LOAN COPY: RETURN TO
AFWL TECHNICAL LIBRARY
KIRTLAND AFB, N.M.

NASA
CR
3263
C.1

TECH LIBRARY KAFB, NM
0062106

NASA Contractor Report 3263

Microwave Remote Sensing of Snowpacks

William H. Stiles and Fawwaz T. Ulaby

CONTRACT NAS5-23777
JUNE 1980

NASA

TECH LIBRARY KAFB, NM
0062106

NASA Contractor Report 3263

Microwave Remote Sensing of Snowpacks

William H. Stiles and Fawwaz T. Ulaby
University of Kansas Center for Research, Inc.
Lawrence, Kansas

Prepared for
Goddard Space Flight Center
under Contract NAS5-23777

National Aeronautics
and Space Administration

**Scientific and Technical
Information Office**

1980

ACKNOWLEDGEMENTS

This investigation was principally supported by NASA/GSFC under contracts and in part by NASA/JSC under contract NAS9-15003. The authors wish to thank the following individuals and their respective organizations for their technical assistance provided in support of the experiment and analysis.

NASA/GSFC
Dr. Albert Rango
Dr. Jim Shiue
Dr. Alfred Chang
Dr. Vincent Salomonson
NASA/ARC
Dr. William Linlor
NASA/LRC
Dr. Lawrence Klein
Eglin AFB
Captain Ted Lane
Resources Consultants, Inc.
Dr. Bruce Jones

Also noted was the guidance provided by Professor R. K. Moore, A. K. Fung and L. F. Dellwig at the University of Kansas and Professor K. R. Carver at New Mexico State University.

The personnel of the Remote Sensing Laboratory experiment team were Mr. Bradford Hanson (leader of the ground truth effort), Mr. D. Brunfeldt, Mr. J. Lyall, Mr. M. Lubben, Mr. K. Scott, Mr. L. Gulley, and Mr. A. Aslam.

TABLE OF CONTENTS

	PAGE
LIST OF FIGURES	v
LIST OF TABLES	xxiii
NOMENCLATURE	xxv
1.0 INTRODUCTION	1
1.1 Significance of Snowpack Hydrology	1
1.2 The Role of Remote Sensing in Snowpack Monitoring	3
1.3 Advantages of Microwave Remote Sensors	6
2.0 DEFINITION OF THE PROBLEM	9
2.1 Target Description	9
2.1.1 Derivation of the backscattering coefficient σ^o equation	12
2.1.2 Derivation of the apparent radiometric temperature T_{ap} equation	13
2.2 Review of Theoretical Models	15
2.3 Statement of the Problem	16
3.0 PHYSICAL PROPERTIES OF SNOW	18
3.1 Snow Characteristics	18
3.2 Snowpack Characteristics	18
3.2.1 Snowpack crystalline structure and grain size	21
3.2.2 Snowpack thermal properties	21
3.2.3 Snowpack optical properties	22
4.0 DIELECTRIC PROPERTIES OF SNOW	26
4.1 Dielectric Properties of Water	26
4.2 Dielectric Properties of Ice	31
4.3 Dielectric Mixing Formulas	41
4.4 Dielectric Properties of Dry Snow	45
4.5 Dielectric Properties of Wet Snow	49
4.6 Attenuation Through Snow	53
4.7 Dielectric Properties of Soils	56
5.0 REVIEW OF MICROWAVE MEASUREMENTS	65
5.1 Reflection Coefficient Measurements	65
5.2 Stratigraphy Measurements	71
5.3 Backscatter Measurements	77

PAGE

5.3.1 Sandia Corporation 77
5.3.2 Ohio State University 77
5.3.3 University of Alaska 77
5.3.4 CRREL 84
5.3.5 Georgia Institute of Technology 84
5.3.6 Rome Air Development Center 84
5.3.7 University of Kansas 94
5.3.8 Airborne and spaceborne observations 94
5.3.9 Summary of active backscatter measurements 97
5.4 Review of Passive Measurements 97
5.4.1 Aerojet General Corporation 99
5.4.2 Helsinki University of Technology 99
5.4.3 University of Berne 106
5.4.4 NASA Goddard 113
5.4.5 ESMR 119
5.4.6 Summary of passive measurements 119
6.0 EXPERIMENT DESCRIPTION 125
6.1 Objectives 125
6.2 Test Site Description 125
6.3 Microwave Sensors 126
6.3.1 MAS 1-8 and MAS 8-18/35 126
6.3.2 Radiometers 136
6.3.2.1 10.69 GHz radiometer 138
6.3.2.2 37 GHz radiometer 140
6.3.2.3 94 GHz radiometer 145
6.4 Ground Truth Instrumentation 149
6.4.1 Snowpack Conditions 150
6.4.1.1 Snow depth and stratification 150
6.4.1.2 Snow density and water equivalent 152
6.4.1.3 Snow wetness 157
6.4.1.3.1 Capacitance measurement of snow wetness 160
6.4.1.3.2 Calorimeter measurement of snow wetness 163
6.4.1.3.3 Comparison of capacitor and calorimeter 169
6.4.1.4 Snow temperature 172
6.4.1.5 Surface roughness 174

PAGE

6.4.1.6 Grain size, shape and texture 174
6.4.2 Soil Conditions 181
6.4.3 Atmospheric Conditions 191
6.5 Data Acquisition 191
6.5.1 Daily Backscatter and Emission Measurements 191
6.5.2 Diurnal Backscatter and Emission Measurements . . . 195
6.5.3 Attenuation Measurements 195
6.5.4 Single Cell Fluctuation Measurement 198
6.5.5 Snowpile Experiment 198
7.0 DATA STATISTICS 201
7.1 Measurement Variability 201
7.1.1 Test Site Spatial Variability 201
7.1.2 Precision of Microwave Measurements 204
7.2 Seasonal Statistics of Active Microwave Data 210
7.3 Seasonal Statistics of Passive Microwave Data 225
7.4 Radar-Radiometer Correlation 226
8.0 MICROWAVE RESPONSE TO SNOWPACK PARAMETERS 238
8.1 Angular Response 238
8.1.1 Active Microwave 238
8.1.2 Response to Roughness 252
8.1.3 Passive Microwave 263
8.1.4 Response to Roughness 266
8.1.5 Summary 266
8.2 Spectral Response 271
8.2.1 Active Microwave 271
8.2.2 Passive Microwave 275
8.2.3 Summary 282
8.3 Diurnal Response 282
8.3.1 Diurnal Experiment on 2/17/77 and 2/18/77 282
8.3.2 Diurnal Experiment on 3/3/77 and 3/4/77 289
8.3.3 Diurnal Experiment on 3/16/77 and 3/17/77 294
8.3.4 Diurnal Experiment on 3/24/77 301
8.3.5 Diurnal Experiment on 3/23/77 308
8.3.6 Summary of Diurnal Response 308
8.4 Response of Snow Wetness 316

PAGE

8.4.1 Active Microwave 316
8.4.2 Passive Microwave 327
8.4.3 Summary 336
8.5 Response to Water Equivalent 336
8.5.1 Active Microwave 338
8.5.2 Passive Microwave 342
8.5.3 Summary 346
8.6 Attenuation of Snow 346
9.0 SIMPLE MODELS FOR SNOWPACK 352
9.1 Active Microwave 352
9.1.1 Proposed Backscattering Coefficient Model 352
9.1.2 Evaluation of the Backscattering Coefficient Model . 355
9.2 Passive Microwave 369
9.2.1 Emissivity Model 369
9.2.2 Evaluation of the Emissivity Model 379
9.3 Summary of Simple Models 383
10.0 CONCLUSIONS AND RECOMMENDATIONS FOR FUTURE EXPERIMENTS 389
10.1 Conclusions 389
10.2 Unanswered Questions 390
10.3 Recommendations for Future Experiments 391
REFERENCES 395

LIST OF FIGURES

		PAGE
Figure 1-1	Satellite-derived snowcover estimates versus measured runoff for the Indus River, 1967-1972	5
Figure 1-2	Partial electromagnetic spectrum showing the percent transmission through the earth's atmosphere and ionosphere	7
Figure 2-1	Snowpack scene configuration	10
Figure 3-1	The meteorological classification of snow crystals according to the scheme of Magono and Lee	19
Figure 3-2	Temperature and humidity conditions for formation of snow crystals in the atmosphere	20
Figure 3-3	Thermal conductivities of snow, sea ice, fresh ice, frozen fine-grained soil, and frozen course-grained soil	23
Figure 3-4	Relationship between snow density and thermal conductivity	24
Figure 3-5	Comparison of calculated and observed reflectance of a nearly fresh snow	25
Figure 4-1	Relative permittivity of water at T = 0°C and T = 20°C using the Debye equation	29
Figure 4-2	Relative permittivity of water at T = 10°C and T = 30°C using the Debye equation	30
Figure 4-3	Rate of attenuation in water	32
Figure 4-4	The loss tangent of ice samples as a function of temperature at a frequency of 10^{10} Hz	34
Figure 4-5	Dielectric properties of ice	35
Figure 4-6	Rate of attenuation in ice as computed using loss tangents	38
Figure 4-7	Attenuation in ice	39
Figure 4-8	Attenuation curve (CP ice)	40

PAGE

Figure 4-9 Attenuation curve (tap-water ice) 40
Figure 4-10 Dielectric properties of dry snow 44
Figure 4-11 Variation of loss tangent of snow with temperature 46
Figure 4-12 A comparison between the rates of attenuation in snow and ice 48
Figure 4-13 Dielectric properties of wet snow 50
Figure 4-14 Effective dielectric constant (a) and loss factor (b) shown as a function of water content for wet snow samples. The data points and theoretical curves are shown 51
Figure 4-15 Effective dielectric constant k'_m and loss factor k''_m versus liquid water content for the glass bead samples 51
Figure 4-16 Dielectric constant of foam rubber with varying wetness 52
Figure 4-17 Skin depth calculated from Linlor's (1975b) data and Sweeney and Colbeck's (1974) data 54
Figure 4-18 Attenuation rates in dB/m for wet snow and pseudo-snow 55
Figure 4-19 Absorption of radiation by snow as a function of temperature 57
Figure 4-20 Microwave beam intensity versus thickness of wet foam polyurethane 60
Figure 4-21 Dielectric properties of soils 62
Figure 4-22 The complex dielectric constant at 10×10^9 Hz as a function of temperature at three water constants 63
Figure 4-23 Skin depth as a function of volumetric water content, frequency, and soil type . . 64
Figure 5-1 The reflection coefficient of a frozen sand surface covered with 10 in. of dry snow 67
Figure 5-2 The reflection coefficient of a frozen sand surface covered with moist snow 68
Figure 5-3 The reflection coefficient of a metallic surface covered with moist snow 69

PAGE

Figure 5-4 The reflection coefficient of a metallic surface covered with 6 in. of dry snow 70

Figure 5-5 The amplitude of reflection coefficient of natural snow surfaces as a function of air temperature at a grazing angle of 2°15' and a frequency of 4 GHz 72

Figure 5-6 Measured reflection signal of snow as a function of temperature at a frequency of 35.26 GHz and an incidence angle of 22.5° 72

Figure 5-7 A comparison of radar and gamma ray determinations of snow depth 73

Figure 5-8a Data record of the snow and ground surfaces, temperature 28°F 74

Figure 5-8b Data record of the snow and ground surfaces, snow melting 74

Figure 5-8c Data record of the snow and ground surfaces, raining 75

Figure 5-9 Profile data for a test site near Pass Lake 76

Figure 5-10 Effects of various depths of melting snow return from one-inch grass at X-band 78

Figure 5-11 Effects of various depths of melting snow return from one-inch grass at Ka-band 78

Figure 5-12 Effects of snow cover upon γ at Ka-band 79

Figure 5-13 Effects of smooth and rough snow covers on a concrete road at Ka-band 79

Figure 5-14 Effects of snow cover upon γ at Ka-band 80

Figure 5-15 Effects of snow cover upon γ at Ka-band 80

Figure 5-16 Effects of snow upon γ at X-band 81

Figure 5-17 Effects of snow upon γ at Ku-band 81

Figure 5-18 Effects of various types of snow cover upon γ at X-band 82

PAGE

Figure 5-19 Effects of various types of snow cover upon γ at Ku-band 82

Figure 5-20 Effects of various types of snow cover upon γ at X-band 83

Figure 5-21 Effects of various types of snow cover upon γ at Ku-band 83

Figure 5-22 Normalized backscatter cross-section for sea ice with varying snow cover, versus angle of incidence 85

Figure 5-23 Normalized backscatter cross-section for frozen ground with wet and dry snow cover, versus angle of incidence . . . 86

Figure 5-24 Typical analog plots of the return from smooth snow at 10 GHz and vertical polarization 87

Figure 5-25 Variation of σ^o as a function of snow temperature at 10 GHz and horizontal polarization 87

Figure 5-26 Radar return from a snow-covered field . . . 88

Figure 5-27 Radar backscatter per unit area from two snow-covered fields as a function of time for 35 GHz and the percent free water present in the top snow layer 89

Figure 5-28 Radar backscatter from snow illustrating the cyclic variations as a function of time 90

Figure 5-29 B-scope display of test area with snow present on the ground 91

Figure 5-30 B-scope display of test area after snow has melted 91

Fgiure 5-31 Angular dependence of σ^o to wet and dry snow at 35 GHz 92

Figure 5-32 Angular dependence of σ^o to wet and dry snow at 98 GHz 92

Figure 5-33 Angular dependence of σ^o to wet and dry snow at 140 GHz 93

Figure 5-34 Angular response of σ^o of short grass and short grass with a 15 cm dry powder snow cover 95

Figure 5-35 Angular response of σ^o of short grass and short grass with a 12 cm wet snow cover 96

PAGE

Figure 5-36 S193 scatterometer as a function of snow depth on January 11, 1974, in Kansas 98

Figure 5-37 Measured dry snow brightness temperatures 100

Figure 5-38 Plate experiment to determine microwave penetration 101

Figure 5-39 Brightness temperature of various depths of snow on a metal plate 102

Figure 5-40 Measured change in brightness temperature with appearance of liquid water 103

Figure 5-41 Measured wet snow brightness temperatures 104

Figure 5-42 Distribution of brightness temperature with area for three types of terrain in the vicinity of South Cascade Glacier, Washington 105

Figure 5-43 Brightness temperatures T_B versus look angle for horizontal (HP) and vertical polarization (VP), April 4, 1978 107

Figure 5-44 Brightness temperature spectral response for a wet snow and a dry snow case 108

Figure 5-45 Brightness temperature versus snow wetness (humidity) 109

Figure 5-46 Diurnal variation of brightness temperature for horizontal (h, open) and vertical (v, block symbols) along with snow wetness (humidity) and refrozen layer thickness (ice) 110

Figure 5-47 Scattering absorption and damping coefficients for dry winter snow 111

Figure 5-48 Scattering, absorption and damping coefficients for dry spring (metamorphosed) snow 112

Figure 5-49 Multispectral data obtained over Bear Lake 115

Fgiure 5-50 Brightness temperature versus snow depth for wet and dry snow 116

PAGE

Figure 5-51 Brightness temperature spectral response to moist snow and frozen ground in Colorado 116

Figure 5-52 Brightness temperature versus snowpile depth 117

Figure 5-53 Brightness temperature of natural snowpack as a function of water equivalent 118

Figure 5-54 Summer melt line in the snow field covering the Greenland continental ice sheet as deduced from Nimbus-5 ESMR data obtained on 21 July 1973 120

Figure 5-55 Snow accumulation and Nimbus-6 ESMR horizontally polarized brightness temperature data (1975-1976) for Williston, North Dakota, U.S.A. 121

Figure 5-56 Snow coverage maps of North America for the period of 15-21 March, 1976 122

Figure 5-57 Nimbus-6 vertically polarized microwave brightness temperature versus water equivalent on the Canadian high plains 123

Figure 6-1 Steamboat Springs test site 127

Figure 6-2 Steamboat Springs test site layout 128

Figure 6-3 Test plot layout 129

Figure 6-4 Closeup of MAS 1-8 RF section 131

Figure 6-5 Closeup of the MAS 8-18/35 RF section 131

Figure 6-6 MAS 8-18 block diagram 132

Figure 6-7 Overall schematic of the 35 GHz radar module 134

Figure 6-8 Functional block diagram of 10.69 GHz radiometer 138

Figure 6-9 Functional block diagram of 37 GHz radiometer 141

Figure 6-10 Calibration curve of 37 GHz H-polarization radiometer 142

Figure 6-11 Calibration curve of 37 GHz V-polarization radiometer 142

Figure 6-12 Functional block diagram, 94 GHz radiometer 146

PAGE

Figure 6-13 Calibration curve of the 94 GHz radiometer 147

Figure 6-14 Snow depth measurement 151

Figure 6-15 Ground truth data acquisition sheet 153

Figure 6-16 Snow stratification profiles were measured. This photograph shows three distinct layers 154

Figure 6-17a The profile view (Feb. 23, 1977) illustrates snowpack stratification 155

Figure 6-17b The boundaries for the layers determined using the methods of section 6 155

Figure 6-18 A given volume of snow was removed from each snow interval with an aluminum cylinder of known volume (500 cc) and placed in a pan. The pan, snow and cylinder were transported to the balance and weighed. The data were then recorded for the appropriate date and time 156

Figure 6-19 The ground truth enclosure is pictured with a cold storage box 156

Figure 6-20 The Mount Rose snow tube was used periodically to measure snow water equivalent 158

Figure 6-21 The split-barrel sampler is a 3-inch PVC tube 4 feet in length which had the lower 3 feet split lengthwise to facilitate viewing of the core 158

Figure 6-22 Comparison of snow wetness measured by various instruments at South Cascade Glacier, Washington 159

Figure 6-23 Dependence of dielectric constant on wetness 161

Figure 6-24 Quality factor of snow capacitor versus wetness 161

Figure 6-25 Dependence of dielectric constant on frequency 161

Figure 6-26 Capacitor Sampling Procedure 162

PAGE

Figure 6-27 The freezing calorimeter, used for measuring the amount of free water present in a sample of snow, consists of a thermos bottle with a thermocouple probe inserted through the lid and extending down into the central cavity of the thermos 164

Figure 6-28 The temperatures of the solution were recorded using a digital thermometer, and the weights of snow and toluene were measured 164

Figure 6-29 Sample data sheet for the freezing calorimeter measurements 166

Figure 6-30 Correlation of the capacitor and calorimetric indices 170

Figure 6-31 A digital thermometer (Doric Trendicator 400, Type T/°C) was used to measure temperature 173

Figure 6-32 Temperature was also measured at 10 cm intervals using thermistors encased in PVC tubing 173

Figure 6-33 The lack of wind resulted in a flat essentially featureless surface (2/27/77). 175

Figure 6-34 Significant surface perturbations were often the result of warm days followed by freezing nights (2/20/77). 175

Figure 6-35 Strong southerly winds caused local drifting and created wind slabbing on the snow surface (3/12/77). 176

Figure 6-36 Surface roughness was determined for two directions, one perpendicular and one parallel to the predominant wind direction. The grid shows one inch divisions. 176

Figure 6-37 Leitz (Model 350) microscope and Fiber Optic light source 177

Figure 6-38 Dendritic snow crystal (P1e) observed from snowfall on 2/24/77 178

Figure 6-39 Stellar snow crystal (P2b) observed from snowfall on 2/28/77 178

PAGE

Figure 6-40 Capped column (CP1a) observed in snowfall on 2/24/77. 179

Figure 6-41 Combination of bullets (C2a) found in snowfall on 2/24/77. 179

Figure 6-42 Stellar snow crystal with light riming (R1d) found in snowfall on 3/2/77 180

Figure 6-43 Very heavily rimed graupel-like snow (R3) observed in snowfall on 2/28/77 180

Figure 6-44 The start of the destructive metamorphism process. Photographed on 2/13/77 182

Figure 6-45 Advanced destructive metamorphism in the surface layer on 2/28/77 182

Figure 6-46 Fused ice particles composing a hard snow crust on 2/15/79. 183

Figure 6-47 Surface hoar crystal photographed on 2/15/79. 183

Figure 6-48 Example of a thin surface ice layer (firn mirror) photographed on 2/21/77. 184

Figure 6-49 One corner of a hexagonal shaped depth hoar crystal on 2/17/77 184

Figure 6-50 Remnants of a depth hoar crystal altered by descructive metamorphism. Photographed on 2/21/78 185

Figure 6-51 Snow Particle Sizes (mm) 186

Figure 6-52 Layer 1 depth hoar crystals on 3/24/77 187

Figure 6-53 Layer 2 small depth hoar crystals on 3/24/77 187

Figure 6-54 Layer 3 old metamorphosed snow on 3/24/77 188

Figure 6-55 Layer 4 old snow on 3/24/77 188

Figure 6-56 Layer 5 old snow on 3/24/77 189

Figure 6-57 Layer 7 old snow on 3/24/77 189

Figure 6-58 Layer 9 old snow on 3/24/77 190

PAGE

Figure 6-59 A three channel Meteorgraph, model M701 recorded atmospheric temperature, relative humidity and atmospheric pressure. This weather station was located between the test plots as illustrated in Figure 6-3 192

Figure 6-60 Two pyranometers were mounted back-to-back to measure incident and reflected solar radiation 192

Figure 6-61 Experiment timetable showing data acquisition periods of the various sensors 193

Figure 6-62 Diagram illustrating the attenuation measurement procedure 196

Figure 6-63 Attenuation measurement 197

Figure 6-64 Diagram illustrating the procedure used to measure the attenuation of the snow at 35.6 GHz as a function of layer thickness (t). 199

Figure 6-65 MAS 8-18/35 and radiometers during one of the snowpile experiments 200

Figure 7-1 Spatial variability of snow depth and density at test site. 203

Figure 7-2 Spatial variability of microwave radiometric temperatures 206

Figure 7-3 Spatial variability of received backscatter power at two frequencies and angles. 208

Figure 7-4 Seasonal average σ^o spectral response at 0° (nadir) and regression equations along with the 5% and 95% limits 211

Figure 7-5 Seasonal average σ^o spectral response at 20° angle of incidence and regression equations along with the 5% and 95% limits 212

Figure 7-6 Seasonal average of σ^o response at 50° angle of incidence and regression equations along with the 5% and 95% limits 213

Figure 7-7 Correlation coefficients between σ^o_{HH} at 1.2 GHz and σ^o_{HH} at other frequencies at 0°, 20° and 50°. 215

Figure 7-8 Correlation coefficients between σ^o_{HH} at 35.6 GHz and σ^o_{HH} at other frequencies at 0°, 20° and 50°. 216

PAGE

Figure 7-9a Histogram of σ^{o}_{HH} at 1.2 GHz and 0° angle of incidence. The number of data sets within each bin is on the horizontal axis. 217

Figure 7-9b Histogram of σ^{o}_{HH} at 8.6 GHz and 0° angle of incidence 218

Figure 7-9c Histogram of σ^{o}_{HH} at 17.0 GHz and 0° angle of incidence 219

Figure 7-9d Histogram of σ^{o}_{HH} at 35.6 GHz and 0° angle of incidence 220

Figure 7-10a Histogram of σ^{o}_{HH} at 1.2 GHz and 50° angle of incidence. 221

Figure 7-10b Histogram of σ^{o}_{HH} at 8.6 GHz and 50° angle of incidence. 222

Figure 7-10c Histogram of σ^{o}_{HH} at 17.0 GHz and 50° angle of incidence. 223

Figure 7-10d Histogram of σ^{o}_{HH} at 35.6 GHz and 50° angle of incidence. 224

Figure 7-11 Seasonal average of T_{ap} and 5% and 95% confidence limits at a) 10.69 GHz and b) 37 GHz. 226

Figure 7-12 Histograms of the T_{ap} measurements in Steamboat Springs at 0° angle of incidence and (a) 10.69 GHz, H-polarization; (b) 37 GHz, H-polarization; and (c) 37 GHz, V-polarization. 227-229

Figure 7-13 Histograms of the T_{ap} measurements in Steamboat Springs at 20° angle of incidence and (a) 10.69 GHz, H-polarization; (b) 37 GHz, H-polarization; and (c) 37 GHz, V-polarization. 230-232

Figure 7-14 Histograms of the T_{ap} measurements in Steamboat Springs at 50° angle of incidence and (a) 10.69 GHz, H-polarization; (b) 37 GHz, H-polarization; and (c) 37 GHz, V-polarization. 233-235

Figure 8-1a Angular Response of σ^{o} at 2.6 GHz to Wet and Dry Snow 239

Figure 8-1b Angular Response of σ^{o} at 8.6 GHz to Wet and Dry Snow 240

PAGE

Figure 8-1c Angular Response of σ^o at 17.0 GHz to Wet and Dry Snow 241

Figure 8-1d Angular Response of σ^o at 45.6 GHz to Wet and Dry Snow 242

Figure 8-2 Path Loss Through 27 sm Snow Depth 243

Figure 8-3 Variation in the angular response of σ^o for several data sets to nearly dry snow over two daytime periods at (a) 2.6 GHz, (b) 7.6 GHz, (c) 17.0 GHz and (d) 35.6 GHz 245, 246

Figure 8-4 Variation in the angular response of σ^o for several data sets with varying wetness over two days of a 26 cm snow layer at (a) 2.6 GHz and (b) 7.6 GHz 247

Figure 8-5 Variation in the angular response of σ^o for several data sets with varying wetness of a 45 cm snow layer at (a) 2.6 GHz and (b) 7.6 GHz . . . 248

Figure 8-6 Polarization and angular response of σ^o at 2.6 GHz to an (a) dry snow condition and (b) wet snow condition 249

Figure 8-7 Polarization and angular response of σ^o to an (a) dry snow condition, linear polarization, (b) wet snow condition, linear polarization, (c) dry snow condition, circular polarization, and (d) wet snow condition, circular polarization 250, 251

Figure 8-8 Snow surface structure (a) regular snow surface, (b) wind generated snow surface 253

Figure 8-9 Effect of surface roughness on σ^o of dry snow at (a) 2.6 GHz, (b) 7.6 GHz, (c) 13.0 GHz, (d) 17.0 GHz, and (e) 35.6 GHz 254-256

Figure 8-10 Effect of surface roughness on σ^o of wet snow at (a) 2.6 GHz, (b) 7.6 GHz, (c) 13.0 GHz, (d) 17.0 GHz, and (e) 35.6 GHz 258-260

Figure 8-11 The effect of varying roughness of wet snow, (a) smooth surface, (b) rough surface, (c) very rough surface, (d) σ^o response at 8.6 GHz, and (e) σ^o response at 17.0 GHz 261, 262

PAGE

Figure 8-12 Angular response of T_{ap} at (a) 10.69 GHz, and (b) 37 GHz to wet and dry snow on 2/21/77 264

Figure 8-13 Angular response of T_{ap} at (a) 10.69 GHz and (b) 37 GHz to wet and dry snow on 2/24 and 2/25/77 . . 265

Figure 8-14 Variation in the angular response of T_{ap} for several data sets to nearly dry snow over two daytime periods at (a) 10.69 GHz and (b) 37 GHz. 267

Figure 8-15 Time variation of the angular response of T_{ap} over the snow melt (a) and (b) and snow freeze (c) and (d) cycles. 268, 269

Figure 8-16 The effect of surface roughness on T_{ap} of (a) dry snow and (b) wet snow at 10.69 GHz. 270

Figure 8-17a Spectral response of σ^o at 0° (nadir) to wet and dry snow 272

Figure 8-17b Spectral response of σ^o at 20° Angle of Incidence to Wet and Dry Snow. 273

Figure 8-17c Spectral Response of σ^o at 50° Angle of Incidence to Wet and Dry Snow. 274

Figure 8-18a Spectral response of σ^o at 20° angle of incidence for HH and HV polarizations 276

Figure 8-18b Spectral response of σ^o at 50° angle of incidence for HH and HV polarizations 277

Figure 8-19a Depolarization Ratio of σ^o at 20° Angle of Incidence to Wet and Dry Snow. 278

Figure 8-19b Depolarization Ratio of σ^o at 50° Angle of Incidence to Wet and Dry Snow. 279

Figure 8-20a Spectral Response of T_{ap} at 50° Angle of Incidence to Wet and Dry Snow 280

Figure 8-20b Spectral Response of ε at 50° Angle of Incidence to Wet and Dry Snow 281

PAGE

Figure 8-21 Diurnal variation of the supportive ground truth data on 2/17 - 2/18/77. m_v is the volumetric snow wetness of the top 5 cm layer 284

Figure 8-22a Diurnal variation of σ^o at 8.6 and 35.6 GHz at 5° angle of incidence 286

Figure 8-22b Diurnal variation of σ^o at 8.6 and 35.6 GHz at 25° angle of incidence 287

Figure 8-22c Diurnal variation of snow wetness and σ^o at 8.6 and 35.6 GHz. (Note that snow wetness scale has been reversed for each of comparison of σ^o.) 288

Figure 8-23a Diurnal variation of T_{ap} at 10.69 and 37 GHz at 5° angle of incidence . . . 290

Figure 8-23b Diurnal variation of T_{ap} at 10.69 and 37 GHz at 25° angle of incidence . . . 291

Figure 8-23c Diurnal variation of snow wetness and T_{ap} at 10.69 and 37.0 GHz 292

Figure 8-24 Diurnal Variation of Ground Truth Data on 3/3 - 3/4/77. m_v is Volumetric Snow Wetness of the Top 5 cm Snow Layer 293

Figure 8-25a Diurnal variation of σ^o between 1 and 35 GHz at 0° (nadir) 295

Figure 8-25b Diurnal Variation of Snow Wetness and σ^o Between 1 and 35 GHz at 20° Angle of Incidence. 296

Figure 8-25c Diurnal Variation of Snow Wetness and σ^o Between 1 and 35 GHz at 50° Angle of Incidence. 297

Figure 8-26a Diurnal Variation of T_{ap} at 10.69 and 37 GHz at 0° (nadir). 298

Figure 8-26b Diurnal Variation of Snow Wetness and T_{ap} at 20° Angle of Incidence 299

Figure 8-26c Diurnal Variation of Snow Wetness and T_{ap} at 50° Angle of Incidence 300

Figure 8-27 Diurnal variation of ground truth data on 3/16 - 3/17/77. m_v is volumetric snow wetness of the top 5 cm layer. 302

PAGE

Figure 8-28a Diurnal variation of snow wetness and σ^o at 2.6, 4.6, and 7.6 GHz at 50° angle of incidence. 303

Figure 8-28b Diurnal variation of snow wetness and σ^o at 8.6, 13.0, 17.0 and 35.6 GHz at 50° angle of incidence 304

Figure 8-28c Diurnal variation of snow wetness and the circular polarized σ^o values at 35.6 GHz and the depolarization ratio ($\sigma^o_{RR}/\sigma^o_{RL}$) at 50° angle of incidence. 305

Figure 8-29 Diurnal variation of T_{ap} at 10.69 GHz at 50° angle of incidence . . . 306

Figure 8-30 Diurnal variation of ground truth data on 3/24/77. m_v is the volumetric snow wetness of the top 5 cm layer 307

Figure 8-31 Diurnal variation of σ^o at 8.6, 17.0 and 35.6 GHz at 50° angle of incidence 309

Figure 8-32 Diurnal variation of T_{ap} at 10.69, 37 and 94 GHz at 50° angle of incidence. 310

Figure 8-33 Snow wetness and temperature variation over the measurement period of the diurnal experiment on 3/23/77 311

Figure 8-34a Time variation of 50° backscatter power at 8.6, 17.0, and 35.6 GHz 312

Figure 8-34b Time variation of 70° backscatter power at 8.6, 17.0, and 35.6 GHz 313

Figure 8-35a Time variation of the 50° radiometric temperature at 10.69, 37 and 94 GHz. 314

Figure 8-35b Time variaton of the 70° radiometric temperature at 10.69, 37 and 94 GHz. 315

Figure 8-36 Magnitude of the σ^o diurnal responses versus the magnitude of the snow wetness response 318

Figure 8-37 Diurnal Response and Hysteresis Effect of σ^o at 8.6 GHz and 55° Angle of Incidence 320

PAGE

Figure 8-38 Diurnal Response and Hysteresis Effect of σ^o at 35.6 GHz and 55° Angle of Incidence. 321

Figure 8-39 Diurnal response and hysteresis effect of σ^o at 8.6 GHz and 50° angle of incidence. 323

Figure 8-40 Diurnal response and hysteresis effect of σ^o at 35/6 GHz and 50° angle of incidence. 324

Figure 8-41 σ^o Response to m_v at 50° Angle of Incidence on 3/16 - 3/17/77. 325

Figure 8-42 Correlation Coefficient and Sensitivity of σ^o to m_v at 50° Angle of Incidence on 3/16 - 3/17/77. . . . 326

Figure 8-43 Correlation coefficient and sensitivity of σ^o and m_v at 0°, 20° and 50° angles of incidence over the measurement period 328

Figure 8-44 Magnitude of the T_{ap} diurnal response versus the magnitude of the snow wetness response. 330

Figure 8-45 Diurnal Response and Hysteresis Effect of T_{ap} at 10.7 GHz and 55° Angle of Incidence. 332

Figure 8-46 Diurnal Response and Hysteresis Effect of T_{ap} at 37 GHz and 55° Angle of Incidence. 333

Figure 8-47 Hysteresis effect of T_{ap} at 10.69 GHz and 50° angle of incidence. . . . 334

Figure 8-48 T_{ap} Response to m_v at 50° Angle of Incidence. 335

Figure 8-49 Scattering Coefficient Response to Snow Water Equivalent at 9 GHz 340

Figure 8-50 Scattering coefficient response to snow water equivalent at 16.6 GHz. . . . 341

Figure 8-51 Radiometric apparent temperature response to snow water equivalent at 10.69 GHz. 343

Figure 8-52 Radiometric apparent temperature response to snow water equivalent at 37 GHz 344

PAGE

Figure 8-53 Radiometric apparent temperature response to snow water equivalent at 94 GHz. 345

Figure 8-54 Dynamic range of snow attenuation values at 2.125 GHz. 347

Figure 8-55 Dynamic range of snow attenuation values at 5.125 GHz. 348

Figure 8-56 Dynamic range of snow attenuation values at 13.8 GHz 349

Figure 8-57 Dynamic range of snow attenuation values at 17.0 GHz 350

Figure 8-58 Measured path loss as a function of snow thickness for three snow conditions 351

Figure 9-1 Snowpile Spectral Response 357

Figure 9-2 Scattering coefficient model applied to two diurnal data groups at 8.6 GHz. . . . 360

Figure 9-3 Scattering coefficient model applied to two diurnal data groups at 17.0 GHz . . . 361

Figure 9-4 Scattering coefficient model and observed σ^{o} value comparison over the experiment duration at 8.6 GHz and 50^{o} angle of incidence 362

Figure 9-5 Scattering coefficient model and observed σ^{o} value comparison over the experiment duration at 17.0 GHz and 50^{o} angle of incidence 363

Figure 9-6 Sensitivity of σ^{o} of deep snow to snow wetness 365

Figure 9-7 Spectral response of the σ^{o} model to snow wetness 365

Figure 9-8 Sensitivity of σ^{o} model to water equivalent and snow wetness for (a) frozen ground at 17.0 GHz, (b) thawed ground at 17.0 GHz, (c) frozen ground at 8.6 GHz, and (d) thawed ground at 8.6 GHz 366

Figure 9-9 Scattering coefficient model and observed σ^{o} value comparison at 8.6 GHz and 20 angle of incidence 367

PAGE

Figure 9-10 Scattering coefficient model and observed σ^o value comparison at 17.0 GHz and 20 angle of incidence 368

Figure 9-11 Scattering coefficient model applied to two diurnal data groups at 8.6 GHz 370

Figure 9-12 Scattering coefficient model applied to two diurnal data groups at 17.0 GHz 371

Figure 9-13 Scattering coefficient model and observed σ^o values over the experiment duration at 8.6 GHz and 50^o angle of incidence 372

Figure 9-14 Scattering coefficient model and observed σ^o values over the experiment duration at 17.0 GHz and 50^o angle of incidence 373

Figure 9-15 Scattering coefficient model and observed σ^o values over the experiment duration at 8.6 GHz and 20^o angle of incidence 374

Figure 9-16 Scattering coefficient model and observed σ^o values over the experiment duration at 17.0 GHz and 20^o angle of incidence 375

Figure 9-17 Sensitivity of σ^o to snow wetness 376

Figure 9-18 Sensitivity of σ^o to water equivalent and snow wetness 377

Figure 9-19 Measured radiometric emissivity reponse to dry snow water equivalent at 10.69 GHz, 37 GHz, and 94 GHz 381

Figure 9-20 Emissivity model (x273.2) and observed apparent temperature comparison at 10.69 GHz 384

Figure 9-21 Emissivity model (x273.2) and observed apparent temperature comparison at 37 GHz . 385

Figure 9-22 Sensitivity of T_{ap} model to water equivalent and wetness at 37 GHz for (a) frozen ground and (b) thawed ground 386

LIST OF TABLES

		PAGE
Table 4-1.	Relaxation Frequency of Water	28
Table 4-2.	Relative Dielectric Constants of Ice	36
Table 4-3.	Millimeter Wave Dielectric Constants of Ice	37
Table 4-4.	Mixing Formulas	42,43
Table 4-5.	Dielectric Constant of Dry Snow	47
Table 4-6.	Loss Caused by Snow and Ice	58
Table 4-7.	Loss Measurements at 35 and 95 GHz	59
Table 5-1.	Summary of Active and Passive Microwave Measurement Programs of Snow	66
Table 5-2.	Observed Brightness Temperatures, in Kelvins	114
Table 6-1.	MAS 1-8 and MAS 8-18/35 Nominal System Specifications	130
Table 6-2.	Radiometer Specifications	137
Table 6-3.	Capacitor Calibration Constants	171
Table 6-4.	Data Base of 1977 Snow Experiment at Steamboat Springs, Colorado	194
Table 7-1.	Mean snowpack depth and standard deviation based on N samples acquired along the perimeter of the test plot as indicated in Figure 7-1	202
Table 7-2.	Mean snowpack water equivalent and standard deviation	205
Table 7-3.	Scatterometer measurement variation with spatial position	209
Table 7-4.	HH Polarized Scattering Coefficient Correlation Matrix	214
Table 7-5.	Correlation Coefficients Between the T_{ap}'s	236
Table 7-6.	Correlation Coefficients Between T_{ap} and the σ^o Closest in Frequency	237

PAGE

Table 8-1. Summary of Microwave and Ground Truth Diurnal Acquisitions 283

Table 8-2. Magnitudes of $\Delta\sigma^{o}$ (dB) in response to the peak snow wetness variations observed during the diurnal experiments . . 317

Table 8-3. Magnitudes of ΔT_{ap} in response to the peak snow wetness variations observed during the diurnal experiments 329

Table 8-4. Summary of the Snowpile Experiment Conditions 337

Table 8-5. Ground Truth for Snowpile Experiments . . . 339

Table 9-1. Coefficients for the Emissivity model applied to dry snowpile data 382

Table 9-2. Coefficients for the Scattering Coefficient Model 387

Table 10-1. Desired Range of Parameters for Determining Dielectric Properties of Snow 392

Table 10-2. Ground Truth Parameters 393

NOMENCLATURE

A_{ill}	Illuminated Area, m^2
B_{bb}	Brightness of a blackbody, J/m^2
c	Velocity of propagation, m/sec
C	Capacitance, farads
C_{tf}	Specific heat of toluene at T_f, cal/g/°C
C_{sf}	Specific heat of ice at T_f, cal/g/°C
C_{ti}	Specific heat of toluene at T_i, cal/g/°C
C_s	Specific heat of ice at T_s, cal/g/°C
ΔC	Change in capacitance with freezing of the snow capacitor
D	Skin depth (field), cm
d	Snow depth, cm
dA	Incremental element of illuminated area, m^2
F	Form number
f	Frequency, Hz
f_o	Relaxation frequency, Hz
f_{IF}	Intermediate frequency, Hz
f_m	Modulation frequency, Hz
Δf	Bandwidth, Hz
G_t	Transmit antenna gain
G_r	Receive antenna gain
H_i	Initial heat content of the calorimeter, cal
H_f	Final heat content of the calorimeter, cal
K	Boltzmann's constant = 1.38×10^{-16} erg/K

k	Complex permittivity, farad/m
k_r	Relative complex permittivity or complex dielectric constant
k_o	Free space permittivity = 8.85×10^{-12} farad/m
k'_r	Real part of the dielectric constant
k''_r	Imaginary part of the dielectric constant
k_s	Relative dielectric constant of snow
k_i	Relative dielectric constant of ice
k_w	Relative dielectric constant of water
k_∞	Optical limit of the dielectric constant
k_{dc}	Static limit of the dielectric constant
L_d	Loss, dB
L_f	Latent heat of fusion of water, 79.7 cal/g
m_v	Snow wetness, percent liquid water by volume
m_s	Soil moisture, percent liquid water by volume
m_{vc}	Snow wetness of the capacitor snow sample, percent by volume
m_w	Snow wetness of the calorimeter snow sample, percent by volume
n	Refractive index
P_r	Received power, watts
P_t	Transmitted power, watts
P_{bb}	Power received from a blackbody, watts
$P(z)$	Pressure profile, mm Hg
Q	Quality factor of the snow capacitor
R	Power reflection coefficient
R_t	Range to target, m
R_c	Range to calibration target, m
S_f	Sensitivity of σ^o to angle of incidence at frequency f, dB/degree

T, T_{phys}	Physical temperature, K
T_B	Brightness temperature, K
T_{ap}	Apparent radiometric temperature of a target, K
T_{sc}	Scattered temperature, K, representing the downward emitted sky radiation scattered by the target in the direction of the antenna
T_{sky}	Downward emitted sky radiation, K
T_g	Ground (soil) contribution to T_B, K
T_s	Snow self-emission contribution to T_B, K
T_{se}	Snow self-emission of a thin layer, K
T_i	Initial temperature of toluene, °C
T_f	Final equilibrium temperature, °C
T_s	Snow sample temperature, °C
T_{air}	Sky physical temperature, K
T_{case}	Ambient temperature of the 94 GHz radiometer case, °C
T_H, T_V	Polarized apparent radiometric temperature for the 37 GHz radiometer, K
$T(z)$	Physical temperature profile, K
$\tan \delta$	Loss tangent
ΔT	Measurement accuracy of the 94 GHz radiometer, K
V_{td}, V_{cd}	Voltage at the mixer output from the delay line, volts
V_t	Voltage at the mixer output from a target, volts
V_c	Voltage at the mixer output from the calibration target, volts
V_H, V_V	Voltage output of the 37 GHz radiometer, volts
V_{94}	Voltage output of the 94 GHz radiometer, volts
W	Snow water equivalent, cm
W_{eff}	Effective water equivalent, cm
W_i	Weight of toluene, g

W_s	Weight of wet snow, g
W_f	Weight of free water in the snow, g
W_d	Weight of dry snow, g
α	Cole-cole distribution parameter
α_a	Attenuation constant (field), nepers/cm
$\gamma_{ij}(\theta,\theta_s)$	Differential bistatic scattering coefficients where i and j are polarization indices
γ_1	Damping coefficient, dB/m
γ_2	Damping coefficient, dB/m
γ_a	Absorption coefficient, dB/m
γ_s	Scattering coefficient, dB/m
$\Gamma_{H_2O}(z)$	Loss due to water vapor absorption, dB/km
$\Gamma_{ox}(z)$	Loss due to oxygen absorption, dB/km
Γ	Total atmospheric attenuation at zenith, dB
$\varepsilon,\varepsilon_1\ (\theta)$	Emissivity
θ	Angle of incidence, relative to nadir, degrees
θ'	Angle of propagation, relative to nadir, degrees
θ_s	Angle of scattered radiation, degrees
κ_e	Snow extinction coefficient (power), nepers/cm
κ_a	Snow absorption coefficient (power), nepers/cm
κ_s	Snow scattering coefficient (power), nepers/cm
κ_{eff}	Effective extinction coefficient, nepers/cm
κ_a'	Snow mass absorption coefficient (power), nepers/(cmW)
κ_s'	Snow mass scattering coefficient (power), nepers/(cmW)
κ_e'	Snow mass extinction coefficient (power), nepers/(cmW)
κ_{ao}	Dry snow mass absorption coefficient (power), nepers/cm
κ_{so}	Dry snow mass scattering coefficient (power), nepers/cm
κ_{eo}	Dry snow mass extinction coefficient (power), nepers/cm

λ	Wavelength, cm
μ	Magnetic permeability, henry/m
μ_r	Relative permeability
μ_o	Free space permeability = $4\pi \times 10^{-7}$ henry/m
ρ	Snow density, g/cm^3
ρ_s	Snow density of the capacitor sample, g/cm^3
$\rho(z)$	Water vapor density profile, g/cm^3
σ^o	Scattering cross-section per unit area (backscattering coefficient), expressed in dB
$\sigma^o_{ii}(\theta,\theta_s)$	Bistatic scattering coefficient
σ^o_{gnd}	Scattering coefficient of the ground
σ^o_{snow}	Scattering coefficient of the snow
σ^o_s	Saturation scattering coefficient of deep snow
σ^o_{sat}	Saturation scattering coefficient on infinite layer of dry snow
σ_i	Ionic conductivity, mho/m
τ_{sa}	Snow-air power transmission coefficient
τ_{gs}	Ground-snow power transmission coefficient
τ	Relaxation time of a dipole, seconds
Ω	Solid angle, sr
τ_d	Optical depth, nepers

1.0 INTRODUCTION

1.1 Significance of Snowpack Hydrology

Snowpack water is the major component of the total water supply for the western United States, Alaska, and many other parts of the world. Since the runoff from snow melt is usually limited to the spring and early summer, conservation of this water is very important. Accurate prediction of runoff is therefore needed on a seasonal, monthly, weekly, and daily basis for flood control, hydroelectric power generation, irrigation, domestic and industrial water supplies, and recreation.

It has been estimated that more than 50 percent of the stream-flow in the western United States results from snow melt (Rooney, 1969; Committee on Polar Research, 1970). In the Colorado River Basin, 75 percent of the runoff is the product of snowpack depletion (U.S. Department of Interior, 1970). In the Pacific Northwest, 80 percent of all electric power is the consequence of hydroelectric generation (Limpert, 1975). Flood damage during the spring thaw has over the years caused many millions of dollars worth of damage. The above are some specific examples illustrating the magnitude of the importance of conservation of water resources resulting from snowpack melt.

A NASA-sponsored Hydrology Panel of the National Academy of Sciences (1969) stated:

> "The changing extent, surface temperature, thickness, water equivalent, and liquid-water content of seasonal snowpack are necessary for engineering design and operation and planning of water projects large and small. In the mountainous areas of the United States, millions of dollars are spent each year at fixed locations to measure snowpack for forecast purposes. Improved forecasts are estimated to be worth 10^7 to 10^8 dollars per year to water users in the western United States alone."

Therefore, investigations into improved methods of estimating snowpack parameters may, in addition to the basic knowledge gained, provide substantial economic dividends. Also, in the face of ever-increasing demands on water supply, the savings may eventually be much greater than the above estimates.

Correct decisions concerning the use of available water supplies can result in large benefits, while incorrect decisions or insufficient data to allow correct decisions may cause substantial losses. As an example, in California, the cost of steam generated electric power was approximately four times that of hydroelectric power (Brown, 1974). This estimate

is surely much higher today with the drastic rise in fuel costs. Therefore, conservation of the water from snow melt can result in large economic savings. Accurate forecasts of water available for irrigation, several months in advance, could save agricultural areas considerable money through advance planning for acreage and types of crops which could be planted, based on the crop water demands. Knowledge of water storage in snowpacks can help the various stream regulation authorities keep reservoir levels as high as possible and still retain optimum flood control capabilities. In addition, with the growing concern for the ecology, better information on water supply may allow more efficient use of existing water control projects and lessen the need for future construction.

As recently as a few years ago, the only inputs to runoff models and water supply forecasts from snow melt consisted of water equivalent (depth of melted snowpack per unit area) measurements at strategically selected points along widely spaced snow courses. After many years of collecting data, statistical relationships are determined to relate the measured water equivalents to expected runoff. These data supply an "index" for forecasting the runoff. The prediction of runoff includes other factors, such as past cumulative runoff and prediction of future precipitation from a "historic normal" of preceding years.

The Soil Conservation Service has traditionally prepared only seasonal runoff forecasts for the western United States. The average error of forecasts prepared on April 1 is 18 percent (U.S. Department of the Interior, 1974). These errors are a result of both post-prediction weather variations and the uncertainty in snow course indices. Prediction has been most accurate when snowpack accumulation was nearest the historic average.

There are many drawbacks in addition to the inherent inaccuracy of the small sample size in using the snow course method of obtaining data for input to runoff models. It would be desirable to increase the snow course sample density for more accurate predictions. Labor costs, however, would make this action prohibitively expensive. Another disadvantage of the present method of snow sampling is the long time-lag between data acquisition and incorporation into the model. Some snow courses are of necessity located in avalanche areas and are therefore very dangerous. Relatively recent developments involving the use of remote snow "pillows" or profiling gauges and satellite telemetry allow remote measurements of water equivalent

(Brown, 1974) and can potentially alleviate the danger of physical sampling in some areas. Even these remote station installations are subject to vandalism and alteration as a result of the presence of people. Expense of these installations limits the number which can be deployed. Also, there is growing pressure to enhance wilderness areas and these remote stations would be an encroachment. The ecological considerations are a major problem in data acquisition since, for example, almost 50 percent of California's snowpack lies within wilderness areas.

The disadvantages of the above methods were evaluated by a NASA survey on space applications (1967):

> "Too few data points are normally available to make reliable estimates of snow cover of watersheds. Methods to monitor vast areas on a periodic basis are required. An airborne or spaceborne sensor that could map synoptically the water content or thickness of snow would be immensely valuable."

Remote sensing methods have the potential of monitoring the required large areas on a periodic basis. The following section examines the usefulness of different types of remote sensors to snowpack monitoring.

1.2 The Role of Remote Sensing in Snowpack Monitoring

Sensors operating in the visible, infrared, thermal infrared, microwave and gamma ray bands have been employed in experiments to examine their potential for remote sensing snowpack properties. The relative effectiveness of the different spectral bands is governed by several factors. The levels of understanding of the different interaction mechanisms are diverse. In addition, the interactions of the electromagnetic radiation of different wavelengths and the snowpack are determined by different characteristics of the snowpack. Also, the volume of past research is largely dependent upon the availability of sensors and access to the data obtained with these sensors. The acquisition time span and dissemination time spans are also important. The participants at the Workshop on the Operational Applications of Satellite Snowcover Observations held in 1975 at South Lake Tahoe, California, stated that reliable snowpack information was required within 72 hours to be relevant (Rango, 1975).

The visible band of the electromagnetic spectrum was the first to be employed in remote sensing of snowpack parameters. Aerial snow surveys have been conducted for many years to supplement snow course data in inaccessible areas. Snow depth is determined by observation or photo-

graphy of calibrated poles. Measurements of areal extent of snow cover from low resolution TIROS, ESSA and ITOS satellite imagery (Fritz, 1962; Barnes and Bowley, 1968a, 1968b) have demonstrated the feasibility of satellite mapping of snow extent. The higher resolution imagery of the Landsat satellite has allowed more accurate determination of the position of snow line and hence areal extent (Meier, 1975). Rango and Salomonson (1975) showed a linear relationship between percent areal coverage at the start of the snow depletion cycle and the seasonal runoff from several watersheds in Pakistan and in Wyoming. Figure 1-1 illustrates the relationship for the Indus River over a period of six years. The use of Landsat imagery for water content estimation versus snow course information has been shown to be cost-effective as an input to runoff models (Sharp, 1975); for a given budget, the accuracy using Landsat imagery and suitable statistical sampling yielded much better precision than the snow course method. The actual method of water content estimation is based on multiple looks over time of the snow areal extent. Visible band remote sensing does have limitations, however; effectively only surface information is available because the penetration depth is very small. Snow depth, density or water equivalent therefore must be estimated. Also, the radiances of snow and some types of clouds are similar and separation is sometimes difficult (Meier, 1975). Since some mountainous areas are clouded a large part of the time, multiple looks may be required to obtain cloud-free images. Another limitation is the dependence on solar radiation.

Thermal infrared devices have been shown to be sensitive to surface temperature, and therefore serve as indicators of surface melting conditions of snowpacks (Barnes and Bowley, 1972). The motivation for this technique is the variation in ambient temperature of melting snow (0°C) to the ambient temperature of snow-free areas which are usually not at 0°C. These sensors have the advantage over visible and near infrared sensors in that solar illumination is not required; however, the spatial resolution of operational thermal infrared sensors is inferior to that of Landsat's visible sensors.

Attenuation by snow cover of the natural emission of gamma rays of the underlying rock can be used to measure snow water equivalent (Peck, et al., 1971; Grasty, et al., 1974). The device utilized is a scintillometer which counts gamma photons. Water equivalent is

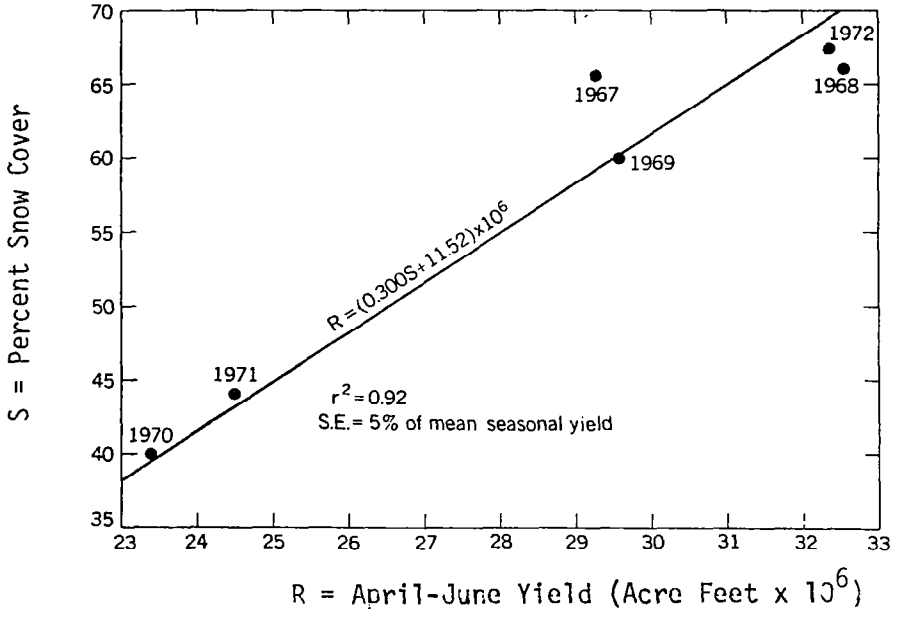


Figure 1-1 Satellite-derived snowcover estimates versus measured runoff for the Indus River, 1967-1972. (Rango and Salomonson, 1975)

calculated from pre-snow radiation levels ratioed to the levels with snow present. Water equivalent estimation using this technique in Ontario gave an accuracy of 1.2 cm for water equivalents between 1.4 and 14.1 cm (Grasty, et al., 1974). The maximum operational altitude for this sensor is on the order of 150 m which severely limits its applicability in mountainous regions (Meier, 1975).

Although limited research has been conducted to date on the use of microwave remote sensing to monitor snowpack parameters, available results point to a promising potential. The penetration depths in snow in the microwave region and the physical snow depths of interest are closer to one another than in any other portion of the spectrum. The possibility of obtaining profile information is immediately suggested. The following section will describe the unique advantages of a microwave remote sensor.

1.3 The Advantages of Microwave Remote Sensors

The degree of transparency of the earth's atmosphere is a serious consideration for satellite platforms. Figure 1-2 illustrates the optical window between 500 THz and 5 THz and the radio window between 300 GHz and 30 MHz. The remaining spectrum is essentially opaque. Figure 1-2 applies only to clear sky conditions; hydrometeors such as light clouds cause greater than 5 dB/km loss at infrared wavelengths and even greater loss at visible wavelengths (Bush and Ulaby, 1977). The loss through the same clouds at 100 GHz is about 0.05 dB/km. At lower frequencies, the loss is even less. The microwave spectrum is therefore relatively independent of cloud cover. High rainfall rates do have a serious attenuating effect at microwave frequencies (Benoit, 1968). The loss results from absorption and scattering from the rain droplets and has been covered extensively in the literature. The operation of optical sensors, however, is prevented by precipitation.

There are two basic types of microwave remote sensors: active and passive. The active sensor is a radar and supplies its own source of illumination. Scatterometers, real-aperture imagers (SLAR), and synthetic aperture imagers (SAR) are examples. The passive sensors are radiometers and receive power from natural emission resulting from molecular and atomic motion.

One of the major advantages of microwave sensors is that the operation is independent of solar illumination. Since solar illumination is not

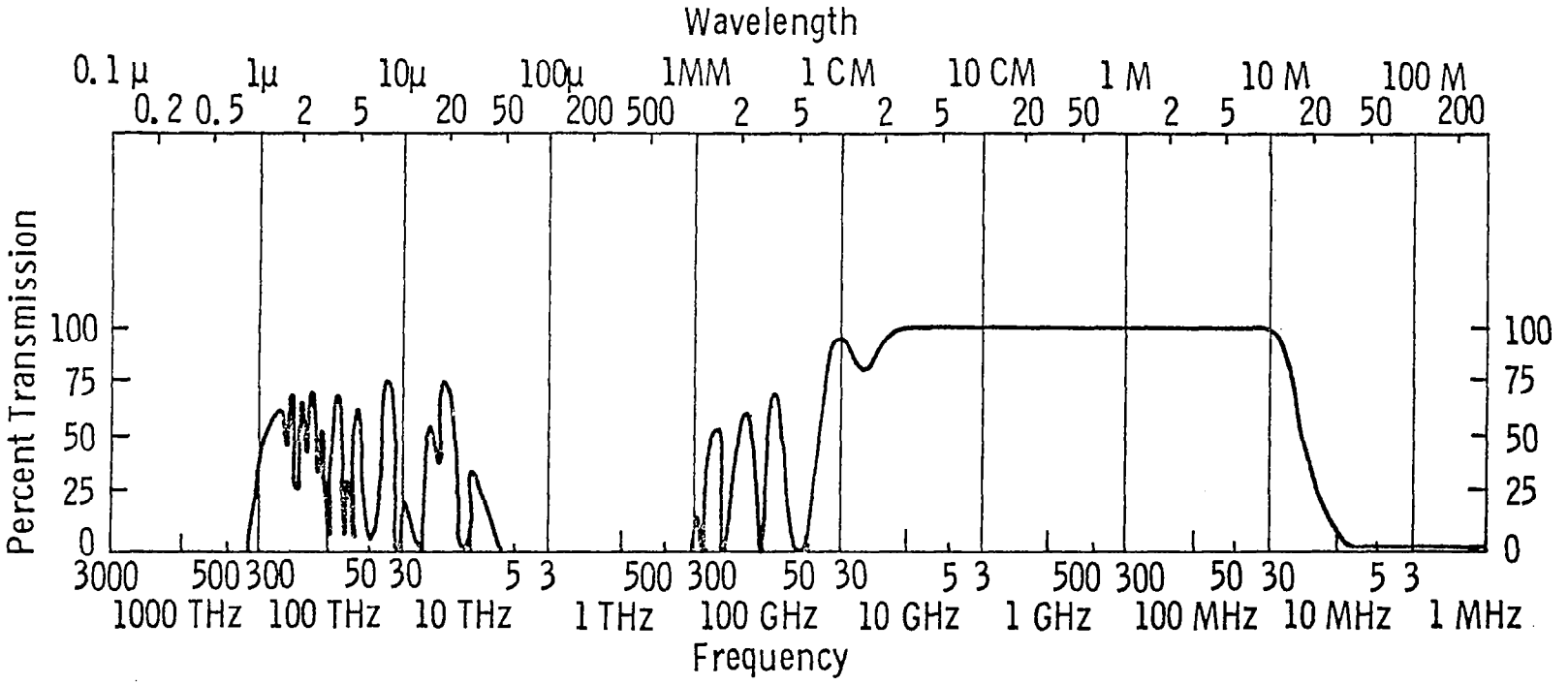


Figure 1-2 Partial electromagnetic spectrum showing the percent transmission through earth's atmosphere and ionosphere. (Thompson, 1971) Atmos. Trans. Hndbk.

required as a source, the restrictions on satellite orbit can be relaxed and nighttime measurements are feasible. Independence of operation, however, does not infer that there are no target changes with respect to solar radiation.

The main limitation of satellite radiometric microwave investigations is spatial resolution. The spatial resolutions of passive sensors are beamwidth limited; the nadir resolution of the Nimbus 5 and Nimbus 6 Electrically Scanning Microwave Radiometers (ESMR), for instance, is approximately 25 km. Even with this limited resolution, snow areal extents on a continental basis have been measured with good correlation to physical measurements (Rango, et al., 1979). The first active sensor to be placed in orbit was the Skylab S-193 Scatterometer. This device was also beam-limited and had a resolution of from 10 km at nadir to about 20 km at 50° incidence angle. A synthetic aperture radar (SAR) imager, on the other hand, has the capability to produce very high resolution images; SEASAT, for example, provided approximately 25 m resolution for its short period of operation. Resolutions of this order can provide information on snow-pack in mountainous areas where the major accumulations are located.

The greater penetration of microwaves over optical waves can also provide knowledge on the depth profile of the snowpack characteristics. Knowledge of the snow profile is precisely the information which would allow implementation of much better runoff models.

The aforementioned advantages warrant an investigation to fill the gaps in the understanding of microwave-snowpack interactions.

2.0 DEFINITION OF THE PROBLEM

The purpose of this study is to investigate the use of microwave remote sensing for snowpack analysis. Before a detailed treatise on the subject can be developed, one must review the basic mechanisms of the electromagnetic wave-target interaction process.

2.1 Target Description

The target or area of observation of the microwave sensor can be characterized by many sets of parameters. It can be described by its physical parameters that we deal with in everyday life. Also the target can be described by its dielectric parameters which determine its interaction with electromagnetic waves. Even if direct contact with the target of interest is not allowed, the information gained at a distance may be related to the physical or dielectric properties or both.

Figure 2-1 illustrates the target configuration. The specific case shown is a snow layer of depth d which may actually consist of several sublayers over an effectively infinite ground layer. θ is the angle of observation by the sensor and θ' is the angle of propagation within the snow layer.

Some of the physical properties describing the snowpack scene are snow surface roughness, snow depth d, snow density ρ, water equivalent W, snow wetness m_v, crystalline structure, stratification, snow inhomogeneities, ground surface roughness, soil moisture m_s and snow physical temperature. The water equivalent is the height of water which would result from complete melt of a column of snow. It is the product of depth and density. Obviously, this group of parameters should adequately specify the scene for the applications of interest. The question is how do these characteristics affect, first, the dielectric properties and then, the remotely sensed parameters.

The two parameters which govern propagation in a medium are the permittivity k and the permeability μ. Normally, k and μ are expressed in terms of the free space values k_o and μ_o, respectively.

$$k = k_r k_o$$
$$\mu = \mu_r \mu_o \qquad (2\text{-}1)$$

where k_r and μ_r are dimensionless.

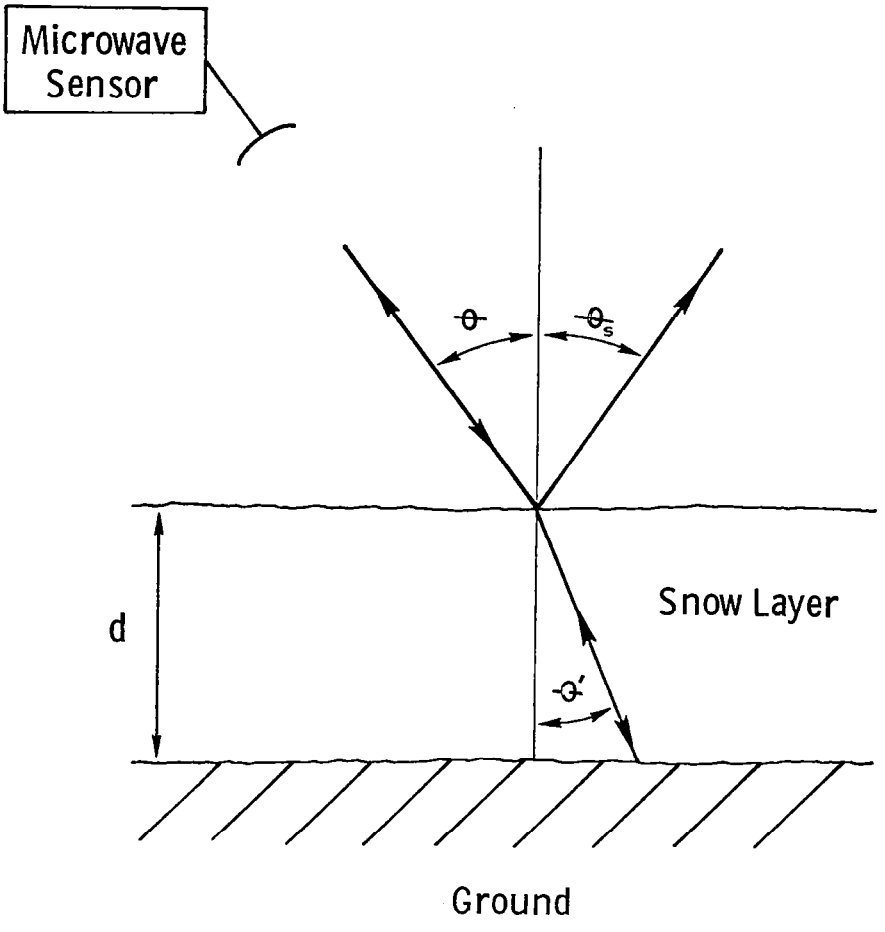


Figure 2-1 Snowpack scene configuration.

For the targets of interest in this study, $\mu_r = 1$. The relative permittivity (or relative dielectric constant), however, is influenced by several of the physical parameters. In general, k_r is complex valued

$$k_r = k'_r - j\, k''_r \qquad (2\text{-}2)$$

and results in absorption and propagation of the wave. The imaginary part k''_r is sometimes represented in the form of the loss tangent, tan δ:

$$\tan\delta = \frac{k''_r}{k'_r} \qquad (2\text{-}3)$$

The field attenuation constant α_a is related to k_r by (Ramo, et al., 1965):

$$\alpha_a = \frac{2\pi}{\lambda} \left\{ \frac{k'_r}{2} \left[\left(1 + \left(\frac{k''_r}{k'_r} \right)^2 \right)^{1/2} - 1 \right] \right\}^{1/2} \qquad (2\text{-}4)$$

where λ is the wavelength and the units of α_a are nepers/unit length. Penetration of a wave into a medium is also related to the loss in the medium. Penetration is characterized by the skin depth D which is the depth at which the magnitude of the electric (or magnetic) field is diminished to 1/e of its value just beneath the surface. If the medium is homogeneous then the equations of this section determine the electromagnetic behavior. However, if the medium consists of particle sizes on the order of the wavelength, then another loss mechanism is manifested in addition to absorption. This loss results from scattering of the wave.

It will be convenient in this study to use power attenuation coefficients. Since the microwave measurements taken over terrain are usually averaged values, phase information is usually lost and the results have the units of power. Therefore at this point, the (power) absorption coefficient κ_a is defined as

$$\kappa_a = 2\, \alpha_a \qquad (2\text{-}5)$$

which represents the power loss due to absorption. A scattering coefficient κ_s, analogous to κ_a, then represents the power lost due to scattering. The total extinction coefficient κ_e is then

$$\kappa_e = \kappa_a + \kappa_s \tag{2-6}$$

with the assumption that κ_a and κ_s are independent. Alternately, the above quantities can be expressed as mass absorption; mass scattering, and mass extinction coefficients:

$$\begin{aligned} \kappa_a' &= \kappa_a/\rho \\ \kappa_a' &= \kappa_a/\rho \\ \kappa_a' &= \kappa_a/\rho \end{aligned} \tag{2-7}$$

where ρ is the density. These quantities will be used in model evaluations in Chapter 9.

The loss factor L_d for a length d is given by:

$$L_d = e^{\tau d} \tag{2-8}$$

where the optical depth τ_d is:

$$\tau_d = \int_0^d \kappa_e \, dh \tag{2-9}$$

If κ_e is constant over the path length then the optical depth becomes:

$$\tau_d = \kappa_e \, d \tag{2-10}$$

Next the equations describing the active and passive microwave/target interaction mechanisms will be examined.

2.1.1 Derivation of the backscattering coefficient σ° equation.

The received power for the active microwave (radar) case is governed by the radar equation for an area extensive target (Moore, et al., 1975 in Manual of Remote Sensing):

$$P_r = \iint_{A_{ill}} \frac{P_t \, G_t \, G_r \, \lambda^2 \, \sigma^\circ \, dA}{(4\pi)^3 \, R_t^4} \tag{2-11}$$

where: P_r = received power

P_t = transmitted power

G_t = transmit antenna gain

G_r = receive antenna gain

σ^o = backscattering coefficient

R_t = target range

dA = differential element of illuminated area

A_{ill} = illuminated area

If the assumption is made that the parameters inside the integral are constant over the illuminated area, the scattering coefficient σ^o can be determined from equation 2-7 by measuring the other quantities. Establishing the relationship of σ^o to the physical and dielectric parameters of snowpacks is one of the major objectives of this investigation.

2.1.2 Derivation of the apparent radiometric temperature T_{ap} equation.

The received power for the passive microwave (radiometer) case results from natural emission of radiation from atomic and molecular vibrations. In the microwave region, the brightness B_{bb} of a blackbody is given by the Rayleigh-Jeans approximation to Plank's formula (Moore, et al., 1975 in Manual of Remote Sensing):

$$B_{bb} = \frac{2kT}{\lambda^2} \qquad (2\text{-}12)$$

where T is the ambient temperature and K is Boltzmann's constant. The resulting output power from a microwave antenna placed inside a blackbody is given by (Moore, et al., 1975 in Manual of Remote Sensing):

$$P_{bb} = KT\Delta f \qquad (2\text{-}13)$$

where Δf is the bandwidth. Most targets are not ideal absorber-emitters of radiation; these targets are often called greybodies. Since power is linear with temperature, the power emitted from a greybody may be represented as the equivalent power of a blackbody radiator with a cooler temperature T_B. The ratio of this temperature, called the brightness temperature, to the thermometric temperature T is the emissivity ε of the material

$$\varepsilon = \frac{T_B}{T} \tag{2-14}$$

For the case of a downward looking ground-based radiometer, the apparent temperature is given by (Janza, et al., 1975 in Manual of Remote Sensing):

$$T_{ap}(\theta) = T_B(\theta) + T_{sc}(\theta) \tag{2-15}$$

where T_B is the brightness temperature of the target and T_{sc} is the component of the downward emitted sky radiation scattered by the target in the direction of the radiometer antenna. As a first order approximation, the target will be described by a specular surface model. If the target is isothermal, the power reflection coefficient $R(\theta)$ and the effective emissivity $\varepsilon(\theta)$ of the target are related by:

$$R(\theta) = 1 - \varepsilon(\theta) \tag{2-16}$$

Therefore, if the average target thermometric temperature is T_{phys} then:

$$T_B(\theta) = \varepsilon(\theta)\, T_{phys} \tag{2-17a}$$

$$T_{sc}(\theta) = [1 - \varepsilon(\theta)]\, T_{sky} \tag{2-17b}$$

Combining equations 2-15 and 2-17,

$$\varepsilon(\theta) = \frac{T_{ap}(\theta) - T_{sky}(\theta)}{T_{phys} - T_{sky}(\theta)} \tag{2-18}$$

where $T_{sky}(\theta)$ is the downward emitted radiometric temperature of the atmosphere. The above result is only valid for emission from a medium with a perfectly smooth surface and isothermal physical temperature. If the surface is rough relative to the wavelength, then the emissivity is described in terms of the scattering properties of the surface. Peake (1969) determined a generalized expression for the polarized emissivity $\varepsilon_i(\theta)$ in terms of the surface differential bistatic scattering coefficients $\gamma_{ii}(\theta, \theta_s)$ and $\gamma_{ij}(\theta, \theta_s)$:

$$\varepsilon_i(\theta) = 1 - \frac{1}{4\pi} \int_{\Omega} [\gamma_{ii}(\theta, \theta_s) + \gamma_{ij}(\theta, \theta_s))]\, d\Omega_s \tag{2-19}$$

where i and j are subscripts designating horizontal or vertical polarization, Ω is the solid angle, and γ is related to σ^o by (Moore, et al., 1975 in Manual of Remote Sensing):

$$\gamma_{ij}(\theta, \theta_s) = \frac{\sigma^o_{ij}(\theta, \theta_s)}{\cos\theta} \qquad (2\text{-}20)$$

For layered media, such as snow over terrain, the emission is governed by scattering and absorption in the snow layer as well as emission from the underlying terrain medium. In this case, $T_B(\theta)$ has to be determined from a solution of the radiative transfer equation.

2.2 Review of Theoretical Models

Since snowpack is a dielectric medium which is both a scatterer and emitter of radiation at microwave frequencies, the medium can be described as either a continuous random medium with large dielectric variation or as a collection of scatterers distributed within a lossy dielectric. Theoretical models which fit both types of dielectric descriptions have been covered extensively in the literature which was reviewed by Ulaby, et al., (1978).

There have been traditionally two approaches to solving problems involving scattering and emission. The first of these makes use of the "radiative transfer theory" originally formulated by Schuster (1905). This type of formulation solves for intensity. The radiative transfer theory was used by Chandrasekhar (1960) to treat scattering and emission in the atmosphere. The general assumptions required for this approach are (1) neglection of diffraction and interference and (2) power is additive (uncorrelated field quantities). The field approach, on the other hand, starts with the wave equations and the scattering and absorption properties of the medium. The average fields and correlation functions of the fields are then derived. This approach can be mathematically rigorous, however, as a result of the generality and complexity of this formulation, many assumptions must be made to obtain actual solutions.

The radiative transfer theories are valid when the effect of phase of the propagating field is random and there is no correlation of the field quantities. With the above restraints, the equations of radiative transfer have been derived by several methods: Tsang and Kong, 1978a; Tatarskii,

1964; Tatarskii and Gertsenshtein, 1963; and Dence and Spence, 1973. Chandrasekhar (1960) provided a reference on general radiative transfer theory. Applications to snowpack or similar mediums have been reported by Tsang and Kong (1975, 1976a, 1977b, 1978b), England (1974, 1975), Chang, et al., (1976), Edgerton, et al., (1971), Zwally (1977), and Stogryn (1970).

The field approach to the solution of scattering and propagation in a continuous random medium may be subdivided into two types. The first type uses the first term of the Neumann series solution to the wave equation. Frisch (1968), Sancer and Varvatsis (1969), Barabanenkov, et al., (1971), and Tsang and Kong (1975, 1976b) have employed variations of this approach. The second type is the renormalized Neumann series approach. The following theoreticians have used variations of this method: Tartarskii (1964), Frisch (1968), Tartarskii and Gertsenshtein (1963), Varvatsis and Sancer (1971), Macrakis (1965), Bourret (1962), Rosenbaum (1967, 1968, 1971), Karal and Keller (1974), Bassamini, et al. (1967), Fung and Fung (1977), Dence and Spence (1973), Kupiec, et al. (1969), Fung (1979), Stogryn (1974), Tsang and Kong (1976a, 1978a), and Tan and Fung (1978), and Fung and Ulaby (1978).

The problems associated with multiple scattering have been investigated by Burke and Twersky (1964), Twersky (1960 to 1967), Lin and Ishimaru (1974), Ishimaru (1975), and Twersky (1978).

A few terms associated with the theoretical models which describe the electromagnetic interactions at the surface and within the medium should be introduced. The surface roughness of a target is known to affect the boundary conditions at that surface. A "smooth surface" occurs when the height variations are much smaller than a wavelength. For a perfectly smooth continuous surface σ^o would be a Dirac delta function at the specular angle. Roughness tends to spread the delta function to all angles. As roughness increases a "rough surface" scatters radiation in accordance with Lambert's Law. In this case, the scattering coefficient σ^o varies as $\cos \theta$.

2.3 Statement of the Problem

The objective of this study is to evaluate the use of microwave remote sensing techniques for obtaining snowpack information. The methodology employed will be to relate σ^o and ε to the physical and

dielectric properties of the snow-ground target. Active and passive microwave sensors were employed in an extensive measurement program in Steamboat Springs, Colorado. Quantitative relationships will be determined (whenever possible) between the snowpack parameters under varying conditions and σ^o and T_{ap} (or ε). If quantitative conclusions are not possible, qualitative inferences will be made.

In Chapters 3 and 4, the physical and dielectric properties of the targets are covered in detail. Terms that will be used in the analysis are defined and past research is reviewed.

Chapter 5 reviews and summarizes the results of previous measurement programs in active and passive microwave remote sensing of snowpacks. Based on this review, areas of needed research are specified.

The description of the experiment is given in Chapter 6. Ground truth techniques, data acquisition procedures and the microwave systems are described.

Chapter 7 covers the statistics of the microwave and ground truth data. In this chapter, seasonal histograms of the microwave data are given.

Chapter 8 gives the analysis of the microwave response to snowpack parameters, and in Chapter 9, the simple models are developed and applied to the experimental data.

The final chapter suggests experiments for a follow-on experiment and summarizes the findings of this investigation.

3.0 PHYSICAL PROPERTIES OF SNOWPACKS

A brief description of the physical properties of snow and snowpacks will provide insight into the dielectric and scattering properties of snow. Snow refers to ice crystals that have grown large enough to fall, and to the resulting deposition on the ground. Almost immediately after reaching the ground, metamorphism commences even if the temperature is well below zero (LaChapelle, 1969). In time, the structure of the snow crystals becomes vastly altered. LaChapelle (1969) described the various snow crystal types and the metamorphic forces on the crystals. The layer of metamorphosed snow covering the ground is referred to as snowpack.

3.1 Snow Characteristics

Snow crystals begin to form when a particle (for example, dust) passes through supercooled air and ice condensation accretes on the particle. In the presence of super saturated air, the crystal will grow and become heavy enough to fall. Many different types of snow crystals can be formed under various atmospheric conditions. The meteorological classification of snow crystals developed by Magono and Lee (1966) is given in Figure 3-1. This classification scheme applies also to falling snow. The different types of snow crystals (Figure 3-1) are formed under different temperature and humidity conditions (Figure 3-2). Bentley (1931) published a book illustrating many photographs of perfectly formed snow crystals. Most crystals reaching the ground, however, bear little resemblance to the symmetrical crystals of Bentley's photographs. Most crystals get broken by wind or covered with "rime", which are small water droplets that under certain atmospheric conditions accumulate on the snow crystals.

The density of freshly fallen snow varies between 0.01 to 0.30 g/cm^3 according to its wetness and crystal type (Figure 3-1). Geographic location, wind and elevation also affect density. Grant and Rhea (1974) measured a density range from 0.02 to 0.15 g/cm^3 in Colorado. More detailed information of snow formation and characteristics may be found in Hobbs (1974).

3.2 Snowpack Characteristics

This section discusses the crystalline structure and grain size, thermal properties, and optical characteristics of snowpacks.

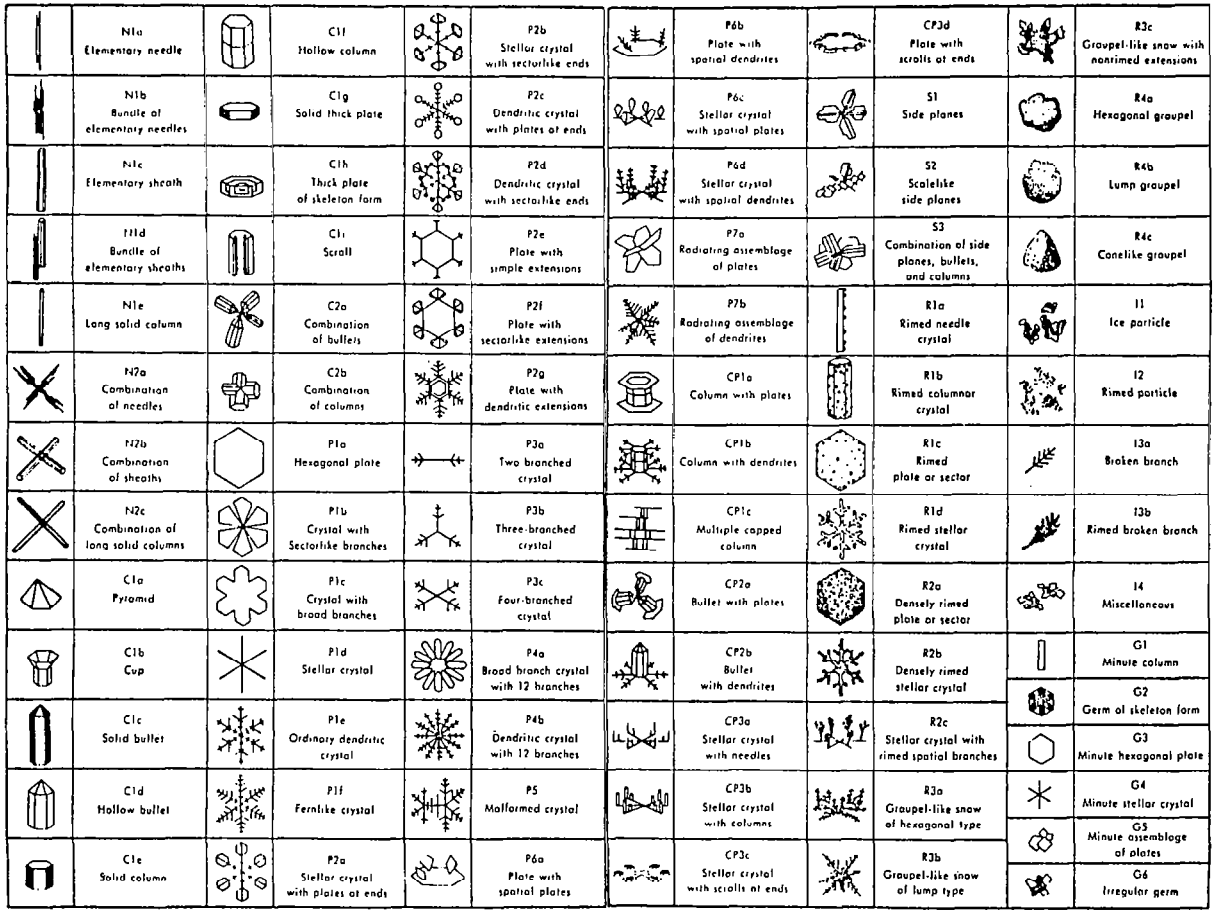


Figure 3-1 The meteorological classification of snow crystals according to the scheme of Magono and Lee. (LaChapelle, 1969)

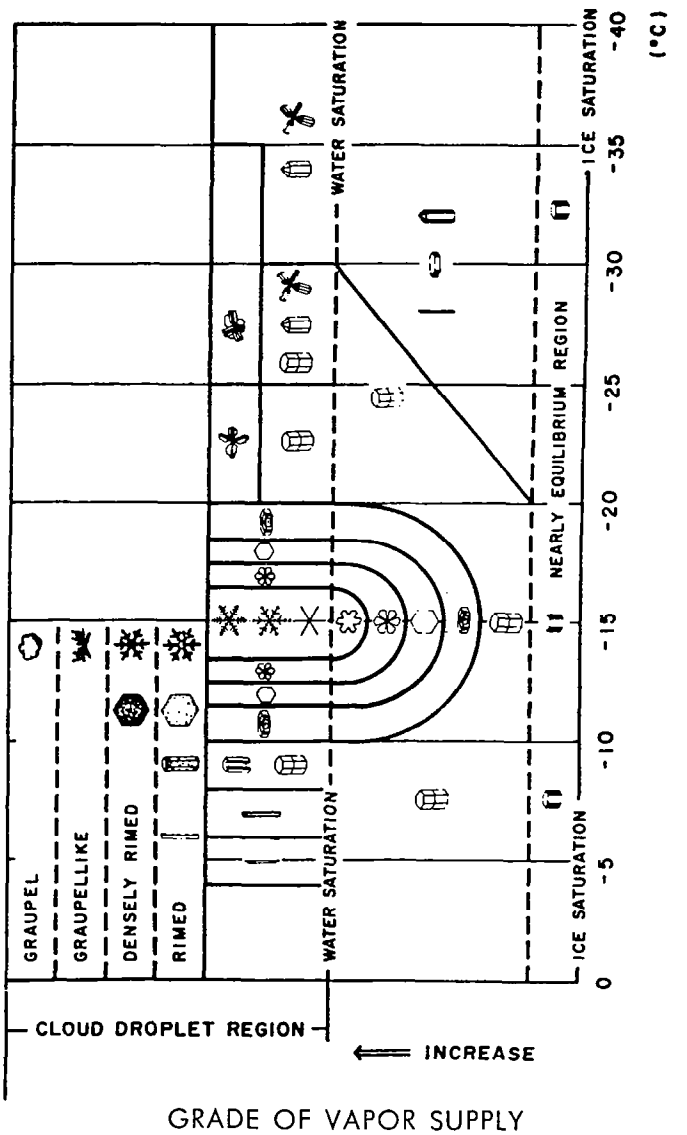


Figure 3-2 Temperature and humidity conditions for formation of snow crystals in the atmosphere. (Magono and Lee, 1966)

3.2.1 Snowpack crystalline structure and grain size

The beautifully shaped intricate patterns of newly formed snow crystals are thermodynamically very unstable. Molecular attraction leads to minimization of the surface area to volume ratio. This process, which results in smoothing the pointed angles of the crystals to rounded ice shapes, is termed destructive metamorphism or equitemperature metamorphism. It only occurs when the snowpack is near isothermal equilibrium. The original snow crystals break up into smaller rounded snow particles. This breaking up process leads to a considerable percentage of the total observed snow compaction.

Surface effects cause another class of crystal metamorphism. Melt-freeze cycles can form a very strong crust. The strength results from bonding of the ice grains. Another surface structure is surface hoar. Sublimation of water vapor from the air on the snow surface is the mechanism of growth. Surface hoar is ice dew which occurs on clear cold nights under high humidity conditions when the dewpoint is reached. A greenhouse effect is sometimes created when absorbed heat causes evaporation which condenses as a thin ice layer at the surface. This condition is designated as firn mirror and can result in considerable snow melt beneath the ice layer.

If large temperature gradients exist within the snowpack, differences in equilibrium vapor pressure will exist at different depths. The net effect is vapor migration toward the lower vapor pressure cold snow. This process, termed constructive or temperature gradient metamorphism, can create very large crystals, on the order of 1 cm in diameter. The vapor pressure gradient is larger with respect to temperature gradient near 0°C. Therefore, since the ground temperature is consistently near 0°C, formation of "depth hoar" is generally at the base of the snowpack. The size of the crystals are related monotonically to the vapor pressure gradient. The larger crystals form at the highest gradients and the characteristic shape of these crystals is hexagonal. As soon as the temperature gradient is removed, however, destructive metamorphism begins.

3.2.2 Snowpack Thermal Properties

Thermal properties of the snowpack affect both absorption of energy from the sun and atmosphere and transfer of this energy through the snowpack. The energy transfer to and from the soil is also important.

The thermal conductivity range for snow of widely differing densities is shown in Figure 3-3 to be much less than the values for soils and ice (Poulin, 1974). Snow cover therefore has a considerable influence on the heat flux. Thermal conductivity also must be a function of wetness, although the exact relationship was not found in the literature. Fowler (1974) measured the thermal conductivity of snow as a function of density (Figure 3-4).

3.2.3 Snowpack Optical Properties

The optical reflectance of snow determines the solar radiation absorbed by the snow. The reflectance is high in the visible region (.4 to .7 μm) and gradually drops through the near-infrared band. The result is reflection of a major component of the incidence radiation and therefore low energy absorption. Choudhury and Chang (1978) have shown that reflectance can be modeled as a function of snow particle size (Figure 3-5). Reflectance is lowered for larger particle sizes and therefore the reflectance of old snow is lower than that of fresh snow. They stated that multispectral scanners might be able to monitor heat flux over a snow covered area. This information could then be used as an input to an energy balance snow melt model.

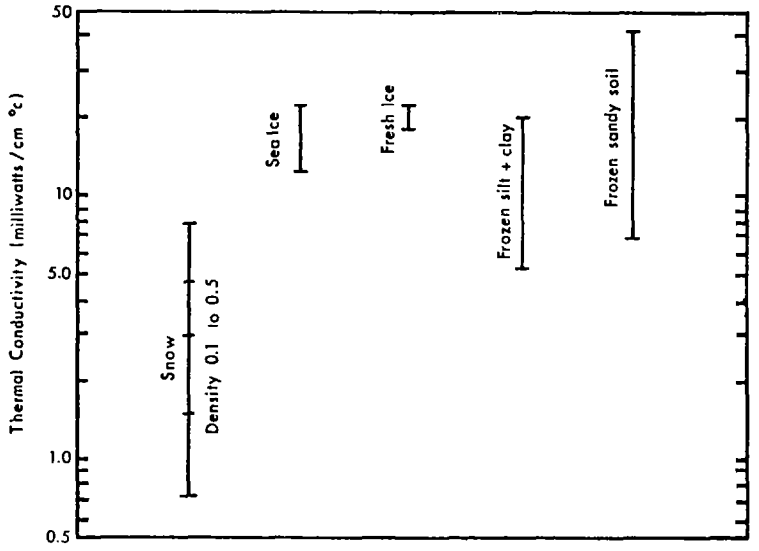


Figure 3-3 Thermal conductivities of snow (0.1-0.5 gm/cm^3), sea ice, fresh ice, frozen fine-grained soil (1-2 gm/cm^3, 10-40% moisture), and frozen coarse-grained soil (1.2-2 gm/cm^3, 5-25% moisture). Soil moisture is percent of dry weight. Extreme values for soil are not included. Sources for these values are from (Poulin, 1974)

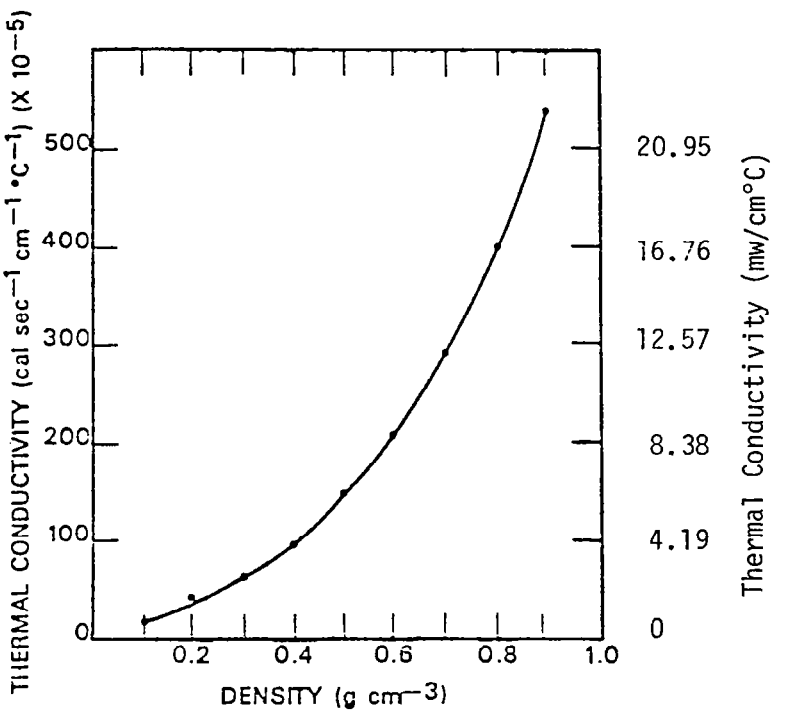


Figure 3-4 Relationship between snow density and thermal conductivity. (Fowler, 1974)

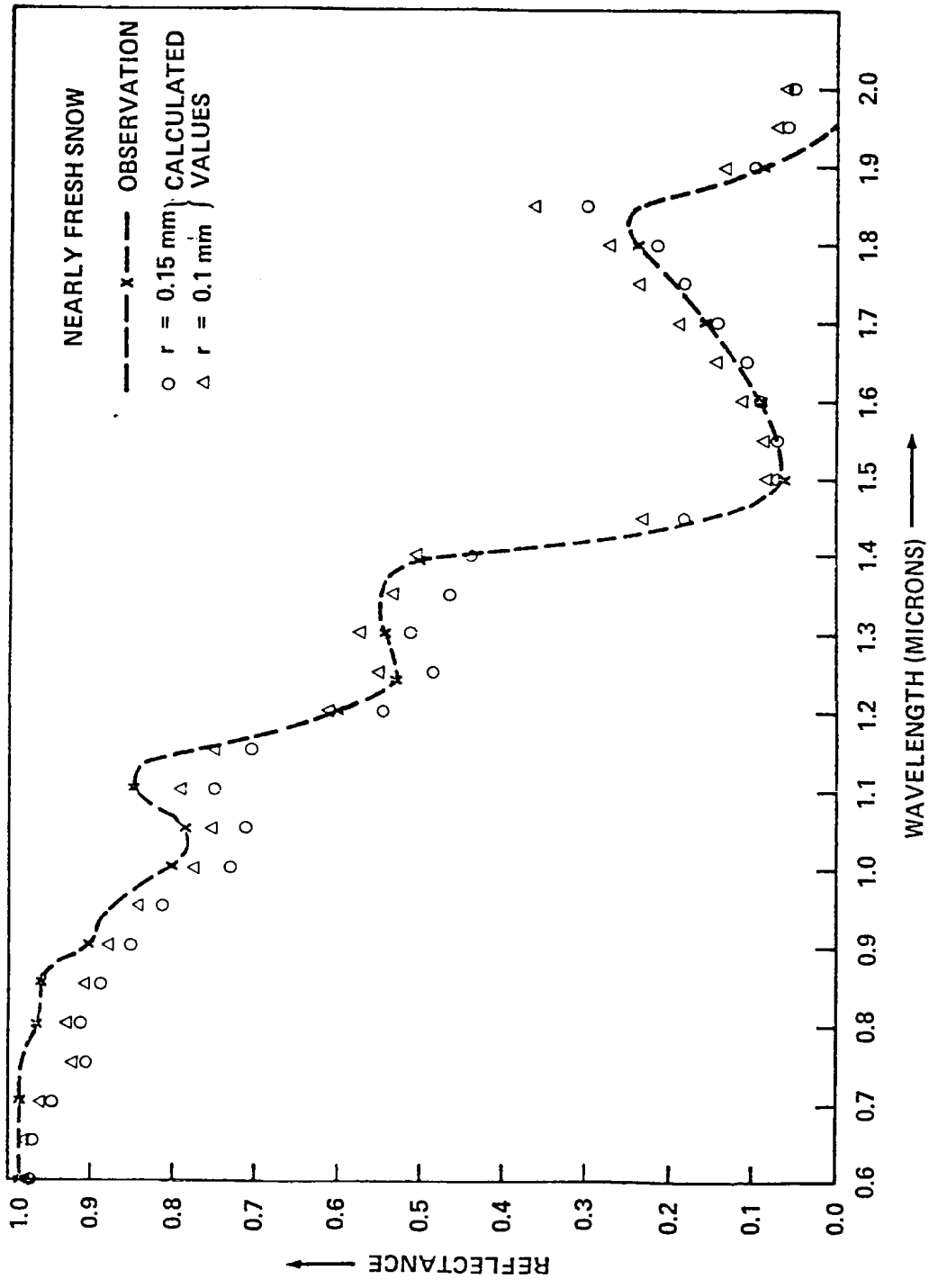


Figure 3-5 Comparison of calculated and observed reflectance of a nearly fresh snow. (Choudhury and Chang, 1978)

4.0 DIELECTRIC PROPERTIES OF SNOW AND SOILS

Electromagnetic wave-snow interaction (absorption, emission and scattering) is governed by the geometrical and electrical (dielectric) properties of the snow medium. The relative dielectric constant of snow k_s, is in general a function of:

a) Microwave frequency;
b) Percentage volume of ice;
c) Percentage volume of air;
d) Percentage volume of free water;
e) Snow temperature;
f) Crystal size and structure of the snow medium; and
g) Presence of impurities.

The strongest effect of the intrinsic snow parameters on k_s is the percentage of free water. Since the snow medium is composed of three distinct components (ice, air, and water), the dielectric properties of each affect the dielectric properties of the mixture. The dielectric properties of water and ice are surveyed first, then the properties of the mixture are examined.

4.1 Dielectric Properties of Water

The dielectric constant of water in the microwave region is governed by the Debye equation:

$$k_\omega = k_\infty + \frac{k_{dc} - k_\infty}{1 - j2\pi\tau f} + j\frac{\sigma_i}{2\pi k_0 f} \qquad (4\text{-}1)$$

where

k_ω = complex relative dielectric constant of water, $k_\omega = k'_\omega - jk''_\omega$
k_∞ = optical limit of dielectric constant
k_{dc} = static limit of dielectric constant
τ = relaxation time of the water molecule dipole
k_0 = permitivity of free space
σ_i = ionic conductivity
f = frequency (Hz)

The Debye equation exhibits a single resonance phenomena at the relaxation frequency f_0:

$$f_o = \frac{1}{2\pi\tau} \tag{4-2}$$

The real and imaginary parts of equation 4-1 in terms of f_o are:

$$k'_w = k_\infty + \frac{k_{dc} - k_\infty}{1 + \left(\frac{f}{f_o}\right)^2} \tag{4-3a}$$

$$k''_w = \left(\frac{f}{f_o}\right) \frac{k_{dc} - k_\infty}{1 + \left(\frac{f}{f_o}\right)^2} + \frac{\sigma_i}{2\pi k_{dc} f} \tag{4-3b}$$

The maximum value of k''_w is located at $f = f_o$. Table 4-1 gives the relaxation frequency as a function of temperature and Figures 4-1 and 4-2 illustrate the frequency behavior. The first term in equation 4-3b causes dielectric loss while the second term causes ohmic loss. The limiting values on the of k'_w and k''_w are:

$$k'_w \cong k_{dc} \qquad \text{for } f << f_o \tag{4-4a}$$

$$k''_w \cong (k_{dc} - k_\infty)(f/f_o) \quad \text{for } f << f_o \tag{4-4b}$$

$$k'_w \cong k_\infty \qquad \text{for } f >> f_o \tag{4-5a}$$

$$k''_w \cong (k_{dc} - k_\infty)/(f/f_o) \text{for } f >> f_o \tag{4-5b}$$

Stogryn (1971) calculated regression fits to obtain the dielectric parameters from several experimenters' data. More recently, Klein and Swift (1975) updated the regression fits. For the case of interest (snow), the ionic conductivity term may (usually) be neglected. Figures 4-1 and 4-2 illustrate the real and imaginary parts of the dielectric constant of water as a function of freuqency. Also the sensitivity to temperature is demonstrated. These curves were calculated using the following regression equations from Stogryn (1971) for pure water:

$$k_{dc}(T) = 87.74 - 0.40008\ T + 9.398 \times 10^{-4} T^2 + 1.41 \times 10^{-6} T^3 \tag{4-6}$$

$$2\Pi\tau(T) = 1.1109 \times 10^{-10} - 3.824 \times 10^{-12} T + 6.938 \times 10^{-14} T^2 - 5.096 \times 10^{-16} T^3 \tag{4-7}$$

$$k_\infty = 4.9$$

where T is in °C.

TABLE 4-1

Relaxation Frequency of Water (Royer, 1973)

T (°C)	f_o(GHz)
0	8.5
10	11.7
20	15.8
30	21.2
40	27.0
50	33.9

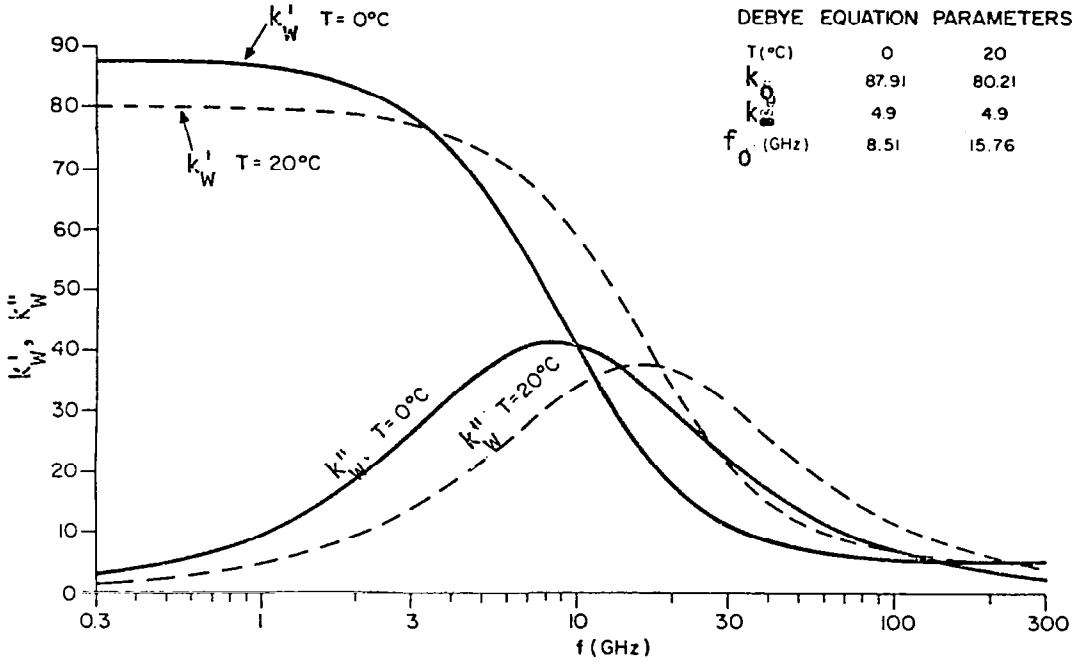


Figure 4-1 Relative permittivity of water at T = 0°C and T = 20°C using the Debye equation. (Royer, 1973)

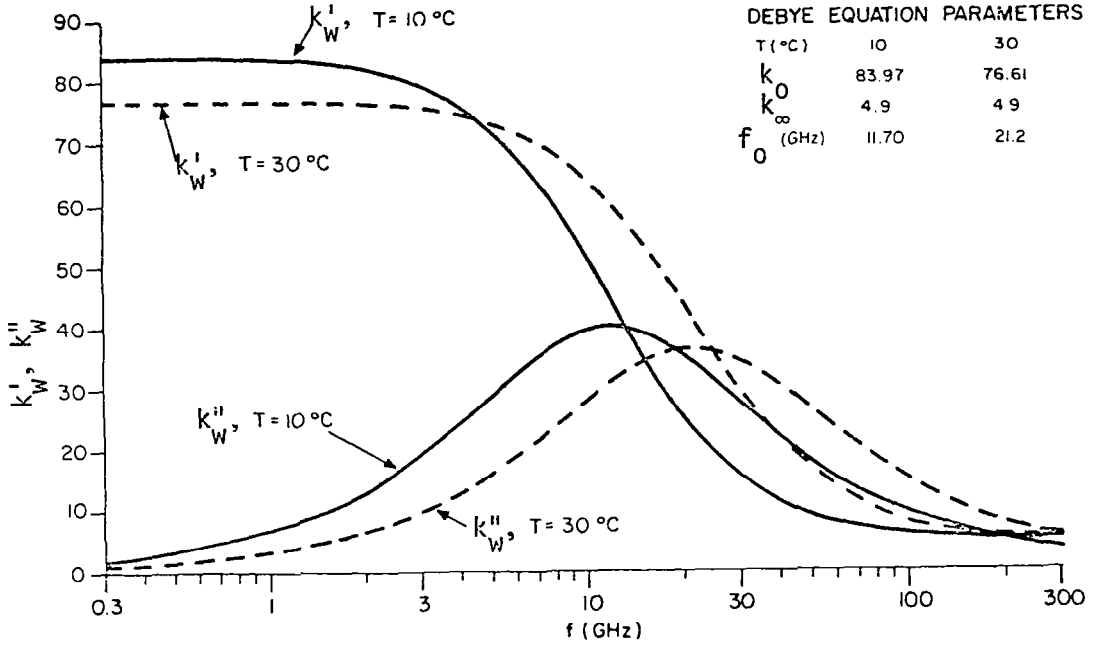


Figure 4-2 Relative permittivity of water at T = 10°C and T = 30°C using the Debye equation. (Royer, 1973).

Since there is some evidence (Blue, 1977) that the single relaxation frequency assumption of the Debye equation is not exact, a more valid equation would allow for a spread in the relaxation frequency. The equation

$$k_\omega = k_\infty + \frac{k_{dc} - k_\infty}{1 - (jf/f_o)^{1-\alpha}} \qquad (4\text{-}8)$$

where α is the distribution parameter proposed by Cole and Cole (1941), permits a distribution of the relaxation frequencies. α is defined over the interval $0 \leq \alpha \leq 1$ and for water α appears to be less than 0.02 (Klein and Swift, 1975). Blue (1979) determined that the Cole-Cole equation did provide an improved fit to his measurements; however, the difference between the Debye and Cole-Cole equations was less than one percent even in the millimeter region.

Water is a very lossy medium throughout the microwave region since the relaxation frequency f_o falls within this region. Figure 4-3 gives the attenuation as a function of frequency and temperature. The attenuation at 1 GHz is 30 to 90 dB/meter (depending upon the physical temperature) and increases rapidly with frequency. Small amounts of free water, therefore, can drastically alter both the real and imaginary parts of the dielectric constant of snow and therefore, induce a large change in its scattering, emission, and attenuation characteristics.

4.2 Dielectric Properties of Ice

The relaxation frequency of ice is temperature dependent, as is water. In ice, the water molecules are bound and therefore not as mobile as for free water; consequently the relaxation frequency is much lower than water's and is on the order of 10 KHz (Evans, 1965). Measurements by Blue (1979) have shown that no absorption or dispersion bands exist at least up to 183 GHz.

If ice is assumed to obey the Debye equation, the optical limit is easily satisfied in the microwave region. At 1 GHz, $f/f_o = 10^5$, for ice, therefore the dielectric properties could be represented by equations 4-5a and 4-5b. Measurements up to 183 GHz indicate that the real part of the dielectric constant of ice is approximately 3.17 in the microwave region and is independent of both frequency and temperature (Evans, 1965; Blue, 1976). The imaginary part is temperature dependent and its variation

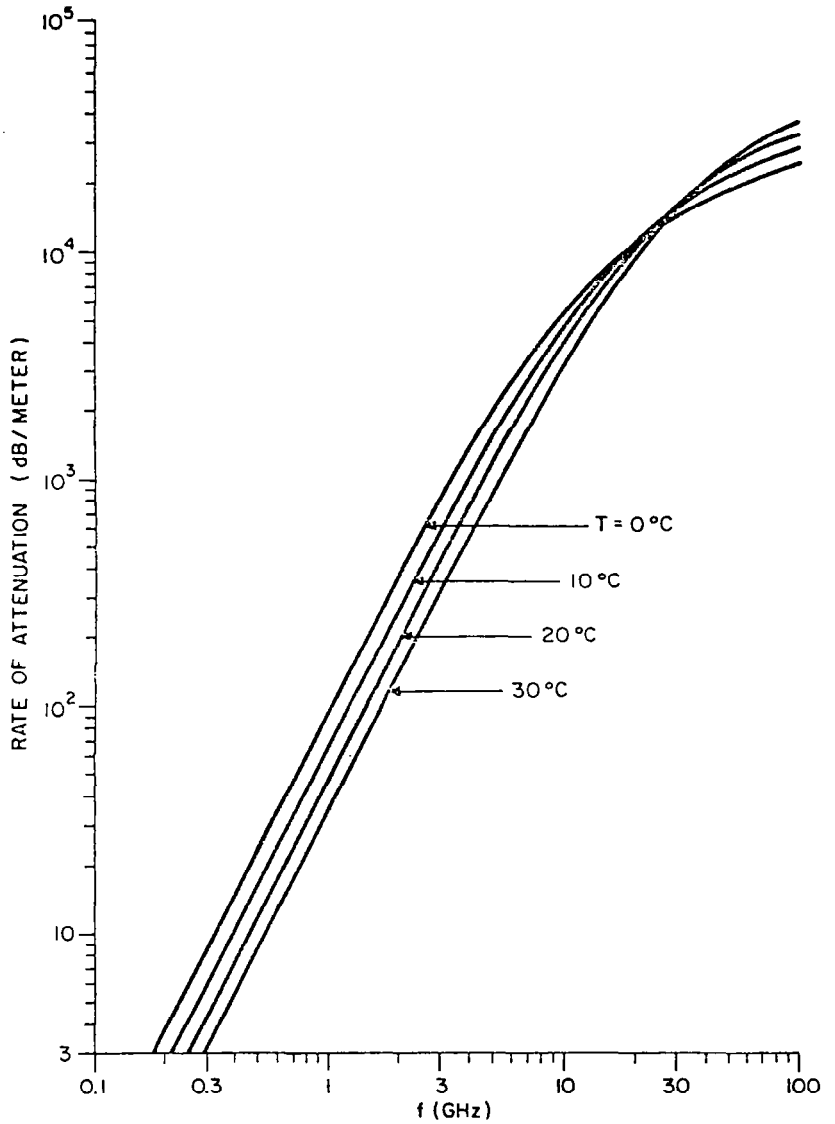


Figure 4-3 Rate of attenuation in water. (Royer, 1973)

is shown in Figure 4-4 at 10 GHz. The large rise near 0°C results from the appearance of free water. Figure 4-5 illustrates the frequency variation of the dielectric properties of ice. The behavior of the real part is in approximate agreement with the Debye equation 4-5a; however the imaginary part (equation 4-5b), represented by the symbol "A" in Figure 4-5, does not agree with the experiment results in the microwave range. For this reason, dielectric properties of ice and snow in the microwave region must rely on experimental data. Very little data exists above 10.0 GHz, and measurements on the dielectric properties of ice above 24 GHz are limited to the results of two groups of experimenters. Table 4-2 gives the results at 35.3 and 94.5 GHz from Perry and Straiton (1972). These data are consistently different from the lower frequency data (Figure 4-5). Gough (1972) stated that these data were in error since measurements at 600 GHz gave $k_i' = 3.2$. He implied that for the value of k_i' to drop between 24 and 600 GHz, a dispersion region would have to exist. If a dispersion region did exist, then the values measured for k_i'' would have been too small. Blue's (1976) measurements (Table 4-3) also indicated that no dispersion region existed. He measured the refractive index n of ice at 99, 136 and 183 GHz. Dielectric constant and refractive index are related by:

$$n = \sqrt{k} \qquad (4\text{-}9)$$

where n and k are in general complex. Since Blue's data agree well with the lower frequency data, the data of Perry and Straiton (1972) are considered questionable.

Attenuation through ice was calculated by Royer (1973) from the data of Lamb (1946), Lamb and Turney (1949), and Cumming (1952). Figures 4-6 and 4-7 give the results as a function of temperature and frequency. The lack of consistency between the data of Lamb and Cumming needs investigation. The attenuation rates at 1.0 GHz are between .015 and .07 db/m or about a factor of at least 10^5 less than the rate for water. Attenuation measurements on ice by Perry and Straiton (1972) are shown in Figures 4-8 and 4-9. Agreement on the real parts of dielectric constant was reasonable; however, the discrepancy in the attenuation data stresses the need for accurate measurements of the imaginary part of the dielectric constant.

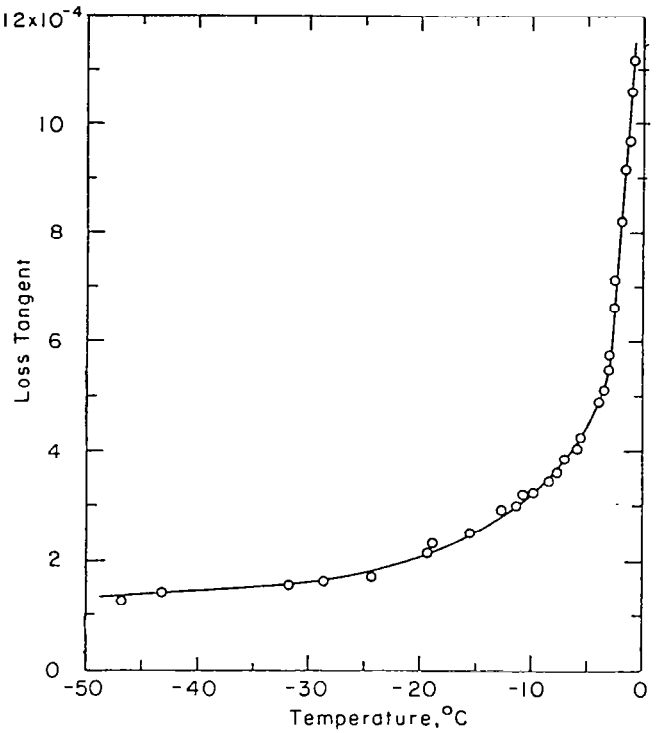
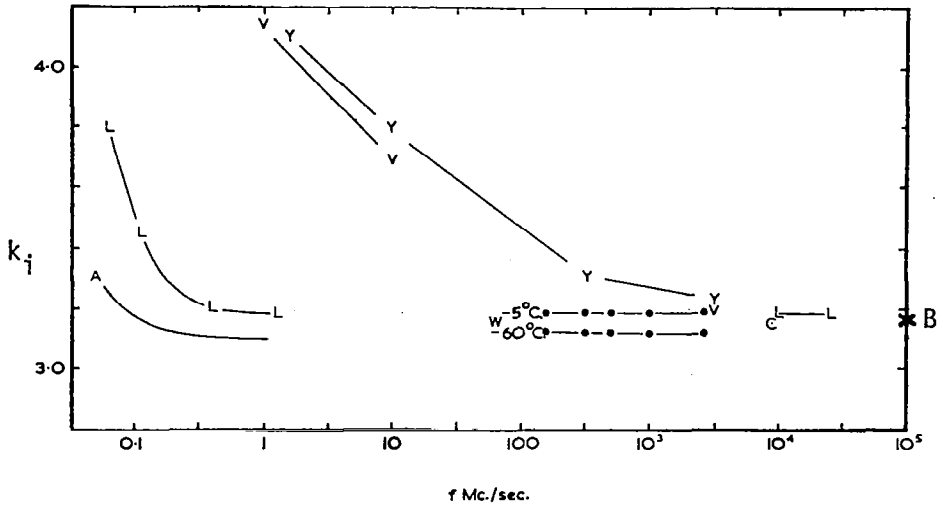
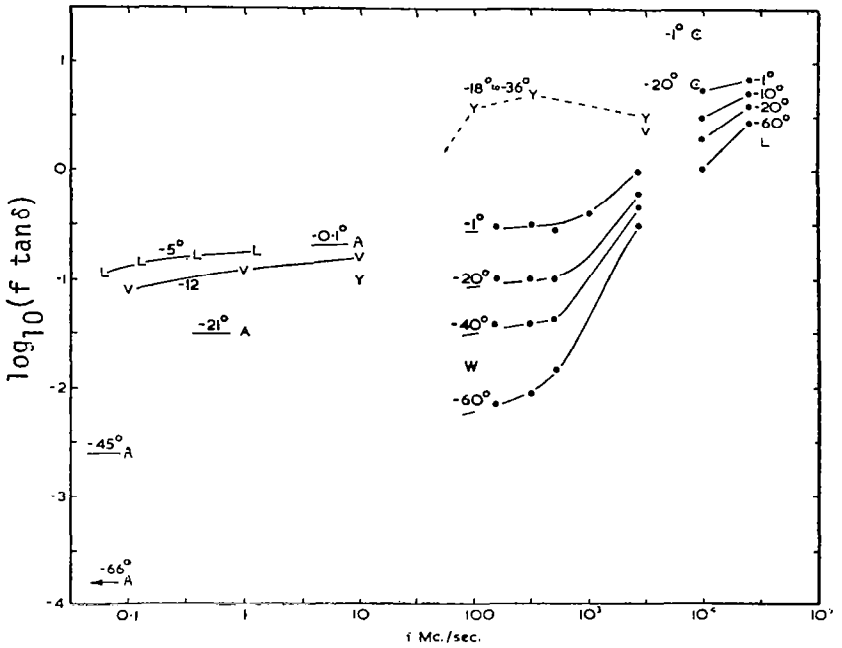


Figure 4-4 The loss tangent of ice samples as a function of temperature at a frequency of 10^{10} Hz. (Lamb and Turney, 1949, quoted in Hoekstra and Spanogle, 1972)



Relative permittivity of ice (ordinates) versus logarithm of radio-frequency (abscissae).



Loss tangent of ice versus radio frequency. The quantity plotted vertically is $\log_{10}$ (f tan δ) where f is the frequency in mc/sec. On the high-frequency tail of a relaxation spectrum this quantity is constant: it has the further useful property that the attenuation of a radio wave (measured in dB/m) passing through the medium is directly proportional to f tan δ. Temperatures are marked in °C.

L: Lamb (1946) and Lamb and Turney (1949) -5°C at low frequencies, 0° to -190°C at high frequencies: distilled water.
C: Cumming (1952) Distilled water, tap water, and melted snow (no observable difference).
A: Auty and Cole (1952) Conductivity water, ice free from stress. Limiting values plotted arbitrarily at 1,000 times the relaxation frequency.
V: Von Hippel (1954) Conductivity water, ice not available.
Y: Yashino (1961) Antarctic ice core samples, not annealed, density 0.91g/cm^3.
W: Westphal (private communication) Greenland ice, annealed, density 0.90g/cm^3
B: Blue (1979)

Figure 4-5 Dielectric properties of ice. (Evans, 1965)

TABLE 4-2

Relative Dielectric Constants of Ice

(Perry and Straiton, 1972)

Frequency (GHz)	k_i'	k_i''	tan δ	Ice Source
35.3	1.91 ± .03	$<4 \times 10^{-3}$	$<2.1 \times 10^{-3}$	deionized H_2O
94.5	1.88 ± .02	$<1.53 \times 10^{-3}$	$<8.1 \times 10^{-4}$	deionized H_2O
35.3	1.89 ± .03	1.14×10^{-1}	6.03×10^{-2}	Tap H_2O
94.5	1.91 ± .02	6.4×10^{-2}	3.35×10^{-2}	Tap H_2O

TABLE 4-3

Millimeter Wave Dielectric Constants of Ice
(Blue, 1979)

Frequency(GHz)	k_i'	$n = \sqrt{k}$
99	$3.17 \pm .27$	$1.78 \pm .08$
136	---	1.78
183	---	1.78

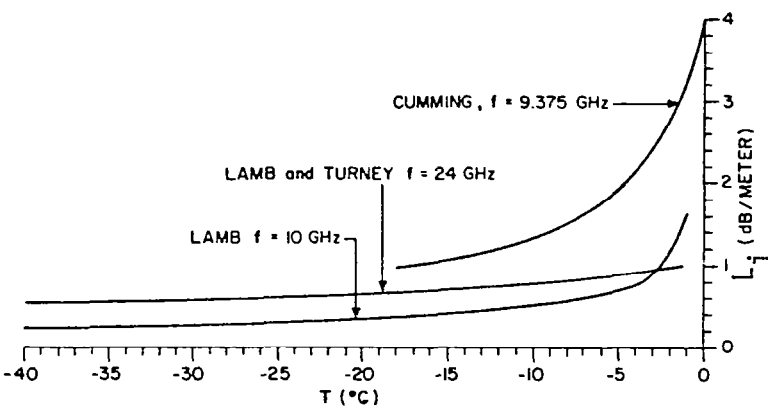


Figure 4-6 Rate of attenuation in ice as computed using loss tangents. (Royer, 1973)

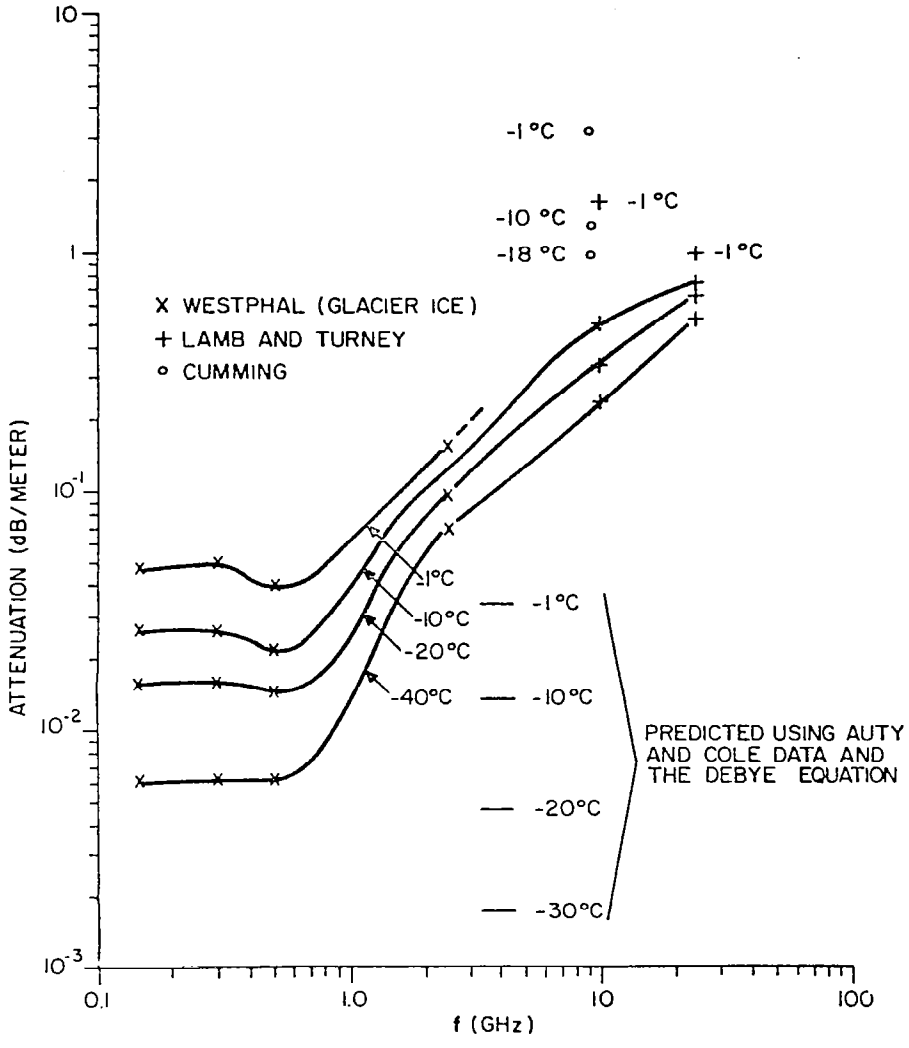


Figure 4-7 Attenuation in ice. (Royer, 1973)

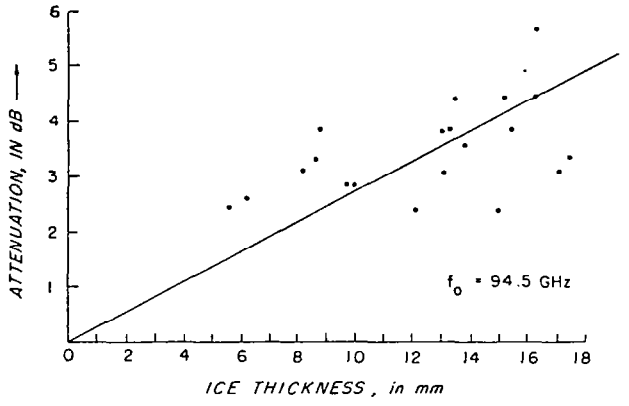


Figure 4-8 Attenuation curve (CP ice). (Perry and Straiton, 1971)

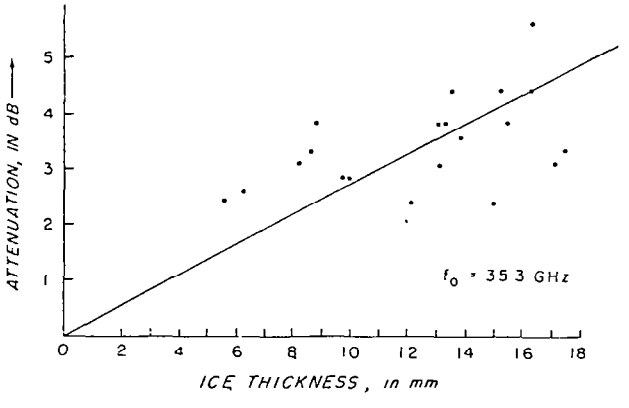


Figure 4-9 Attenuation curve (tap-water ice). (Perry and Straiton, 1971)

4.3 Dielectric Mixing Formulas

The dielectric properties of snow are difficult to quantify. In addition to the varying volumetric proportions of ice, water, and air, structure is a significant factor. Several mixing formulas have been proposed. Table 4-4 (Poe, 1971; Sweeny and Colbeck, 1974) is a summary of formulas for the dielectric properties of a mixture consisting of two components. The form number F is introduced to account for structure in the dielectric medium. No frequency dependence is inherent to these mixing formulas. As the wavelength of interest approaches the order of the snow crystal size, scattering effects may become significant and the form number may require different values as a function of frequency.

The Weiner (1910) formula was used by Evans (1965) to fit the dielectric constant data of dry snow. The variation in structure, which can be modeled with the form number, may be seen in Figure 4-10. The numerical values of the form number can vary from F = 0 (vertical particles), to F = 2 (spherical particles), to infinity (for elongated horizontal particles). Values for freshly fallen snow are normally between 2 and 10 (Evans, 1965). Royer (1973) also used the Weiner formula and found that F = 3.5 gave a good fit to Cumming's data for k'_s. Prediction of the imaginary part of the dielectric constant was found to be less accurate; F = 2 was an approximate fit. A deficiency of the Weiner formula is that different values of the form number are required for k'_s and k''_s.

The Bottcher formula was used by Cumming (1952) to fit the real part of the dielectric constant of dry snow at 9.375 GHz. Lack of structure dependence limits this formula's general applicability.

Edgerton, et al. (1971) used the wet snow (Weiner) formula to represent the dielectric constant of wet snow. The best fit for their data was obtained with F = 32.

The Pierce formula has not been applied specifically to snow. The deLoor formula has been employed by Sweeny and Colbeck (1974) to fit wet snow data at 6 GHz. This formula is more complex than the other formulas in that it can represent a three parameter three-dimensional structure. The model is valid for a mixture of ellipsoidal particles with varying size within a dielectric medium. The A_j are the depolarization factors for the particles for each of the three axes. Another benefit of this model is the allowance for bound water. Since a fraction of the water

TABLE 4-4

Mixing Formulas

Weiner:

$$\frac{k_{ds} - 1}{k_{ds} + F} = \rho_i \frac{k_i - 1}{k_i + F} + (1 - \rho) \frac{k_o - 1}{k_o + F}$$

where: ρ_i = volumetric fraction of ice

k_o = dielectric constant of air

k_i = dielectric constant of ice

k_{ds} = dielectric constant of dry snow

F = form number

Bottcher:

$$\frac{k_{ds} - k_o}{3\, k_{ds}} = \rho_i \frac{k_i - k_o}{k_i + 2\, k_{ds}}$$

Wet Snow (Weiner):

$$k_{ws} = \frac{k_w \rho_w U + k_{ds} (1 - \rho)}{\rho_w U + (1 - \rho_w)}$$

where:

$$U = \frac{k_{ds} + F}{k_w + F}$$

k_{ws} = dielectric constant of wet snow

k_w = dielectric constant of bulk water

ρ_w = volumetric fraction of water

Pierce:

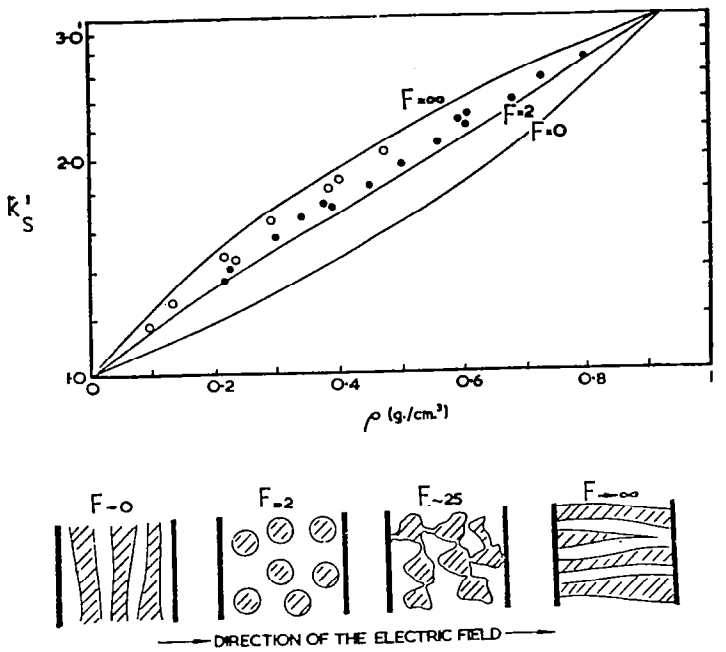
$$k_{ds} = k_i + \frac{(1 - \rho_i)(1 - F)}{1 - (1 - \rho_i)F} (k_o - k_i)$$

deLoor

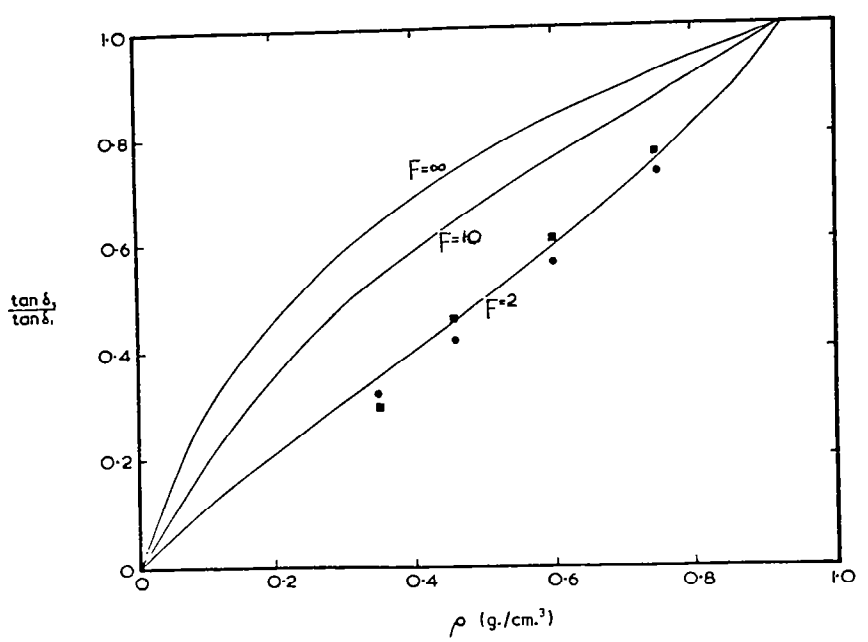
$$k_{ws} = k_{ds} + \frac{\rho_w}{3} (k_w - k_{ds}) \sum_{j=1}^{3} \frac{1}{1 + \left[\left(\frac{k_w}{k_n}\right) - 1\right] A_j}$$

where: k_n = dielectric constant of bound water

A_j = particle depolarization factor for each of the three major axes (Sweeney and Colbeck, 1974)



Relative permittivity of snow (ordinates) vs. density (abscissa). The upper curves are computed as explained in section 2.4 for snow particles having the characteristic Formzahl values u = 0, 2, 10 and ∞ in Weiner's formula and taking the relative permittivity of solid ice to be 90 at low frequencies. The lower curves are for the limiting value of the permittivity at high frequencies, taken to be 3.2 for solid ice. Measured valued: 0 due to Kuroiwa (1956) at frequencies less than 1 Mc/sec. and at 3 Mc/sec., due to Cumming (1952) at 9.375 Mc/sec. The sketches beneath the graphs show how snow structure is related to the Formzahl.



Loss tangent of snow versus density (abscissa). The quantity plotted vertically is the ratio of the loss tangent of the ice/air mixture forming snow to that of the solid ice. Smooth curves are plotted for different values of the Formzahl in Weiner's formula assuming that tan δ is much less than unity for the solid ice considered. Measured values are due to Cumming (1952) at 9.375 Mc/sec., at 0°C, at -8°C.

Figure 4-10 Dielectric properties of dry snow. (Evans, 1965)

is bound to the ice crystals in the snow, its dielectric constant is effectively reduced from its bulk properties. Therefore, models which treat all water as unbound cannot accurately predict dielectric constant.

4.4 Dielectric Constant of Dry Snow

Figure 4-10 shows measured values of the real part of the dielectric constant k_s of dry snow as a function of snow density. The loss tangent $\tan \delta_s$ normalized to the loss tangent of ice is also shown in Figure 4-10. As density increases, the real part and loss tangent approach the values for ice. Since the real part of the dielectric constant of ice was temperature independent, the real part of the dielectric constant of snow is also independent of temperature. The temperature dependence of $\tan \delta_s$ is illustrated in Figure 4-11. The data for these curves were obtained from measurements of reflection and transmission from a snow-filled waveguide section (Cumming, 1952). Edgerton, et al. (1971) fit Cumming's loss tangent data of dry snow with the following polynomial:

$$\tan \delta_s = 0.756 \times 10^{-9} \exp \left\{ 0.0574\ T + \frac{3.277}{A^2} - \frac{4.67}{A^3} + \frac{1.55}{A^4} \right\} \qquad (4\text{-}10)$$

where $A = (273.5 - T)$ and T is temperature in K for $T < 273$ K.

Table 4-5 gives results of later experiments reported by Edgerton, et al. (1971). These measurements were made using an ellipsometer to measure reflection coefficient. The ellipsometer operates at a fixed angle of incidence and measures the bistatic reflection coefficient as a function of polarization rotation around the axis of propagation. Calculations then yield the real and imaginary parts of k_r.

As previously mentioned in the mixing formula section, scattering may cause a frequency dependence in snow which is not explicitly accounted for by present measurement techniques or mixing theory. Effects of crystal size have not to date been experimentally quantified. Therefore, measurements are required to determine the variation of the dielectric constant of snow with frequency and to quantify the scattering loss in the snow medium.

Attenuation calculations through snow referenced to ice were made by Royer (1973) using Cumming's data and are shown in Figure 4-12. At 35 GHz however, the scattering loss can make the attenuation through snow greater than the attenuation through ice. Section 4.6 covers the attenuation measurements on snow.

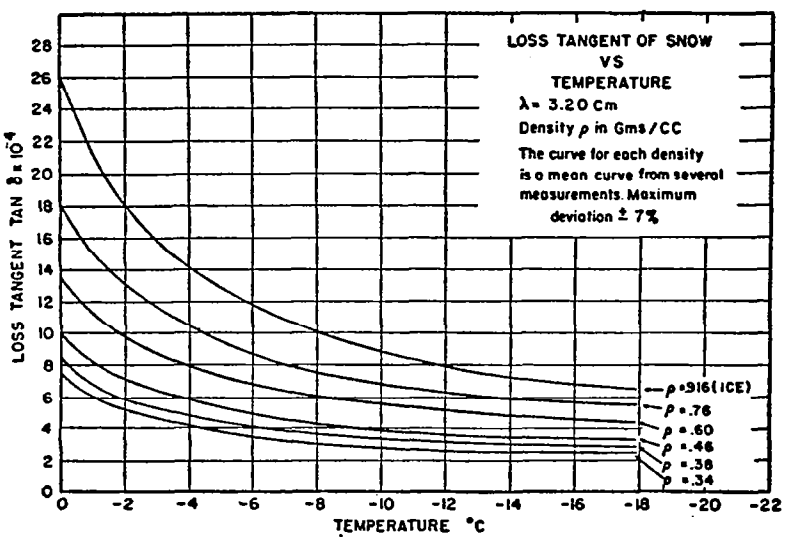


Figure 4-11 Variation of loss tangent of snow with temperature. (Cumming, 1952)

Table 4-5

Dielectric Constant of Dry Snow

Freq (GHz)	k'_s	k''_s	Temp°C	Density g/cm^3	Grain Size (mm)	Source
37	2.77*	<.03	- 2	.5	1-2	Edgerton et al. (1971)
13.6	2.76*	<.03	-20	.52	.5-1.0	Edgerton et al. (1971)
37	1.9	<.05	-10	.5	.5	Edgerton et al. (1971)
13.6	2.3	<.06	-10	.5	.5	Edgerton et al. (1971)

*The high values were explained as resulting from difficulty in sample preparation.

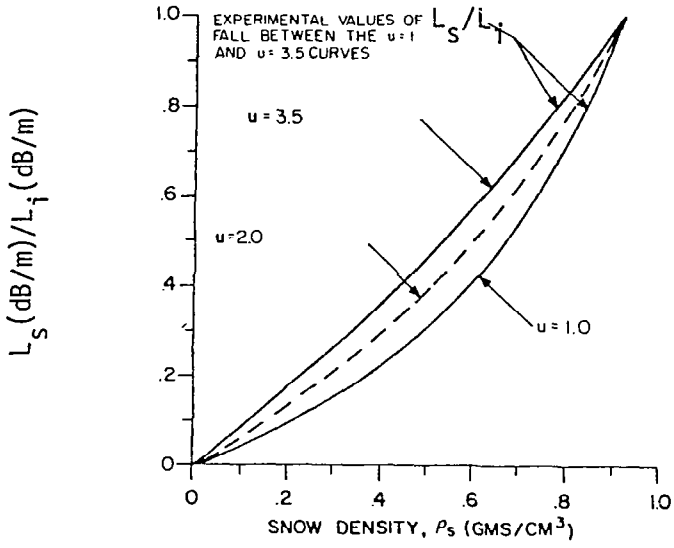


Figure 4-12 A comparison between the rates of attenuation in snow and ice. $F=u$ = 3.5 for computing k'_s/k'_i (Royer, 1973)

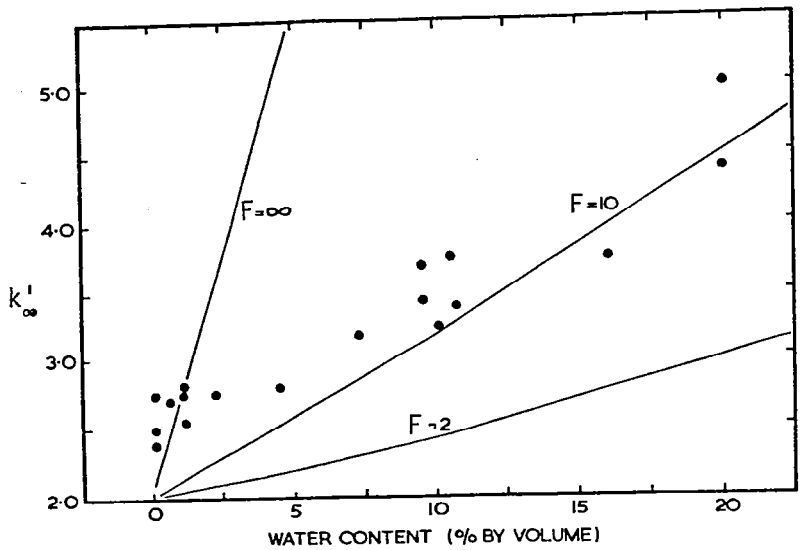
4.5 Dielectric Properties of Wet Snow

Small amounts of free water can significantly change the dielectric properties of snow. Experimental data compiled by Evans (1965) are illustrated in Figure 4-13. The Weiner mixing formula was applied with $k_o = 2.0$ (dry snow) and $k_i = 80$ (water). The Weiner model is observed to be a poor fit at low wetness values; however, this problem was believed to be due to a systematic error in the wetness measurements. Wetness measurement of snow is an arduous problem, which is examined in detail in section 6.3.1.3. The variation in loss tangent is shown in Figure 4-13 to increase with density.

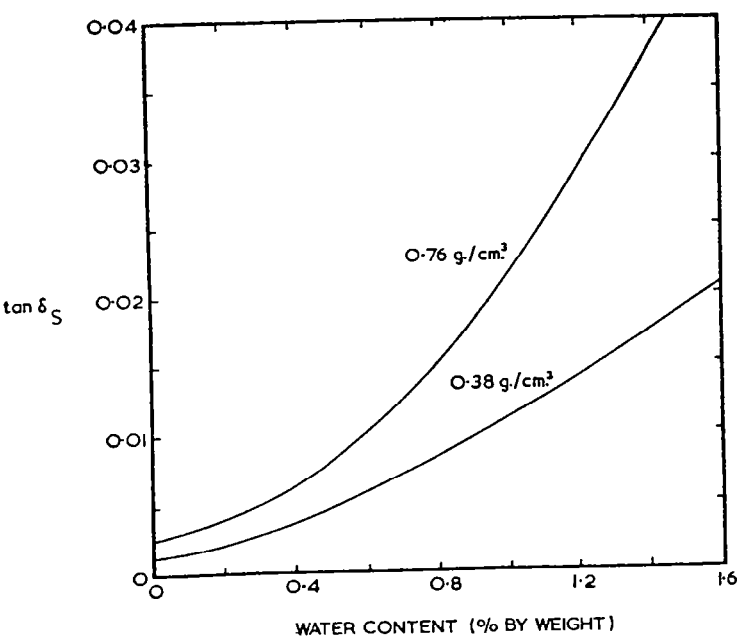
Sweeney and Colbeck (1974) made measurements of the dielectric constant of wet snow at 6 GHz using a microwave slotted line waveguide technique. Measurements with and without the sample inside a shorted waveguide section allow calculation of the dielectric constant (assuming no scattering loss). Their results for wet snow are illustrated in Figure 4-14. The scatter of the data points was believed to be the result of sample preparation problems. In order to decrease the scatter and to permit application of a model, glass beads were measured (Figure 4-15). The deLoor mixing formula fits the data well except near the saturation end of the curve. The imaginary parts of the snow and glass bead data are surprisingly similar, indicating that at least at this frequency wetness is the dominant loss factor. The difference in the real parts is a result of the dielectric constants of the support medium and the free water.

In another attempt to simplify the measurement problem and to approximate the structure of dry snow, Linlor (1975b) made measurements at 9.3 GHz using foam rubber as the supporting medium. Results for the real part are shown in Figure 4-16. This method allowed easy measurement of moisture; the drawback is the neglect of any interaction that occurs between free water and the ice crystal structure. Also, for zero wetness, an offset is observed if a comparison is made with dry snow.

Reliable measurements of the dielectric constant above 10 GHz of wet snow are non-existent and therefore need to be measured.



Permittivity of wet snow at high frequencies (ordinates) vs. volume percentage of liquid water (absciss The permittivity of the dry snow is assumed to be 2.0 corresponding to specific gravity of approximately 0.5. The continuing lines are calculated from Weiner's mixing formula and the measured values are due to Kuroiwa (1956). There is a system error in his measurement of the free water content. Ambach (1963, p. 174-177) has given result for snow of much lower density.



Loss tangent of snow (ordinates) vs. free water content in per cent by weight (abscissa). Mean curves are shown for two snow samples of denisty 0.76 and 0.38 g/cm^3, temperature 0°C, radio frequency 9.375 Mc/sec (after Cumming, 1952).

Figure 4-13 Dielectric properties of wet snow. (Evans, 1965)

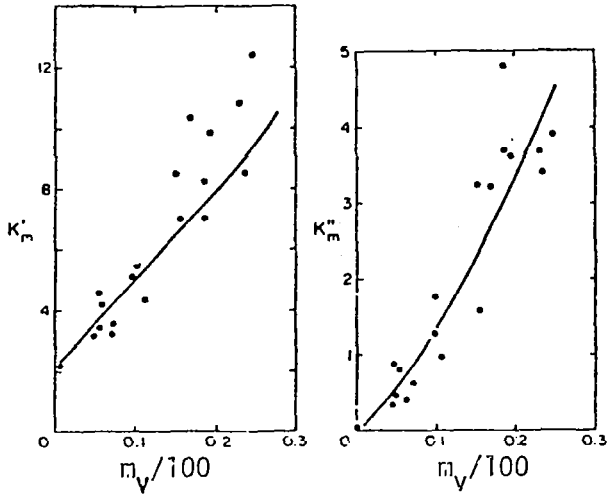


Figure 4-14 Effective dielectric constant (a) and loss factor (b) shown as a function of water content for the wet snow samples. The data points and theoretical curves are shown. (Sweeny and Colbeck, 1974)

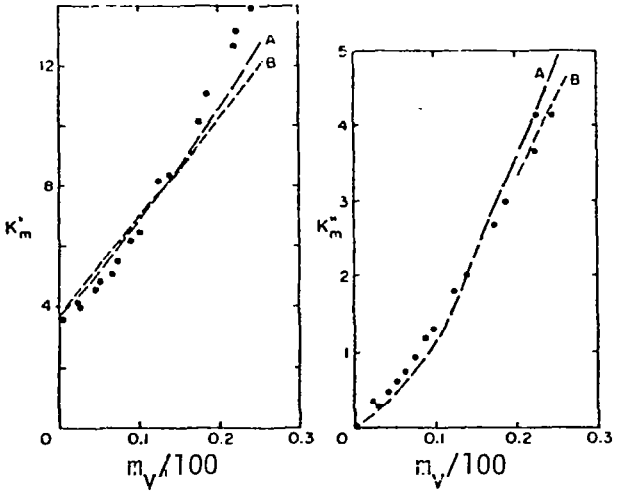


Figure 4-15 Effective dielectric constant K'_m and loss factor K''_m versus liquid water content for the glass bead samples. The experimental points and two theoretical curves are shown. (Sweeny and Colbeck, 1974)

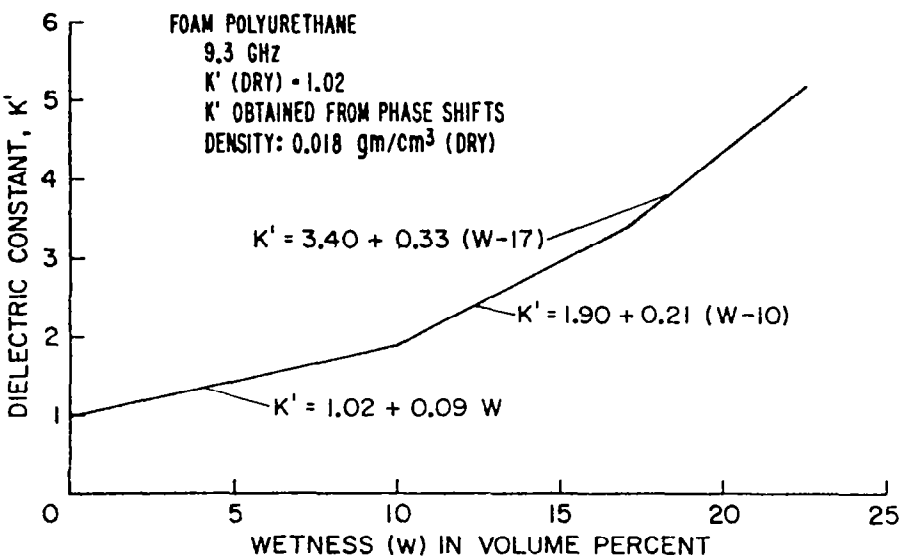


Figure 4-16 Dielectric constant of foam rubber with varying wetness. (Linlor, 1975b)

4.6 Attenuation Through Snow

Attenuation resulting from absorption is given by equations 2-4 and 2-5. For the case of dry snow or even wet snow, experimental evidence indicates that:

$$k_s'' << k_s' \tag{4-11}$$

With this condition:

$$\alpha_a = \frac{\pi k_s''}{\lambda \sqrt{k_s'}} \tag{4-12}$$

Attenuation rate in db/m is given by:

$$L = -8.68\ \alpha_a \tag{4-13}$$

The field skin depth D is given by $1/\alpha_a$, therefore:

$$D = \frac{\lambda \sqrt{k_s'}}{\pi k_s''} \tag{4-14}$$

Figure 4-17 shows skin depth calculations for wet snow and glass beads from Sweeney and Colbeck (1974) and wet foam rubber from Linlor (1975b). Good agreement is observed among the sets of data. At higher frequencies, where snow structure is known to be a factor, the data on pseudo-snow would probably not be as valid. Figure 4-18 illustrates the same data plotted as attenuation rate. The University of Kansas data will be discussed in Chapter 9.

If power loss measurements are made through a layer, this loss is composed of two parts, mismatch loss and attenuation loss. Moreover, since the measurement is performed with coherent transmission, the two types of losses cannot be easily decoupled (even with multiple thickness measurements) because of the interference effects caused by multiple reflections, unless the measurements cover a wide range of thickness at intervals smaller than the propagation wavelength in the snow medium. Most "attenuation" measurements made on snow have been performed at a single frequency and a single thickness. Valid attenuation rates cannot be determined from these values.

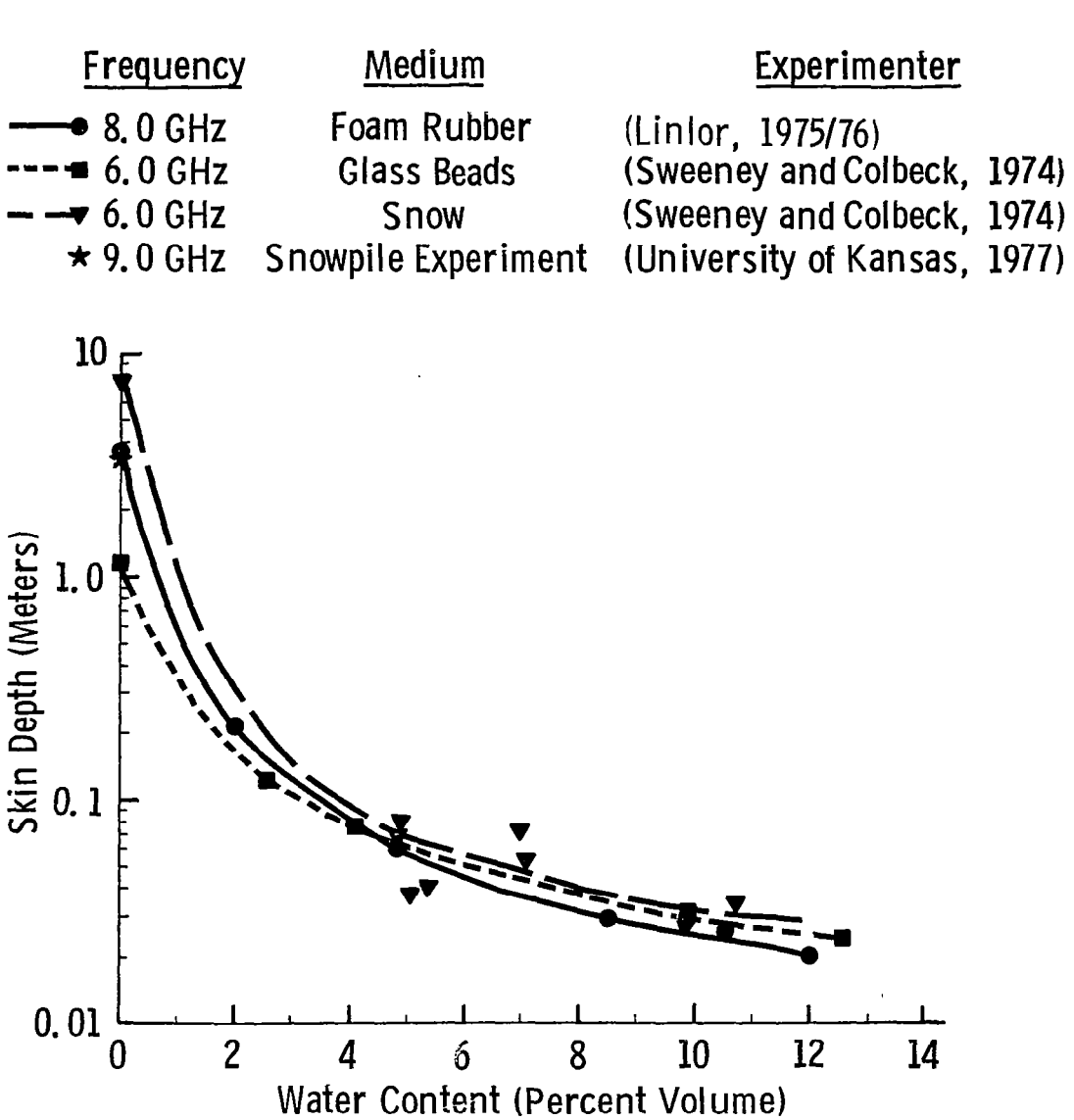


Figure 4-17 Skin depths calculated from Linlor's (1975b) data and Sweeny and Colbeck's (1974) data.

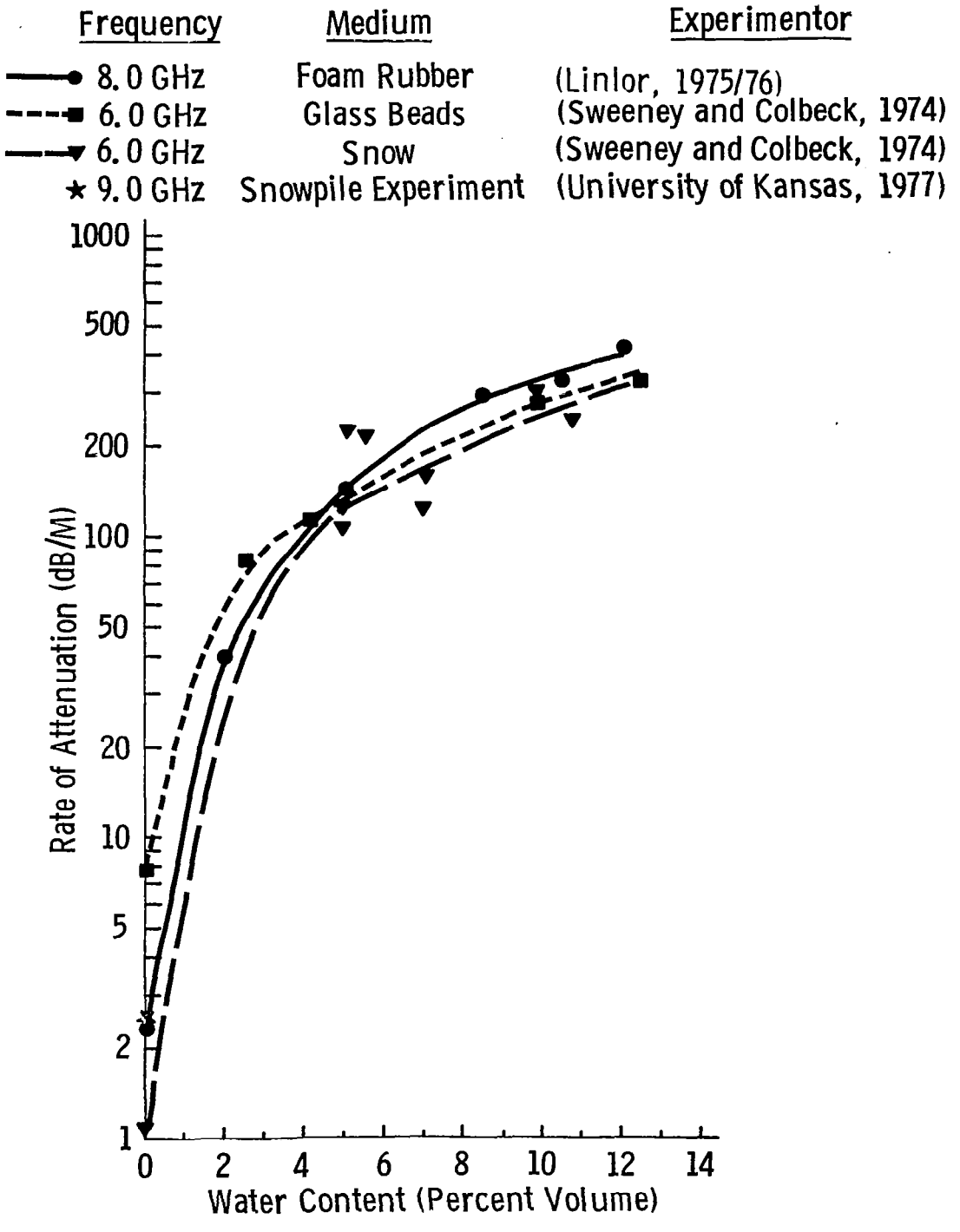


Figure 4-18 Attenuation rates in dB/m for wet snow and psuedo-snow.

Battles and Crane (1965, 1966) employed interferometry techniques at frequencies between 31 and 38 GHz to measure loss from artifically creat snow. The loss was measured as a function of temperature and is illustrate in Figure 4-19. The loss shows a slow decrease with decreasing temperature for dry snow. This result is expected and correlates with the results for ice (Figure 4-6). A dramatic increase in the loss is seen as the temperature nears the melting point and some moisture appears at the surface. To investigate the loss for different types of snow, Battles and Crane (1966) artificially created snow with four different densities. The results are given in Table 4-6. The higher losses for the locally packed and ice crystal cases were postulated to be the result of scattering, which in some cases, causes the loss through snow to be larger than through ice.

Currie, et al. (1977) made measurements using pulsed radars operating at 35 and 95 GHz. Table 4-7 presents the data used for calculating attenuation rate. Their attenuation rates were calculated by comparing the return from a corner reflector positioned behind a wall of snow with the return measured from the same corner reflector placed above the wall of snow. The loss through a 3.5 cm layer of dry snow crust was measured to be 3 dB. Then an attenuation coefficient of 43 dB/m was calculated. For the low loss (3 dB) case, however, mismatch could be the dominant loss factor. Therefore extrapolation of loss measurements to attenuation rate is not valid. Linlor (1975b) made loss measurements at several frequencies on foam rubber to approximate the snow structure (Figure 4-20). An equivalent method to the multilayer procedure of decoupling the two loss terms is the use of multifrequency loss measurements.

As a result of the lack of appropriate theories to model the dielectric behavior of snow and as a result of the paucity of reliable data, the relationship of physical snow parameters to dielectric propertie is dubious. Inferences can be made, however comprehensive measurements are needed.

4.7 Dielectric Properties of Soils

If the penetration depth of the active or passive microwave system is greater than the snow depth, then effects of soil conditions must be considered. The relative dielectric constant of soils may be modeled by

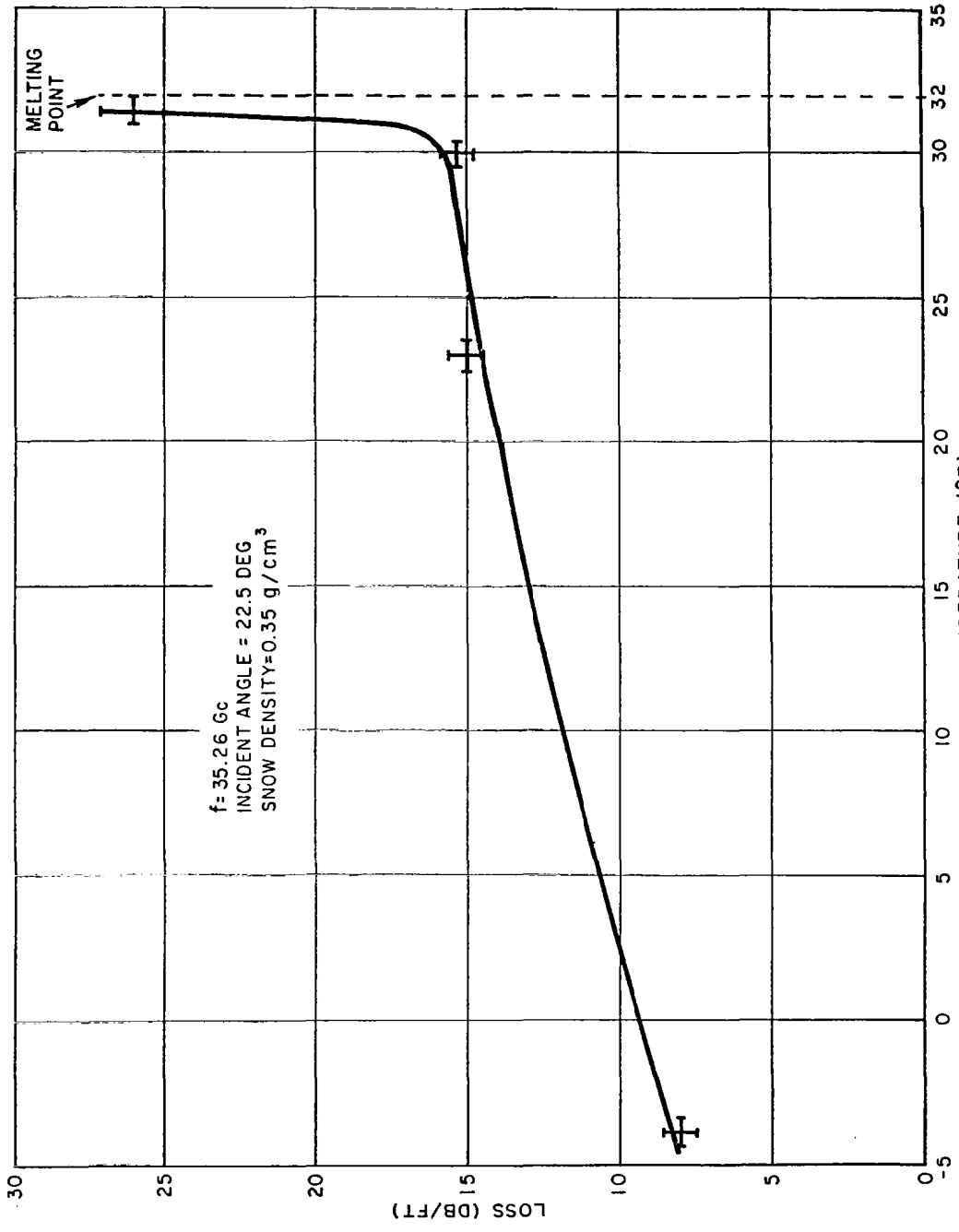


Figure 4-19 Absorption of radiation by snow as a function of temperature. (Battles and Crane, 1965)

Table 4-6

Loss Caused by Snow and Ice (Battles and Crane, 1966)

Type	Thickness (cm)	Density (g/cm^3)	Loss (dB)
Fine loose snow	14.0	.2	2.5
Locally packed loose snow	14.0	.33	7.2
Large ice crystals	14.0	.39	9.2
Packed snow	14.0	.47	1.4
Ice	5.1	.92	1.2

Table 4-7

Loss Measurements at 35 and 95 GHz (Currie et al., 1977)

Snow Condition	Frequency	Layer Thickness (cm)	Loss (dB)
Wet Snow	95	6.0	30
Dry Snow Crust	35	4.6	21
Dry Snow Crust	35	5.0	5
Dry Snow Crust	95	5.0	30
Dry Snow Crust	35	3.5	3
Wet Snow Crust	35	3.5	11

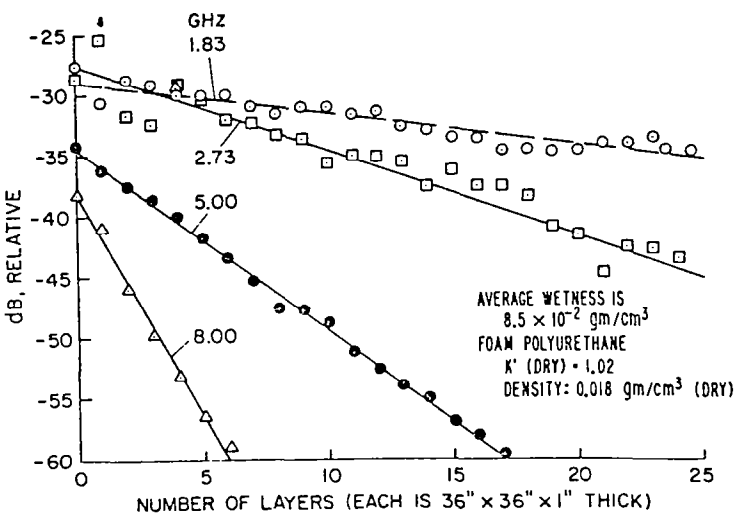
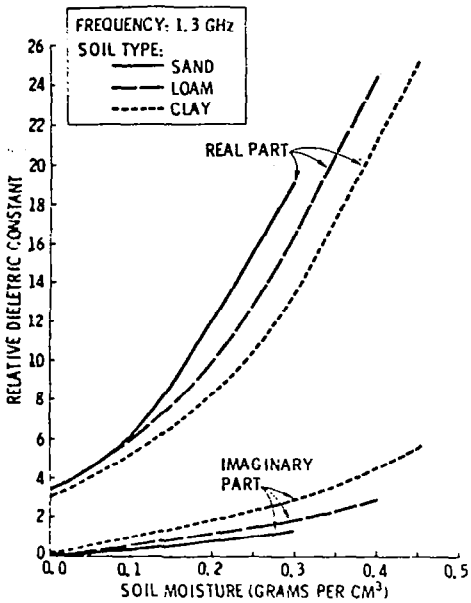
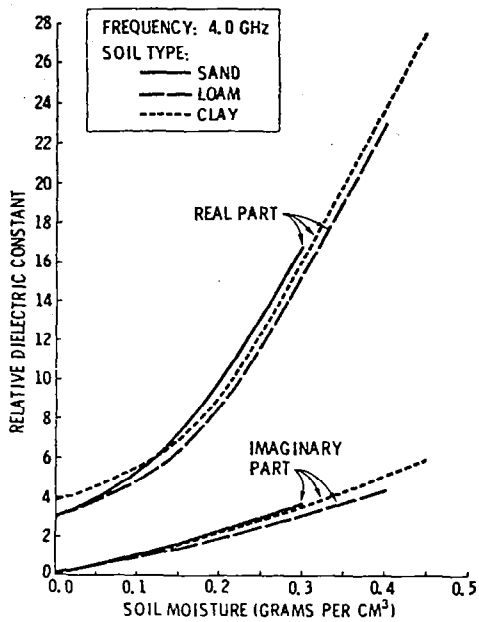


Figure 4-20 Microwave beam intensity versus thickness of wet foam polyurethane. (Linlor, 1975b)

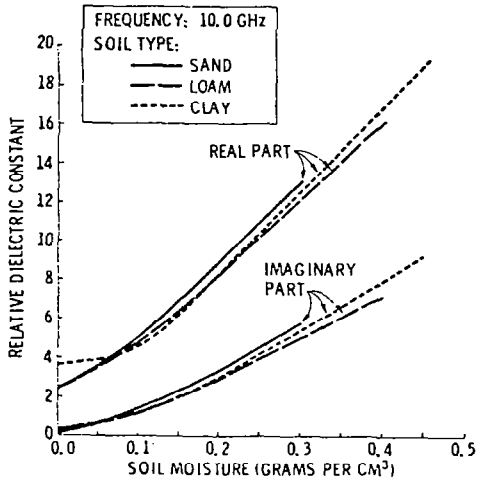
the same mixing formulas of Section 4.3. The dielectric constant is a function of soil type and soil moisture content. The dominant parameter is moisture content. Figure 4-21 illustrates the sensitivity to soil moisture. The temperature of the soil also determines the state of the moisture in the soil (ice or water) and therefore the dielectric constant. Figure 4-22 shows the effects of temperature. Skin depth as a function of soil type, frequency, and soil moisture is given in Figure 4-23. Comparison with Figure 4-17 indicates that at low wetness, the skin depth in soil is less than the skin depth of snow. In Figure 4-23, 0.1 g/cm^3 is approximately 10 percent by volume. Therefore, at higher wetness values (greater than 10 percent) the skin depths are comparable. A detailed description of soil dielectric properties may be found in the work by Cihlar and Ulaby (1974).



Representative dielectric constant values as a function of volumetric water content for sand, loam, and clay at 1.3 GHz.

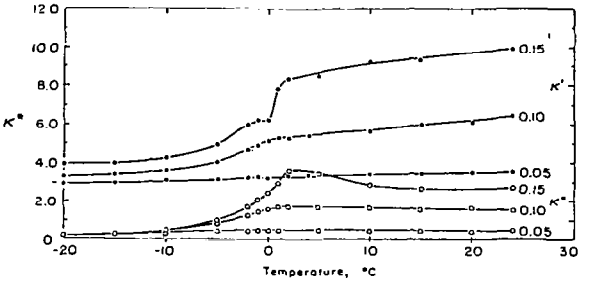


Representative dielectric constant values as a function of volumetric water content for sand, loam, and clay at 4.0 GHz.

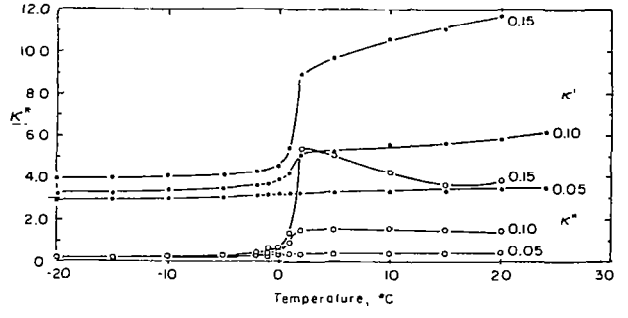


Representative dielectric constant values as a function of volumetric water content for sand, loam, and clay at 10.0 GHz.

Figure 4-21 Dielectric properties of soils. (Cihlar, 1974)



(a)



(b)

Figure 4-22 The complex dielectric constant at 10 x 10^9 Hz as a function of temperature at three water constants (g H_2)/g soil) for (a) Goodrich clay and (b) Fairbanks silt. (Hoekstra and Delaney, 1974)

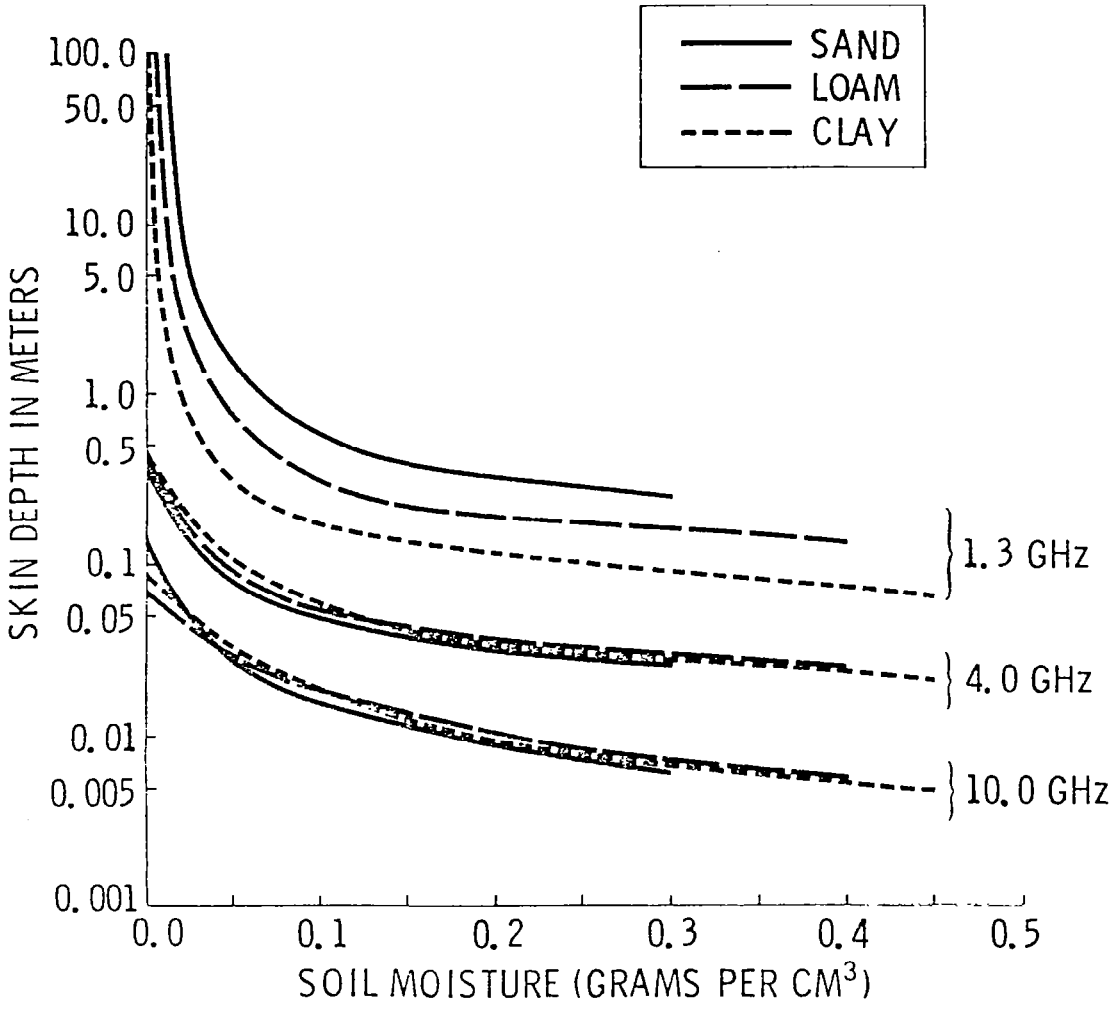


Figure 4-23 Skin depth as a function of volumetric water content, frequency, and soil type. (Cihlar, 1974)

5.0 REVIEW OF MICROWAVE MEASUREMENTS

Pioneering microwave measurements of snow were conducted in the 50's and early 60's (Cumming, 1952; Cosgriff, 1960). At that time, the knowledge of the microwave properties of snow was limited. Since that time, considerable progress has been made both in the accuracy and precision of the sensors and in the understanding of the interaction mechanisms. As this learning process advanced, more and more detailed ground truth has been required to further the understanding.

Several types of active and passive experiments have been conducted during the past twenty years. This section will review some of these investigations and compare experimenters' results whenever possible. The first part reviews reflection coefficient measurements; the second part covers snowpack stratigraphy profilers; the third part covers backscatter coefficient measurements; and the fourth part covers passive measurements. Table 5-1 summarizes the past microwave measurement programs.

5.1 Reflection Coefficient Measurements

In addition to his investigation of the dielectric properties of ice and snow, Cumming (1952) looked at the effects of snow on the magnitude of the reflection coefficient (Γ) at 9.375 GHz. He measured the reflection coefficient from a frozen sand surface without snow cover, with a 10-inch dry granular snow cover shown in Figure 5-1 and a 9-inch slightly moist (<.25%) snow cover illustrated in Figure 5-2. He concluded "that the reflection of the air-snow boundary was predominant" since the angular response did not show interference patterns and because of the agreement with calculated values assuming an infinite layer of snow. To separate the effects of snow and target, Cumming made reflection coefficient measurements on a flat metallic platform. For the case of wet snow cover shown in Figure 5-3, the attenuation through 10 inches of snow was high enough that the contribution of the reflection from the perfectly conducting plate was almost negligible. The reflection coefficient from the dry snow cover, shown in Figure 5-4, however, illustrated significant effects of multiple reflections in the snow layer. Hence, for backscatter measurements, snow tends to mask the underlying terrain unless the snow is dry and its thickness is small.

TABLE 5-1

Summary of Microwave Measurement Programs of Snow

TYPE OF MEASUREMENT	ORGANIZATION	YEAR	FREQUENCY	ANGLE OF INCIDENCE	REFERENCE
Reflection Coefficient	National Research Council, Canada	1952	9.375 GHz	40-88	Cumming (1952)
Reflection Coefficient	Japan	1958	4 GHz	88	Suzuki and Hasegawa (1958)
Reflection Coefficient	Naval Ordinance Laboratory	1966	35.26 GHz	22.5	Battles and Crane (1966)
Snow Stratigraphy--Short Pulse	Colorado State University	1972	2.7 GHz	0	Vickers and Rose (1972)
Snow Stratigraphy--FM-CW	Canadian Communication Research Center	1973	8-12 GHz	0	Venier and Cross (1972)
Snow Stratigraphy--FM-CW	National Bureau of Standards	1977	8-12 GHz	0	Ellerbruch et al. (1977)
Backscatter	Sandia Laboratories	1959	3.8 GHz	0-30	Janza et al. (1959)
Backscatter	Ohio State University	1960	10, 15.5 and 35 GHz	10-80	Cosgriff et al. (1960)
Backscatter	University of Alaska	1972	35 GHz	0-70	Sackinger (1972)
Backscatter	Cold Regions Res. and Eng. Lab.	1972	10, 35 and 95 GHz	89	Hoekstra and Spangole (1972)
Backscatter	Georgia Institute of Technology	1977	35 and 95 GHz	75-82	Currie et al. (1977)
Backscatter	Rome Air Development Center	1978?	35, 98 and 145 GHz	0-75	Hayes et al. (1979)
Backscatter	University of Kansas	1975	1-8 GHz	0-70	Ulaby et al. (1977)
Backscatter	University of Kansas	1977	1-18 and 35 GHz	0-70	Stiles et al. (1977)
Imagery (AN/APQ97)	University of Kansas	1970	35 GHz	----	Waite and MacDonald (1970)
SKYLAB S-193 Scatterometer	University of Kansas	1975	13.9 GHz	5	Eagleman et al. (1975)
Apparent Temperature	Aerojet General Corp.	1965 to 1971	1.4, 6, 13.4 and 37 GHz	----	Edgerton et al. (1971)
Apparent Temperature	University of Berne	1977	4.9, 10.5, 21, 35 and 95 GHz	0-65	Schanda and Hofer (1977)
Apparent Temperature	University of Berne	1978	4.9, 10.5, 21, 35 and 95 GHz	0-65	Matzler et al. (1979)
Apparent Temperature	Helsinki University of Technology	1978	4.8 and 36.8 GHz	0-70	Tiuri et al. (1978)
Apparent Temperature	NASA Goddard	----	1.4, 2.7, 5, 10.7, 19.3 and 37 GHz	45	Schmugge et al. (1974)
Apparent Temperature	NASA Goddard	1977	1.4, 17.6, 21.4 and 37 GHz	48	Hall, et al. (1978)
Apparent Temperature	NASA Goddard	1978	5, 10.7, 18, and 37 GHz	0-85	Shiue, et al. (1978)
ESMR	------	----	19.35 GHz	50	Gloersen and Salomonson(1975)
ESMR	------	----	37 GHz	50	Rango, et al. (1976)
Nimbus-5	------	----	22.2 and 31.4 GHz	0	Kunzi, et al. (1978)

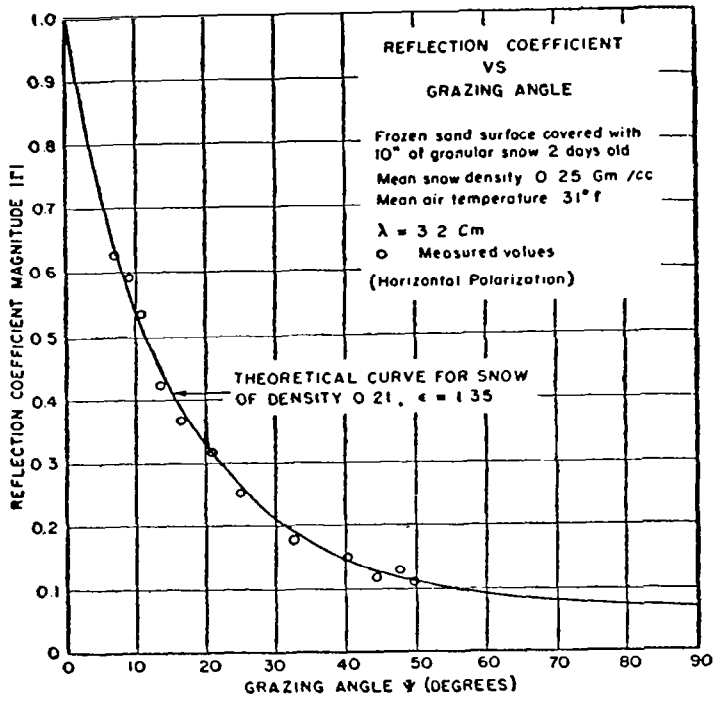


Figure 5-1 The reflection coefficient of a frozen sand surface covered with 10 in. of dry snow. (Cumming, 1952)

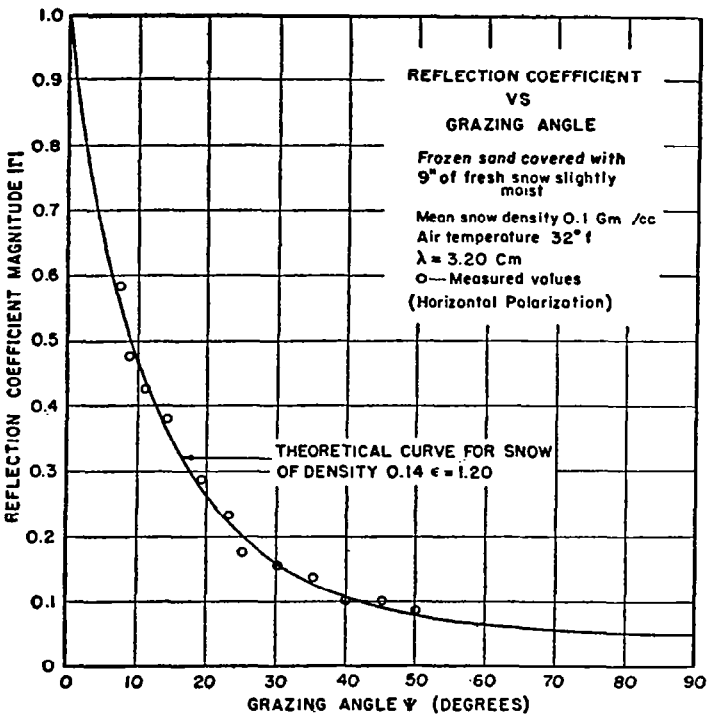


Figure 5-2 The reflection coefficient of a frozen sand surface covered with moist snow. (Cumming, 1952)

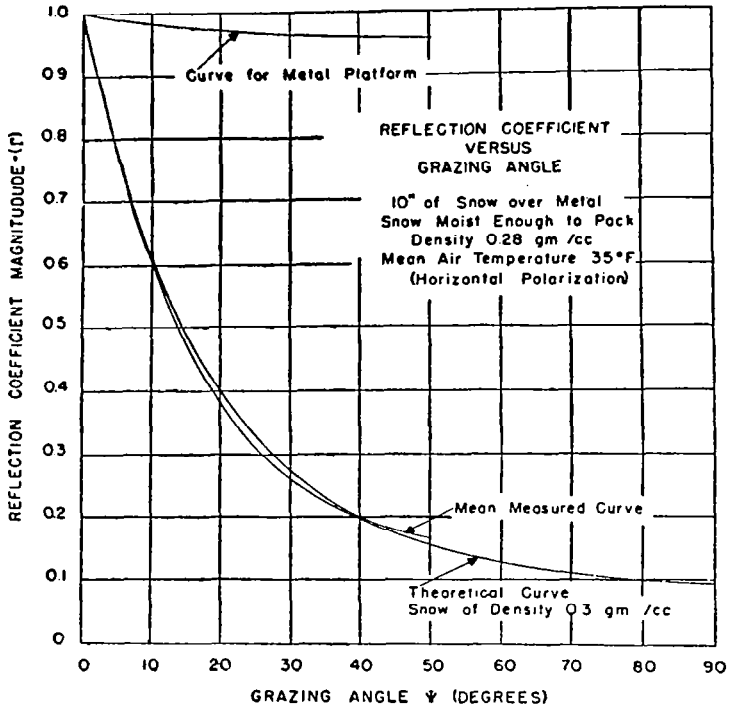


Figure 5-3 The reflection coefficient of a metallic surface covered with moist snow. (Cumming, 1952).

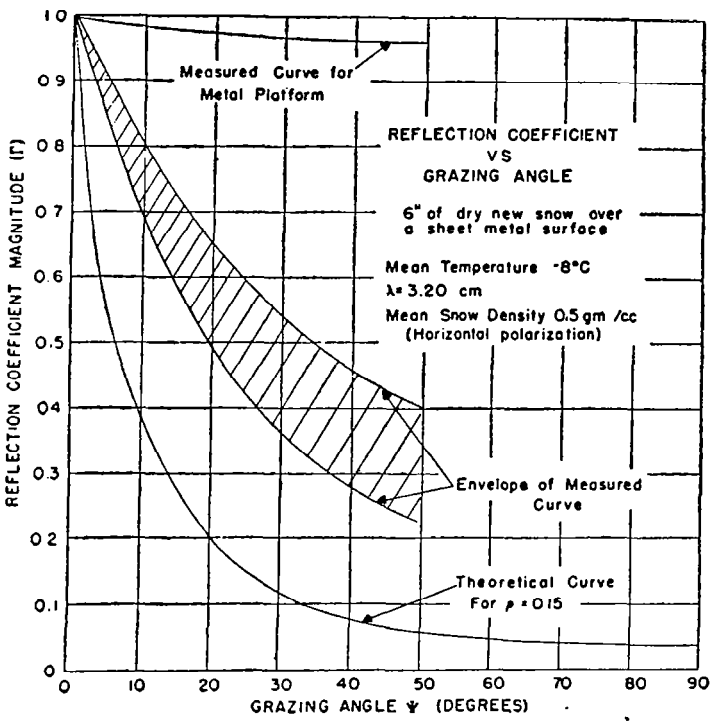


Figure 5-4 The reflection coefficient of a metallic surface covered with 6 in. of dry snow. Theoretical curve is computed for snow density ρ = 0.15 gm/cc. (Cumming, 1952)

The dependence of reflection coefficient of snow on air temperature gives some indication of the effects of snow wetness. Suzuki and Hasegawa's (1958) results at 4 GHz and a grazing angle of 2.25° are illustrated in Figure 5-5. A substantial increase in Γ is shown. The effects of the transition near the 0°C point seem too small. Figure 5-6 from Battles and Crane (1966) shows a much more dramatic effect near 0°C. These measurements, however, were at a much higher frequency (35.26 GHz) and closer to nadir (67.5° grazing angle). Only a small increase in Γ is observed for a temperature increase from -20°C to -1°C; then there is a dramatic rise for temperatures between -1°C and 0°C. This increase results from the appearance of free water.

5.2 Stratigraphy Measurements

These measurements use radar ranging to snowpack layer boundaries as a method of profiling and characterizing the snowpack. Abrupt changes in dielectric constant at layer boundaries will produce reflections. Both pulsed and FM-CW systems have been used.

Vickers and Rose (1972) used a short pulse (1 ns) 2.7 GHz radar to find the snow depth by measuring the two-way transit time of the radar pulse. Figure 5-7 shows snow depth estimated from their data with depth measured by a Gamma Ray nuclear profiler. A similar system has been used to measure lake ice thickness from a helicopter (Vickers et al., 1973).

FM modulation was used in an investigation conducted by Venier and Cross (1972) with the Canadian Communications Research Centre. The time delay (or range) to the snow surface and ground surface is translated to a frequency difference. Their system operated at nadir and was swept in frequency from 8 to 12 GHz. Figures 5-8a, 5-8b and 5-8c show examples of their measurements for dry snow, melting snow, and snow during a rain. The scattering coefficients of the snow surface were calculated to be -4 dB, 0 dB, and +4 dB, respectively.

The National Bureau of Standards (Ellerbruch et al. 1977 and 1978) also have employed an FM-CW system and a FFT processor to translate the results to time and then range. Figure 5-9 shows the radar and ground truth response profiles for a snow target.

These three experiments show that a short pulse or an FM-CW radar can be used to delineate layers within a snowpack. Quantitative analyses on the effects of snow density, snow wetness and crystal structure have not been performed.

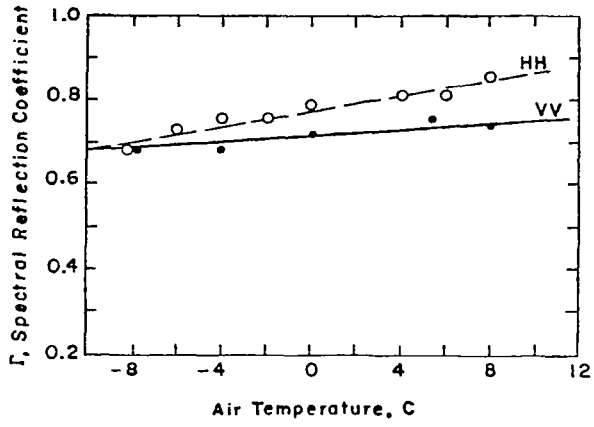


Figure 5-5 The amplitude of reflection coefficient of natural snow surfaces as a function of air temperature at a grazing angle of 2° 15' and a frequency of 4 GHz. (Suzuki and Hasegawa, 1958)

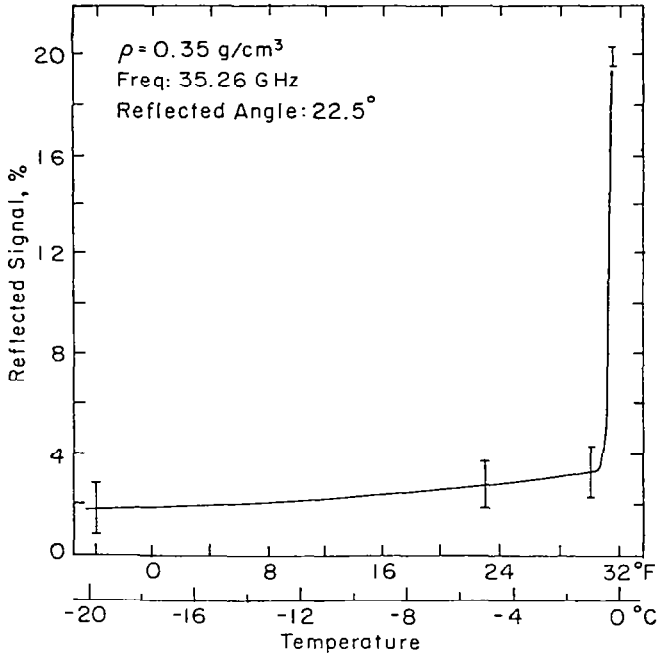


Figure 5-6 Measured reflection signal of snow as a function of temperature at a frequency of 35.26 GHz and an incidence angle of 22.5°. (Battles and Crane, 1966)

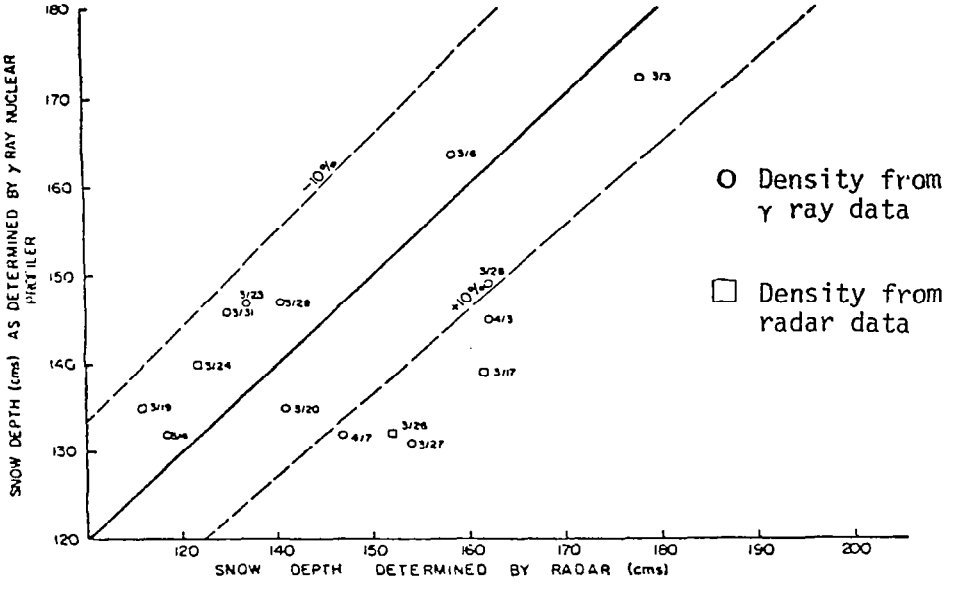


Figure 5-7 A comparison of radar and gamma ray determinations of snow depth. (Vickers and Rose, 1972)

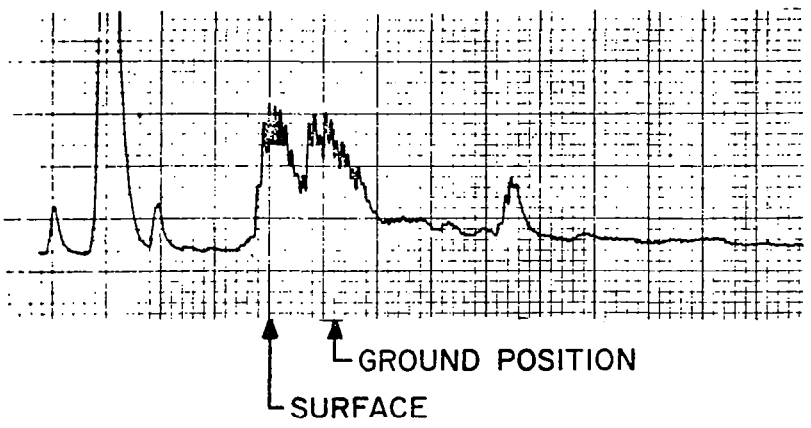


Figure 5-8a Data record of the snow and ground surfaces, temperature 28°F. (Venier and Cross, 1972)

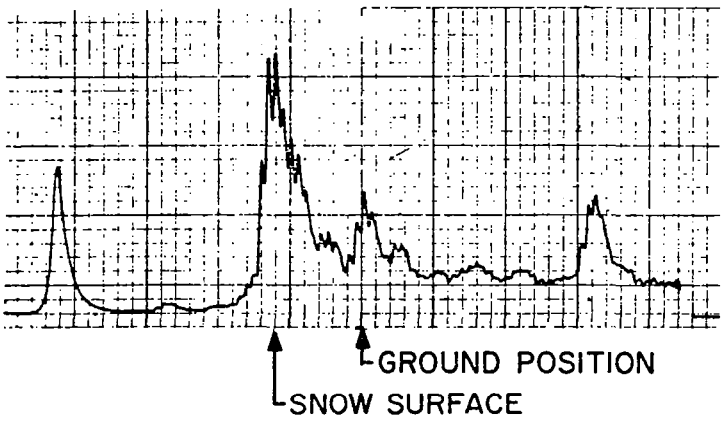


Figure 5-8b Data record of the snow and ground surfaces, snow melting. (Venier and Cross, 1972)

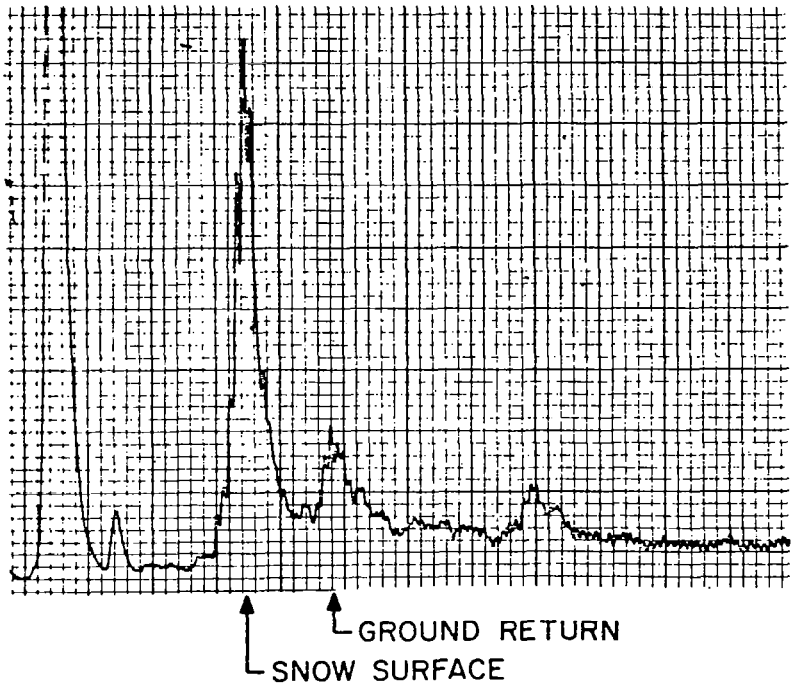


Figure 5-8c Data record of the snow and ground surfaces, raining. (Venier and Cross, 1972)

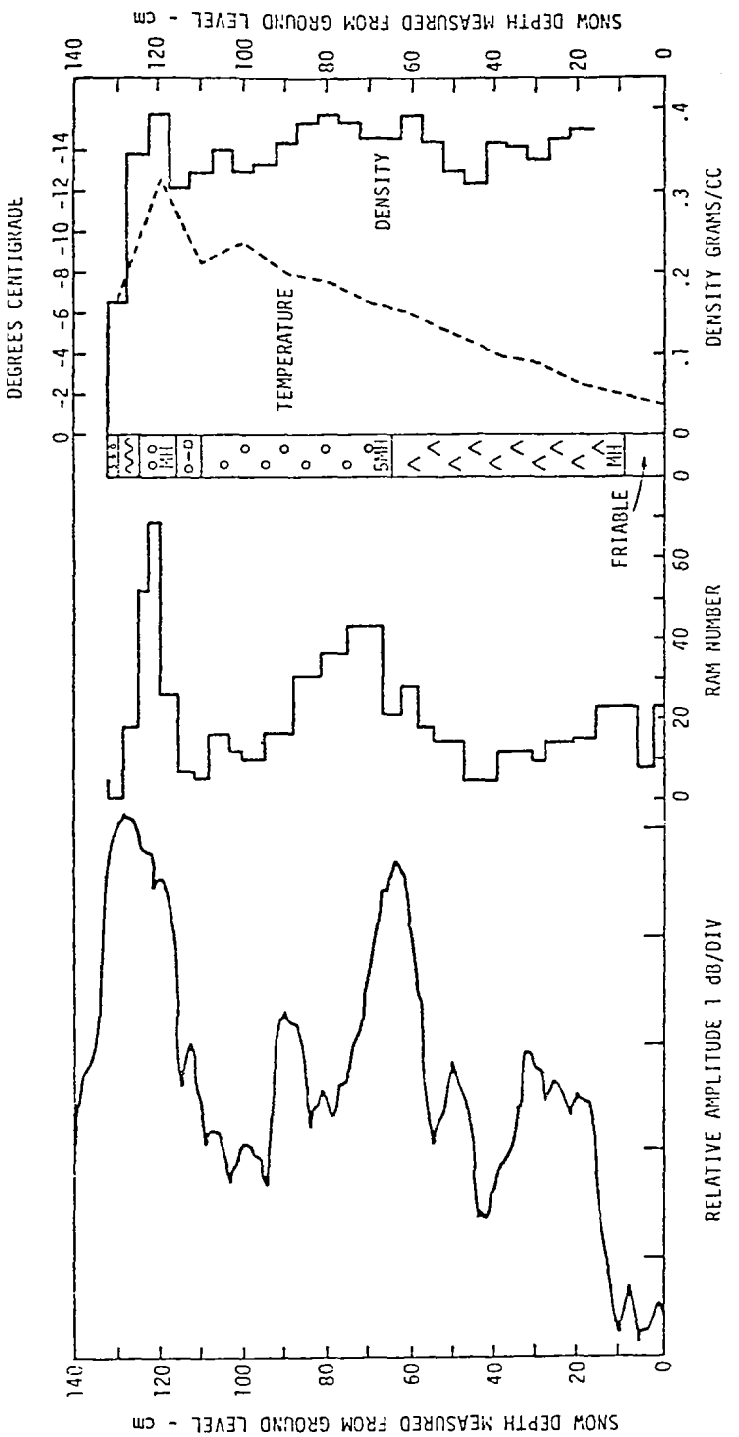


Figure 5-9 Profile data for a test site near Pass Lake. (Ellerbruch, et al., 1978)

5.3 Backscatter Measurements

Backscatter measurements will be stressed since these measurements have the greatest relevance to this investigation. Most of the measurement programs have been ground based. A brief section covers airborne and spaceborne observations.

5.3.1 Sandia Corporation

Early measurements on "snow covered farmland" were made by Sandia Corporation in 1959 (Janza et al., (1959)). Angular response at 415 MHz and 3.8 GHz were obtained. Since no other ground truth were acquired, no quantitative conclusions can be made.

5.3.2 Ohio State University

As a part of Ohio State Universitys' Terrain Handbook II which included backscatter measurements from a very wide variety of targets, Cosgriff et al. (1960), observed concrete and grass targets with and without snow cover. Data was obtained at grazing angles from 10° to 80° (angles of incidence from 80° to 10°) and at three frequencies: 10 GHz (X-Band), 15.5 GHz (Ku-Band) and 35 GHz (Ka-Band). The radar cross section per unit area γ was used to describe the terrain. These data are reproduced in Figures 5-10 to 5-21. The following observations can be made:

(1) In most cases, dry snow cover causes an increase in γ (Figures 5-13 to 5-21). The only exception is for HH polarization at Ku-Band on grass (Figures 5-17 and 5-21). This exception could be a result of a soil moisutre difference.

(2) Wet snow causes a decrease in γ of grass (Figures 5-10 and 5-11) of up to 17 dB at Ka-Band and 10° grazing angle.

(3) γ of dry rough snow is approximately 2 dB higher than the γ of smooth snow (Figures 5-13, 5-20 and 5-21).

The Ohio State University data for many years has provided useful information on the qualitative effects of snow cover. Quantitative conclusions about snow were not the objectives of the experiment.

5.3.3 University of Alaska

The backscatter behavior of snow-covered ice at 35 GHz was investigated by Sackinger (1972) of the Institute of Artic Environmental Engineering at the University of Alaska. The system operated in a amplitude modulated CW mode. The reported values of σ° are generally too high since they

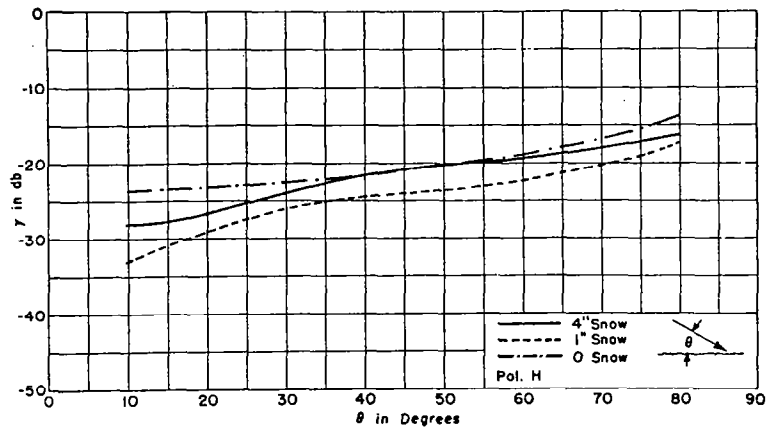


Figure 5-10 Effects of various depths of melting snow return from one-inch grass at X-band. (Cosgriff, et al., 1969).

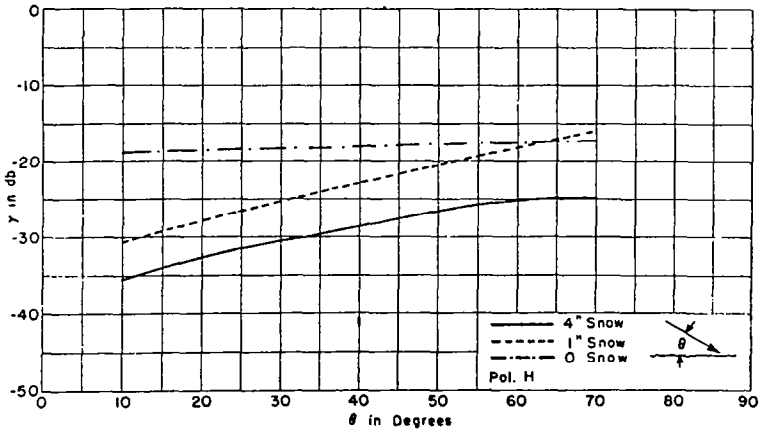


Figure 5-11 Effects of various depth of melting snow on return from one-inch grass at Ka-band. (Cosgriff, et al., 1960)

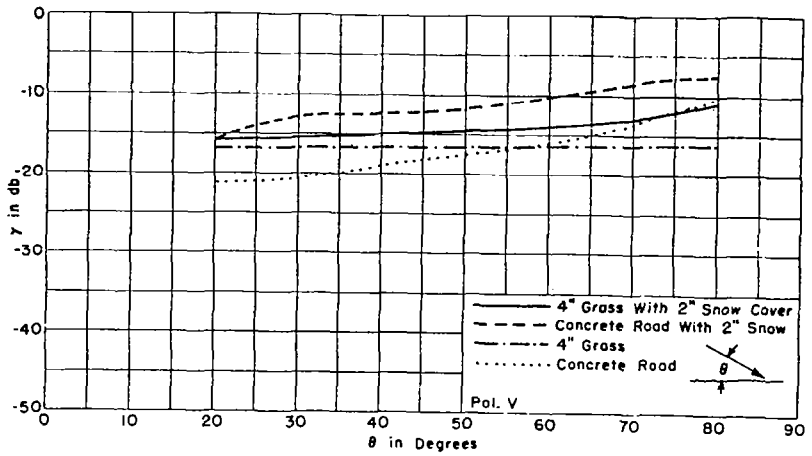


Figure 5-12 Effects of snow cover upon γ at Ka-band. (Cosgriff, et al., 1960)

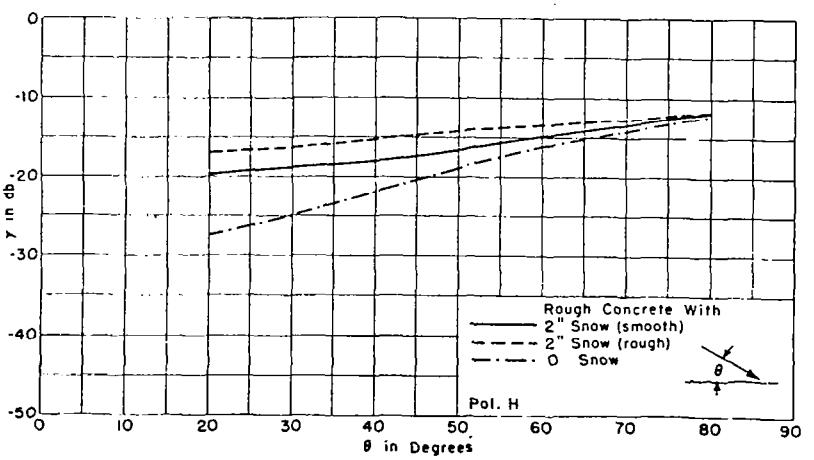


Figure 5-13 Effects of smooth and rough snow covers on a concrete road at Ka-band. (Cosgriff, et al., 1960)

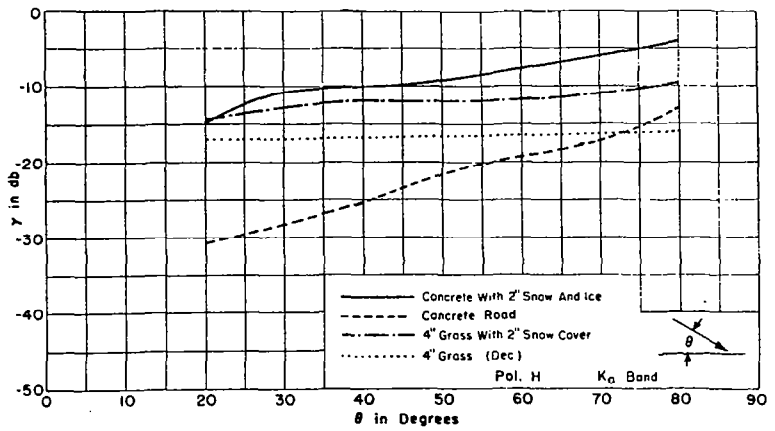


Figure 5-14 Effects of snow cover upon γ at Ka-band. (Cosgriff, et al., 1960)

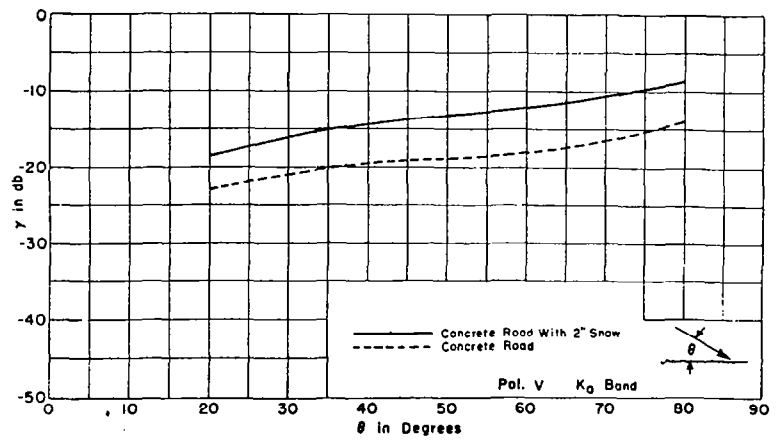


Figure 5-15 Effects of snow cover upon γ at Ka-band. (Cosgriff, et al., 1960)

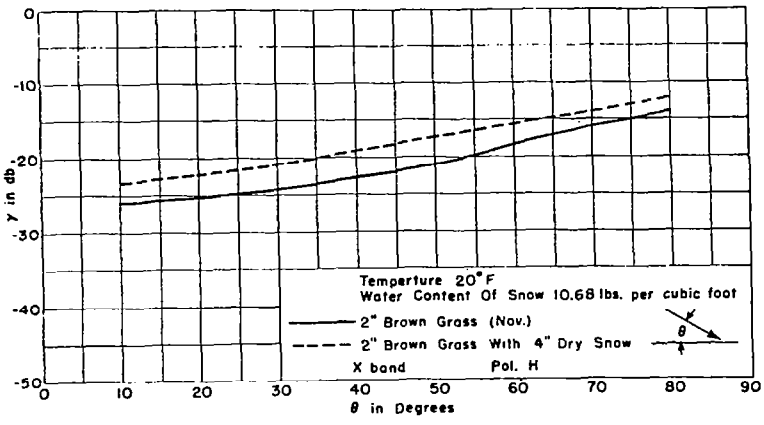


Figure 5-16 Effects of snow upon γ at X-band. (Cosgriff, et al., 1969)

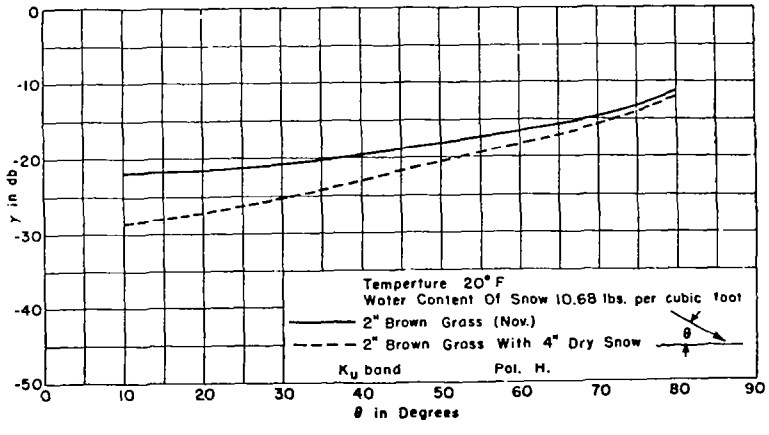


Figure 5-17 Effects of snow upon γ at Ku-band. (Cosgriff, et al., 1960)

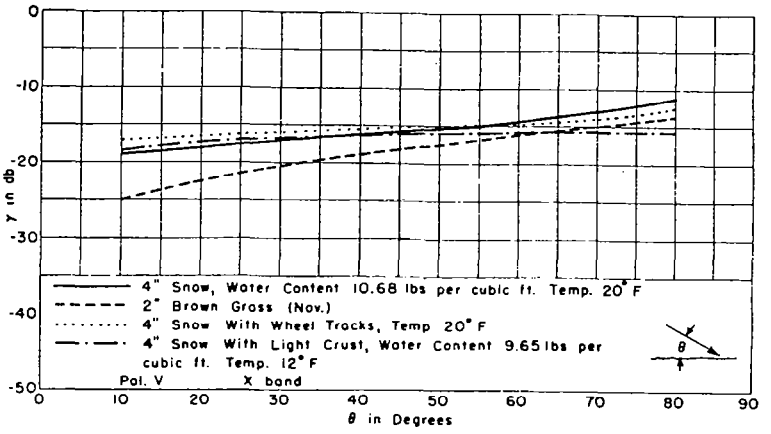


Figure 5-18 Effects of various types of snow cover upon γ at X-band. (Cosgriff, et al., 1960)

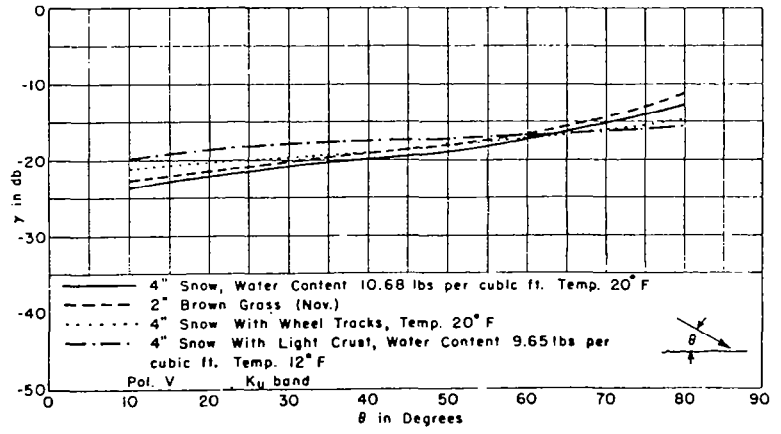


Figure 5-19 Effects of various types of snow cover upon γ at Ku-band. (Cosgriff, et al., 1960)

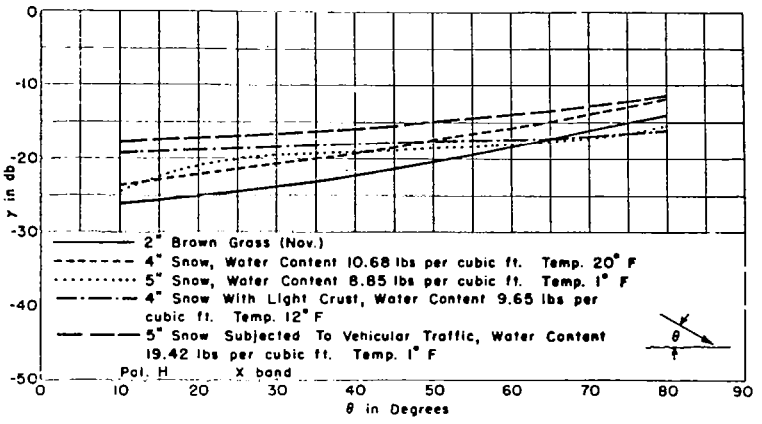


Figure 5-20 Effects of various types of snow cover upon γ at X-band. (Cosgriff, et al., 1960).

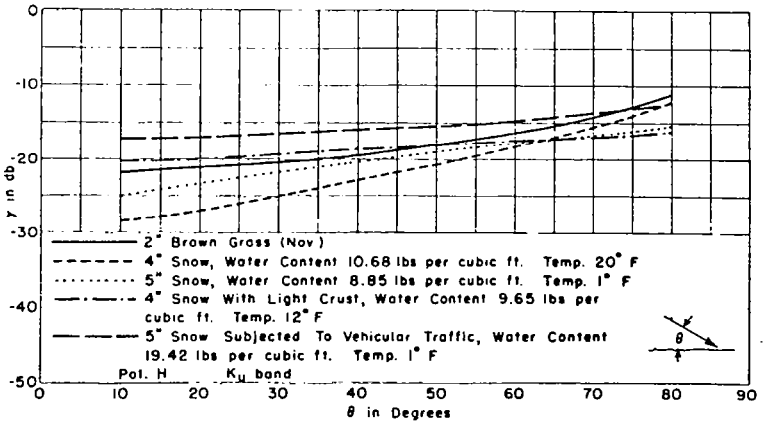


Figure 5-21 Effects of various types of snow cover upon γ at Ku-band. (Cosgriff, et al., 1960).

recorded peak values. The data are smoother than the one independent sample measurements would predict, however, the smoothness is a result of the peaking process. Figures 5-22 and 5-23 illustrate sample data. As a result of neglecting signal fading (see Section 7.1), quantitative conclusions again cannot be made.

5.3.4 CRREL

Hoekstra and Spangole (1972) of the Cold Regions Research and Engineering Laboratory of the U.S. Army Corps of Engineers reported backscatter measurements at grazing angles of 0.3° to 1.0°. Figure 5-24 illustrates a typical pulse return. Figure 5-25 shows the dramatic change in σ° as the snow temperature approaches 0°C and the snow becomes wet.

5.3.5 Georgia Institute of Technology

The Engineering Experiment Station of Georgia Institute of Technology performed penetration and backscatter measurements on snow at 35 and 94 GHz (Currie et al., 1977). Grazing angles from 8° to 15° were observed. Reported σ° values are based on peak values of the pulse return. This procedure will reduce signal scintillation but the value obtained is not the average value of scattering coefficient or σ°. At a 15° grazing angle, the range resolution was about 8 meters. The range swath observed from Figure 5-26 suggests that the antenna beamwidth allowed returns from about 40 meters in range. This indicates that this data could have been processed to 5 independent samples consequently reducing the confidence interval on the σ° value. This data must be used carefully since the "measured" values are "peak" values and therefore are probably larger than the true σ° value. Figures 5-27 and 5-28 illustrate σ° values versus time. Figures 5-29 and 5-30 are B-Scope displays of the fairly homogeneous target area and clearly show the effects of fading.

5.3.6 Rome Air Development Center

Hayes and his colleagues of the Propagation Branch of the Electromagnetic Sciences Division, Rome Air Development Center have performed millimeter wave backscatter and attenuation measurements of snow at 35, 98 and 145 GHz. They made the following observations (Hayes, et al., 1979):

(1) Snow wetness lowers the σ° values of dry snow.

(2) The effects of snow wetness on VV polarization decrease with increasing frequency and increase or stay constant with increasing angle of incidence (Figures 5-31 to 5-33).

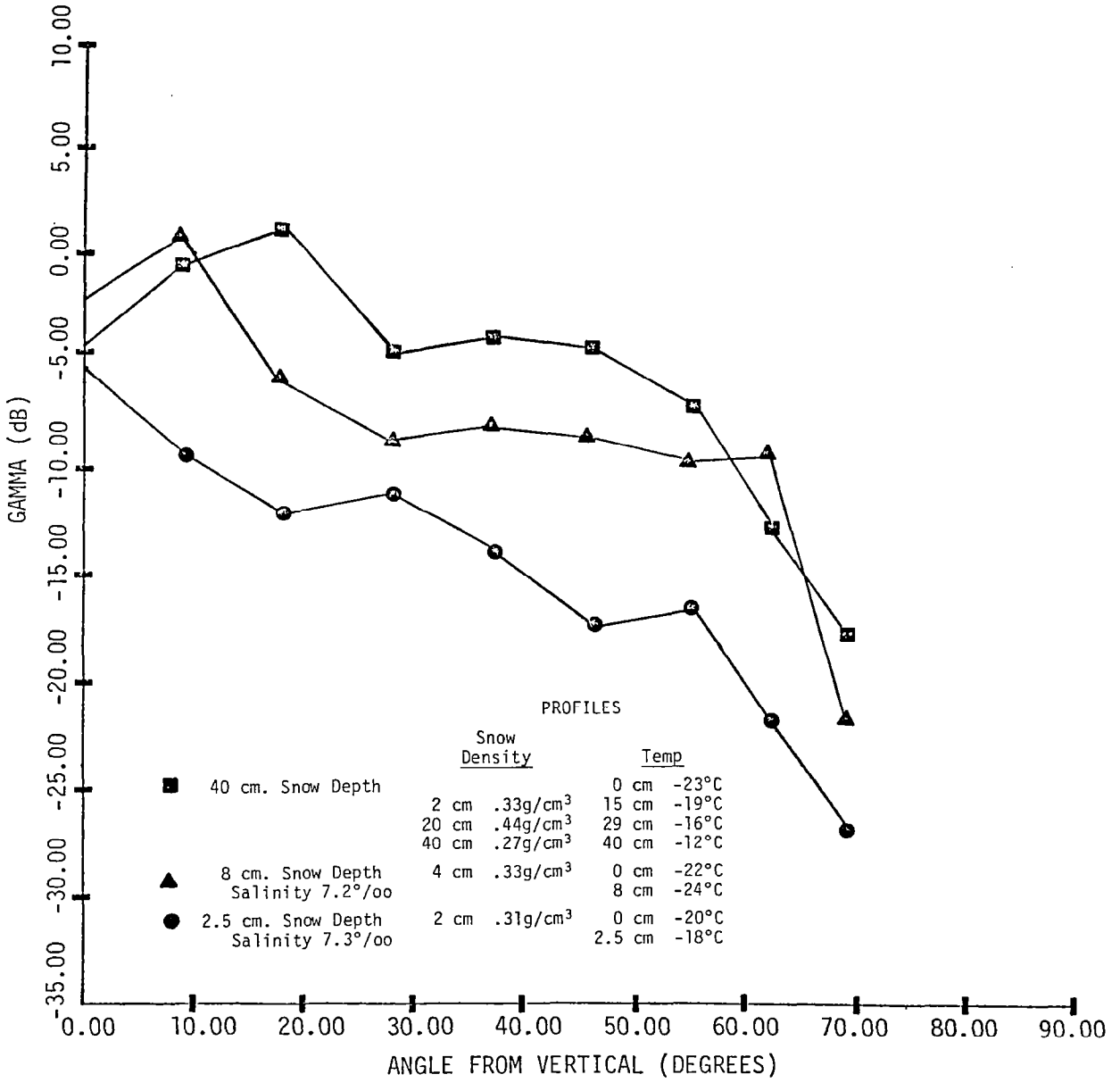


Figure 5-22 Normalized backscatter cross-section for sea ice with varying snow cover, versus angle of incidence. (Sackinger, 1972)

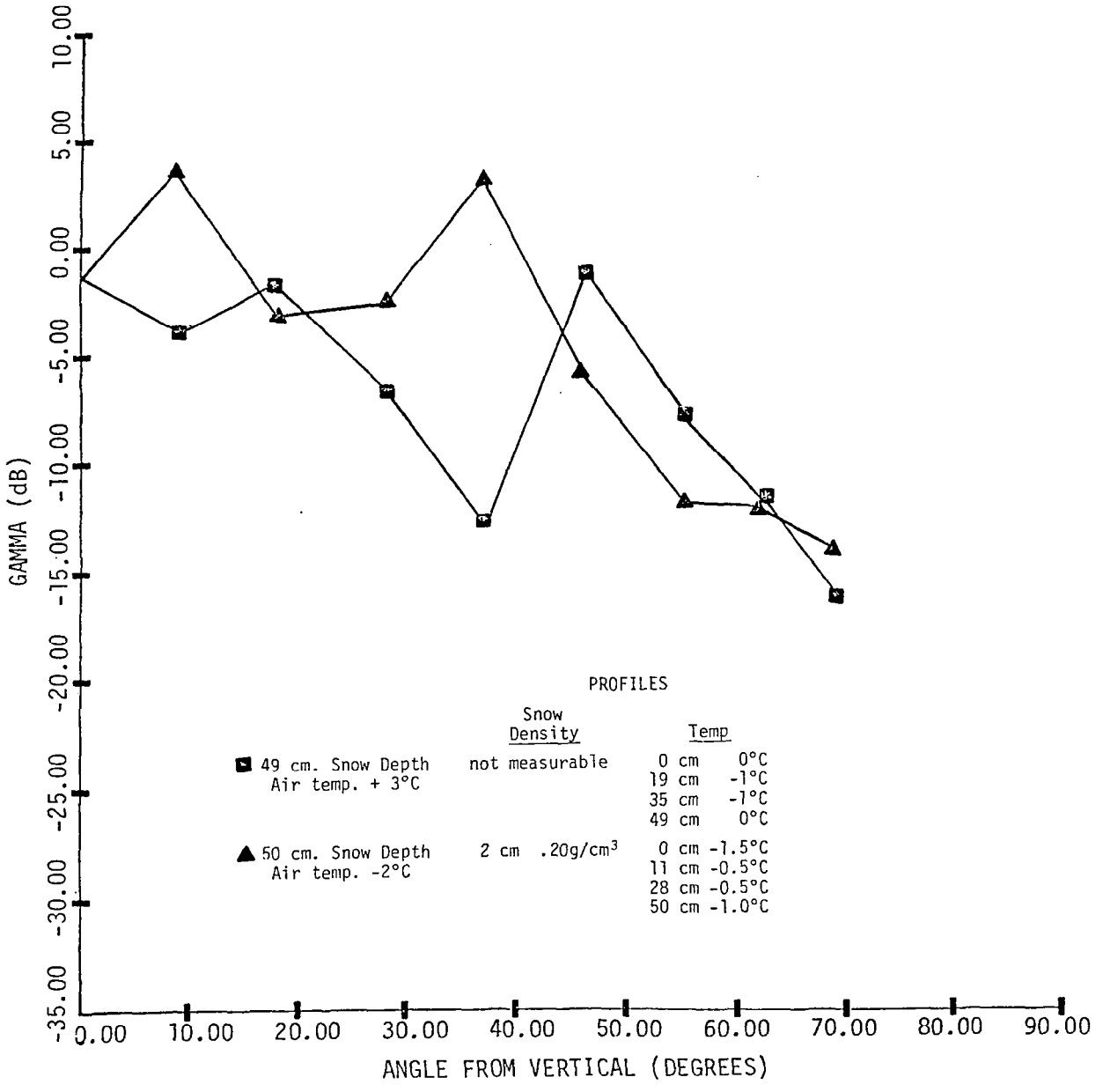


Figure 5-23 Normalized backscatter cross-section for frozen ground with wet and dry snow cover, versus angle of incidence. (Sackinger, 1972)

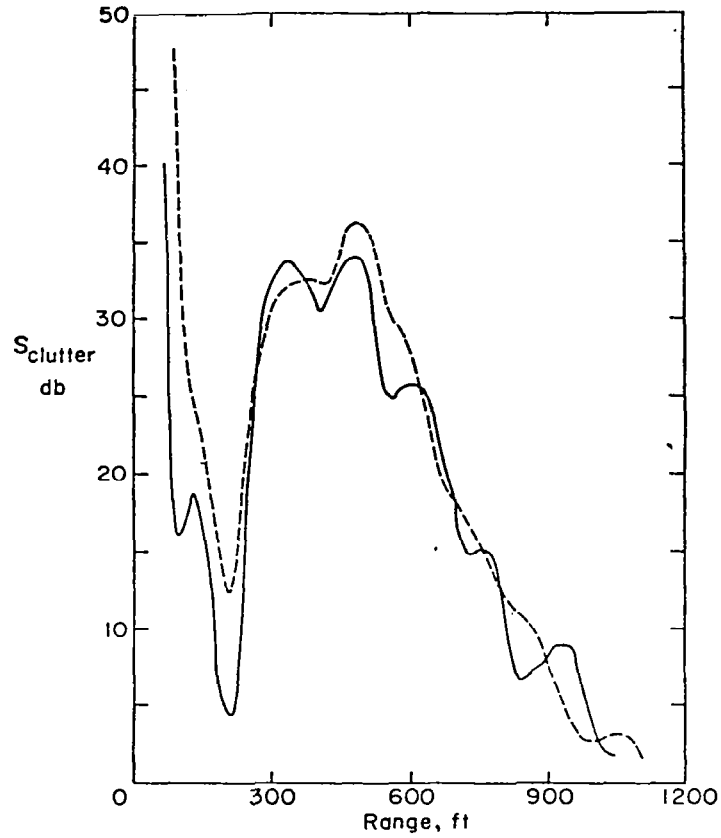


Figure 5-24 Typical analog plots of the return from smooth snow at 10 GHz and vertical polarization. The solid line represents returns at fixed frequency; the broken line represents returns with a 40 MHz bandwidth and simultaneous sweep of transmitter and receiver. (Hoekstra and Spangole, 1972)

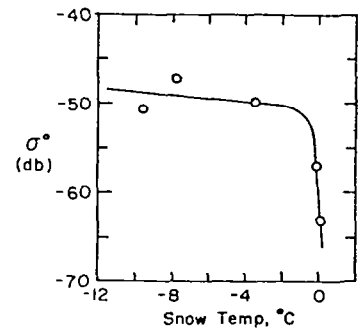


Figure 5-25 Variation of σ^o as a function of snow temperature at 10 GHz and horizontal polarization. (Hoekstra and Spangole, 1972)

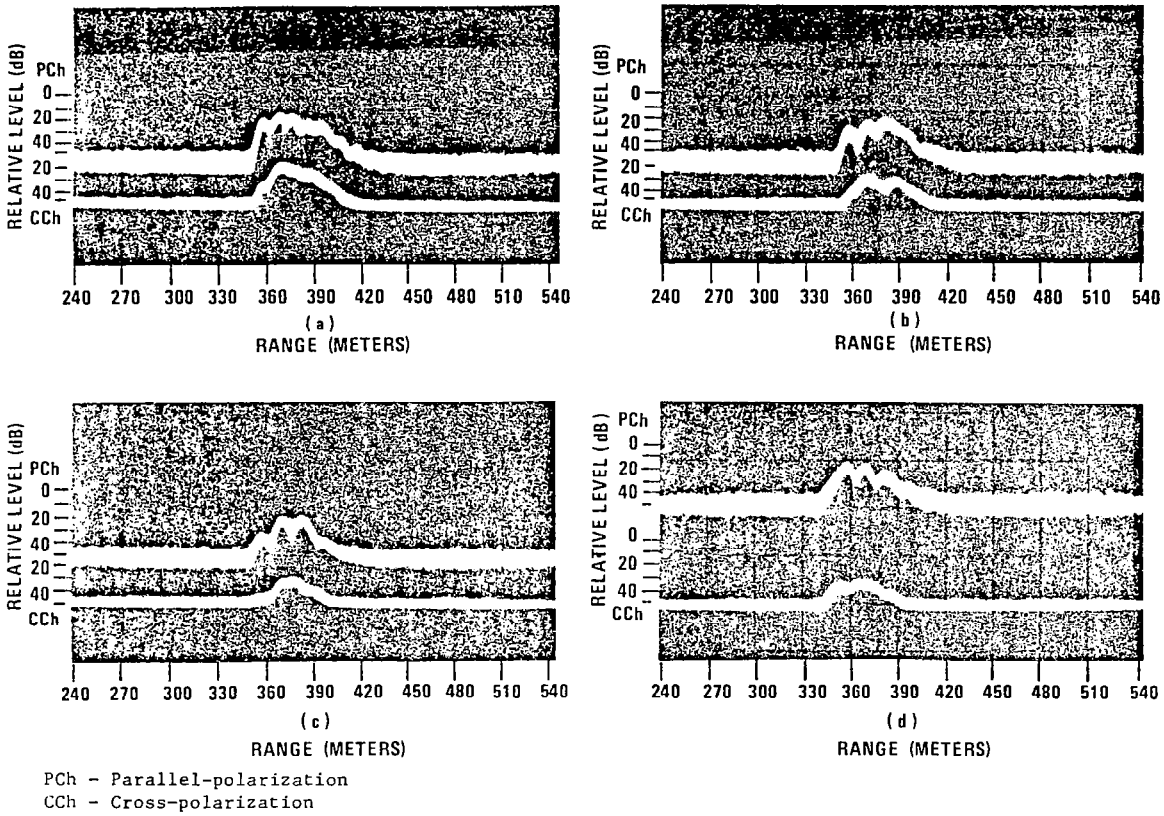


Figure 5-26 Radar return from a snow-covered field at times of (a) 0700, (b) 0800, (c) 0830, and (d) 1004; 34.7 GHz, horizontal polarization, 15° depression angle. (Currie, et al., 1977)

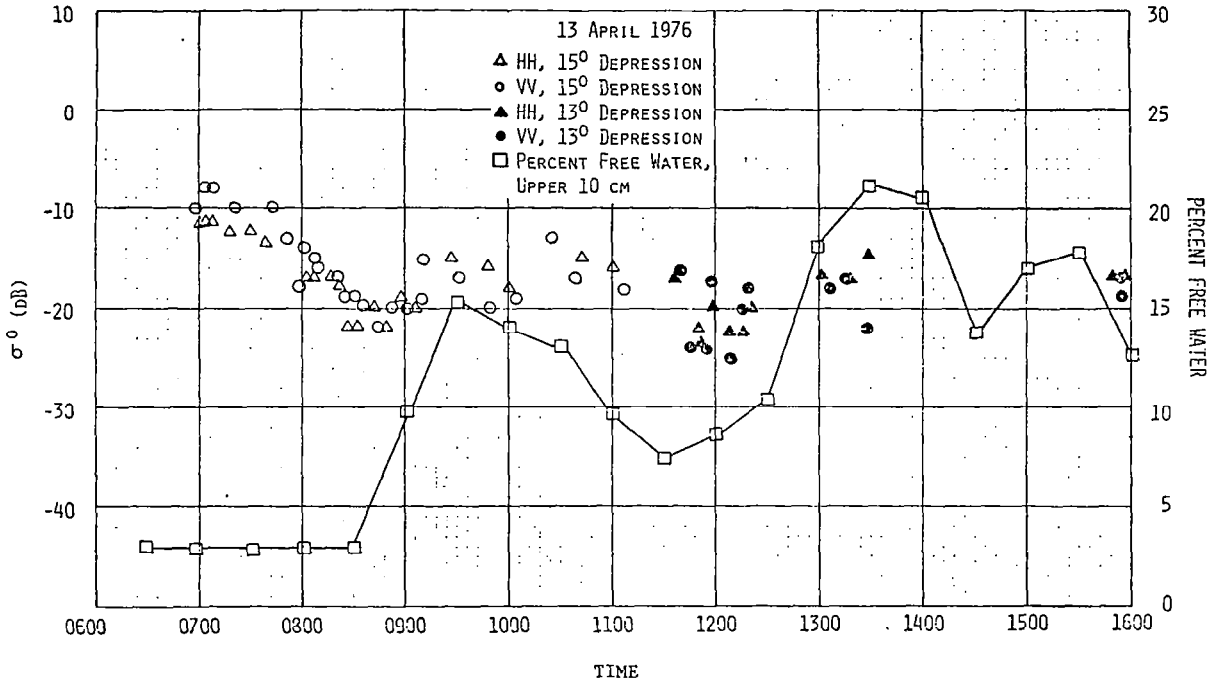


Figure 5-27 Radar backscatter per unit area from two snow-covered fields as a function of time for 35 GHz and the percent free water present in the top snow layer. (Currie, et al., 1977)

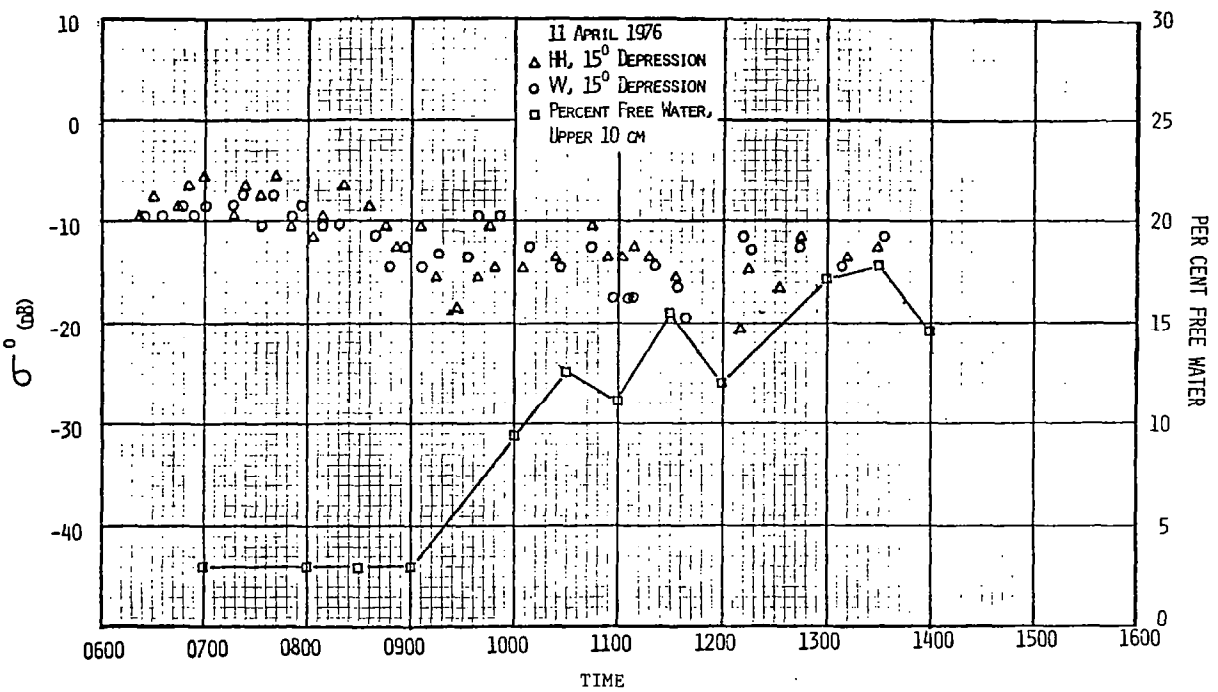


Figure 5-28 Radar backscatter from snow illustrating the cyclic variations as a function of time; 35 GHz. (Currie, et al., 1977)

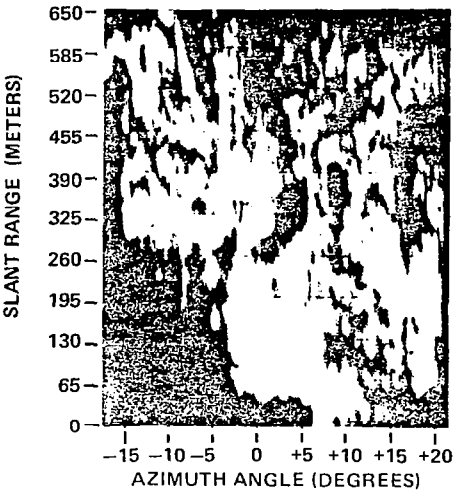


Figure 5-29 B-scope display of test area with snow present on the ground. (Currie, et al., 1977)

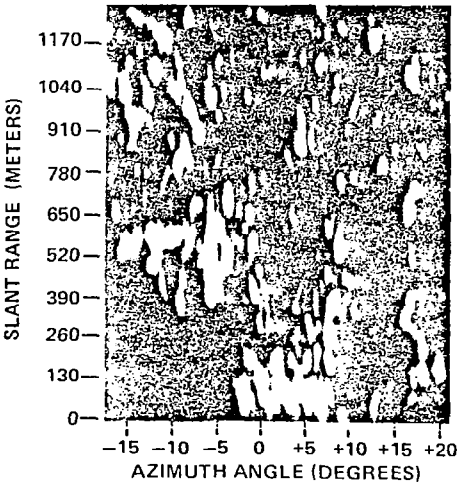


Figure 5-30 B-scope display of test area after snow has melted (area is very wet). (Currie, et al., 1977)

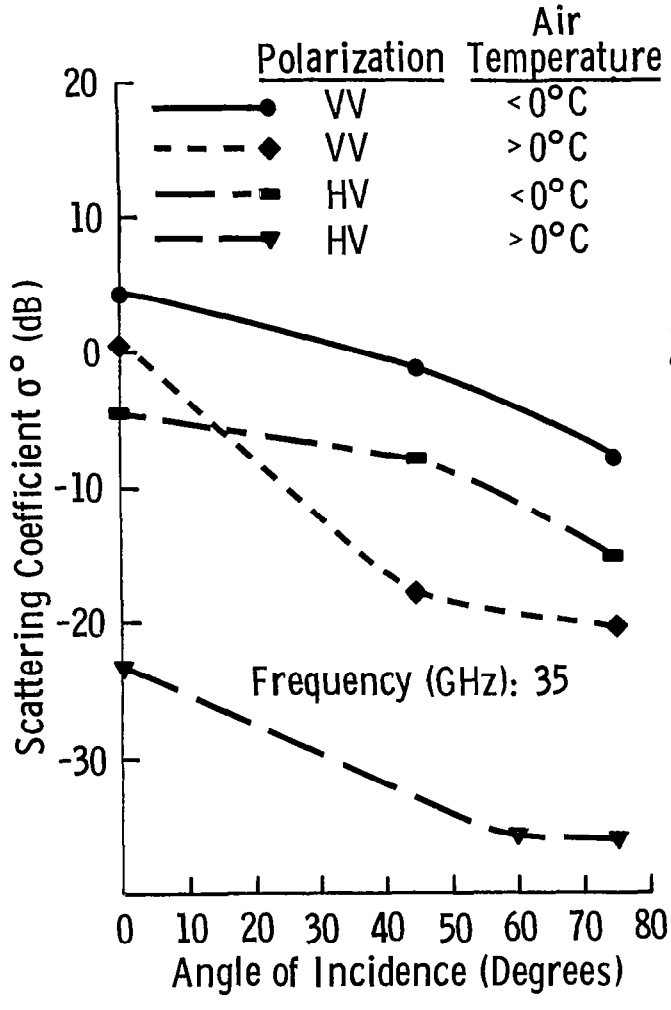


Figure 5-31 Angular Dependence of σ^{o} to wet and dry snow at 35 GHz. (Hayes, et al., 1979)

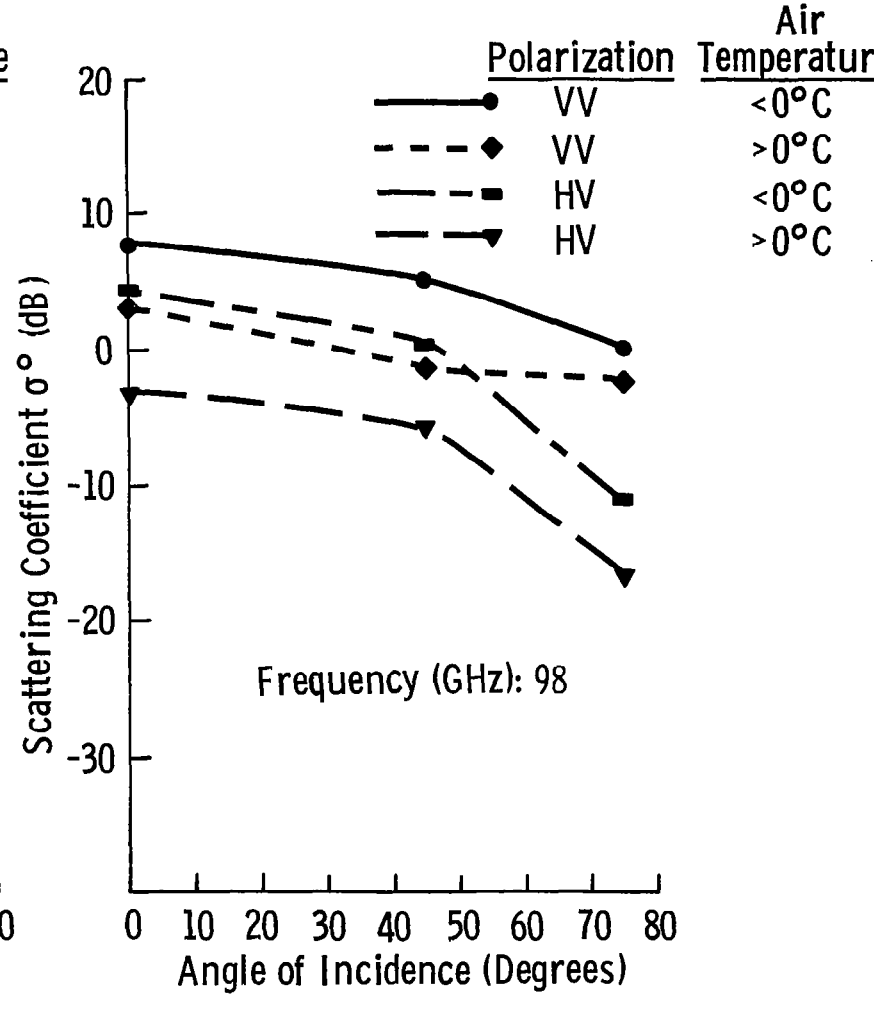


Figure 5-32 Angular dependence of σ^{o} to wet and dry snow at 98 GHz. (Hayes, et al., 1979)

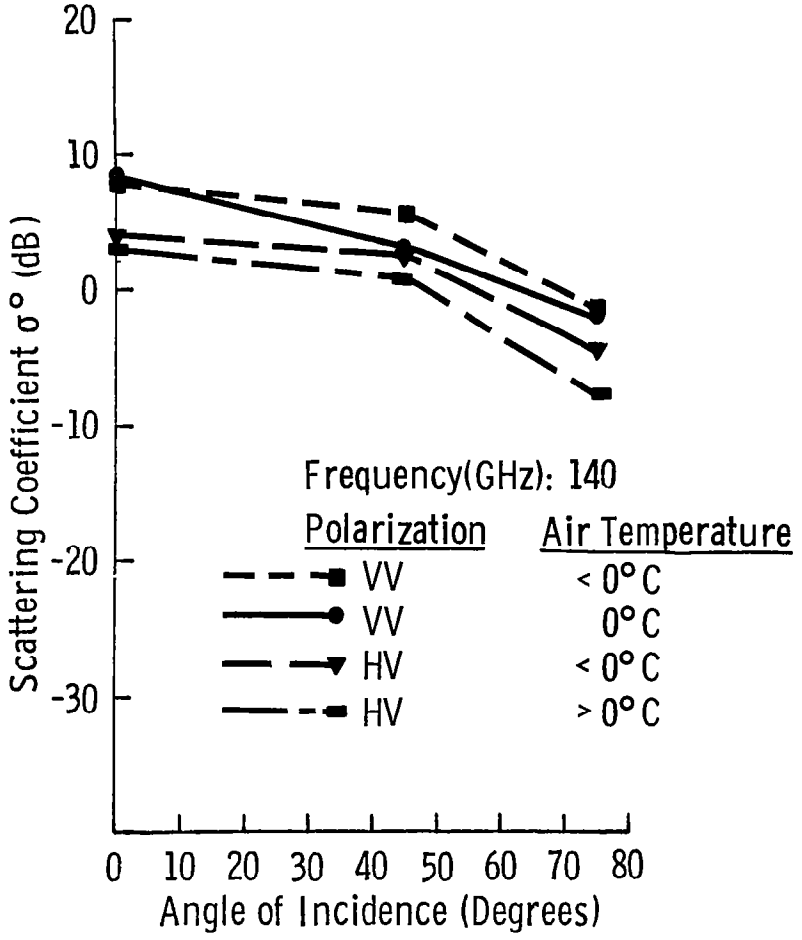


Figure 5-33 Angular dependence of σ° to wet and dry snow at 140 GHz. (Hayes, et al., 1979)

They attribute the lack of sensitivity to wetness at 98 and 145 GHz to roughness or the decrease in the difference between the dielectric constants of ice and water at these frequencies.

(3) The effects of wetness on HV polarization are similar to VV polarization with the exception of 35 GHz at nadir which dropped 25 dB upon the appearance of wetness (Figure 5-31).

5.3.7 University of Kansas

The Remote Sensing Laboratory of the University of Kansas conducted an experiment during 1975 to investigate the backscatter properties of snow. Since then, other experiments have been conducted in Lawrence, Kansas; (Stiles, et al., 1976; and Ulaby, et al., 1977) Steamboat Springs, Colorado (Stiles, et al., 1977; and Ulaby and Stiles, 1977) and Brookings, South Dakota. This dissertation deals mainly with the Steamboat Springs data; additional information gained from later experiments will also be incorporated.

The MAS 1-8 was used in 1975 to obtain data over the 1-8 GHz region at angles of incidence between 0° (nadir) and 70°. The maximum depth of the snow cover was 15 cm. The measurements indicated that dry snow has a small effect on the soil backscatter over the 1-8 GHz frequency range (Figure 5-34) and that wet snow causes σ^{o} to decrease away from nadir (Figure 5-35). Also shown is the increasing sensitivity to wetness with increasing frequency.

5.3.8 Airborne and Spaceborne Observations

There have been a limited number of experiments using airborne or spaceborne active microwave sensors. Waite and McDonald (1970) investigated some K-Band SLAR imagery and observed that new dry snow had little effect on the underlying target return. High returns were observed from old perennial snow and this was postulated to be the result of volume scattering from inhomogeneities in the snow. This hypothesis was supported by the apparent independence of the radar return to angle of incidence over the old snow areas. The effect of old snow on cross polarization was observed to be larger than the effect on like polarization.

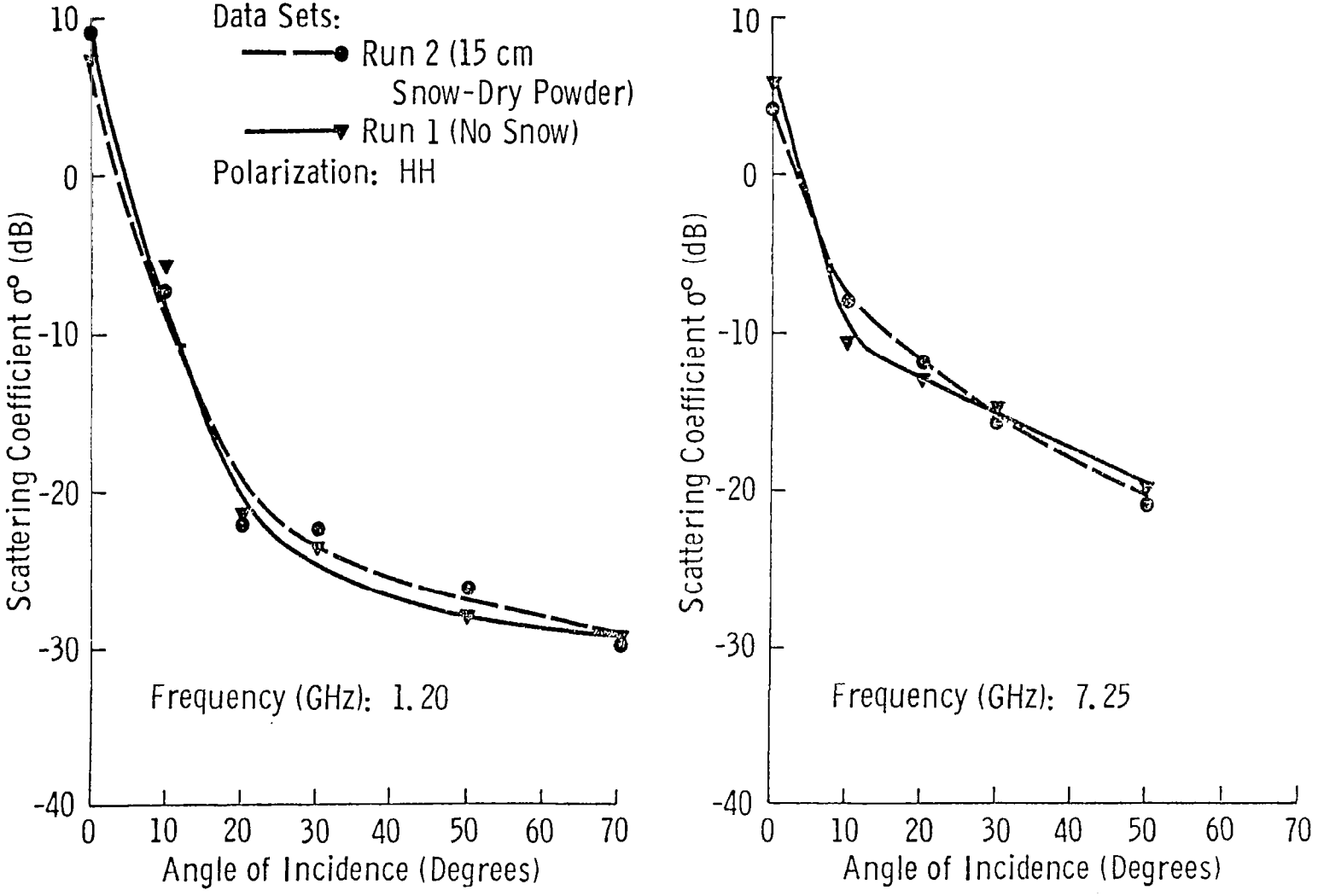


Figure 5-34 Angular response of σ^{o} of short grass and short grass with a 15 cm dry powder snow cover. (Ulaby, et al., 1977)

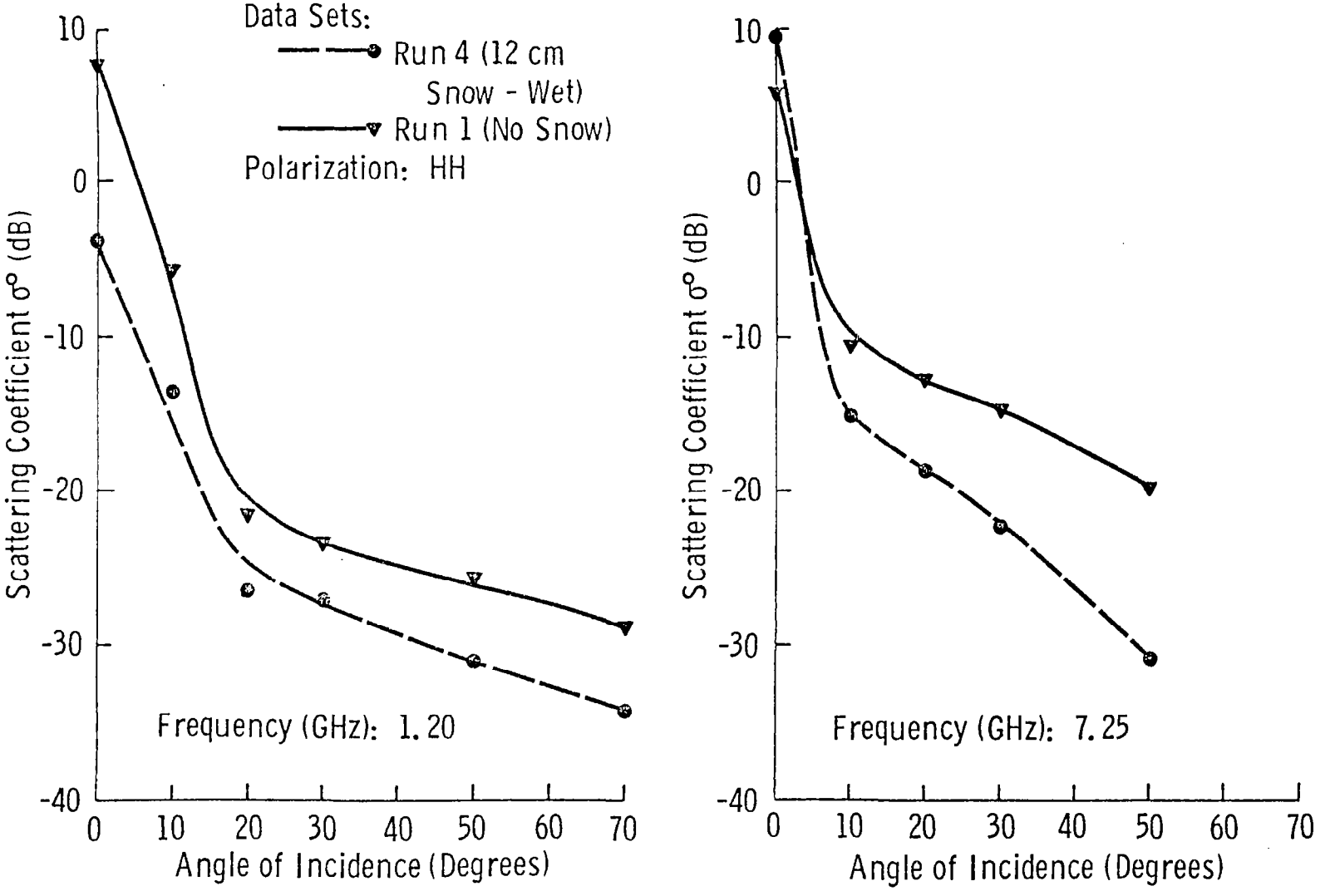


Figure 5-35 Angular response of σ^{o} of short grass and short grass with a 12 cm wet snow cover. (Ulaby, et al., 1977)

The only reported measurements from an orbital platform were obtained at 13.9 GHz from the S-193 scatterometer on Skylab. Eagleman et al. (1975) reported a positive correlation of σ^{o} to snow depth (Figure 5-36). The resolution cell size and the ground truth sampling density prevented definitive conclusions about the radar return from snow covered surfaces.

5.3.9 Summary of Active Backscatter Measurements

For detailed analyses of the σ^{o} response, high quality ground truth data are required. These ground truth measurements should include as a minimum: snow depth, snow water equivalent, snow wetness, and some information of the ground conditions. The Georgia Institute of Technology data are the only data in the literature to have very complete ground truth. The remote sensing value of this information can only be qualitative, however, since the σ^{o} values were obtained at high angles of incidence (greater than 75°) and at 35 and 94 GHz only.

Active microwave measurements in the 1 to 35 GHz frequency range over incidence angles from 0° to 70° on snowpacks are needed along with reliable ground truth to allow evaluation of the active microwave remote sensing potential and to furnish valuable information to the theoretician for development of better models for scattering from snowpacks.

5.4 Passive Measurements

The earliest radiometric snow measurements were performed by the Air Force Ballistic Systems Division in 1962. The radiometric resolution was only $\pm$5K, however, which was too crude for quantitative conclusions (Janza, et al., 1975 in Manual of Remote Sensing). The more recent experiments are covered in the sections that follow. The term used to characterize the measured radiation is "brightness temperature." It should be noted that this is the brightness temperature of the scene observed by the antenna which includes ground self-emission as well as atmospheric attenuation and emission effects.

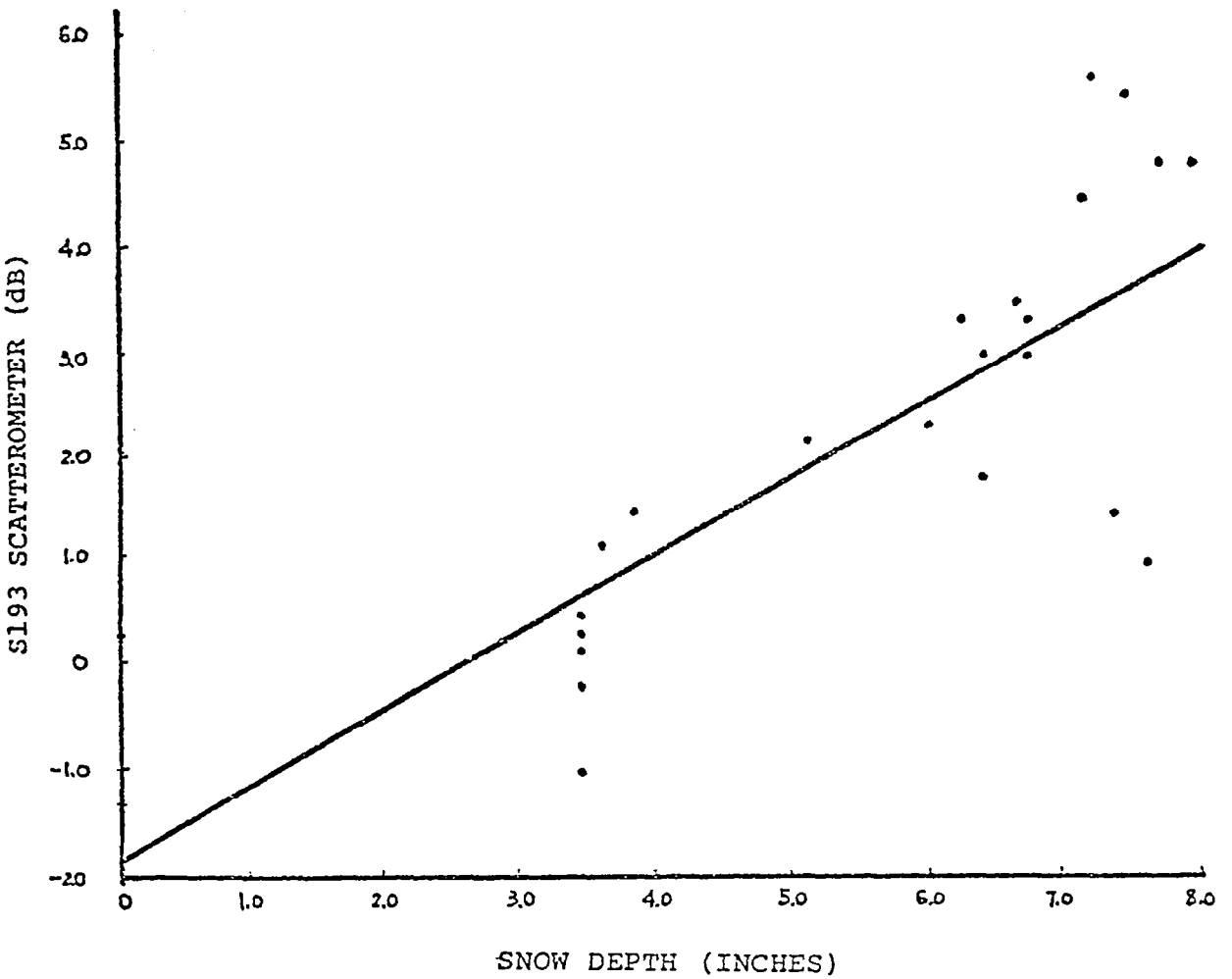


Figure 5-36 S193 Scatterometer as a function of snow depth on January 11, 1974, in Kansas. Angle of incidence is 5° and f = 13.9 GHz. (Eagleman, et al., 1975)

5.4.1 Aerojet General Corporation

The fundamental understanding of the microwave emission from snowpacks is based on experiments conducted by Edgerton and his colleagues between 1965 and 1971.

The microwave response to water equivalent of dry snow is shown in Figures 5-37 to 5-39. Figure 5-37 (Edgerton, et al., 1971) illustrates the brightness temperature response to water equivalent of dry snow over a natural soil surface. The increased sensitivity to water equivalent with increasing frequency is shown. Also noted is the "unusually" low brightness temperature at 13.4 and 37 GHz (Edgerton et al., 1968). Brightness temperatures as low as 120 K to 150 K were observed. The emission from a snow layer over a cold background (a metal plate) is given in Figure 5-38 (Meier and Edgerton, 1971). Saturation depth or the depth at which the snow layer may be treated as infinite are seen to be frequency dependent. The 0.8 cm data are near saturation at 30 cm water equivalent while the 2.2 cm data are still changing and the 21 cm data have shown very little response. The "60 cm snow" and "51 cm snow, packed" data points in Figure 5-39 indicate that the parameter affecting the brightness is water equivalent and not snow depth.

The microwave response to snow wetness is illustrated in Figures 5-40 and 5-41. In Figure 5-41, the diurnal response of brightness to snow wetness is observed. The high brightness temperature response to wet snow is in contrast to the low brightness temperature of wet soil. This phenomenon points to a different scatter mechanism in snow as opposed to the scatter mechanism from soil. The low brightness temperature of dry snow was attributed to volume scattering. The response to wetness is observed to saturate above approximately 2 percent water by volume. The combined effects of wetness and water equivalent could not be separated (Figure 5-41). Meier (1972) found that classification of dry snow, wet snow, and vegetated ground was possible in measurements at Mount Ranier, Washington (Figure 4-42).

5.4.2 Helsinki University of Technology

The Radio Laboratory of Helsinki University of Technology recently reported the results of microwave radiometric observations of snow in Finland (Tiuri, et al., 1978). The brightness temperature at 4.8 and

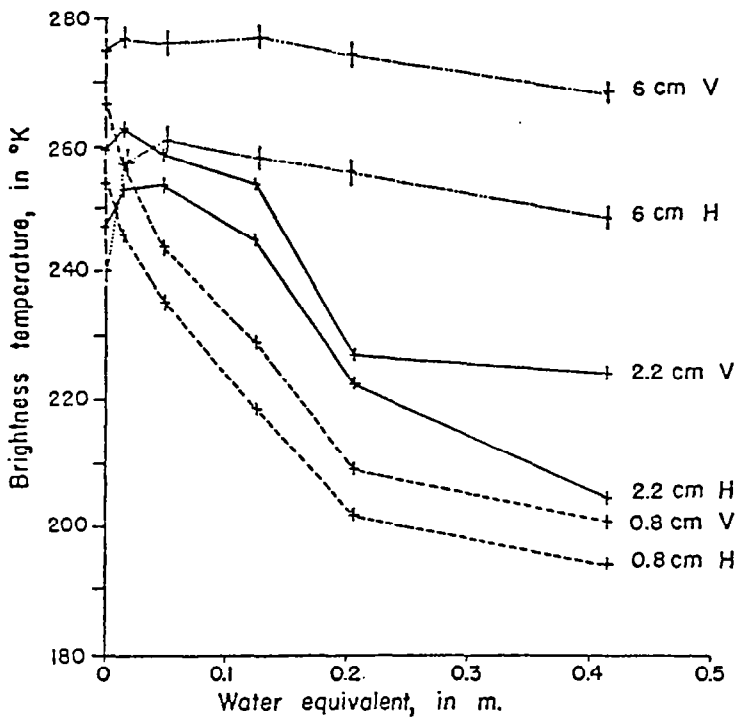


Figure 5-37 Measured dry snow brightness temperatures. These are given as a function of snow mass per unit area (water equivalent), 45° viewing angle, at 3 wavelengths and 2 polarizations (H = horizontal, V = vertical polarization). Absolute values of brightness temperature at 6 cm wavelengths are not known, but relative variations in brightness are correct. Measurement errors indicated by short dashes. Crater Lake, Oregon, March 23, 1970. (Meier and Edgerton, 1971)

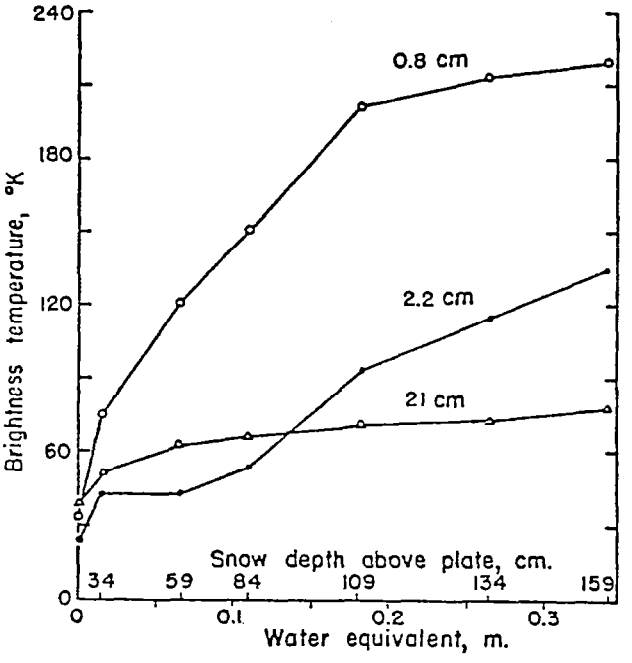


Figure 5-38 Plate experiment to determine microwave penetration. Aluminum plate inserted at various depths in a dry snowpack in situ and microwave emission measured at 20° viewing angle from nadir at 3 wavelengths. Snow ranged in density from 60 kg/m^3 at top to 370 kg/m^3 at base, with ice layers at 58, 85, and 103 cm below the top. Crater Lake, Oregon, December 16, 1968. (Meier and Edgerton, 1971)

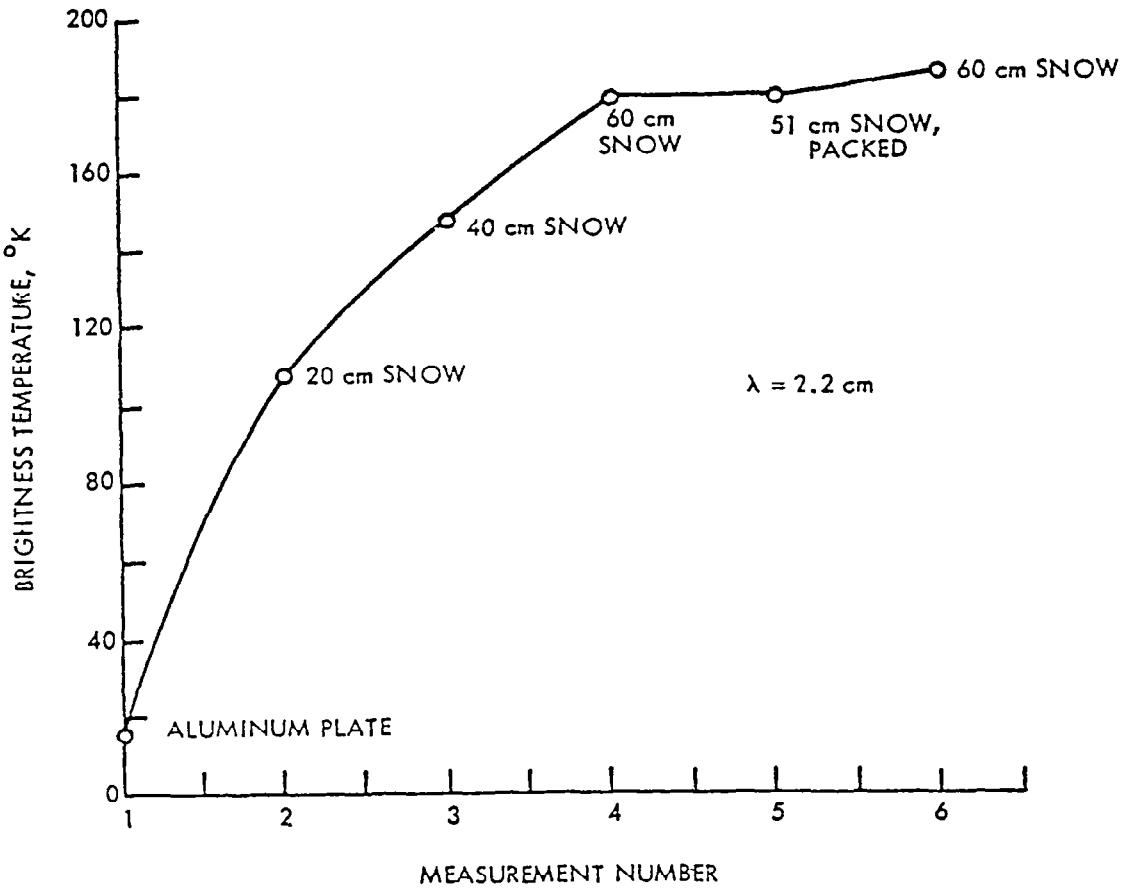


Figure 5-39 Brightness temperature of various depths of snow on a metal plate. Note that the first 60 cm snow and the 51 cm snow packed points are for the same total snow mass. (Edgerton, et al., 1971)

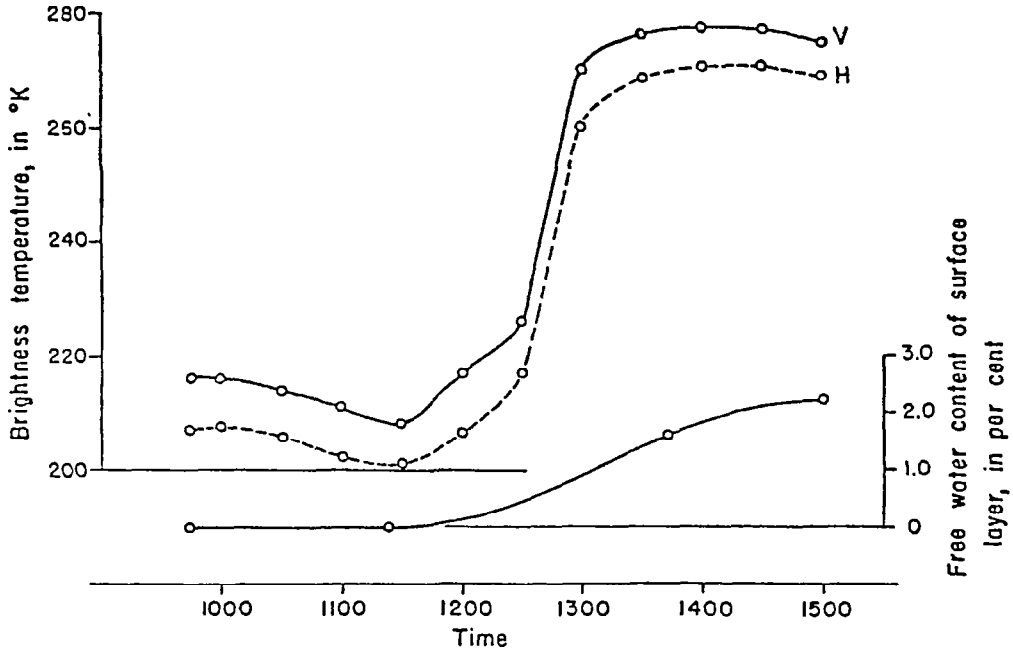


Figure 5-40 Measured change in brightness temperature with appearance of liquid water. Graph shows microwave emission at 0.8 cm, 45° viewing angle for a snowpack in situ as a function of time. Prior to 1200 hours, the whole snowpack was cold and dry. By 1500 hours, the appreciable liquid water had appeared in upper layers but lower part of the snowpack was relatively dry. Snow density 517 kg/m, thickness 0.8 m. Crater Lake, Oregon, March 22, 1970. (Meier and Edgerton, 1971)

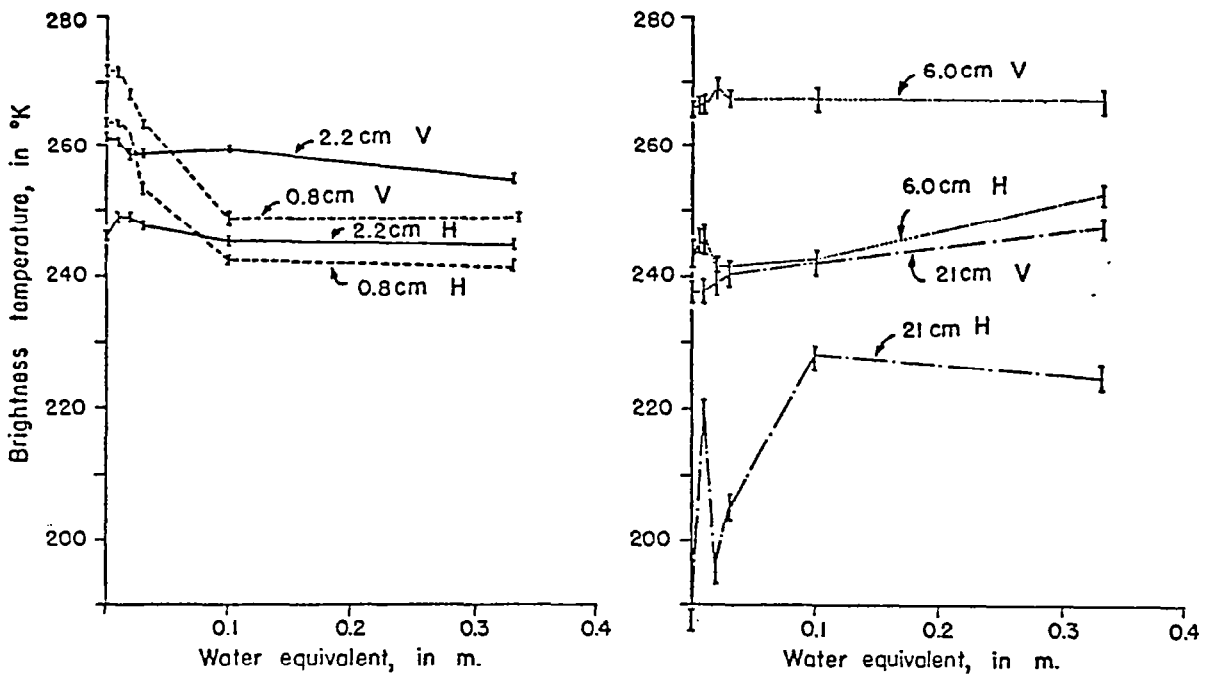


Figure 5-41 Measured wet snow brightness temperatures. These are given as a function of snow mass per unit area (water equivalent), 45° viewing angle at 4 wavelengths and 2 polarizations. Absolute values of brightness temperature at 6 cm wavelength are not known, but relative variations in brightness are correct. Measurement errors indicated by short dashes. Crater Lake, Oregon, May 14, 1970. (Meier and Edgerton, 1971)

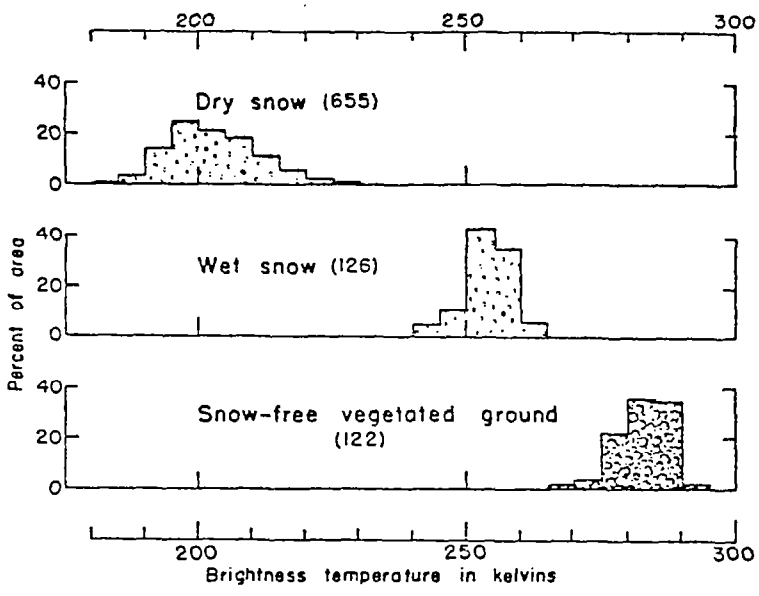


Figure 5-42 Distribution of brightness temperature with area for three types of terrain in the vicinity of South Cascade Glacier, Washington. The dry-snow data were obtained March 8, 1971; the wet-snow and snow free, vegetated-ground data were obtained June 18, 1968. Figures in parentheses indicate number of observations (resolution cells). (Meier, 1972)

36.8 GHz was observed to be relatively independent of incidence angle (Figure 5-43) for both dry (9 am) and wet (3 pm) snow conditions. The response to snow wetness variation is small at 4.9 GHz and approximately 60 K at 36.8 GHz. Thus, these measurements qualitatively agree with the Aerojet General results.

5.4.3 University of Berne

Schanda and Hofer of the Institute of Applied Physics at the University of Berne reported preliminary results of brightness temperature observation of snow at 4.9, 10.5, 21, 35 and 95 GHz (Schanda and Hofer, 1977). Figure 5-44 presents the spectral response of brightness temperature for dry snow conditions (9:10 to 10:20) and wet snow conditions (14:05 to 15:15). The difference in brightness temperature between wet and dry conditions generally increases with frequency. The variation of brightness temperature with humidity (snow wetness) in the top 15 cm layer was observed (Figure 5-45) to have a hysteresis effect that increased with increasing frequency (Hofer and Mätzler, 1979). In addition, the humidity at which the response saturates is low at 36 and 94 GHz, while there is no saturation at 4.9 and 10.5 GHz. There is a response reversal at 10.5 GHz above about 4 percent humidity. Below 4 percent, the curve resembles the saturation effect representative of the higher frequencies, however, above 4 percent the response resembles the 4.9 GHz data. Figure 5-46 shows the same results plotted as a diurnal experiment. During a late season diurnal period for which wetness was never zero, the 36 GHz brightness temperatures remained high over the period while the lower frequency data illustrated a considerable drop in T_b due to high snow wetness values during the daytime (private communication, Hofer, 1979).

Attenuation rates for snow were calculated from brightness temperature measurements of a snow layer of known thickness over a metal plate. Two simple models were used (Mätzler, et al., 1979). Figures 5-47 and 5-48 illustrate the results. The first model included the effects of multiple reflections but neglected interference effects. γ_1 is the power damping (or attenuation) coefficient for this model. In the second model, volume scattering γ_s and absorption γ_a were included in a radiative transfer model. The combined effects of absorption and scattering are given by γ_2, a power damping coefficient (Mätzler, et al., 1979):

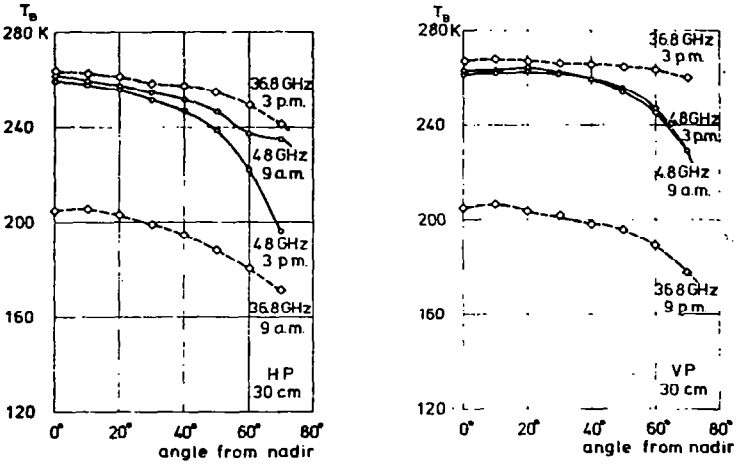


Figure 5-43 Brightness temperatures T_B versus look angle for horizontal (HP) and vertical polarizations (VP), April 4, 1978. (Tiuri, et al., 1978)

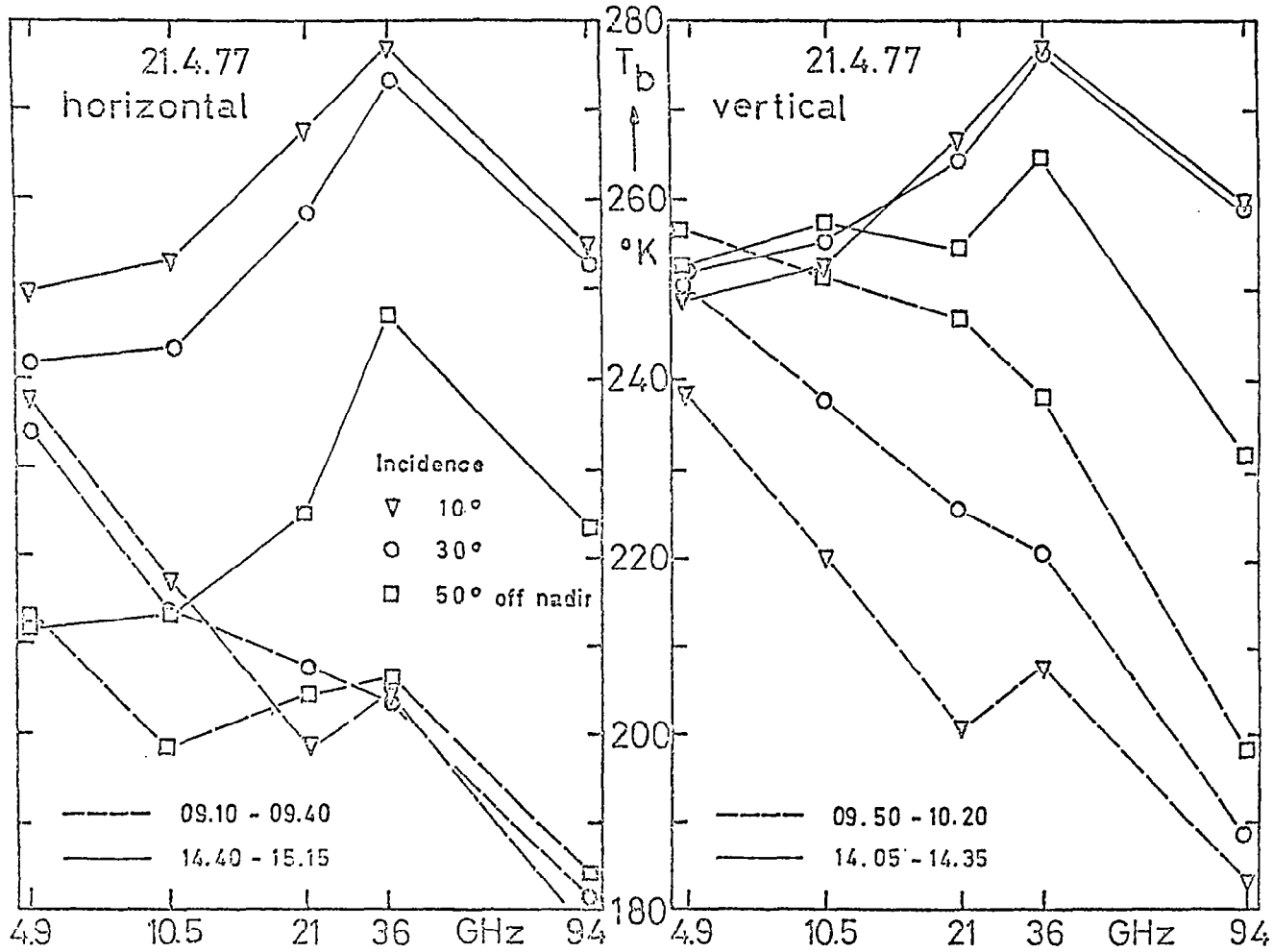


Figure 5-44 Brightness temperature spectral response for a wet snow and a dry snow case. (From Schanda and Hofer, 1977)

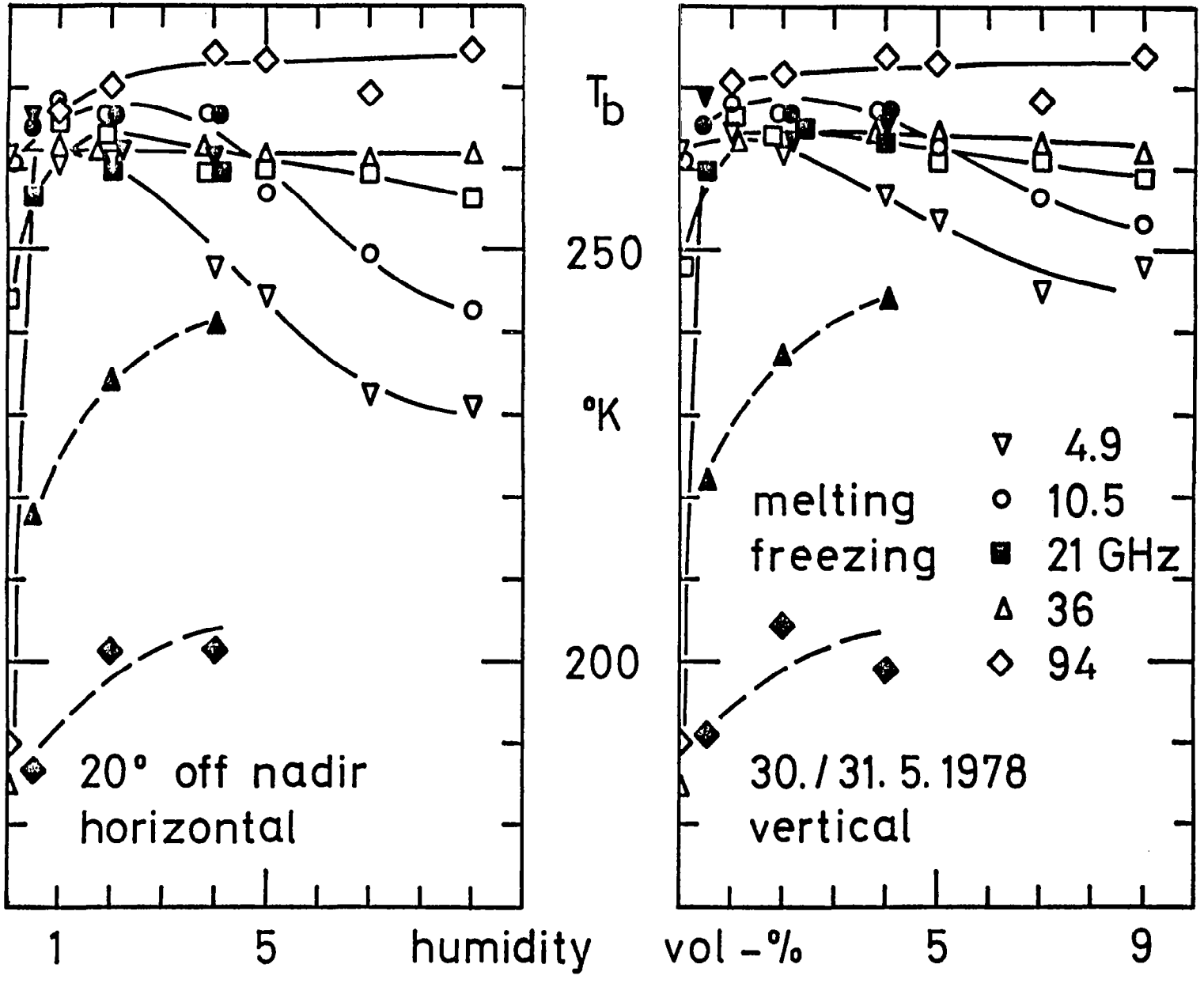


Figure 5-45 Brightness temperature versus snow wetness (humidity). (From Hofer and Matzler, 1979)

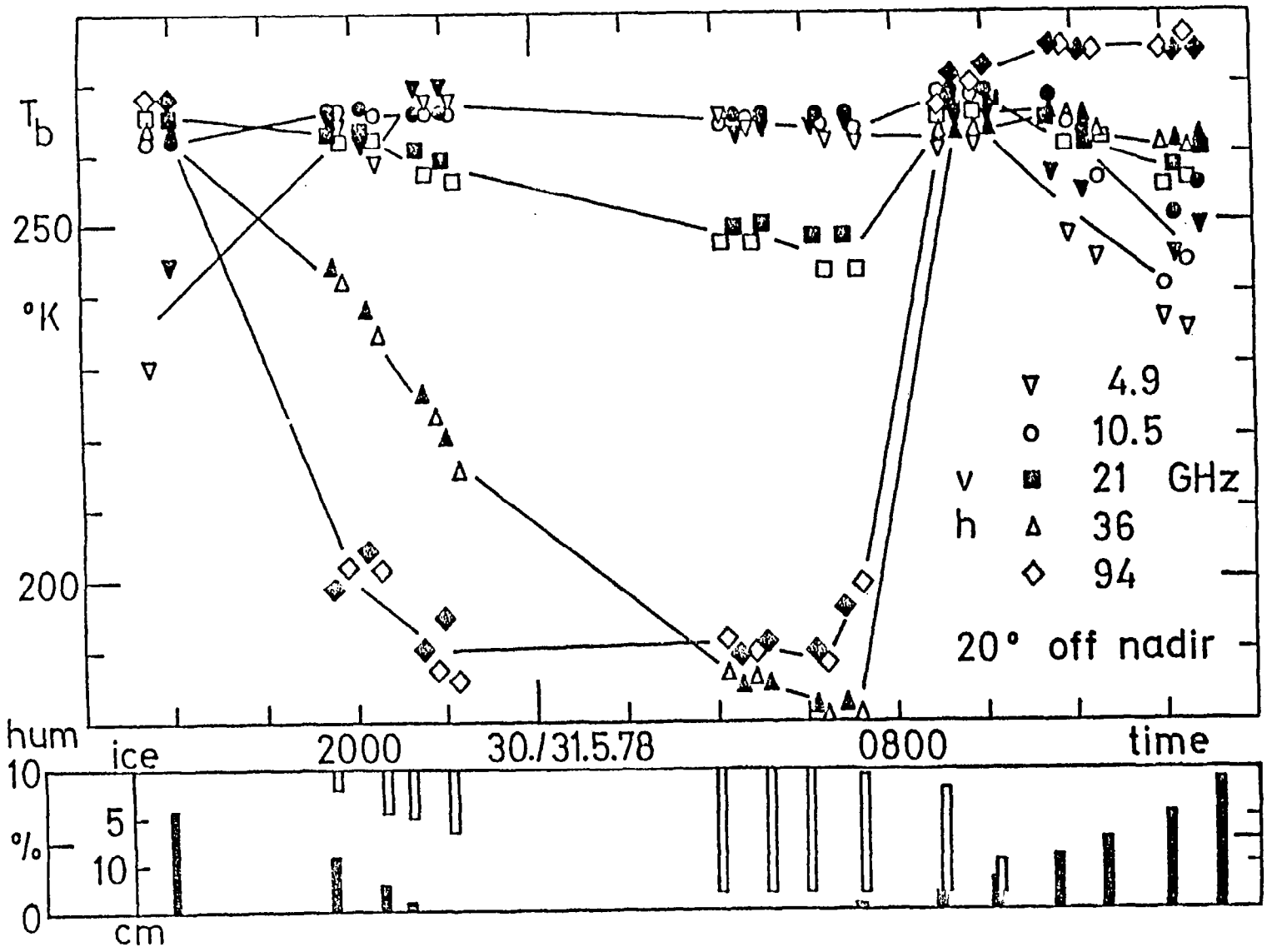


Figure 5-46 Diurnal variations of brightness temperature for horizontal (h, open) and vertical polarization (v, block symbols) along with snow wetness (humidity) and refrozen layer thickness (ice). (Hofer and Matzler, 1979)

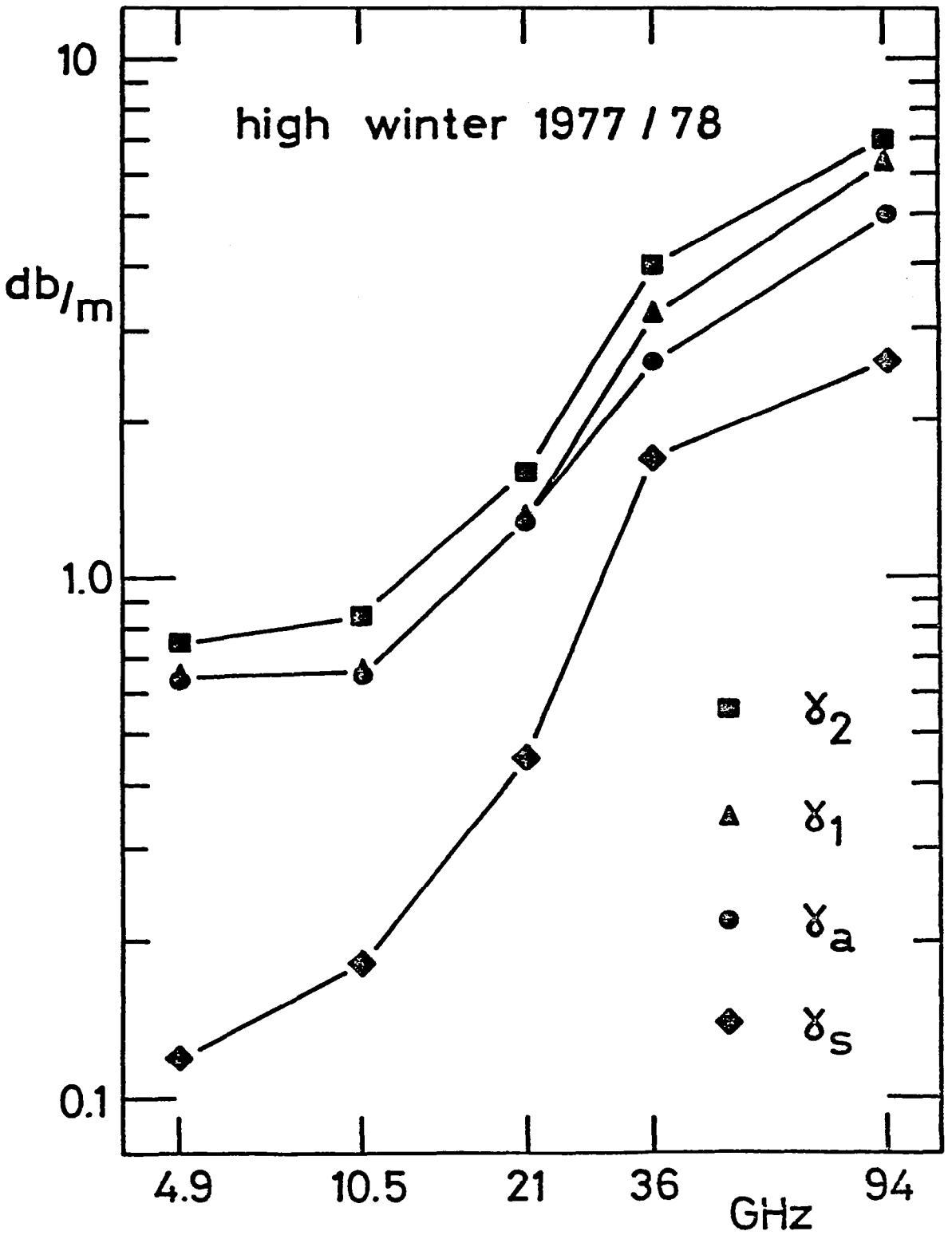


Figure 5-47 Scattering, absorption and damping coefficients for dry winter snow. (Hofer and Matzler, 1979)

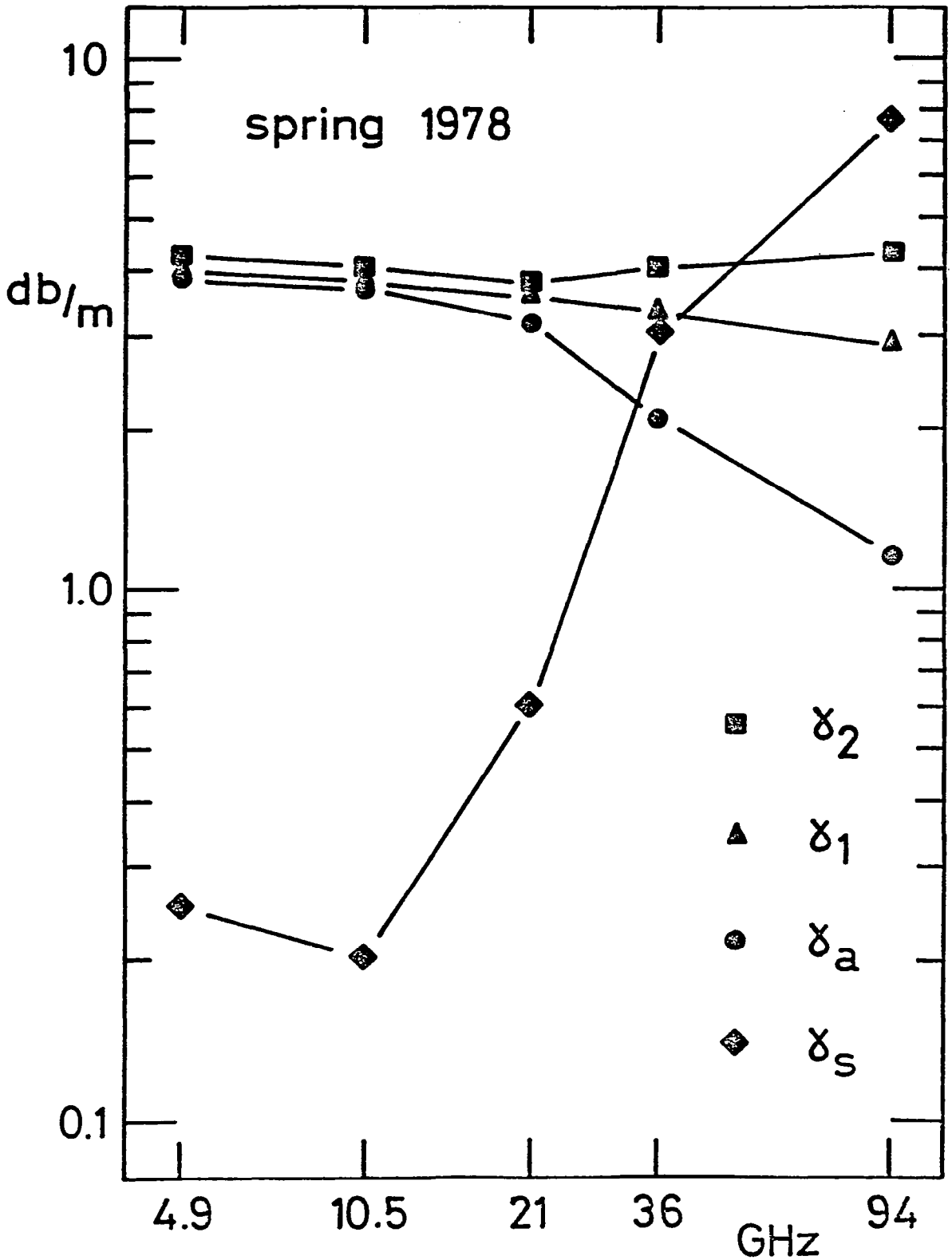


Figure 5-48 Scattering, absorption and damping coefficients for dry spring (metamorphosed) snow. (Hofer and Matzler, 1979)

$$\gamma_2 = \sqrt{\gamma_a^2 + 2\gamma_a\gamma_s} \qquad (5\text{-}1)$$

γ_1 and γ_2 from the two models agree well for both the dry winter snow and dry metamorphosed spring snow. For the dry winter case absorption and scattering are observed to increase with frequency. For the dry spring snow, on the other hand, the coefficients with the exception of scattering are constant with frequency. Moist snow with a wetness of 1 to 3 per cent by volume exhibited power damping coefficients greater than 30 dB/meter at all frequencies from 4.9 to 94 GHz (Mätzler, et al., 1979).

5.4.4 NASA Goddard

Airborne measurements of T_b have been conducted by the NASA Goddard Space Flight Center since 1971. Schmugge, et al (1974) reported results (Table 5-2) of measurements over Bear Lake, Utah and Steamboat Springs, Colorado. Penetration to underlying wet soil and water was given as the reason for the very low temperatures at the 21 cm wavelength. The shorter wavelengths responded more to the bulk snow properties, but some ground effect was still seen in the Bear Lake pass. Figure 5-49 illustrates the greater effect of the lake at the longer wavelengths. More recently, Hall, et al. (1978) reported the response to snow depth at two wavelengths (Figure 5-50). Except for the data points noted in Figure 5-50, the observations were obtained over dry snow. Figure 5-51 shows that the effect of ground conditions (frozen or thawed) is small at λ = .8 cm while it is very important at λ = 21 cm. The snow depths were a trace for the frozen ground condition and 2.5 cm for the thawed ground condition.

During the winter of 1977-1978 an experiment was conducted in Colorado using radiometers operating at 5, 10.7, 18 and 37 GHz. Shiue, et al. (1978) reported preliminary results which showed that large crystal sizes caused lower brightness temperatures at 37 GHz for all angles of incidence than did small crystal sizes for similar snow depths. The variation of brightness temperature with depth displayed a smaller slope (Figure 5-52) than Edgerton's, et al. (1971) data given in Figure 5-37. The small slope was attributed to the large 3-5 mm crystal grain size. Also T_B of naturally occurring snow was measured (Figure 5-53) as a function of water equivalent.

TABLE 5-2

Observed Brightness Temperatures, in Kelvins (Schmugge, et al., 1974)

	Snow Thickness (m)	21 cm	11 cm	6 cm	2.8 cm	1.55 cm	0.8 cm Horiz.	0.8 cm Vert.	IR 10-12μm
Bear Lake Alt. 1805 m	.15	123	156	163	193	206	198	231	268
Steamboat Springs Alt. 2070 m	.8	212	235	246	243	215	211	235	266

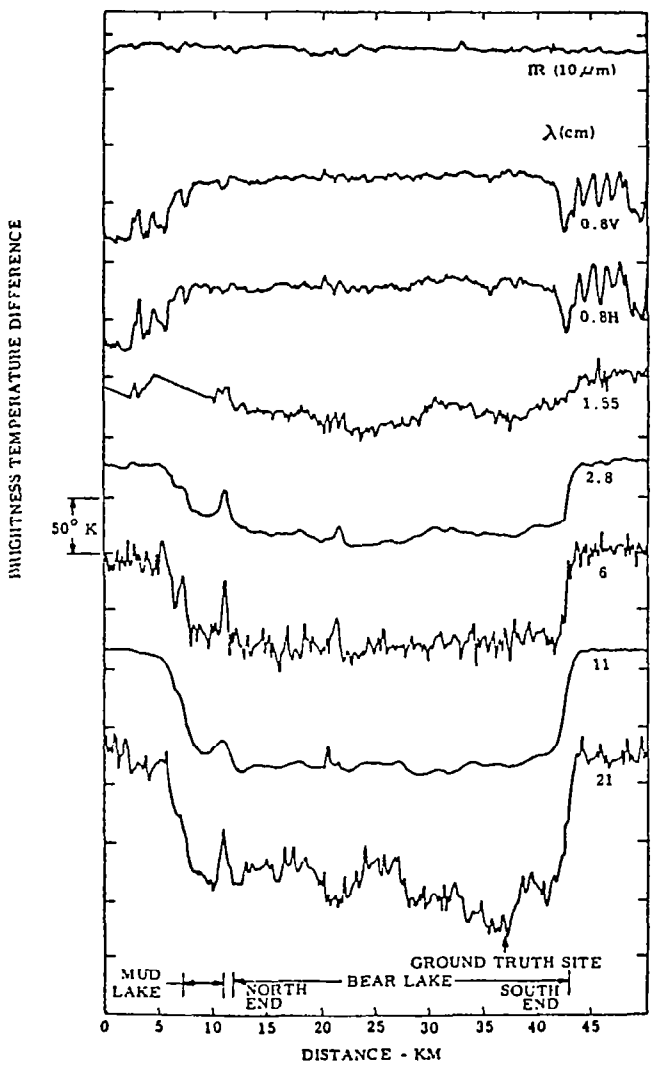


Figure 5-49 Multispectral data obtained over Bear Lake. The H and V refer to the horizontal and vertical channels of the 0.8 cm radiometer which viewed the surface at an angle of 45°. The remaining radiometers were nadir viewing. (Schmugge, et al., 1974)

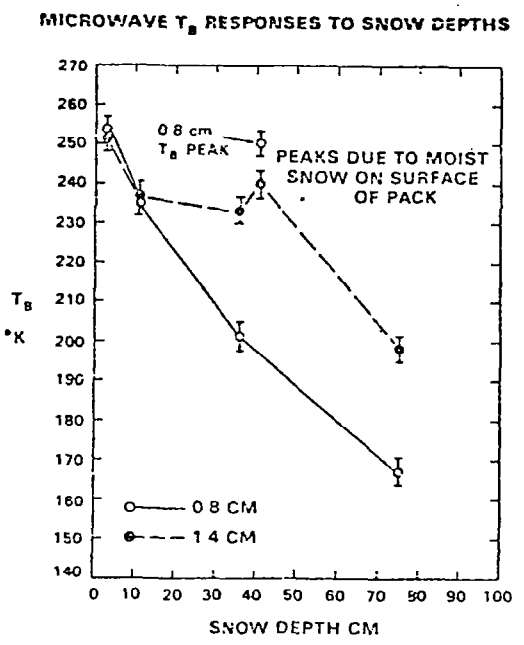


Figure 5-50 Brightness temperature versus snow depth for wet and dry snow. (Hall, et al., 1978)

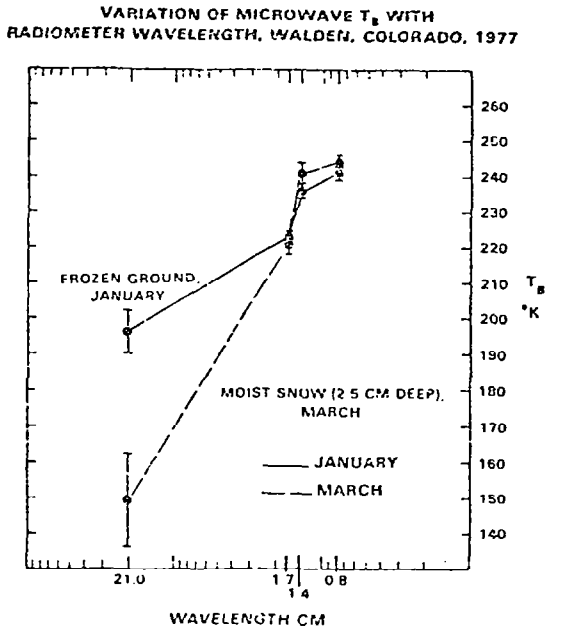


Figure 5-51 Brightness temperature spectral response to moist snow and frozen ground in Colorado. (Hall, et al., 1978)

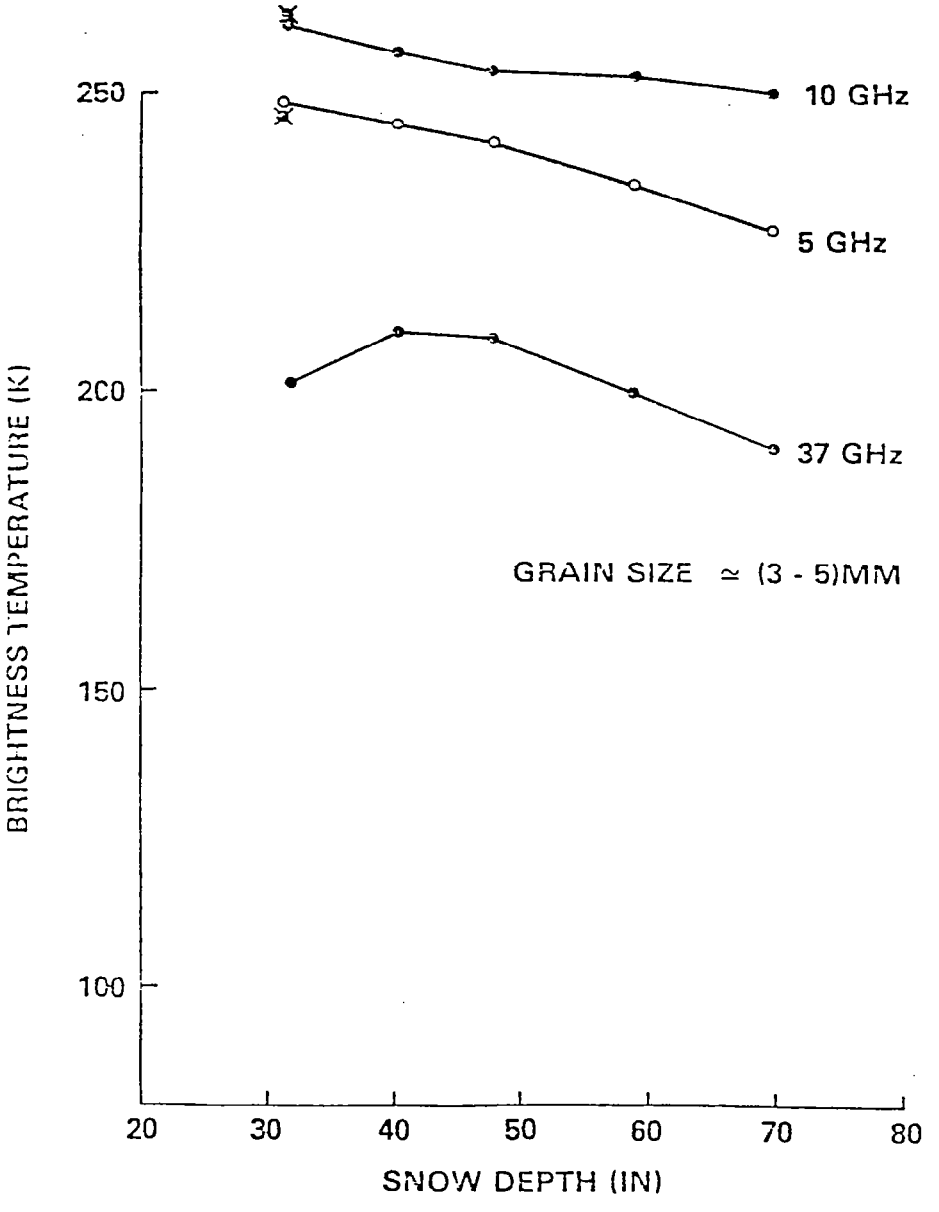
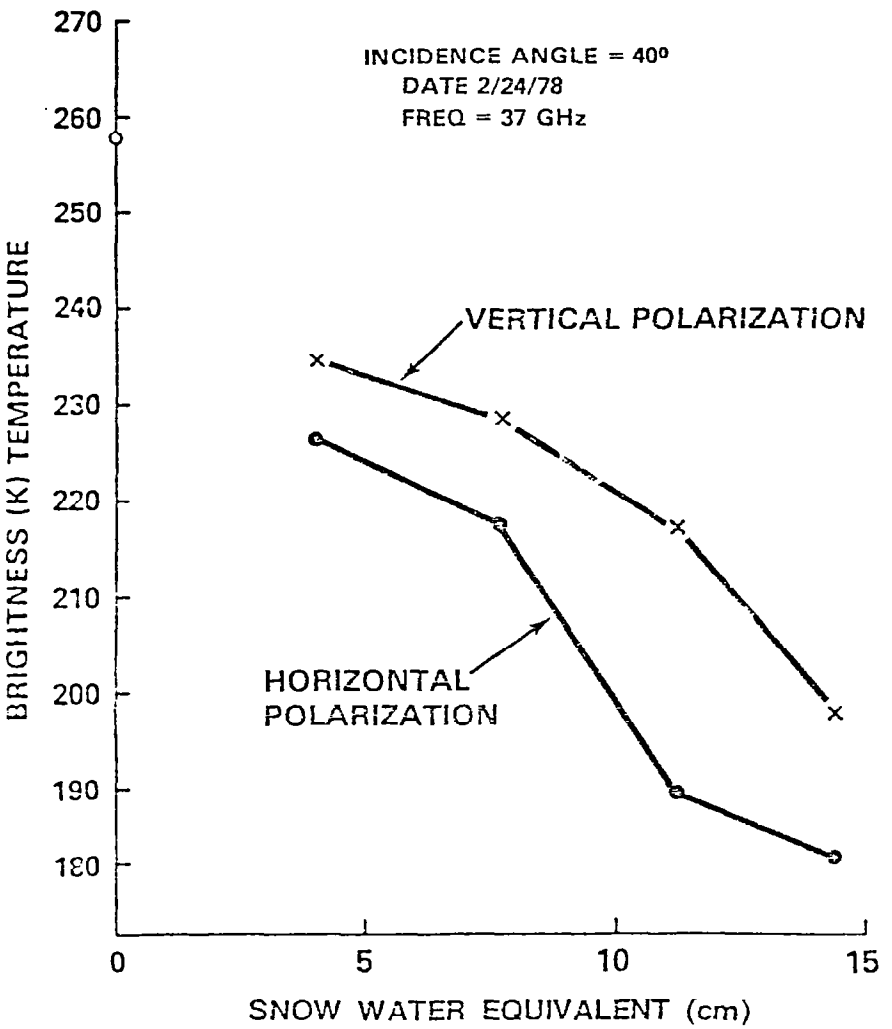


Figure 5-52 Brightness temperature vs. snowpile depth. (Shiue, et al., 1978)



Note 1: 0 is a Nadir Measurement for bare soil.

Note 2: The right most data point is measured by 35 GHz radiometer.

Figure 5-53 Brightness temperature of natural snowpack as a function of water equivalent. (Shiue, et al., 1978)

5.4.5 ESMR

The Electronically Scanning Microwave Radiometer (ESMR) on the Nimbus-5 satellite has been operational since 1972 (Rango, et al., 1979). Its low resolution limits observation to large glacial areas. Nimbus-5 data was used by Gloersen and Salomonson (1975) to map snow extent over Greenland (Figure 5-54). Also on the Nimbus-5 are nadir viewing radiometers operating at 22.2, 31.4, 53.65, 54.9 and 58.8 GHz. Kunzi, et al. (1976) used the 22.2 and 31.4 GHz channels to observe signatures from ice and snow. The mean brightness temperature and brightness temperature gradients were calculated. The gradient over snow covered ground was always less than -0.4 K/GHz while the gradient over bare ground was always greater than -0.4 K/GHz. They therefore concluded that a two frequency radiometer system could be used for large scale mapping of snow extent.

The ESMR on Nimbus-6 operating at λ = 0.81 cm was used by Rango, et al. (1979) to measure snow accumulation (Figure 5-55), and snow areal extent over North America (Figure 5-56) and to determine snow depth over the high plains of Canada. High negative correlation of brightness temperature to snow water equivalent was observed over short and high grass prairie for dry snow. The linear fit is illustrated in Figure 5-57 for dry snow. Wetness was observed to cause a large increase in brightness temperature, as expected, and the sensitivity to snow water equivalent was noted to be greater for the Nimbus-6 ESMR (λ = 0.81 cm) than for the Nimbus-5 ESMR (λ = 1.55 cm).

5.4.6 Summary of Passive Measurements

Analogous to the analyses of the active data, comprehensive ground truth data are required for interpretation of passive results. Edgerton did obtain passive data with variations in both water equivalent and snow wetness. More recent measurements (Schanda and Hofer, 1977; Shiue, et al., 1978) have looked in detail at the effects of wetness and water equivalent. Also the feasibility of snow extent mapping has been demonstrated (Gloersen and Salomonson, 1975; Rango, et al., 1979). Any superiority of passive microwave remote sensing over active microwave remote sensing or vice versa cannot be shown because of the lack of comprehensive active measurements and the lack of simultaneous active and passive measurements. Therefore, although more extensive passive microwave measurement programs have been performed, the need for

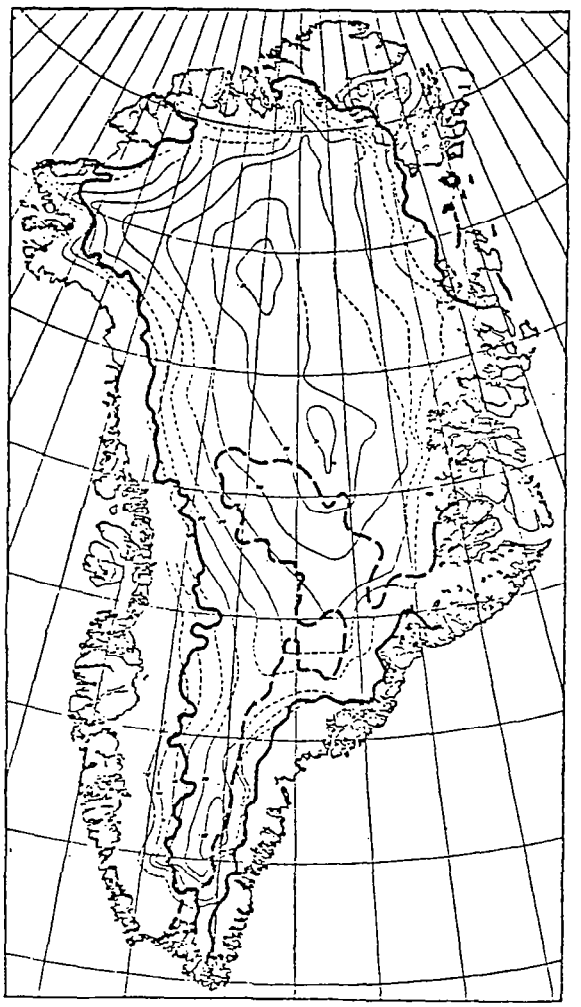


Figure 5-54 The thick solid line is the summer melt line in the snow field covering the Greenland continental ice sheet as deduced from Nimbus-5 ESMR data obtained on July 21, 1973. The area to the east of the thick dashed line is that in which the highest microwave brightness temperatures were observed on January 11, 1973. (Gloersen and Salomonson, 1975)

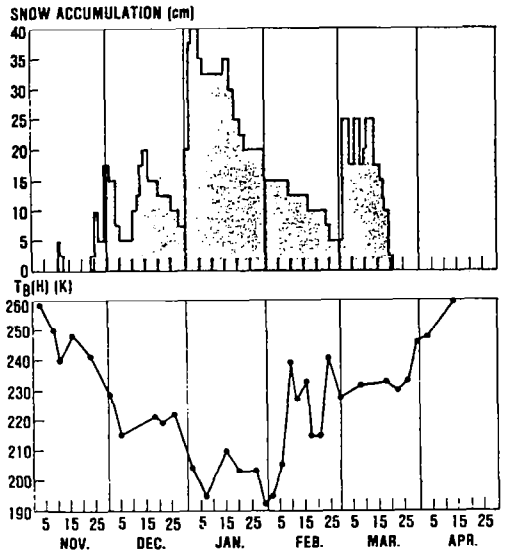
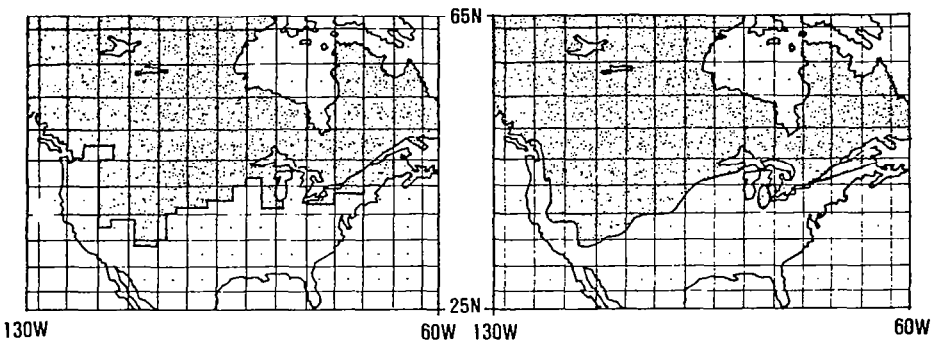
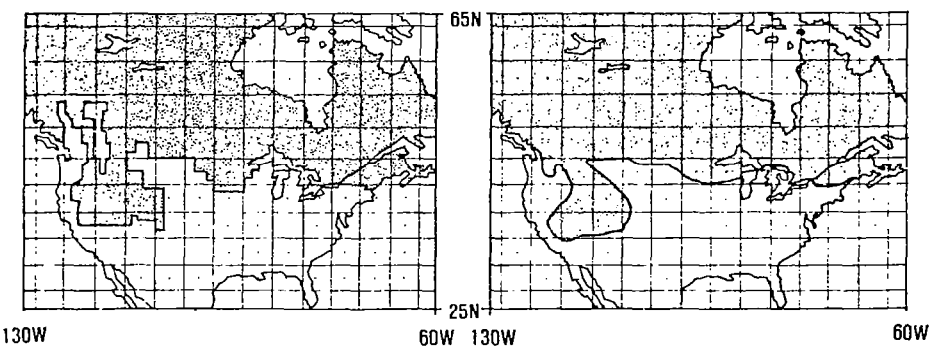


Figure 5-55 Snow accumulation and Nimbus-6 ESMR horizontally polarized brightness temperature data (1975-1976) for Williston, North Dakota, U.S.A. (Rango, et al., 1979)



DERIVED FROM NIMBUS-6 ESMR DATA. THE AREA SHADED REPRESENTS SNOW COVER.

SNOW BOUNDARY MAP BY NOAA-NESS. THE AREA SHADED REPRESENTS SNOW COVER.



DERIVED FROM NIMBUS-6 ESMR DATA. THE AREA SHADED REPRESENTS SNOW COVER.

SNOW BOUNDARY MAP BY NOAA-NESS. THE AREA SHADED REPRESENTS SNOW COVER.

Figure 5-56 Snow coverage maps of North America for the period of March 15-21, 1976. (Rango, et al., 1979)

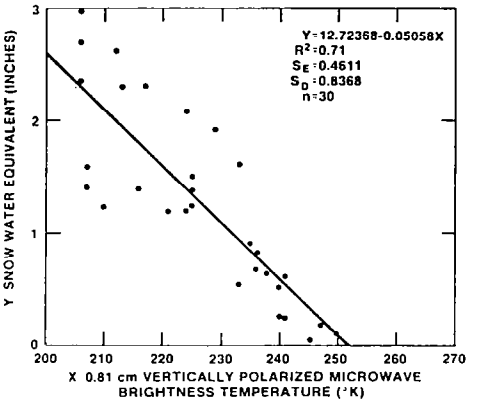


Figure 5-57 Nimbus-6 vertically polarized microwave brightness temperature versus snow water equivalent on the Canadian high plains. Nimbus-6 data from daytime pass March 15, 1976 summarized by one degree latitude-longitude grid; water equivalent data from March 15, 1976 summarized over same grid; data included from short and high grass prairie areas only. (Rango, et al., 1979)

conducting simultaneous active and passive microwave measurements over angles of incidence from 0° to 70° is clear.

6.0 EXPERIMENT DESCRIPTION

This chapter states the objectives and provides a description of the snow experiment perfromed in Steamboat Springs, Colorado in 1977. In general it can also serve as a guide in setting up future experiments in microwave remote sensing of snow. Test site selection, microwave sensors, ground truth sensors and techniques, and data acquisition are covered in detail.

6.1 Objectives

The general objective of this study, covered in Chapter 2, is to evaluate the use of microwave remote sensing techniques for monitoring snowpack conditions that are of hydrologic significance. This objective was to be achieved by the following detailed tasks:

(1) To obtain high quality ground truth information to include, but not limited to snow depth, temperature, density, snow wetness, water equivalent and underlying soil moisture.

(2) To experimentally determine the influence of snowpack parameters (depth, water equivalent, wetness, density, stratification,temperature, soil moisture, etc.) under naturally occurring conditions on the radar return as a function of the radar sensor parameters (frequency, polarization, angle of incidence). The frequency range of 1 to 35 GHz, linear polarization combinations, and 0° to 70° angle of incidence were desired.

(3) To experimentally determine the microwave radiometric response to snowpack parameters under naturally occurring conditions at X-Band (10.69 GHz), Ka-Band (37 GHz), and W-Band (94 GHz).

(4) To develop empirical and theoretical models to represent the microwave/snowpack interactions (Chapters 2 and 9).

6.2 Test Site Selection and Description

The following criteria were used for the site selection:

1. The target area had to be flat, fairly homogeneous and unobstructed.
2. The depth of the snowpack had to be "adequate".

3. The area had to be accessible.

4. The area had to be close to the University of Kansas.

A site survey was conducted on three areas in Colorado and Steamboat Springs was chosen. A 40-acre hay field approximately seven miles south of town was rented from Mr. Ben Hibbert of Steamboat Springs. Figure 6-1 shows the test site before the first snowfall. The surface was very flat and was covered with close-cut hay, approximately 6 cm in height.

The experiment layout is illustrated in Figure 6-2. Test plot #1 was the main test area for observation with the microwave sensors. Test plot #2 contained buried enclosures for the attenuation experiment. It was also to serve as the back-up area for the main test plot. The radar trucks were parked between plots #1 and #2 and remained stationary for the duration of the experiment. Connections were made to the electric company and the telephone company for the experiment duration. Figure 6-3 shows the trucks and ancillary equipment in place at the test site.

Ground truth data were gathered in a snowpit near the northeastern corner of test plot #1. Periodically, the homogeneity of the test area was checked by sampling the perimeter of the test area. Description of this verification is given in section 7.1.1.

6.3 Microwave Sensors

Microwave measurements of the snowpack were made with both active and passive sensors. The MAS 1-8 and MAS 8-18/35 scatterometers and three microwave radiometers were employed. The following sections describe these systems.

6.3.1 MAS 1-8 and MAS 8-18/35

The MAS systems are both mobile truck mounted wideband FM-CW radars. These systems are calibrated to make absolute radar cross section measurements. Figure 6-3 shows the systems in operation at the test site. Each MAS system is mounted on its own hydraulic boom. The operator's console and data processing equipment are housed in the instrumentation van.

System specifications are given in Table 6-1. Closeups of the antennas are shown in Figures 6-4 and 6-5. Each system is computer controlled; data formatting and processing are handled by the minicomputer. A block diagram of the MAS 8-18 is shown in Figure 6-6, and except for the difference in frequency coverage, the MAS 1-8 block diagram is similar

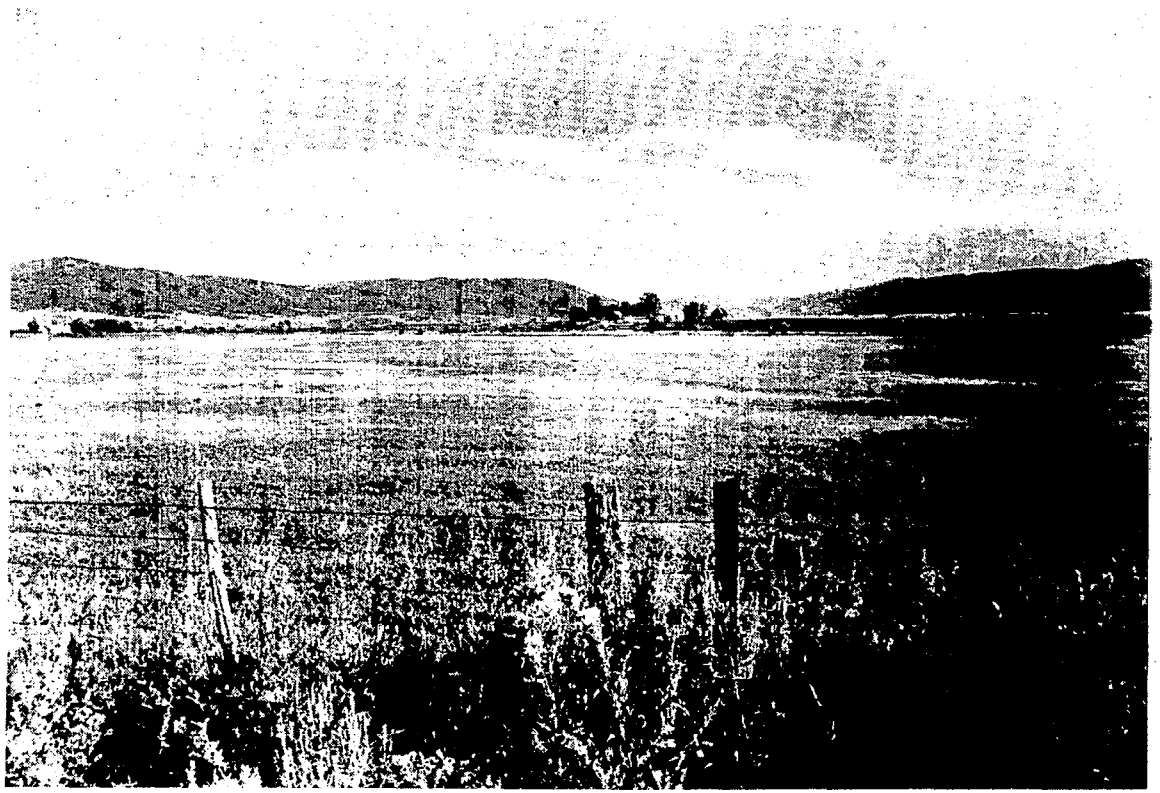


Figure 6-1 Steamboat Springs test site

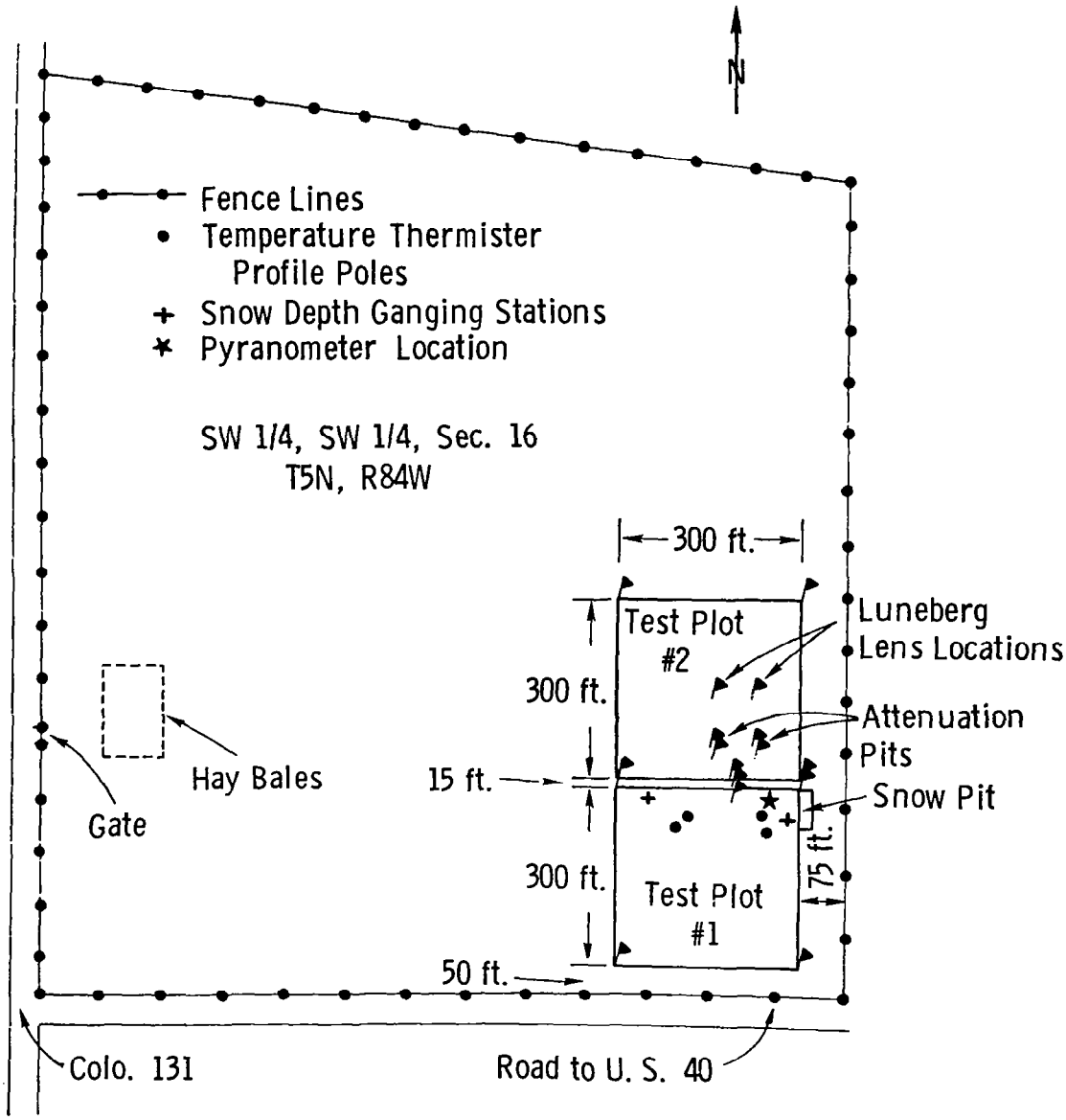


Figure 6-2 Steamboat Springs test site layout.

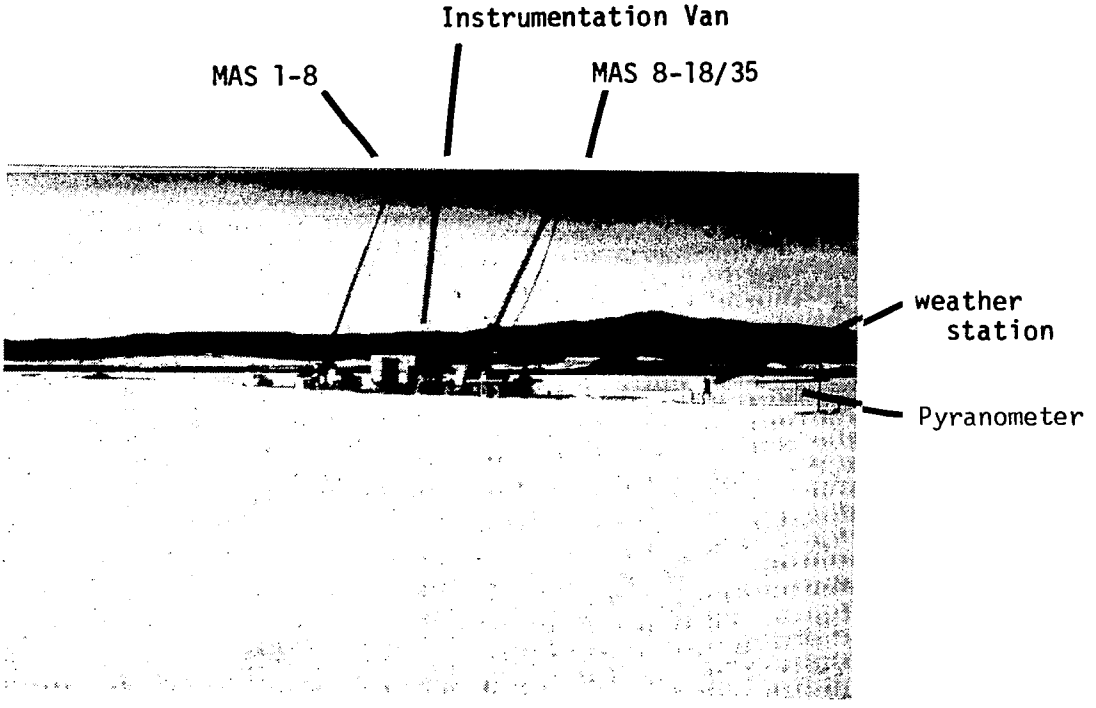


Figure 6-3 Test plot layout.

TABLE 6-1

MAS 1-8 and MAS 8-18/35 Nominal System Specifications

	MAS 1-8	MAS 8-18	35 GHz Channel
Type	FM-CW	FM-CW	FM-CW
Modulating Waveform	Triangular	Triangular	Triangular
Frequency Range	1-8 GHz	8-18 GHz	35.6 GHz
FM Sweep: Δf	400 MHz	800 MHz	800 MHz
Transmitter Power	10 dBm	10 dBm	1 dBm
Intermediate Frequency	50 KHz	50 KHz	50 KHz
IF Bandwidth	10 KHz	10 KHz	10 KHz
Antennas			
Height above Ground	20 m	26 m	26 m
Type	122 cm Reflector	46 cm Reflector	Scalar Horn
Feeds	Crossed Log-Periodic	Quad-Ridged Horn	----
Polarization Capabilities	HH, HV, VV	HH, HV, VV	HH, HV, VV, RR, RL, LL
Beamwidth	12° at 1.25 GHz to 1.8° at 7.25 GHz	4° at 8.6 GHz to 2° at 17.0 GHz	3°
Incidence Angle Range	0° (nadir)-80°	0° (nadir)-80°	0° (nadir)-80°
Calibration:			
Internal	Signal Injection (delay line)	Signal Injection (delay line)	Signal Injection (delay line)
External	Luneberg Lens Reflector	Luneberg Lens Reflector	Luneberg Lens Reflector

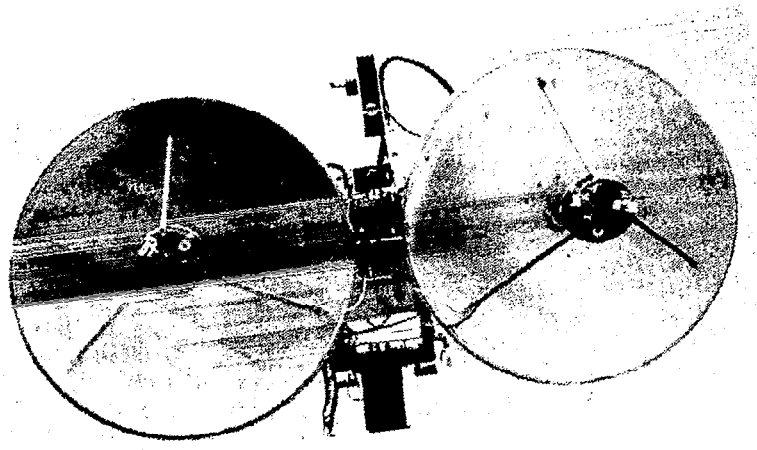
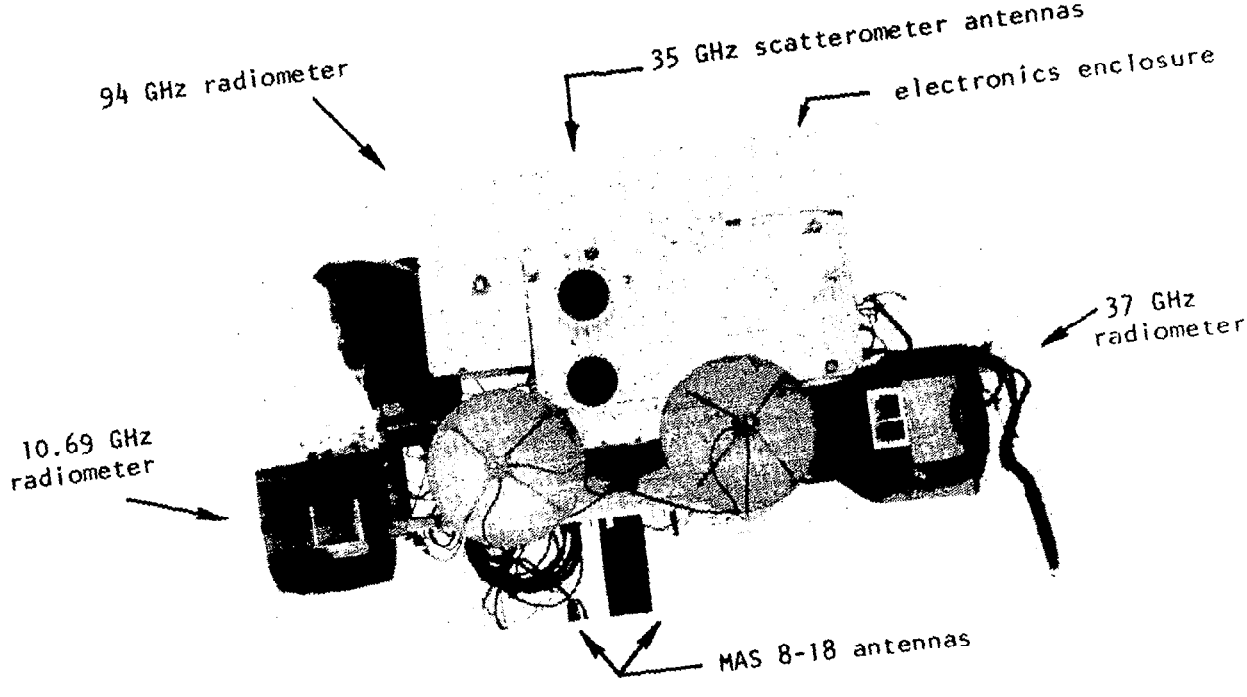


Figure 6-4 Closeup of MAS 1-8 RF section.



Closeup of the MAS 8-18/35 RF section.

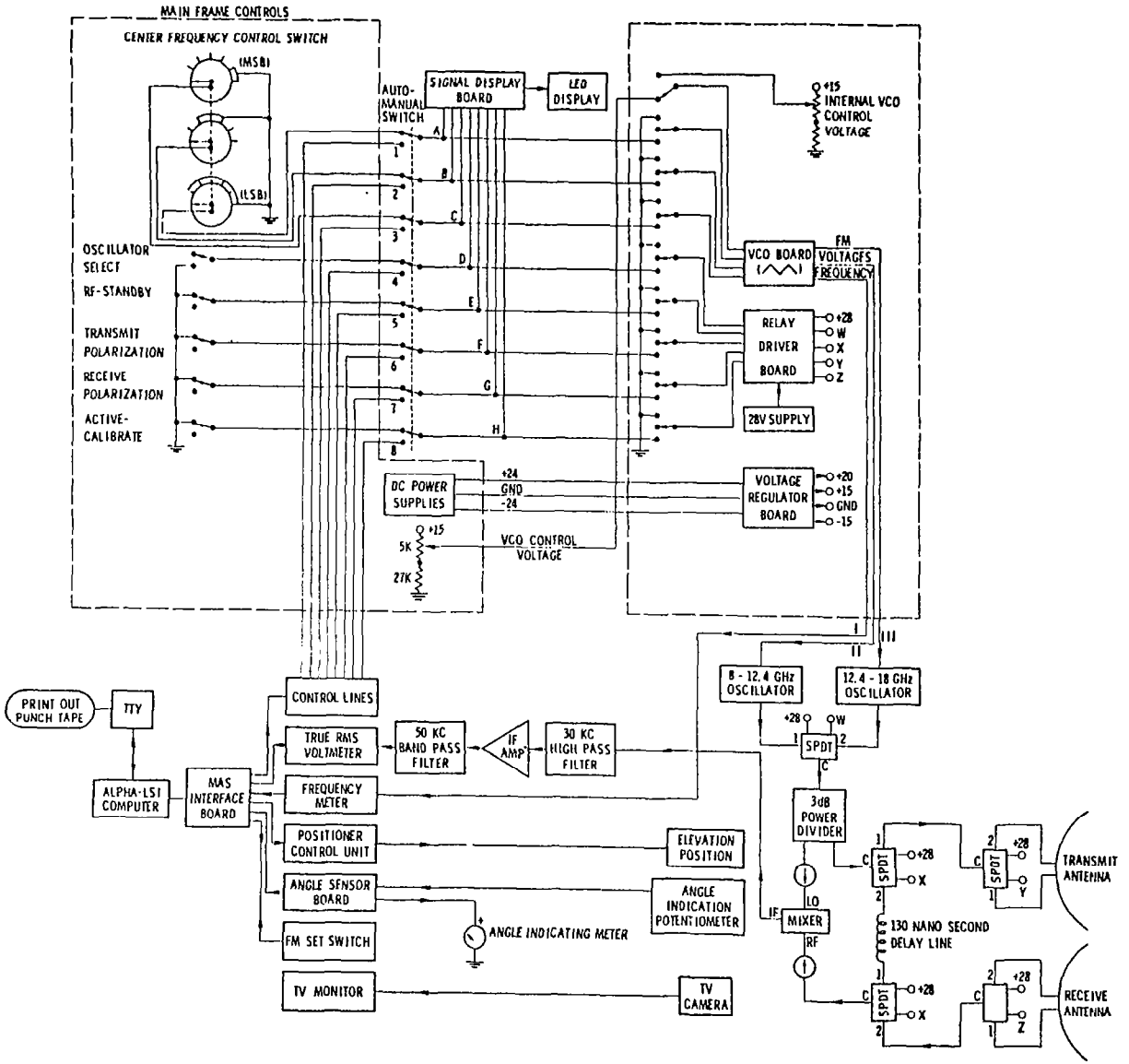


Figure 6-6 MAS 8-18 block diagram.

in configuration to the MAS 8-18. The 35 GHz channel is a dual conversion scatterometer. The block diagram of the RF module is given in Figure 6-7. Detailed information on the MAS systems are contained in reports by Ulaby, et al. (1979), Brunfeldt, et al. (1979) and Stiles, et al. (1979).

Radar data were acquired at eight frequencies between 1.125 GHz and 7.75 GHz for MAS 1-8, while MAS 8-18/35 acquired data at 11 frequencies between 8.6 and 17.0 GHz, in addition to 35.6 GHz. The systems operate in three polarization configurations, HH (horizontal transmit-horizontal receive), HV (horizontal transmit-vertical receive), and VV (vertical transmit-vertical receive). In addition, at 35.6 GHz, RR (right circular transmit-right circular receive), RL (right circular transmit-left circular receive), and LL (left circular transmit-left circular receive) polarization capabilities are available. Data can be obtained at any angle of incidence between 0° and 80° from nadir. Receive power levels are converted to scattering cross section by a two-step calibration procedure. Short-term power variations due to oscillator power, mixer temperature, etc., are normalized by referencing the backscattered power to the power transmitted through a coaxial delay line of known loss. Actual calibration to radar cross section value is accomplished by referencing the target return power to the power returned from an object of known radar cross section. A Luneberg lens reflector is used for this purpose. The radar cross-section of the Luneberg lens reflector has been calibrated against a metal plate. For calibration in the field, the lens is preferred over the sphere as a calibration target because of its larger radar cross-section and it is favored over other calibration targets (metal plate, corner reflector, etc.) because of its wide azimuthal and elevation beamwidths. The calculation of σ° or scattering coefficient results from evaluating the radar equation for an area extensive target (Section 2.1).

$$P_r = \iint_A \frac{P_t\, G_t\, G_r\, \lambda^2 \sigma^\circ\, dA}{(4\pi)^3\, R^4_t} \qquad (6\text{-}1)$$

If the assumption is made that the parameters inside the integral are constant over the illuminated area, the radar equation becomes:

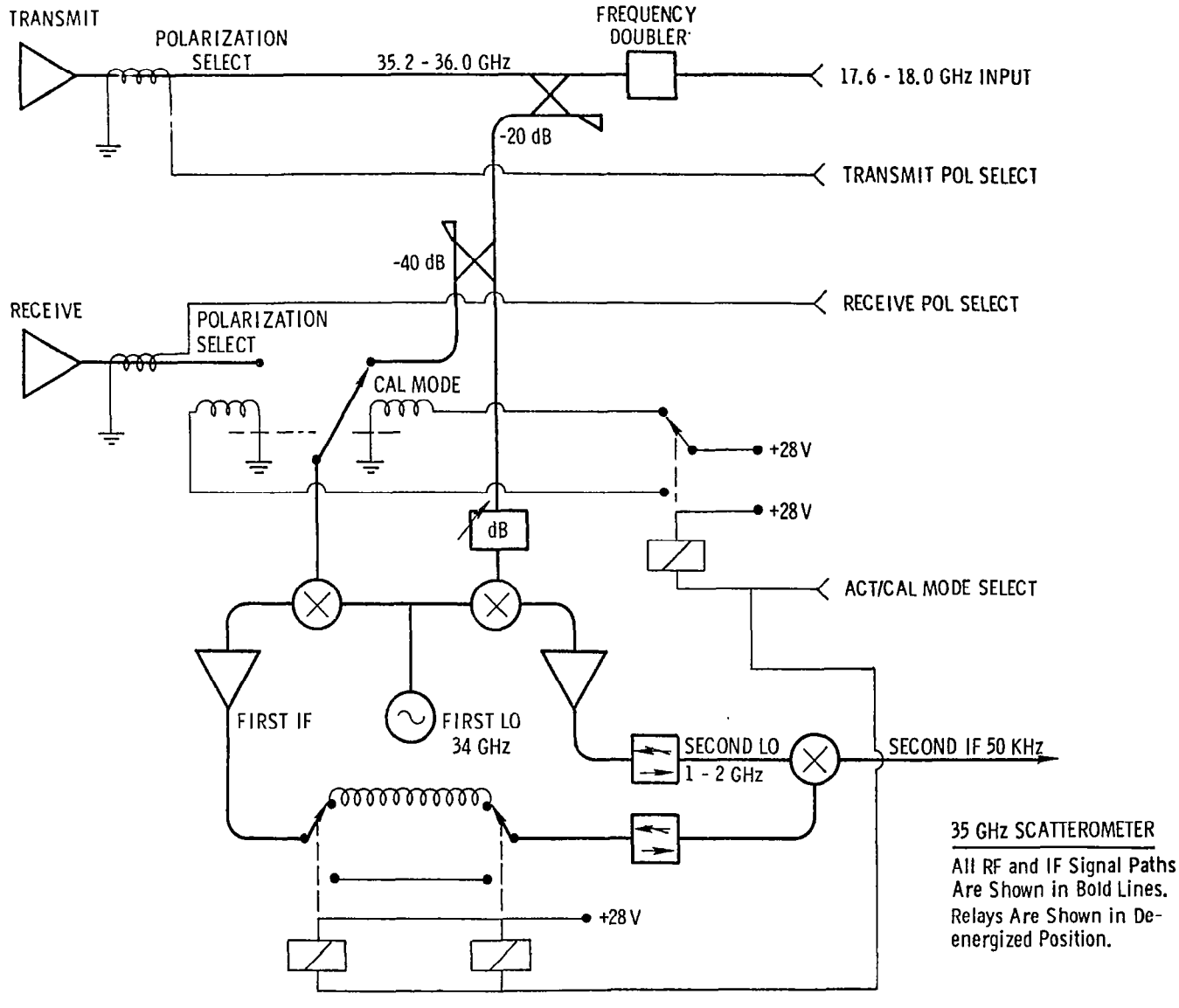


Figure 6-7 Overall Schematic of the 35 GHz Radar Module

$$P_r = \left[\frac{P_t\ G_t\ G_r\ \lambda^2 \sigma^\circ A_{ill}}{(4\pi)^3\ R^4_t}\right] \qquad (6\text{-}2)$$

Note that P_r represents the received power at the receive antenna terminal. If we introduce an unknown constant K_t to represent the effects of cable loss, mixer conversion loss etc., we can write

$$V_t = K_t \left[\frac{P_t\ G_t\ G_r\ \lambda^2\ \sigma^\circ\ A_{ill}}{(4\pi)^3\ R^4_t}\right]^{1/2} \qquad (6\text{-}3)$$

where V_t is the voltage at the mixer output.

Shortly before or after recording the return from the target of interest, switches at the transmit and receive RF lines are actuated to replace the transmit antenna-receive antenna path with a coaxial delay line of loss L. Thus, the voltage received in this configuration is given by:

$$V_{td} = K_t\ [P_t\ L]^{1/2} \qquad (6\text{-}4)$$

The ratio of the two voltages, M_t, is given by:

$$M_t = \frac{V_t}{V_{td}} = \left[\frac{G_t\ G_r\ \lambda^2\ \sigma^\circ\ A_{ill}}{(4\pi)^3\ R^4_t\ L}\right]^{1/2} \qquad (6\text{-}5)$$

Thus any variations in P_t or K_t are removed by this internal calibration technique.

In addition to internal calibration, external calibration is also conducted by recording the voltage corresponding to the return from a standard target of known radar cross section, in this case a Luneberg lens reflector. The measured voltage is given by:

$$V_c = K_c \left[\frac{P_t\ G_t\ G_r\ \lambda^2 \sigma_c}{(4\pi)^3\ R^4_c}\right]^{1/2} \qquad (6\text{-}6)$$

where K_c is the receiver transfer constant during calibration against the lens, R_c is the range to the lens and σ_c is the radar cross section of the lens. Again, internal calibration with the delay line is conducted shortly before recording the voltage due to the calibration target:

$$V_{cd} = K_c\ [P_t\ L]^{1/2} \qquad (6\text{-}7)$$

and the ratio is given by:

$$M_c = \frac{V_c}{V_{cd}} = \left[\frac{G_t\, G_r \lambda^2 \sigma_c}{(4\pi)^3\, R_c^4\, L}\right]^{1/2} \qquad (6\text{-}8)$$

Combining Eqs. 6-5 and 6-8 yields the following expression for σ^o in dB.

$$\sigma^o\,(dB) = 20 \log M_t - 20 \log M_c + 10 \log \sigma_c - 20 \log A_{ill} + 40 \log R_t - 40 \log R_c \qquad (6\text{-}9)$$

The first two quantities are measured and recorded by the system and σ_c is known (measured by the manufacturer) with respect to a flat plate. R_t and R_c are determined through measurement of the modulation frequency f_m:

$$R_t = \frac{f_{IF} c}{4 \Delta f f_m} \qquad (6\text{-}10)$$

where

c = the velocity of propagation

f_{IF} = intermediate frequency

Δf = bandwidth of FM sweep

f_m = modulation frequency

Finally, A_{ill} is calculated from the geometry on the basis of measured values of the beamwidths (for each frequency-polarization configuration) and the range R_t.

6.3.2 Radiometers

Passive microwave data were acquired with radiometers operating at 10.69, 37 and 94 GHz. These devices were all obtained for this experiment from outside organizations. The manufacturer's specifications are given in Table 6-2.

The 10.69 and 37 GHz radiometers were operated with 1 second integration time. The effective integration time for the 94 GHz radiometer was 67 ms. Data were taken at the same angles as the scatterometer since the radiometers were located on the boom with the MAS 8-18/35. Calibration of the radiometers was checked when possible by looking at the sky or microwave absorber.

TABLE 6-2

Radiometer Specifications

Manufacturer	Aerojet	Aerojet	Sperry
Frequency	10.69 GHz	37 GHz	94 GHz
Type	Dicke	Dicke	Total-power
Polarization	H	H and V	H
Bandwidth	200 MHz	300 MHz	730 MHz
Sensitivity (Δt min)	.2K (1-sec.)	.5K (1-sec.)	3.5K
Accuracy	1K	$\pm$1K	$\pm[.05(300-T_s)+6]$
Temperature Range	50-350K	0-500K	0-500K
Approx. Gain (Volt/K)	-.012	.010	.020
AGC	No	Yes	Yes

6.3.2.1 10.69 GHz Radiometer

The block diagram of the 10.69 GHz radiometer is given by Figure 6-8. The following equations were used to convert the measured voltages and physical temperatures of components to T_{ap}, the radiometric temperature of the scene viewed by the antenna:

$$T_{HL} = \frac{t_{hl}}{1.108} + \frac{t_{hl} + t_{sw}}{136.8} + \frac{t_{sw}}{12.06} \qquad (6\text{-}11)$$

$$T_{WL} = \frac{t_{wl}}{1.106} + \frac{t_{wl} + t_{sw}}{136.5} + \frac{t_{sw}}{12.38} \qquad (6\text{-}12)$$

$$G = \frac{V_{CAL} - V_{BL}}{T_{HL} - T_{WL}} \qquad (6\text{-}13)$$

$$T_R = T_{HL} - \frac{V_{ANT} - V_{BL}}{G} \qquad (6\text{-}14)$$

$$T_{in} = 1.042 \left[T_R - \frac{t_1 + t_2}{239.7} - \frac{t_2 + t_{sw}}{738.6} - \frac{t_{sw}}{34.25} \right] \qquad (6\text{-}15)$$

$$T_{ap} = 1.009\, L_{ANT} \left[T_{in} - t_{ANT} \left(1 - \frac{1}{L_{ANT}} \right) (.9951) - \frac{T_{RAD}}{440.5} \right] \qquad (6\text{-}16)$$

where

t_{hl} = physical temperature of hot load

t_{sw} = physical temperature of Dicke switch

t_{wl} = physical temperature of warm load

t_1 = physical temperature of waveguide 1

t_2 = physical temperature of waveguide 2

t_{ANT} = physical temperature of antenna

L_{ANT} = loss of the antenna

G = gain factor

T_{HL} = radiometric temperature of hot load

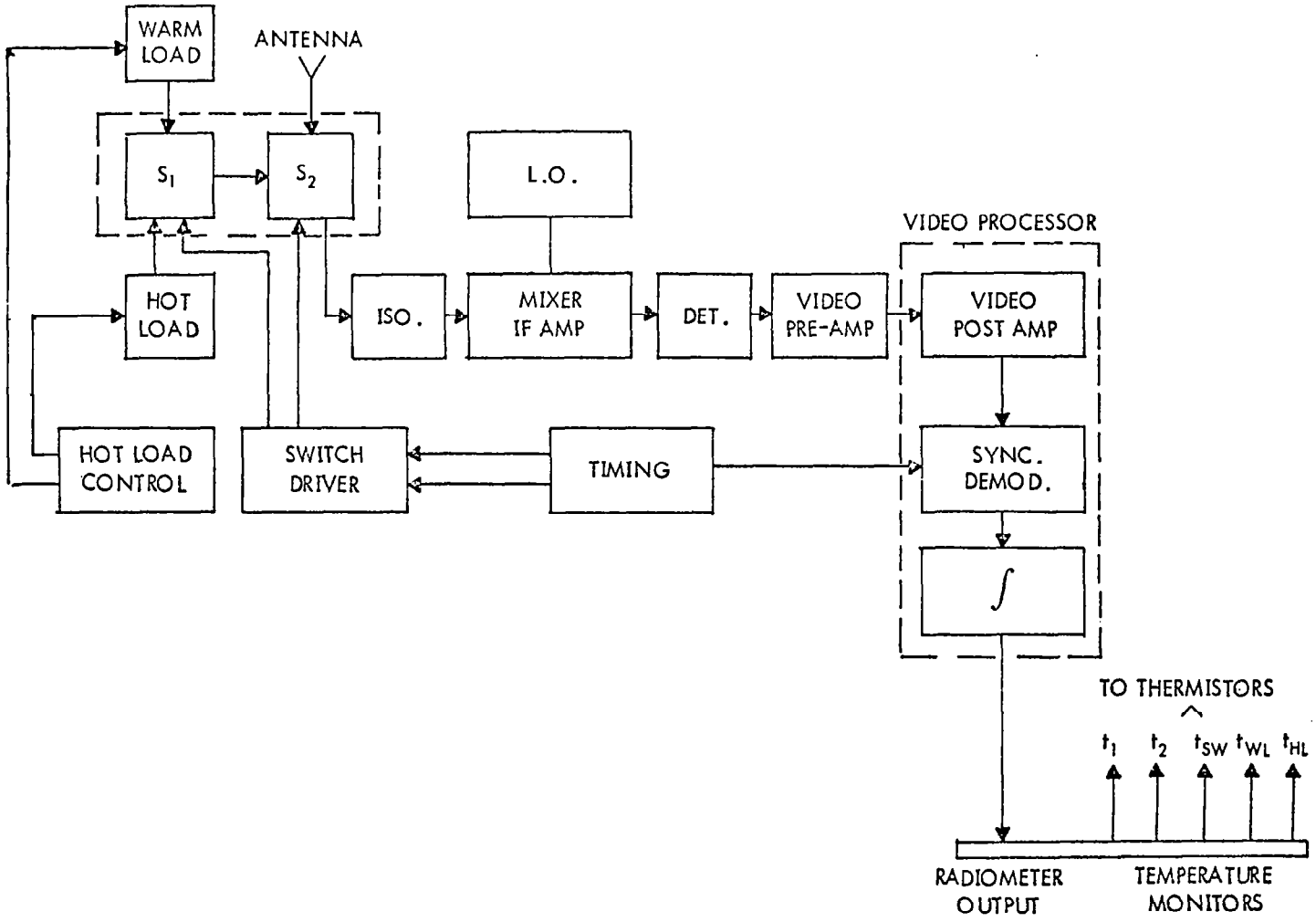


Figure 6-8 Functional block diagram of 10.69 GHz radiometer. (Aerojet)

T_{WL} = radiometric temperature of warm load

T_{in} = radiometric temperature at receiver input

T_{ap} = radiometric temperature at the input to the antenna

V_{ANT} = voltage measured with receiver connected to the antenna

V_{CAL} = voltage measured with receiver connected to the warm load

V_{BL} = voltage measured with receiver connected to the hot load

T_{RAD} = radiometric temperature of energy emitted by the radiometer RF section

Equations 6-11 to 6-15, provided by the radiometer manufacturer's manual (Aerojet), represent the system transfer function between the input to the receiver (T_{in}) and the final output voltages. Equation 6-16 relates T_{ap} to T_{in} by taking into account absorption and mismatch losses of the antenna and waveguide section. The mismatch losses were measured and supplied by Dr. Lawrence Klein, then with NASA Langley Research Center. By matching Equation 6-16 against calculated values of T_{in}, from measurements of the emission from an anechoic absorber of known physical temperature, L_{ANT} is found to be approximately equal to 1.0.

6.3.2.2 37 GHz Radiometer

The 37 GHz radiometer used during the experiment was a dual polarized Dicke type manufactured by Aerojet General Corporation (Figure 6-9). Calibration of the radiometer was performed at the University of Kansas after completion of the Steamboat Springs experiment. The following calibration equations relating the voltages at the output (V_H, V_V) to the input radiometric temperatures for horizontal and vertical polarizations (T_H, T_V) were developed using a linear regression based on radiometric sky measurements and radiometric measurements of the microwave absorber:

$$T_H = 95.06\ V_H - 1.02 \qquad (6\text{-}17)$$

$$T_V = 102.8\ V_V - 23.52 \qquad (6\text{-}18)$$

Figures 6-10 and 6-11 show the calibration curves. The above equations were employed in the calibration of the 37 GHz data in a preliminary report (Stiles, et al., 1977).

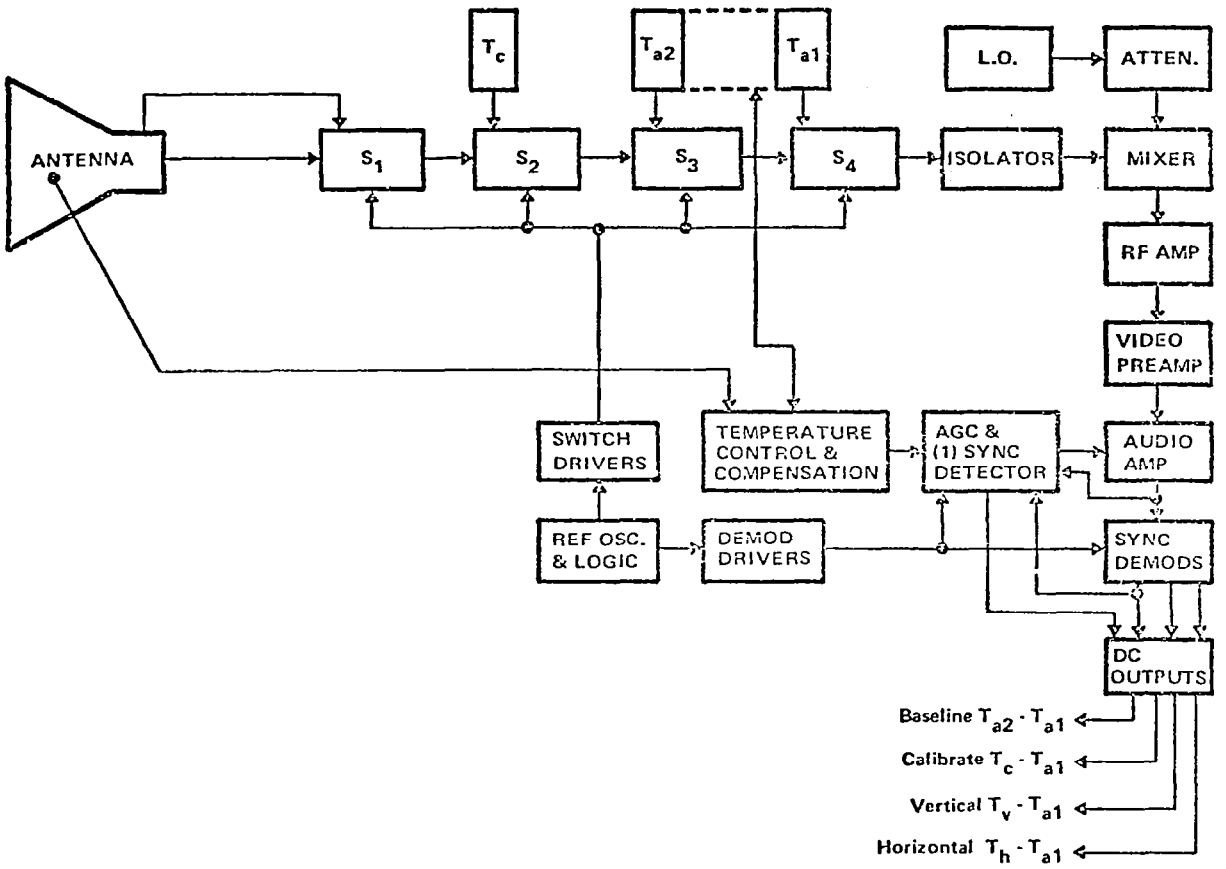


Figure 6-9 Functional block diagram of 37 GHz radiometer.

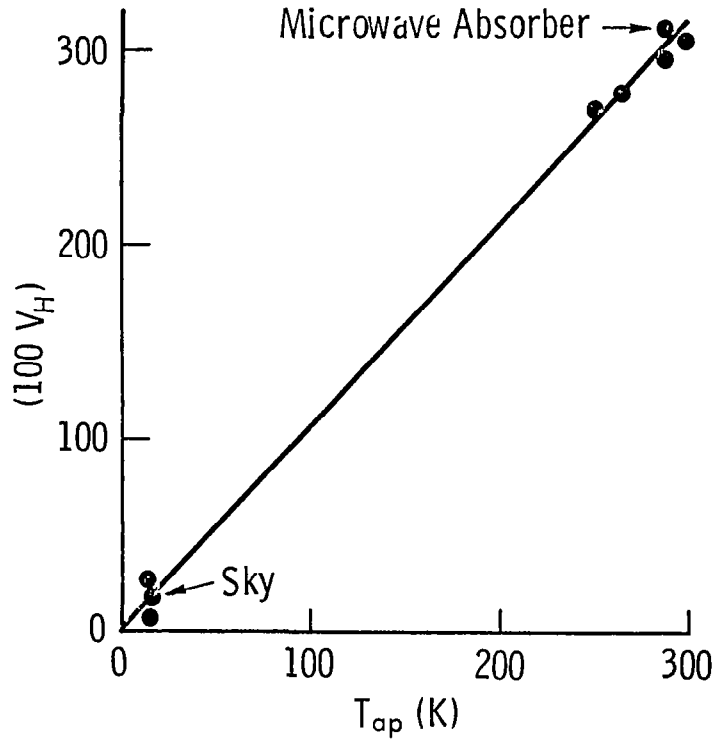


Figure 6-10 Calibration curve of 37 GHz H-polarization radiometer.

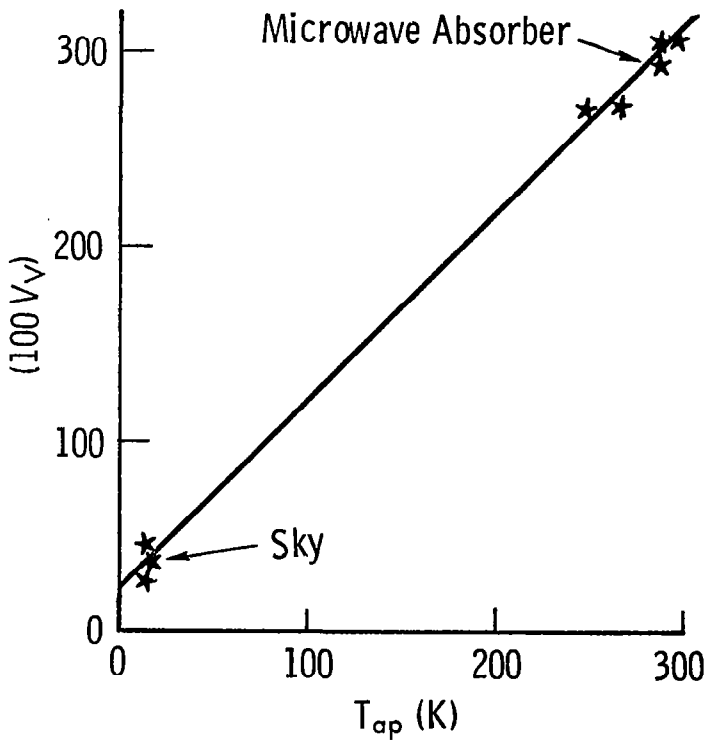


Figure 6-11 Calibration curve of 37 GHz V-polarization radiometer.

Examination of the radiometric sky temperature measurements obtained during the experiment and calibrated using equations (6-17) and (6-18), indicated that as a result of equipment problems, five distinct quasi-stable operational states existed over the experiment duration. As a result, a procedure to recalibrate the radiometer for each state separately needed to be developed.

For a linear system, a two point calibration is sufficient to describe the system characteristics. Therefore, a calculation of radiometric sky temperature was utilized as the "cold" calibration point. The "hot" calibration point was determined from measurements of the microwave absorber or from measurements of wet snow at nadir. A paucity of data on the absorber required the use of the wet snow data as a calibration point (previous observations as well as those reported in Chapter 8 indicate that the emissivity of wet snow is approximately unity at nadir). Linear fits were then calculated for these two points.

The radiometric sky temperature was calculated from the radiative transfer equation (Moore, et al., 1975 in Manual of Remote Sensing)

$$T_{sky} = \int_0^\infty \sec\theta\, T(z)\, \kappa_a(z)\, \exp\left[-\sec\theta \int_0^z \kappa_a(h)\, dh\right] dz \qquad (6\text{-}19)$$

where θ is the angle of incidence, $T(z)$ is the atmospheric temperature profile and $\kappa_a(z)$ is the absorption coefficient profile. A standard atmospheric model (Valley, 1965) was assumed for the temperature and pressure variations:

$$T(z) = \begin{cases} T(0) - 6.5\, z & 0 < z < 11 \text{ km} \\ T(11) & 11 < z < 25 \text{ km} \\ T(11) + 30\,(z-25) & 25 < z < 47 \text{ km} \end{cases} \qquad (6\text{-}20)$$

$$P(z) = P(0) \exp(-z/2.1) \qquad (6\text{-}21)$$

where $P(0)$ and $T(0)$ are the sea level pressure and temperature respectively. The water vapor density is given by:

$$\rho(z) = \rho(0) \exp(-z/2.1) \qquad (6\text{-}22)$$

where $\rho(0)$ is the sea level value in g/m^3 (Malkevich, 1963).

The altitude of Steamboat Springs is 2.0 km. Average surface weather data were transferred to sea level using the above models; the resulting values are

$$T(0) = 286 \text{ K}$$
$$P(0) = 760 \text{ mm}$$
$$\rho(0) = 6.0 \text{ g/m}^3$$

The form of the loss Γ(dB/km) with temperature and pressure is given by Tolbert, et al. (1964) for both water vapor (Γ_{H_2O}) and oxygen (Γ_{ox})

$$\Gamma_{H_2O}(z) = \Gamma_{H_2O}(0) \frac{(P(z)/P(0))^2}{(T(z)/T(0))^3} e^{-.5z} \qquad (6\text{-}23)$$

$$\Gamma_{ox}(z) = \Gamma_{ox}(0) \frac{(P(z)/P(0))^2}{(T(z)/T(0))^4} \qquad (6\text{-}24)$$

where $\Gamma_{H_2O}(0)$ and $\Gamma_{ox}(0)$ are the sea level values. The absorption coefficient $\Gamma(z)$ is given by:

$$\kappa_a(z) = (\Gamma_{ox}(z) + \Gamma_{H_2O}(z))/10 \log_{10} e \qquad (6\text{-}25)$$

Sea level values of the loss factor are:

$$\Gamma_{ox}(0) = .027 \text{ dB/km}$$

$$\Gamma_{H_2O}(0) = .09 \text{ dB/km}$$

The above values were obtained from Fraser, et al. (1975), in Manual of Remote Sensing). The water vapor value was estimated for a water vapor density of 6.0 g/m^3

Inserting the above relationships into Equation (6-19) yields:

$$T_{sky} = 11.96 \text{ K} \qquad (6\text{-}26)$$

Radiometric measurements on microwave absorber (assuming unity emissivity) must equal the physical temperature. Eccosorb CV-3 was used as the absorbing material. For cases where such measurements were not made, an alternative reference was needed. For snow, the radiometric

temperature can never exceed 273K. Edgerton, et al. (1971) and Schanda and Hofer (1977) measured maximum temperatures on wet snow at 37 GHz from 260 to 265 K. These values correspond to effective emissivities from .95 to .97. Since some of the data obtained with the 37 GHz radiometer prior to recalibration exceeded 273 K, the new calibration procedure introduced a correction equation to lower these apparent values to agree with the maximum temperature of 265 K measured by the other experimenters.

For each of the five periods, all sky measurements were averaged to obtain a mean value. Also, all nadir data corresponding to stable (saturated) wet snow conditions were averaged. For each polarization, the correction equation was generated by linearly relating calculated values of sky and wet snow apparent temperatures to the values provided by the first calibration procedure. Using the above procedure, calibration equations were generated for each of the five periods.

6.3.2.3 94 GHz Radiometer

The 94 GHz radiometer, manufactured by Sperry Microwave Electronics Co., is shown in block diagram form in Figure 6-12. This device is a total power radiometer using a reference signal to achieve automatic gain stabilization. The technical manual (Sperry, 1977) gives the following relationship between output voltage (V_{94}) and input radiometric temperature (T_{ap}).

$$T_{ap} = 50\ V_{94} \qquad (6\text{-}27)$$

Temperature measurement accuracy is given by

$$\Delta T = \pm\ [.05\ (300\text{-}T_{ap}) + 6]\ K \qquad (6\text{-}28)$$

where T_{ap} is the radiometric apparent temperature of the scene under observation. Absolute accuracy therefore improves with increasing apparent temperature.

An attempt at calibration of this instrument was made after the conclusion of the Steamboat Springs experiment. Radiometric sky measurements along with radiometric measurements of a microwave absorber at various physical temperatures provided the calibration line of Figure 6-13. The linear regression is given by

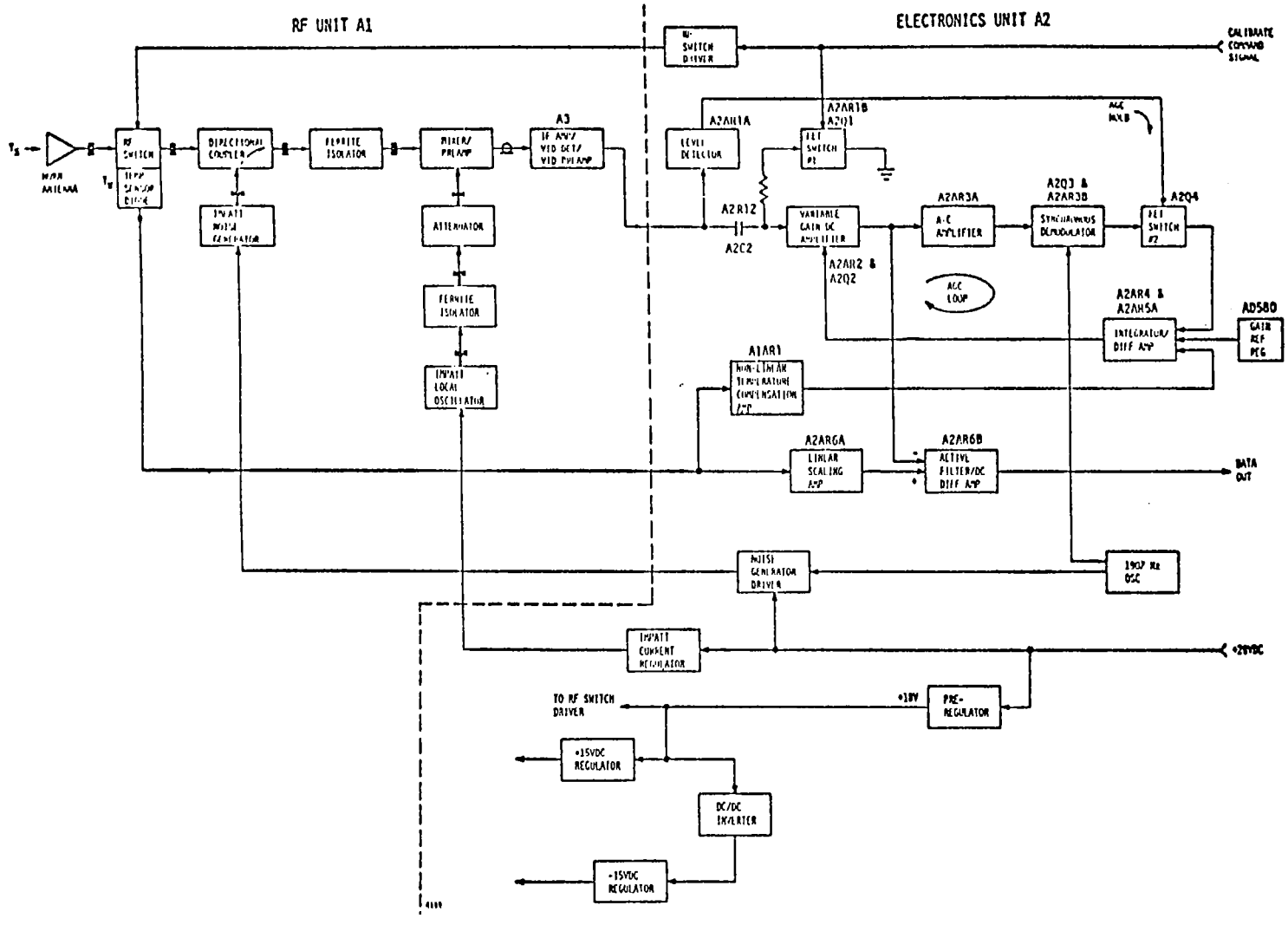


Figure 6-12 Functional block diagram 94 GHz radiometer (Sperry).

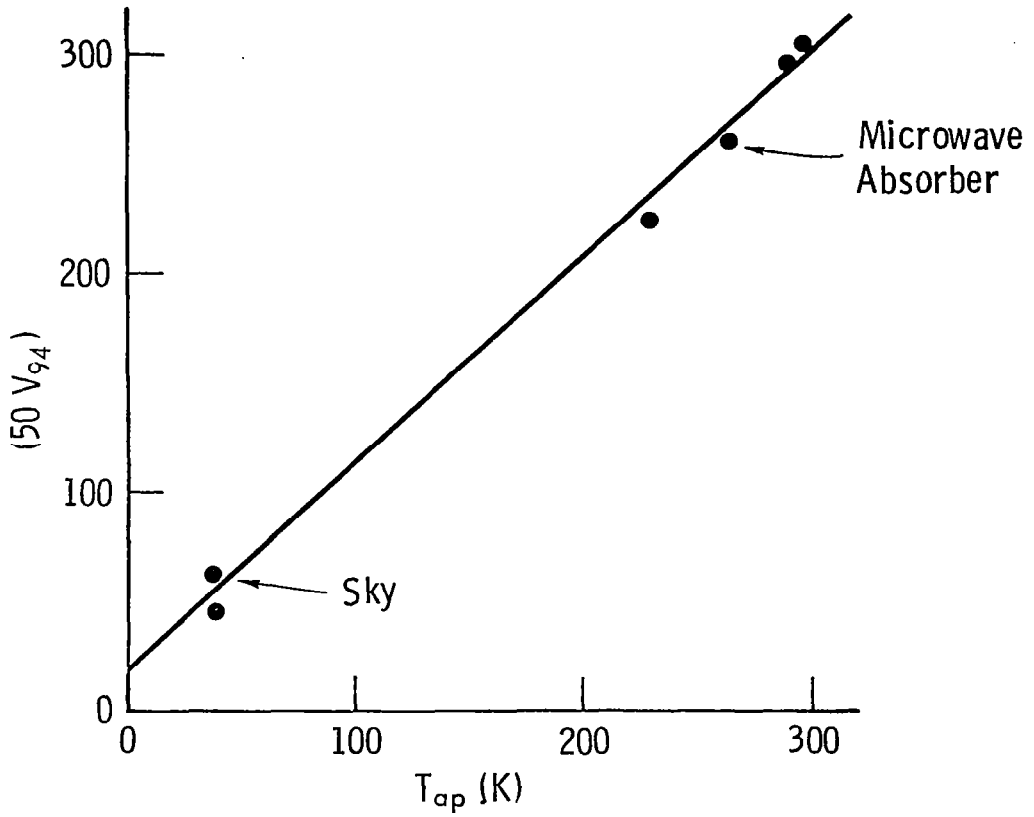


Figure 6-13 Calibration of the 94 GHz radiometer.

$$T_{ap} = 53.4\ V_{94} - 20.86 \qquad (6\text{-}29)$$

This equation was developed while the radiometer operated under constant ambient temperature. Equation (6-29) was employed for the preliminary report presentations (Stiles, et al., 1977). Examination of apparent temperature data obtained by employing equation (6-29) revealed that this calibration equation was inadequate because of system transfer function variations with ambient temperature. Although the ambient temperature of the radiometer RF section was to be maintained constant by a temperature control unit, malfunction of this control unit caused damage to the RF unit from accidental overheating before the start of the experiment. Thus a new calibration procedure was needed which incorporated the dependence on ambient temperature. The following method was used. Calibration, assuming linearity, can be achieved with two measurements. A calculation of the radiometric sky temperature was used for the "cold" calibration point. Sky temperature was calculated from the effects of water vapor and oxygen absorption lines. Inputs to this model included the surface values of temperature, pressure and absolute humidity which were in turn inserted into a standard atmospheric model. Radiometric emission measurements of a microwave absorber at a known temperature were used for the "hot" calibration point. The emissivity of the absorbing material was assumed to be unity; therefore, the radiometric and physical temperatures w assumed equal. The method used is similar to the 37 GHz radiometer calibration. The radiometric sky temperature was calculated from equation (6-1 using the standard atmospheric model and extrapolating the average Steamboa Springs weather data to sea level values. The resulting surface values of absorption coefficient,

$$\Gamma_{ox}(0) = 0.065 \text{ dB/km}$$
$$\Gamma_{H_2O}(0) = 0.3 \text{ dB/km} \qquad (6\text{-}30)$$

were obtained from the Manual of Remote Sensing (Fraser, et al., 1975) for $\rho = 6\ g/m^3$. Evaluation of equation (6-19) yields

$$T_{sky} = 30.6\ K \qquad (6\text{-}31)$$

To investigate the validity of the assumption of an average sky temperature calculation, the variation in radiometric temperature versus atmospheric temperature was examined. The ratio of T_{sky} to the physical temperature was approximately 0.1. The maximum variation in atmospheric temperature was 22°C or a 2.2 K change in sky temperature. Hence, the error due to variation in atmospheric temperature was ignored.

An inverse relationship between the ambient case temperature (T_{case}) and the voltage at the output of the radiometer (V_{94}) was observed. The data indicated both an absolute level shift and gain sensitivity variation with variations in ambient temperature.

The reference point for corrections for ambient temperature variations was chosen as the center of the allowable operating range, 25° to 35°C. A calibration equation was then developed through the application of a multiple linear regression on the three variables affecting the output. These variables are:

a) (T_{ap}) -- either calculated sky temperature or absorber physical temperature

b) (T_{case} - 30) -- case temperature relative to 30°C

c) (50 V_{94}) x (T_{case} - 30) -- gain variation term

The resulting calibration equation is

$$T_{ap} = .9183\ (50\ V_{94}) - .00548\ (50\ V_{94})\ (T_{case} - 30) + 2.446\ (T_{case} - 30) - 12.54 \qquad (6\text{-}32)$$

Using equation (6-32), the calculated T_{ap} and the estimated T_{ap} values were fit with a correlation coefficient of 0.99. If the variation with case temperature were to be ignored, the standard deviation of the error between the calibration points and the regression line would double in magnitude to 17.7 K.

6.4 Ground Truth Instrumentation and Techniques

This section describes the instrumentation, procedures and techniques used for the acquisition of ground truth. The choice of ground truth parameters and the sampling frequency of each were governed by the significance each parameter was expected to play in the wave-target interaction process

and by the available time and manpower associated with the acquisition of the microwave data. As will be discussed later, the results indicate that in some cases the sampling rate and temporal precision of specific snow parameters were insufficient to provide complete understanding of the microwave response to these snow parameters. On the other hand, some snow parameters were over sampled.

6.4.1 Snowpack Conditions

The snow measurements were obtained from a snowpit at the northeast corner of test plot #1. A single pit was chosen because the time span required for multiple pit sampling was prohibitive. The snowpit was enlarged such that each succeeding measurement was from undisturbed snow. The pit was back-filled after each measurement to cover any exposed grass. This procedure was necessary to prevent the spread of melting due to the higher thermal emissivity of grass over snow. Comparison with the ground truth data around the perimeter of the plot is given in section 7.1.1. The validity of using the snowpit data as representative of the entire test plot is shown. The following parameters were observed:

1. Depth
2. Stratification
3. Density
4. Water Equivalent
5. Wetness
6. Temperature
7. Grain size
8. Surface Roughness

6.4.1.1 Snow depth and stratification

Two permanent gauging stations for snow depth (Figure 6-14) were located at opposite ends of the test plot. These stations were monitored daily. Depth was also monitored in conjunction with the snow stratification measurements.

A vertical cut was made in undisturbed snow as the first step in obtaining a stratification profile. The thickness and position of each distinct layer within the snowpack were determined and recorded. A layer boundary is defined by a variation in either snow density or crystal structure. In some cases, the density may change only slightly

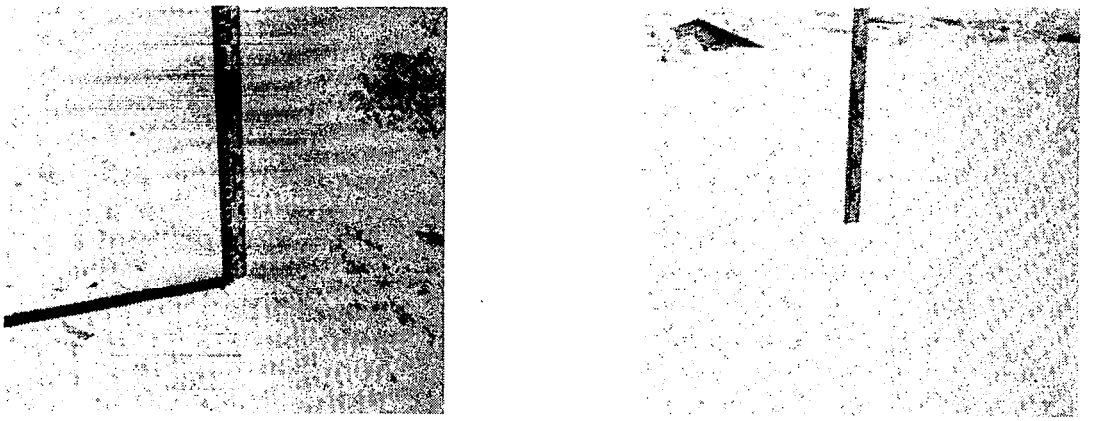


Figure 6-14 Snow depth measurement.

but the crystalline structure change may be significant. Figure 6-15 illustrates a sample ground truth data sheet. Stratification is indicated in the lower picture of the figure. Also any distinguishing characteristics of the layers are noted.

Since layers are not always easily separable, a few of the techniques for distinguishing layers will be examined. Figure 6-16 illustrates a case when three layers were easily distinguishable. The layer boundaries occurred at 12, 20 and 25 cm AGL (above ground level).

A qualitative method for determining boundaries, when not clearly visible, is achieved through the use of a plastic card. A card is inserted vertically into the snowpack and moved gently up and down. Snow layers of differing densities will apply differing resistances to motion. This method was used to determine the layer boundary at 31 cm in Figure 6-17 Figure 6-17b shows the layer boundaries. This boundary at 31 cm AGL was characterized by such a slight variation in density that later in the day it could not be found. It was therefore deleted in the final form of the data and the range from 25 cm to 39 cm was considered to be a single layer.

Another method used for separation of layers was based on tonal variations under direct sunlight. Backlighting was found to be optimal; however, this method required special care in slicing out a snow vertical profile for observation.

After the boundaries were determined, numbered layer codes were assigned. The oldest and lowest layer was designated "1", then newer layers were assigned increasing numbers. Nine layers was the maximum number observed during this investigation. The ninth layer resulted from the last snowfall observed toward the end of the snow season.

6.4.1.2. Snow density and water equivalent

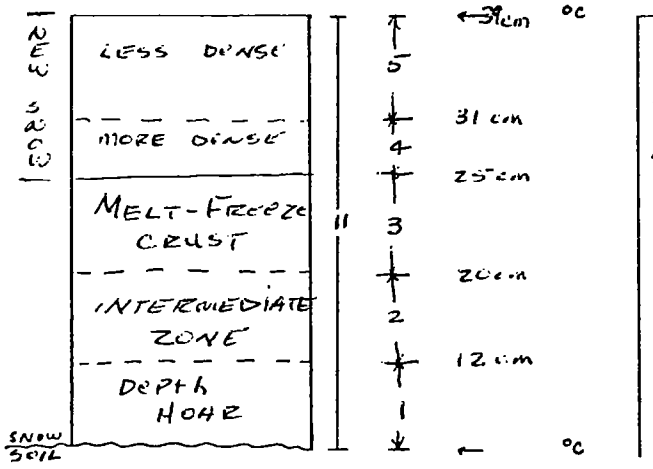
Snow density of each layer can be measured once the boundaries of the layers are established. A known volume of snow was weighed and the density calculated. The water equivalent, the total amount of water contained in the form of snow per unit area, is the product of density and depth. The measurements of density employed two snow coring tubes, a balance, and two containers for transporting the snow cores. Snow samples of known volume (500 ml) were removed from each layer of the snow (Figure 6-18a). The snow sampling cylinders were inserted carefully into the snowpack along an imaginary horizontal line, then the coring tube and container and snow sample were weighed. Figure 6-18b illustrates

GROUND TRUTH - DATA ACQUISITION

DATE 2-23-77 (MONTH DAY YEAR) TIME 0900 OBSERVER BCH

SAMPLING HOR. / VERT	SNOW DEPTH (cm)	TARE OF INSTR. (gm)	INSTR. + SNOW (gm)	SNOW AVG. (gm)	DENSITY AVG. (g/cc)	WATER EQUIV. (in.)	SNOW TEMP. (°C)	SNOW WATER
11	39	133.04	455.56		0.182			
5	36	441.49 443.45	478.45 477.96	35.50	0.071			
4	28	441.49 443.45	502.95 505.78	61.88	0.124			
3	21	441.49 443.45	602.91 606.00	161.98	0.324			
2	15	441.49 443.45	566.51 568.39	124.98	0.250			
1	7	441.49 443.45	537.89 537.50	95.23	0.190			

NOTE: "11" TAKEN WITH 3 inch PVC SNOW CORER FOR AVG. ρ.
" 1 " TAKEN WITH 500 ML DENSITY TUBE FOR INDIVIDUAL LAYERS OF SNOW



Photographs

ROLL # 8 FRAMES 6

FRAME # 6 - 12 /pc

Figure 6-15 The data obtained from the snow profile illustrated in Figure 5b would be recorded as shown in the lower left corner. The density data are recorded on the top half of this form while photographic data are indicated in the lower right corner.

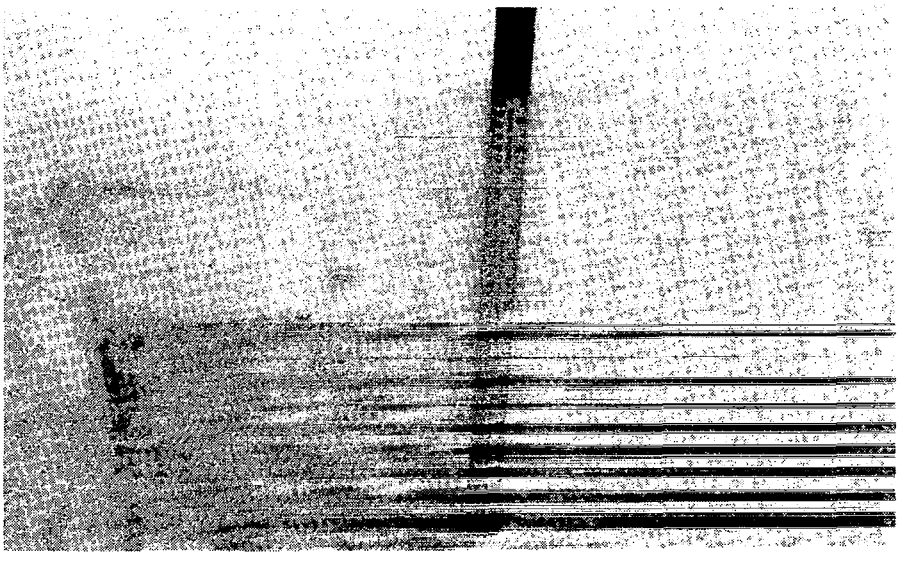


Figure 6-16 Snow stratification profiles were measured. This photograph shows three distinct layers.

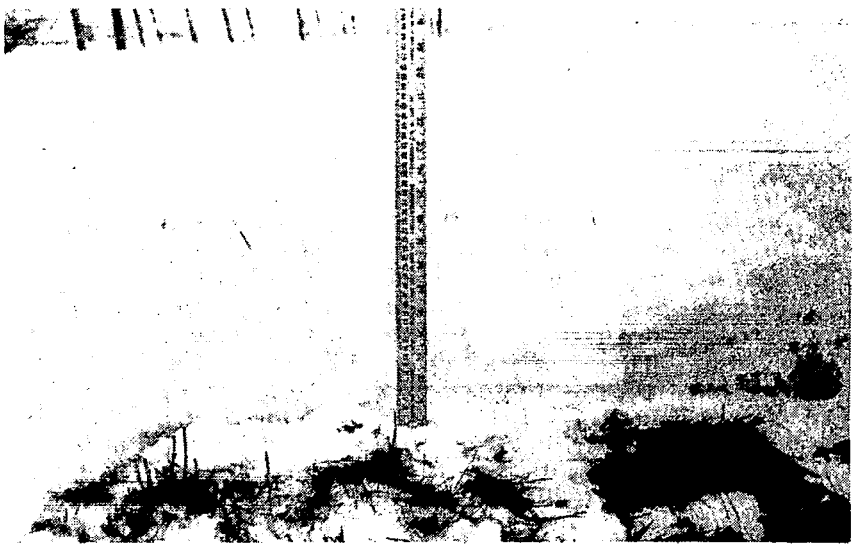


Figure 6-17a The profile view (February 23, 1977) illustrates the snowpack stratification.

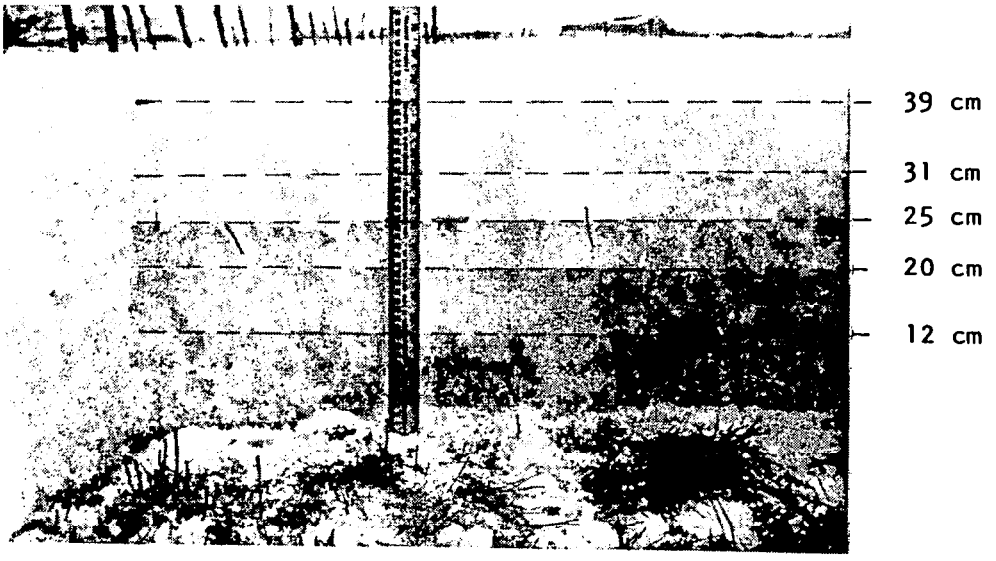
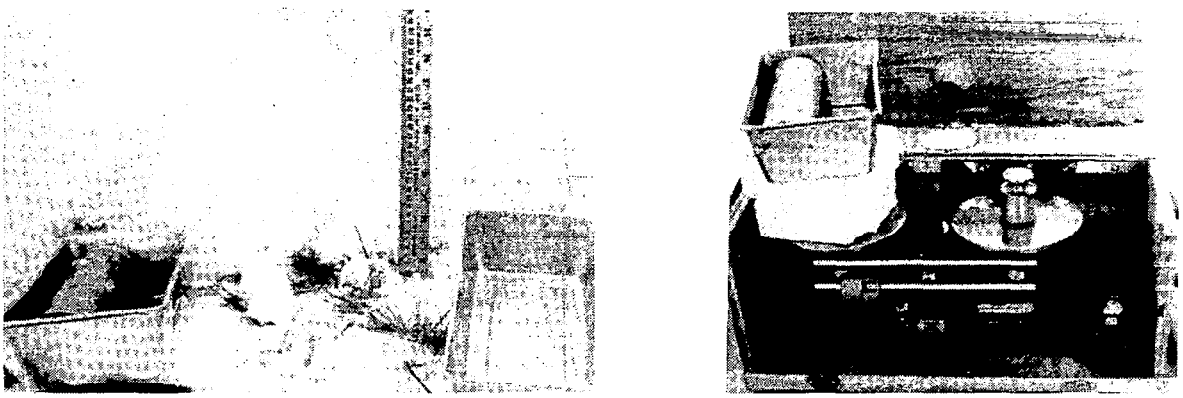


Figure 6-17b The boundaries for the layers determined using the methods of section 4.1.



(a) (b)

Figure 6-18 A given volume of snow was removed from each snow interval with an aluminum cylinder of known volume (500 cc) and placed in a pan. The pan, snow and cylinder were transported to the balance and weighed. The data were then recorded for the appropriate date and time.

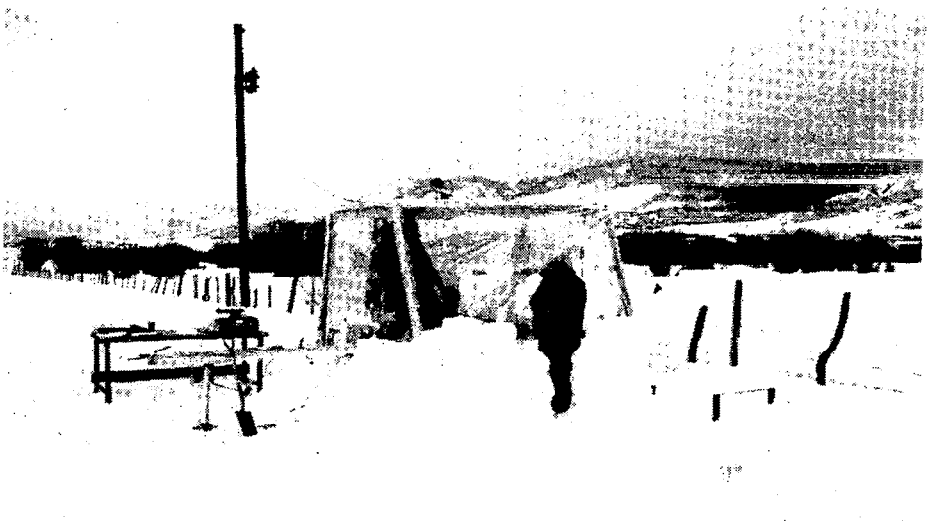


Figure 6-19 The ground truth enclosure is pictured with a cold storage box in the right foreground for dry ice to cool the calorimeter and toulene. Another storage area was maintained at the snowpack temperature for housing the snow sampling apparatus.

the procedure. The results of density calculations for each layer on February 23, 1977 are given in Figure 6-15. Each layer was sampled twice to remove sampling and weighing errors. If the two measurements differed by more than 10 grams, the measurements were repeated. Since the density measurements were repeated at least twice daily and since variations over time for a given layer were small, variations within the layer can be assumed to be small also.

Very low density snow could not be sampled by the coring method. Thin layers also presented a similar problem. In these cases, a rectangular volume was sampled. Other problems occurred when the snow was extremely wet. For these cases, cooling the sampling tube decreased adhesion of the snow to the tube. The adhesion problem can be solved by using PVC or other plastic type tubing. To avoid errors resulting from wind-induced vibration on the scales, an enclosure, shown in Figure 6-19, was constructed as a wind and snowfall shield.

The use of sandwich bags is encouraged for sample containers in future measurements. Cleanup of the sample containers and the errors involved with the high tare weights of these containers would then be reduced. The time to sample five layers can be reduced significantly from the 45 minute period required for the method employed in this experiment.

Snow water equivalent was measured with the Mount Rose snow tube or a split barreled sampler and also calculated from a summation of the water equivalent calculations for each layer. The Mount Rose snow tube shown in Figure 6-20 is used by the Soil Conservation Service and other Federal and state agencies with a portable scale for field measurements of water equivalent. The small diameter of the tube, however, introduced errors which were somewhat alleviated by the larger split barrel sampler shown in Figure 6-21. The measurement of the total snow column as sampled by the split barrel sampler was designated Layer 11.

6.4.1.3 Snow Wetness

Snow wetness is the percent free water in the snowpack. The units can be either per cent by weight or by volume. Percent by volume is used in this report. Wetness is one of the most difficult and time-consuming snow parameters to be measured of snow. Edgerton and Sakamoto (1970) investigated several techniques of measuring snow wetness. Their results, shown in Figure 6-22, indicate a large variation in the measured values of wetness among the six methods. It was pointed out that the centrifuge

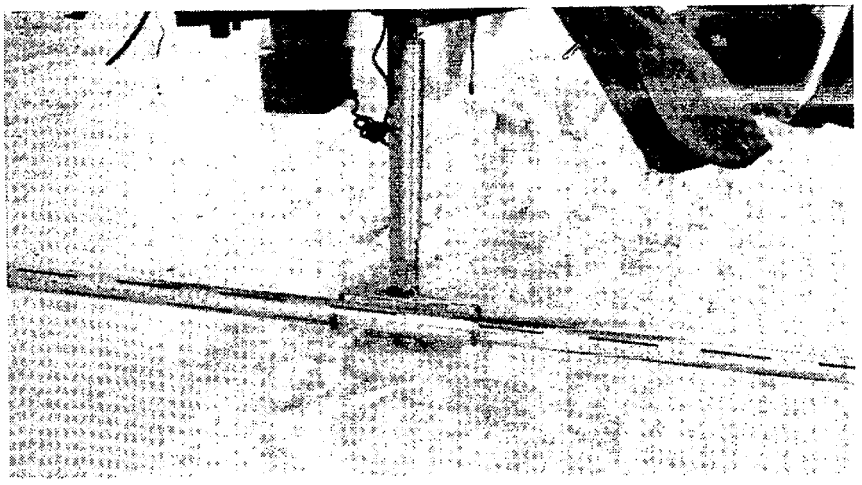


Figure 6-20 The Mount Rose snow tube was used periodically to measure snow water equivalent.

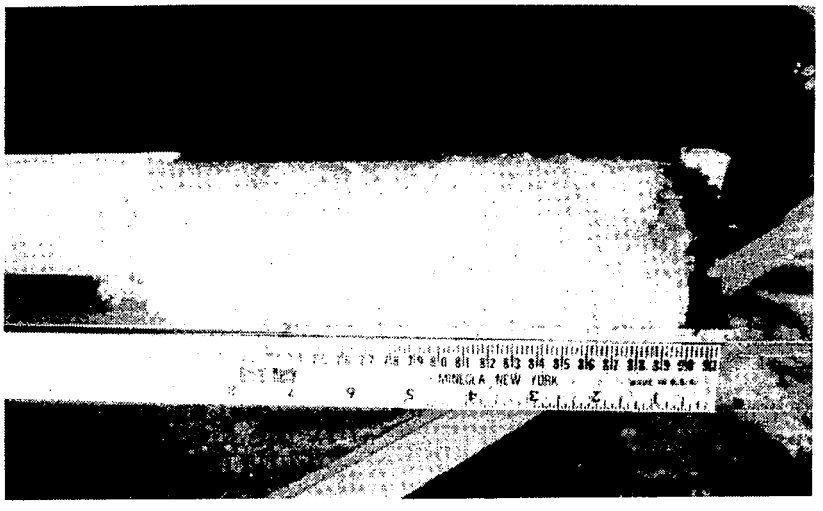


Figure 6-21 The split-barrel sampler is a 3-inch PVC tube 4 feet in length which had the lower 3 feet split lengthwise to facilitate viewing of the core.

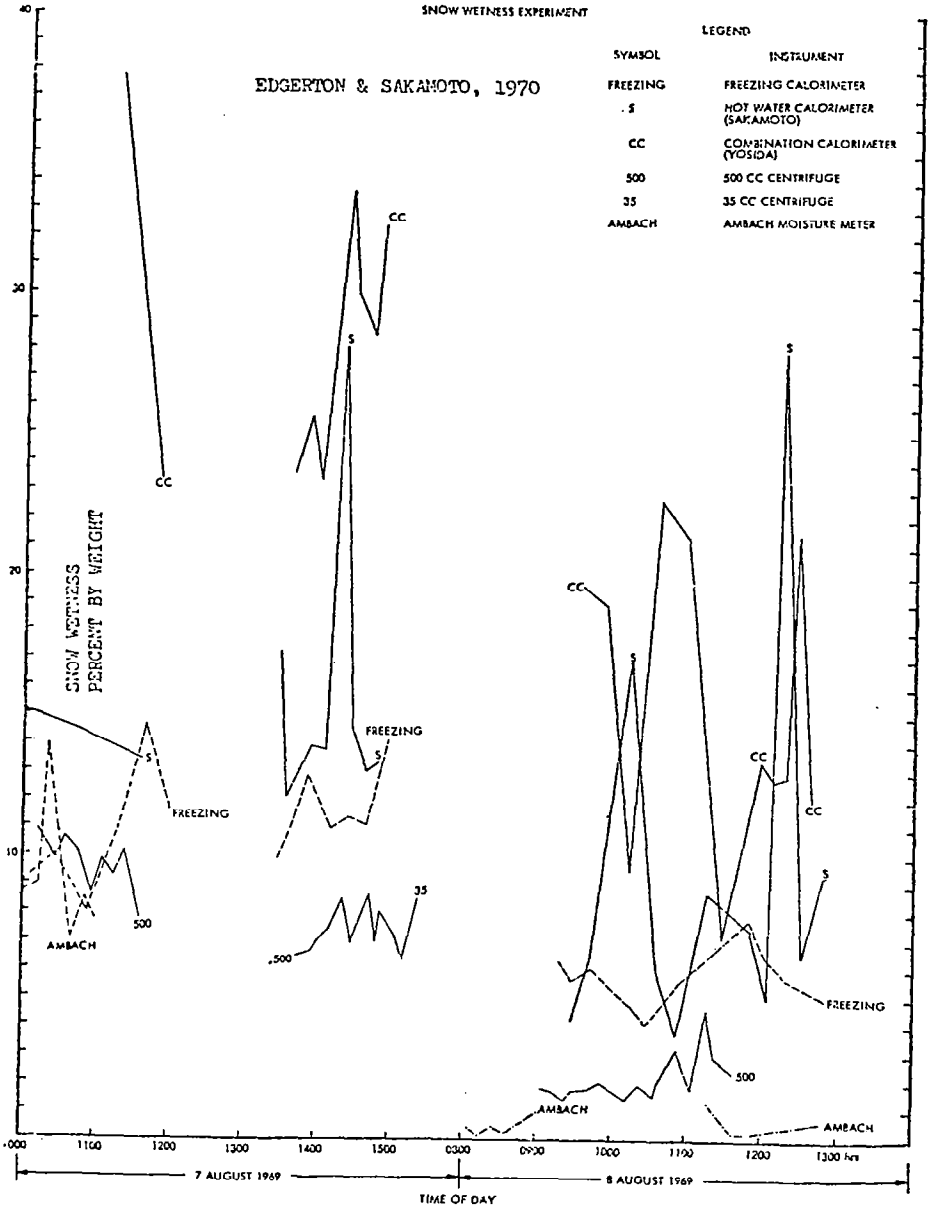


Figure 6-22 Comparison of Snow Wetness Measured by Various Instruments at South Cascade Glacier, Washington. (Edgerton & Sakamoto, 1970)

technique cannot extract all the water and the residual liquid is a function of the snow grain size and the spin rate of the centrifuge (Yosida, 1967). The melting calorimeter induces large errors since the wetness values of interest are small and therefore represent a small part of the total heat transfer. Among the various snow wetness measurement techniques, the freezing calorimetric technique is considered to be the most accurate. Since Edgerton and Sakamoto's study, Linlor (1975) has proposed the use of a capacitance technique which allows removal of the snow structure dependence. Hence, for the purposes of this investigation, it was decided to use both the freezing calorimetric and capacitance techniques.

6.4.1.3.1 Capacitance measurement of snow wetness

The use of a capacitor to measure the free water content of snow was proposed by Ambach (1958) and tested by Linlor (1975a) who loaned us his equipment for this experiment. The amount of free water in the snow affects the dielectric constant of the snow-filled capacitor, and hence its Q and capacitance. Figures 6-23 and 6-24 show the experimental relationships between dielectric constant or Q and the amount of free water. The response of dielectric constant, and therefore capacitance, is a linear function of wetness. Determination of wetness from capacitance is simpler than using the Q because of linearity. Also, low frequencies give the most sensitivity to wetness. Figure 6-25 illustrates the variation of capacitance and Q with frequency. A trade-off is involved between sensitivity (low frequency desirable) and Q (high frequency desirable). The problem with using Q measurements alone is that the structure of the snow and of the capacitor will affect the Q. Therefore an alternative is to measure the change in capacitance between a snow sample with free water, and the same sample after freezing with dry ice. For this case, the change in capacitance is independent of structure and is a function of only the free water. The measurements of capacitance and Q were made with a parallel plate capacitor with inside dimensions of 12" x 12" x 1' and an HP-4342A Q-meter at the following frequencies: 100 KHz, 230 KHz, 500 KHz, 1.0 MHz and 3.2 MHz. Figure 6-26 shows the procedure employed in obtaining and preparing the samples and in making the measurements with the Q-meter.

The measurement procedure is as follows:

1. Note the location, layer and time of the sample.
2. Bring the capacitor temperature to 0°C.

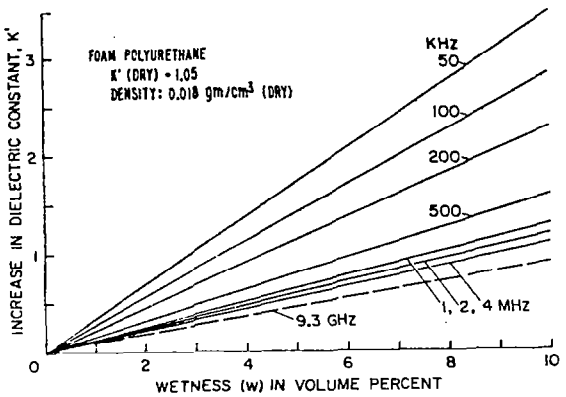


Figure 6-23 Dependence of dielectric constant on wetness (Linlor, 1975a)

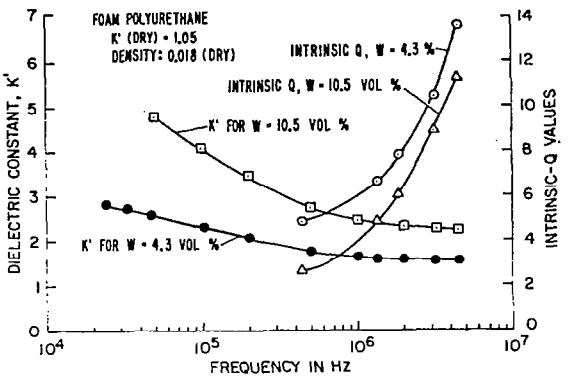


Figure 6-25 Dependence of dielectric constant on frequency (Linlor, 1975a)

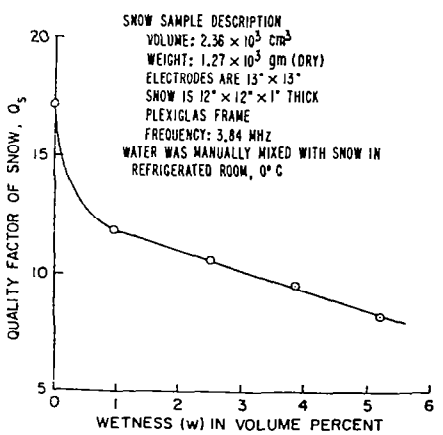


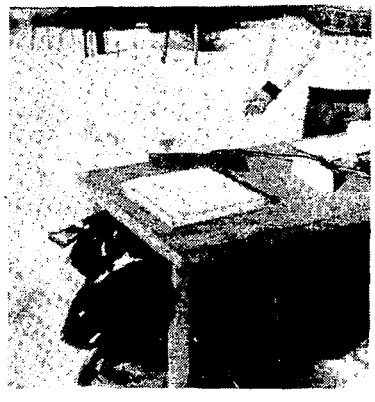
Figure 6-24 Quality factor of snow capacitor versus wetness (Linlor, 1975a)



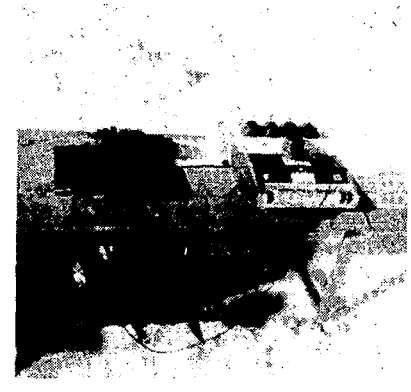
(a) Obtaining sample.



(b) Preparing snow capacitor.



(c) The filled snow capacitor.



(d) Measurement of capacitance and Q showing Q-meter, inductors and snow capacitor.

Figure 6-26 Capacitor Sampling Procedure.

3. Measure Q_0 and capacitance C_0 of the empty capacitor.

4. Fill the capacitor with snow to obtain a uniform layer while altering the density as little as possible.

5. Measure the Q_s and capacitance C_s of the snow filled capacitor.

6. Freeze the sample.

7. Measure the Q_f and capacitance C_f of the snow filled capacitor after freezing.

8. Record the air gap (if present) between the snow dielectric and the plate of the capacitor.

9. Record the weight of the snow sample.

Three wetness indicators were calculated from these measurements:

1. $\Delta C/C = (C_s - C_f)/C_0$
2. C_s (6-33)
3. Q_s

Linlor (1975a) showed that

$$\Delta C = A\, m_{vc} \tag{6-34}$$

where A is a calibration constant and m_{vc} is the snow wetness by volume. Since the density of the snow sample is usually altered in loading the capacitor, the volume wetness of the snowpack is related to m_{vc} by

$$m_v = \frac{\rho_s}{\rho}\, m_{vc} \tag{6-35}$$

where ρ_s is the density of the snow capacitor sample and ρ is the undisturbed snow density.

The basic drawback of the capacitance method is the calibration procedure. The calibration constant was determined through comparison to the values measured by the freezing calorimeter (Section 6.4.1.3.3).

6.4.1.3.2 Freezing calorimeter measurement of snow wetness

The calorimetric method of measuring snow wetness was investigated by Leaf (1966), who concluded that the freezing technique was more accurate than the melting technique for snowpack wetness measurement.

The calorimeter is an insulating container with provisions for measuring temperature. Figure 6-27 shows the thermos bottle with terminals for the internal thermocouple thermometer. A known amount of

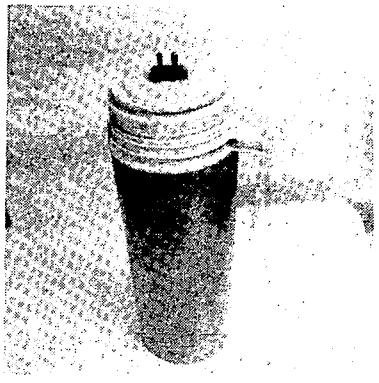


Figure 6-27 The freezing calorimeter, used for measuring the amount of free water present in a sample of snow, consists of a thermos bottle with a thermocouple probe inserted through the lid and extending down into the central cavity of the thermos.

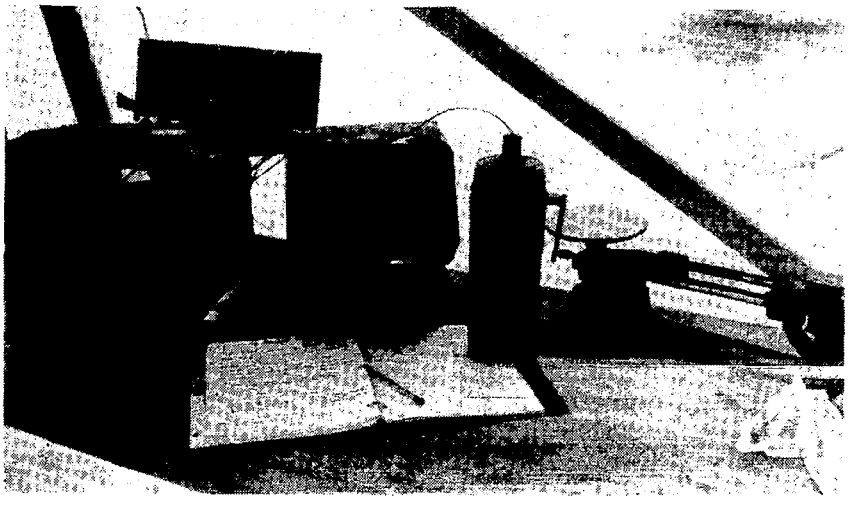


Figure 6-28 The temperatures of the solution were recorded using a digital thermometer, and the weights of snow and toluene were measured.

toluene (cooling agent) was allowed to reach equilibrium inside the calorimeter, then the wet snow was added and the solution again allowed to reach equilibrium. Weight and temperature measurements at the two equilibrium temperatures allow calculation of the wetness. Figure 6-28 illustrates the equipment used in obtaining the sample and performing the calorimeter measurements. Figure 6-29 shows the data sheet used in the recording process.

If the calorimeter is assumed lossless, heat will be conserved between initial and final states:

$$H_i = H_f \tag{6-36}$$

where

H_i = initial heat content of all constituents

H_f = final heat content of the solution

The heat content of the final solution of toluene and ice is

$$H_f = T_f(W_i + E_c)\, C_{tf} + T_f W_s\, C_{sf} \tag{6-37}$$

where

T_f = final equilibrium temperature

W_i = weight of toluene

E_c = calorimeter constant

W_s = total weight of snow

C_{tf} = specific heat of toluene at t_f

C_{sf} = specific heat of ice at t_f

The two terms are the heat content of the toluene and calorimeter, and the heat content of the ice. The heat content of the initial constituents (toluene, snow, free water) is

$$H_i = T_i\, (W_i + E_c)\, C_{ti} + L_f W_f + T_s W_d C_s + T_s W_f C_w \tag{6-38}$$

COLD CALORIMETER DATA SHEET

DATE _____, 1977 TIME _____ OBSERVER _____

SAMPLE # _____ SNOW TEMP. _____ AIR TEMP. __

(1) TARE WEIGHT CALORIMETER _____

(2) WEIGHT CALORIMETER + TOLUENE _____ T_1 __

(3) WEIGHT CALORIMETER + TOLUENE + SNOW _____ T_2 __

(4) CALORIMETER CONSTANT (E) _____

NOTE: ALL WEIGHTS RECORDED IN GRAMS
ALL TEMPERATURES RECORDED IN °C

Figure 6-29 Sample data sheet for the freezing calorimeter measurements.

where

T_i = initial temperature of toluene

T_s = snow temperature

W_f = weight of free water in snow

W_d = weight of dry snow, S = D + F

C_{ti} = specific heat of toluene at t_i

C_s = specific heat of snow at t_s

C_w = specific heat of water at t_s

L = heat of fusion of water = 79.7 cal/g

The first term of Equation 6-38 is the initial heat content of the toluene and calorimeter and the second term is the heat required to change the state of the free water to ice. The third term is the heat content of the ice component of the snow and the last term is the heat content of the free water in the snow. If the temperature of the snow (T_s) is less than 0°C, then the last term of Equation (6-38) should be changed to $T_s W_f C_s$, since there should be no free water.

Using equations 6-36, 6-37 and 6-38 and solving for the fraction of free water yields:

$$\frac{m_w}{100} = \frac{W_f}{W_s} = \frac{(W_i + E_c)(T_f C_{tf} - T_i C_{ti})}{W_s(T_s C_w + L_f)} + \frac{T_f W_s C_{sf} - T_s W_d C_s)}{W_s(T_s C_w + L_f)} \qquad (6\text{-}39)$$

The volumetric wetness is then

$$m_v = \rho m_w \qquad (6\text{-}40)$$

where ρ is the snow density.

The procedure used for this measurement is as follows:

1. Weigh the empty calorimeter, measure its temperature and record the results.

2. Add 300 ml of toluene, shake gently 4 to 5 minutes or until the temperature stabilizes. The toluene must be well below 0°C.

3. Weigh and measure the temperature of the calorimeter and cold toluene.

4. Remove the cap and add the snow sample. The snow volume should be approximately 500 ml. Replace the cap and shake gently for 3 minutes or until the temperature stabilizes.

5. Weigh and measure the final temperature of the calorimeter, toluene and snow sample.

6. Clean the calorimeter.

The total time to perform this measurement and clean up was about 45 minutes. For monitoring of the wetness change in the surface layer on a warm sunny day, this time resolution was not as small as desired. In future experiments, this time interval can be reduced by using smaller sample sizes and by using several calorimeters. The surface layer is the most dynamic and therefore was sampled most often. A profile was also desired, so the following procedure was developed for sequential sampling of snowpack wetness profile. This procedure was begun once the surface layer had become wet.

1. Sample the surface layer.

2. Sample the second layer and resample the first layer.

3. If the second layer seemed wet, then the third layer was sampled. If not, layers one and two were sampled alternately.

4. The first layer was sampled every other time and deeper layers only if the layer above them showed signs of increasing wetness.

Several observations were made about these measurements. If the snow temperature was below about -3°C, then the wetness was zero; however, from -2° to 0°C varying wetnesses were observed. If the following approximations are made in equation (6-39):

$$C_{tf} = C_{ti}$$

$$C_s = C_{sf} \qquad (6\text{-}41)$$

$$T_s = 0$$

then the resulting equation is the version employed by Leaf (1966):

$$\frac{m_w}{100} = \frac{W_f}{W_s} = \frac{(W_i + E_c)(T_f - T_i)C_t}{W_s L_f} + \frac{T_f C_s}{L_f} \qquad (6\text{-}42)$$

6.4.1.3.3 Comparison of the calorimeter and capacitance snow wetness measurements

Comparison of the two methods used for determining snow wetness shows promise; however, the results were not as good as had been hoped. There was a definite correlation between the two methods of wetness measurements, but the linear correlation coefficient was only 0.7. The three wetness indicators using the capacitance method were compared with the calorimeter measurements of wetness. The constant A should have been determined in a laboratory test which was not done, so the value will be estimated using the calorimeter data as a reference.

Two snow wetness indicators were calculated from the calorimetric method. The first one, based on equation (6-42) and used by Leaf (1966), does not include the snow temperature as a parameter, and the second one is based on equation (6-39) which does include the effects of snow temperature.

Linear correlation coefficients were calculated for all combinations of the wetness indices at each of the five capacitor frequencies. The 500 MHz frequency was excluded due to equipment problems. Figure 6-30 shows the frequency variation of the correlation coefficient of each of the two calorimetric indices with $\Delta C/C$ and with C_s. Correlation of the calorimeter indices to Q_s of the snow sample was low and was neglected from the analysis. Correlation coefficients and sensitivity generally increase with frequency. The 1.0 MHz frequency is seen to be optimum. Also the $\Delta C/C$ index gave the highest correlation. The C_s index is comparable in performance to the $\Delta C/C$ index. Also the calorimetric index with corrections for snow temperature is only marginally better than Leaf's index.

The results of the linear regressions are of the form:

$$\Delta C/C = A\, m_v + B$$
$$C_s = A'\, m_v + B' \qquad (6\text{-}43)$$

The constants A, B, A' and B' are given in Table 6-3 for the various frequencies, with m_v determined by Leaf's method. It should be noted that the constants A' and B' are applicable only to the capacitor employed and new relationships would be required for any other capacitor.

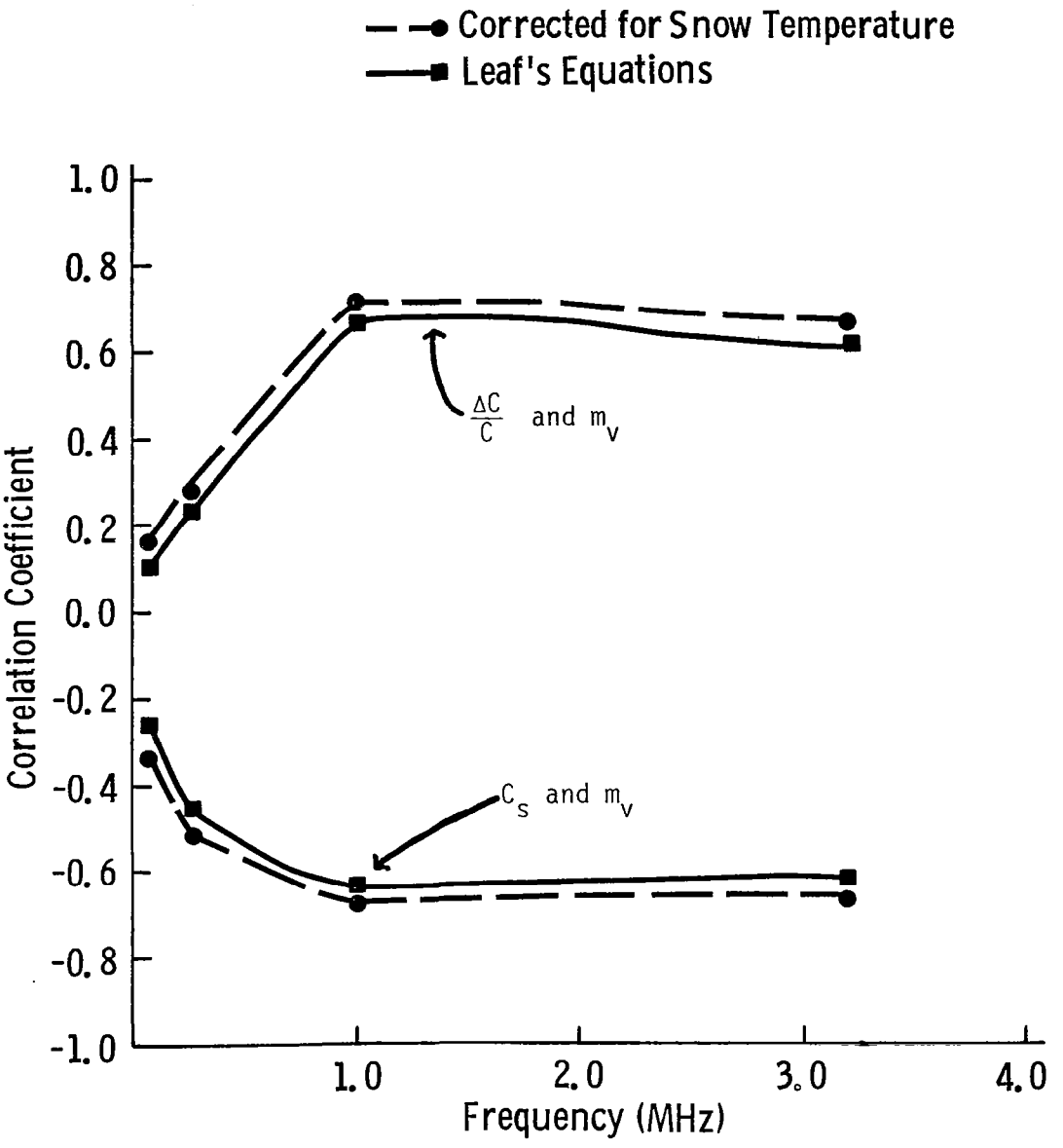


Figure 6-30 Correlation coefficient of the capacitor and calorimeter indices.

TABLE 6-3

Capacitor Calibration Constants

Constant	100 KHz	230 KHz	1.0 MHz	3.2 MHz
A	.103	.063	.043	.040
B	.004	.004	.014	.014
A'	139.5	154.7	137.5	150.8
B'	-2.34	-3.82	-4.56	-4.93

For field measurements, C_s may be the superior indicator of wetness since dry ice for freezing (required for both $\Delta C/C$ and the calorimeter) is not necessary, and therefore the convenience may justify the reduced accuracy.

The inclusion of the effect of snow temperature seems to have little improvement on the results. Experimental inaccuracies may have been larger than the expected improvement from the effects of snow temperature variation.

Some of the problems leading to low correlations were related to operator fatigue and errors. Still others seem to be inherent in the methods. The capacitor method is inaccurate at high wetness conditions for several reasons. The Q_s of very wet snow can fall beneath the Q-meter sensitivity. Also, insertion of the snow sample into the capacitor becomes difficult and a uniform layer cannot be achieved without substantial alteration of the snow characteristics.

6.4.1.4 Snow Temperatures

Temperature profiles of the snowpack were measured at approximately 60 minute intervals (30 minute intervals near sunrise and sunset). The temperature was monitored by two methods. A digital thermometer (the same unit was used for monitoring soil temperature) was used to record the snow temperatures (Figure 6-31). Thermocouple temperature probes (stainless steel, 12 inches in length x 3/32 inches in diameter) were placed at 2 cm intervals by inserting them into a matrix of holes drilled in a 120 cm length of 1 inch by 2 inch cedar. The probe positioner was driven into the ground approximately 5 cm which positioned the first drilled hole at ground level. Temperatures were recorded up to a height of 4 cm above the surface of the snow and at 60 cm and 100 cm (AGL), thus providing information with respect to atmospheric temperatures for various heights above the surface of the snow cover. The back up system measured the snow temperature at 10 cm intervals and is illustrated in Figure 6-32. Thermistors were encased in PVC tubing poles which were placed in the field before the first snowfall. The thermistors were measured with a bridge circuit.

Continuous monitoring of snow temperatures at a few intervals within the snowpack would be very desirable during periods of change from dry to wet and wet to dry snow conditions.



Figure 6-31 A digital thermometer (Doric Trendicator 400, Type T/°C) was used to measure temperature. Note the temperature profile positioner at the left.

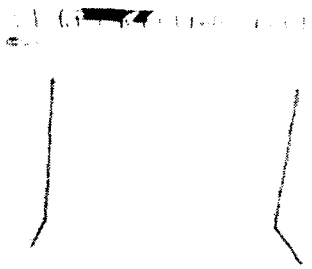


Figure 6-32 Temperature was also measured at 10 cm intervals using thermisters encased in PVC tubing.

6.4.1.5 Surface Roughness

The roughness of the surface was measured only when there was wind induced drifting. The lack of significant wind during snowfall led to the featureless surface illustrated by Figure 6-33. Most data sets were taken on this visually smooth surface. Warm days resulted in increased surface roughness as illustrated in Figure 6-34. The roughness profile for these cases was not obtained. High winds on March 11 and March 20 created a surface configuration of wind slabs, as shown in Figure 6-35. The grid shown in Figure 6-36 was used to measure surface roughness with a grid spacing of 1 inch.

The major problem with this technique was the inability to accurately measure the microrelief such as that seen in Figure 6-34, which might influence the short wavelength emission and backscatter behavior. For example, at 94 GHz, accurate measurements for small surface irregularities are more critical than at 1.0 GHz; the roughness panel does not provide the necessary detail. One possible method for obtaining small scale relief may be to photograph the surface of the snow during early morning or late evening to accentuate shadows induced by the microrelief on the surface.

6.4.1.6 Snow Grain Size and Structure

Snow crystal parameters were observed using a microscope. Figure 6-37 shows the microscope and fiber optic light source used to minimize heating effects on the snow sample. A single lens reflex camera was attached to obtain photomicrographs with an extent of approximately 1.5 x 2.3 mm.

Figures 6-38 to 6-43 illustrate some of the different types of snow crystals observed over the experiment duration. The classification is given in Figure 3-1 and was discussed in Chapter 3. These crystal types are all formed near or above the water saturation line (Figure 3-2) but over a wide temperature range. The riming on the crystal in Figure 6-43 has totally obscured the crystal and is almost to the stage of graupel or "pellet snow". Although the percentages of the different types of crystals of each snowfall would have been valuable, this information was not obtained. Snowfall was generally dry with a density range of 0.05 to 0.19 g/cm^3.

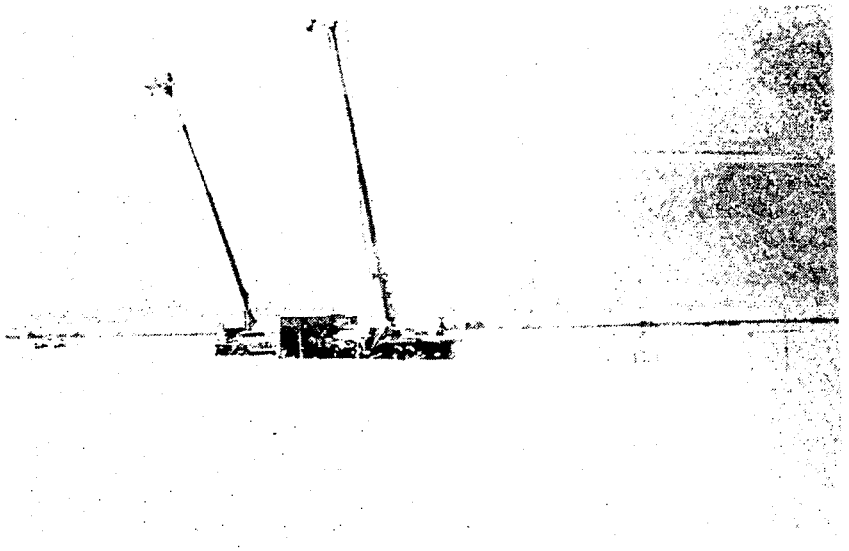


Figure 6-33 The lack of wind resulted in a flat essentially featureless surface (2/27/77).

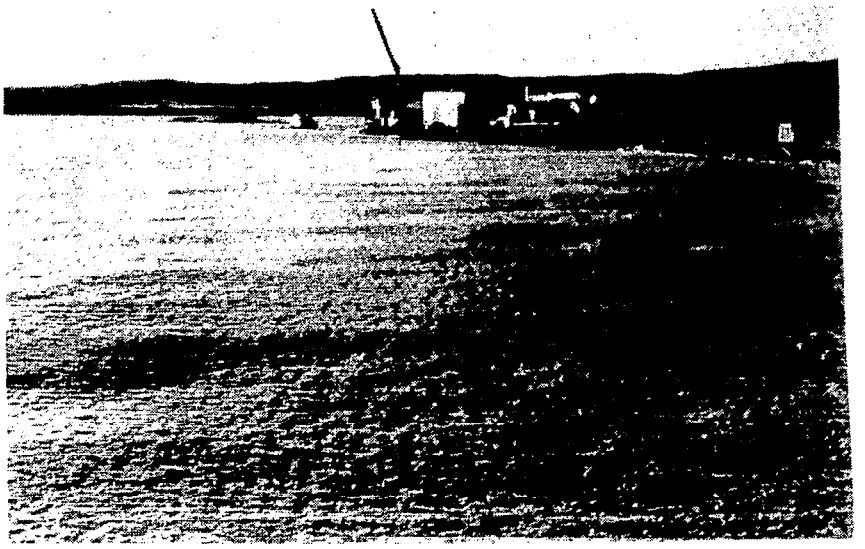


Figure 6-34 Significant surface perturbations were often the result of warm days followed by freezing nights (2/20/77).



Figure 6-35 Strong southerly winds caused local drifting and created wind slabbing on the snow surface (3/12/77).

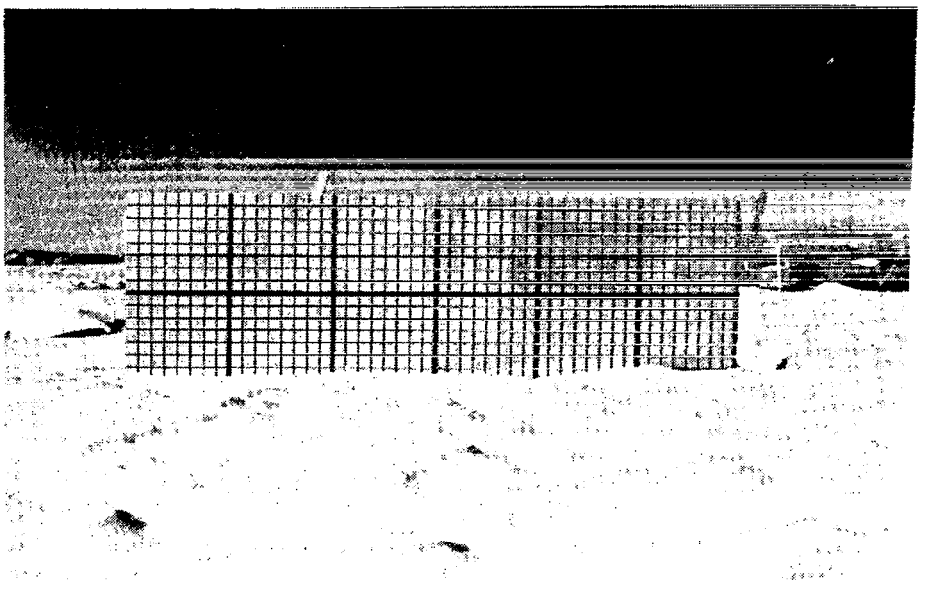


Figure 6-36 Surface roughness was determined for two directions, one perpendicular and one parallel to the predominant wind direction. The grid shows one inch divisions.

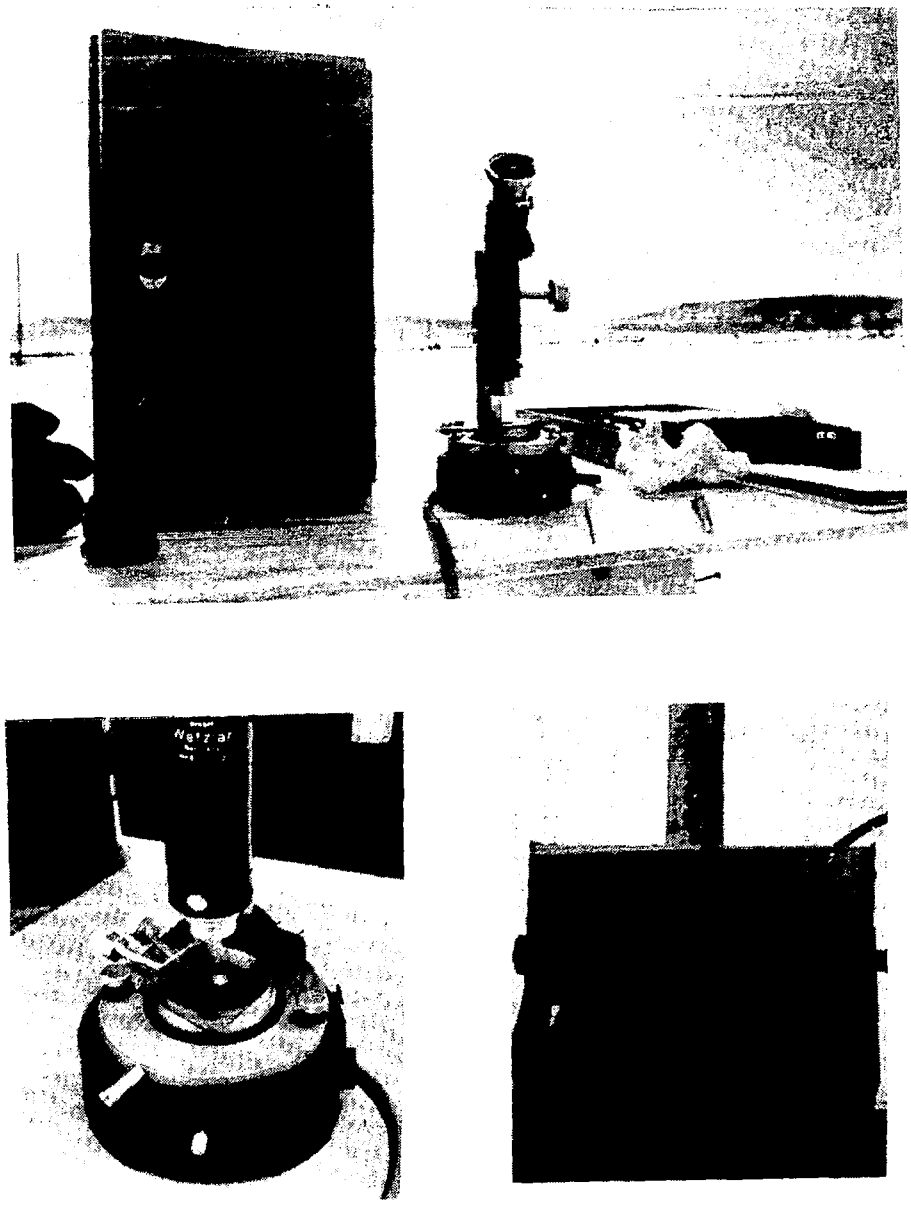


Figure 6-37 Leitz (Model 350) microscope and Fiber Optic light source.

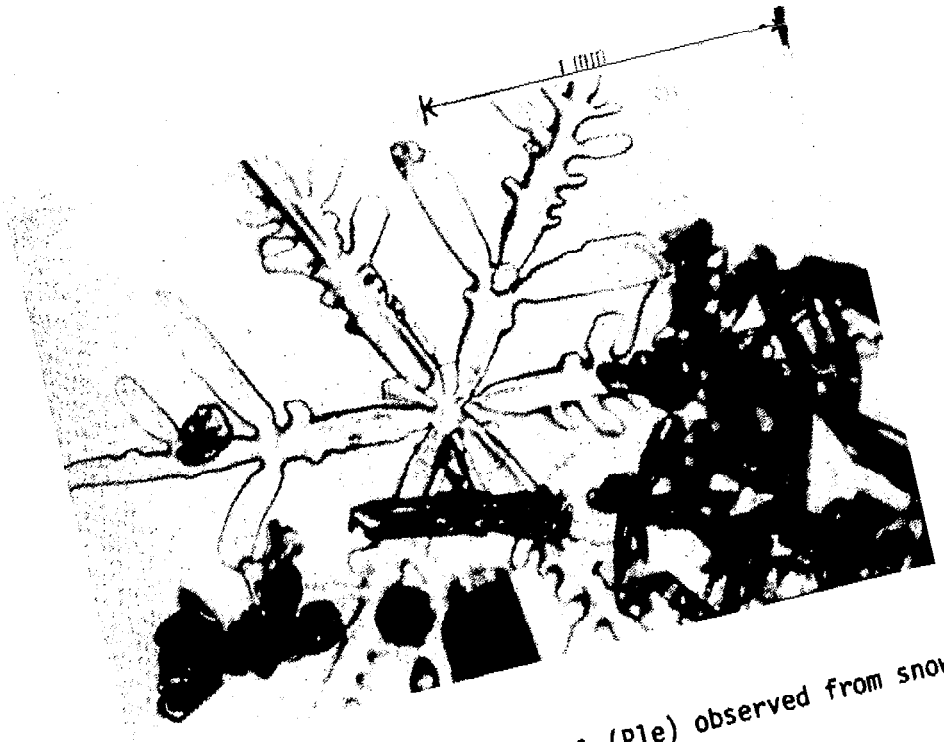
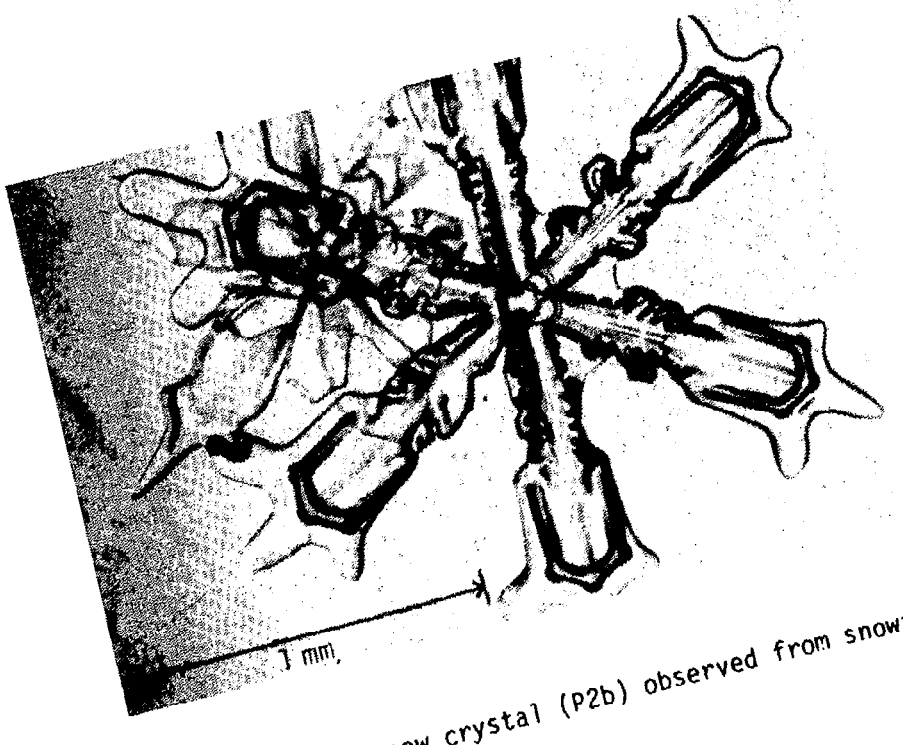


Figure 6-38 Dendritic snow crystal (P1e) observed from snowfall on 2/24/77.



snow crystal (P2b) observed from snowfall

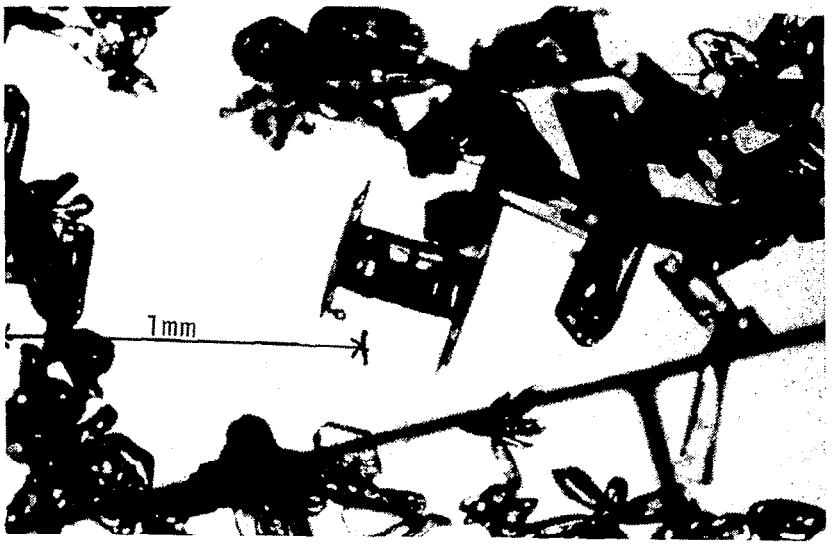


Figure 6-40 Capped column (CP1a) observed in snowfall on 2/24/77.

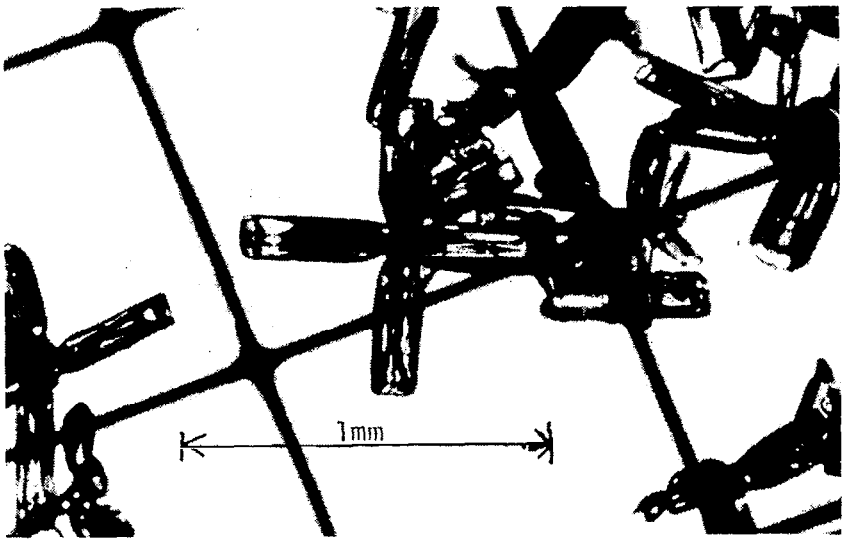


Figure 6-41 Combination of bullets (C2a) found in snowfall on 2/24/77.

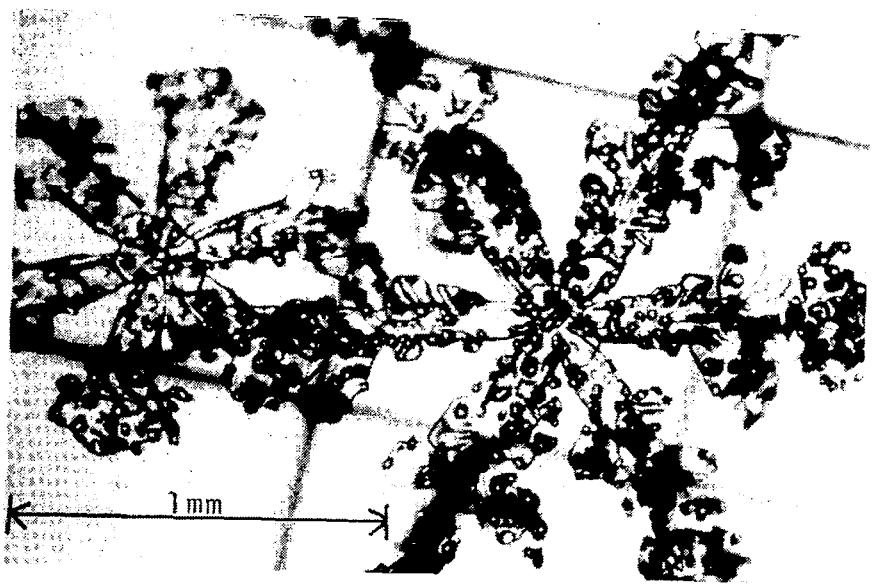


Figure 6-42 Stellar snow crystal with light riming (R1d) found in snowfall on 3/2/77.

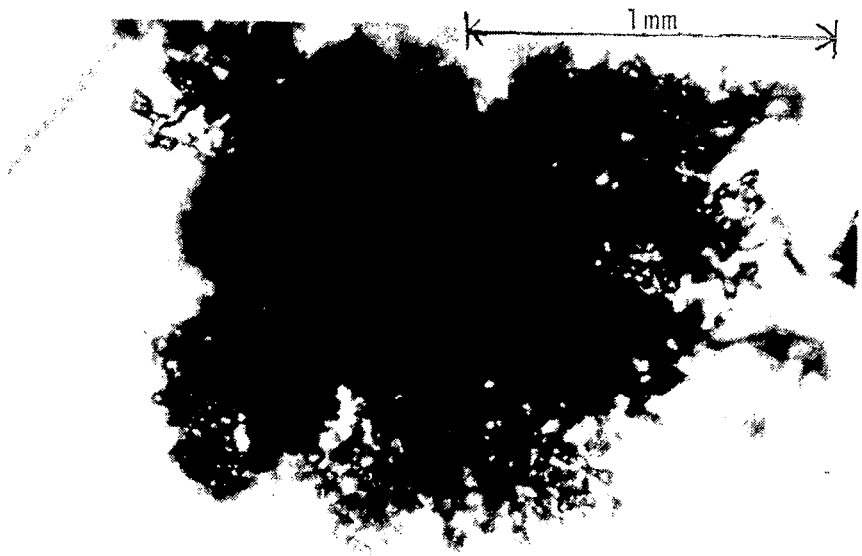


Figure 6-43 Very heavily rimed graupel-like snow (R3) observed in snowfall on 2/28/77.

The results of metamorphism are shown in Figures 6-44 to 6-50. The stages of destructive metamorphism are shown in Figures 6-44 and 6-45, while different types of surface effects are given in Figures 6-46 to 6-48. The final product of constructive metamorphism, depth hoar (Figure 6-49), undergoes destructive metamorphism (Figure 6-50) if the temperature gradient is removed. Crystal photographs were obtained at five to ten day intervals, or for new snow layers. Crystal sizes were observed from approximately 0.2 mm to 8 mm. Figure 6-51 gives the particle size history for each layer for the experiment duration in Steamboat Springs. These sizes represent estimates of the largest crystal dimensions for that layer at the times indicated. Figures 6-52 to 6-58 are photographs of the snow crystals on a 1 cm x 1 cm grid showing the variation in crystal size for the layers present on 3/24/77.

6.4.2 Soil Conditions

Observations of microwave scattering data for soils and vegetation have been shown by Ulaby, et al., (1979) to be affected by the following, in approximately their order of importance:

1. Vegetation geometry and moisture content
2. Soil moisture
3. Surface roughness
4. Soil texture

The underlying vegetation consisted of short (6 cm) hay in its winter state. The surface was smooth and the hay resembled any coarse, dead, dry winter grass. For the purposes of this experiment, the contributions due to the grass were neglected or at least assumed constant.

An additional factor must be included in any characterization of soils in a winter climate. Frozen soil exhibits dielectric properties similar to dry soil. For this reason, one does not want to make the erroneous conclusion that because the microwave properties indicate "dryness" that the soil really is without frozen moisture. Section 4.7 includes a more complete description of the soil properties.

Soil temperature was monitored hourly and soil moisture was determined approximately twice daily when the soil was in the thawed state. The temperature was recorded at three depths: soil surface, 2 cm and 5 cm below the soil surface. The sensors were described in Section 6.4.1.4. Soil moisture was measured on a volume basis. The snow was cleared from an area and the soil sampled using a standard tube-type soil sampler.

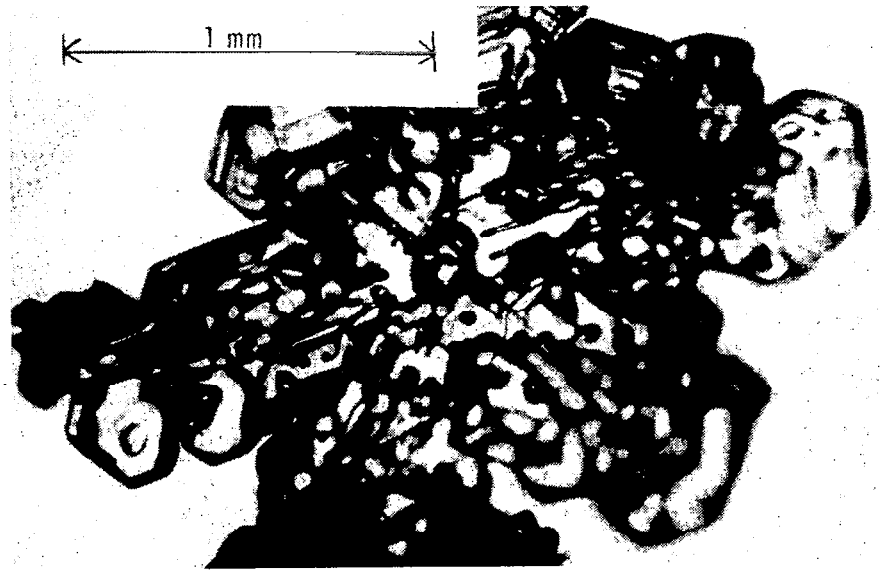


Figure 6-44 The start of the destructive metamorphism process. Photographed on 2/13/77.



Figure 6-45 Advanced destructive metamorphism in the surface layer on 2/28/77.



Figure 6-46 Fused ice particles composing a hard snow crust on 2/15/79.

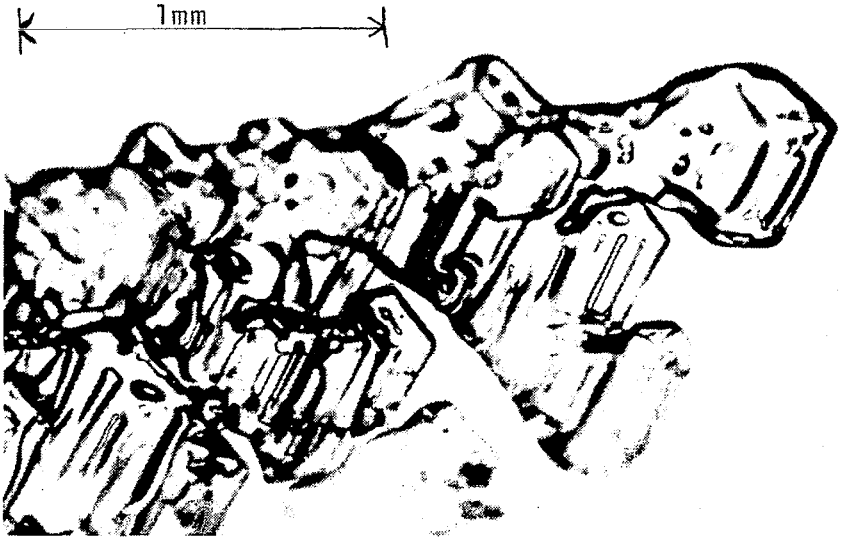


Figure 6-47 Surface hoar crystal photographed on 2/15/79.

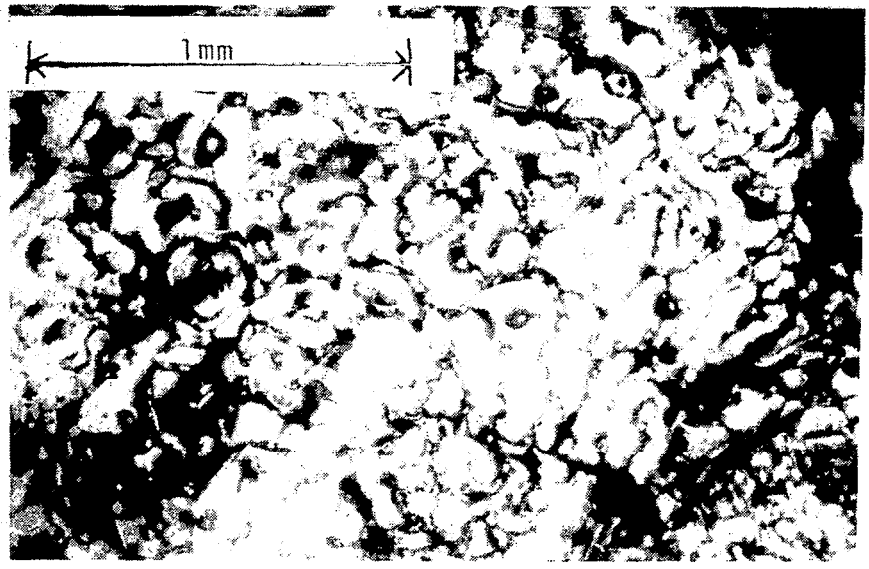


Figure 6-48 Example of a thin surface ice layer (firn mirror) photographed on 2/21/77.

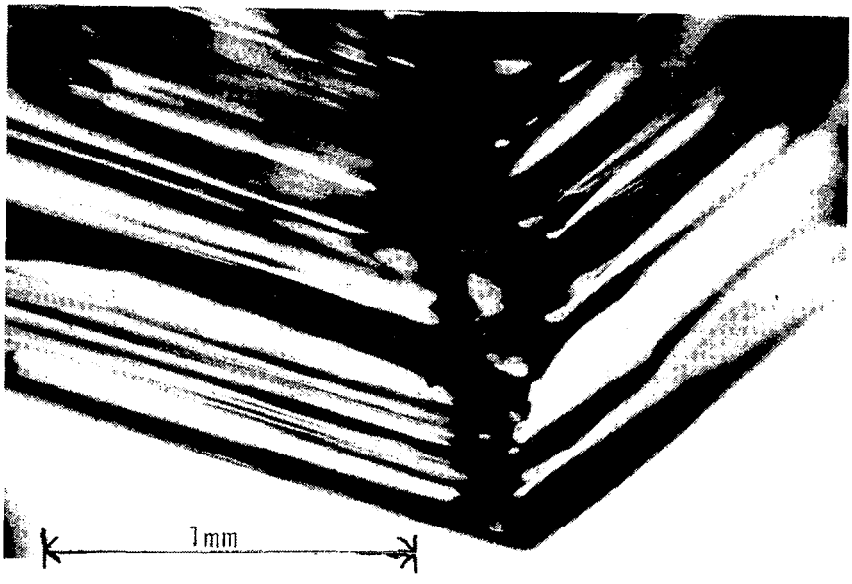


Figure 6-49 One corner of a hexagonal shaped depth hoar crystal on 2/17/77.

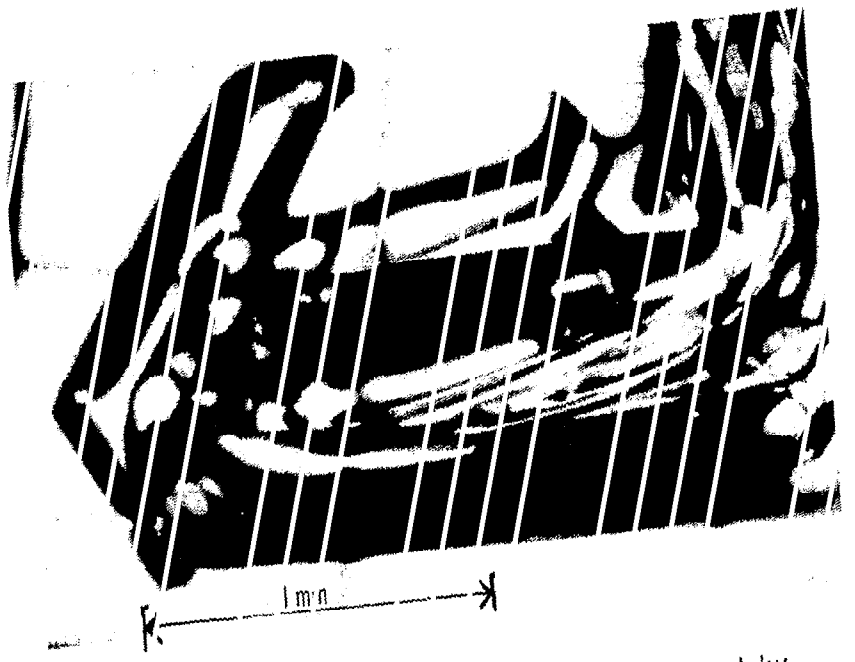


Figure 6-50 Remnants of a depth hoar crystal altered by destructive metamorphism. Photographed on 2/21/78.

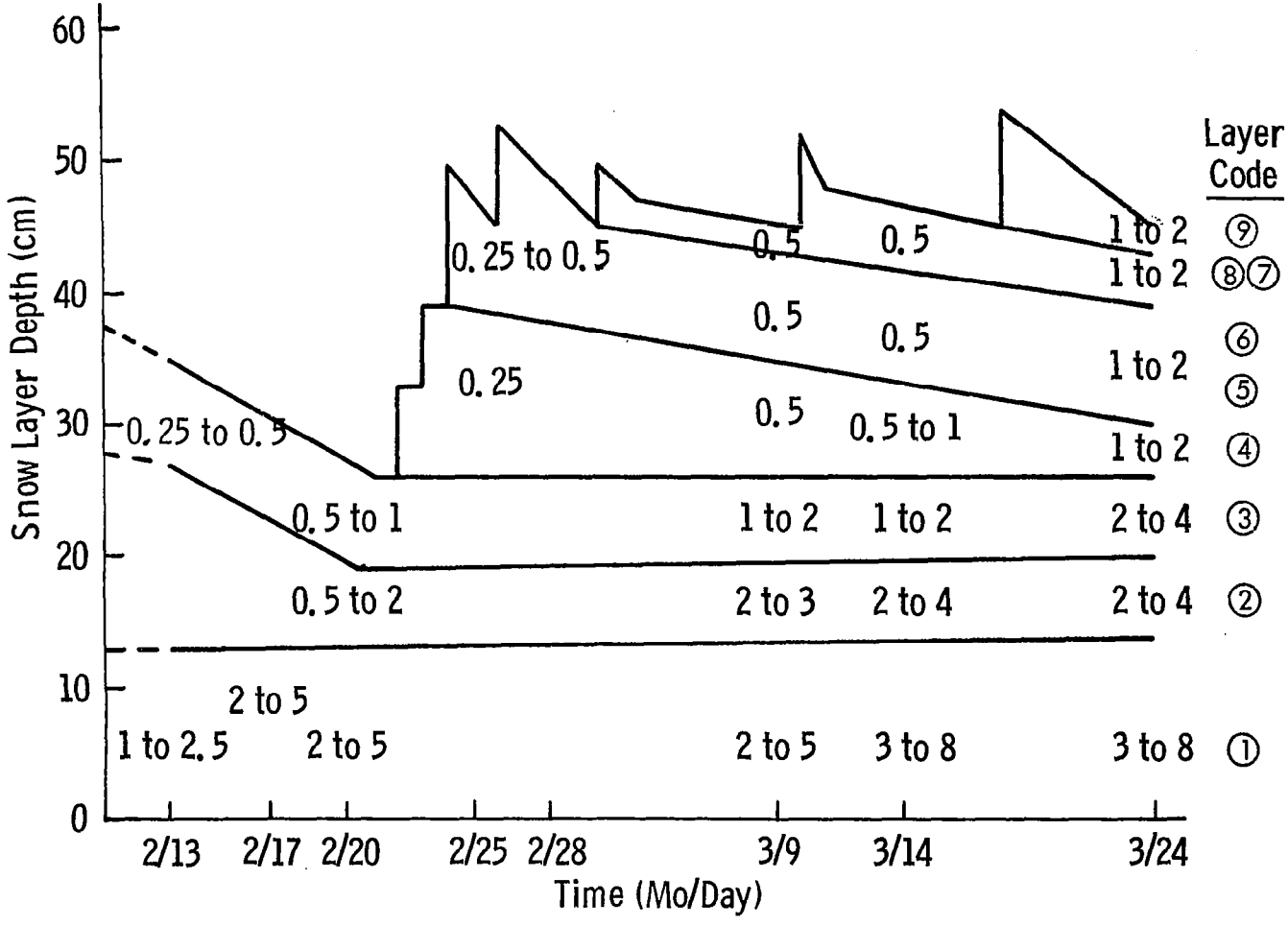


Figure 6-51 Snow Particle Sizes (mm)

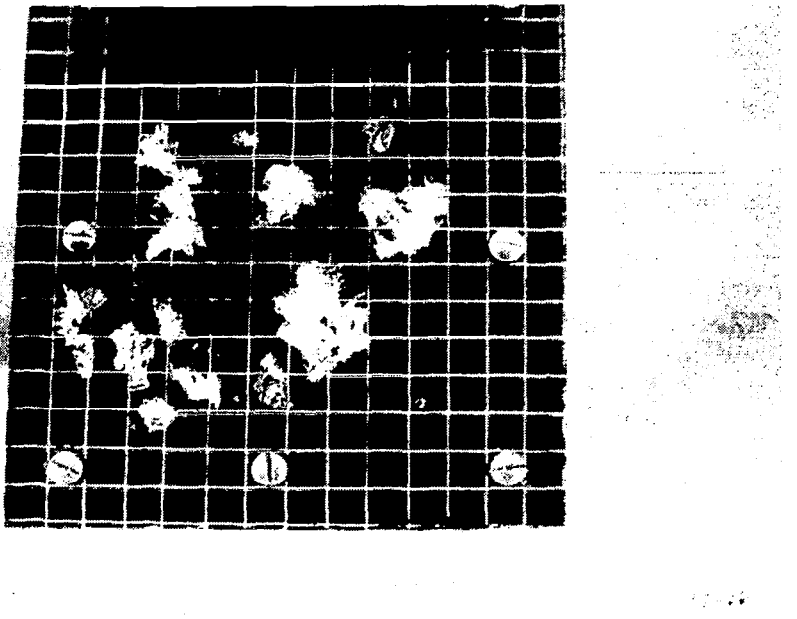


Figure 6-52 Layer 1 depth hoar crystals on 3/24/77. 1 cm x 1 cm grid

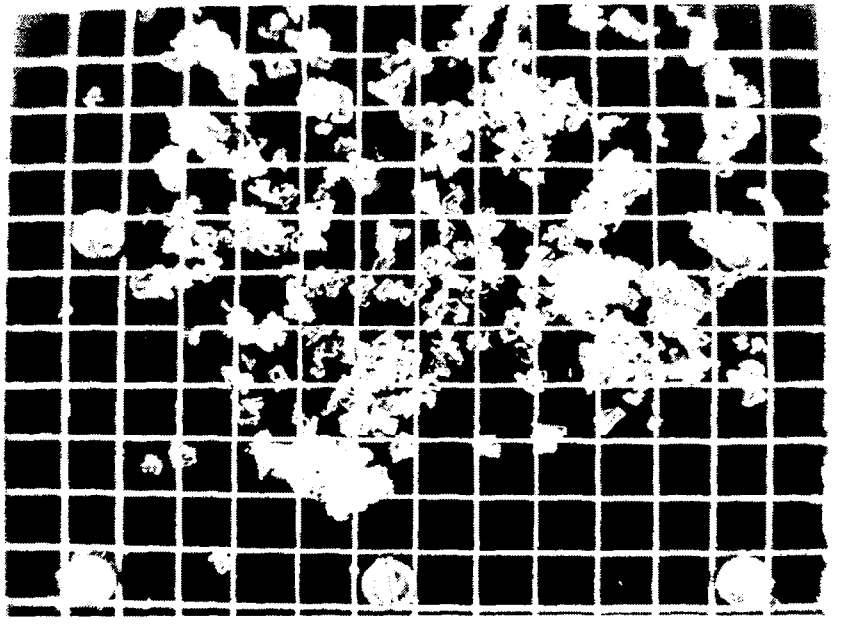


Figure 6-53 Layer 2 small depth hoar crystals on 3/24/77. 1 cm x 1 cm grid

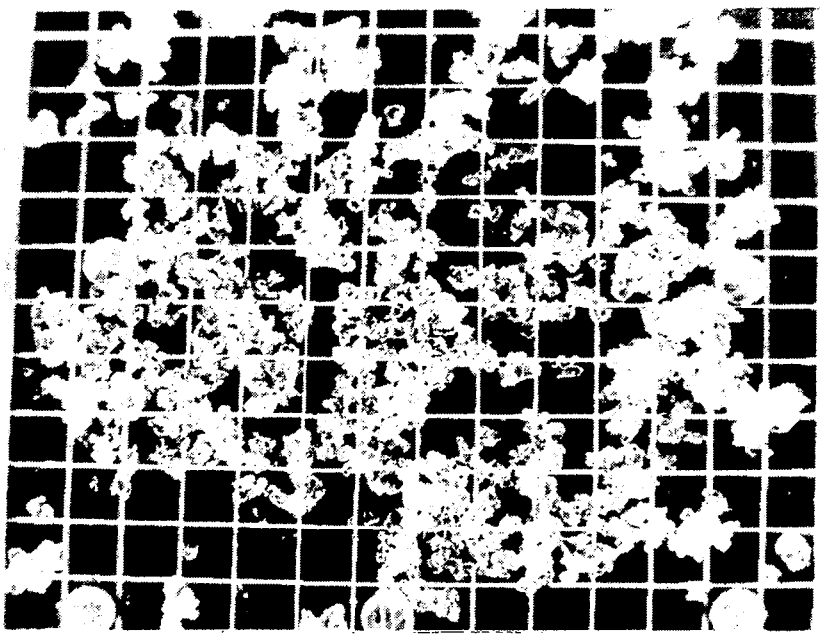


Figure 6-54 Layer 3 old metamorphosed snow on 3/24/77. 1 cm x 1 cm grid

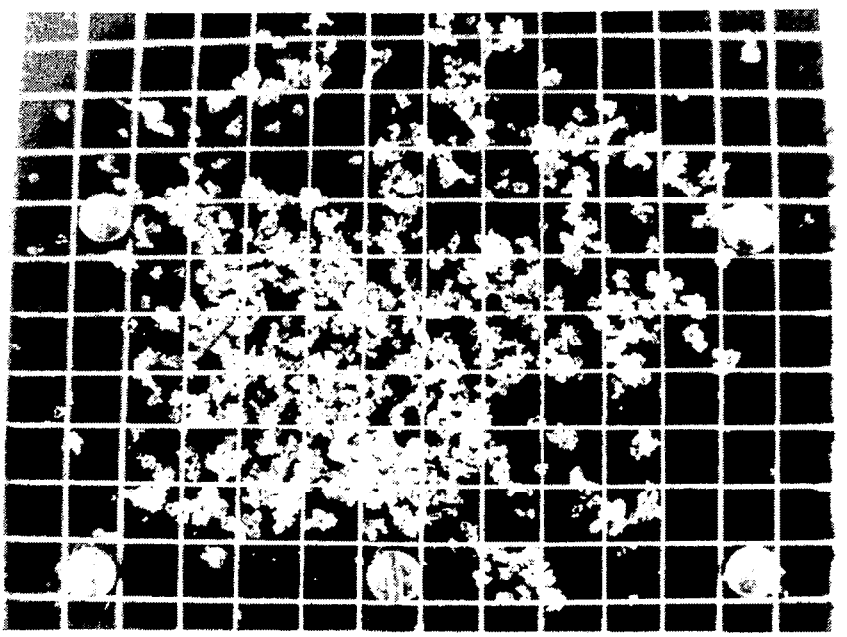


Figure 6-55 Layer 4 old snow on 3/24/77. 1 cm x 1 cm grid

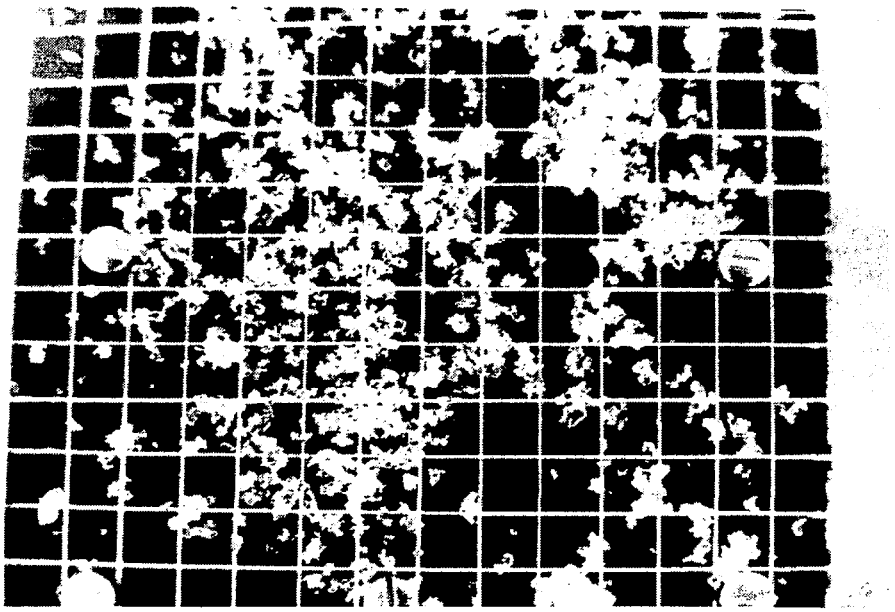


Figure 6-56 Layer 5 old snow on 3/24/77. 1 cm x 1 cm grid

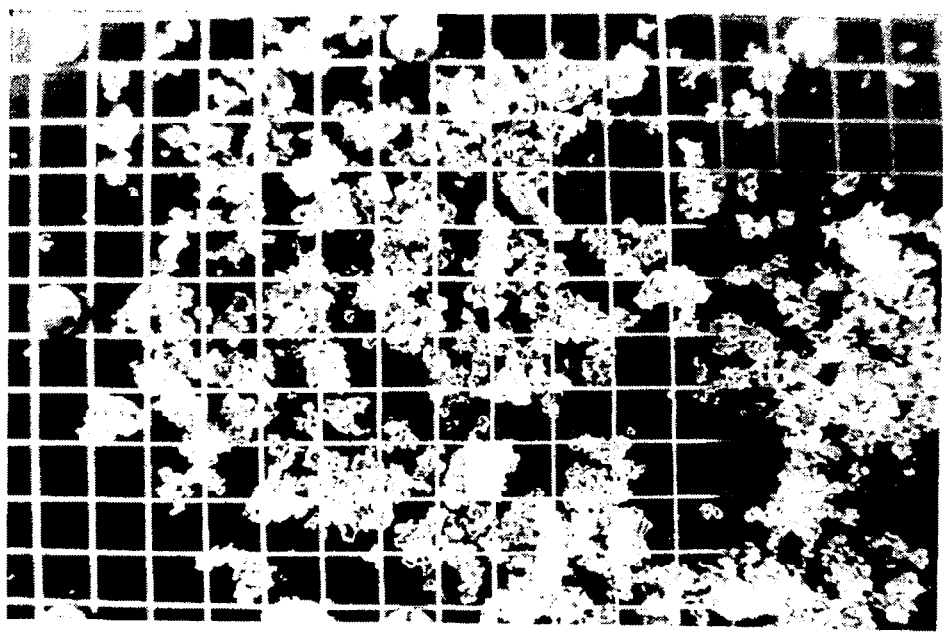


Figure 6-57 Layer 7 old snow on 3/24/77. 1 cm x 1 cm grid

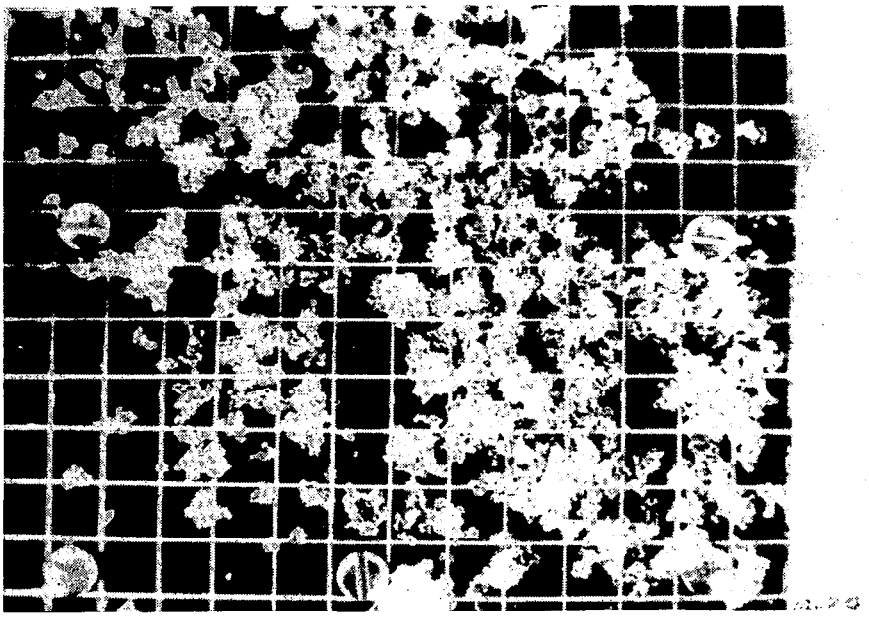


Figure 6-58 Layer 9 old snow on 3/24/77. 1 cm x 1 cm grid

Sampling of frozen soils is a time-consuming process. Freeze depth could only be determined, with the available means, by visual observation. Also, the frozen to thawed boundary was not a boundary at all but a zone in which frozen and liquid water coexisted. Actual determination of the effective soil moisture would require calorimetric or capacitance techniques. In this case, however, the problem is even more difficult since specific heats of the soils would have to have been determined. As a result of the above complications, the sampling technique and data on the soils were two of the weak points of the experiment.

6.4.3 Atmospheric Conditions

A weather station installed at the test site (Figure 6-59) monitored atmospheric temperature, relative humidity and atmospheric pressure. The weather instrument, a Meteorograph, Model M701 (Weather Measure Corporation, Sacramento, California), recorded data on a 24-hour strip chart with one minute resolution. This system proved adequate throughout the course of the experiment.

Solar radiation data were recorded with two pyranometers (Spectro-Lab, Model SR71) mounted such that one recorded incident radiation while the other recorded reflected radiation. The mounting and two pyranometers are shown in Figure 6-60. Both units were connected to a dual channel, strip chart recorder.

6.5 Data Acquisition

This section describes the specific experiments performed to better understand the microwave characteristics of snowpacks. Figure 6-61 gives the experiment timetable for the data acquisition and the periods during which each of the systems were operational. Table 6-4 provides a summary of the data acquired.

6.5.1 Daily Backscatter and Emission Measurements

The daily data sets covered a more complete set of sensor parameters than the special experiments. The MAS 1-8 and MAS 8-18/35 operated at all system frequencies and polarizations. The incidence angles observed were: 0°, 10°, 20°, 30°, 50° and 70°. Spatial averaging was employed to reduce the effects of fading. The radar returns from 20 resolution cells were averaged at 0°. The number of spatial samples was decreased with increasing angle to a minimum of five at 70°. The microwave radiometers

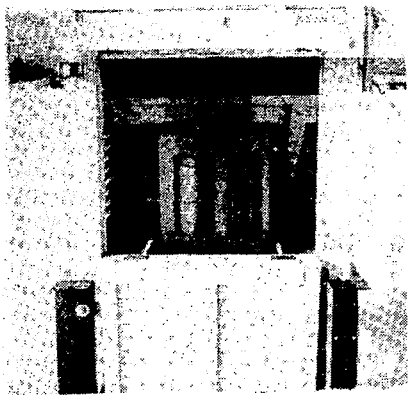


Figure 6-59 A three channel Meteorgraph, model M701 recorded atmospheric temperature, relative humidity and atmospheric pressure. This weather station was located between the test plots as illustrated in Figure 6-3.

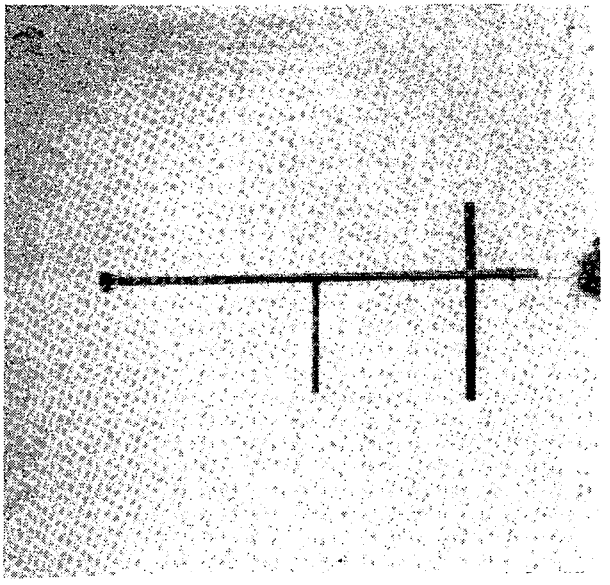


Figure 6-60 Two pyranometers were mounted back-to-back to measure incident and reflected solar radiation.

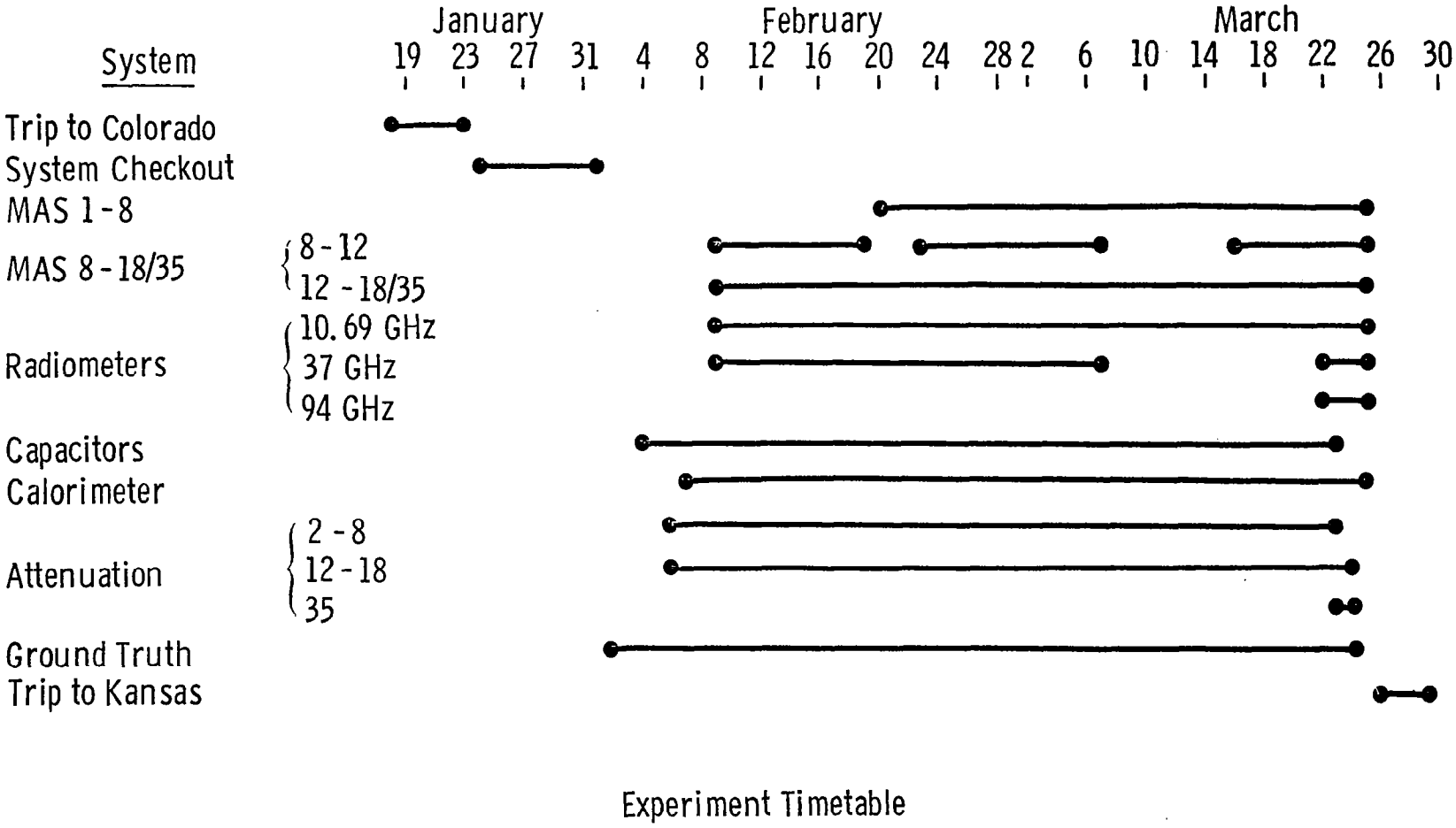


Figure 6-61 Experiment timetable showing data acquisition periods of the various sensors.

TABLE 6-4

Data Base of 1977 Snow Experiment
at Steamboat Springs, Colorado

SYSTEM	DATA SETS
MAS 1-8	
Diurnal subsets	34
Regular sets	43
TOTAL	77
MAS 8-18/35	
Diurnal subsets	87
Regular sets	31
TOTAL	118
Radiometers	
X-band	
Diurnal subsets	87
Regular sets	31
TOTAL	118
37 GHz	
Diurnal subsets	66
Regular sets	17
TOTAL	83
94 GHz	
Diurnal subsets	17
Attenuation Sets	
2-8 GHz	67
12-18 GHz	40
35 GHz	4
Capacitance Measurements	201
Calorimeter Measurements	217
Temperature Profiles	270
Ground Truth Sets	198
Photographs	576

measured five cells at each angle of incidence. In addition to the remotely sensed data, ground truth was taken with each set.

Between one and three daily sets were obtained depending on snow conditions and equipment status. Approximately three hours were required per data set. The desired time period for the daily sets were predawn, noon and late afternoon. These time periods covered the widest range of snow conditions within one day.

6.5.2 Diurnal Backscatter and Emission Measurements

Four diurnal data sequences were conducted. This measurement program was implemented to observe short-term variation in snow conditions such as appearance of free water in the snowpack and structural changes within the layers. Each diurnal experiment consisted of continuous data acquisition over a 28-hour period commencing at 6:00 a.m.

To improve the temporal resolution of the variations under observation, the time span of an individual data set was reduced by reducing the number of system parameters at which measurements were made. Generally, only HH polarization was observed with the exception of the 35.6 GHz scatterometer for which all polarizations were measured. Also, only 0°, 20° and 50° angles of incidence were sampled. The time span for a data set was reduced to approximately 1.5 hours. For the last two diurnals, only 50° data were acquired and the time span was approximately 0.75 hours. The ground truth data sets were obtained at hourly intervals except for the calorimeter and capacitance measurements which required a slightly longer duration.

6.4.3 Attenuation Measurements

One basic question in the study of snow is that of microwave penetration. Section 4.6 covers past measurements of attenuation through snow. To measure snow attenuation, two boxes (for each radar system) were placed in the field before the first snowfall. Figure 6-62 illustrates the placement. The MAS 1-8 and MAS 8-18/35 were used as transmit sources. The one-way path loss was measured with a small 2-8 GHz cavity backed spiral antenna, a 12.4-18.0 GHz waveguide horn and a Boonton power meter. Figure 6-63 shows the measurement system. The power loss was measured at six frequencies in the 2-8 GHz band and at five frequencies in the 12.4-18.0 GHz band for two snow thicknesses. The one-way loss is not totally due to attenuation, in fact for low loss cases, the dominant loss factor may be due to mismatch at the snow-air interfaces.

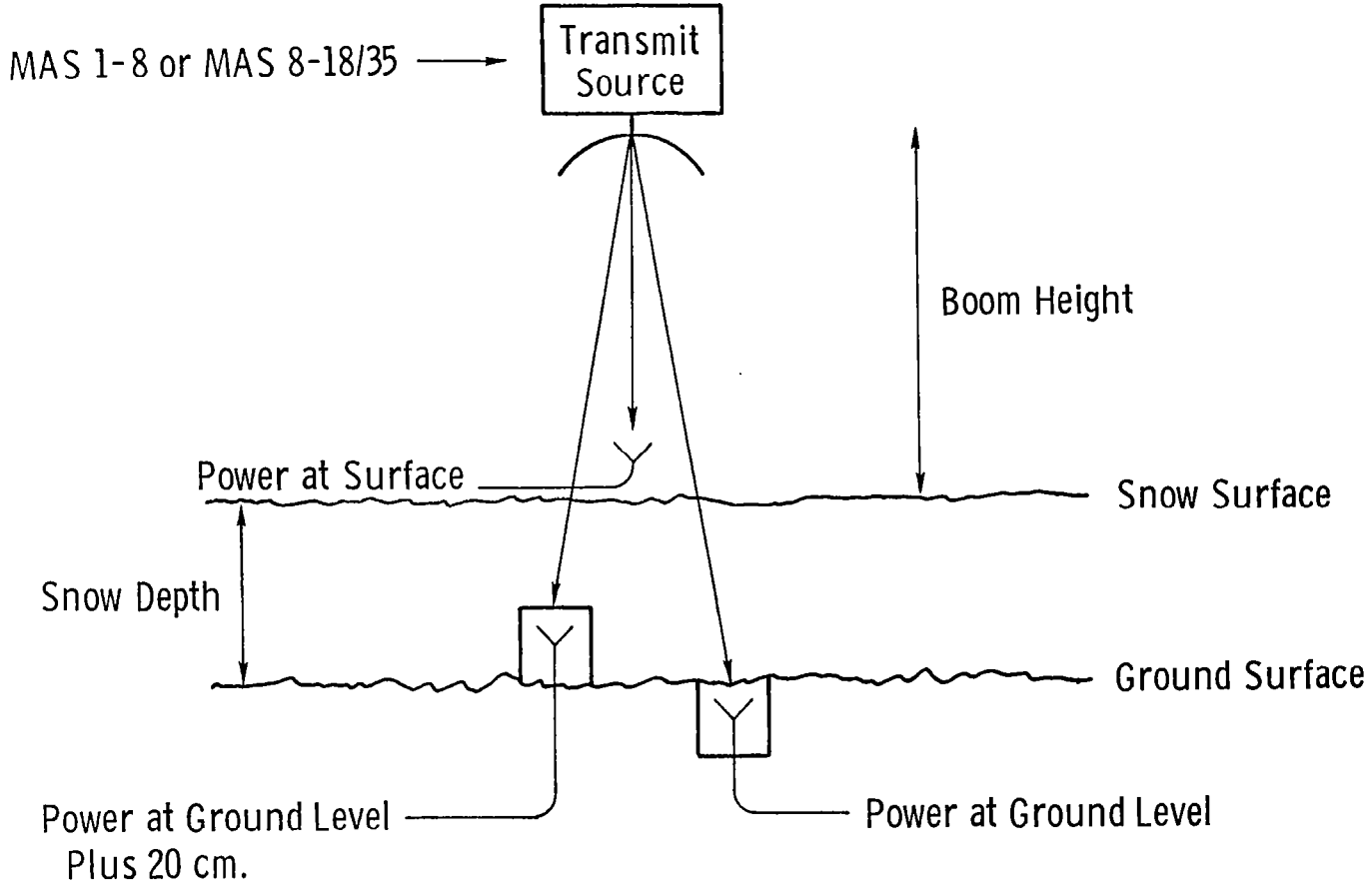
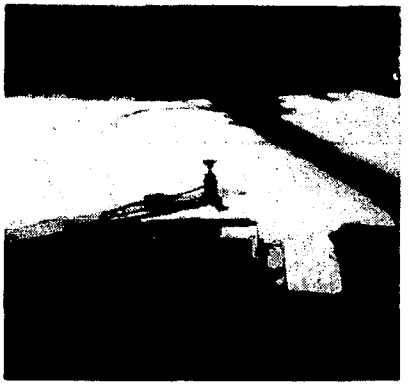


Figure 6-62 Diagram illustrating the attenuation measurement procedure.



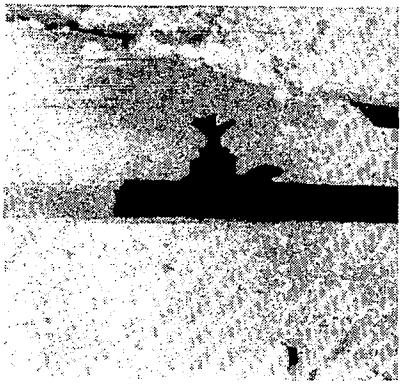
a) Attenuation pit showing the power meter, antenna and shadow of the MAS 8-18/35 transmit source.



b) Surface level power measurement.



c) Closeup of the antenna and power meter and antenna box at +20 cm above ground level.



d) Closeup of the receive horn.

Figure 6-63 Attenuation measurement.

Also, an experiment was carried out independently to measure attenuation at 35 GHz. The path loss in this case was measured horizontally. Readings were taken for varying snow thicknesses and for three snow conditions. Figure 6-64 illustrates the layout. A signal generator and doubler were used for a transmit source. The receiver consisted of a crystal detector and a VSWR meter. Sensitivity was limited by the equipment and alignment. Alignment of the antennas was accomplished by manually peaking the VSWR meter reading.

6.5.4 Single Cell Fluctuation Measurement

This experiment is a variation on the diurnal experiments already described. In this case it was desirable to observe the microwave response for a single observation cell. The look direction and position were therefore set and the scattering and emission properties measured for 12 hours during the daytime. Measurements at all system polarizations and frequencies were taken at 50° and 70° angles of incidence.

6.5.5 Snowpile Experiment

During the winter of 1976-1977, Colorado experienced the most severe drought in the last 10 years and as a result, the snowpack in the test area reached a maximum of only 57 cm. To test the microwave response to snow depth, an artificial snowpack was created by piling snow up to depths of 144 and 170 cm (three experiments were conducted). Figure 6-65 shows a photograph of the MAS 8-18/35 and radiometers in operation during this experiment. Since the size of the target allowed only one independent look (spatially), adjacent frequencies were averaged for the MAS 8-18/35. The error bars associated with the radar measurements were still quite large due to signal fading since only one spatial sample was obtained.

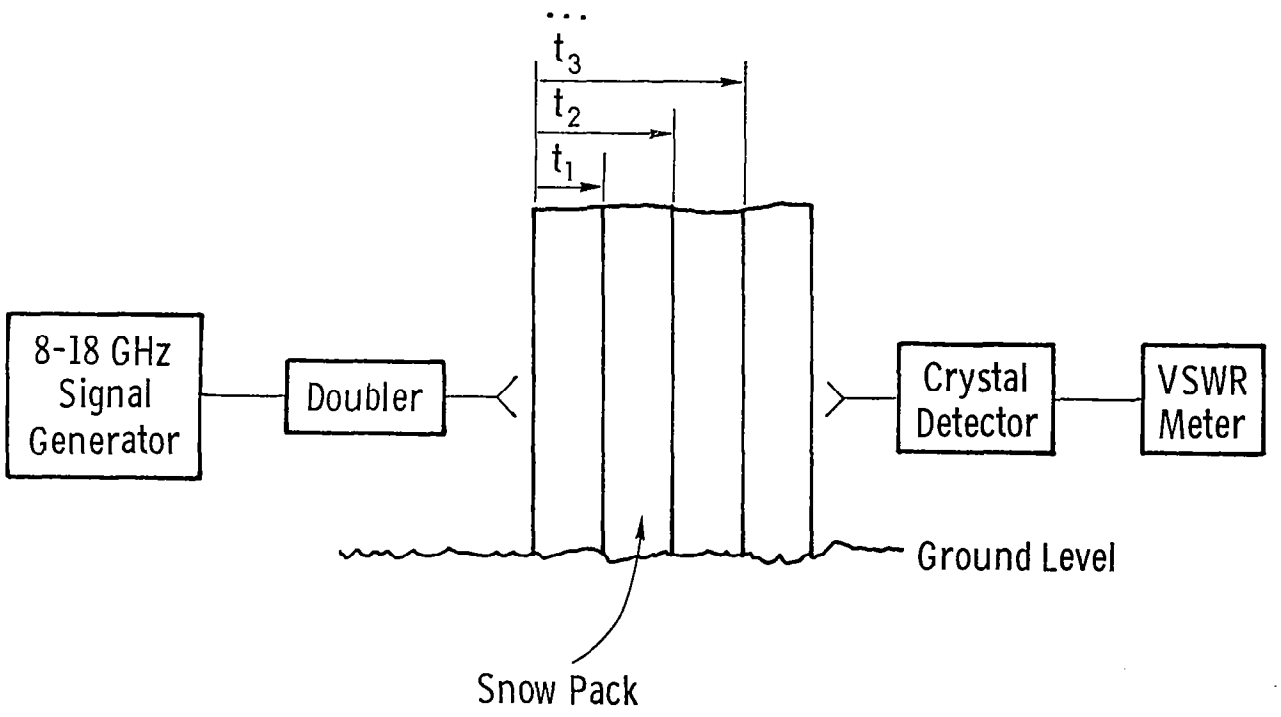


Figure 6-64 Diagram illustrating the procedure used to measure the attenuation of the snow at 35.6 GHz as a function of layer thickness (t).

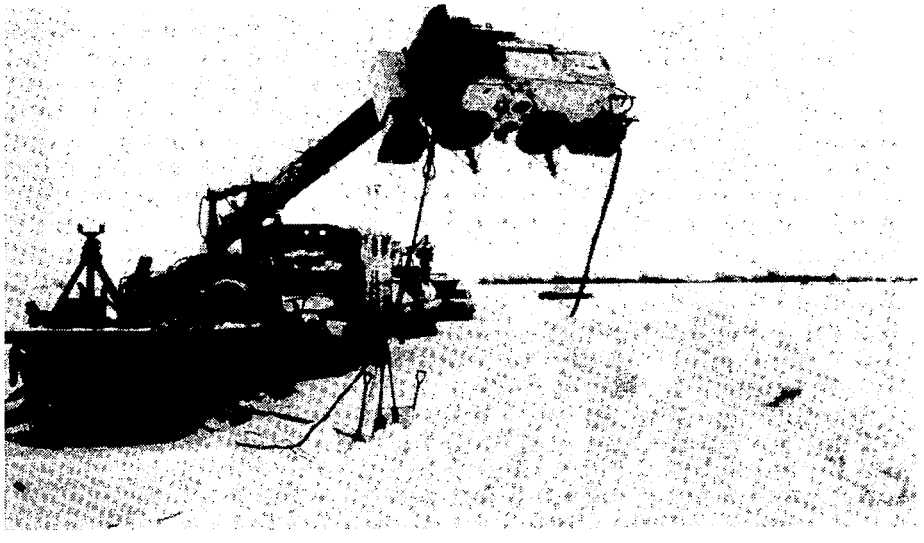


Figure 6-65 MAS 8-18/35 and radiometers during one of the snowpile experiments.

7.0 DATA STATISTICS

Knowledge of the statistics of both the ground truth and the microwave measurements can facilitate the interpretation of the snow/microwave interaction. The pre-experiment assumption of test site homogeneity had to be tested and retested periodically as snow conditions changed. Only if the target statistics are known can the radar and radiometer data statistics be interpreted in terms of the ground truth parameters. The seasonal variation is also investigated. This information is valuable to the radar and radiometer engineers interested in clutter and to remote sensing system designers.

7.1 Measurement Variability

This section examines the horizontal spatial variability of the test site and the measurement precision of the radar system.

7.1.1 Test Site Spatial Variability

Ground truth data were obtained in a snowpit along the northeastern corner of the test plot. A single pit was chosen to minimize the time span required for each complete ground truth set. To test the applicability of the ground truth data obtained in the snowpit to the rest of the field, four tests were periodically made to examine the uniformity of the snow parameters across the field. Table 7-1 provides a summary of the snow depth variations of the snowpack. Figure 7-1 shows the snow depth and water equivalent variation. The samples were acquired along the perimeter of the field (at the locations indicated in Figure 7-1) for the first three tests. The last test, which was performed at the end of the last microwave data set, sampled the interior of the field itself at the numbered locations.

It is clear from Table 7-1 that the snowpack was spatially uniform in depth as indicated by the depth standard deviation. Before the March 14, 1977 test, high winds had caused the back edge of the test plot to drift and reduced the snow depth in that area. These points were not really in the radar field of view, since at 70° angle of incidence, the

TABLE 7-1

Mean Snowpack Depth and Standard Deviation Based on N Samples Acquired Along the Perimeter of the Test Plot as Indicated in Figure 7-1

Date	N	Mean Depth $\bar{h}$ (cm)	Standard Deviation σ_h (cm)
February 15, 1977	11	31.3	1.1
March 12, 1977	9	46.7	1.9
March 14, 1977	21	37.9	1.9
March 14, 1977	12 (excluding far range, points E through N in Fig. 6-1	39.2	1.4
March 26, 1977	15	40.3	1.8

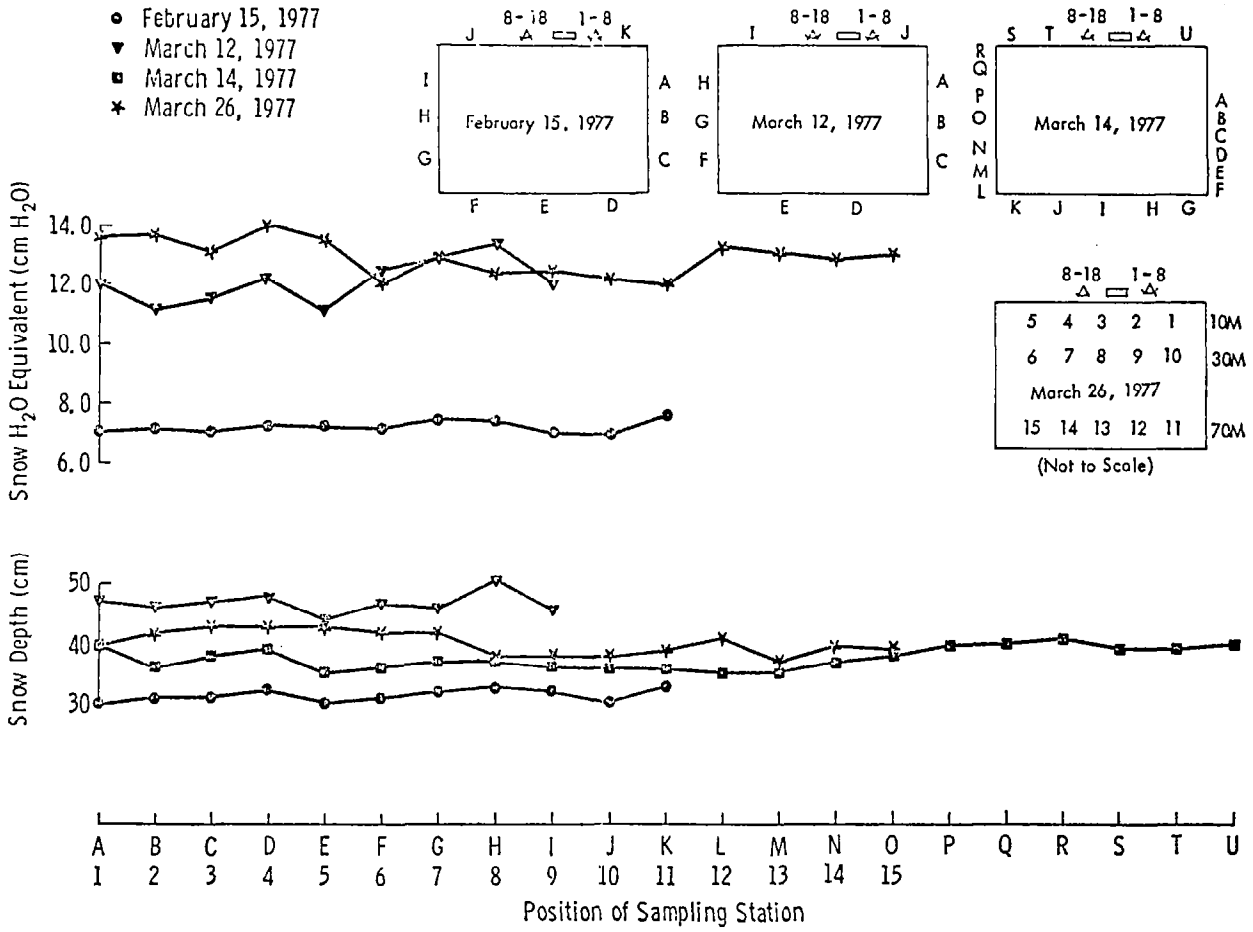


Figure 7-1 Spatial variability of snow depth and density at test site.

maximum ground range of the radar was 90 meters and the outer perimeter of the field was at a range of 110 meters. If the measurements along the back edge of the plot are deleted, the standard deviation of the snow depth reduces to 1.4 cm.

In addition to measuring the snowpack height, depth profiles were obtained for the snowpack density. The combination of height and density profile was used to calculate the snow water equivalent W (cm). Figure 7-1 includes plots of W as a function of position around the field for the February 15, 1977 and March 12, 1977 tests and for the interior of the field for the March 26, 1977 test. Table 7-2, a summary of the measurement statistics on water equivalent, shows the homogeneity of the field.

With the equipment, time and manpower available, determination of horizontal spatial variability in wetness was not possible. Since the density and solar radiation were uniform across the field, it is reasonable to assume horizontal homogeneity.

7.1.2 Precision of Microwave Measurements

Having established in the previous section that the snowpack was fairly uniform, both in terms of depth and water equivalent, we now proceed to examine the measurement variability of the microwave sensors. The spatial homogeneity of the snowpack indicates that the microwave measurement variability should be predominately due to system precision or within data set temporal variation. The temporal variations within a data set are a problem when rapid change of snow wetness occurs during the data set time span. The spatial homogeneity of the snowpack is necessary to average data from different spots across the field, thereby improving the measurement precision of the microwave sensors, particularly the radar. The system precision in the radiometers was mainly due to amplifier gain variations. The radar, on the other hand as a result of coherence, exhibits signal fading characteristics which limit the individual sample measurement precision.

Figure 7-2 shows the 10.69 GHz and 37 GHz radiometric temperatures for 13 measurements at 13 different spots across the field. The positions of the spots were chosen randomly and the data were acquired over a span of approximately two hours during the late hours of the night during which the snowpack conditions remained essentially constant. According to Figure 7-2, the 10.69 GHz radiometric temperature variation

TABLE 7-2

Mean Snowpack Water Equivalent and Standard Deviation

Date	N	Mean Water Equivalent $\bar{w}$ (cm)	Standard Deviation σ_w (cm)
February 15, 1977	11	7.3	0.22
March 12, 1977	9	12.1	0.71
March 26, 1977	15	12.9	0.61

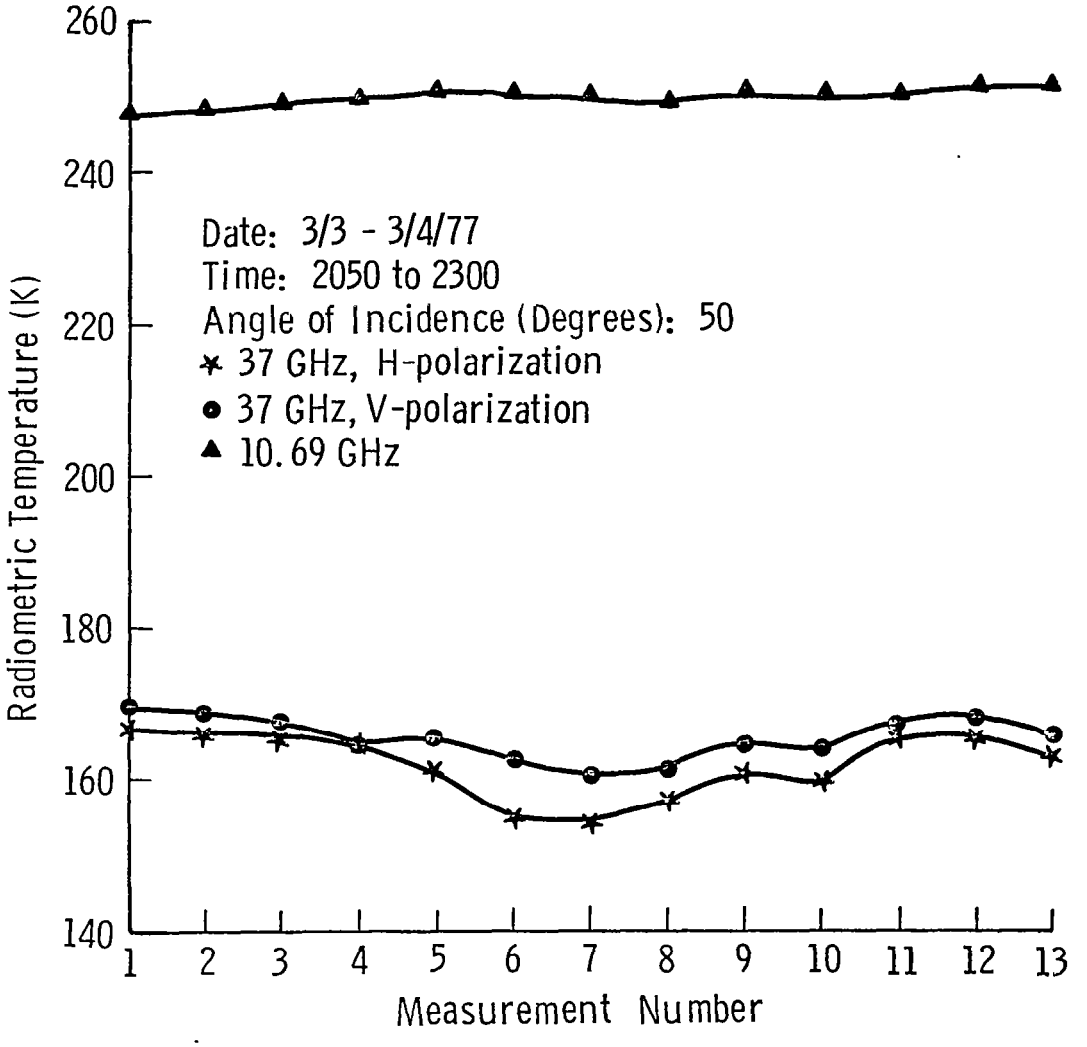


Figure 7-2 Spatial variability of microwave radiometric temperatures.

was only 3 K. At 37 GHz, the total variation is 9 K for the vertically polarized channel and 12 K for the horizontally polarized channel. About 5 K of that variation can be explained as a response to variations in the downward emitted sky radiometric temperature. The remainder is probably due to small variations in the snowpack properties over the two-hour measurement period. It may also be argued that the observed variation is totally due to drift in the amplifier gain of the radiometer receiver. In either case, the variation is small in comparison to the change (greater than 80 K) observed during the diurnal cycles (Section 8.4) which was in response to variation in snow wetness.

Fading in the received power from a radar causes signal fluctuations that must be reduced to obtain an acceptable estimate of the mean of the fading distribution. The effects of fading and measurement precision have been examined in more detail by Stiles et al. (1979). Both frequency averaging and spatial averaging were employed to improve the estimate of σ^{o}. Variability of the radar data is shown in Figure 7-3 for 17.0 GHz and 35.6 GHz at 5° and 55°. Table 7-3 provides a list of the measured values of the received power, the mean value, and the variance of the received power. Also provided in Table 7-3 are the number of independent samples calculated on the basis of the measured data (N calc) and on the basis of Rayleigh fading and frequency averaging (N pred). Rayleigh statistics have been shown to give a good estimate of the fading distribution within a homogeneous field (Bush and Ulaby, 1975). Two values of the predicted number of independent samples are given in Table 7-3, the smaller value corresponds to the assumption that the backscatter is only from the snowpack surface while the larger value corresponds to the assumption that the entire snowpack depth contributes to the backscatter. Comparison of the calculated and predicted values of N clearly demonstrates that Rayleigh fading is a good descriptor of the fading statistics of the snowpack at 17.0 GHz; however at 35.6 GHz, the variance appears to be less than that predicted by Rayleigh statistics.

The variations in Figure 7-3 at 17.0 GHz are in agreement with Rayleigh fading predictions using the MAS system parameters. The much larger variation in the 5° data than the 55° data is a result of the smaller number of independent samples per spatial measurement. This is the reason for acquiring more spatial samples near nadir than at high angles.

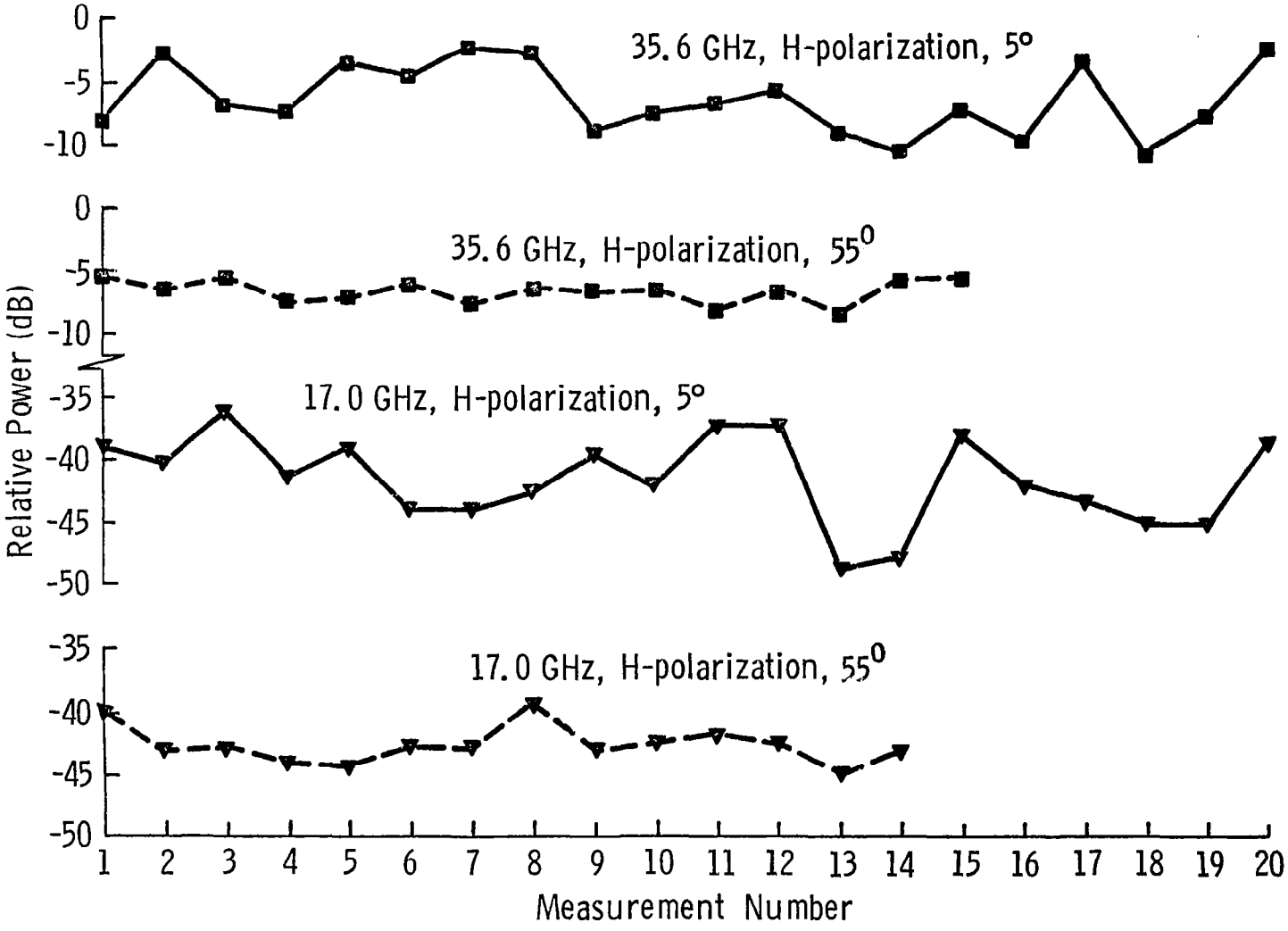


Figure 7-3 Spatial variability of received backscatter power at two frequencies and angles.

TABLE 7-3

Scatterometer Measurement Variation with Spatial Position

Date: 2/18/77 Time: 0300 Angle of Incidence (degrees): 5			Date: 3/3/77 Time: 2045 Angle of Incidence (degrees): 50		
Measurement Number	Measured Received Power (dB)		Measurement Number	Measured Received Power (dB)	
	17.0 GHz	35.6 GHz		17.0 GHz	35.6 GHz
1	-38.9	- 8.3	1	-40.1	- 5.6
2	-40.3	- 2.7	2	-43.2	- 6.5
3	-36.1	- 6.9	3	-42.8	- 5.7
4	-41.6	- 7.3	4	-44.1	- 7.7
5	-39.2	- 3.5	5	-44.3	- 7.3
6	-44.0	- 4.6	6	-42.8	- 6.2
7	-44.0	- 2.4	7	-43.0	- 7.8
8	-42.7	- 2.9	8	-39.4	- 6.5
9	-39.9	- 9.0	9	-43.1	- 6.8
10	-42.4	- 7.4	10	-42.5	- 6.6
11	-37.4	- 6.8	11	-41.8	- 8.0
12	-37.2	- 5.8	12	-42.7	- 6.6
13	-48.9	- 9.2	13	-42.8	- 8.7
14	-47.8	-10.8	14	-45.1	- 6.0
15	-38.2	- 7.1	15	-43.3	- 5.8
16	-42.1	- 9.8			
17	-43.5	- 3.5			
18	-45.3	-10.9			
19	-45.2	- 7.9			
20	-38.7	- 3.3			
$\mu_{\overline{W}}$	9.02×10^{-5}	.270	$\mu_{\overline{W}}$	5.64×10^{-5}	.214
$\sigma^2_{\overline{W}}$	4.02×10^{-9}	.0264	$\sigma^2_{\overline{W}}$	4.569×10^{-10}	.00173
$N_{calc} = \frac{\mu^2}{\sigma^2}$	2.0	2.8	$N_{calc} = \frac{\mu^2}{\sigma^2}$	7.0	26.5
N_{pred} (no penetration)	1	1	N_{pred} (no penetration)	7	13
N_{pred} (complete penetration 35 cm)	1.9	1.9	N_{pred} (complete penetration 35 cm)	10.8	16.5

Since the field was shown to be relatively homogeneous and since the microwave measurement variations can be explained by fading in the active case and sky effects for the passive case, in the future analyses, the response of the averaged σ^o and T_{ap} values will be attributed solely to ground truth characteristic variations.

7.2 Seasonal Statistics of Active Microwave Data

For the radar designer interested in clutter, seasonal averages and expected dynamic range are important parameters for characterizing snow backscatter. Seasonal averages also give an overall look at the behavior of σ^o of snowpacks. The spectral response of the averaged σ^o of all the Steamboat Springs active data are given at 0°, 20° and 50° for HH and HV polarizations in Figures 7-4 to 7-6. Also given are the linear fits to the data. The slopes increase monotonically with frequency. The cross-polarized data is seen to increase at a faster rate than the like-polarized data. The result is a decreasing polarization ratio with increasing frequency and increasing angle of incidence. This behavior results from the increased effect of volume scattering at the higher frequencies. The 5% and 95% bounds of the scattering coefficients over the season are also given in Figures 7-4 to 7-6. These curves define the region containing all data except extreme outliers. The 5% to 95% dynamic range decreases slightly with increasing angle of incidence and is about the same for both like and cross polarization configurations.

Correlation coefficients were calculated between combinations of nine different frequencies at 0°, 20° and 50° and are given in Table 7-4. Figure 7-7 illustrates the correlation coefficients as a function of frequency with respect to 1.2 GHz. The rapid decorrelation with increasing frequency results from the decreasing effects of the underlying soil and increasing dominance of the snow layer. The reason for the lower values at 20° is not clear. Figure 7-8 shows the correlation coefficients with respect to 35.6 GHz. Again, the correlation coefficient is seen to decrease as the frequency difference to the reference frequency increases. The decrease in this case is not rapid and only becomes rapid below 8 GHz. The 8 to 17 GHz data points are seen to be closely correlated.

Histograms of the σ^o data over the season at 1.2, 8.6, 17.0 and 35.6 GHz are given in Figure 7-9 at 0° and in Figure 7-10 at 50° angle of incidence. A larger number of data sets were taken at 50° which

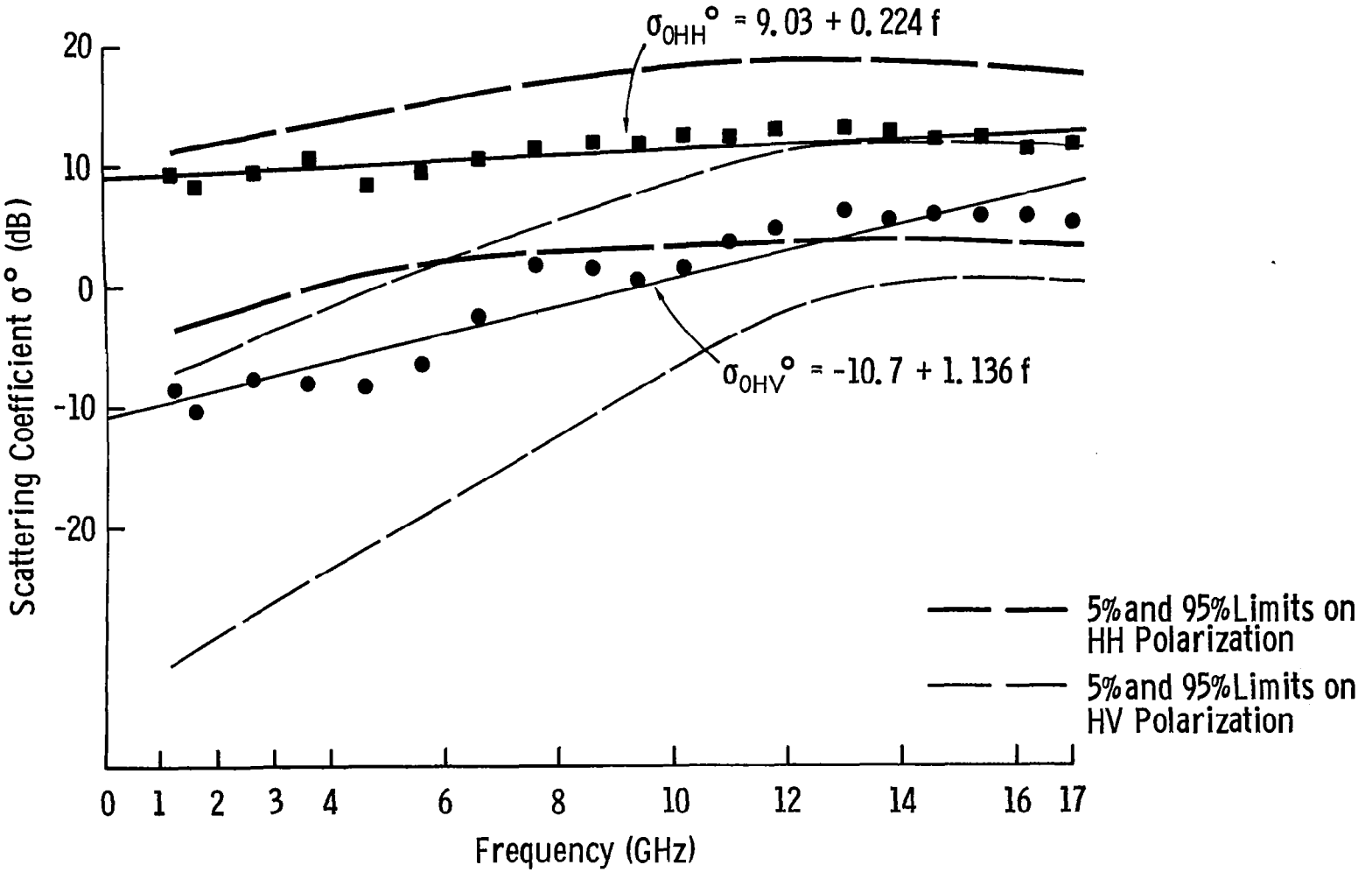


Figure 7-4 Seasonal average σ^{o} spectral response at 0^{o} (nadir) and regression equations along with the 5% and 95% limits.

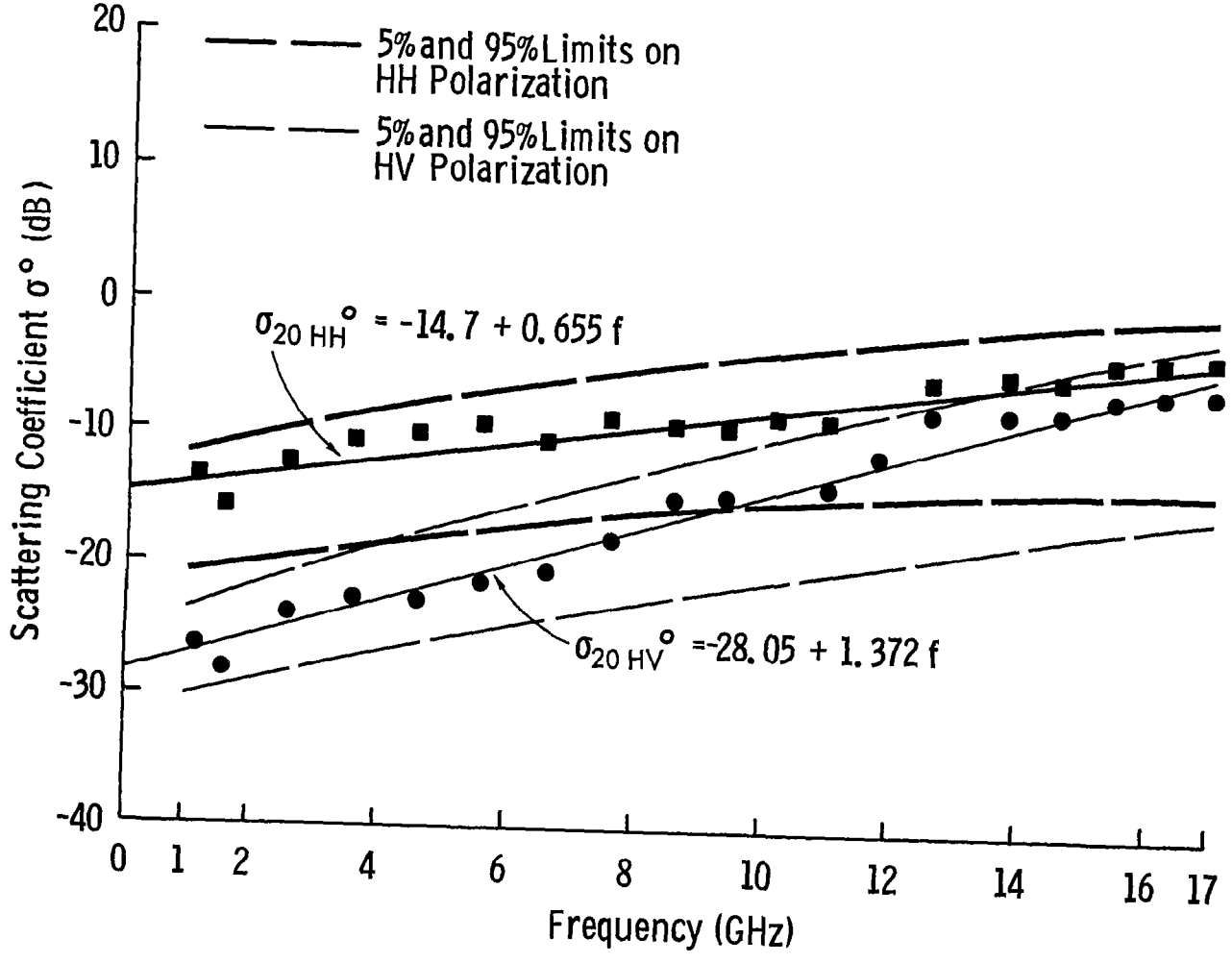


Figure 7-5 Seasonal average σ^{o} spectral response at 20^{o} angle of incidence and regression equations along with the 5% and 95% limits.

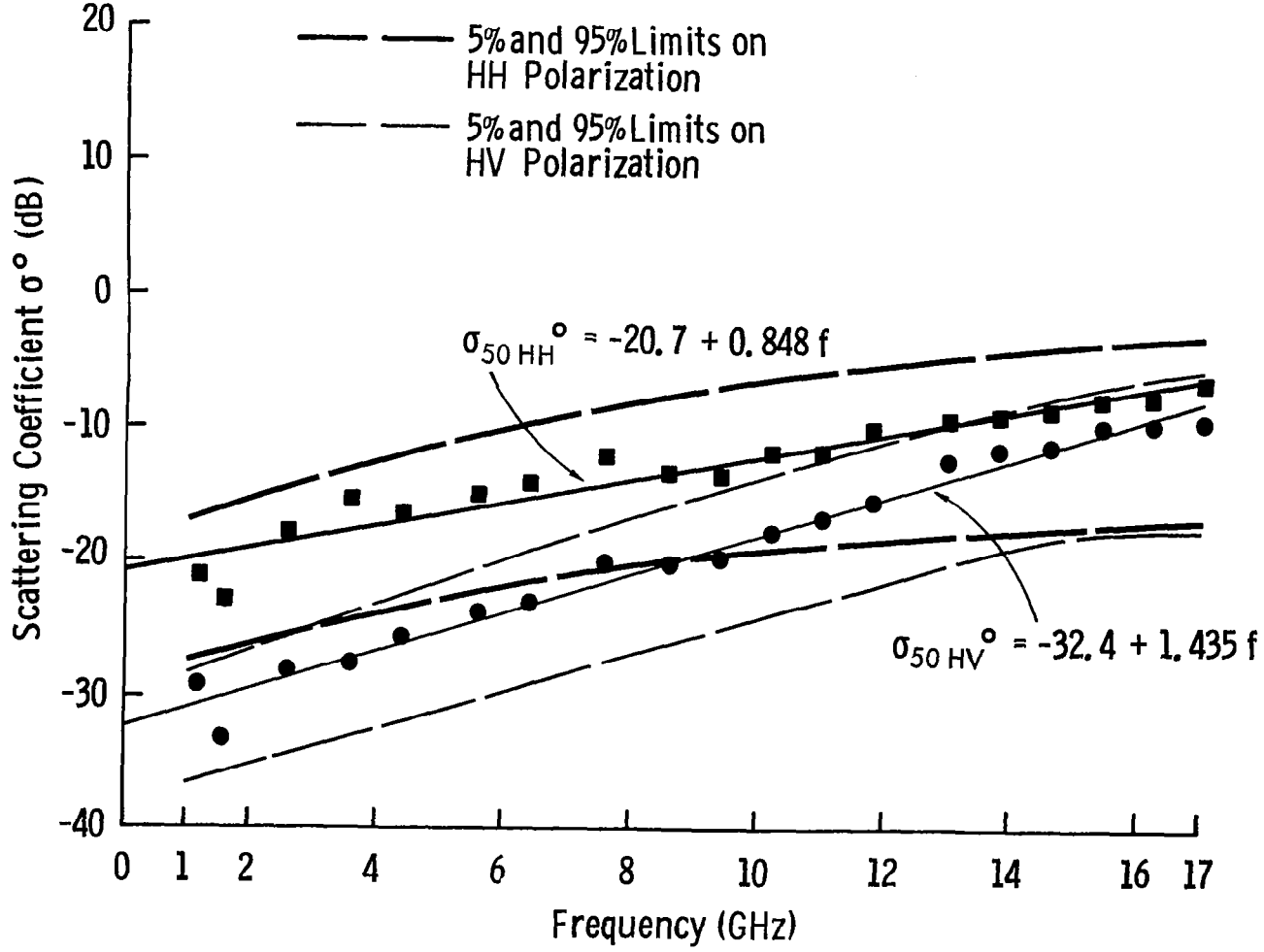


Figure 7-6 Seasonal average of σ^{o} response at 50^{o} angle of incidence and regression equations along with the 5% and 95% limits.

TABLE 7-4

HH Polarized Scattering Coefficient Correlation Matrix

		Frequency								
ANGLE	FREQ	1.2	2.6	4.6	7.6	8.6	11.0	13.0	17.0	35.6
0^o	1.2	1.0								
	2.6	0.58	1.0							
	4.6	0.71	0.42	1.0						
	7.6	0,33	0.49	0.29	1.0					
	8.6	0.59	0.79	-0.83	0.87	1.0				
	11.0	0.41	0.66	-0.88	0.85	0.94	1.0			
	13.0	-0.09	0.31	-0.16	0.43	0.95	0.96	1.0		
	17.0	0.04	0.08	-0.25	0.80	0.88	0.91	0.59	1.0	
	35.6	-0.41	-0.07	-0.01	-0.10	0.32	0.32	0.32	0.49	1.0
20^o	1.2	1.0								
	2.6	0.37	1.0							
	4.6	0.29	0.64	1.0						
	7.6	-0.41	0.06	0.40	1.0					
	8.6	-0.21	-0.66	0.58	0.49	1.0				
	11.0	-0.25	-0.69	0.72	0.58	0.95	1.0			
	13.0	-0.33	-0.11	0.26	0.59	0.97	0.98	1.0		
	17.0	-0.43	-0.24	0.18	0.59	0.96	0.97	0.94	1.0	
	35.6	-0.64	-0.41	-0.06	0.56	0.85	0.87	0.80	0.90	1.0
50^o	1.2	1.0								
	2.6	0.95	1.0							
	4.6	0.74	0.74	1.0						
	7.6	0.49	0.54	0.87	1.0					
	8.6	0.22	0.25	0.59	0.81	1.0				
	11.0	0.01	0.05	0.43	0.72	0.96	1.0			
	13.0	-0.17	-0.13	0.34	0.62	0.91	0.97	1.0		
	17.0	-0.33	-0.31	0.18	0.48	0.76	0.87	0.95	1.0	
	35.6	-0.08	0.06	0.40	0.45	0.74	0.74	0.75	0.76	1.0

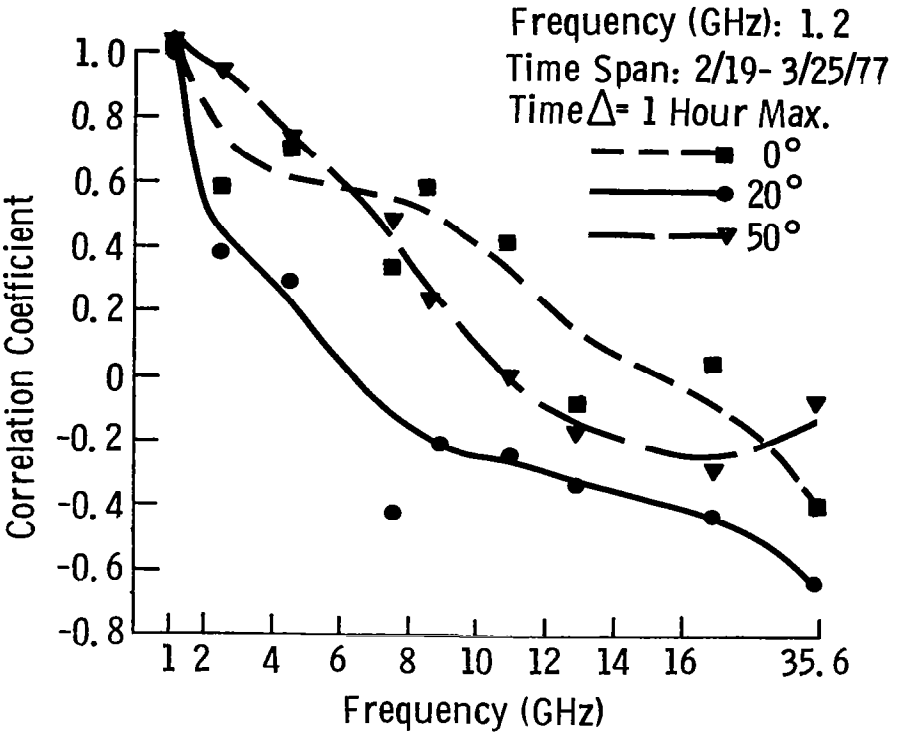


Figure 7-7 Correlation coefficients between σ^{o}_{HH} at 1.2 GHz and σ^{o}_{HH} at other frequencies at 0°, 20° and 50°.

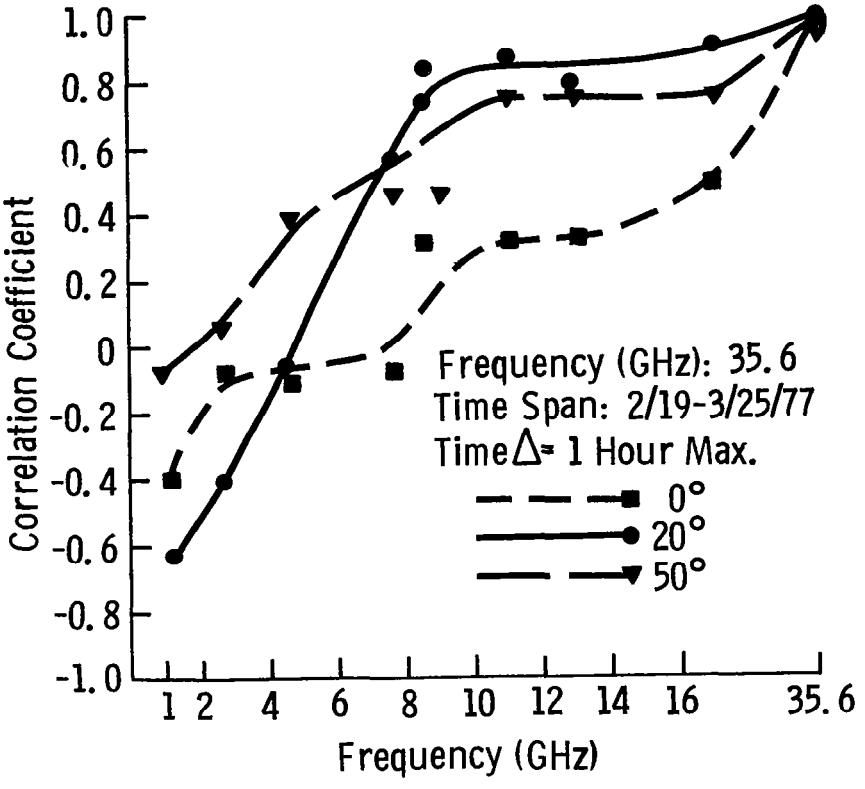


Figure 7-8 Correlation coefficients between σ^{o}_{HH} at 35.6 GHz and σ^{o}_{HH} at other frequencies at 0°, 20° and 50°.

HISTOGRAM OF VARIABLE 1 00HH1.2

SYMBOL X COUNT 51 MEAN 8.518 ST.DEV. 3.334

σ^{o}(dB)

INTERVAL NAME		FREQUENCY INT.	FREQUENCY CUM.	PERCENTAGE INT.	PERCENTAGE CUM.
-20.000	+	0	0	0.	0.
-19.000	+	0	0	0.	0.
-18.000	+	0	0	0.	0.
-17.000	+	0	0	0.	0.
-16.000	+	0	0	0.	0.
-15.000	+	0	0	0.	0.
-14.000	+	0	0	0.	0.
-13.000	+	0	0	0.	0.
-12.000	+	0	0	0.	0.
-11.000	+	0	0	0.	0.
-10.000	+	0	0	0.	0.
-9.0000	+	0	0	0.	0.
-8.0000	+	0	0	0.	0.
-7.0000	+	0	0	0.	0.
-6.0000	+	0	0	0.	0.
-5.0000	+	0	0	0.	0.
-4.0000	+	0	0	0.	0.
-3.0000	+x	1	1	2.0	2.0
-2.0000	+	0	1	0.	2.0
-1.0000	+	0	1	0.	2.0
0.0000	+x	1	2	2.0	3.9
1.0000	+	0	2	0.	3.9
2.0000	+x	1	3	2.0	5.9
3.0000	+	0	3	0.	5.9
4.0000	+x	1	4	2.0	7.8
5.0000	+xx	2	6	3.9	11.8
6.0000	+xx	2	8	3.9	15.7
7.0000	+xxxx	4	12	7.8	23.5
8.0000	+xxxxxx	6	18	11.8	35.3
9.0000	+xxxxxxx	7	25	13.7	49.0
10.000	+xxxxxxxxx	9	34	17.6	66.7
11.000	+xxxxxx	6	40	11.8	78.4
12.000	+xxxxxxxx	8	48	15.7	94.1
13.000	+xx	2	50	3.9	98.0
14.000	+x	1	51	2.0	100.0
15.000	+	0	51	0.	100.0
16.000	+	0	51	0.	100.0
17.000	+	0	51	0.	100.0
18.000	+	0	51	0.	100.0
19.000	+	0	51	0.	100.0
20.000	+	0	51	0.	100.0
LAST	+	0	51	0.	100.0

5 10 15 20 25 30 35 40 45 50 55 60 65 70 75 80

Figure 7-9a Histogram of σ^{o}_{HH} at 1.2 GHz and 0° angle of incidence. The number of data sets within each bin is on the horizontal axis.

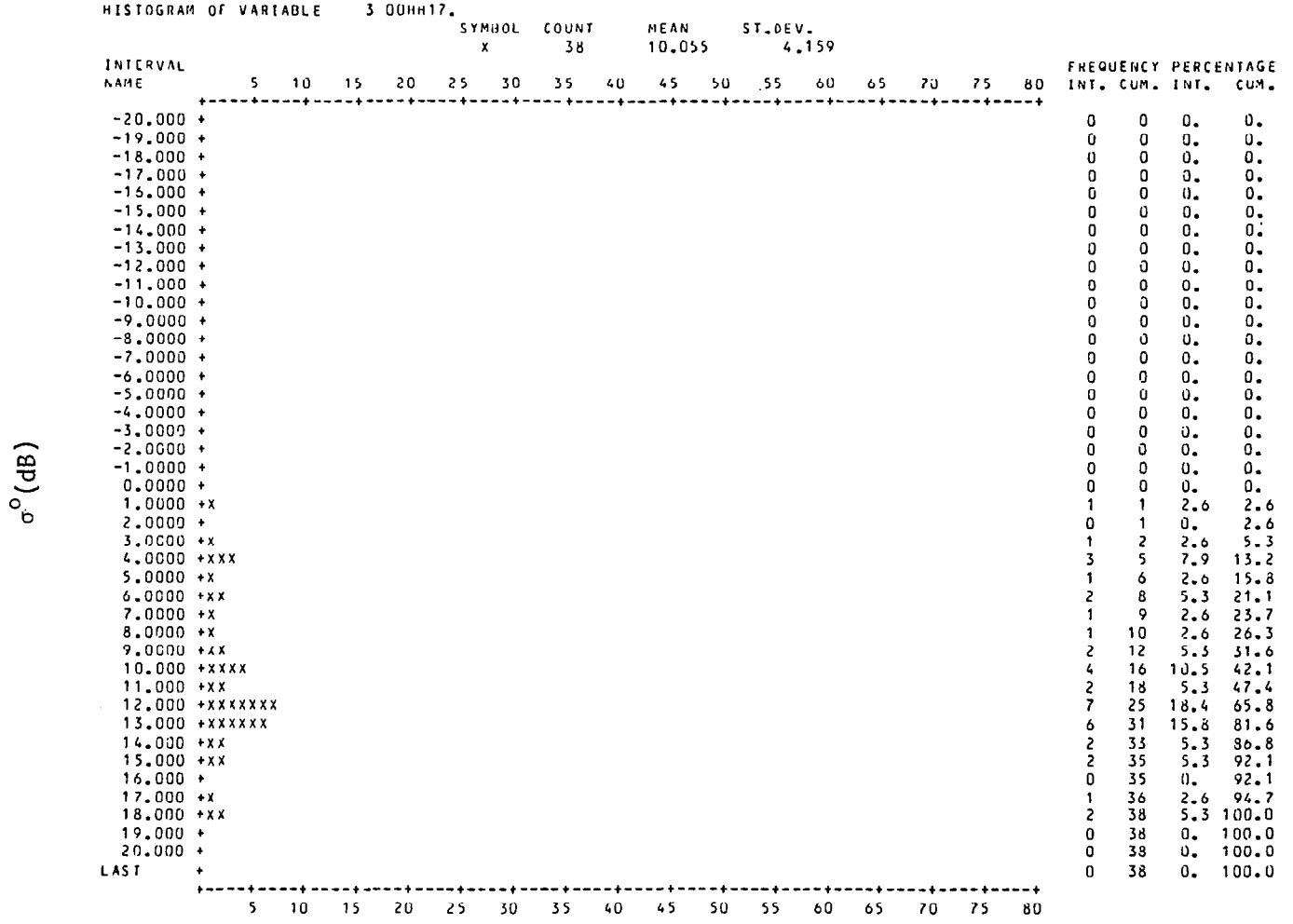
HISTOGRAM OF VARIABLE 2 00HH8.6

SYMBOL	COUNT	MEAN	ST.DEV.
X	19	11.074	3.593

INTERVAL NAME	FREQUENCY INT.	FREQUENCY CUM.	PERCENTAGE INT.	PERCENTAGE CUM.
-20.000	0	0	0.	0.
-19.000	0	0	0.	0.
-18.000	0	0	0.	0.
-17.000	0	0	0.	0.
-16.000	0	0	0.	0.
-15.000	0	0	0.	0.
-14.000	0	0	0.	0.
-13.000	0	0	0.	0.
-12.000	0	0	0.	0.
-11.000	0	0	0.	0.
-10.000	0	0	0.	0.
-9.0000	0	0	0.	0.
-8.0000	0	0	0.	0.
-7.0000	0	0	0.	0.
-6.0000	0	0	0.	0.
-5.0000	0	0	0.	0.
-4.0000	0	0	0.	0.
-3.0000	0	0	0.	0.
-2.0000	0	0	0.	0.
-1.0000	0	0	0.	0.
0.0000	0	0	0.	0.
1.0000	0	0	0.	0.
2.0000	0	0	0.	0.
3.0000	0	0	0.	0.
4.0000	0	0	0.	0.
5.0000	1	1	5.3	5.3
6.0000	1	2	5.3	10.5
7.0000	2	4	10.5	21.1
8.0000	0	4	0.	21.1
9.0000	0	4	0.	21.1
10.000	3	7	15.8	36.8
11.000	2	9	10.5	47.4
12.000	2	11	10.5	57.9
13.000	4	15	21.1	78.9
14.000	2	17	10.5	89.5
15.000	0	17	0.	89.5
16.000	1	18	5.3	94.7
17.000	0	18	0.	94.7
18.000	0	18	0.	94.7
19.000	0	18	0.	94.7
20.000	1	19	5.3	100.0
LAST	0	19	0.	100.0

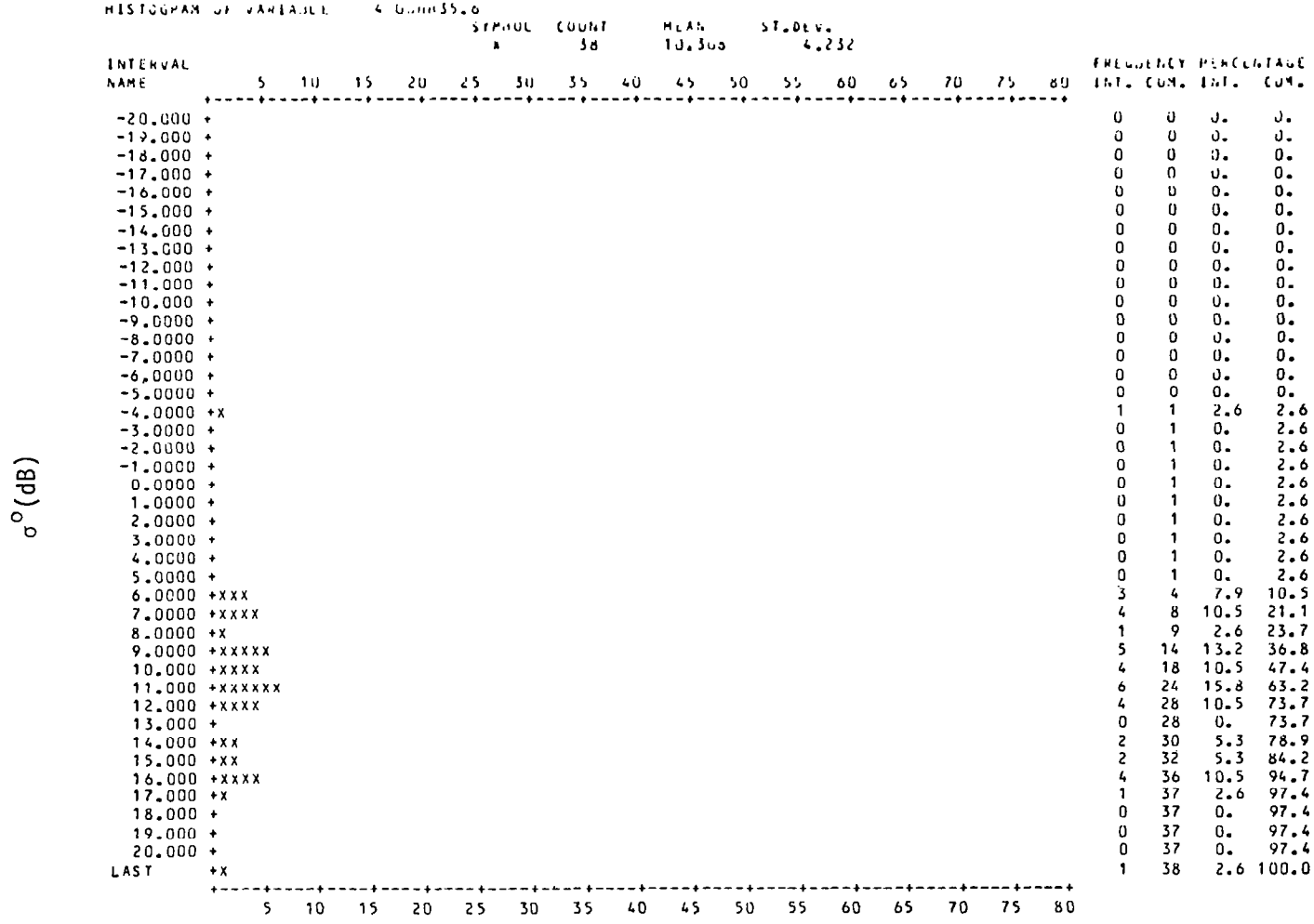
σ^{o}(dB)

Figure 7-9b Histogram of σ^{o}_{HH} at 8.6 GHz and 0° angle of incidence.



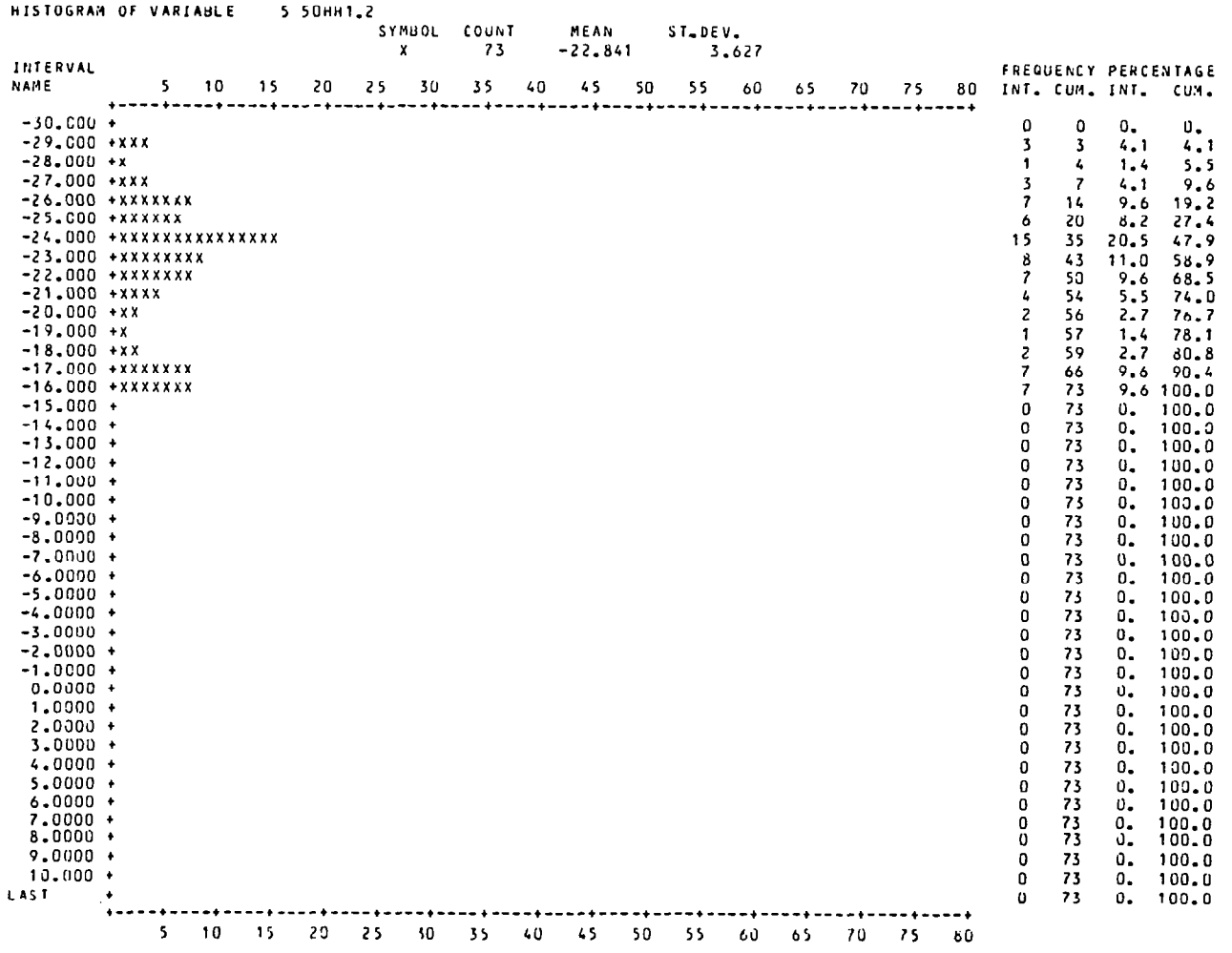
σ^{o}(dB)

Figure 7-9c Histogram of σ^{o}_{HH} at 17.0 GHz and 0° angle of incidence.



σ^{o}(dB)

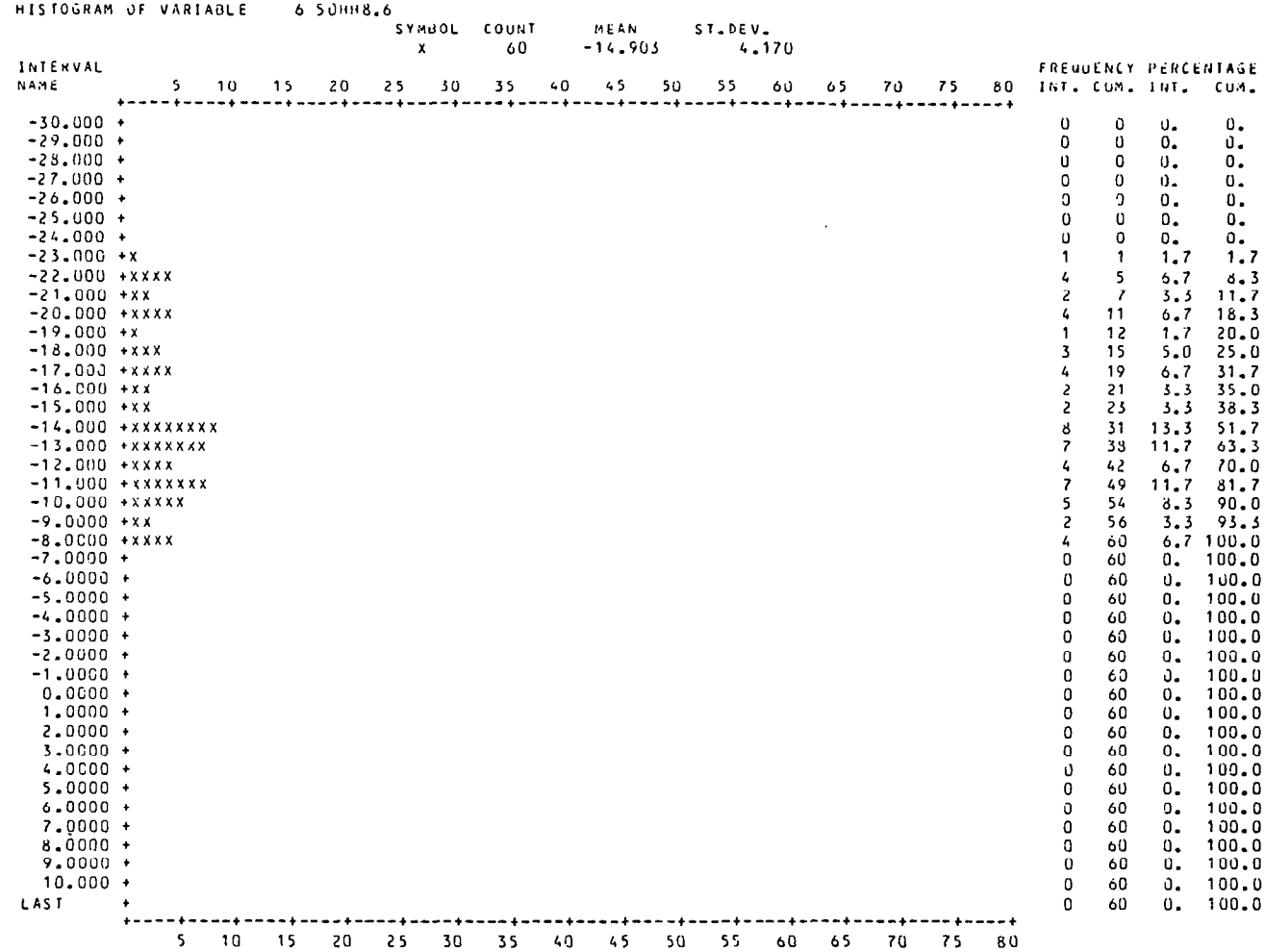
Figure 7-9d Histogram of σ^{o}_{HH} at 35.6 GHz and 0° angle of incidence.



σ^{o}(dB)

Figure 7-10a Histogram of σ^{o}_{HH} at 1.2 GHz and 50° angle of incidence.

σ^0(dB)



HISTOGRAM OF VARIABLE 6 SOHH8.6

SYMBOL	COUNT	MEAN	ST.DEV.
X	60	-14.903	4.170

INTERVAL NAME	FREQUENCY INT.	FREQUENCY CUM.	PERCENTAGE INT.	PERCENTAGE CUM.
-30.000	0	0	0.	0.
-29.000	0	0	0.	0.
-28.000	0	0	0.	0.
-27.000	0	0	0.	0.
-26.000	0	0	0.	0.
-25.000	0	0	0.	0.
-24.000	0	0	0.	0.
-23.000	1	1	1.7	1.7
-22.000	4	5	6.7	8.3
-21.000	2	7	3.3	11.7
-20.000	4	11	6.7	18.3
-19.000	1	12	1.7	20.0
-18.000	3	15	5.0	25.0
-17.000	4	19	6.7	31.7
-16.000	2	21	3.3	35.0
-15.000	2	23	3.3	38.3
-14.000	8	31	13.3	51.7
-13.000	7	38	11.7	63.3
-12.000	4	42	6.7	70.0
-11.000	7	49	11.7	81.7
-10.000	5	54	8.3	90.0
-9.0000	2	56	3.3	93.3
-8.0000	4	60	6.7	100.0
-7.0000	0	60	0.	100.0
-6.0000	0	60	0.	100.0
-5.0000	0	60	0.	100.0
-4.0000	0	60	0.	100.0
-3.0000	0	60	0.	100.0
-2.0000	0	60	0.	100.0
-1.0000	0	60	0.	100.0
0.0000	0	60	0.	100.0
1.0000	0	60	0.	100.0
2.0000	0	60	0.	100.0
3.0000	0	60	0.	100.0
4.0000	0	60	0.	100.0
5.0000	0	60	0.	100.0
6.0000	0	60	0.	100.0
7.0000	0	60	0.	100.0
8.0000	0	60	0.	100.0
9.0000	0	60	0.	100.0
10.000	0	60	0.	100.0
LAST	0	60	0.	100.0

Figure 7-10b Histogram of σ^0_{HH} at 8.6 GHz and 50° angle of incidence.

HISTOGRAM OF VARIABLE 7 SOHH17.0

SYMBOL	COUNT	MEAN	ST.DEV.
X	86	-8.488	4.287

INTERVAL NAME	FREQUENCY INT.	FREQUENCY CUM.	PERCENTAGE INT.	PERCENTAGE CUM.
-30.000	0	0	0.	0.
-29.000	0	0	0.	0.
-28.000	0	0	0.	0.
-27.000	0	0	0.	0.
-26.000	0	0	0.	0.
-25.000	0	0	0.	0.
-24.000	0	0	0.	0.
-23.000	0	0	0.	0.
-22.000	0	0	0.	0.
-21.000	0	0	0.	0.
-20.000	0	0	0.	0.
-19.000	0	0	0.	0.
-18.000	1	1	1.2	1.2
-17.000	0	1	0.	1.2
-16.000	4	5	4.7	5.8
-15.000	3	8	3.5	9.3
-14.000	3	11	3.5	12.8
-13.000	6	17	7.0	19.8
-12.000	2	19	2.3	22.1
-11.000	4	23	4.7	26.7
-10.000	6	29	7.0	33.7
-9.0000	8	37	9.3	43.0
-8.0000	3	40	3.5	46.5
-7.0000	13	53	15.1	61.6
-6.0000	5	58	5.8	67.4
-5.0000	8	66	9.3	76.7
-4.0000	7	73	8.1	84.9
-3.0000	4	77	4.7	89.5
-2.0000	6	83	7.0	96.5
-1.0000	2	85	2.3	98.8
0.0000	1	86	1.2	100.0
1.0000	0	86	0.	100.0
2.0000	0	86	0.	100.0
3.0000	0	86	0.	100.0
4.0000	0	86	0.	100.0
5.0000	0	86	0.	100.0
6.0000	0	86	0.	100.0
7.0000	0	86	0.	100.0
8.0000	0	86	0.	100.0
9.0000	0	86	0.	100.0
10.000	0	86	0.	100.0
LAST	0	86	0.	100.0

σ^o(dB)

Figure 7-10c Histogram of σ^o_{HH} at 17.0 GHz and 50° angle of incidence.

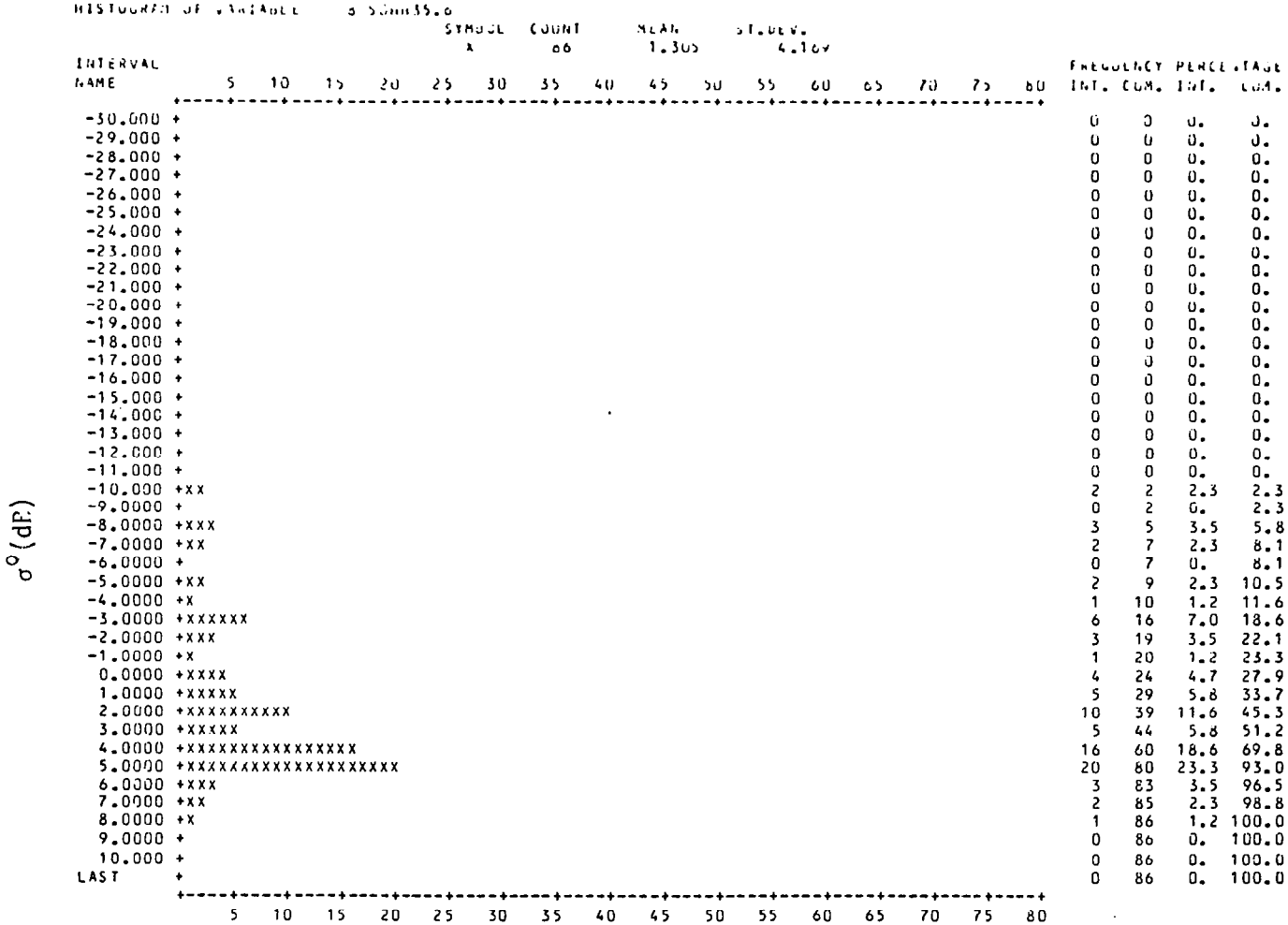


Figure 7-10d Histogram of σ°_{HH} at 35.6 GHz and 50° angle of incidence.

tends to smooth the histograms. The distributions are seen to be unimodal and have a wide dynamic range.

7.3 Seasonal Statistics of Passive Microwave Data

The seasonal averages and 5% and 95% limits of the passive data T_{ap} are given in Figure 7-11. The greater dynamic range of the 37 GHz apparent temperatures is clear. Histograms of the apparent temperature for each frequency and angle of incidence are shown in Figures 7-12 to 7-14. The 10.69 GHz histograms are observed to be unimodal, while the 37 GHz histograms are bimodal. The bimodal distributions result from a dominating effect of snow wetness at 37 GHz. The upper mode corresponds to wet snow conditions and the lower mode corresponds to dry snow conditions.

Correlation coefficients were found to be very high (Table 7-5) between vertical and horizontal T_{ap}'s at 37 GHz at all angles of incidence. The high correlation was not unexpected; however, these results indicate little additional information was gained from the dual polarized radiometer as opposed to a singly polarized radiometer. The correlation coefficients between T_{ap} at 37 GHz and 10.69 GHz were approximately 0.6, independent of the incidence angle. The response to different depths within the snowpack at the two frequencies causes the low correlation values.

7.4 Radar-Radiometer Correlation

Correlation coefficients were also calculated between σ^{o} at 10.2 GHz and T_{ap} at 10.69 GHz and between σ^{o} at 35.6 GHz and T_{ap} at 37 GHz. These relationships (Table 7-6) generally are negative because of the inverse responses of the active and passive measurements to snow wetness at all frequencies. Correlation coefficients are seen to increase with frequency and angle of incidence. Increasing effects of the snow at higher angles of incidence and at the higher frequency cause the increasingly negative values.

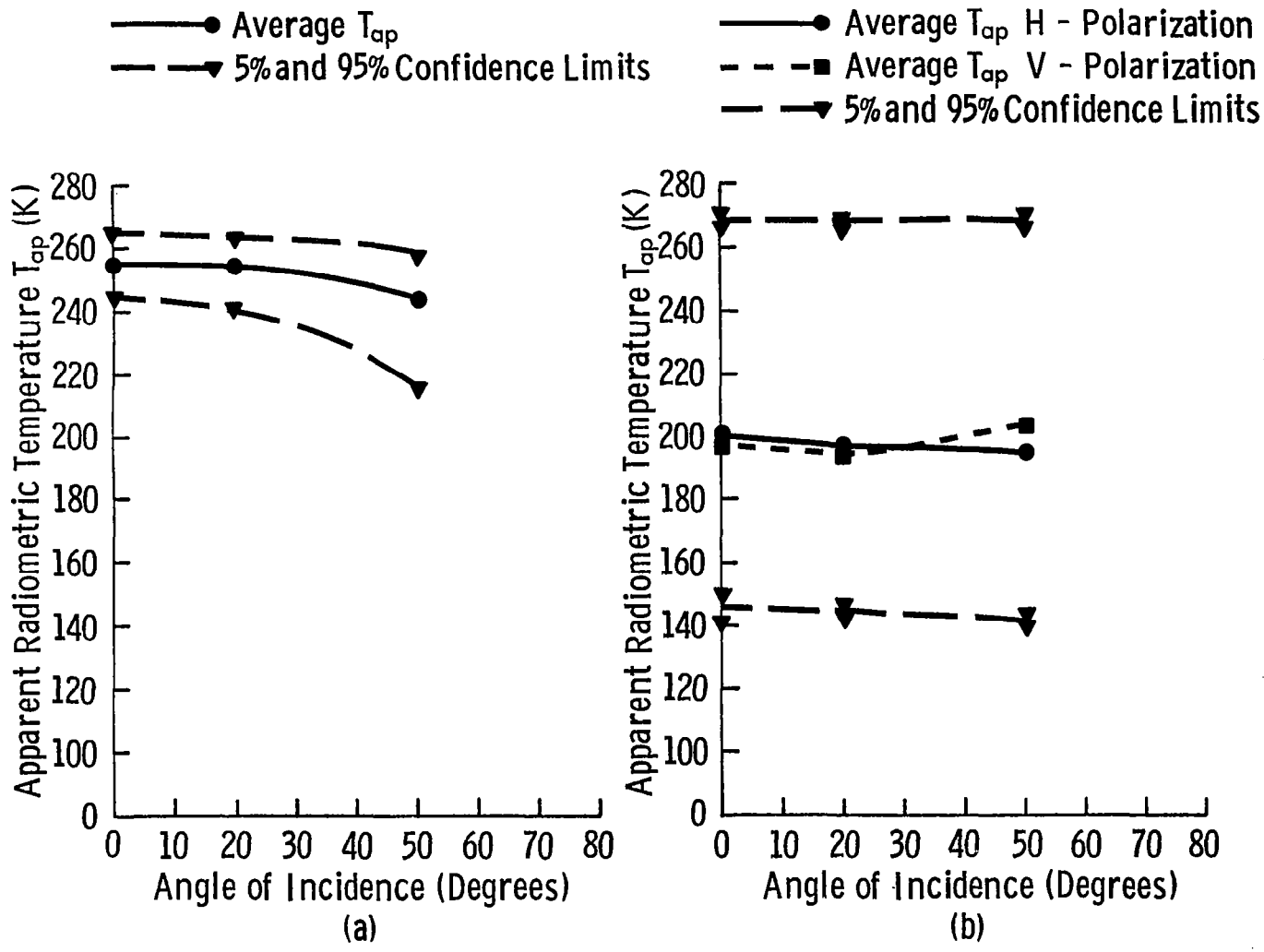
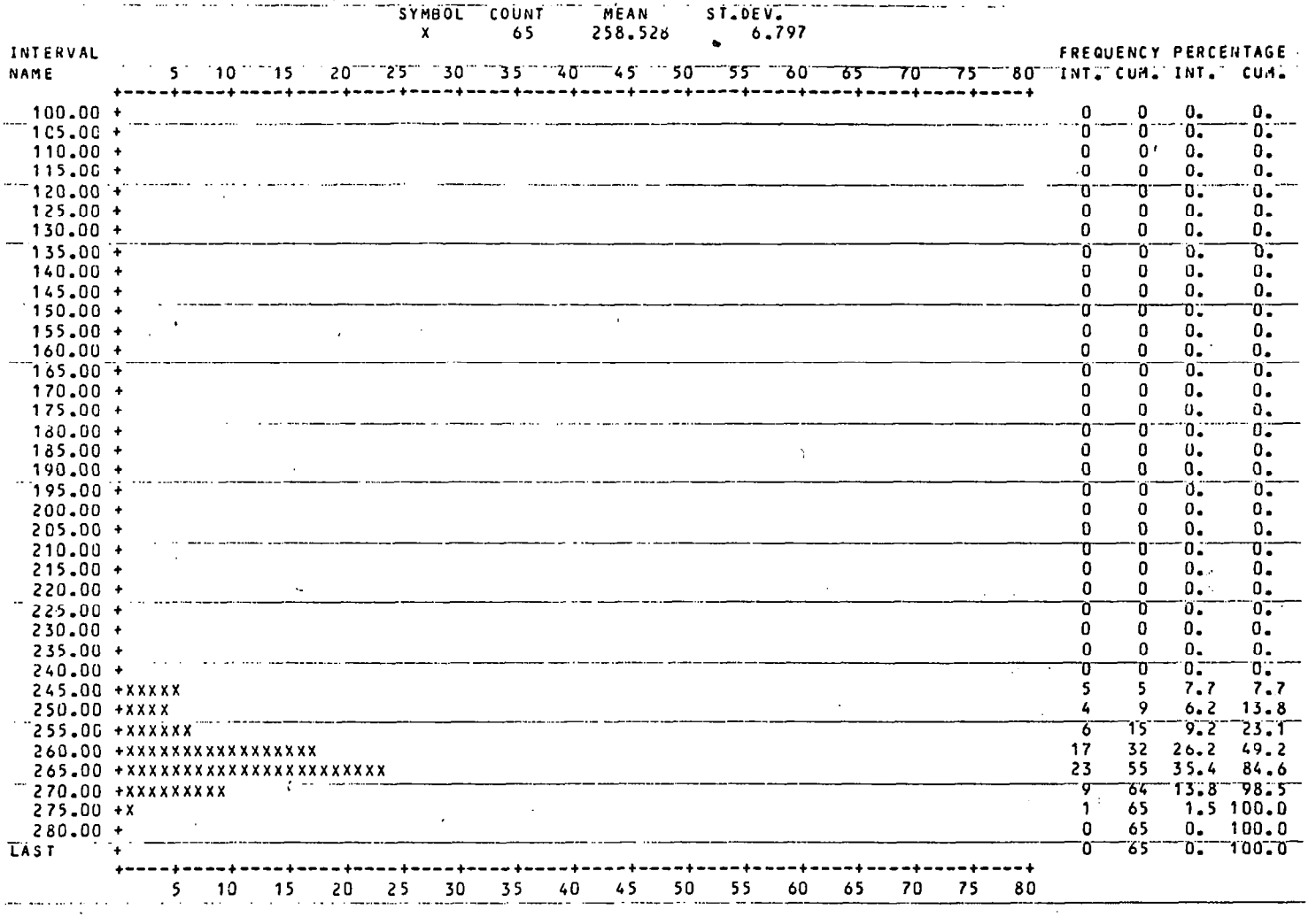


Figure 7-11 Seasonal averages of T_{ap} and 5% and 95% confidence limits at a) 10.69 GHz and b) 37 GHz.



(a)

Figure 7-12 Histograms of the T_{ap} measurements in Steamboat Springs at 0° angle of incidence and (a) 10.69 GHz, H-polarization; (b) 37 GHz, H-polarization; and, (c) 37 GHz, V-polarization.

HISTOGRAM OF VARIABLE 2 37H

SYMBOL X | COUNT 65 | MEAN 162.174 | ST.DEV. 97.893

INTERVAL NAME	5 10 15 20 25 30 35 40 45 50 55 60 65 70 75 80	FREQUENCY INT.	CUM.	PERCENTAGE INT.	CUM.
100.00	+XXXXXXXXXXXXXXX	15	15	23.1	23.1
105.00	+	0	15	0.	23.1
110.00	+	0	15	0.	23.1
115.00	+	0	15	0.	23.1
120.00	+	0	15	0.	23.1
125.00	+	0	15	0.	23.1
130.00	+	0	15	0.	23.1
135.00	+	0	15	0.	23.1
140.00	+	0	15	0.	23.1
145.00	+	0	15	0.	23.1
150.00	+XXX	3	18	4.6	27.7
155.00	+XX	2	20	3.1	30.8
160.00	+XX	2	22	3.1	33.8
165.00	+XXXX	4	26	6.2	40.0
170.00	+	0	26	0.	40.0
175.00	+XXX	3	29	4.6	44.6
180.00	+XX	2	31	3.1	47.7
185.00	+XXXX	4	35	6.2	53.8
190.00	+XXX	3	38	4.6	58.5
195.00	+XXX	3	41	4.6	63.1
200.00	+X	1	42	1.5	64.6
205.00	+	0	42	0.	64.6
210.00	+	0	42	0.	64.6
215.00	+X	1	43	1.5	66.2
220.00	+XX	2	45	3.1	69.2
225.00	+X	1	46	1.5	70.8
230.00	+	0	46	0.	70.8
235.00	+	0	46	0.	70.8
240.00	+	0	46	0.	70.8
245.00	+X	1	47	1.5	72.3
250.00	+	0	47	0.	72.3
255.00	+XX	2	49	3.1	75.4
260.00	+XXX	3	52	4.6	80.0
265.00	+XX	2	54	3.1	83.1
270.00	+XXXXXXX	7	61	10.8	93.8
275.00	+XXXX	4	65	6.2	100.0
280.00	+	0	65	0.	100.0
LAST	+	0	65	0.	100.0

5 10 15 20 25 30 35 40 45 50 55 60 65 70 75 80

(b)

HISTOGRAM OF VARIABLE 3 37V

SYMBOL	COUNT	MEAN	ST.DEV.
X	65	150.388	101.663

INTERVAL NAME	5 10 15 20 25 30 35 40 45 50 55 60 65 70 75 80	FREQUENCY INT.	FREQUENCY CUM.	PERCENTAGE INT.	PERCENTAGE CUM.
100.00	+XXXXXXXXXXXXXXXXX	18	18	27.7	27.7
105.00	+	0	18	0.	27.7
110.00	+	0	18	0.	27.7
115.00	+	0	18	0.	27.7
120.00	+	0	18	0.	27.7
125.00	+	0	18	0.	27.7
130.00	+	0	18	0.	27.7
135.00	+	0	18	0.	27.7
140.00	+	0	18	0.	27.7
145.00	+XX	2	20	3.1	30.8
150.00	+X	1	21	1.5	32.3
155.00	+XX	2	23	3.1	35.4
160.00	+X	1	24	1.5	36.9
165.00	+XXXXX	5	29	7.7	44.6
170.00	+XX	2	31	3.1	47.7
175.00	+XX	2	33	3.1	50.8
180.00	+XXXXX	5	38	7.7	58.5
185.00	+XX	2	40	3.1	61.5
190.00	+XXX	3	43	4.6	66.2
195.00	+X	1	44	1.5	67.7
200.00	+X	1	45	1.5	69.2
205.00	+	0	45	0.	69.2
210.00	+	0	45	0.	69.2
215.00	+X	1	46	1.5	70.8
220.00	+	0	46	0.	70.8
225.00	+	0	46	0.	70.8
230.00	+X	1	47	1.5	72.3
235.00	+	0	47	0.	72.3
240.00	+	0	47	0.	72.3
245.00	+X	1	48	1.5	73.8
250.00	+X	1	49	1.5	75.4
255.00	+X	1	50	1.5	76.9
260.00	+X	1	51	1.5	78.5
265.00	+XXXX	4	55	6.2	84.6
270.00	+XXXXXXXXXX	10	65	15.4	100.0
275.00	+	0	65	0.	100.0
280.00	+	0	65	0.	100.0
LAST	+	0	65	0.	100.0

5 10 15 20 25 30 35 40 45 50 55 60 65 70 75 80

(c)

HISTOGRAM OF VARIABLE 1 10.69H

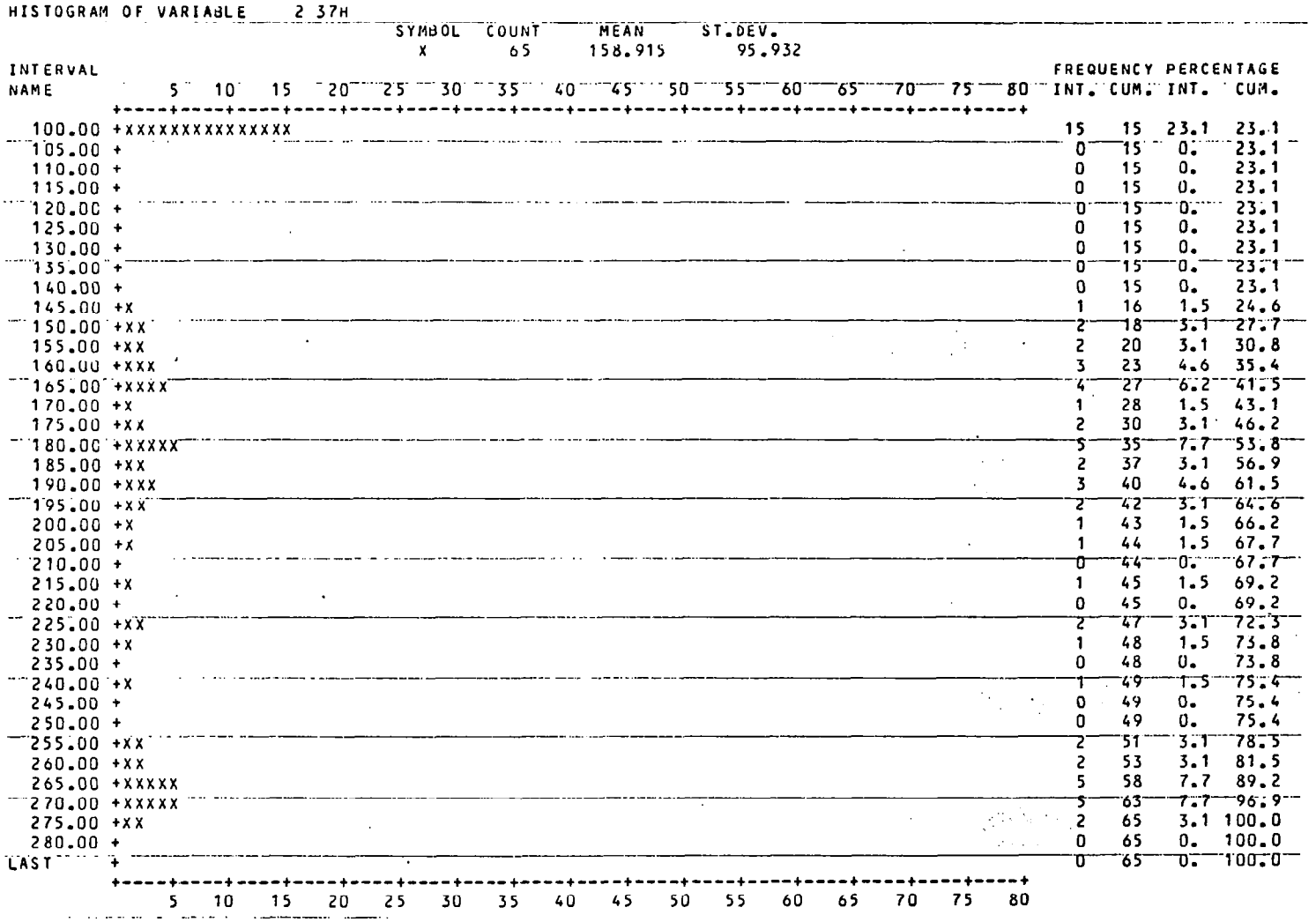
SYMBOL COUNT MEAN ST.DEV.
x 65 257.711 7.473

INTERVAL NAME	5 10 15 20 25 30 35 40 45 50 55 60 65 70 75 80	FREQUENCY INT.	CUM.	PERCENTAGE INT.	CUM.
100.00	+	0	0	0.	0.
105.00	+	0	0	0.	0.
110.00	+	0	0	0.	0.
115.00	+	0	0	0.	0.
120.00	+	0	0	0.	0.
125.00	+	0	0	0.	0.
130.00	+	0	0	0.	0.
135.00	+	0	0	0.	0.
140.00	+	0	0	0.	0.
145.00	+	0	0	0.	0.
150.00	+	0	0	0.	0.
155.00	+	0	0	0.	0.
160.00	+	0	0	0.	0.
165.00	+	0	0	0.	0.
170.00	+	0	0	0.	0.
175.00	+	0	0	0.	0.
180.00	+	0	0	0.	0.
185.00	+	0	0	0.	0.
190.00	+	0	0	0.	0.
195.00	+	0	0	0.	0.
200.00	+	0	0	0.	0.
205.00	+	0	0	0.	0.
210.00	+	0	0	0.	0.
215.00	+	0	0	0.	0.
220.00	+	0	0	0.	0.
225.00	+	0	0	0.	0.
230.00	+	0	0	0.	0.
235.00	+	0	0	0.	0.
240.00	+X	1	1	1.5	1.5
245.00	+XXXXXX	6	7	9.2	10.8
250.00	+XXX	3	10	4.6	15.4
255.00	+XXXX	4	14	6.2	21.5
260.00	+XXXXXXXXXXXXXXXXXX	19	33	29.2	50.8
265.00	+XXXXXXXXXXXXXXXXXXXXXXXXXXX	27	60	41.5	92.3
270.00	+XXXX	4	64	6.2	98.5
275.00	+X	1	65	1.5	100.0
280.00	+	0	65	0.	100.0
LAST	+	0	65	0.	100.0

5 10 15 20 25 30 35 40 45 50 55 60 65 70 75 80

(a)

Figure 7-13 Histograms of the T_{ap} measurements in Steamboat Springs at 20° angle of incidence and (a) 10.69 GHz, H-polarization; (b) 37 GHz, H-polarization; and (c) 37 GHz, V-polarization.



HISTOGRAM OF VARIABLE 2 37H

SYMBOL X | COUNT 65 | MEAN 158.915 | ST.DEV. 95.932

INTERVAL NAME	5 10 15 20 25 30 35 40 45 50 55 60 65 70 75 80	FREQUENCY INT.	FREQUENCY CUM.	PERCENTAGE INT.	PERCENTAGE CUM.
100.00	+XXXXXXXXXXXXXXX	15	15	23.1	23.1
105.00	+	0	15	0.	23.1
110.00	+	0	15	0.	23.1
115.00	+	0	15	0.	23.1
120.00	+	0	15	0.	23.1
125.00	+	0	15	0.	23.1
130.00	+	0	15	0.	23.1
135.00	+	0	15	0.	23.1
140.00	+	0	15	0.	23.1
145.00	+X	1	16	1.5	24.6
150.00	+XX	2	18	3.1	27.7
155.00	+XX	2	20	3.1	30.8
160.00	+XXX	3	23	4.6	35.4
165.00	+XXXX	4	27	6.2	41.5
170.00	+X	1	28	1.5	43.1
175.00	+XX	2	30	3.1	46.2
180.00	+XXXXX	5	35	7.7	53.8
185.00	+XX	2	37	3.1	56.9
190.00	+XXX	3	40	4.6	61.5
195.00	+XX	2	42	3.1	64.6
200.00	+X	1	43	1.5	66.2
205.00	+X	1	44	1.5	67.7
210.00	+	0	44	0.	67.7
215.00	+X	1	45	1.5	69.2
220.00	+	0	45	0.	69.2
225.00	+XX	2	47	3.1	72.3
230.00	+X	1	48	1.5	73.8
235.00	+	0	48	0.	73.8
240.00	+X	1	49	1.5	75.4
245.00	+	0	49	0.	75.4
250.00	+	0	49	0.	75.4
255.00	+XX	2	51	3.1	78.5
260.00	+XX	2	53	3.1	81.5
265.00	+XXXXX	5	58	7.7	89.2
270.00	+XXXXX	5	63	7.7	96.9
275.00	+XX	2	65	3.1	100.0
280.00	+	0	65	0.	100.0
LAST	+	0	65	0.	100.0

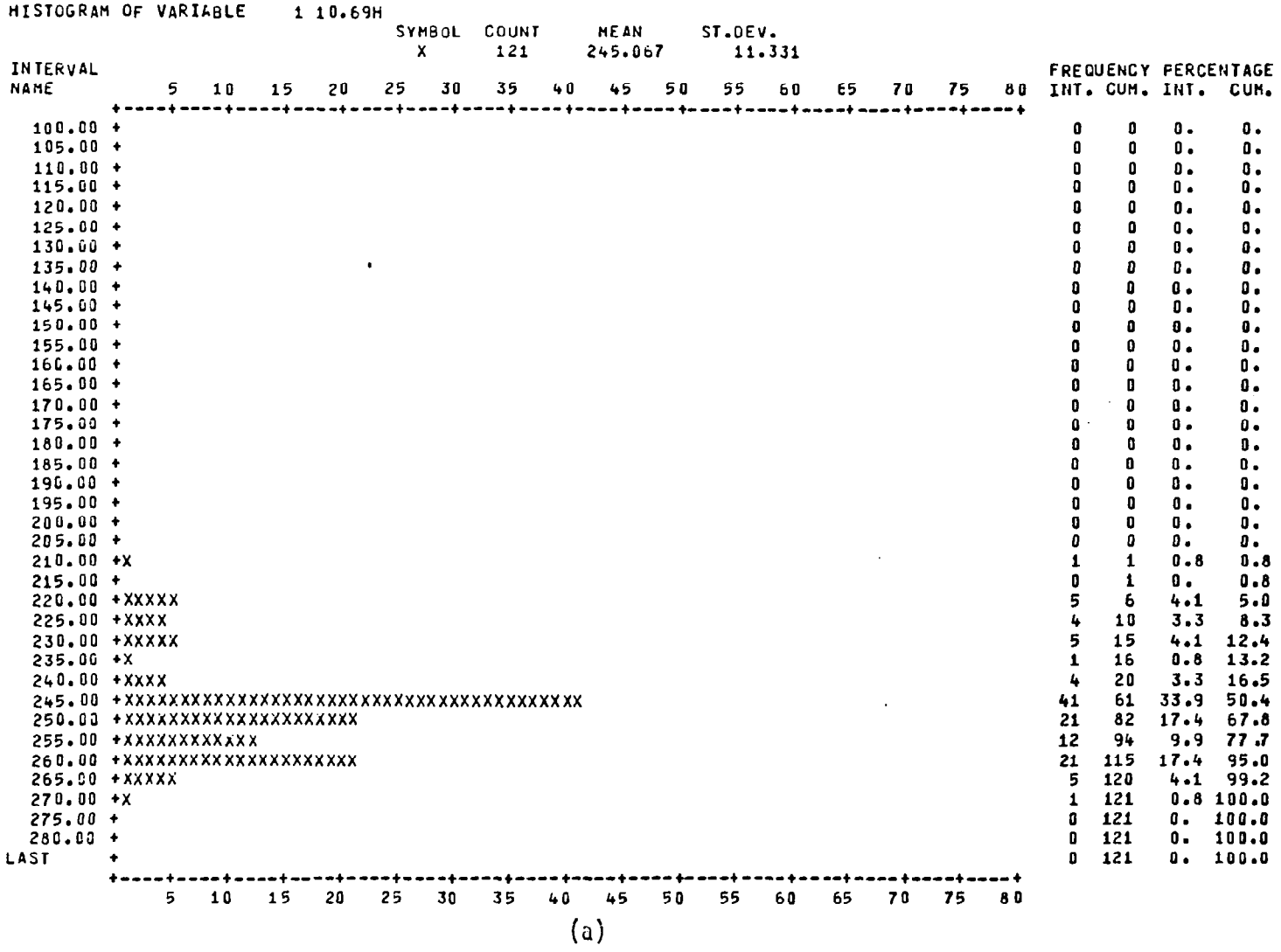
(b)

HISTOGRAM OF VARIABLE 3 37V

SYMBOL	COUNT	MEAN	ST.DEV.
X	65	149.063	101.024

INTERVAL NAME	5 10 15 20 25 30 35 40 45 50 55 60 65 70 75 80	FREQUENCY INT.	CUM.	PERCENTAGE INT.	CUM.
100.00	+XXXXXXXXXXXXXXXXX	18	18	27.7	27.7
105.00	+	0	18	0.	27.7
110.00	+	0	18	0.	27.7
115.00	+	0	18	0.	27.7
120.00	+	0	18	0.	27.7
125.00	+	0	18	0.	27.7
130.00	+	0	18	0.	27.7
135.00	+	0	18	0.	27.7
140.00	+	0	18	0.	27.7
145.00	+XX	2	20	3.1	30.8
150.00	+X	1	21	1.5	32.3
155.00	+XXX	3	24	4.6	36.9
160.00	+X	1	25	1.5	38.5
165.00	+XXXXXX	6	31	9.2	47.7
170.00	+X	1	32	1.5	49.2
175.00	+XXX	3	35	4.6	53.8
180.00	+XX	2	37	3.1	56.9
185.00	+XXX	3	40	4.6	61.5
190.00	+XXX	3	43	4.6	66.2
195.00	+XX	2	45	3.1	69.2
200.00	+	0	45	0.	69.2
205.00	+X	1	46	1.5	70.8
210.00	+	0	46	0.	70.8
215.00	+	0	46	0.	70.8
220.00	+	0	46	0.	70.8
225.00	+X	1	47	1.5	72.3
230.00	+	0	47	0.	72.3
235.00	+X	1	48	1.5	73.8
240.00	+X	1	49	1.5	75.4
245.00	+X	1	50	1.5	76.9
250.00	+	0	50	0.	76.9
255.00	+X	1	51	1.5	78.5
260.00	+XX	2	53	3.1	81.5
265.00	+XXX	3	56	4.6	86.2
270.00	+XXXXXX	6	62	9.2	95.4
275.00	+XXX	3	65	4.6	100.0
280.00	+	0	65	0.	100.0
LAST	+	0	65	0.	100.0
	5 10 15 20 25 30 35 40 45 50 55 60 65 70 75 80				

(c)



(a)

Figure 7-14 Histograms of the T_{ap} measurements in Steamboat Springs at 50° angle of incidence and (a) 10.69 GHz, H-polarization; (b) 37 GHz, H-polarization; and (c) 37 GHz, V-polarization.

HISTOGRAM OF VARIABLE 2 37H

SYMBOL	COUNT	MEAN	ST.DEV.
X	121	167.969	79.681

INTERVAL NAME	5 10 15 20 25 30 35 40 45 50 55 60 65 70 75 80	FREQUENCY INT.	FREQUENCY CUM.	PERCENTAGE INT.	PERCENTAGE CUM.
100.00	+XXXXXXXXXXXXXXXX	17	17	14.0	14.0
105.00	+	0	17	0.	14.0
110.00	+	0	17	0.	14.0
115.00	+	0	17	0.	14.0
120.00	+	0	17	0.	14.0
125.00	+	0	17	0.	14.0
130.00	+	0	17	0.	14.0
135.00	+	0	17	0.	14.0
140.00	+XXXXXX	6	23	5.0	19.0
145.00	+XXXXX	5	28	4.1	23.1
150.00	+XX	2	30	1.7	24.8
155.00	+XXXXXXXXXXX	12	42	9.9	34.7
160.00	+XXXXXXXXX	10	52	8.3	43.0
165.00	+XXXXXXXX	8	60	6.6	49.6
170.00	+XXXX	4	64	3.3	52.9
175.00	+XX	2	66	1.7	54.5
180.00	+XX	2	68	1.7	56.2
185.00	+XXX	3	71	2.5	58.7
190.00	+X	1	72	0.8	59.5
195.00	+XX	2	74	1.7	61.2
200.00	+XXXXXX	6	80	5.0	66.1
205.00	+X	1	81	0.8	66.9
210.00	+	0	81	0.	66.9
215.00	+	0	81	0.	66.9
220.00	+X	1	82	0.8	67.8
225.00	+	0	82	0.	67.8
230.00	+XX	2	84	1.7	69.4
235.00	+XXXXX	5	89	4.1	73.6
240.00	+XXX	3	92	2.5	76.0
245.00	+XXXX	4	96	3.3	79.3
250.00	+XXXXXXX	7	103	5.8	85.1
255.00	+XXXXXXXXX	9	112	7.4	92.6
260.00	+XXX	3	115	2.5	95.0
265.00	+	0	115	0.	95.0
270.00	+XXXX	4	119	3.3	98.3
275.00	+XX	2	121	1.7	100.0
280.00	+	0	121	0.	100.0
LAST	+	0	121	0.	100.0

(b)

HISTOGRAM OF VARIABLE 3 37V

SYMBOL	COUNT	MEAN	ST.DEV.
X	121	175.423	86.622

INTERVAL NAME	5 10 15 20 25 30 35 40 45 50 55 60 65 70 75 80	FREQUENCY INT.	FREQUENCY CUM.	PERCENTAGE INT.	PERCENTAGE CUM.
100.00	+XXXXXXXXXXXXXXXXXX	19	19	15.7	15.7
105.00	+	0	19	0.	15.7
110.00	+	0	19	0.	15.7
115.00	+	0	19	0.	15.7
120.00	+	0	19	0.	15.7
125.00	+	0	19	0.	15.7
130.00	+	0	19	0.	15.7
135.00	+	0	19	0.	15.7
140.00	+	0	19	0.	15.7
145.00	+XXX	3	22	2.5	18.2
150.00	+XXX	3	25	2.5	20.7
155.00	+X	1	26	0.8	21.5
160.00	+XXXXX	5	31	4.1	25.6
165.00	+XXXXXX	6	37	5.0	30.6
170.00	+XXXXXXXXX	9	46	7.4	38.0
175.00	+XXXXXXXXX	9	55	7.4	45.5
180.00	+XXXXXXXXX	9	64	7.4	52.9
185.00	+XXXXX	5	69	4.1	57.0
190.00	+	0	69	0.	57.0
195.00	+XX	2	71	1.7	58.7
200.00	+XX	2	73	1.7	60.3
205.00	+	0	73	0.	60.3
210.00	+XX	2	75	1.7	62.0
215.00	+X	1	76	0.8	62.8
220.00	+XXXXX	5	81	4.1	66.9
225.00	+X	1	82	0.8	67.8
230.00	+	0	82	0.	67.8
235.00	+	0	82	0.	67.8
240.00	+XX	2	84	1.7	69.4
245.00	+XX	2	86	1.7	71.1
250.00	+XX	2	88	1.7	72.7
255.00	+XXX	3	91	2.5	75.2
260.00	+XXXXXXXX	8	99	6.6	81.8
265.00	+XXXXXXX	7	106	5.8	87.6
270.00	+XXXXX	5	111	4.1	91.7
275.00	+XXXXXXXXXX	10	121	8.3	100.0
280.00	+	0	121	0.	100.0
LAST	+	0	121	0.	100.0
	5 10 15 20 25 30 35 40 45 50 55 60 65 70 75 80				

(c)

TABLE 7-5

Correlation Coefficients Between the T_{ap}'s

Comparison	Angle	Correlation Coefficient
T_{37H} vs. T_{37V}	0^o	0.997
T_{37H} vs. T_{37V}	20^o	0.994
T_{37H} vs. T_{37V}	50^o	0.993
T_{37H} vs. $T_{10.69H}$	0^o	0.572
T_{37H} vs. $T_{10.69H}$	20^o	0.647
T_{37H} vs. $T_{10.69H}$	50^o	0.593

TABLE 7-6

Correlation Coefficients between T_{ap} and the σ^o Closest in Frequency

Comparison	Angle	Correlation Coefficient
$\sigma^o_{35.6HH}$ vs. T_{37H}	0^o	-0.399
$\sigma^o_{35.6HH}$ vs. T_{37H}	20^o	-0.843
$\sigma^o_{35.6HH}$ vs. T_{37H}	50^o	-0.903
$\sigma^o_{10.2HH}$ vs. $T_{10.69H}$	0^o	0.148
$\sigma^o_{10.2HH}$ vs. $T_{10.69H}$	20^o	-0.673
$\sigma^o_{10.2HH}$ vs. $T_{10.69H}$	50^o	-0.703

8.0 MICROWAVE RESPONSE TO SNOWPACK PARAMETERS

This chapter covers the active and passive microwave response to snowpack parameters. Qualitative effects and quantitative effects (when they can be determined) of snow depth, snow density, water equivalent, snow wetness, crystal structure and surface roughness on σ^o and T_{ap} are examined. Diurnal changes are also discussed.

8.1 Angular Response

8.1.1 Active Microwave

The angular response of σ^o with wet and dry snow conditions is shown in Figures 8-1a to 8-1d at four frequencies. The apparent independence of the σ^o response to snow wetness (m_v) at 2.6 GHz is illustrated in Figure 8-1a. This observation, along with loss measurements through the snowpack on the same date (Figure 8-2), suggests that the contribution of the snowpack to the return power at this frequency is small and that the observed return is primarily due to backscatter from the underlying soil. Since the ground was frozen at this time, the dielectric constant of the soil was similar to that of dry soil. As frequency increases, the contribution of the snowpack increases and the contribution to the return power of the underlying soil decreases. This dependence is deduced from Figure 8-2. The path loss, which includes mismatch effects at the layer boundaries, shows a general increase from 2 dB to 7 dB (through the 27 cm layer) between 2 GHz and 17 GHz for the dry snow condition. The frequency response of the loss between 2 and 8 GHz is much steeper for the wet snow case, and in the upper frequency range the loss could not be measured because the received signal was lower than the detector's noise floor. The net effect is that at the high microwave frequencies, penetration into the wet snow is small. The effective "smoothing" of the surface when the snow becomes wet is also evident from the angular response curves (Figures 8-1b to 8-1d) which show a steeper decrease in σ^o with angle for the wet snow than the dry snow conditions. The trend toward insensitivity to incidence angle with increasing frequency for dry snow conditions is indicative of increasing surface roughness or volume scatter. It will be shown later that the predominant mechanism is volume scatter. The sensitivity of σ^o to snow wetness also is seen to increase with increasing frequency, particularly at angles away from nadir.

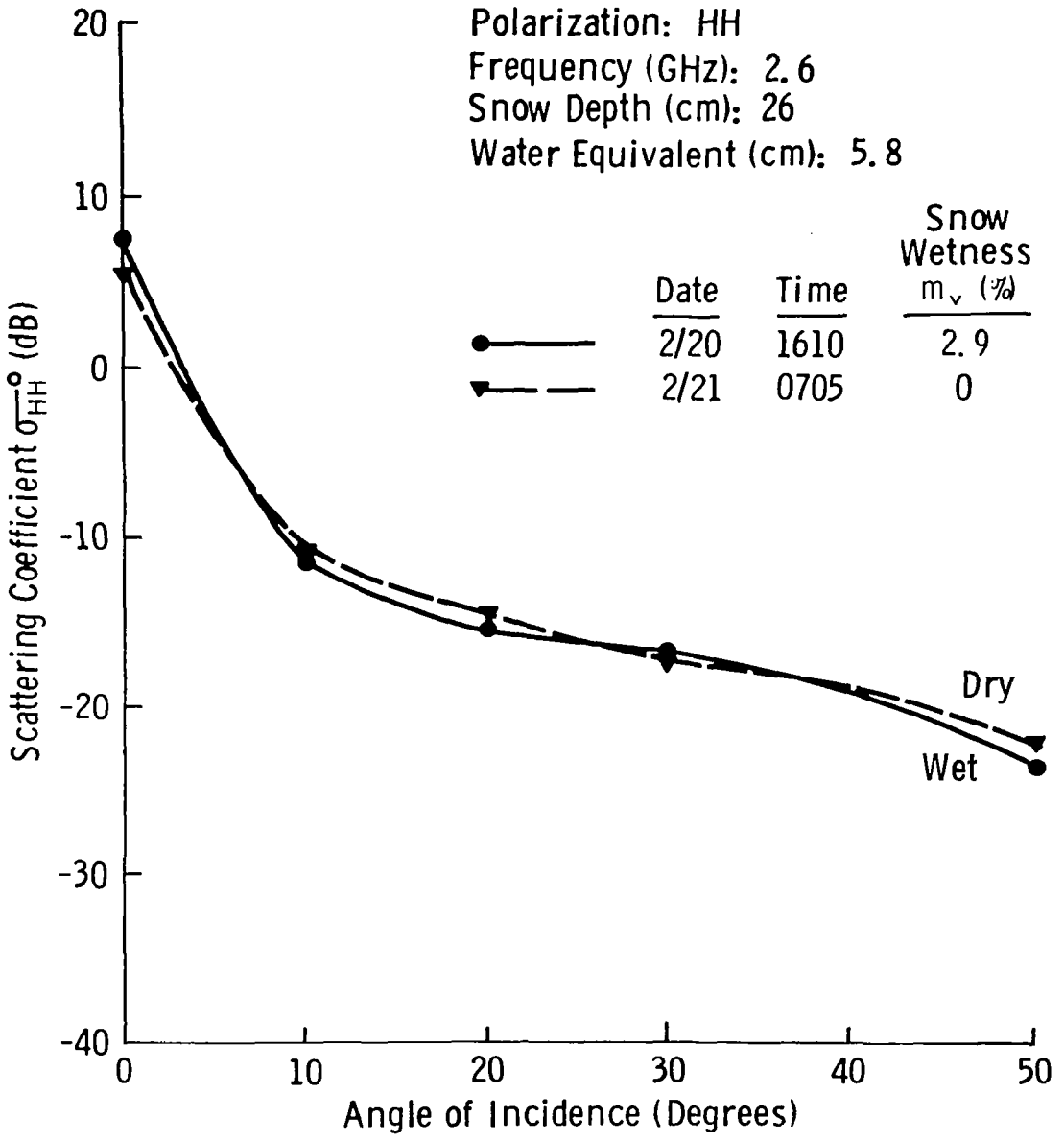


Figure 8-1a Angular Response of σ^o at 2.6 GHz to Wet and Dry Snow

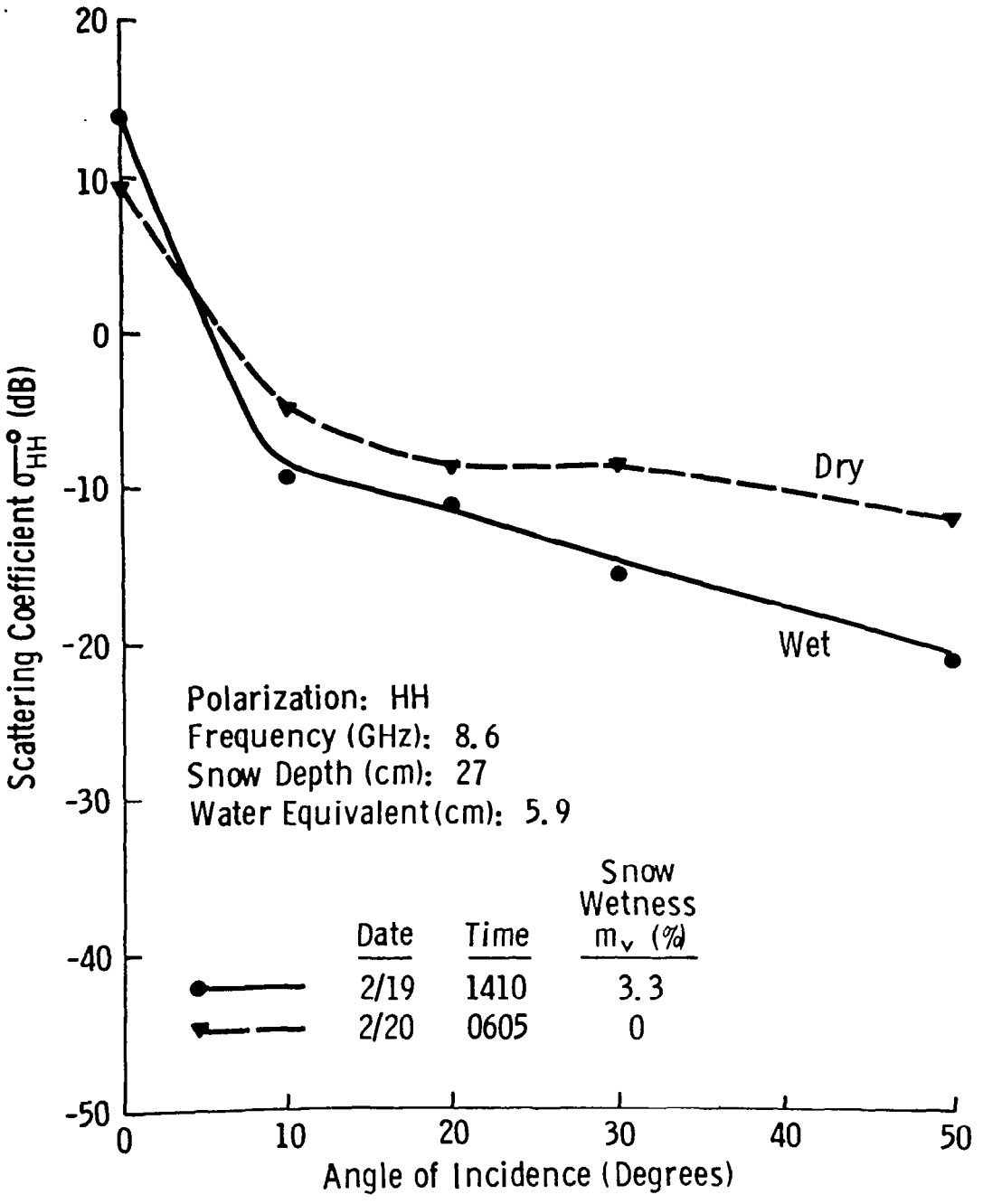


Figure 8-1b Angular Response of σ^{o} at 8.6 GHz to Wet and Dry Snow

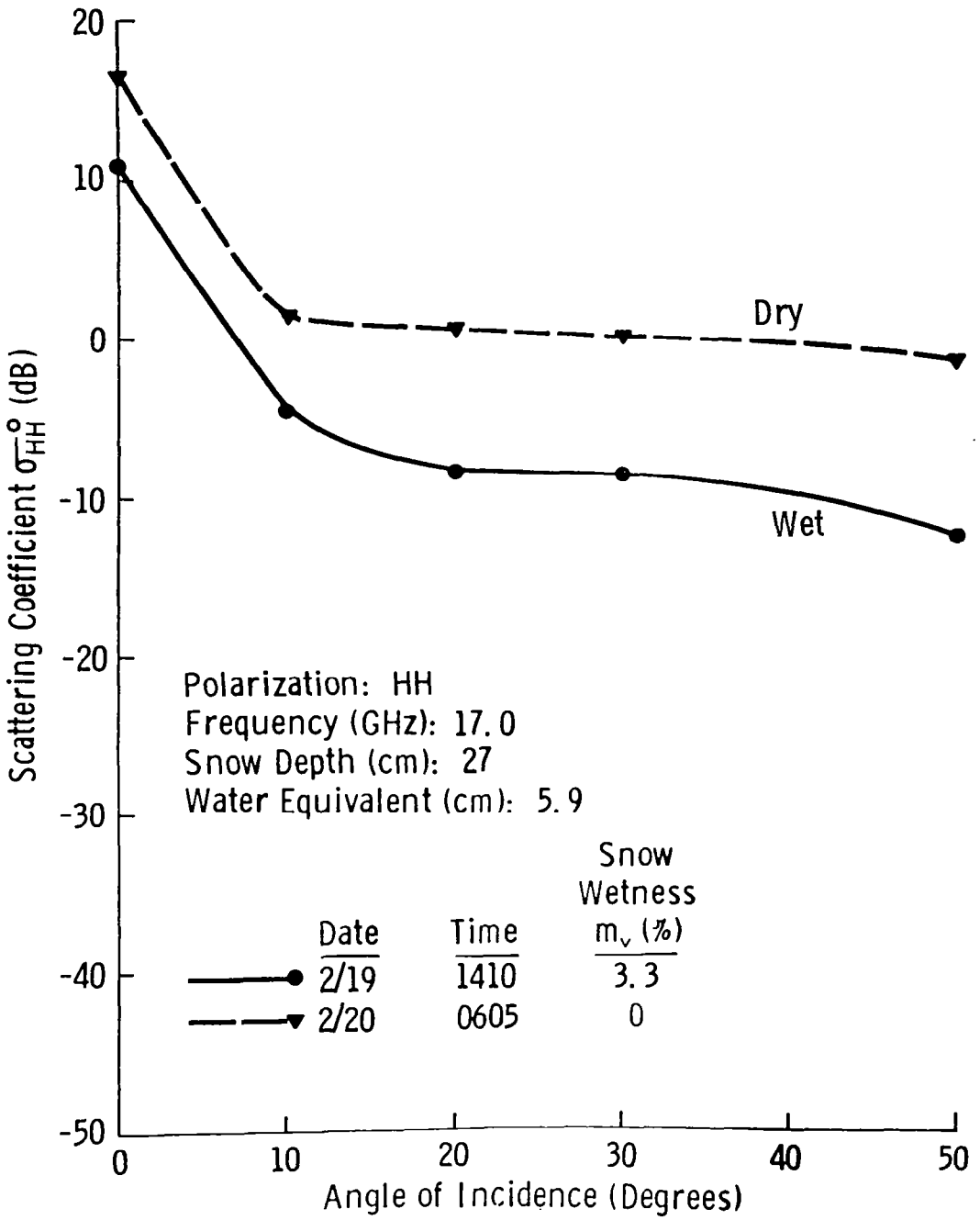


Figure 8-1c Angular Response of σ^{o} at 17.0 GHz to Wet and Dry Snow

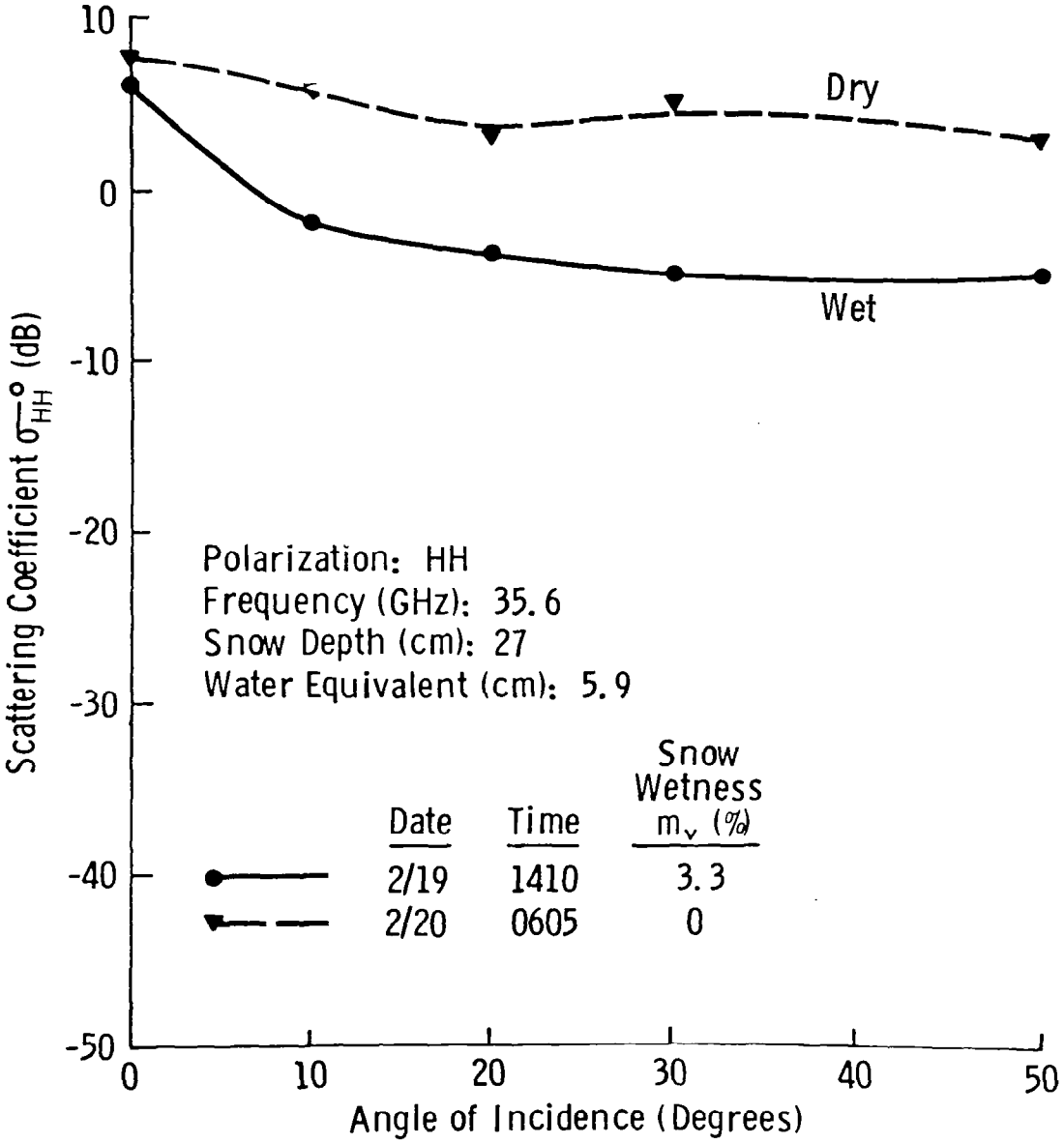


Figure 8-1d Angular Response of σo at 35.6 GHz to Wet and Dry Snow

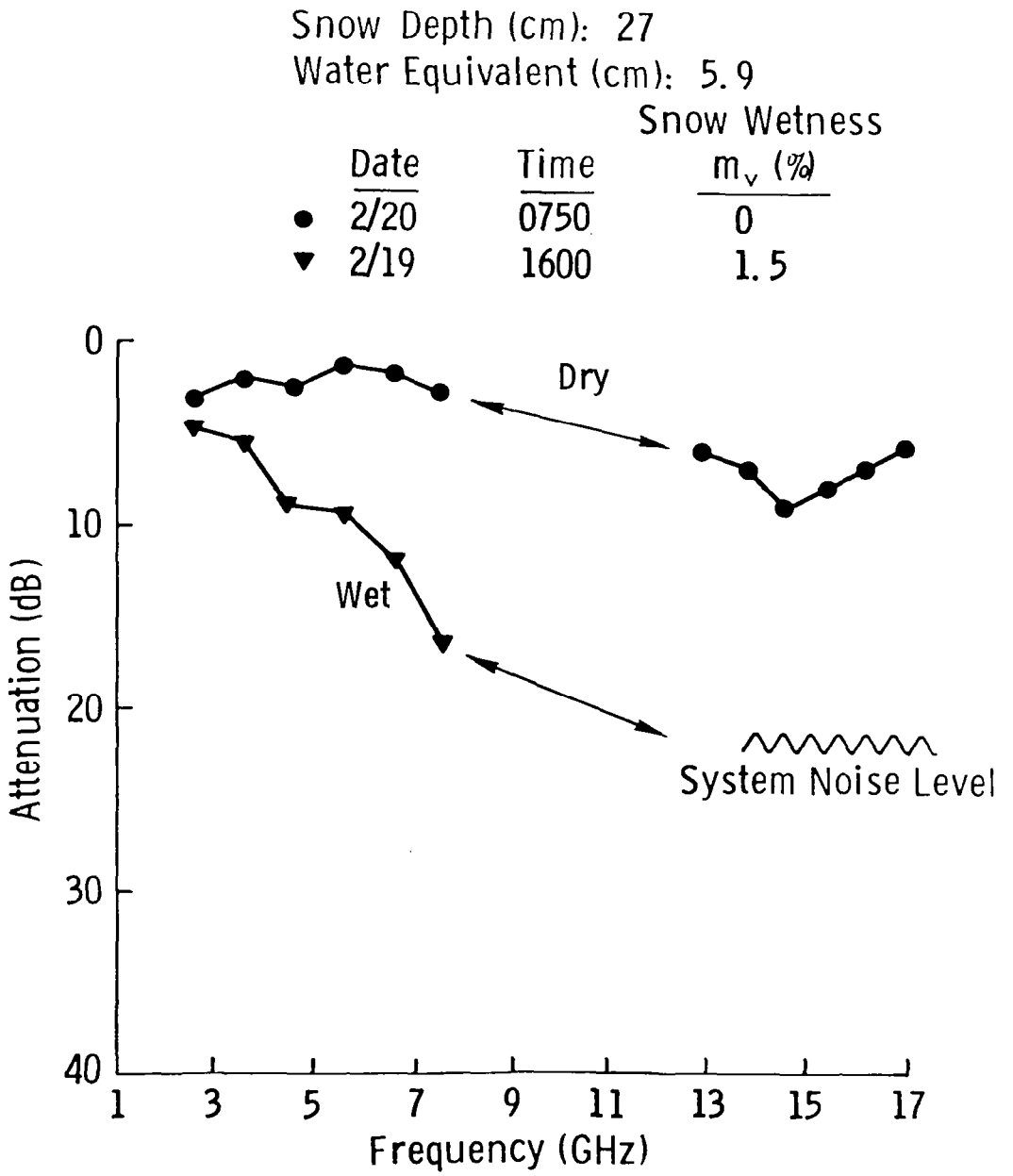


Figure 8-2 Path Loss Through 27 cm Snow Depth

The hypothesis that the σ^o variation between the curve pairs in Figures 8-1b to 8-1d resulted mainly from the wetness variation is further validated by Figures 8-3a to 8-3d. These measurements, during a three day period between 2/25 and 2/27/77, represent approximately dry snow conditions (although the calorimeter measurements indicated up to 2% snow wetness for a few thin layers within the snowpack). The vertical range of variation of σ^o among the curves shown is relatively small compared with the magnitude of the change attributed to wetness seen in Figure 8-1. The differences in the data sets are partially system induced but may also reflect slight changes in crystalline structure or other factors which were not measured.

Angular responses of σ^o of wet and dry snow conditions for two snow depths are shown in Figures 8-4 and 8-5. At 2.6 GHz, the σ^o data on 3/23/77 are similar in value to the σ^o data on 2/21/77. The slightly higher values observed on 3/23/77 may be the result of the thaw in the underlying soil, since the σ^o response is shown to be relatively independent of snow wetness at this frequency. The σ^o responses at 7.6 GHz for wet snow on both dates are similar, while the σ^o response for dry snow on 3/23/77 (W = 12.7 cm) is about 5 dB higher than the σ^o response on 2/21/77 (W = 5.9 cm) at angles away from nadir. The higher σ^o values for the dry conditions may be the increased backscatter resulting from the increase in water equivalent or increased backscatter from the thawed soil.

Evaluation of the polarization response adds insight into the scattering properties of the snowpack. Figures 8-6a and 8-6b illustrate the σ^o response at 2.6 GHz for wet and dry snow conditions. The behavior is again observed to be independent of wetness for all polarization combinations. The magnitude and shape of VV and HH are similar but the magnitude of the HV σ^o values are on the order of 10 dB below the like polarization components. This cross-polarization behavior is typical of surface scattering observed for other backscatter targets (e.g., soils, dense vegetation canopies, asphalt, etc.). In contrast, Figures 8-7a and 8-7b show the σ^o response at 35.6 GHz. Again HH and VV are similar in shape; the difference between the HH and VV curves may be due to a calibration bias. The high values of depolarization (approximately -3 dB) point toward volume scattering. The circular polarization σ^o values at

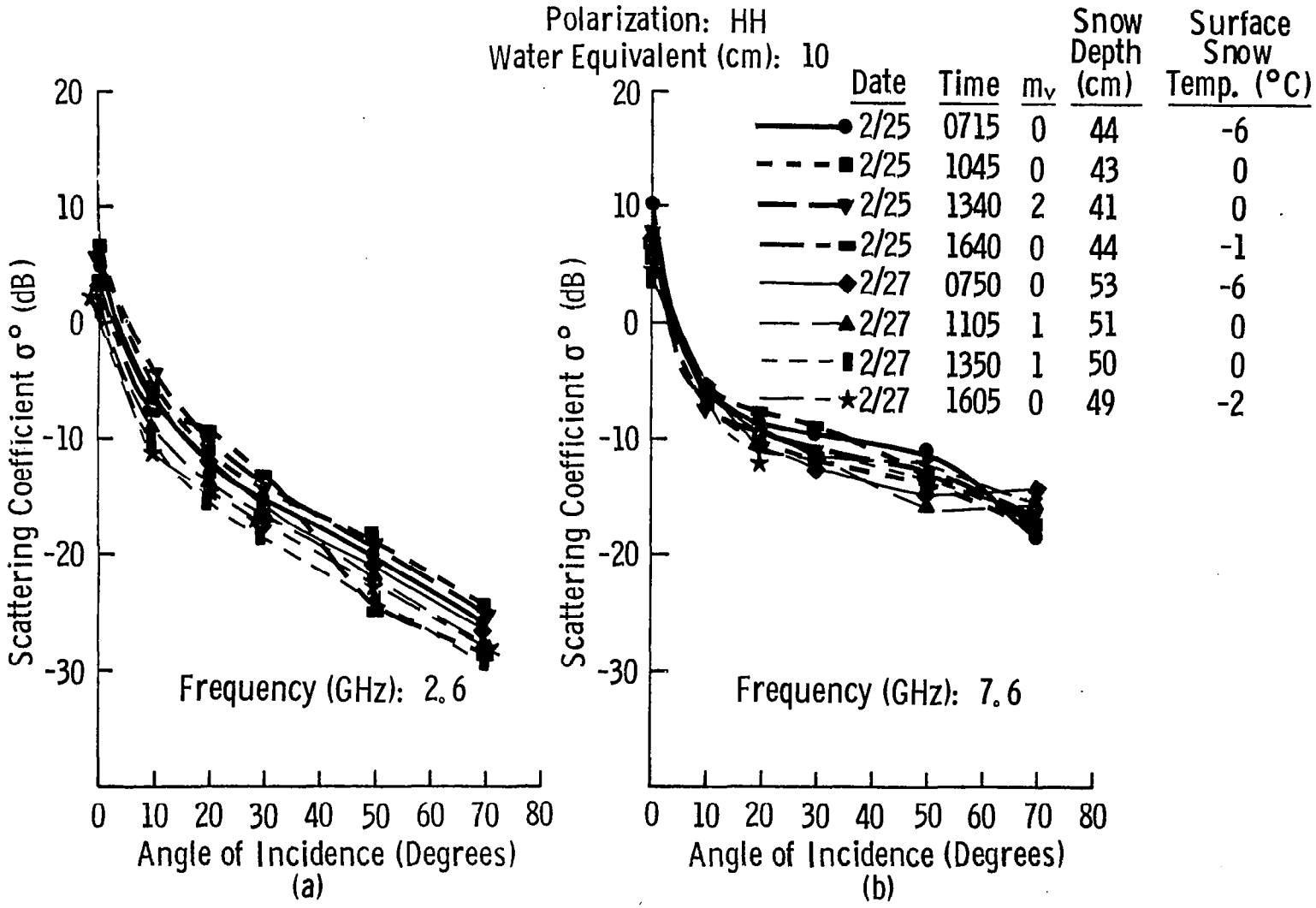
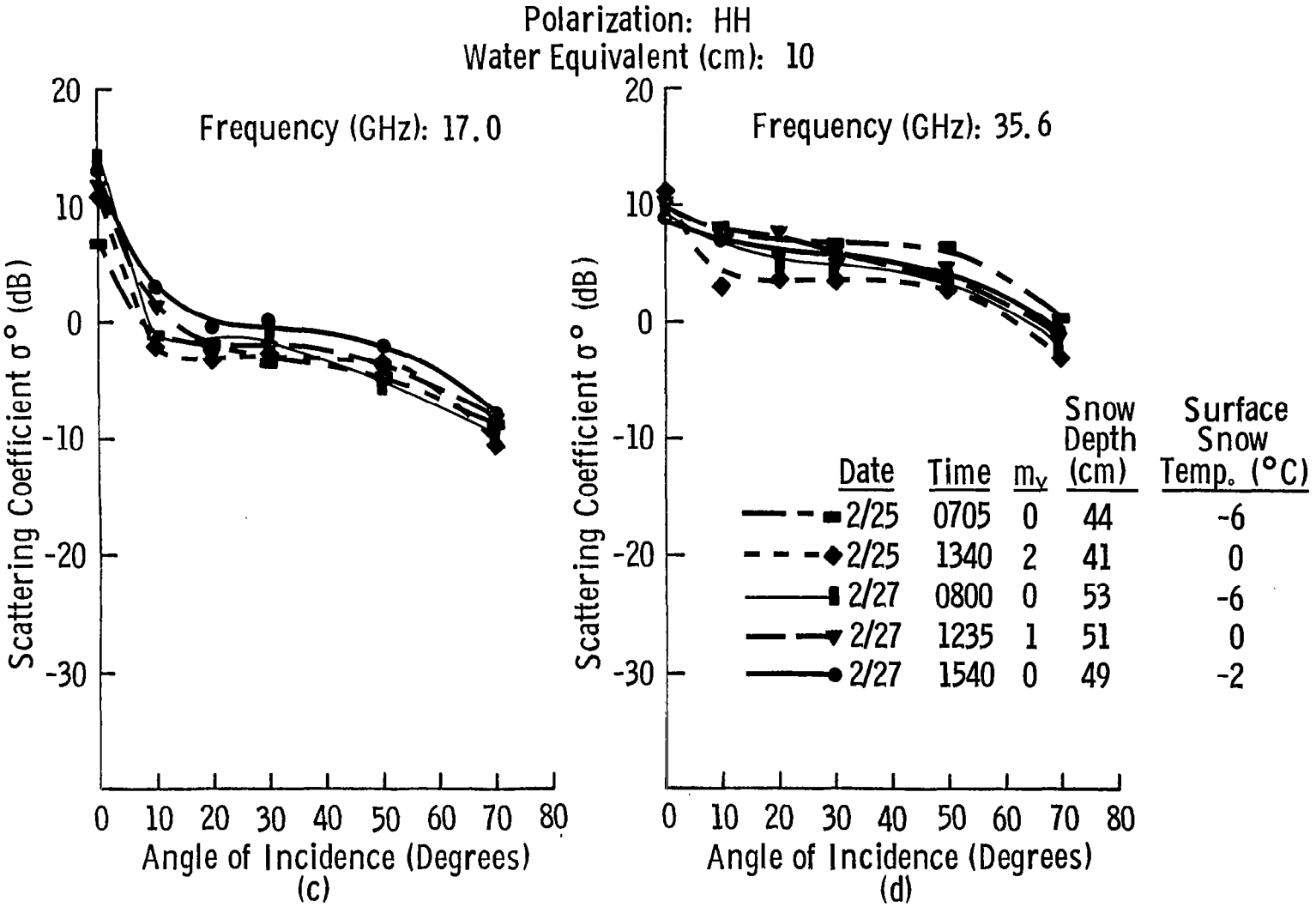


Figure 8-3 Variation in the angular response of σ° for several data sets to nearly dry snow over two daytime periods at (a) 2.6 GHz, (b) 7.6 GHz, (c) 17.0 GHz and (d) 35.6 GHz.


Polarization: HH
Water Equivalent (cm): 10
Frequency (GHz): 17.0
Frequency (GHz): 35.6
Scattering Coefficient σ° (dB)
20
10
0
-10
-20
-30
0 10 20 30 40 50 60 70 80
Angle of Incidence (Degrees)
(c)
(d)
Date Time m_v Snow Depth (cm) Surface Snow Temp. (°C)
2/25 0705 0 44 -6
2/25 1340 2 41 0
2/27 0800 0 53 -6
2/27 1235 1 51 0
2/27 1540 0 49 -2

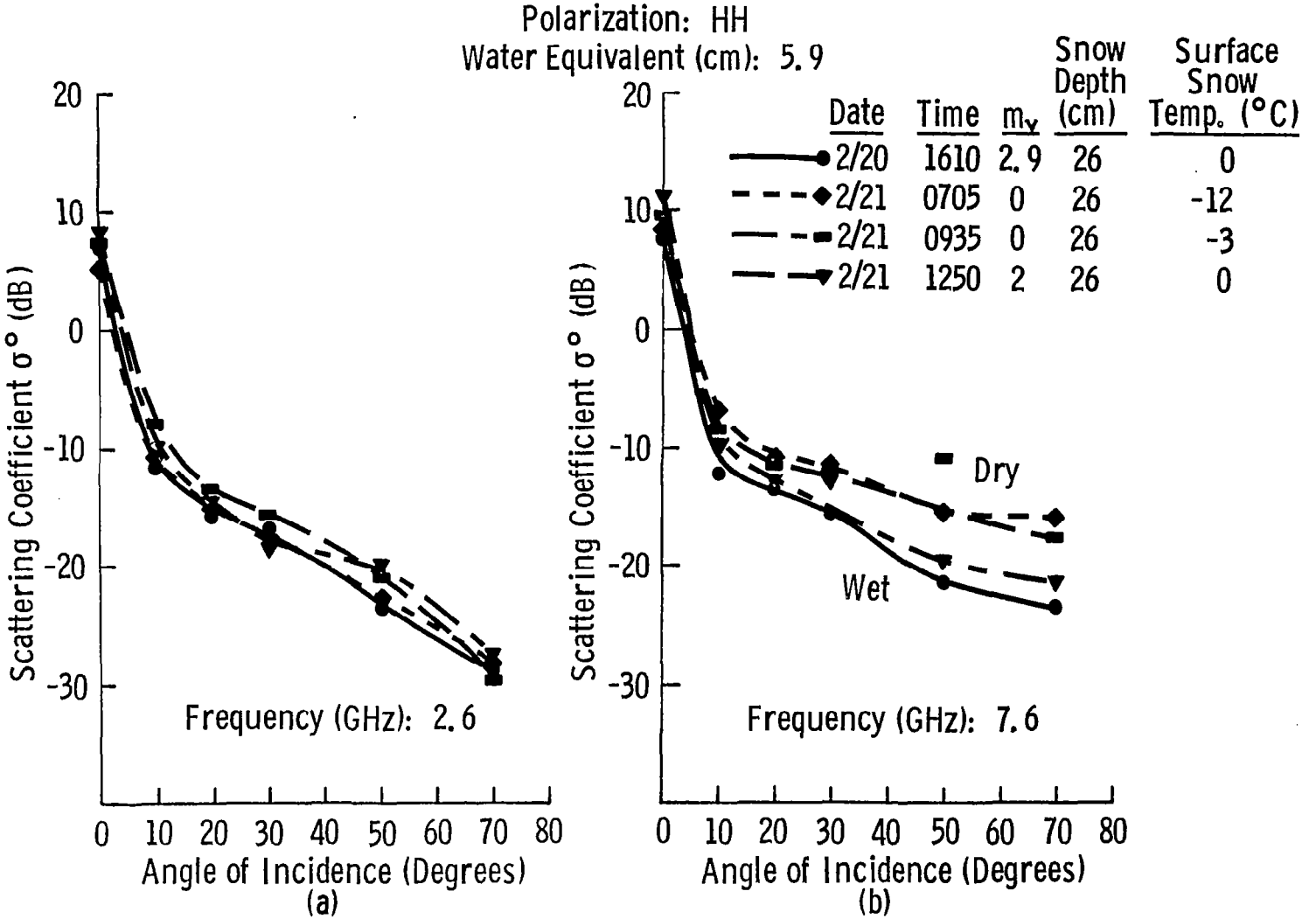


Figure 8-4 Variation in the angular response of σ° for several data sets with varying wetness over two days of a 26 cm snow layer at (a) 2.6 GHz and (b) 7.6 GHz.

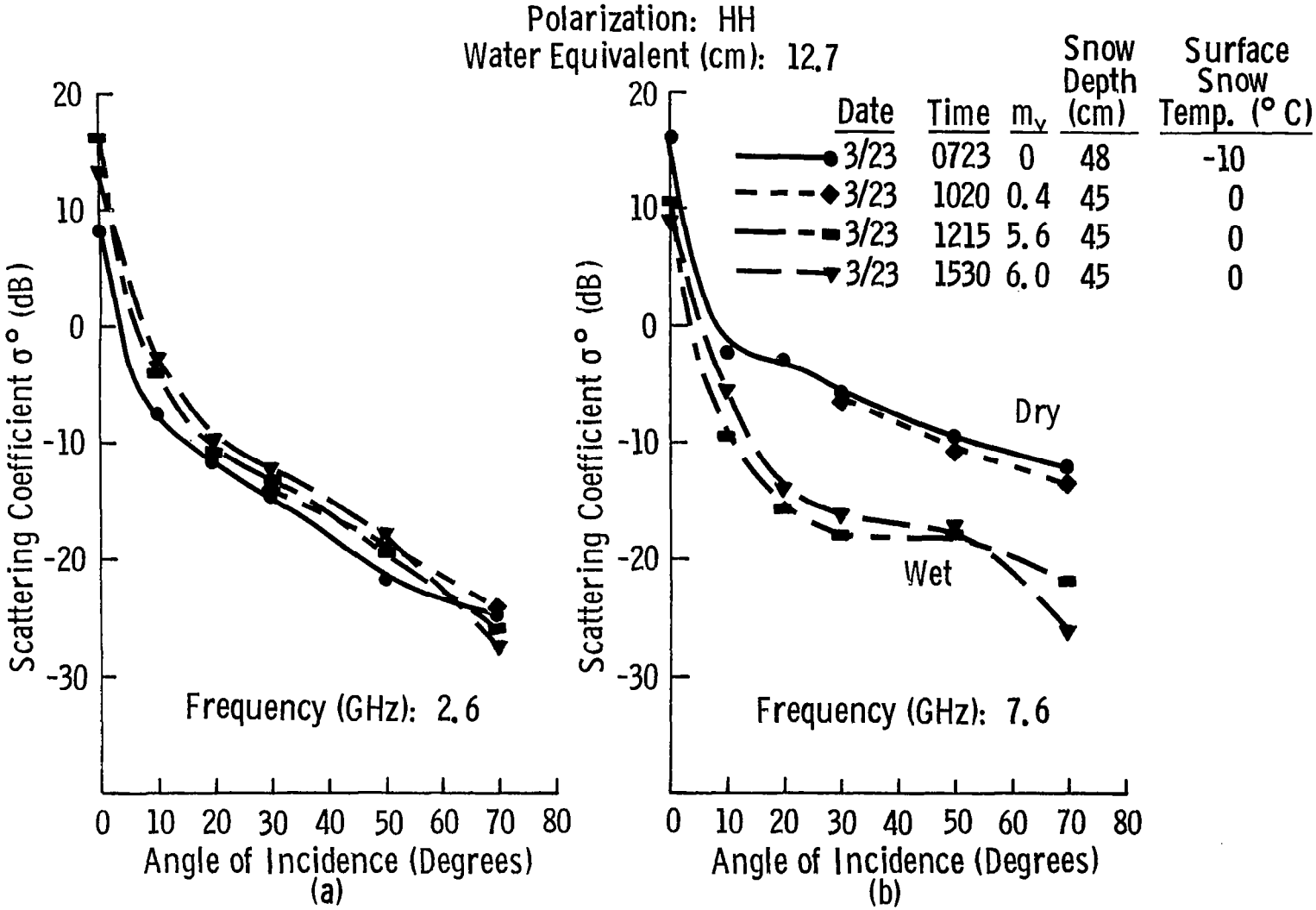


Figure 8-5 Variation in the angular response of σ^{o} for several data sets with varying wetness of a 45 cm snow layer at (a) 2.6 GHz and (b) 7.6 GHz.

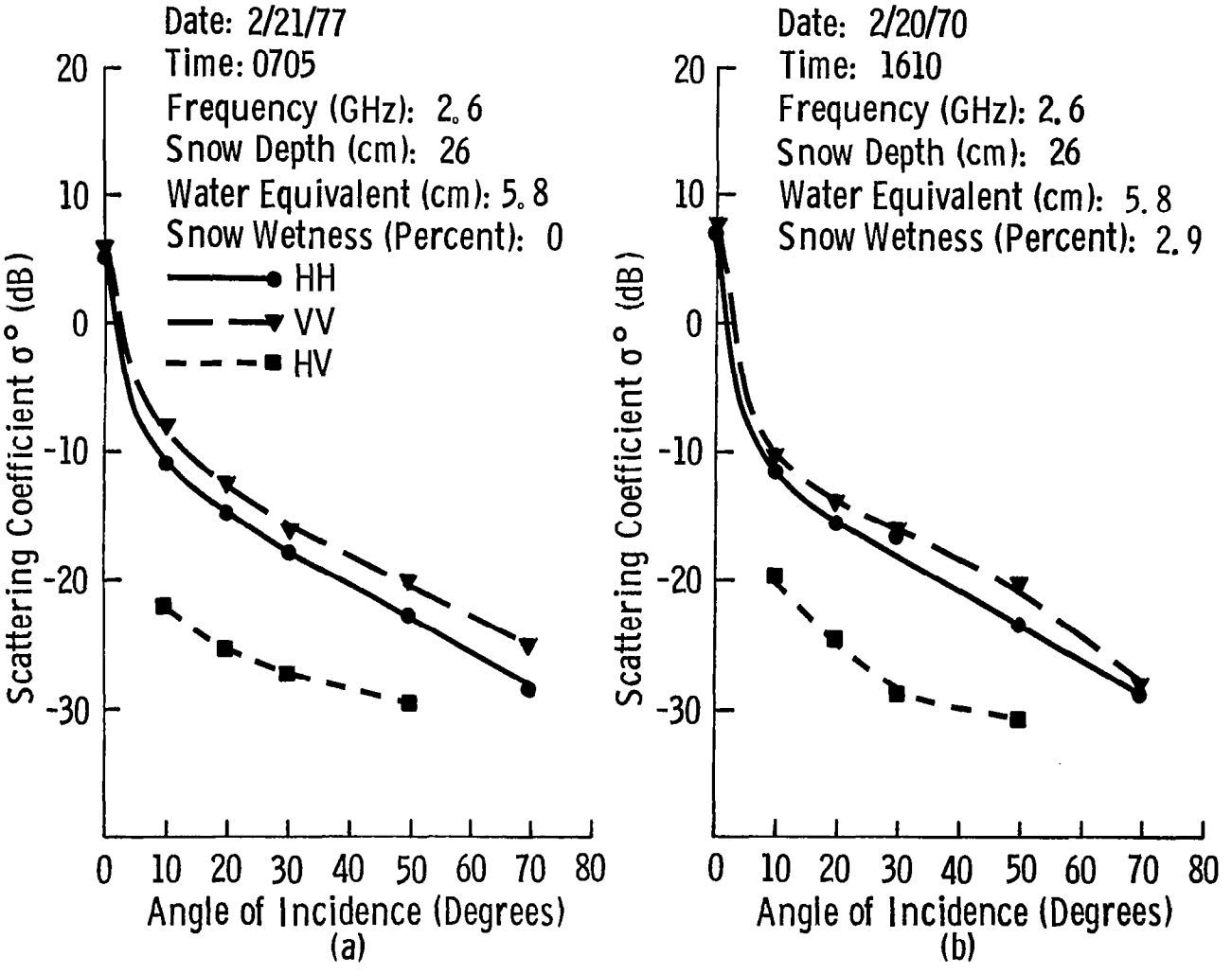


Figure 8-6 Polarization and angular response of σ^{o} at 2.6 GHz to an (a) dry snow condition and (b) wet snow condition.

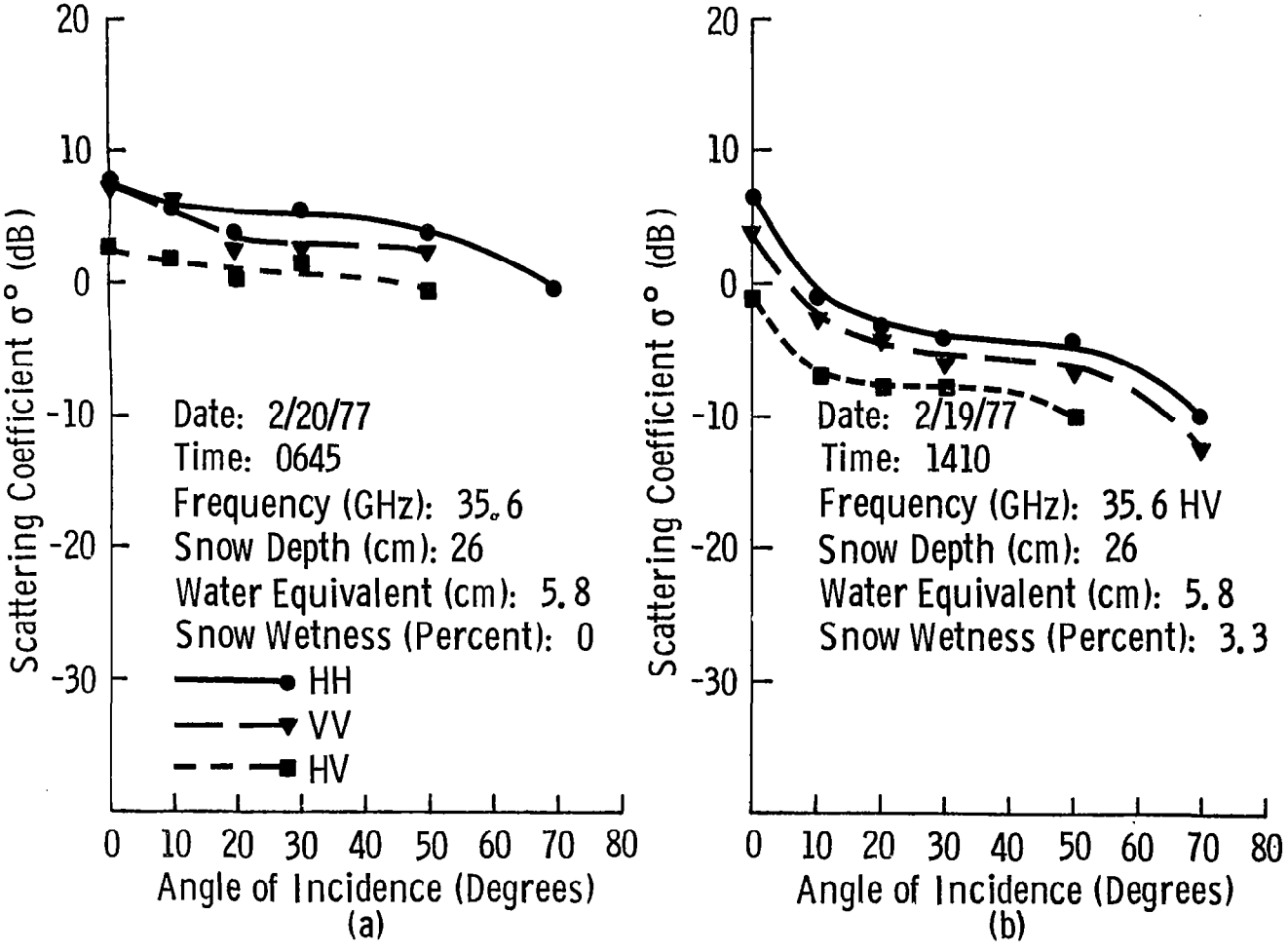
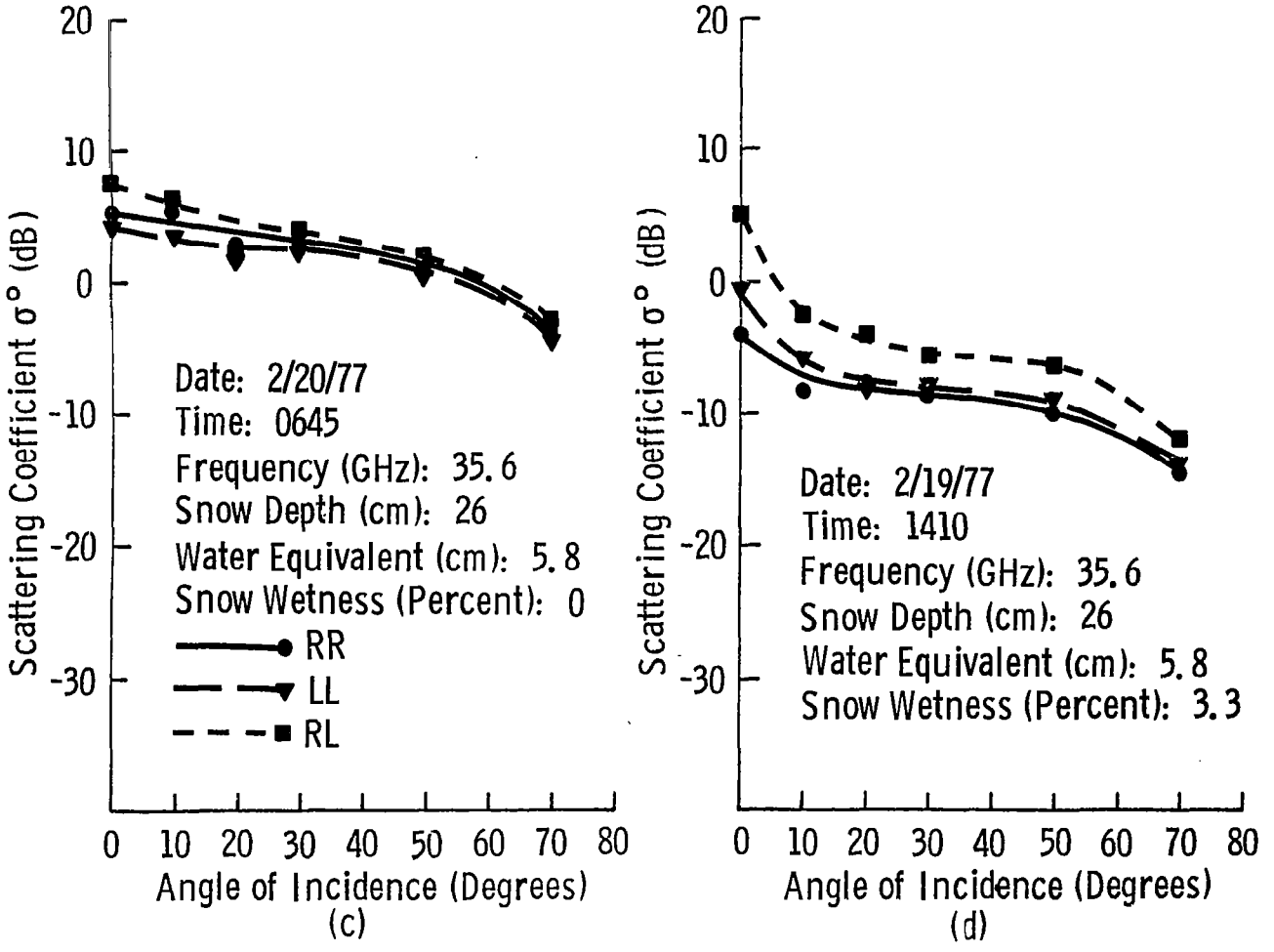


Figure 8-7 Polarization and angular response of σ^{o} to an (a) dry snow condition, linear polarization, (b) wet snow condition, linear polarization, (c) dry snow condition, circular polarization, and (d) wet snow condition, circular polarization.


20
10
0
-10
-20
-30
Scattering Coefficient σ° (dB)
Date: 2/20/77
Time: 0645
Frequency (GHz): 35.6
Snow Depth (cm): 26
Water Equivalent (cm): 5.8
Snow Wetness (Percent): 0
RR
LL
RL
0 10 20 30 40 50 60 70 80
Angle of Incidence (Degrees)
(c)
Date: 2/19/77
Time: 1410
Frequency (GHz): 35.6
Snow Depth (cm): 26
Water Equivalent (cm): 5.8
Snow Wetness (Percent): 3.3
(d)

35.6 GHz are given in Figures 8-7c and 8-7d for wet and dry snow conditions. The RL-polarization configuration is the like polarization in the circular mode, while RR and LL are the cross polarized configurations. Almost no difference is observed between the different polarization σ^o curves of dry snow (indicating volume scatter) while a 3 dB difference is observed for wet snow (indicating rough surface scatter). Also note that the overall shapes of the σ^o curves for circular polarization are similar to the like polarization shapes.

8.1.2 Response to Roughness

Surface roughness has been shown to cause a very significant effect on the microwave properties of soil targets (Ulaby, et al., 1978b). The influence of surface roughness on snow can also be significant, depending on the snow conditions.

For example, strong southerly winds on 3/11/77 created the surface appearance shown in Figure 8-8b. Data sets obtained before and after the occurrence of this change in surface structure allow qualitative analysis of the effect of surface roughness on σ^o. Photographs and sketches illustrating the shapes of the horizontal profiles of the surfaces are shown in Figure 8-8 for the two conditions. The "regular" snow surface is characterized by high spatial frequency variations with small amplitudes, while the "wind generated" surface is characterized by large smooth facets connected by ridges. In the "wind generated" case, the microwave sensor look direction was downwind.

The angular responses of σ^o for the two dry snow surface conditions are shown in Figure 8-9. The difference between the two cases is less than 3 dB for all angle-frequency combinations. Thus, for backscatter from dry snow, surface geometry is not a significant factor. This behavior is not surprising since backscatter by the surface is small in comparison to volume scatter in the snow medium. Surface backscatter is governed by the contrast in the dielectric constant of the snow medium to that of air; for dry snow, this contrast is about 1.5 to 1. Thus, the air-snow discontinuity is small for dry snow, in comparison to a soil surface, for example. Volume scatter on the other hand is governed by the size of the ice crystals relative to the wavelength, the dielectric contrast between the snow crystals and that of the snow medium (typically 3.2 to 1.5), and the depth of the snow medium.

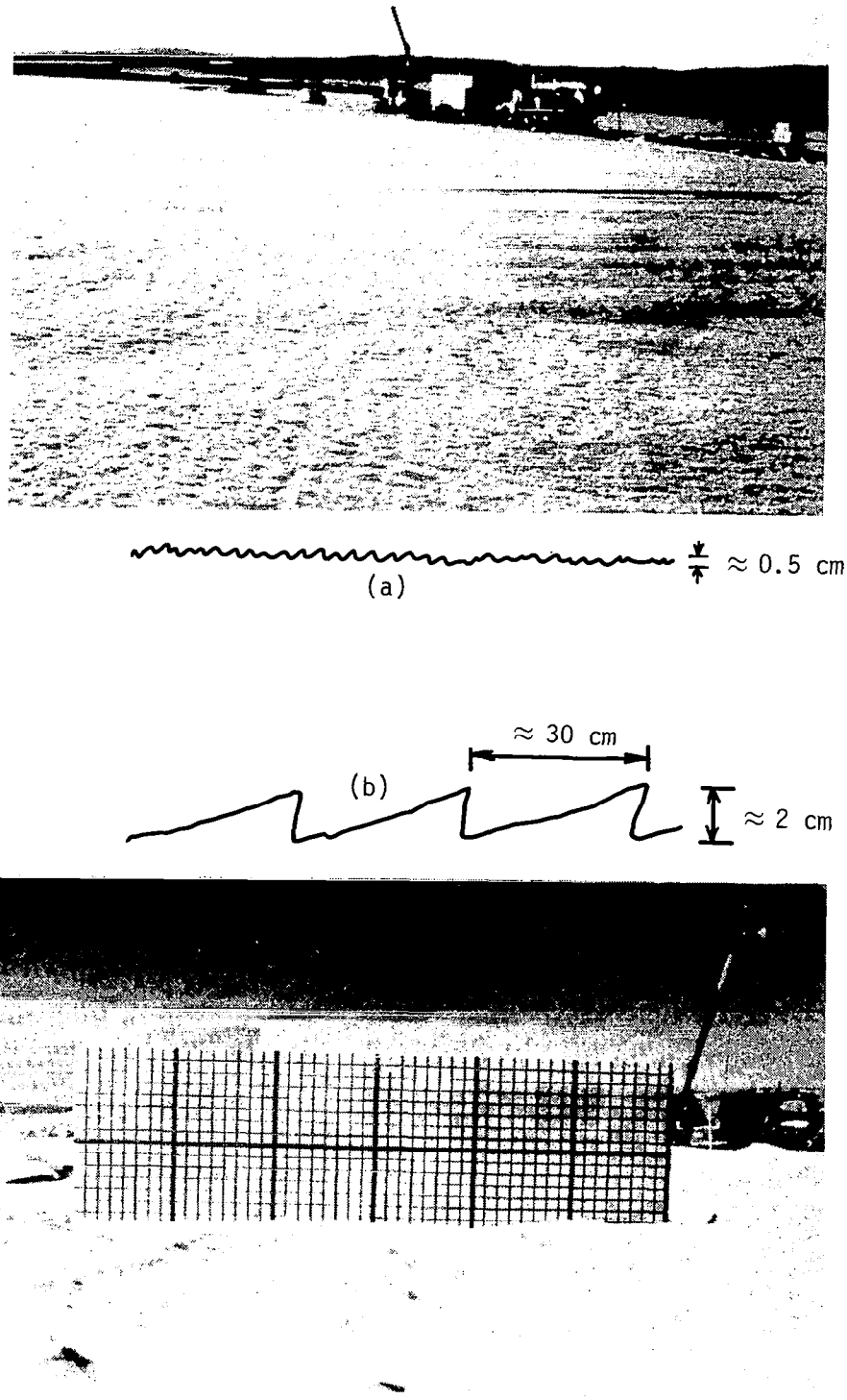


Figure 8-8 Snow surface structure: (a) regular snow surface, (b) wind-generated snow surface

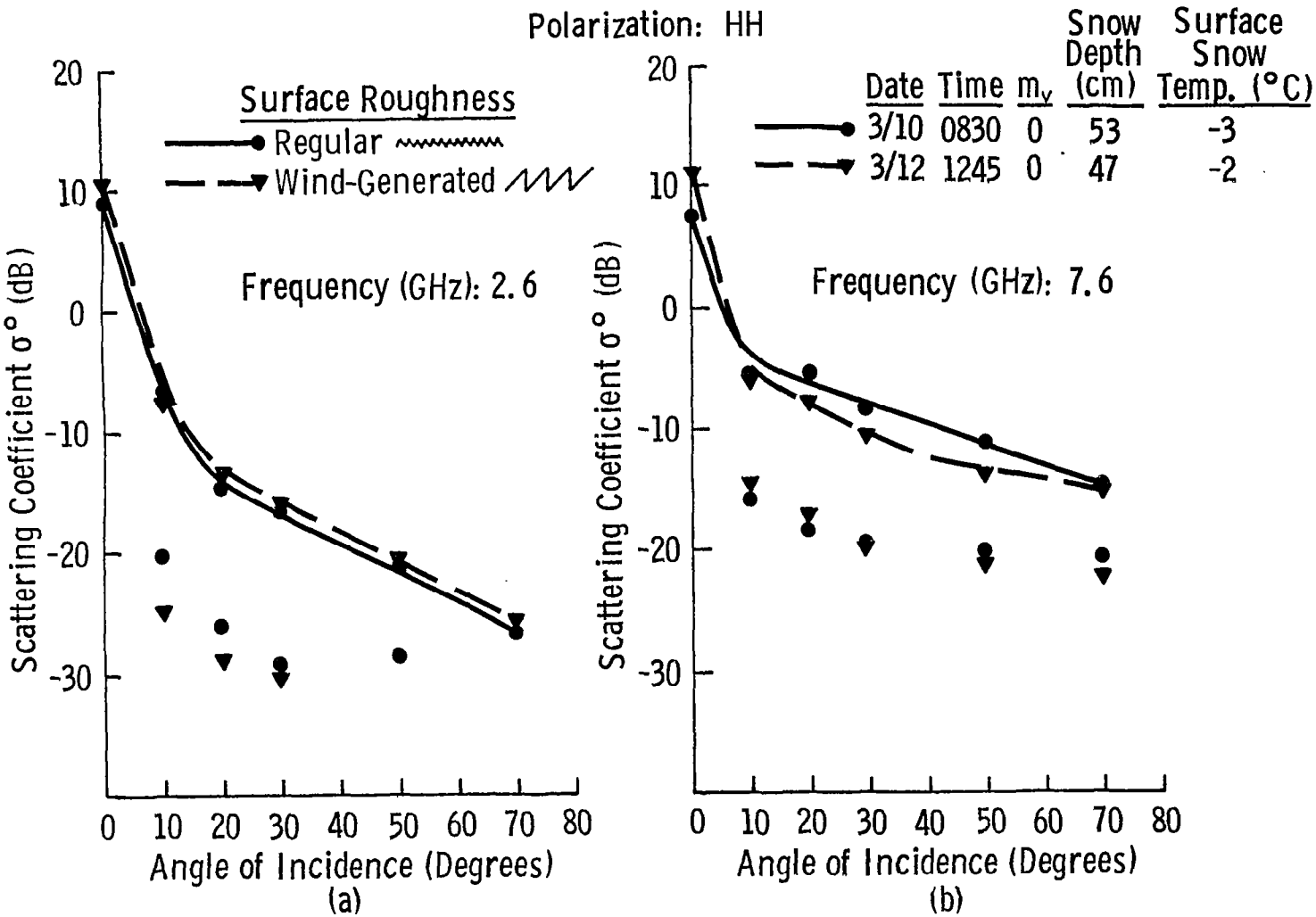
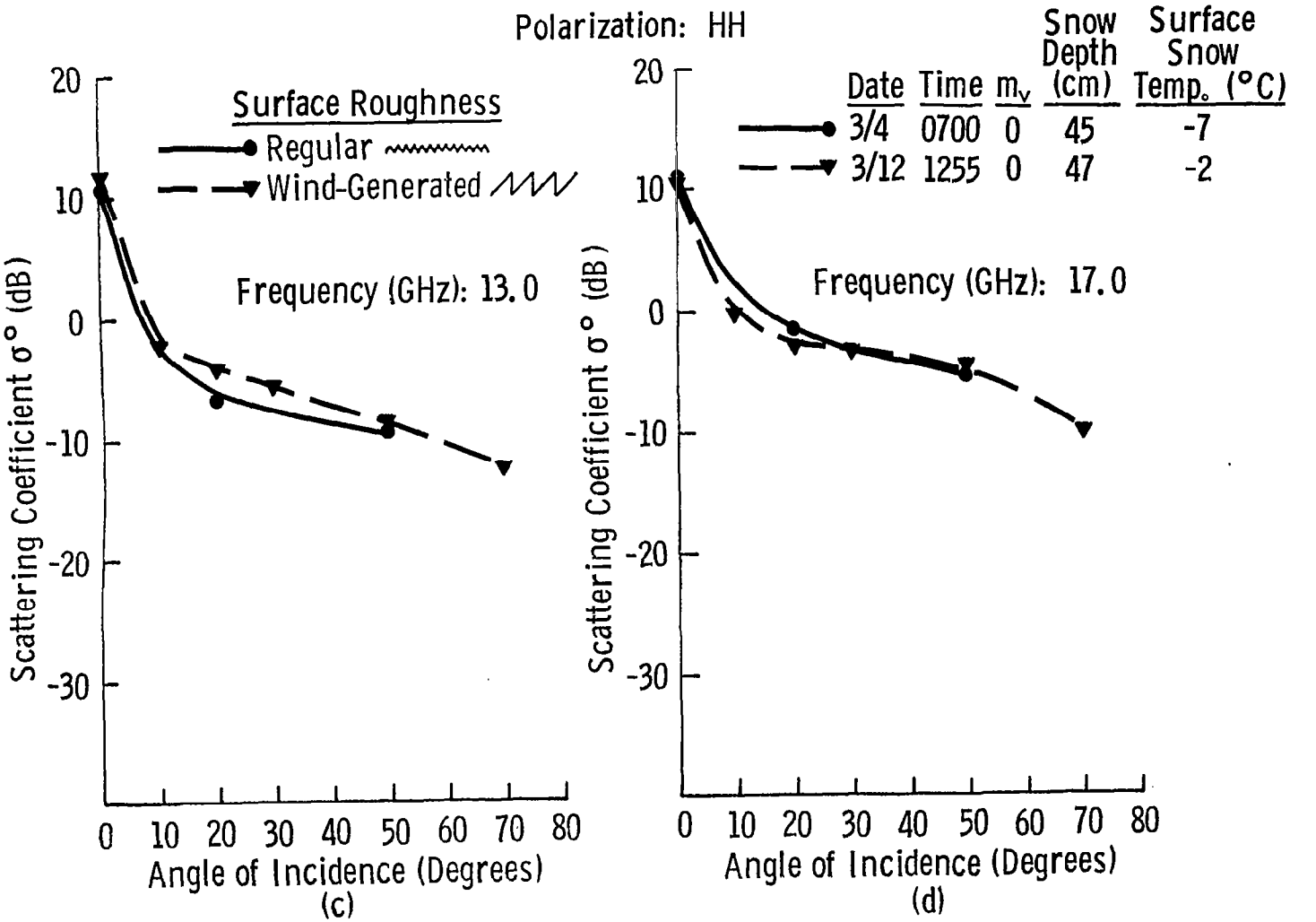
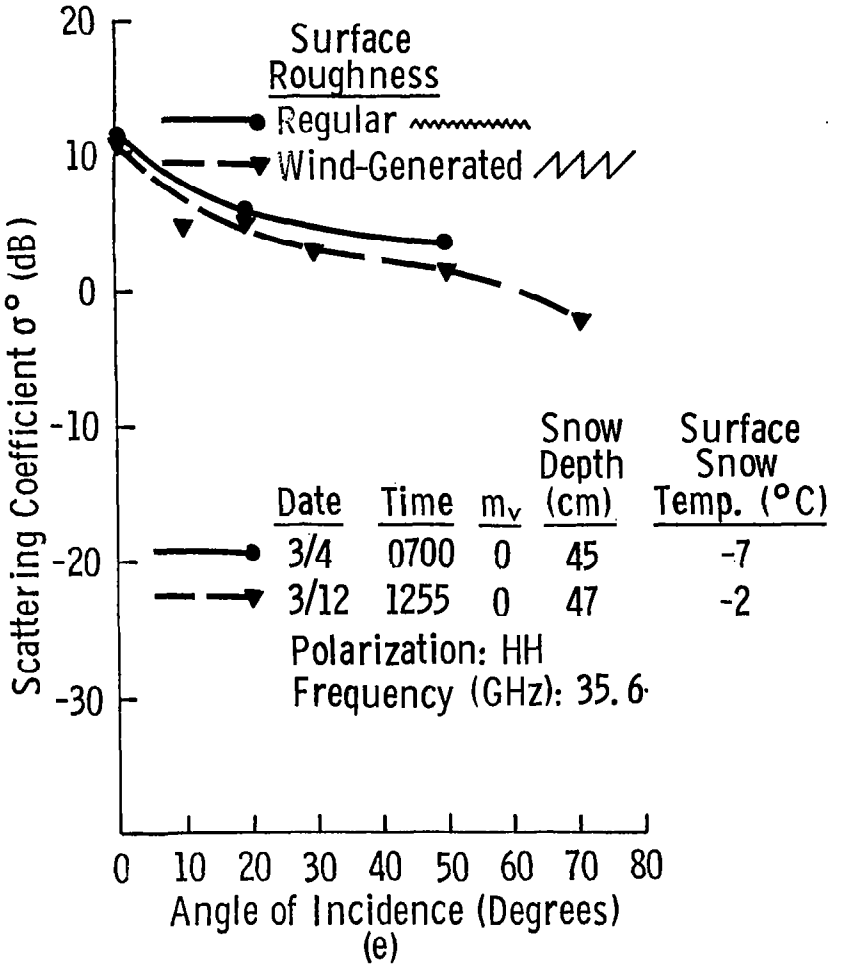


Figure 8-9 Effect of surface roughness on σ^o of dry snow at (a) 2.6 GHz, (b) 7.6 GHz, (c) 13.0 GHz, (d) 17.0 GHz, and (e) 35.6 GHz.


Polarization: HH
Surface Roughness
Regular
Wind-Generated
Frequency (GHz): 13.0
Scattering Coefficient σ° (dB)
Angle of Incidence (Degrees)
(c)
Date Time m_v Snow Depth (cm) Surface Snow Temp. (°C)
3/4 0700 0 45 -7
3/12 1255 0 47 -2
Frequency (GHz): 17.0
Scattering Coefficient σ° (dB)
Angle of Incidence (Degrees)
(d)


Surface Roughness
Regular
Wind-Generated
Scattering Coefficient σ° (dB)
20
10
0
-10
-20
-30
Date
Time
m_v
Snow Depth (cm)
Surface Snow Temp. (°C)
3/4 0700 0 45 -7
3/12 1255 0 47 -2
Polarization: HH
Frequency (GHz): 35.6
0 10 20 30 40 50 60 70 80
Angle of Incidence (Degrees)
(e)

When the snow surface layer is wet, the situation is quite different, especially at the higher microwave frequencies. Snow wetness reduces the penetration depth and increases the dielectric constant of the snow medium, which leads to less volume scatter (smaller ice crystal to medium dielectric contrast and shallower depth of penetration) and more surface scatter. Therefore, for wet snow, the effects of surface roughness on σ^{o} should be more significant than was observed earlier for dry snow. This conclusion is supported by the observations shown in Figure 8-10. At 2.6 GHz, the "wind generated" faceted snow surface appears electromagnetically rougher than the "regular" snow surface because the wavelength is comparable to the average distance between ridges. Consequently, σ^{o} of the faceted snow surface is higher in level than that of the regular surface. As frequency is increased, the high spatial frequency surface structure of the regular surface becomes the dominant feature characterizing the surface roughness, rather than the low spatial frequency of the surface ridges. The facets are smoother in appearance than the surface of the regular snow; hence, at the shorter wavelengths, the faceted surfaces appear electromagnetically smoother than the regular snow surface. Accompanying this reversal in relative roughness between 2.6 and 35.6 GHz is a reversal in the relative magnitudes of σ^{o} of the two snow surfaces, as illustrated in Figure 8-10.

Recent measurements in Brookings, South Dakota indicate that large scale artifically-induced roughness can cause drastic changes in the angular response of wet snow. Scattering coefficient data were obtained at one site with the three scales of surface roughness illustrated in Figures 8-11a, 8-11b and 8-11c. As one might expect, as the surface roughness of wet snow increases, the dynamic range of the angular response decreases. This behavior is shown in Figures 8-11d and 8-11e. The "rough" surface was created by walking across the snow surface; therefore, the roughness at nadir was only slightly affected by the foot prints while at the higher angles there was significant effect. In creating the "very rough" surface, many small snow balls were formed by kicking at the snow surface. The resulting effect was a rough surface at all angles of incidence. These effects of surface roughness thus agree with the previous results on wet snow (Figure 8-10) and extend those results to rougher surfaces.

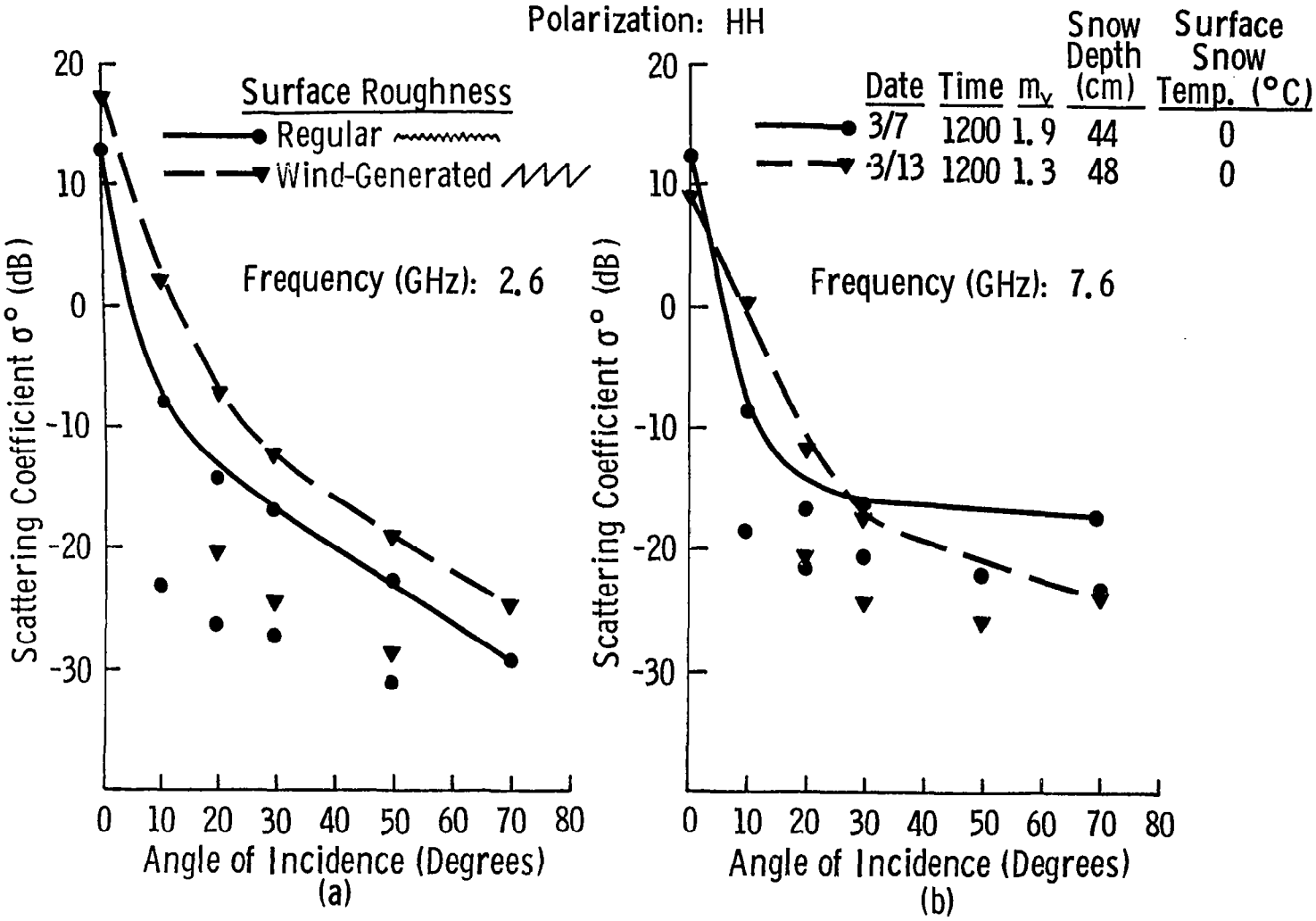
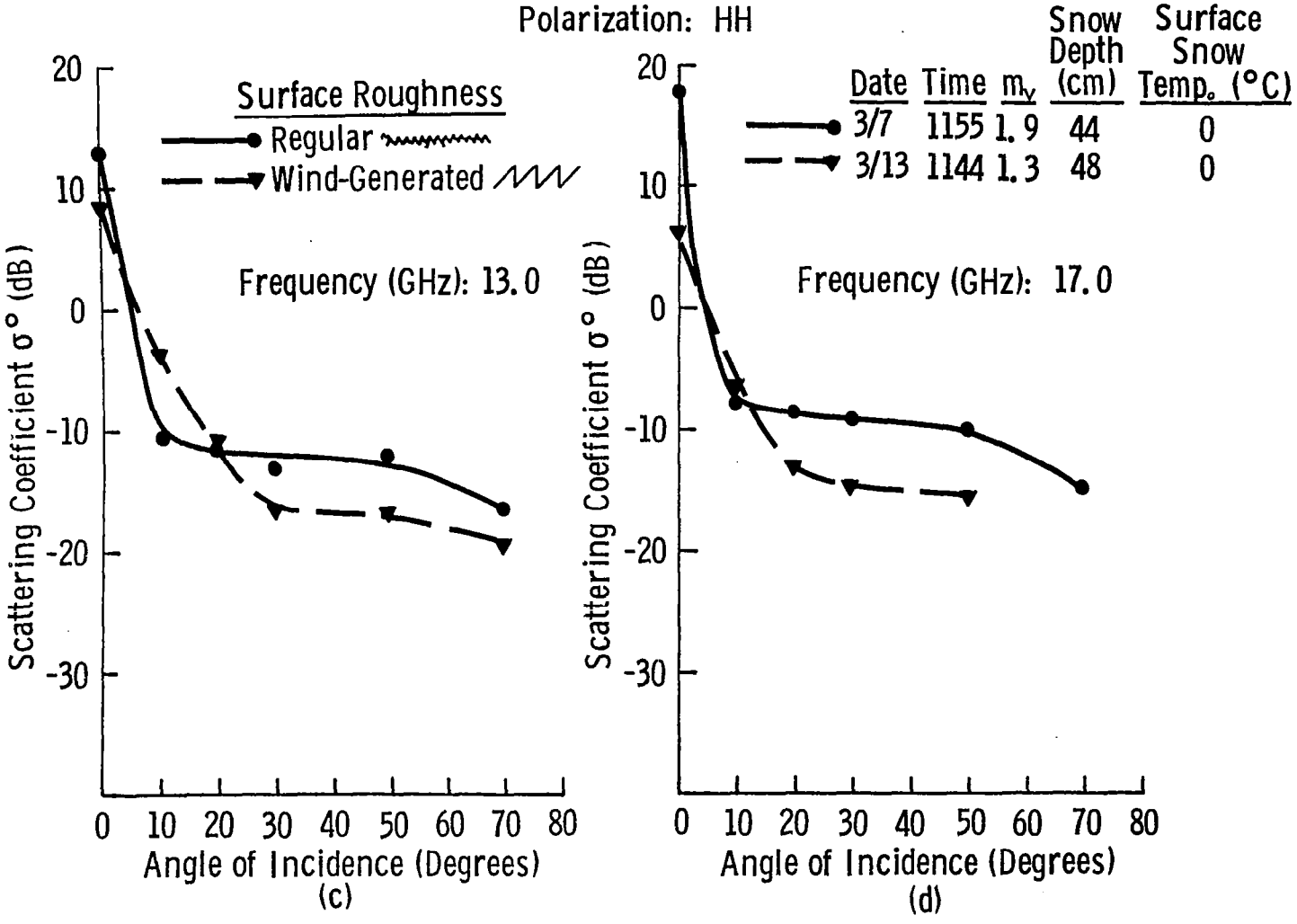
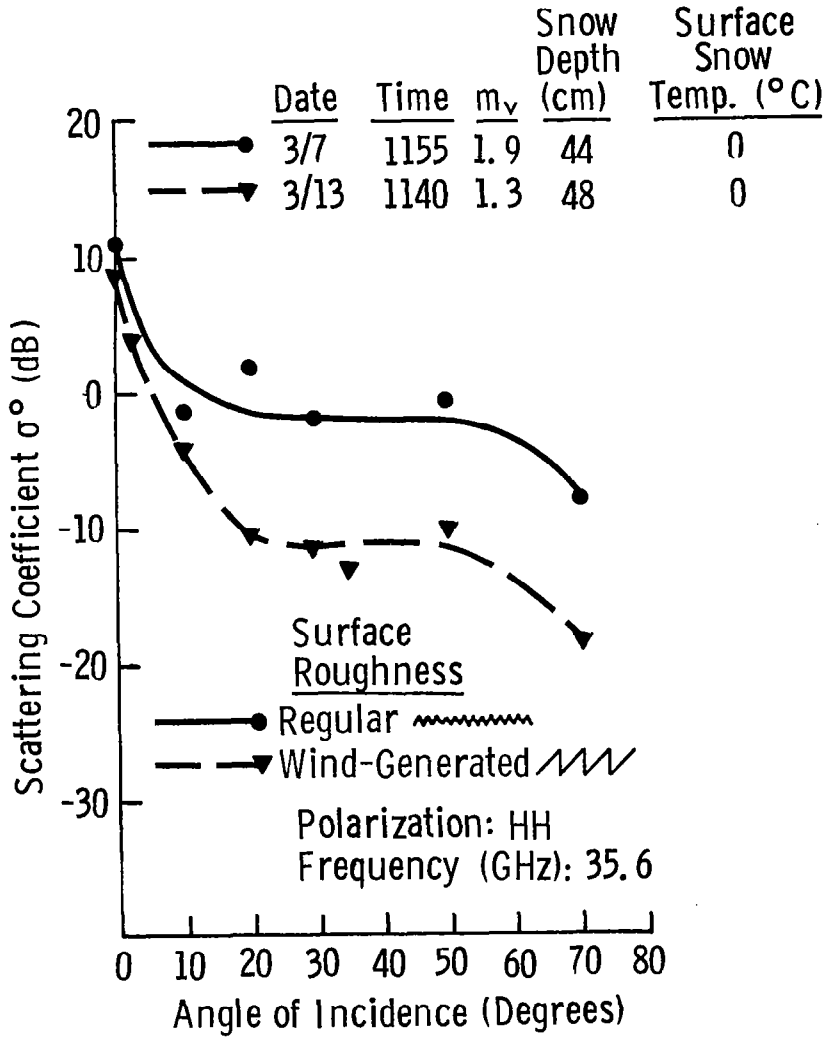


Figure 8-10 Effect of surface roughness on σ^{o} of wet snow at (a) 2.6 GHz, (b) 7.6 GHz, (c) 13.0 GHz, (d) 17.0 GHz, and (e) 35.6 GHz.


Polarization: HH
Surface Roughness
Regular
Wind-Generated
Frequency (GHz): 13.0
Scattering Coefficient σ° (dB)
Angle of Incidence (Degrees)
(c)
Date Time m_v Snow Depth (cm) Surface Snow Temp. (°C)
3/7 1155 1.9 44 0
3/13 1144 1.3 48 0
Frequency (GHz): 17.0
Scattering Coefficient σ° (dB)
Angle of Incidence (Degrees)
(d)


Date
Time
m_v
Snow Depth (cm)
Surface Snow Temp. (°C)
3/7 1155 1.9 44 0
3/13 1140 1.3 48 0
Scattering Coefficient σ° (dB)
20
10
0
-10
-20
-30
Surface Roughness
Regular
Wind-Generated
Polarization: HH
Frequency (GHz): 35.6
0 10 20 30 40 50 60 70 80
Angle of Incidence (Degrees)

(e)

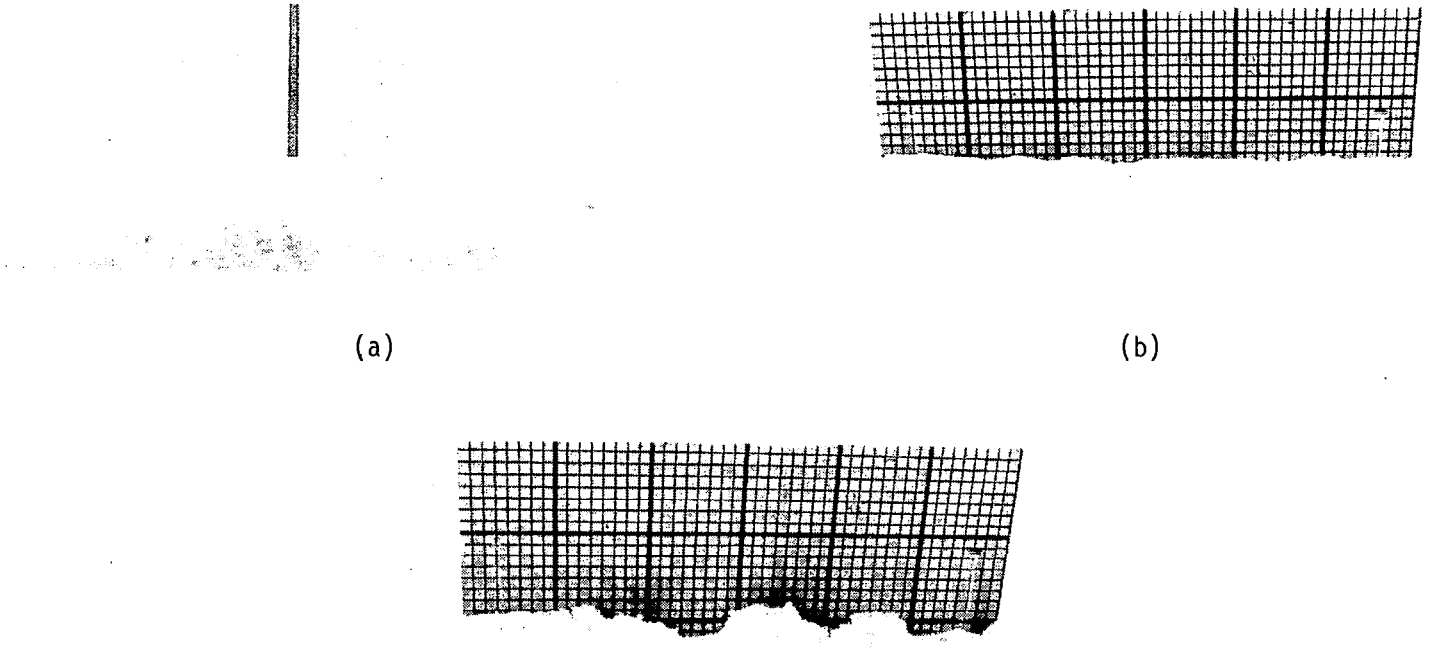
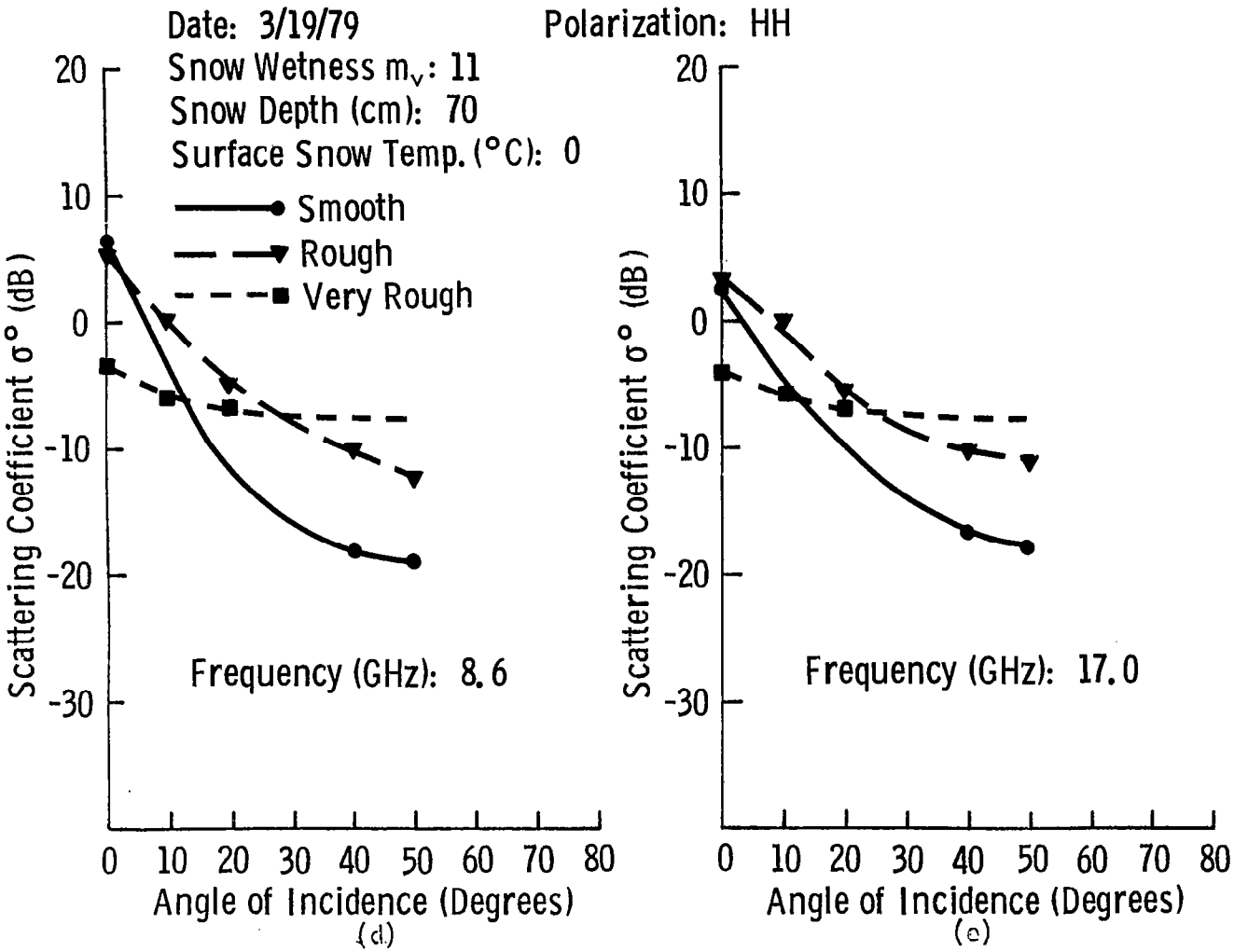


Figure 8-11 The effect of varying roughness of wet snow, (a) smooth surface, (b) rough surface, (c) very rough surface, (d) σ^{o} response at 8.6 GHz and (e) σ^{o} response at 17.0 GHz.


Date: 3/19/79
Polarization: HH
Snow Wetness m_v: 11
Snow Depth (cm): 70
Surface Snow Temp. (°C): 0
Smooth
Rough
Very Rough
Scattering Coefficient σ° (dB)
20
10
0
-10
-20
-30
Frequency (GHz): 8.6
Frequency (GHz): 17.0
0 10 20 30 40 50 60 70 80
Angle of Incidence (Degrees)
(d)
(e)

8.1.3 Passive Microwave

The angular behavior of the apparent temperature T_{ap} with wet and dry snow conditions observed on 2/21/77 is shown in Figure 8-12. The angular shapes of T_{ap} are relatively insensitive to angle of incidence near nadir and decrease more rapidly as the angle increases. T_{ap} is seen to be lower for dry snow than for wet snow at all incidence angles and at both frequencies, in contrast with the σ^{o} responses to wet and dry snow which sometimes intersected (Figure 8-1). The 5 K to 11 K offset in apparent temperature is a result of both the wetness and the thermometric snow temperature difference (14.6°C at the surface). Separation of the above effects is not possible without knowledge of the exact emission mechanism. At 37 GHz, a large sensitivity (>100K) to snow wetness is observed. The thermometric snow temperature does have an effect on T_{ap}; however, at 37 GHz the response to wetness is much larger. The very low apparent temperatures of dry snow have been observed by other experimenters (Section 5.4) and result from scattering by the snow particles which causes a decrease in the emission from the medium and consequently a decrease in T_{ap}. The effects of scattering are much more apparent at 37 GHz than at 10.69 GHz because the wavelength (.81 cm) is on the order of the size of the largest observed snow crystals (Section 6.4.1.6).

The response of T_{ap} to wetness in snow is the inverse (for the range of values observed in this experiment) of the response to wetness observed for soils. Soil targets act primarily as surface scatterers and therefore T_{ap} decreases as wetness increases (Schmugge, et al., 1974b). For snow, T_{ap} increases as wetness increases. This response follows from the increase of absorption and the reduction of scattering in the snow medium which leads to a blackbody behavior.

Figure 8-13 gives the wet and dry case variation for a greater snow depth. Except for a slight decrease in the slope of T_{ap} between 0° and 70°, the 10.69 GHz response is similar to Figure 8-12. At 37 GHz, the angular slopes between 0° and 50° are also similar to Figure 8-12; however, the dry snow level on 2/25/77 is 35 K higher than on 2/21/77. The higher T_{ap} for deep dry snow may be the result of the lower scattering in the new snow layer (26 to 45 cm AGL) because of the smaller crystal sizes in this layer (.5 to 1 mm). A similar effect of crystal size was noted by Shiue, et al., (1978).

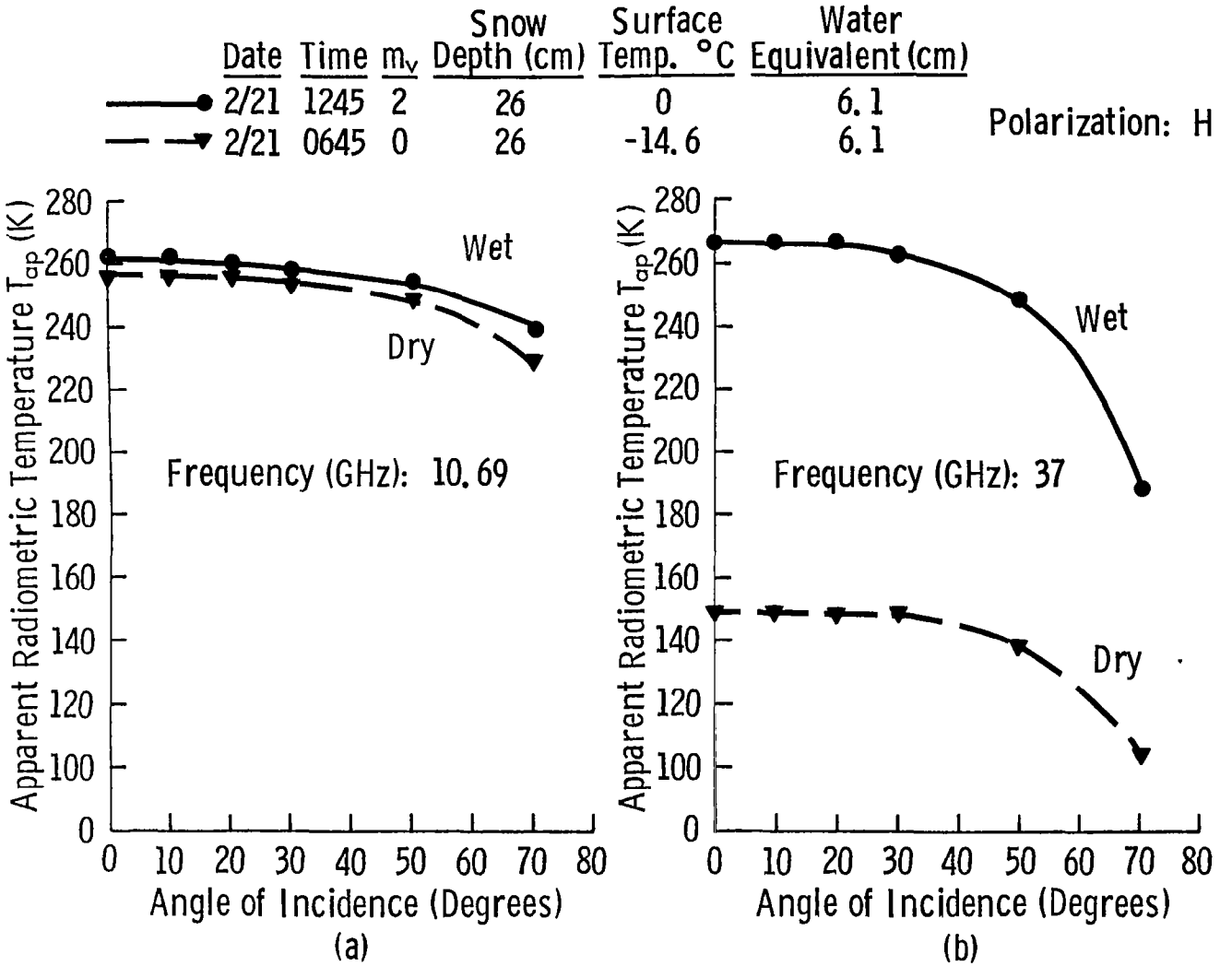


Figure 8-12 Angular response of T_{ap} at (a) 10.69 GHz and (b) 37 GHz to wet and dry snow on 2/21/77.

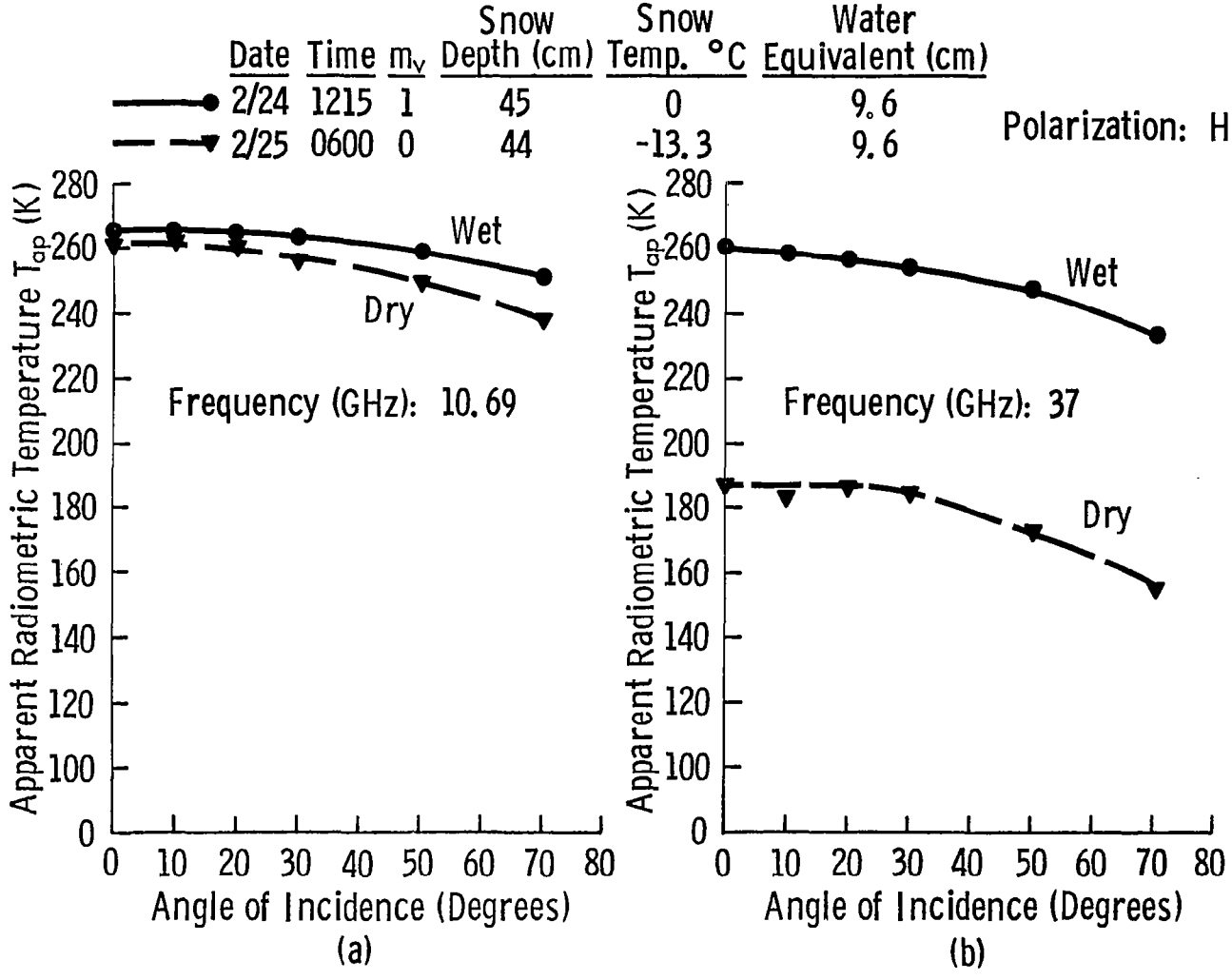


Figure 8-13 Angular response of T_{ap} at (a) 10.69 GHz and (b) 37 GHz to wet and dry snow on 2/24 and 2/25/77.

The variation of the T_{ap} values over periods when the snowpack was approximately dry is greater than the σ^o variation because of the dependence on physical temperature. Figure 8-14 shows five data sets obtained over a three day period when the σ^o data (Figure 8-3) showed approximately constant values. The 10.69 GHz apparent temperatures changed only slightly over the five data sets, while the T_{ap} data at 37 GHz on 2/25/77 at 1505 did show wetness effects. Comparison with 35.6 GHz active data is not possible because 35.6 GHz σ^o data were not acquired due to radar system problems.

The incoherent nature of the radiometric measurements means that better inherent time resolution was available for T_{ap} than for the scatterometer measurements since spatial averaging was not required for the former. The improved time resolution allows observation of the melt and freeze situations occurring in the morning and late evening respectively. Figure 8-15 shows that the angular shape does not change appreciably with increasing or decreasing wetness, while the level does change considerably. Figures 8-15a and 8-15b illustrate the melt phase while 8-15c and 8-15d show the freeze phase.

8.1.4 Response to Roughness

Figure 8-16a shows the effect of surface roughness of dry snow on T_{ap} at 10.69 GHz. The apparent temperature of the faceted snow surface is lower than that of the "regular" snow surface by approximately 5 to 15 K. For the wet case, the effects of roughness should be greater. Figure 8-16b illustrates this fact. More information would have been gained from the response at 37 GHz, but equipment problems did not allow acquisition of 37 GHz T_{ap} data on 3/13/77.

8.1.5 Summary of the Microwave Angular Response

The major findings concerning the active microwave angular response to snowpack parameters are:

1) Snow wetness has a minor effect on σ^o at 2.6 GHz, however, the sensitivity to wetness increases with increasing frequency.
2) The sensitivity of σ^o to wetness generally increases with increasing angle of incidence and results in a lowering of σ^o at angles away from nadir.
3) The scatter mechanism seems to vary. For wet snow, σ^o is governed by surface scatter at all frequencies. For dry snow, volume scattering is responsible for the σ^o

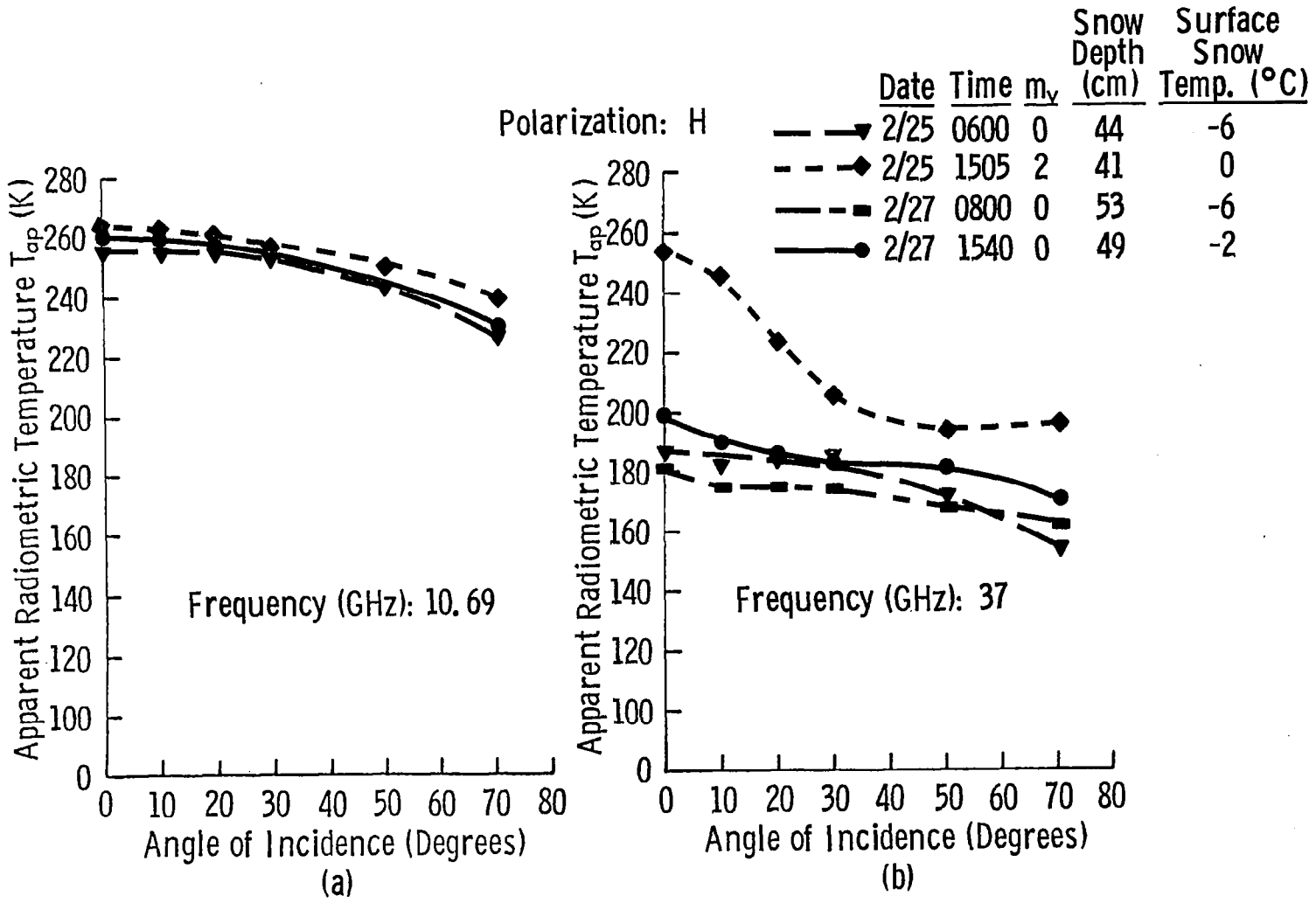


Figure 8-14 Variation in the angular response of T_{ap} for several data sets to nearly dry snow over two daytime periods at (a) 10.69 GHz and (b) 37 GHz.

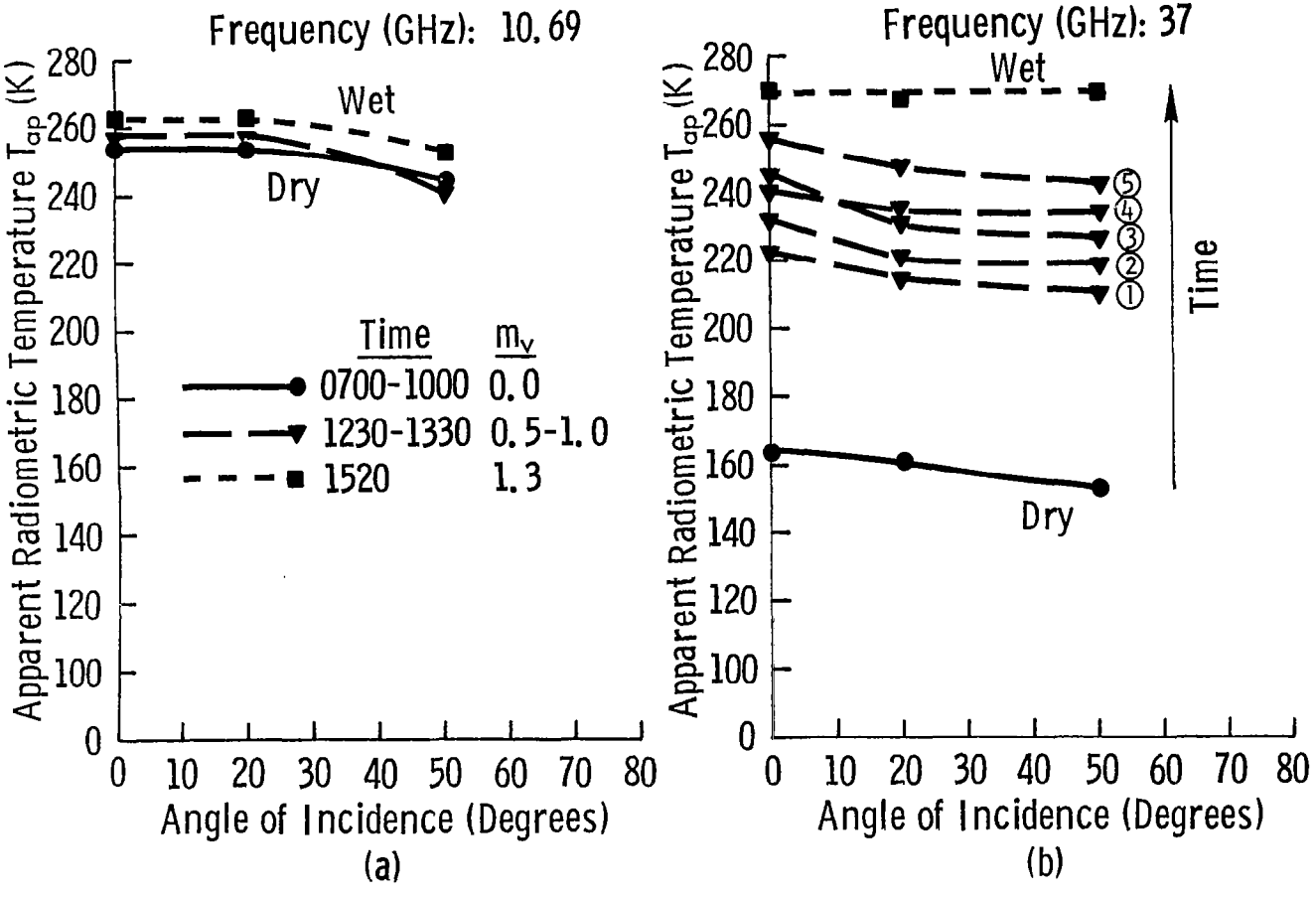
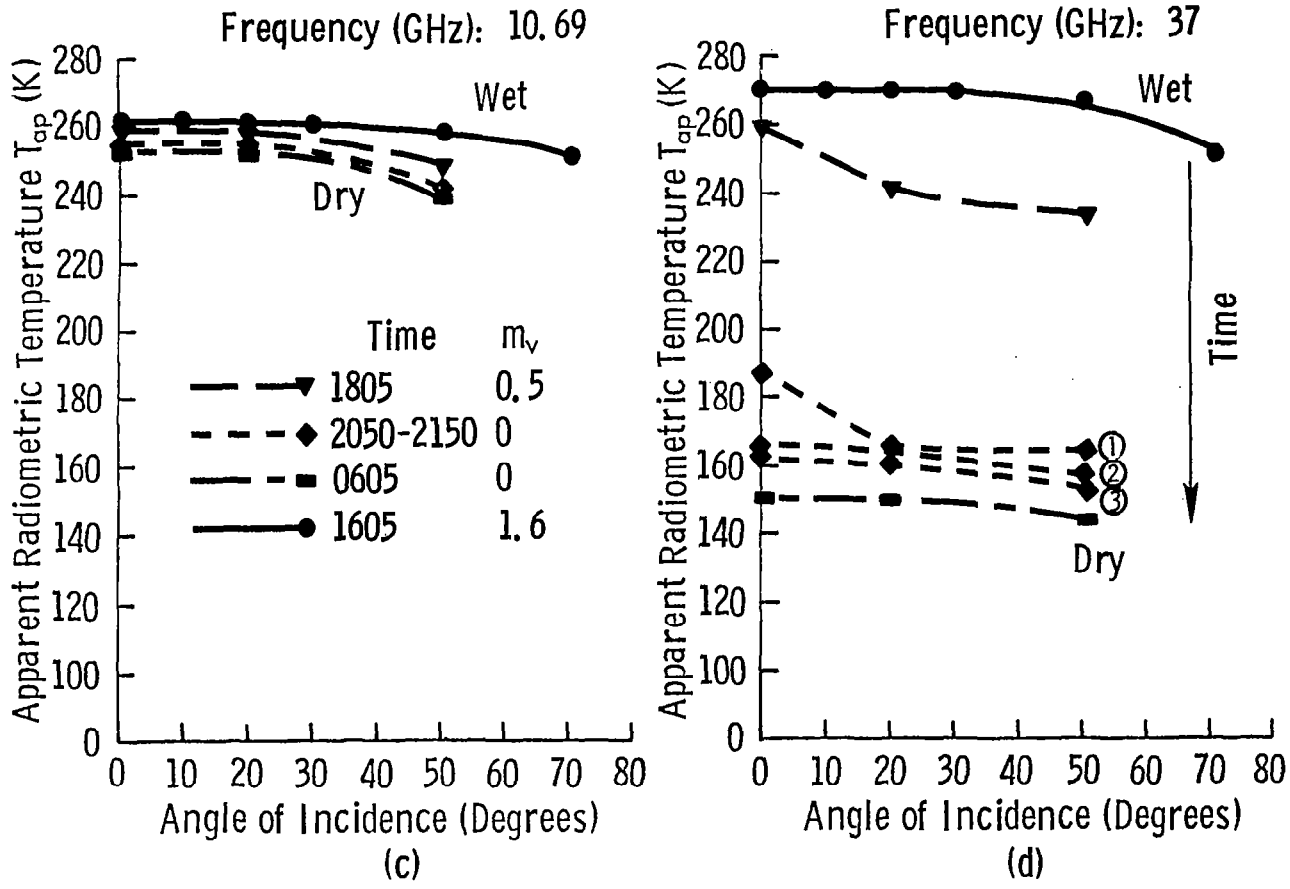


Figure 8-15 Time variation of the angular response of T_{ap} over the snow melt (a) and (b) and snow freeze (c) and (d) cycles.

Date: 3/3-3/4/77
Snow Depth (cm): 48
Water Equivalent (cm): 10.5
Polarization: H



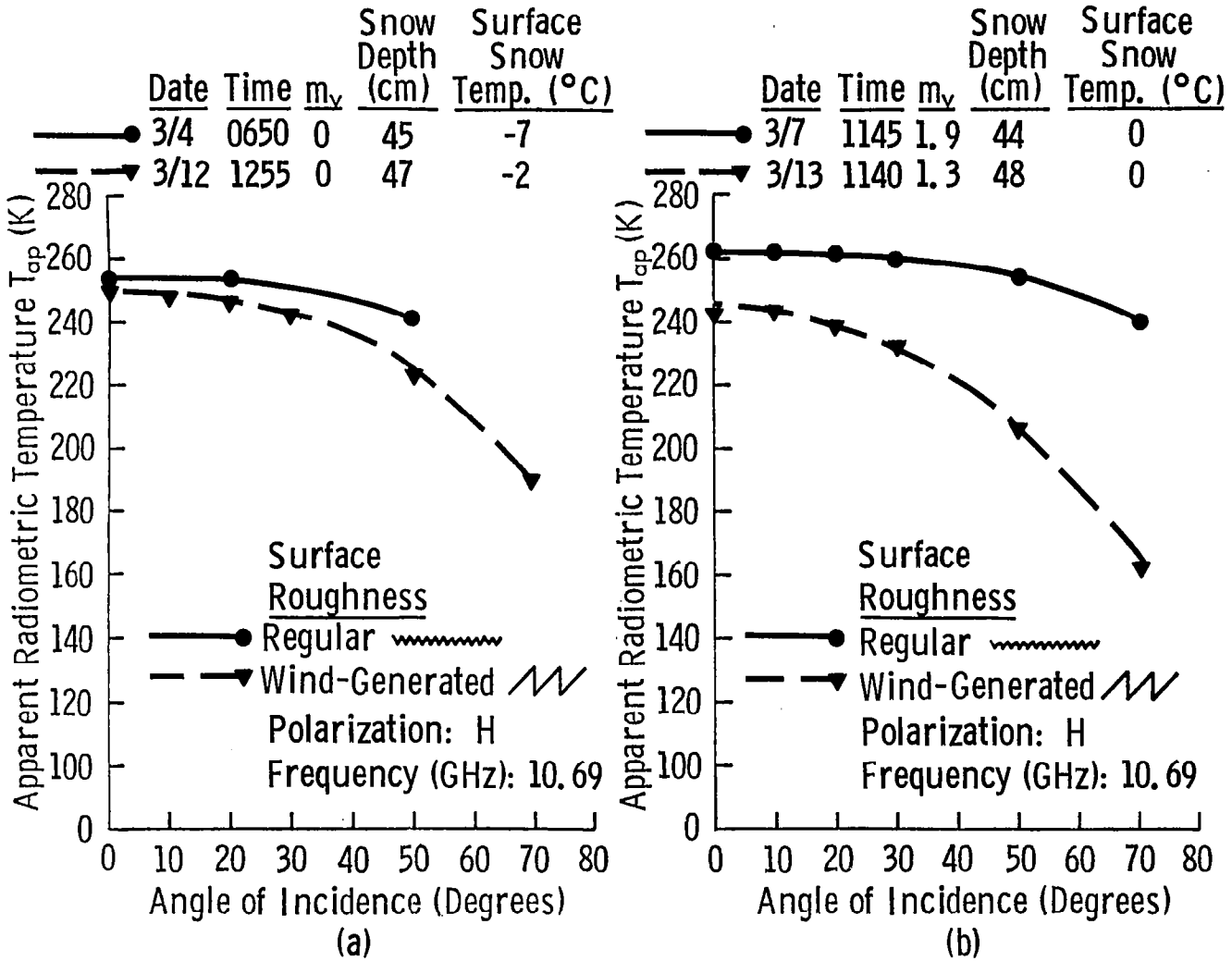


Figure 8-16 The effect of surface roughness on T_{ap} of (a) dry snow and (b) wet snow at 10.69 GHz.

behavior at the higher frequencies and soil contributions are important at the lower frequencies.

4) Surface roughness effects are relatively minor (less than 3 dB) when the snow is dry.
5) Surface roughness is very important when wetness is present.

The major findings of the T_{ap} angular response analyses are:

1) The response of T_{ap} to wetness is the inverse of the response of σ^o to wetness; but in a similar manner, the sensitivity also increases with frequency.
2) Unlike σ^o which shows little sensitivity to m_v at angles near nadir, T_{ap} exhibits approximately the same response to wetness at all angles.
3) Volume scattering effects are much more apparent at 37 GHz than at 10.69 GHz.
4) The angular response shape does not change appreciably with variations in snow wetness.
5) Surface roughness increases T_{ap} particularly for wet snow.

8.2 Spectral Response

8.2.1 Active Microwave

The spectral response of σ^o for wet and dry snow conditions is illustrated in Figures 8-17a, 8-17b and 8-17c at three angles of incidence. At nadir, generally higher σ^o values were observed for the wet snow condition than were observed for the dry snow condition, although there were a few exceptions. The σ^o response is relatively flat with frequency at nadir; however, σ^o increases significantly with frequency at angles of 20° and above. The rate of increase of σ^o is greater for dry snow than for wet snow. The diverging wet snow and dry snow σ^o curves result in increased sensitivity to wetness with increasing frequency. At both 20° and 50°, snow wetness causes a decrease in σ^o from the dry case of about 1 dB at 1 GHz to 12 dB at 35 GHz at 20° and 15 dB at 35 GHz at 50°. These facts in addition to the loss data in Figure 8-2 indicate that the return at 1 GHz is dominated by the ground contribution with minor influence of the snowpack. With increasing frequency and the resulting

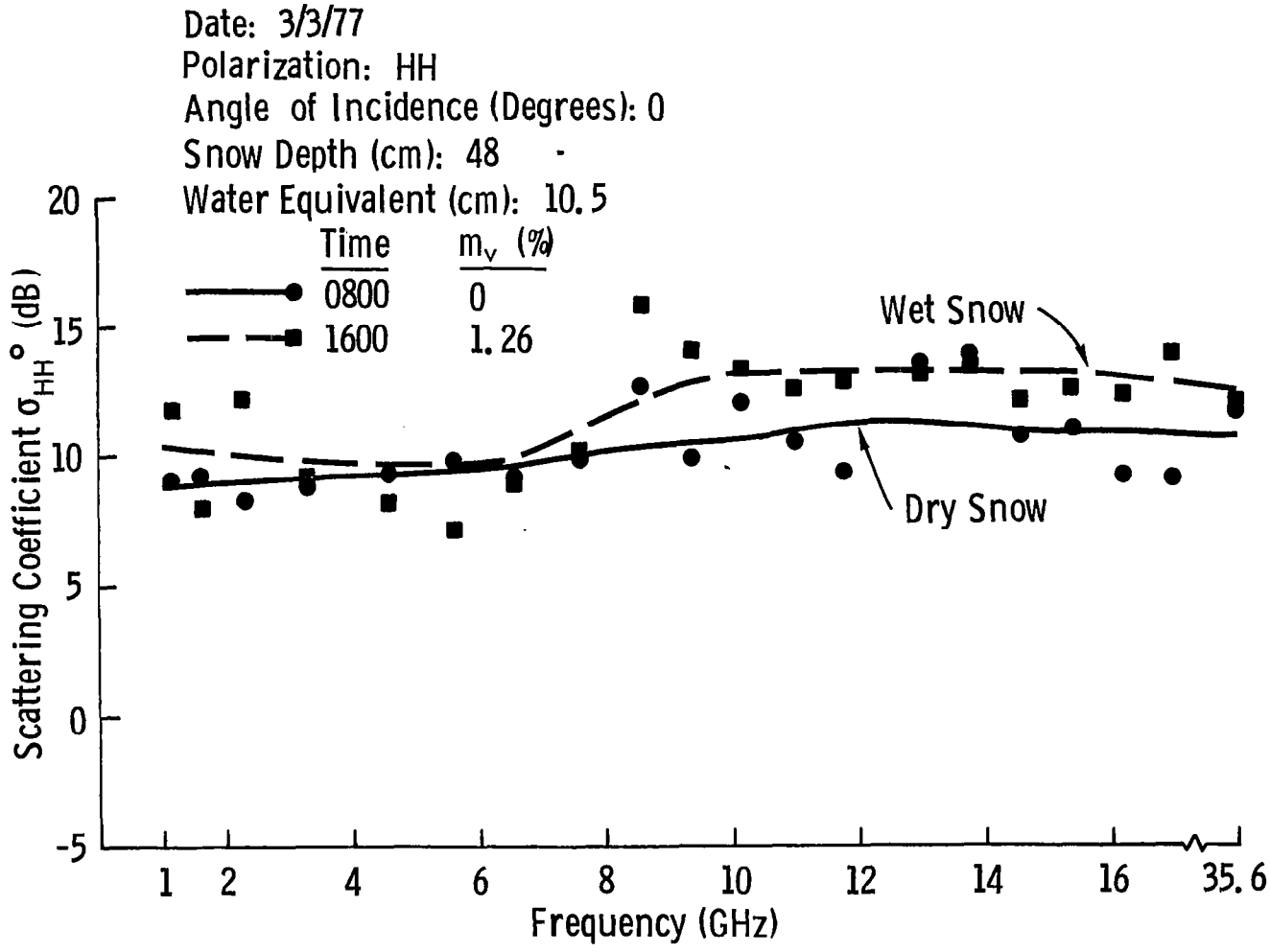


Figure 8-17a Spectral response of σ^o at 0^o (nadir) to wet and dry snow.

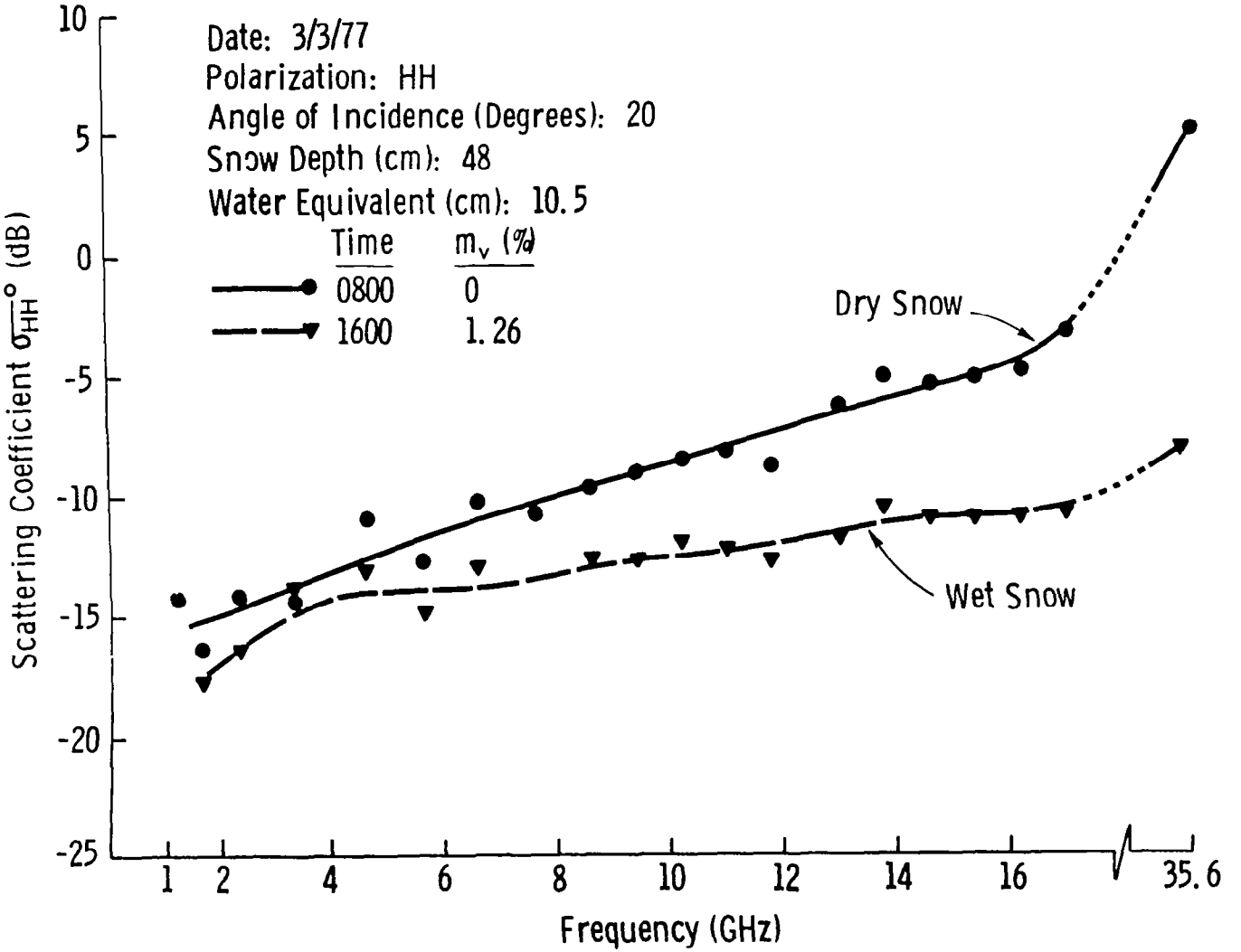


Figure 8-17b Spectral Response of σ° at 20° Angle of Incidence to Wet and Dry Snow

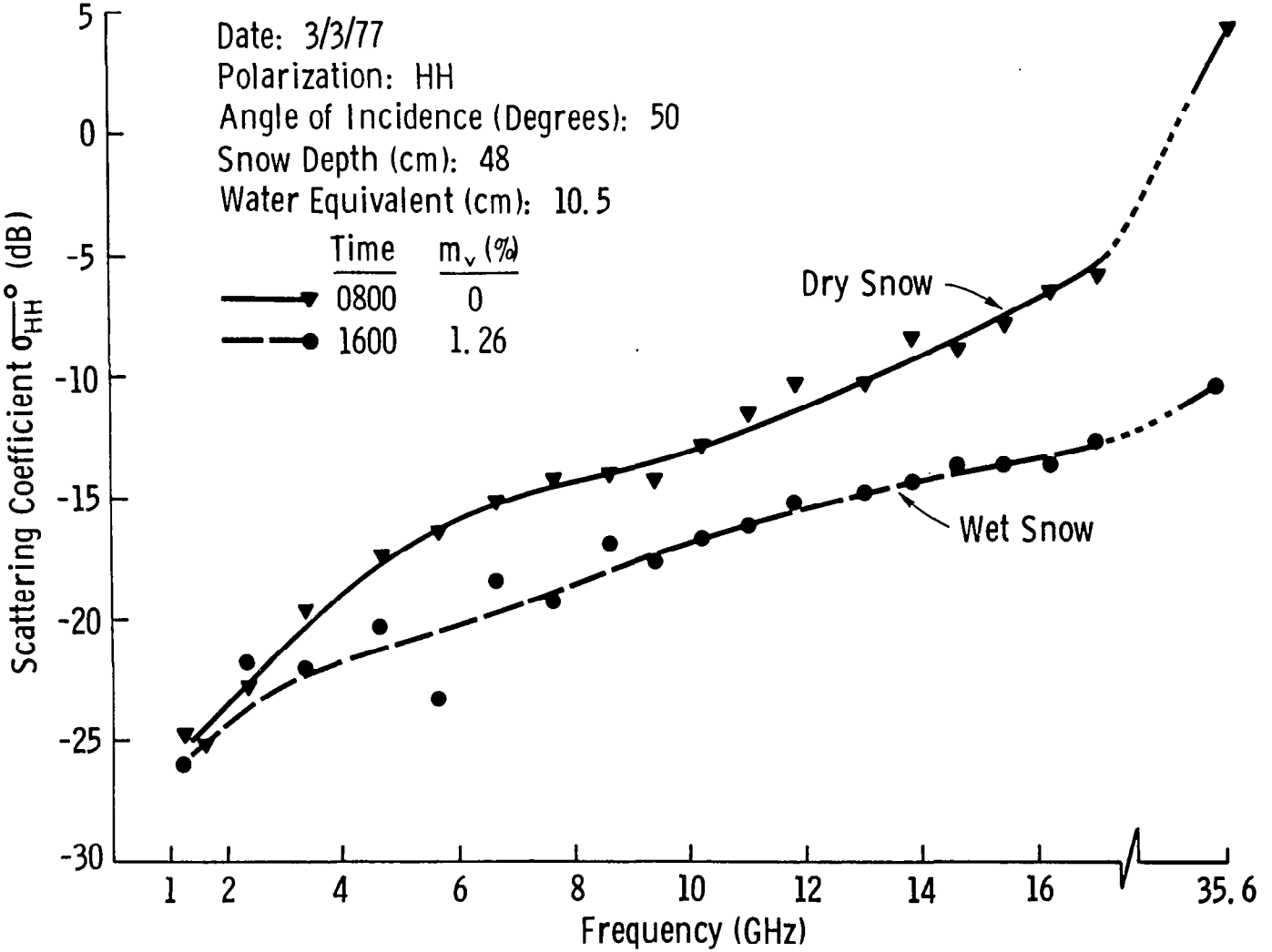


Figure 8-17c Spectral Response of σ^o at 50° Angle of Incidence to Wet and Dry Snow

increase in snow path loss, the ground contribution is diminished and the backscatter from the snowpack predominates. The combination of the effects of frequency and wetness cause a reversal in the relative roles of the underlying ground and the snowpack as either increases.

The spectral response of σ^o is shown for another period during the experiment in Figures 8-18a and 8-18b for both HH and HV polarizations. The similarity of the HH data to the curves in Figures 8-17b and 8-17c is evident although the level is slightly higher on 2/20/77 at the higher frequencies. The behavior of the HV polarization σ^o value is similar to the HH polarization response, although the rate of increase is considerably greater. This behavior is illustrated by the wet and dry snow depolarization ratio ($\sigma^o_{HV}/\sigma^o_{HH}$) spectral responses in Figures 8-19a and 8-19b. It is observed that the depolarization ratio increases rapidly over the 1 to 10 GHz region and then assumes an approximately constant trend for higher frequencies at both 20° and 50° angles of incidence. The effect of snow wetness on depolarization ratio is smaller at 50° than at 20° over the 1-8 GHz region.

8.2.2 Passive Microwave

The spectral response of T_{ap} at a 50° angle of incidence is shown in Figure 8-20a for wet and dry snow conditions. The difference between the two curves, attributed to snow wetness, shows a large increase between 10.7 GHz and 37 GHz, followed by a slight decrease between 37 GHz and 94 GHz, thus suggesting that microwave emission is more sensitive to wetness variations at 37 GHz than at 94 GHz. This is an erroneous conclusion, however, because T_{ap} includes reflected sky temperature contributions which are considerably larger at 94 GHz than at 37 GHz.

In conjunction with the radiometric measurements of the snow, T_{sky} was measured at 30° from zenith. If the measured T_{sky} at 30° zenith angle is employed in the following equation (Moore, et al., 1975 in Manual of Remote Sensing):

$$T_{sky} = T_{air} (1 - e^{-\tau \sec\theta}) \qquad (8\text{-}1)$$

where T_{air} is the sky physical temperature, the zenith attenuation τ can be calculated. Then T_{sky} can be found at other observation angles.

If the T_{ap} values are then converted to emissivity using Equation (2-14), the sensitivity to wetness is observed to increase between 37 GHz and 94 GHz (Figure 8-20b).

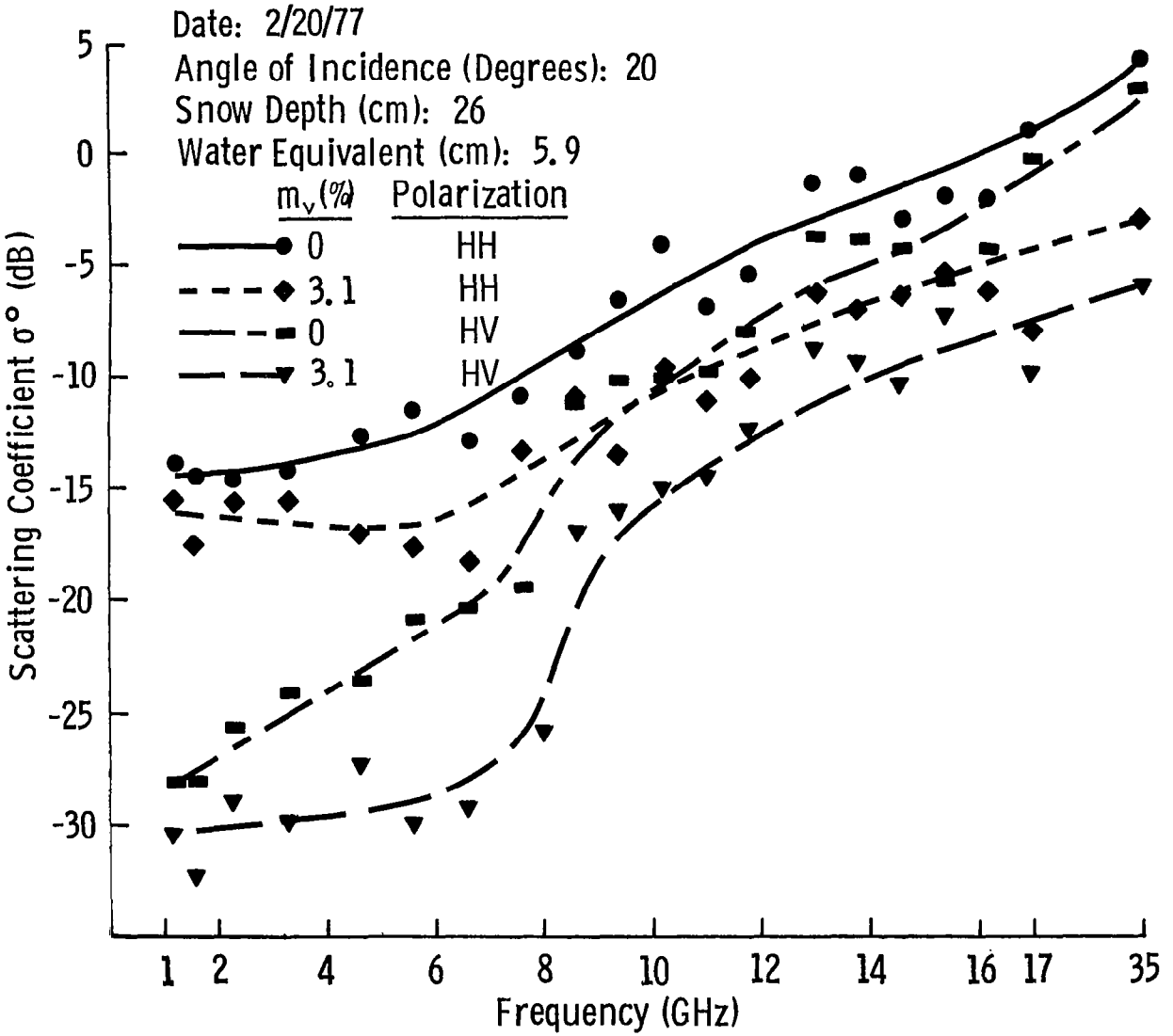


Figure 8-18a Spectral response of σ^o at 20^o angle of incidence for HH and HV polarizations.

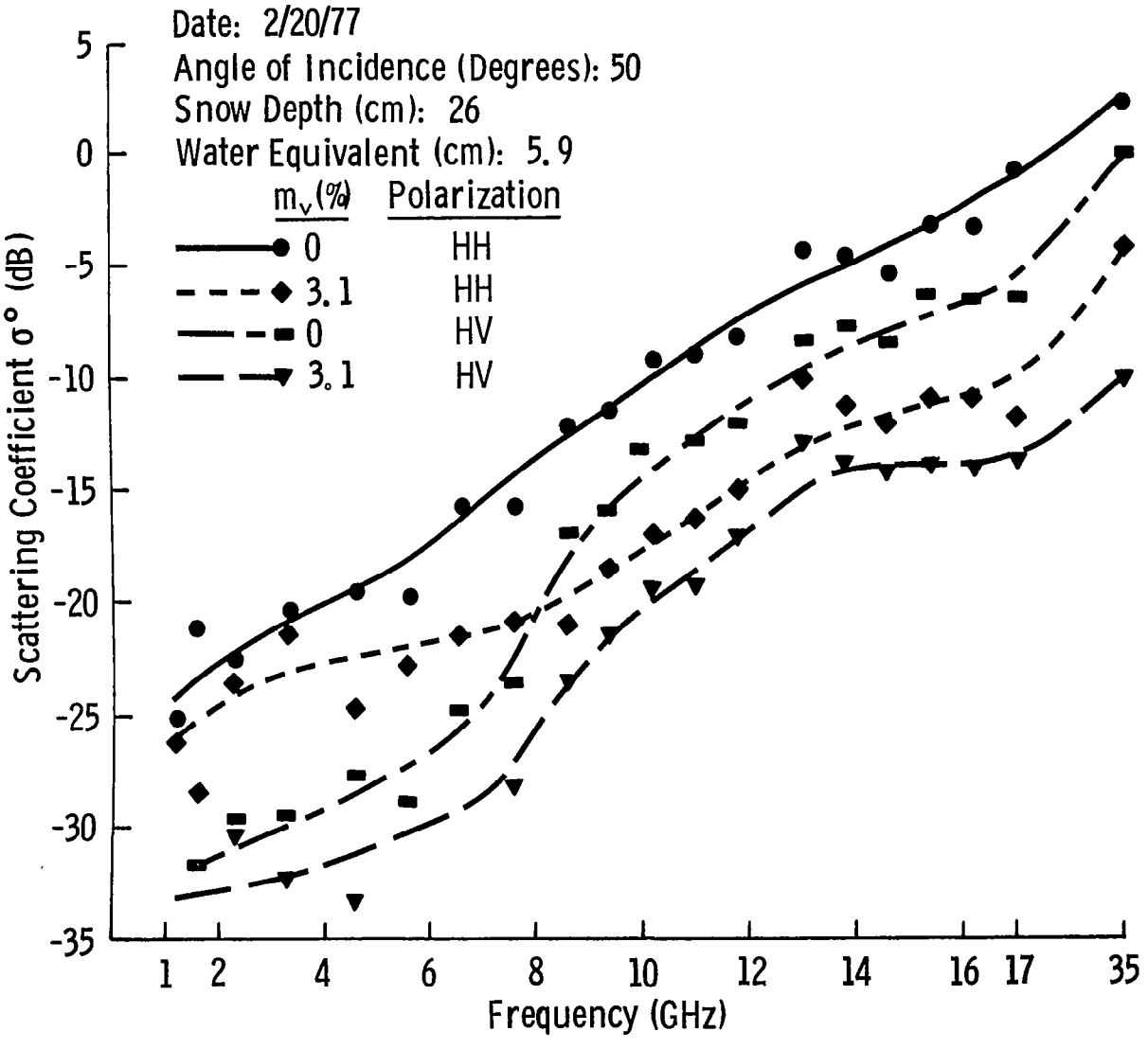


Figure 8-18b Spectral response of σ^o at 50^o angle of incidence for HH and HV polarizations.

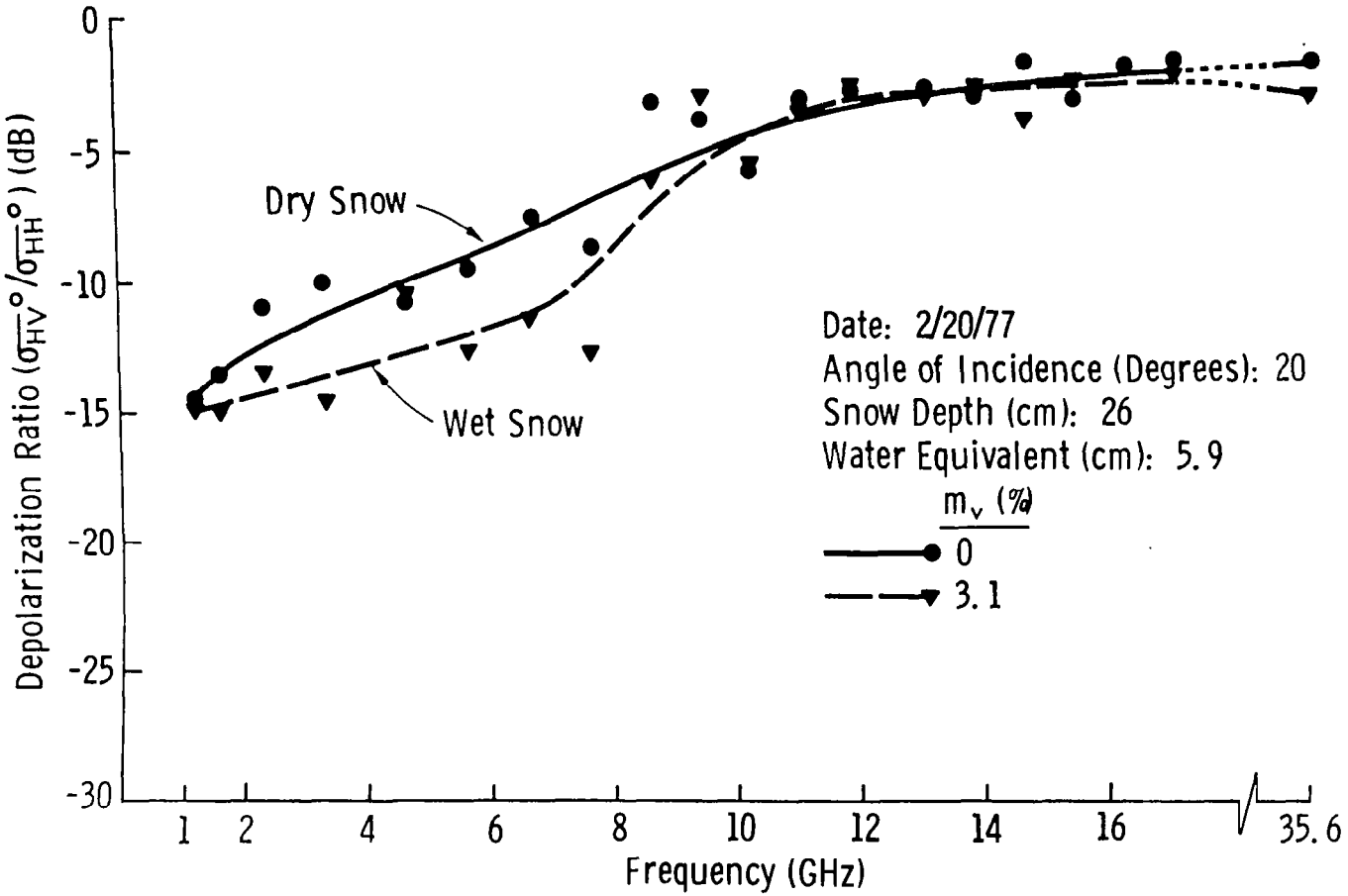


Figure 8-19a Depolarization Ratio of σ° at 20° Angle of Incidence to Wet and Dry Snow

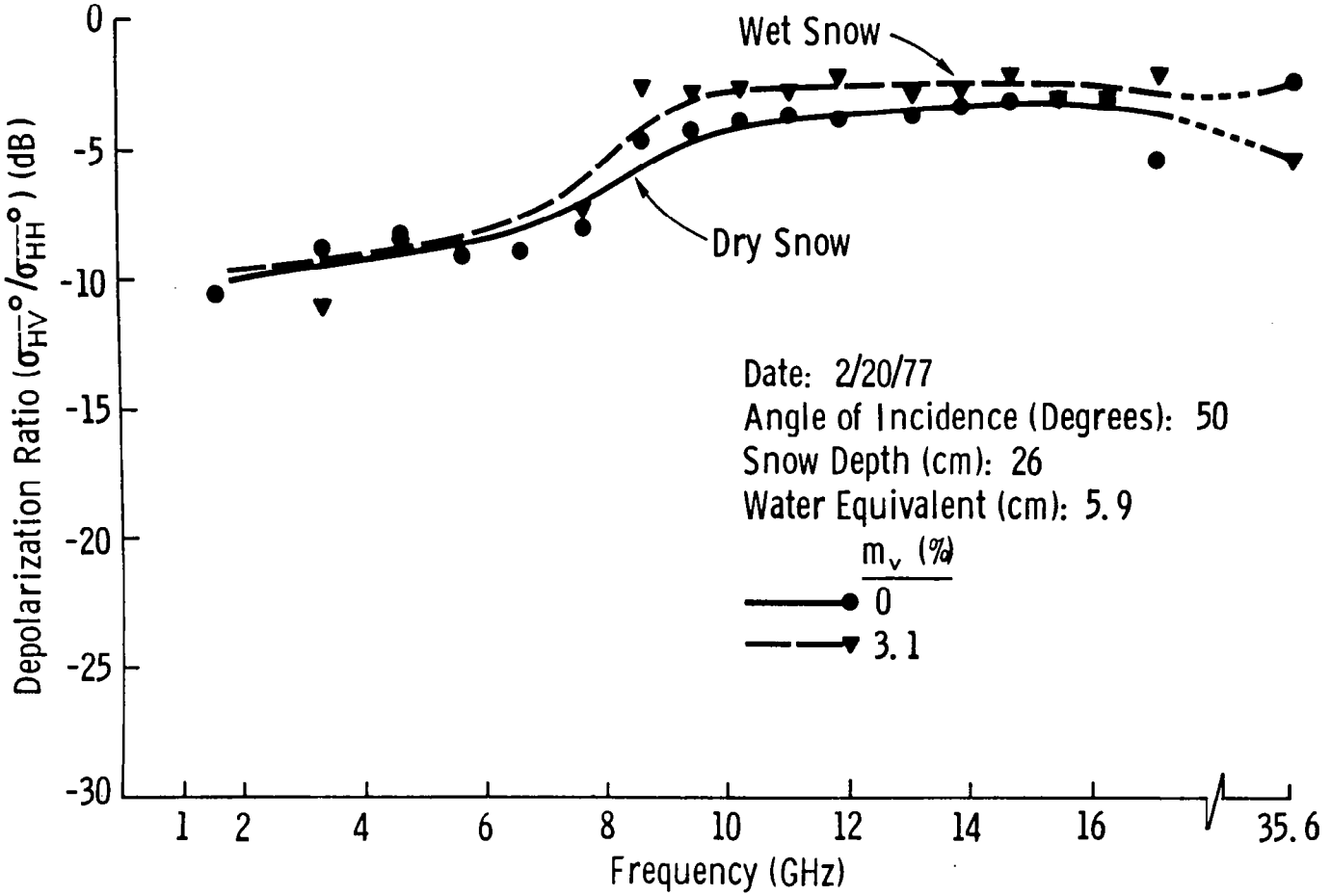


Figure 8-19b Depolarization Ratio of σ^o at 50° Angle of Incidence to Wet and Dry Snow

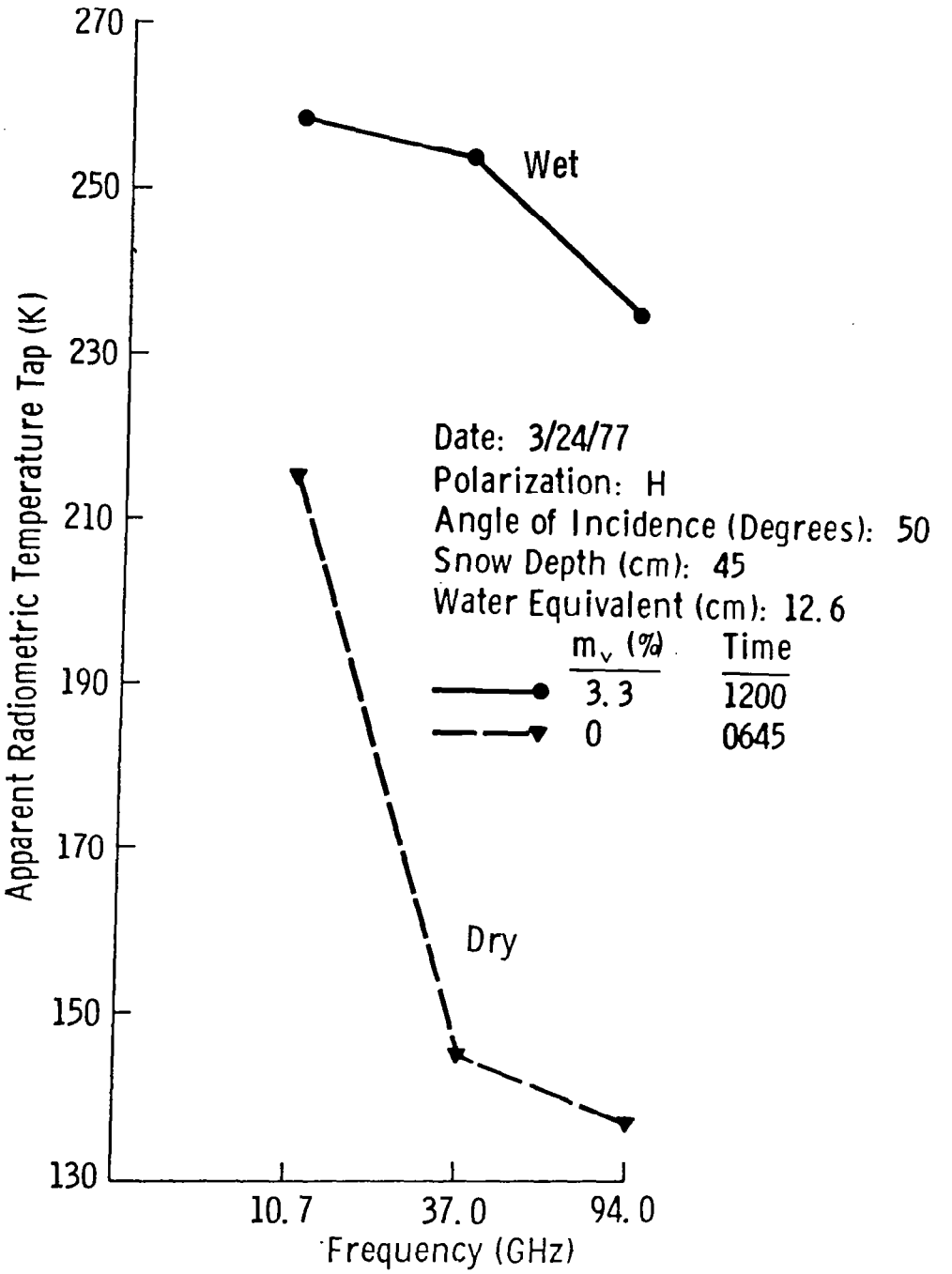


Figure 8-20a Spectral Response of Tap at 50° Angle of Incidence to Wet and Dry Snow

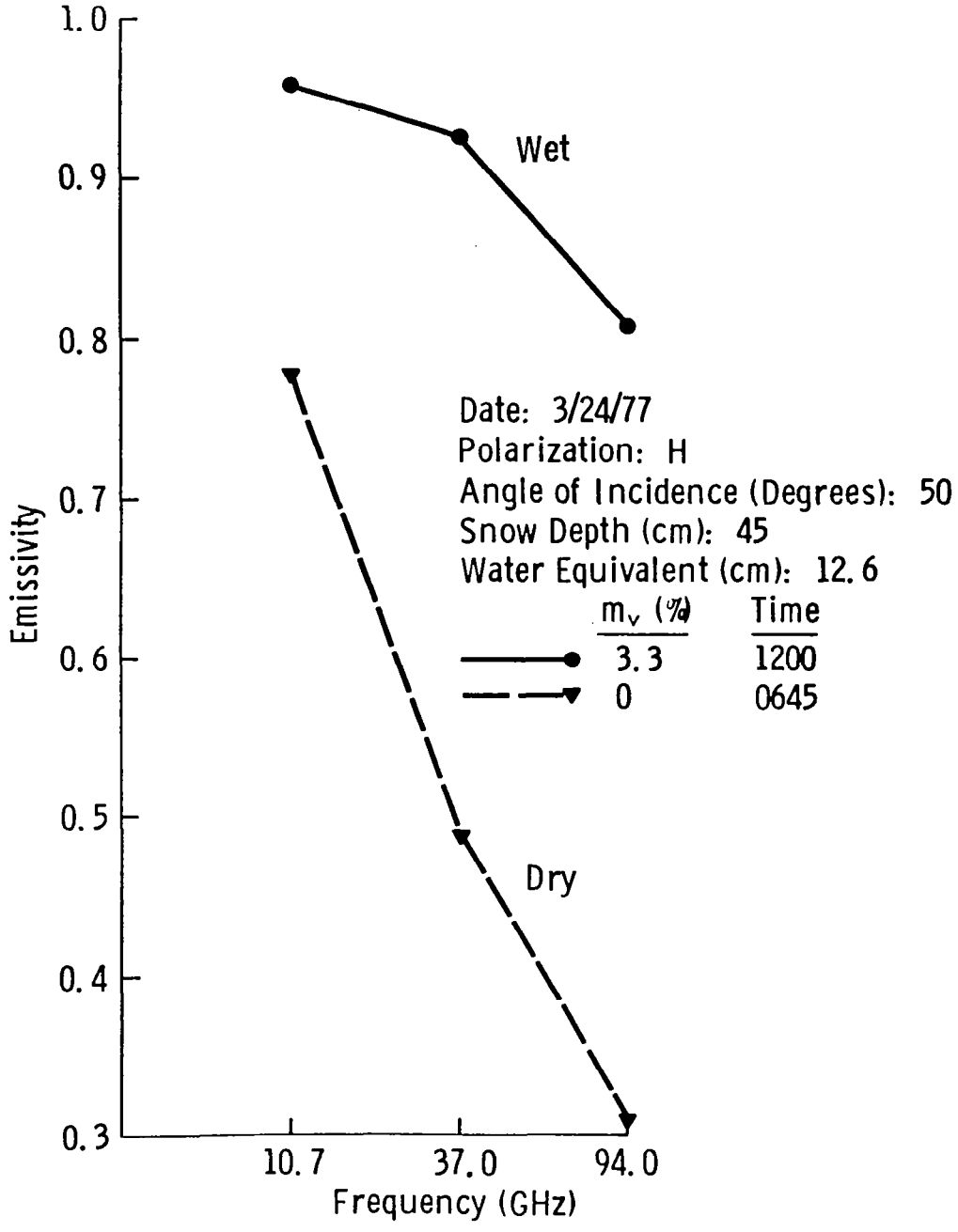


Figure 8-20b Spectral Response of Tap at 50° Angle of Incidence to Wet and Dry Snow

8.2.3 Summary of the Microwave Spectral Response

The additional information concerning the active microwave response to snowpack parameters gained from spectral analyses is:

1) The rate of increase of σ^o with frequency is greater for dry snow than for wet snow at angles away from nadir.
2) The depolarization ratio of σ^o increases with frequency to approximately -2 dB at 35 GHz and 50° indicating a volume scatter mechanism at the higher frequencies.

For the passive case, the following information was gained from the spectral response:

1) The sensitivity of emissivity to snow wetness increases with frequency between 10.69 and 94 GHz.

8.3 Diurnal Response

To investigate the effects of diurnal changes in snowpack conditions on σ^o and T_{ap}, data were obtained over four diurnal periods. Also one diurnal measurement program was conducted during which the microwave sensors observed one resolution cell instead of obtaining spatial averaging. Sections 6.5.2 and 6.5.4 describe these experiments. As stated in those sections, the number of system parameters was decreased to provide better temporal resolution. Table 8-1 gives the microwave and ground truth data acquired during these experiments.

Analysis of the data shows similar qualitative patterns for all of the diurnal experiments. For this reason they will be covered chronologically with detailed analyses being added for later experiments only when new information is ascertained.

8.3.1 Diurnal Experiment of 2/17/77 and 2/18/77

In the first experiment on 2/17/77 and 2/18/77, continuous microwave measurements were obtained with the MAS 8-18/35 and the 10.69 and 37 GHz radiometers. Microwave data were obtained at 5°, 25° and 55° angles of incidence. Continuous ground truth sampling was also performed. Figure 8-21 illustrates the diurnal variations of the incident solar flux, snow wetness and the ground, snow and air temperatures. The snow depth was approximately 30 cm with a water equivalent of 6.3 cm. There were three discernable snow layers when the surface was frozen in a crust while only two layers could be found near midday when the surface had melted. The

TABLE 8-1

Summary of Microwave and Ground Truth Diurnal Data Acquisitions

	2/17 - 2/18	3/3 - 3/4	3/16 - 3/17	3/23	3/24
Active microwave					
MAS 1-8	---	---	I	---	---
MAS 8-18/35	X	X	X	X	X
'assive Microwave					
10.69 GHz	X	X	X	X	X
37 GHz	X	X	---	X	X
94 GHz	---	---	---	X	X
ngles Observed	5^o,25^o,55^o	0^o,20^o,50^o	50^o	50^o,70^o	50^o
round Truth					
Snow Depth	X	X	X	X	X
Snow Density Profile	X	X	X	X	X
Snow Wetness	X	X	X	X	X
Snow Temperature Profile	X	X	X	X	X
Snow Stratification	X	X	X	X	X
Soil Temperature	X	X	X	X	X
Soil Moisture	X	X	X	X	X
Air Temperature	X	X	X	X	X
Barometric Pressure	X	X	X	X	X
Relative Humidity	X	X	X	X	X
Solar Radiation	X	---	X	---	X

otes: X = Data were acquired; --- = Data not acquired; I = Incomplete diurnal data acquisition.

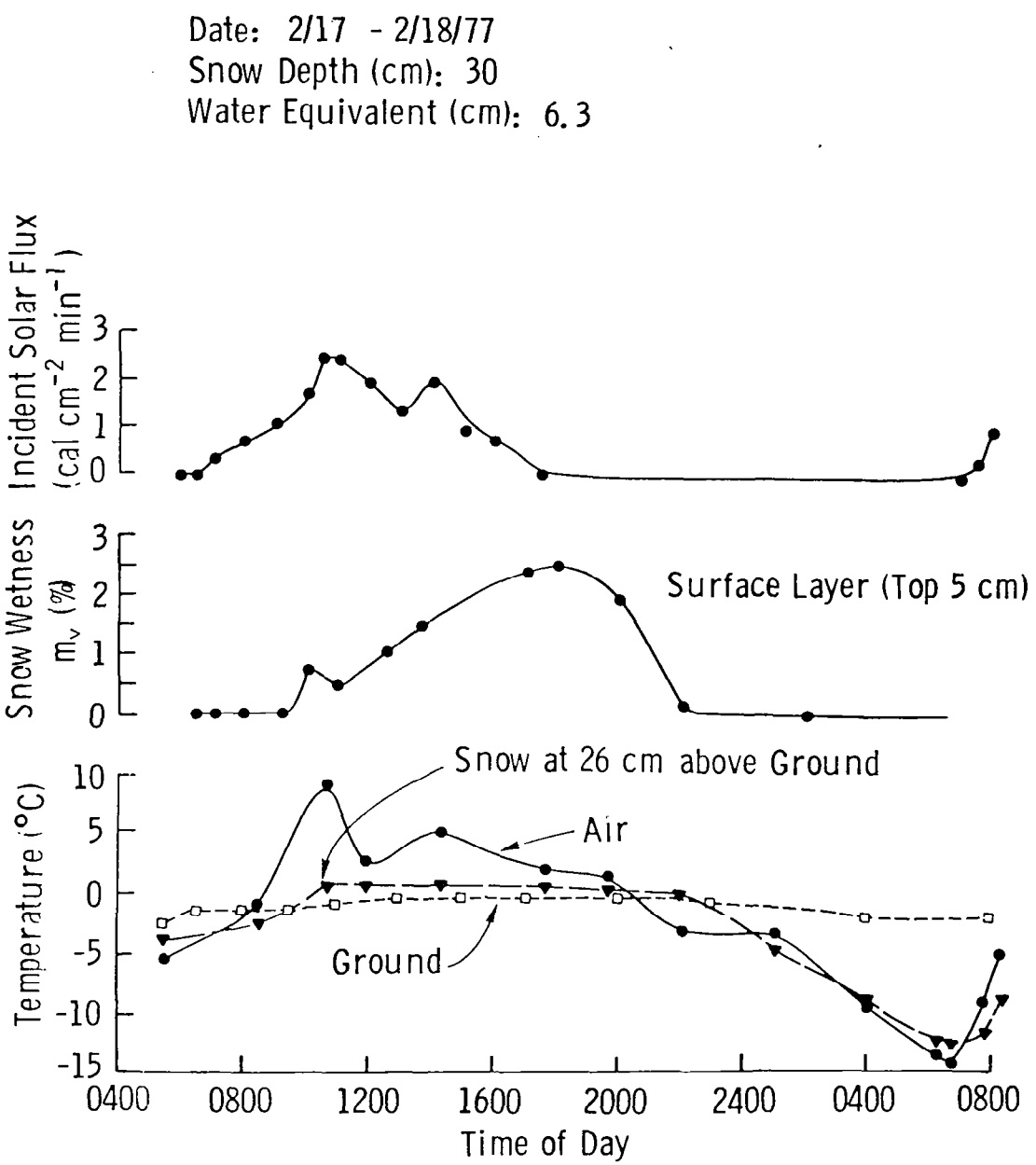


Figure 8-21 Diurnal variation of the supportive ground truth data on 2/17 - 2/18/77. m_v is the volumetric snow wetness of the top 5 cm layer.

sky was generally light overcast. An increase in the overcast around midday is responsible for the observed dip in the incident solar flux (Figure 8-21). The air temperature is observed to lag the solar flux. Temperatures were also obtained at 2 cm intervals within the snowpack. The air temperature exhibited the largest diurnal variation (+9°C to -14°C). The snow temperature at 26 cm was considered representative of the "surface layer" temperature. Since the major heat exchange takes place at the snow-air boundary, the temperature of the snowpack showed increasing response time lag and decreasing sensitivity to the air temperature variation as a function of depth from the snow surface. Consequently, the ground temperature varied only slightly. The ground was in the frozen state throughout this diurnal period. The surface layer snow temperature reached 0° at about 1030 hours and remained near 0°C until 2200 hours by which time the cooler air caused refreezing. As the snow temperature approached 0°C, free water began to appear in the surface layer. Melting generally occurred from the surface down, so the time lag of wetness behind the air temperature is a function of the thickness of the surface layer used in measuring wetness. The time lag of a thinner surface layer would have been smaller as a result of the lower thermal inertia. The dip in snow wetness at 1100 hours (Figure 8-21) may be the result of the drop in air temperature at about the same time or it may be a measurement inaccuracy.

The diurnal response of σ° at 8.6 GHz and 35.6 GHz at three angles of incidence is shown in Figures 8-22a, 8-22b and 8-22c. The behavior of the σ° response is observed to vary inversely with the snow wetness. The magnitude of the change in σ° between the dry and wettest snow conditions is seen to increase with increasing frequency and angle of incidence. At 35 GHz, the σ° difference varies from 4 dB at 5° to 12 dB at 25° and 13 dB at 55°. The change in backscatter coefficient (between wet and dry snow conditions) at 8.6 GHz goes from 2 dB at 5° to 5 dB at 25° and 6 dB at 55°. Also noted is the slight time shift between the σ° and snow wetness values. This time shift will be discussed in Section 8.4 in more detail; it is attributed to the difference between the microwave sensor penetration depth and the snow wetness measurement depth. The smaller penetration depth for the 35.6 GHz frequency has the effect of allowing σ° to vary more rapidly than the σ° value at 8.6 GHz.

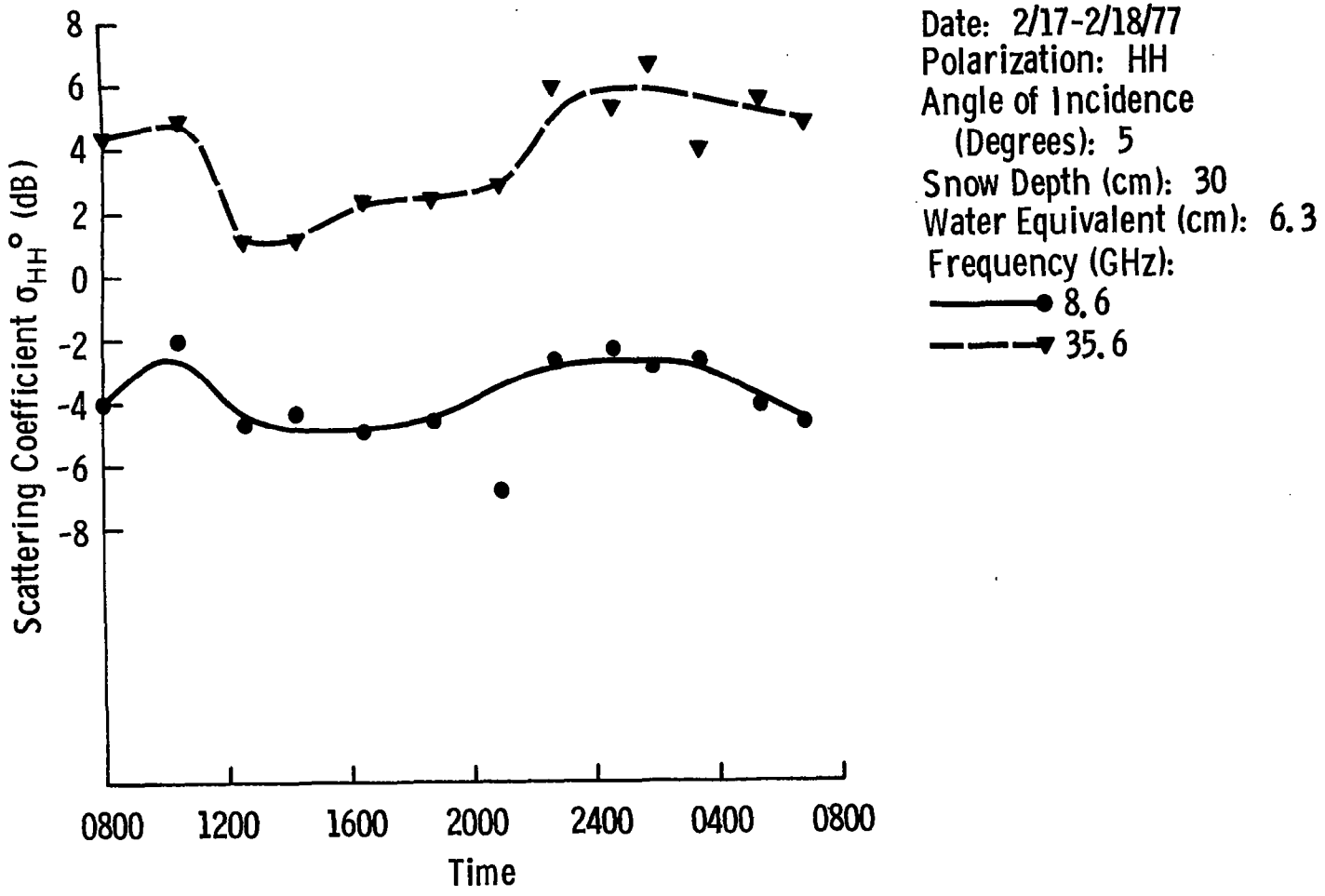


Figure 8-22a Diurnal variation of σ^{o} at 8.6 and 35.6 GHz at 5^{o} angle of incidence.

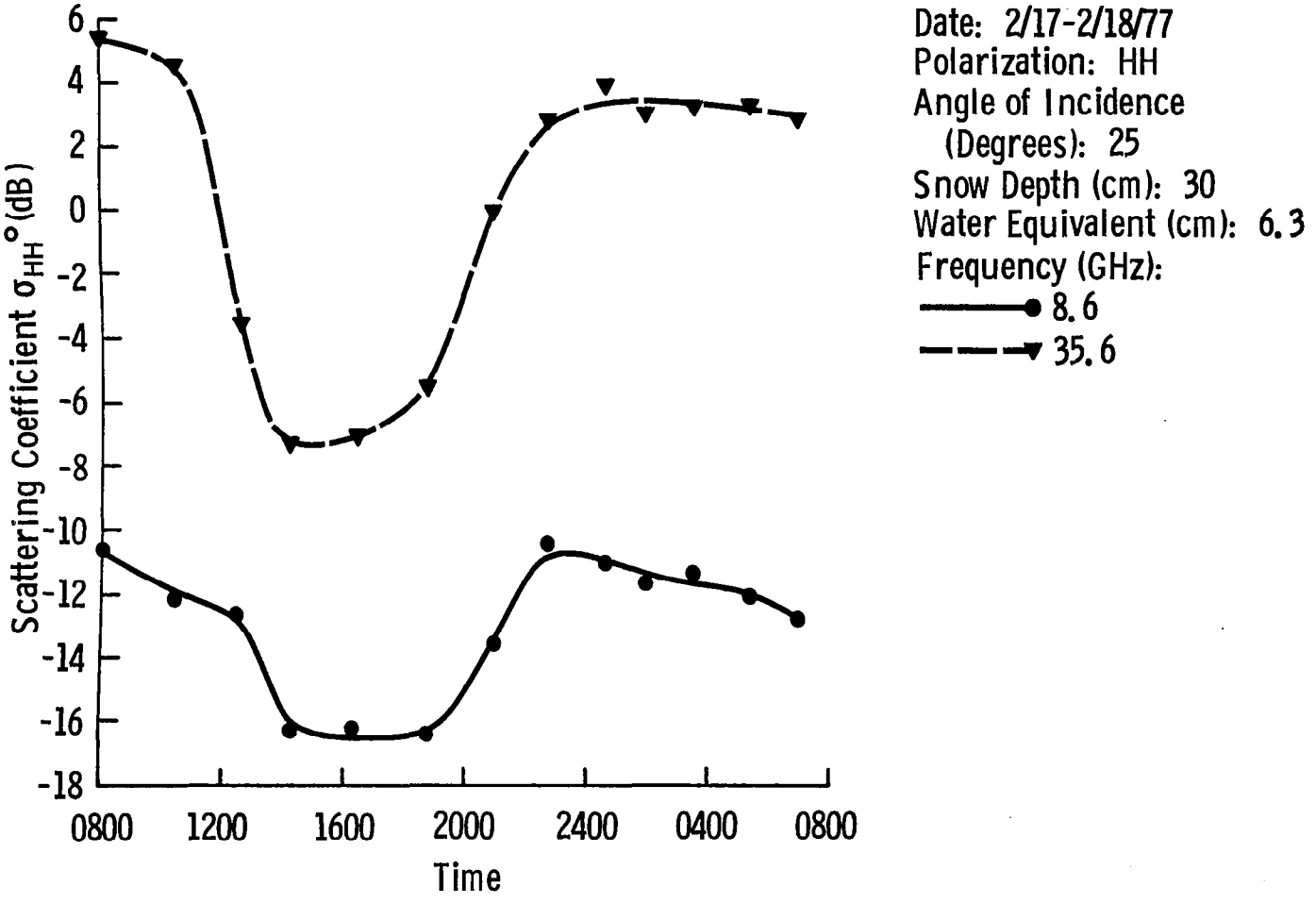


Figure 8-22b Diurnal variation of σ° at 8.6 and 35.6 GHz at 25° angle of incidence.

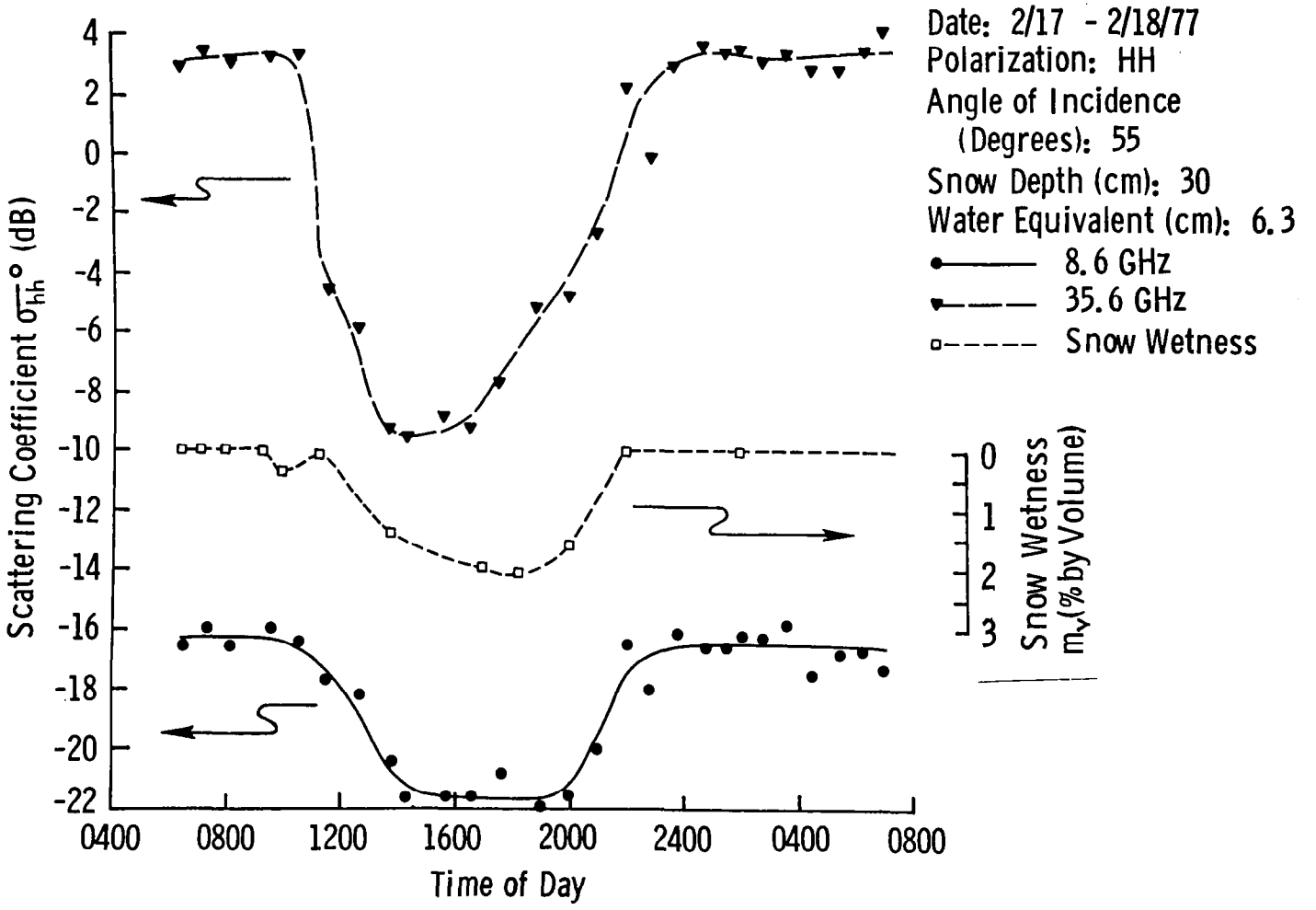


Figure 8-22c Diurnal variation of snow wetness and σ° at 8.6 and 35.6 GHz. (Note that snow wetness scale has been reversed for ease of comparison with σ°.)

The faster rate of change of σ^o upon melting and freezing is most noticeable at 55° which is attributed to a smaller vertical penetration depth than the lower angles. In this case, only a thin surface layer is affecting the response at 35.6 GHz.

The passive data are given in Figures 8-23a, 8-23b and 8-23c. The T_{ap} response varies directly with wetness for all angles of incidence for the 37 GHz radiometer. The T_{ap} response at 10.69 GHz is also in general directly related to wetness; however, this cannot be discerned from the small variations of the 5° and 25° data. Over this diurnal experiment, the variation of T_{ap} at 10.69 GHz increased from a small value at 5° to about 25 K at 55°. The response at 37 GHz, on the other hand, shows a large sensitivity to snow wetness at all angles. The variation between the wet and dry conditions increases slightly with angle from 76 K at 5° to 80K at 25° and 90 K at 55°. A similar time shift (as with the active data) is observed between T_{ap} and measured samples of snow wetness. The midday decrease in the 10.69 GHz curve appears to be related to the dip in solar flux. It may also be in response to very wet snow conditions similar to those observed by Hofer and Mätzler (Figure 5-45). The rapid response of T_{ap} at 37 GHz to snow wetness indicates that this sensor is responding to a very thin surface layer. The trends of T_{ap} at both frequencies after 2200 hours and after the snow had refrozen result from thermometric temperature changes. The snow temperature near the surface follows closely the air temperature (Figure 8-21) while deeper within the snowpack the temperature change is much smaller. This fact explains the decrease in T_{ap} at 37 GHz since it responds to a thin surface layer while the 10.69 GHz T_{ap}, which remains approximately constant after 2200 hours, is responding to contributions from the whole snowpack for which the average temperature changes only slightly.

8.3.2 Diurnal Experiment on 3/3/77 and 3/4/77

The second diurnal experiment was performed on 3/3/77 to 3/4/77. Figure 8-24 gives the applicable ground truth for these dates. The snow depth was 48 cm, hence the 47 cm temperature measurement is used to characterize the surface temperature. Snowfall since 2/18/77 had increased the water equivalent to 10.5 cm. The sky was slightly overcast and light snow fell until about 1200 hours after which the sky cleared. During this diurnal observation, the air temperature was above freezing

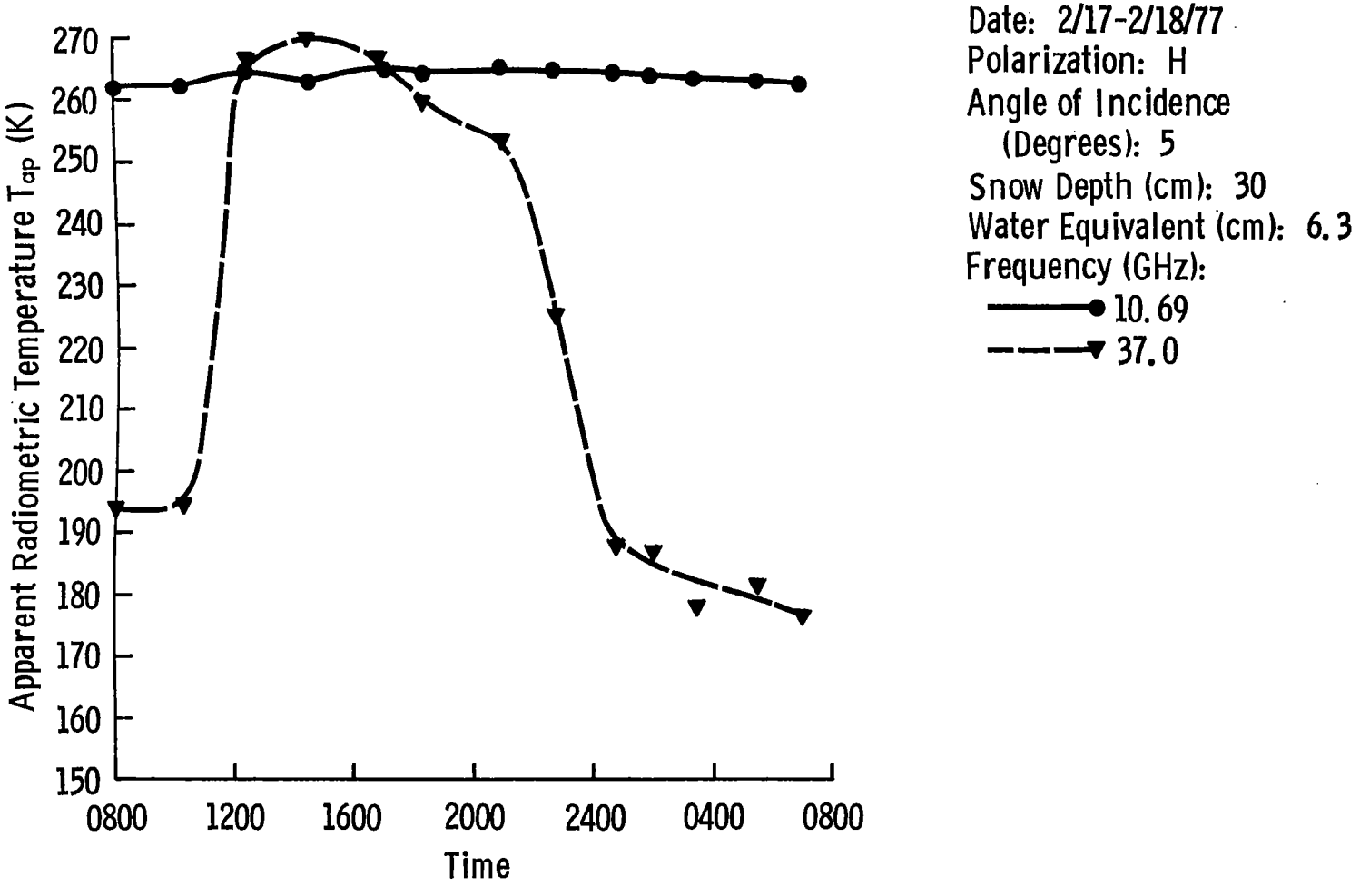
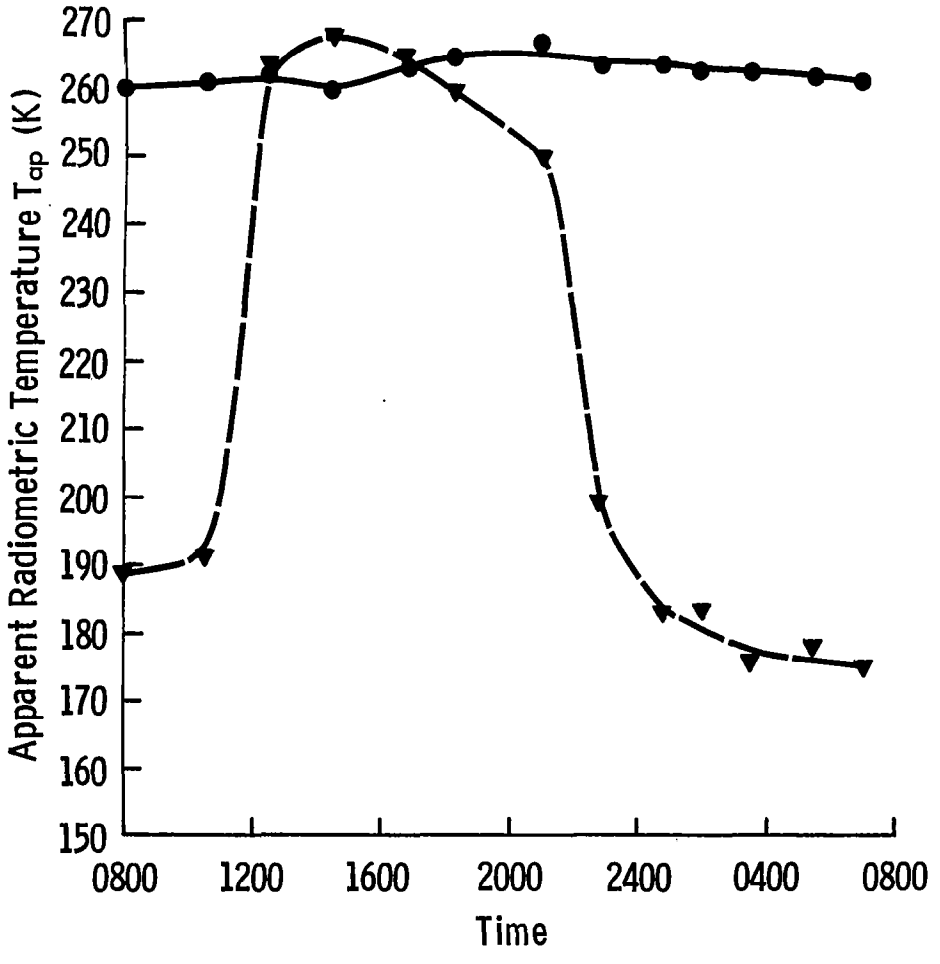


Figure 8-23a Diurnal variation of T_{ap} at 10.69 and 37 GHz at 5^{o} angle of incidence.



Date: 2/17-2/18/77
Polarization: H
Angle of Incidence
(Degrees): 25
Snow Depth (cm): 30
Water Equivalent (cm): 6.3
Frequency (GHz):
10.69
37.0

Figure 8-23b Diurnal variation of T_{ap} at 10.69 and 37 GHz at 25° angle of incidence.

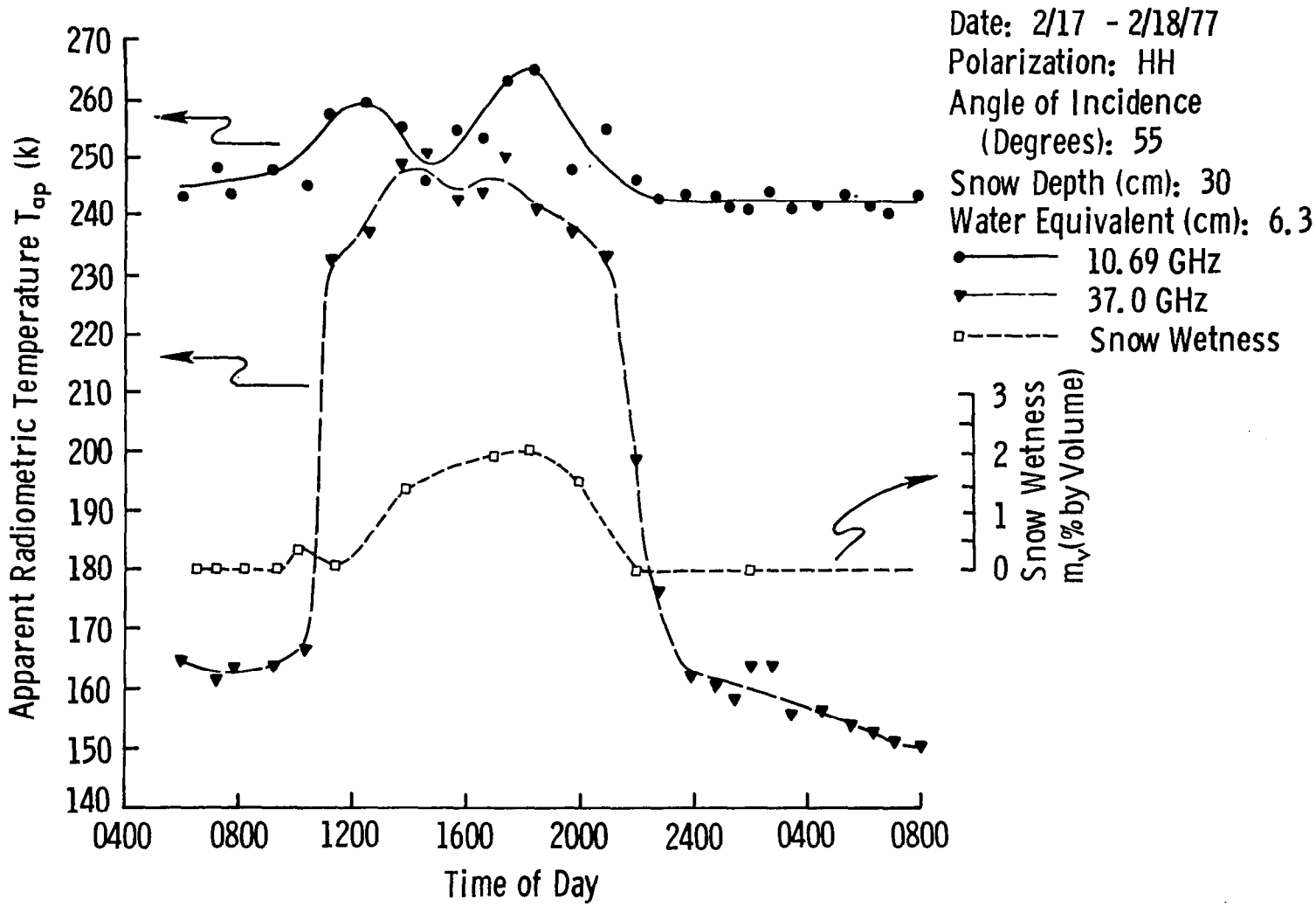


Figure 8-23c Diurnal variation of snow wetness and T_{ap} at 10.69 and 37.0 GHz.

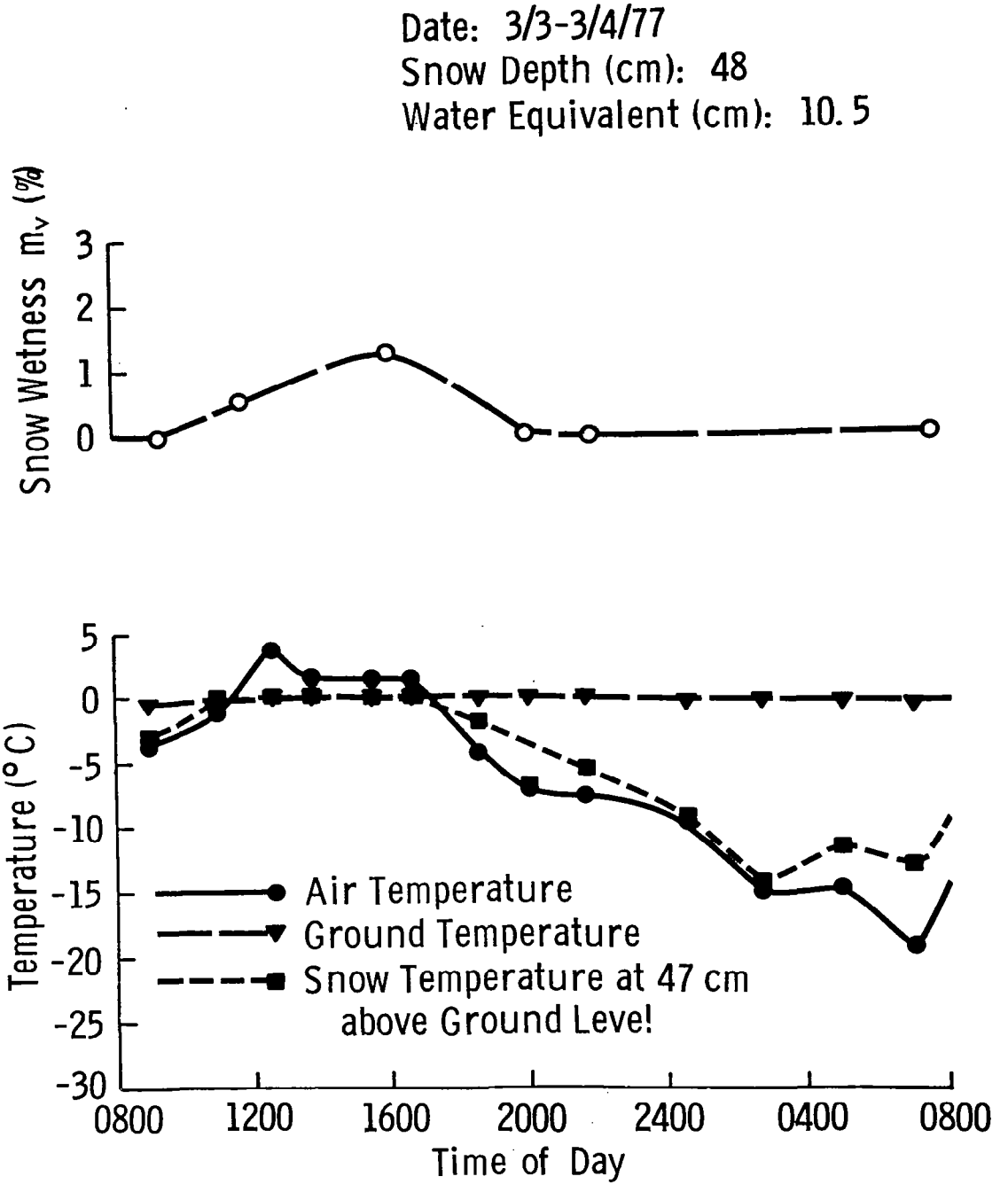


Figure 8-24 Diurnal Variation of Ground Truth Data on 3/3 - 3/4/77. m_v is Volumetric Snow Wetness of the Top 5cm Snow Layer.

for only about four hours. The surface wetness was therefore less than was observed on 2/17/77 and the ground layer was semi-frozen. Ice crystals were observed in the soil samples but the samples were not hard frozen. The time lag of snow wetness in the upper 5 cm layer with respect to the surface snow temperature during the refreezing cycle was observed to be about two hours.

The σ^o diurnal variation is illustrated in Figures 8-25a, 8-25b and 8-25c for five frequencies between 1.2 GHz and 35.6 GHz. Similar to the first diurnal, away from nadir the shape of the σ^o response is the inverse of the snow wetness response. The exception at 20° for 1.2 GHz is attributed to the larger ground contribution at the lower frequency. Since the sensitivity to soil wetness is direct and the sensitivity to snow wetness is inverse, these effects tend to cancel each other at lower frequencies. At 0° (nadir) the diurnal variation in σ^o is observed to dip at 1730 hours above 8.6 GHz; while below 8.6 GHz, no dip is apparent. This dip, however, occurs two hours later than the dip observed at 20° and 50° in response to wetness. Hence, its cause is not understood. As was observed before, there does seem to be a time shift between the σ^o and m_v diurnal behavior. The magnitude of the observed dip between 1200 and 2000 hours at 20° increases with frequency from 0 dB at 1.2 GHz to about 12 dB at 35 GHz. An analogous but more pronounced response to snow wetness is observed at 50° angle of incidence.

The passive data for the 3/3/77 to 3/4/77 diurnal experiment are given in Figures 8-26a, 8-26b and 8-26c. The T_{ap} response follows the same general pattern as the 2/17/77 diurnal; however, the direct response of T_{ap} at 10.69 GHz to snow wetness is more apparent. A slight increase in sensitivity to wetness with increasing angle of incidence is also observed. At 37 GHz, an increase of about 100 K to 120 K is observed between dry and wet snow conditions at all angles, which is comparable to the increase observed for the previous diurnal experiment although the change in wetness is only half as great.

8.3.3 Diurnal Experiment on 3/16/77 and 3/17/77

The third experiment was conducted from 3/16/77 to 3/17/77. Better time resolution was achieved by concentration on one angle of incidence, 50°. Unfortunately, system problems were encountered with the MAS 1-8

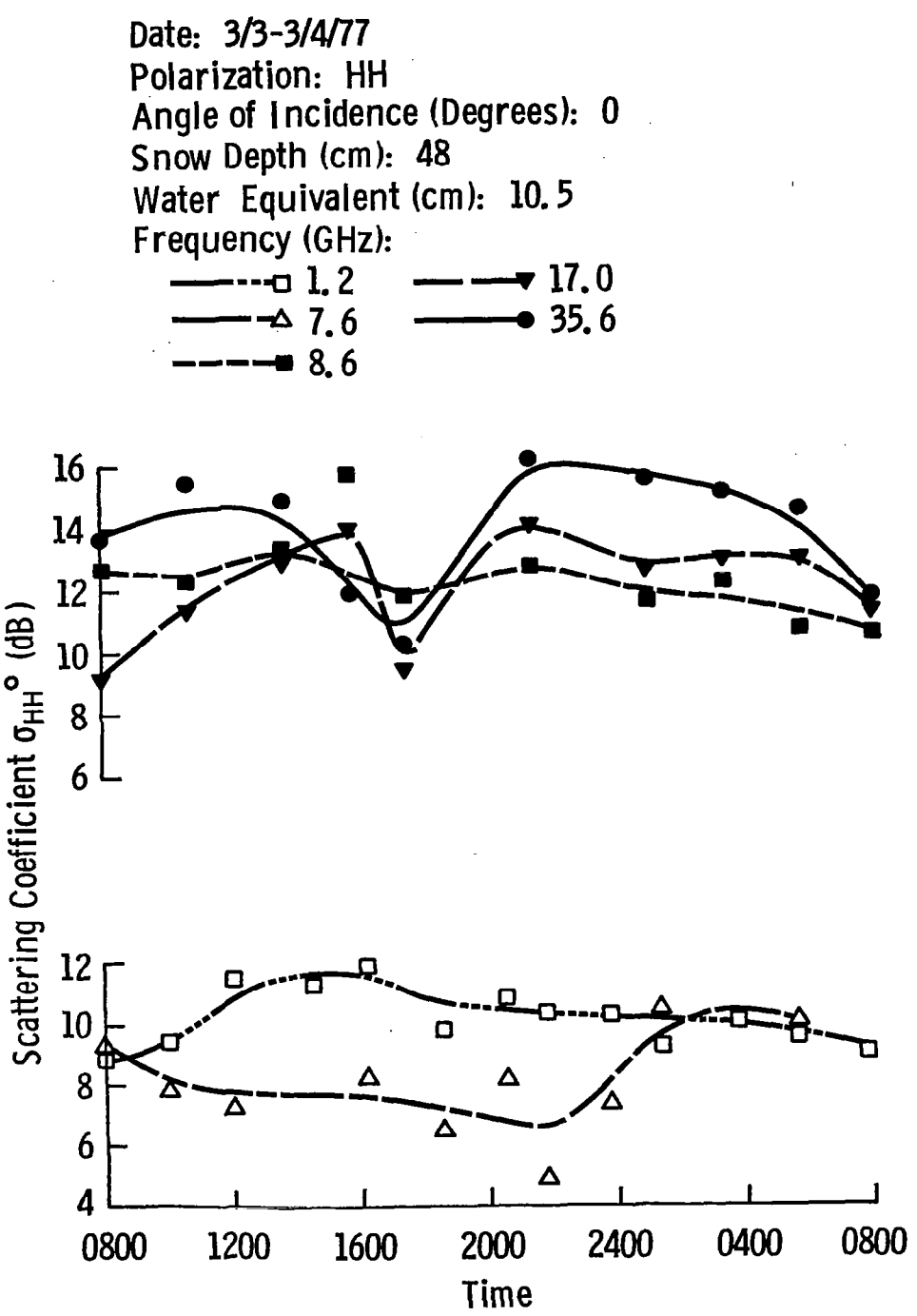


Figure 8-25a Diurnal variation of σ° between 1 and 35 GHz at 0° (nadir).

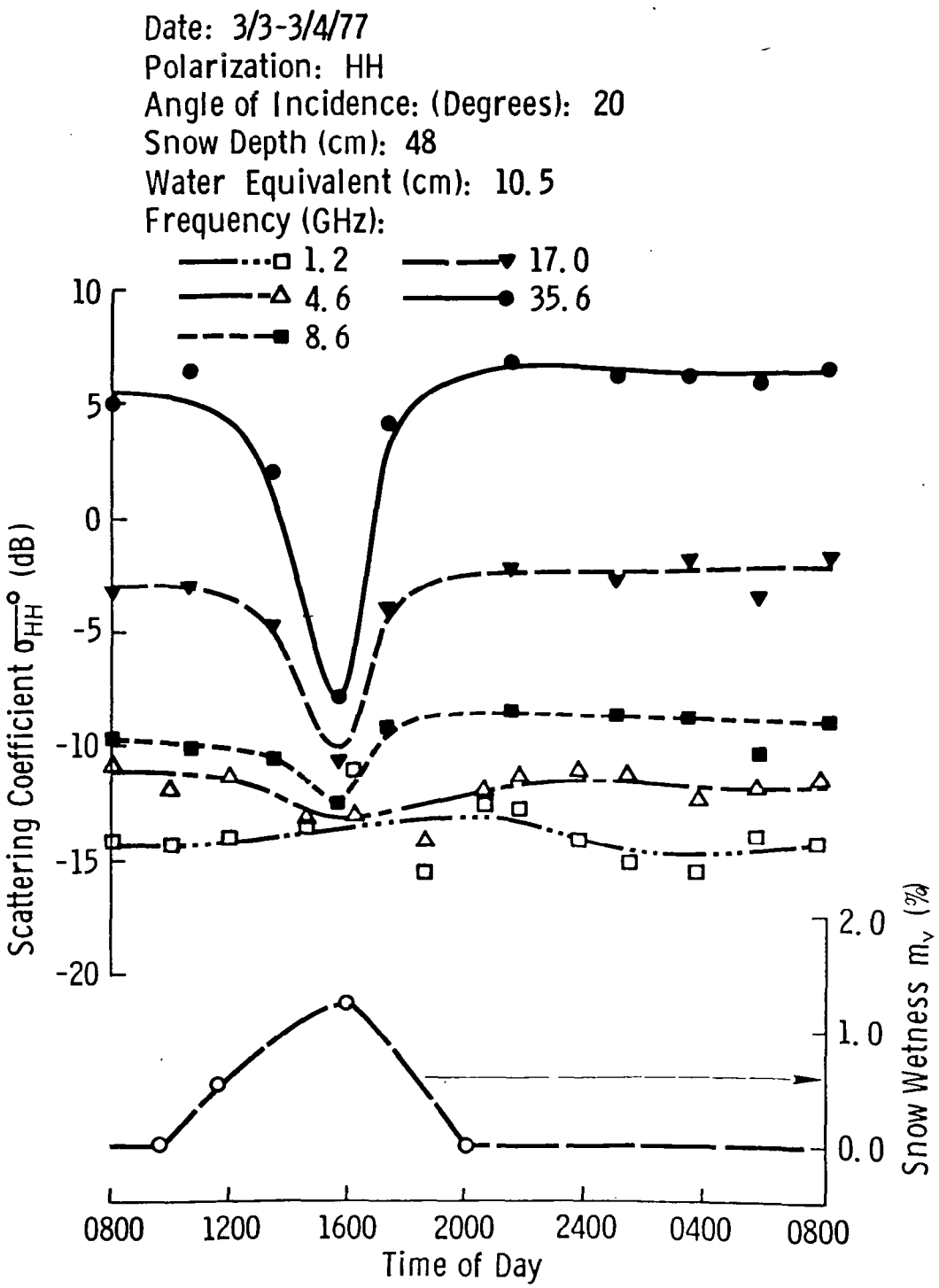


Figure 8-25b Diurnal Variation of Snow Wetness and σ° Between 1 and 35 GHz at 20° Angle of Incidence

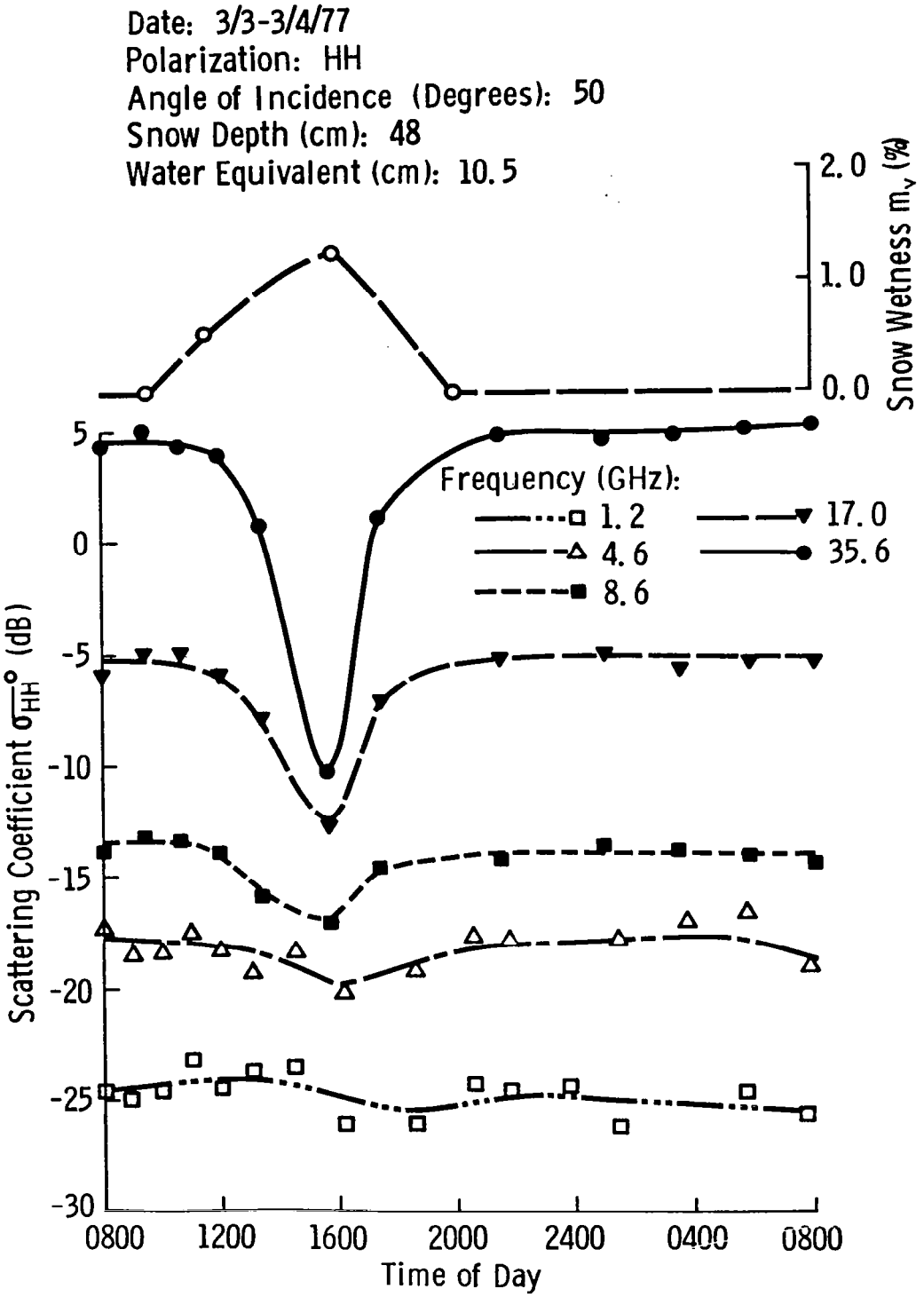


Figure 8-25c Diurnal Variation of Snow Wetness and σ° Between 1 and 35 GHz at 50° Angle of Incidence

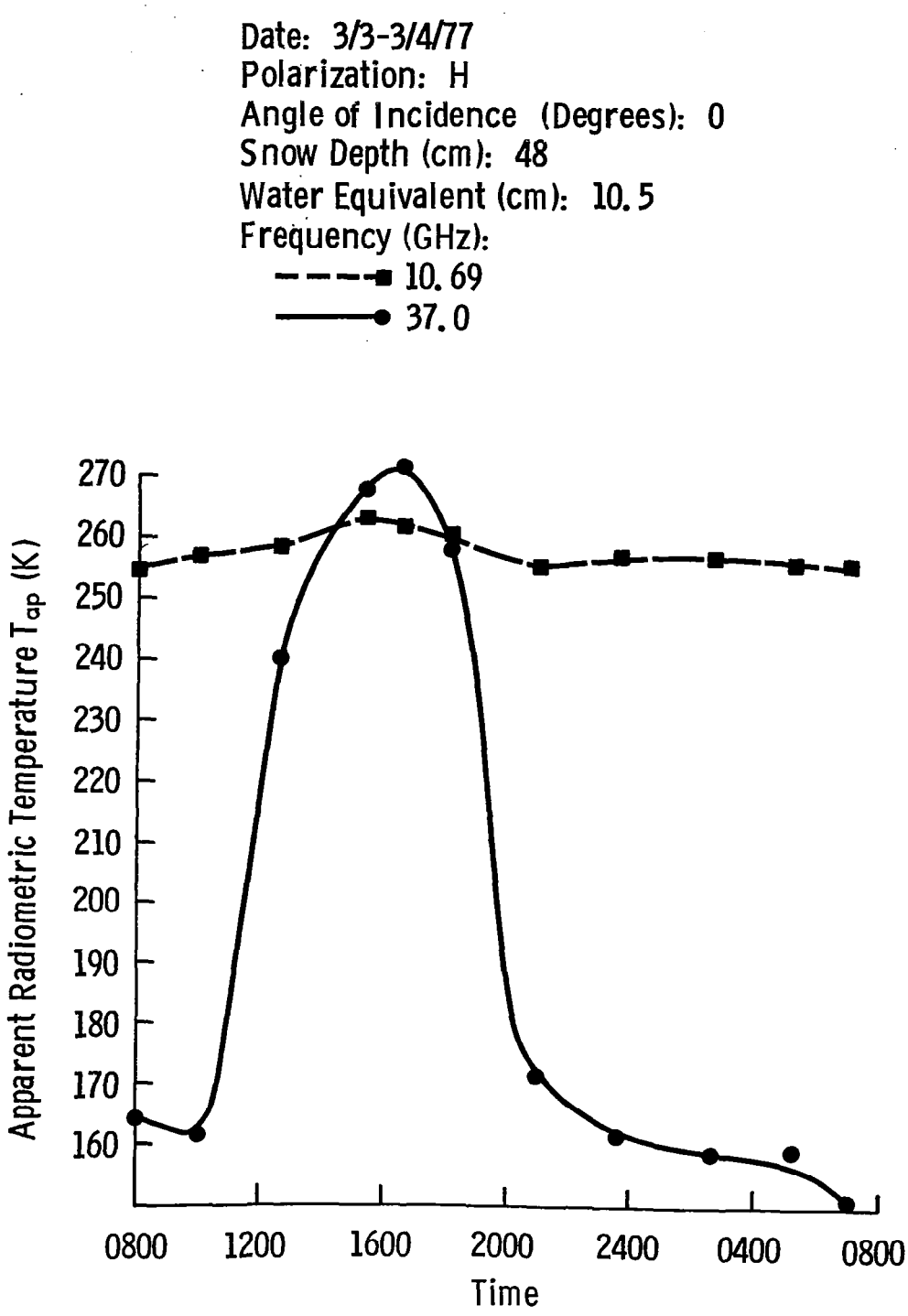


Figure 8-26a Diurnal variation of T_{ap} at 10.69 and 37 GHz at 0° (nadir).

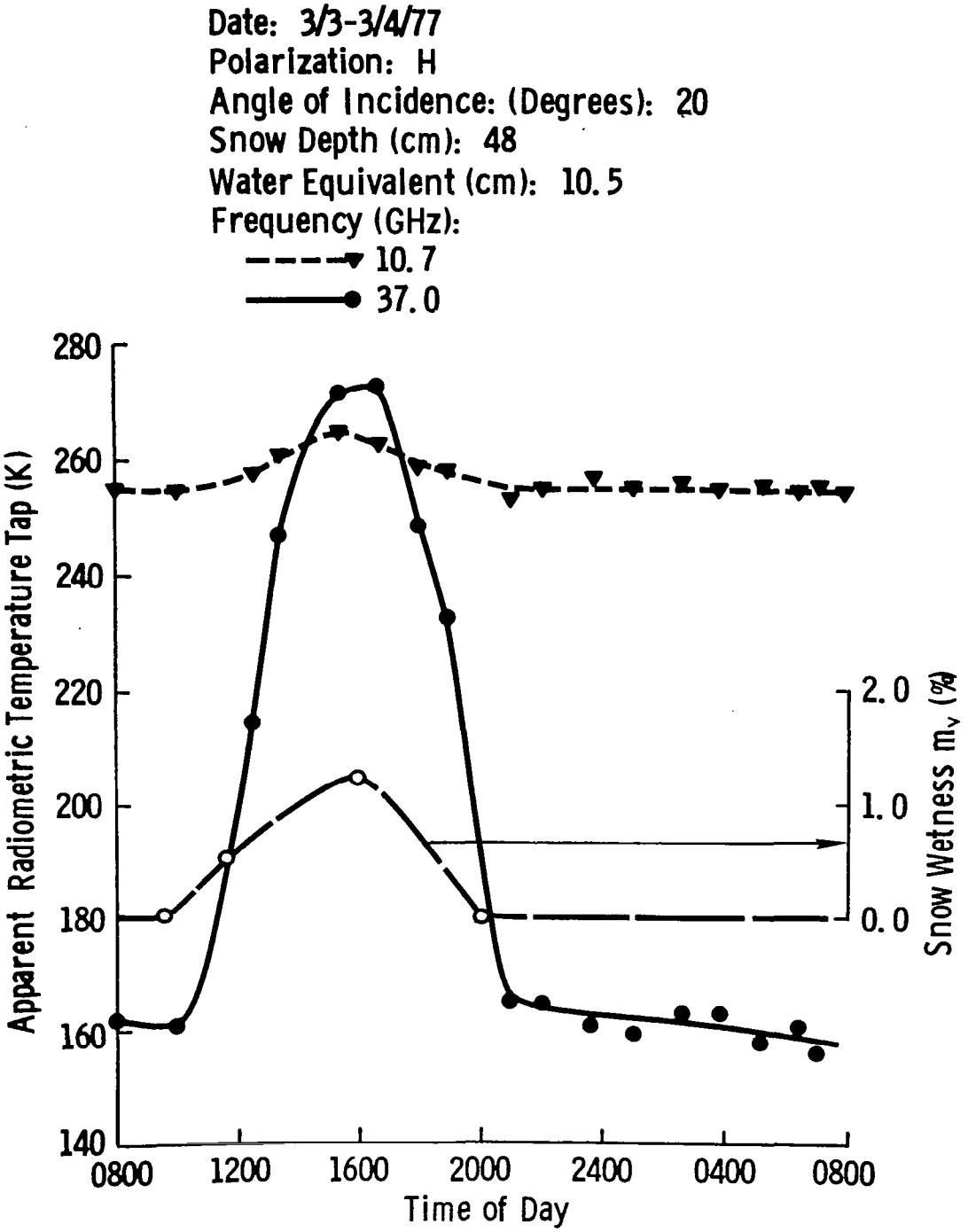


Figure 8-26b Diurnal Variation of Snow Wetness and Tap at 20° Angle of Incidence

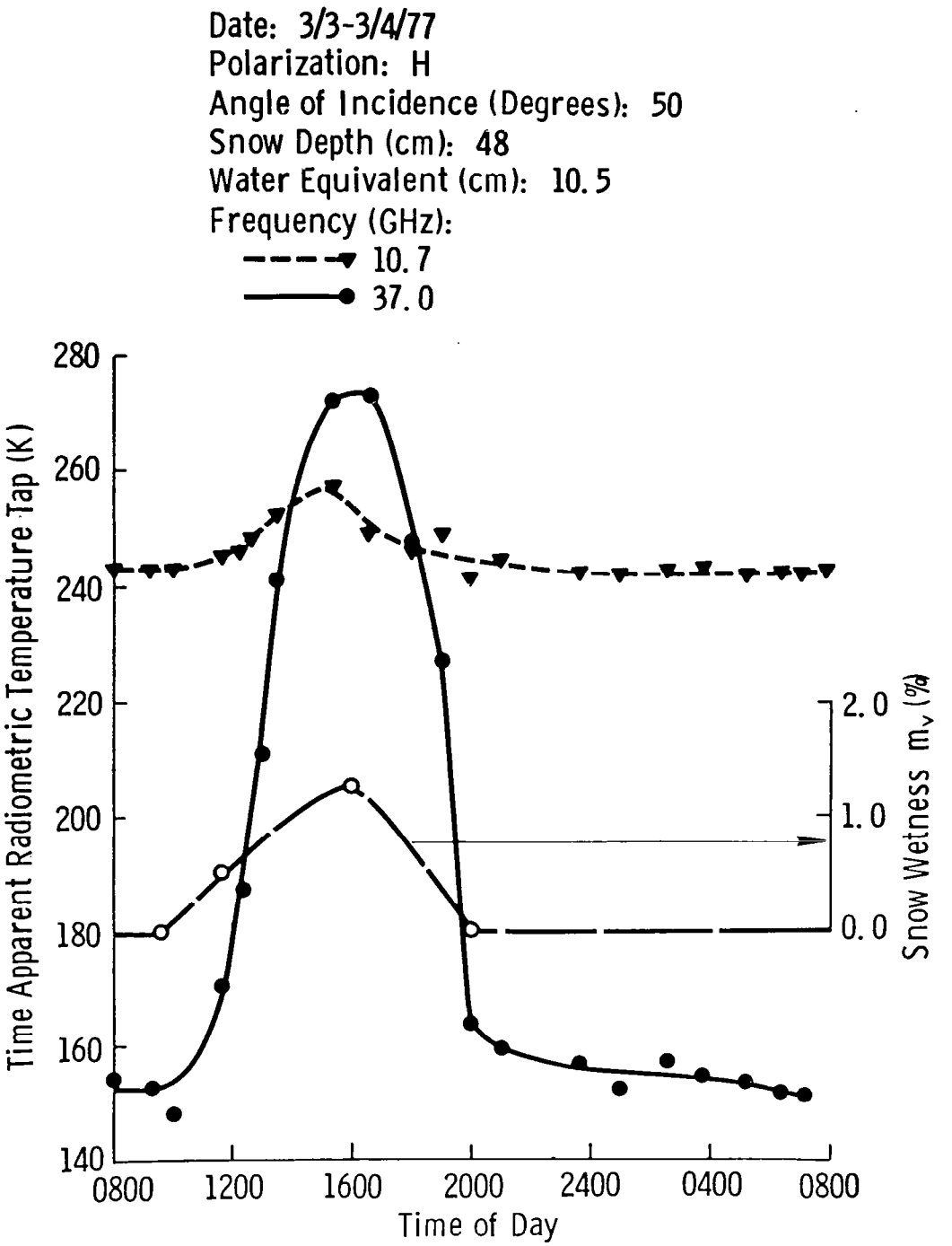


Figure 8-26c Diurnal Variation of Snow Wetness and Tap at 50° Angle of Incidence

during the snow melt phase and the 37 GHz radiometer was not operational. The snow depth was 45 cm with an increase in water equivalent over the previous diurnals to 13.5 cm. Other ground truth parameters are furnished in Figure 8-27, where the wetness is shown for two snow layers.

The σ^o diurnal variation is shown in Figures 8-28a, 8-28b and 8-28c. The very slow temperature change upon refreezing resulted in a slower response of σ^o at all frequencies than was observed in the previous diurnal experiments. Figures 8-28a and 8-28b give the HH polarization response at seven frequencies. The increase in sensitivity to snow wetness is obvious with increasing frequency. Also noticed is the decreasing time required to reach the frozen equilibrium state with increasing frequency. This behavior is attributed to the decreasing thickness of the surface layer affecting the σ^o response with higher frequencies; the smaller the thickness of a surface snow layer, the faster can its wetness respond to air temperature variations. Further discussion of this subject is provided in Section 8.4.1.

The circularly polarized σ^o behavior and depolarization ratio ($\sigma^o_{RR}/\sigma^o_{RL}$) are given in Figure 8-28c. An increase in sensitivity to wetness is apparent for the cross polarization component (RR polarization). Wet snow is observed to be a weak depolarizer as opposed to dry snow which is a strong depolarizing medium, especially at the higher frequencies. Also the HH and RL σ^o response shapes are seen to be similar.

T_{ap} at 10.69 GHz is shown in Figure 8-29. The 35 K magnitude response results from snow wetness values that were higher than the first two diurnal experiment values.

8.3.4 Diurnal Experiment on 3/24/77

The last diurnal experiment was performed on 3/24/77. Only sixteen hours were covered by the measurements with the MAS 8-18/35 and the radiometers. The diurnal variation of ground truth parameters is shown in Figure 8-30 while the active and passive data are given in Figures 8-31 and 8-32, respectively. The σ^o behavior is similar to the other diurnals. The hump in the midday response is related to the dip in wetness; however, the time offset is again observed. Although the snow wetness measurements were obtained for only the surface layer (Figure 8-30), the temperature profile information indicated that the snow deeper within the snowpack remained wet after the surface layer had refrozen. The σ^o values confirm that the lower layers were wet.

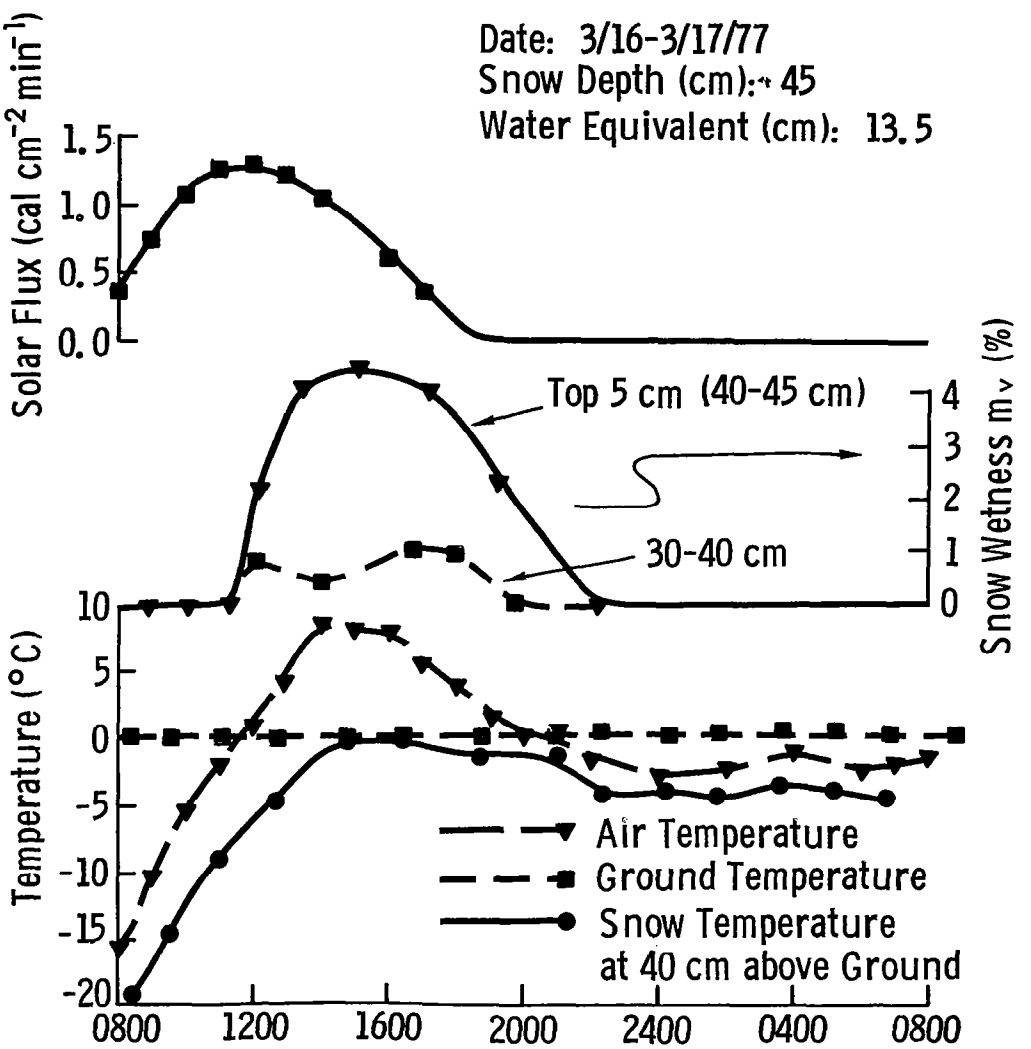


Figure 8-27 Diurnal variation of ground truth data on 3/16 - 3/17/77. m_v is volumetric snow wetness of the top 5 cm layer.

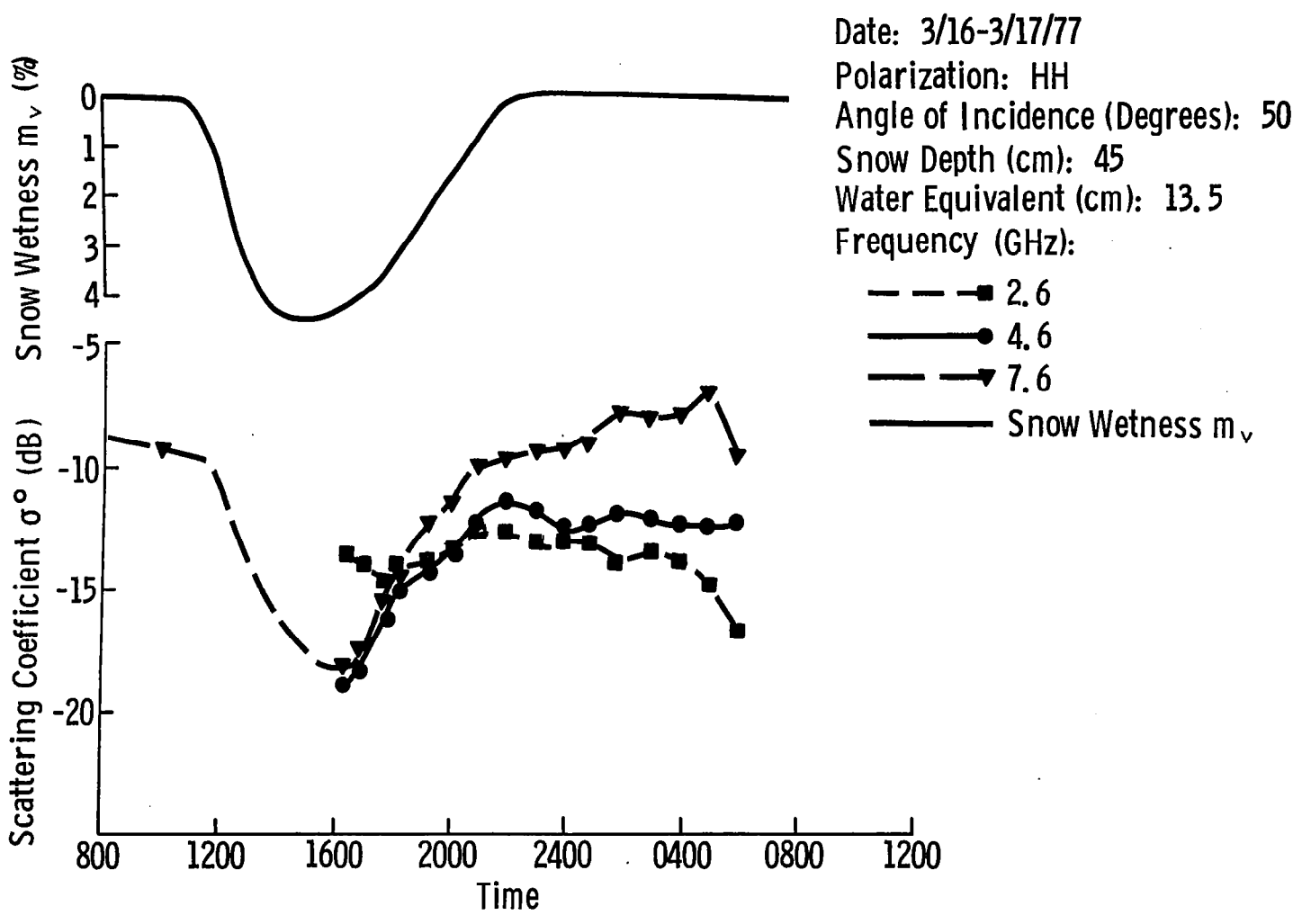


Figure 8-28a Diurnal variation of snow wetness and σ^o at 2.6, 4.6 and 7.6 GHz at 50^o angle of incidence.

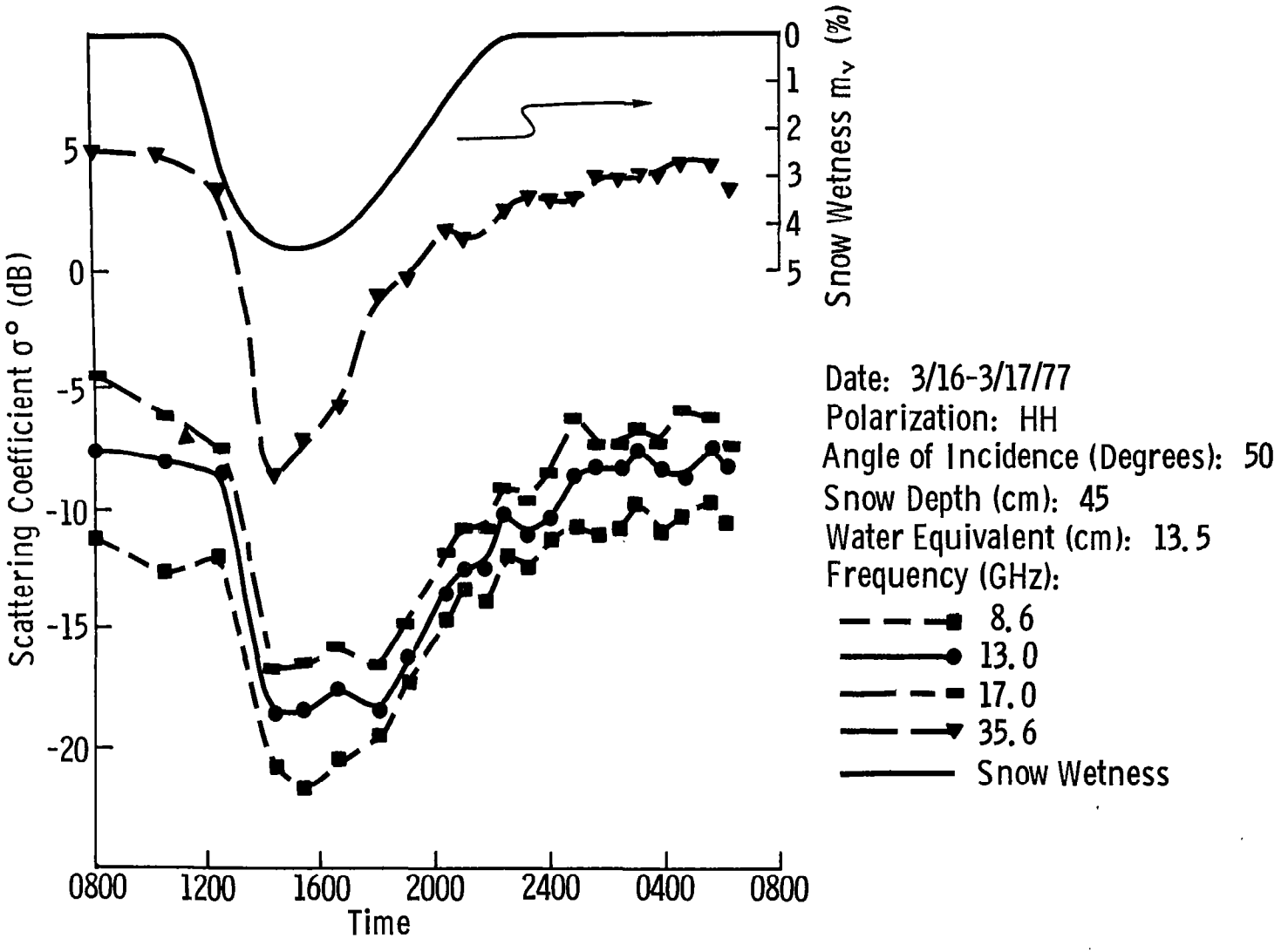


Figure 8-28b Diurnal variation of snow wetness and σ^{o} at 8.6, 13.0, 17.0 and 35.6 GHz at 50^{o} angle of incidence.

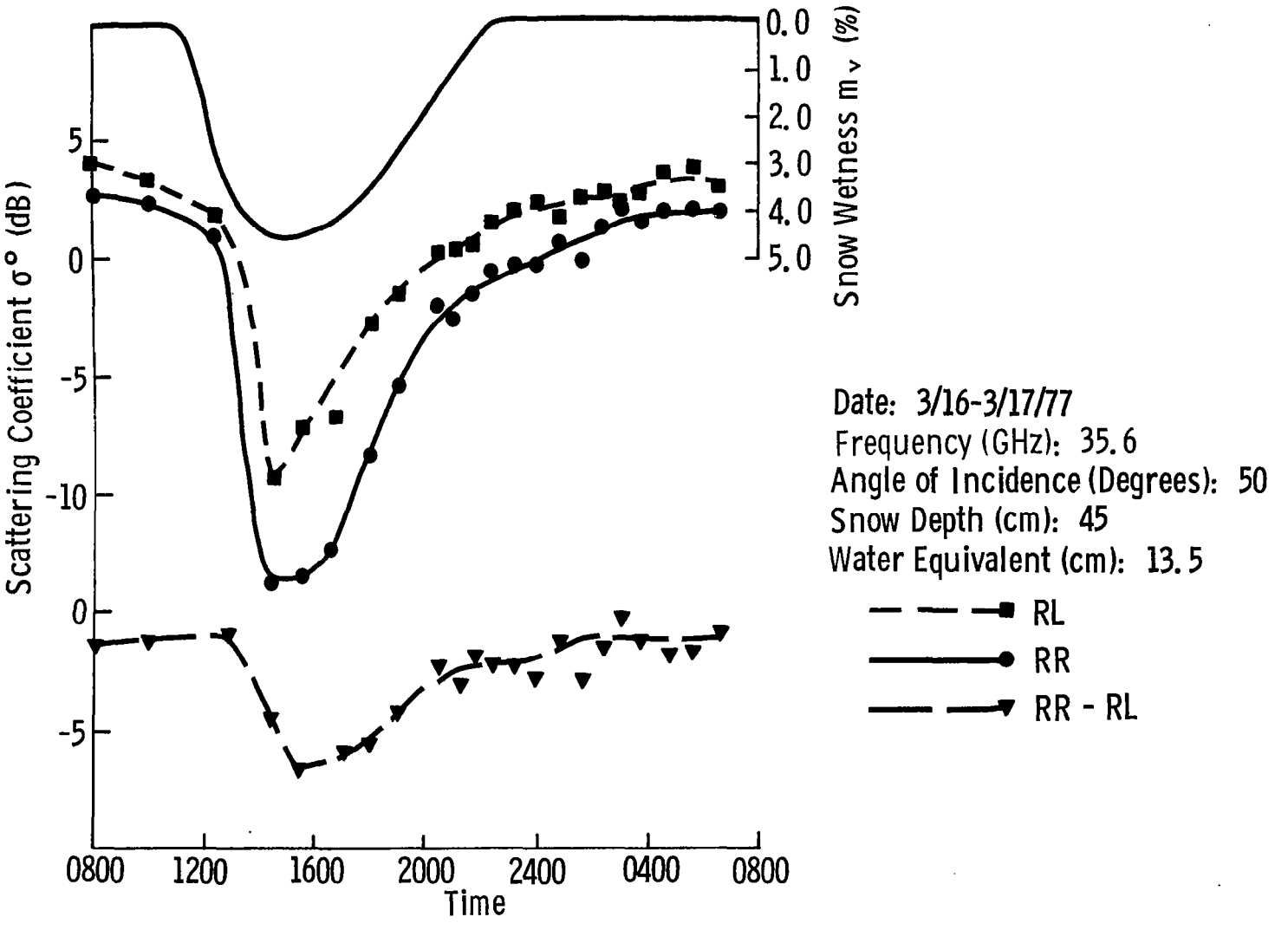


Figure 8-28c Diurnal variation of snow wetness and the circular polarized σ^o values at 35.6 GHz and the depolarization ratio (σ_{RR}/σ_{RL}) at 50^o angle of incidence.

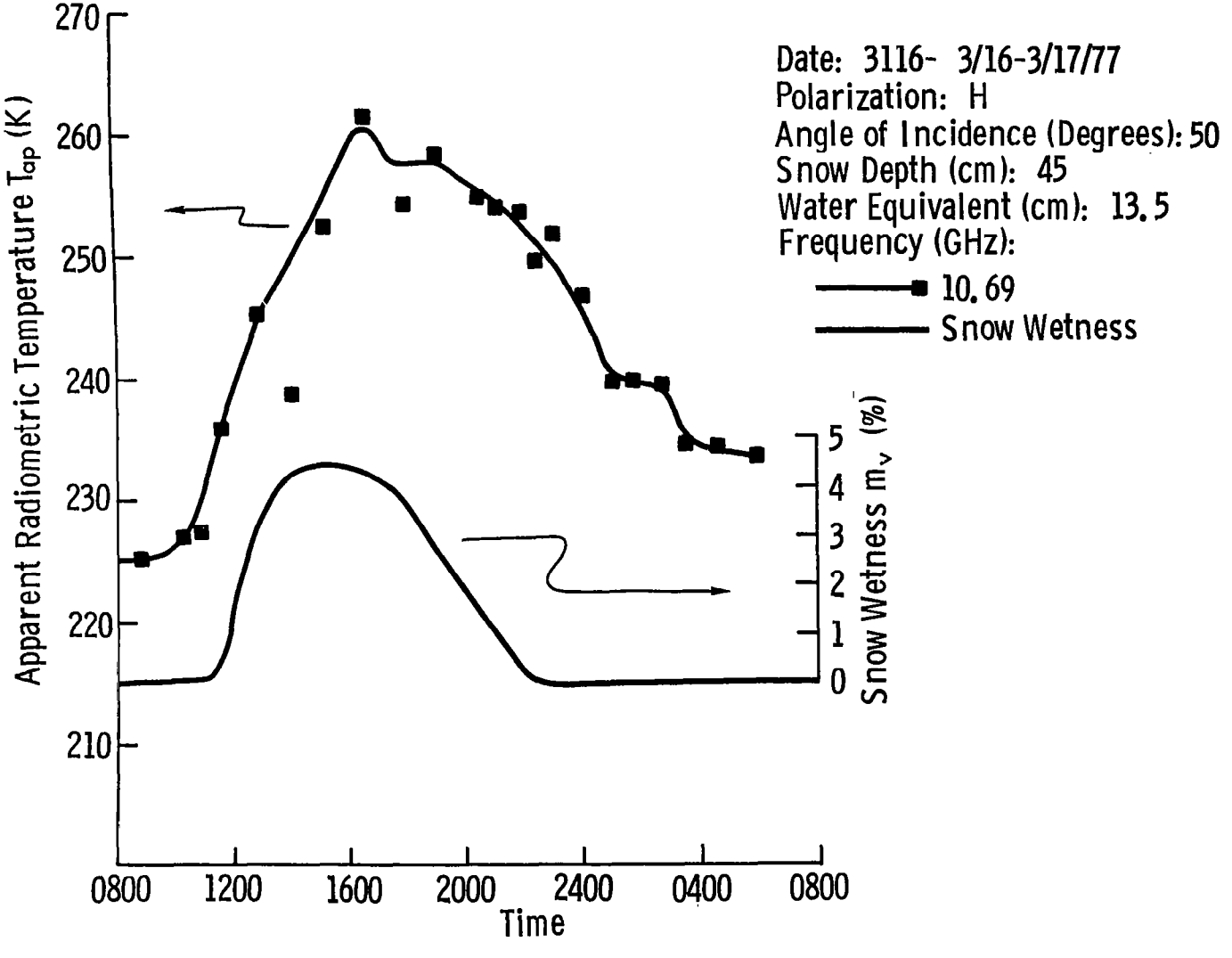


Figure 8-29 Diurnal variation of T_{ap} at 10.69 GHz at 50^{0} angle of incidence.

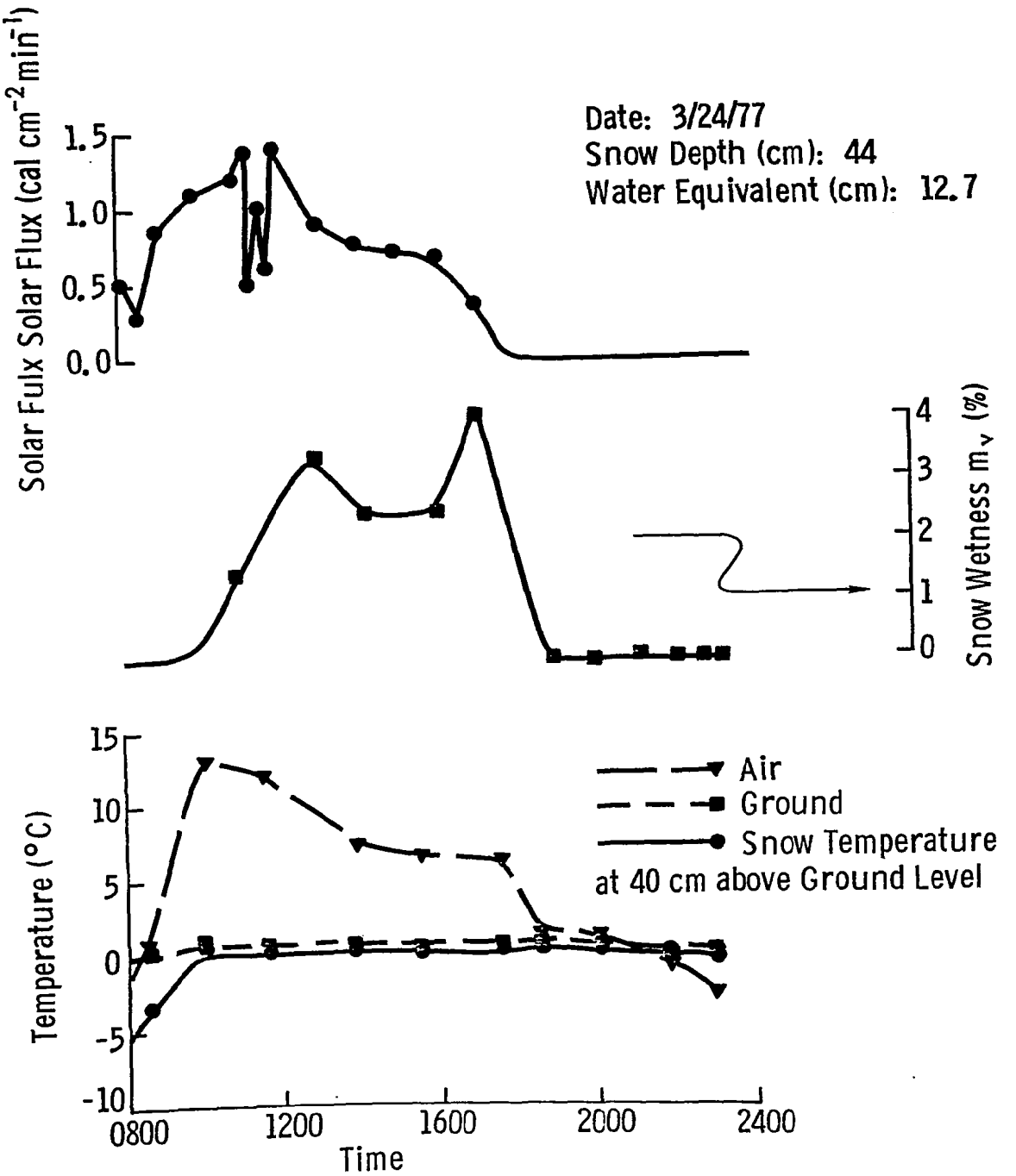


Figure 8-30 Diurnal variation of ground truth data on 3/24/77. m_v is the volumetric snow wetness of the top 5 cm layer.

At 8.6 GHz, the scattering coefficient at 2400 hours is 6 dB lower than its dry morning value; while σ^o is 4.5 and 2.0 dB lower at 17.0 and 35.6 GHz, respectively. Since the depth of penetration is inversely proportional to frequency and since the refreezing of the snowpack is from the surface downward, the σ^o values at 2400 hours at the higher frequencies are closer to the dry σ^o values.

The T_{ap} response at 10.69 GHz showed a larger change with snowmelt than for any of the other diurnal experiments. Wetness in subsurface layers explains the high T_{ap} value at 2400 hours. Effects of subsurface wetness from 2000 to 2400 hours are seen to decrease at 37 GHz and become negligible at 94 GHz. The 37 GHz T_{ap} values again show an inverse response to the 35.6 GHz σ^o values and a direct relationship to the snow wetness. At 94 GHz T_{ap} is observed to respond much quicker to snow wetness than at 37 GHz. This effect is especially noticeable between 1700 and 2400 hours. Also, it can be seen that cloud cover can cause rapid variation in the 94 GHz response by observing the solar flux and T_{ap} between 1100 and 1200 hours. The rapid change at 94 GHz is attributed to rapid change in wetness of a very thin surface layer when the snow is wet. Since the measured snow wetness is the average of the top 5 cm layer, it does not show the faster change associated with the very thin surface layer. Again it should be noted that the actual sensitivity of t .e snow emission is greater at 94 GHz than at 37 GHz (see Section 8.2.2).

8.3.5 Diurnal Experiment on 3/23/77

The diurnal measurements completed on 3/23/77 were for the specific purpose of investigating the diurnal response of a single resolution cell of the snowfield. Two angles of incidence were observed: 50° and 70°. Figure 8-33 gives the ground truth data and Figures 8-34 and 8-35 show the microwave data. The trends were identical at both 50° and 70°, with both active and passive responses saturating after 1200 hours. The accuracy of the 94 GHz data is questionable, however, due to system problems associated with control of the RF section environment.

8.3.6 Summary of the Diurnal Response

The conclusions from the diurnal experiments are:

1) The dynamic range of σ^o due to wetness (change in σ^o due to a corresponding change in m_v) increases with

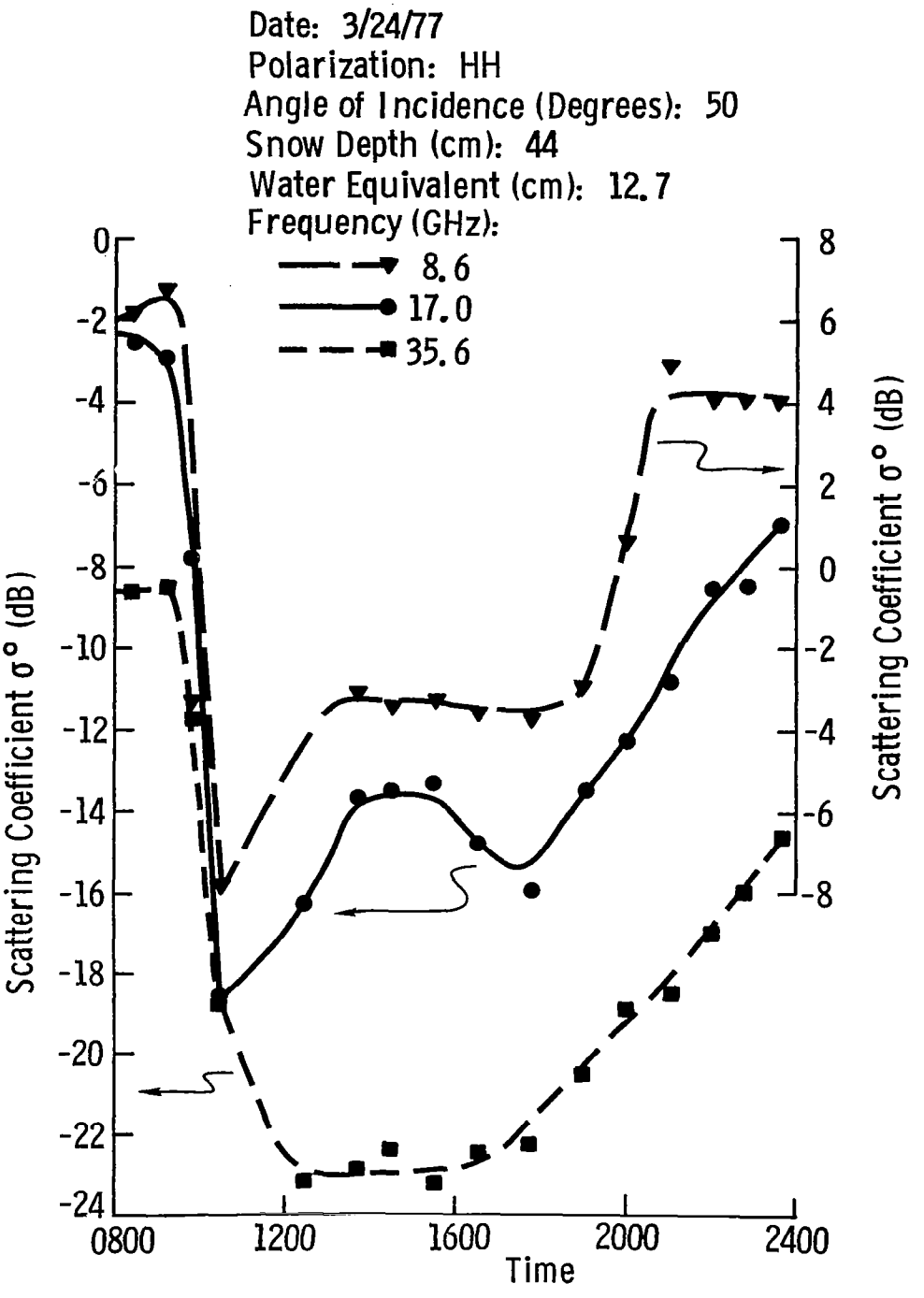


Figure 8-31 Diurnal variation of σ^{o} at 8.6, 17.0 and 35.6 GHz at 50^{o} angle of incidence.

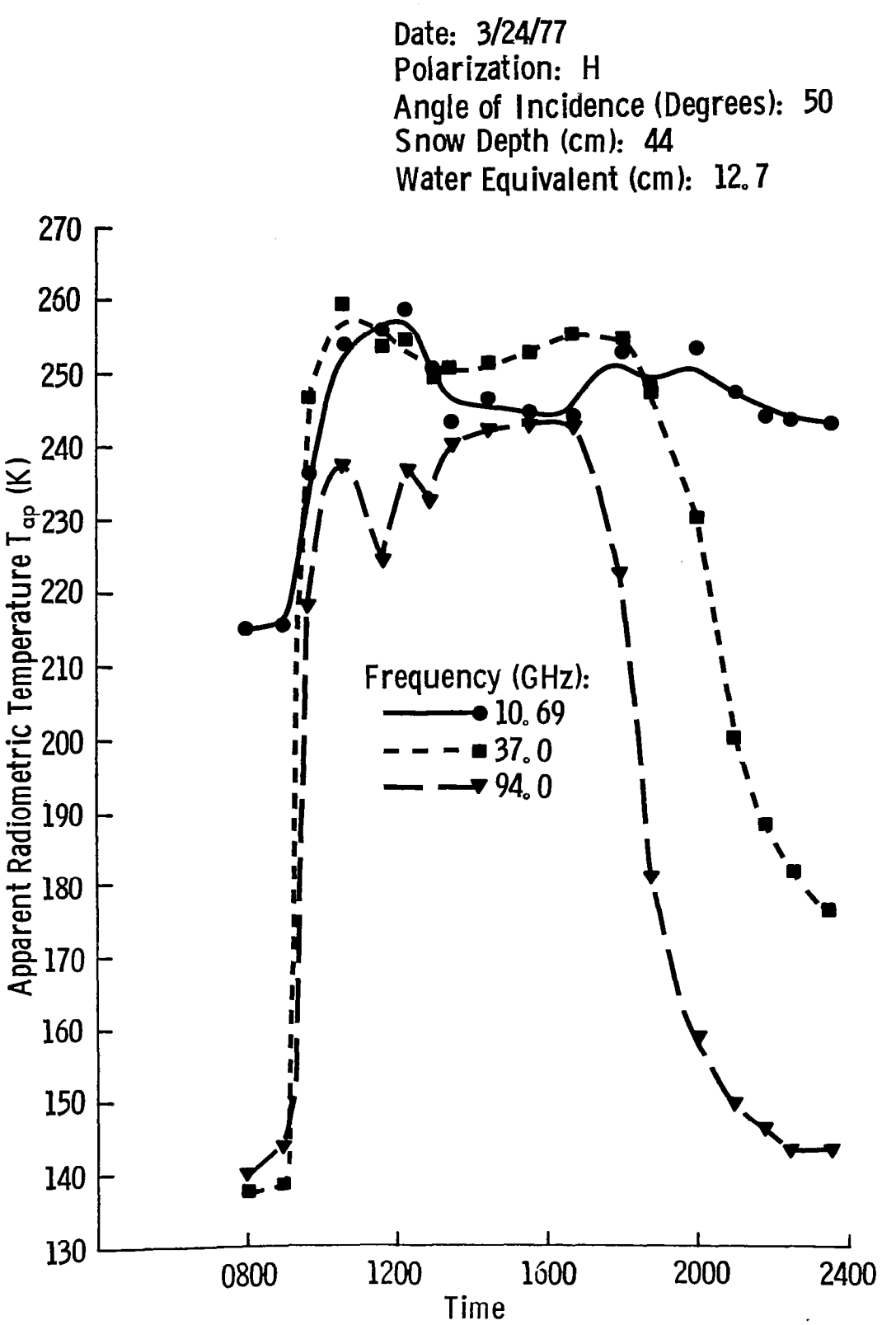


Figure 8-32 Diurnal variation of T_{ap} at 10.69, 37 and 94 GHz at 50^{o} angle of incidence.

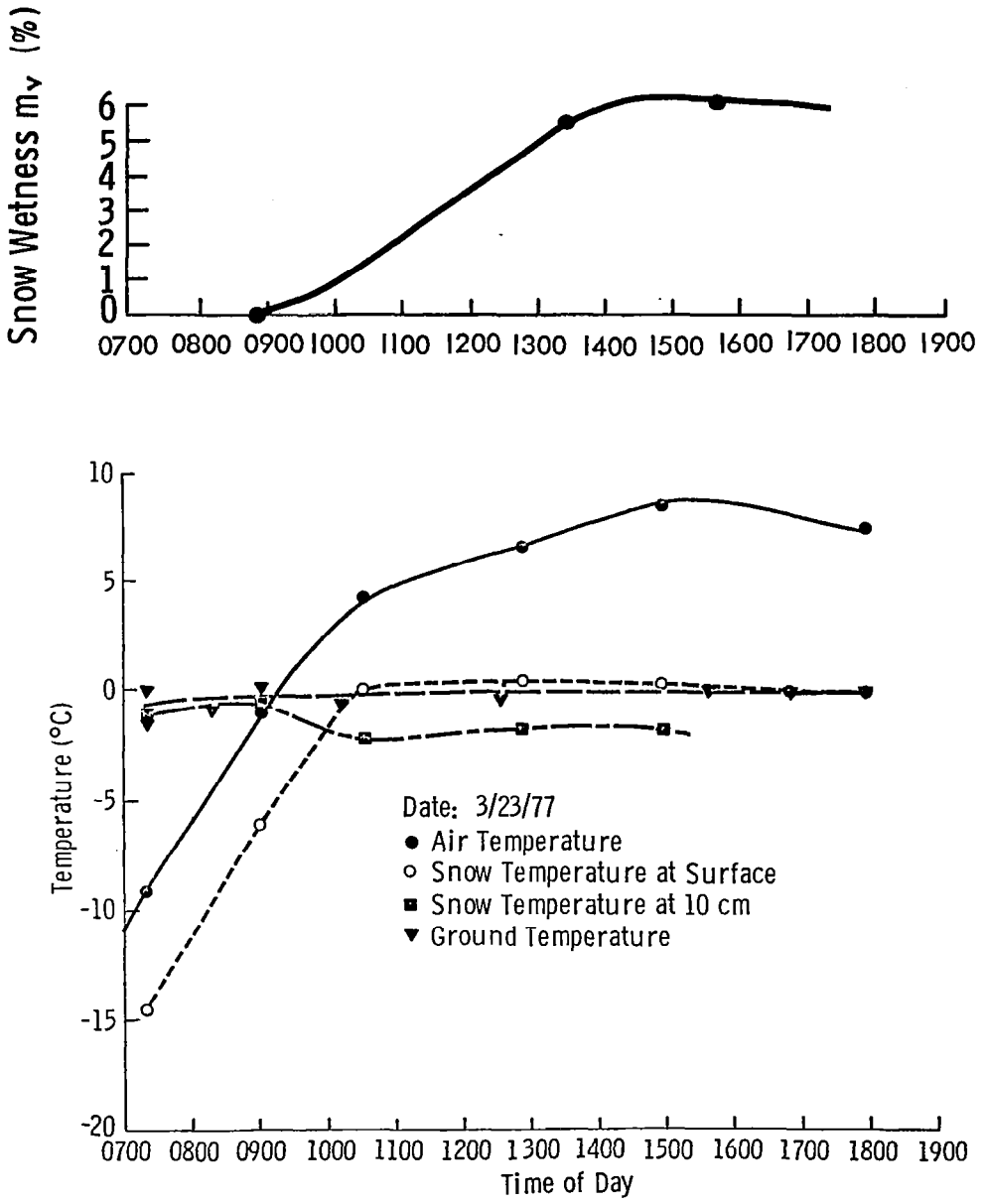


Figure 8-33 Snow wetness and temperature variation over the measurement period of the diurnal experiment on 3/23/77.

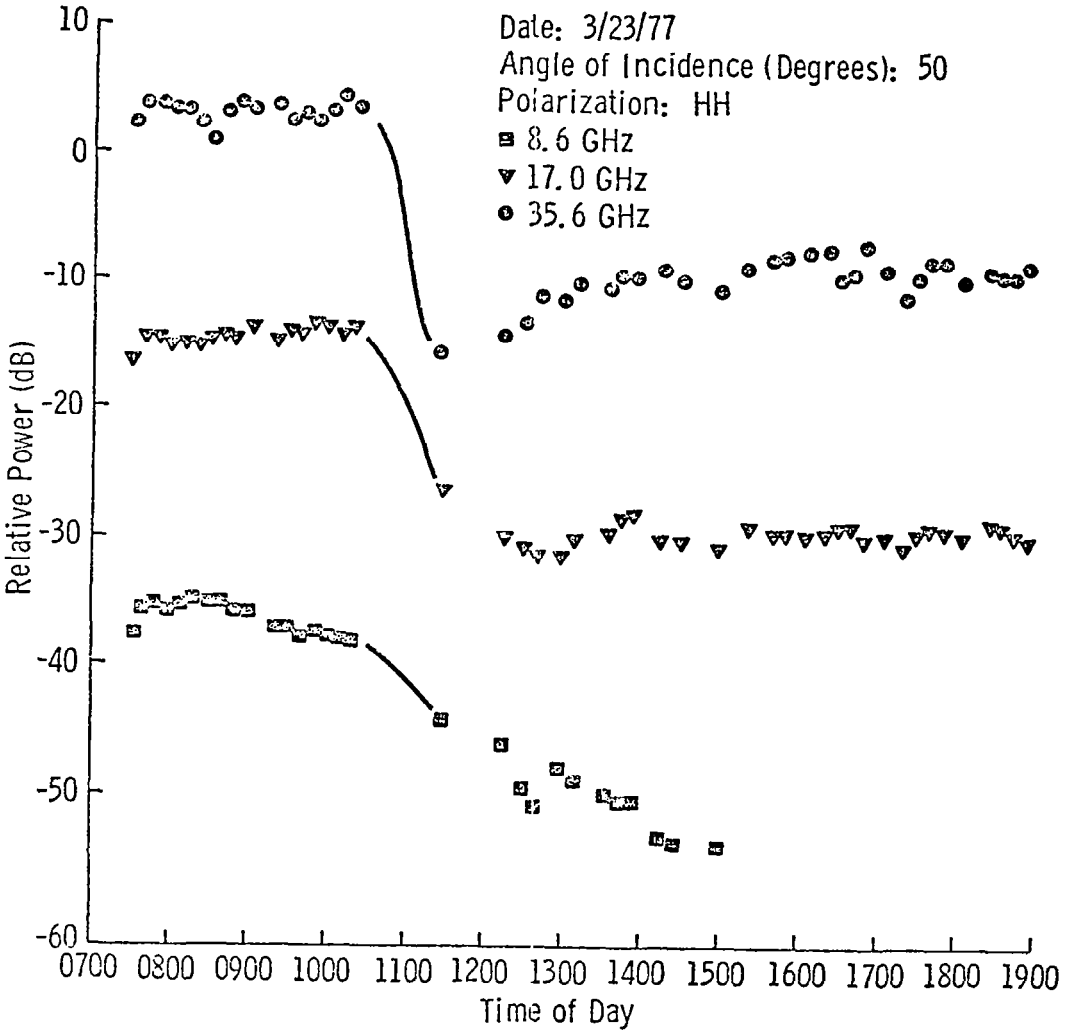


Figure 8-34a Time variation of 50° backscatter power at 8.6, 17.0, and 35.6 GHz.

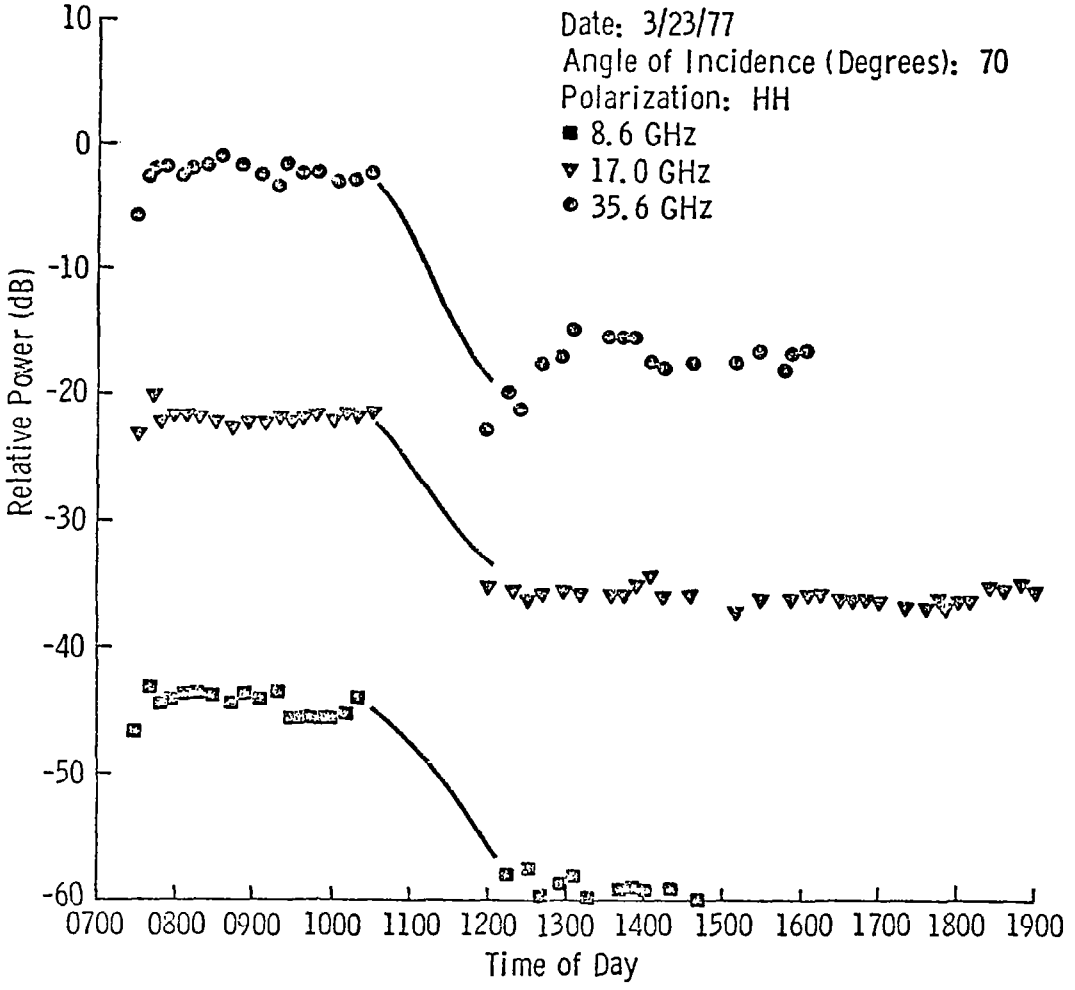


Figure 8-34b Time variation of 70° backscatter power at 8.6, 17.0, and 35.6 GHz.

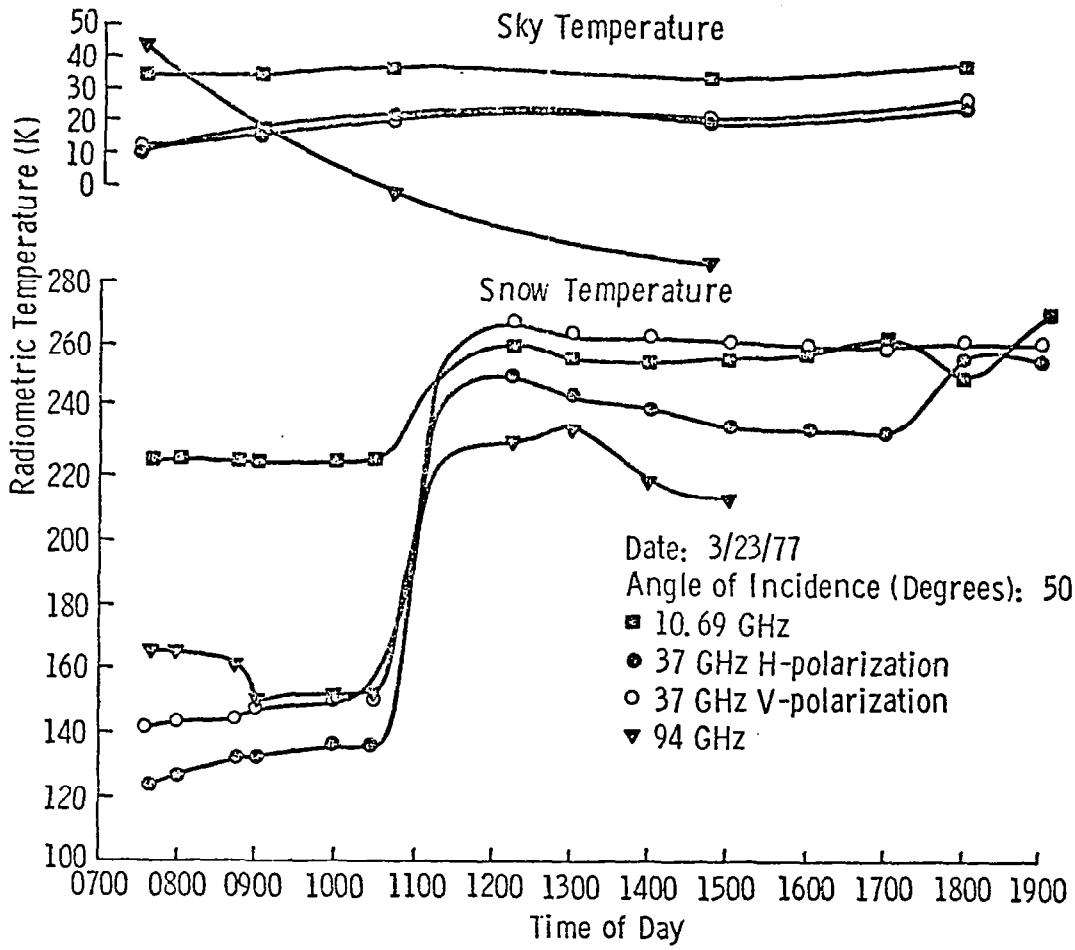


Figure 8-35a Time variation of the 50° radiometric temperature at 10.69, 37 and 94 GHz.

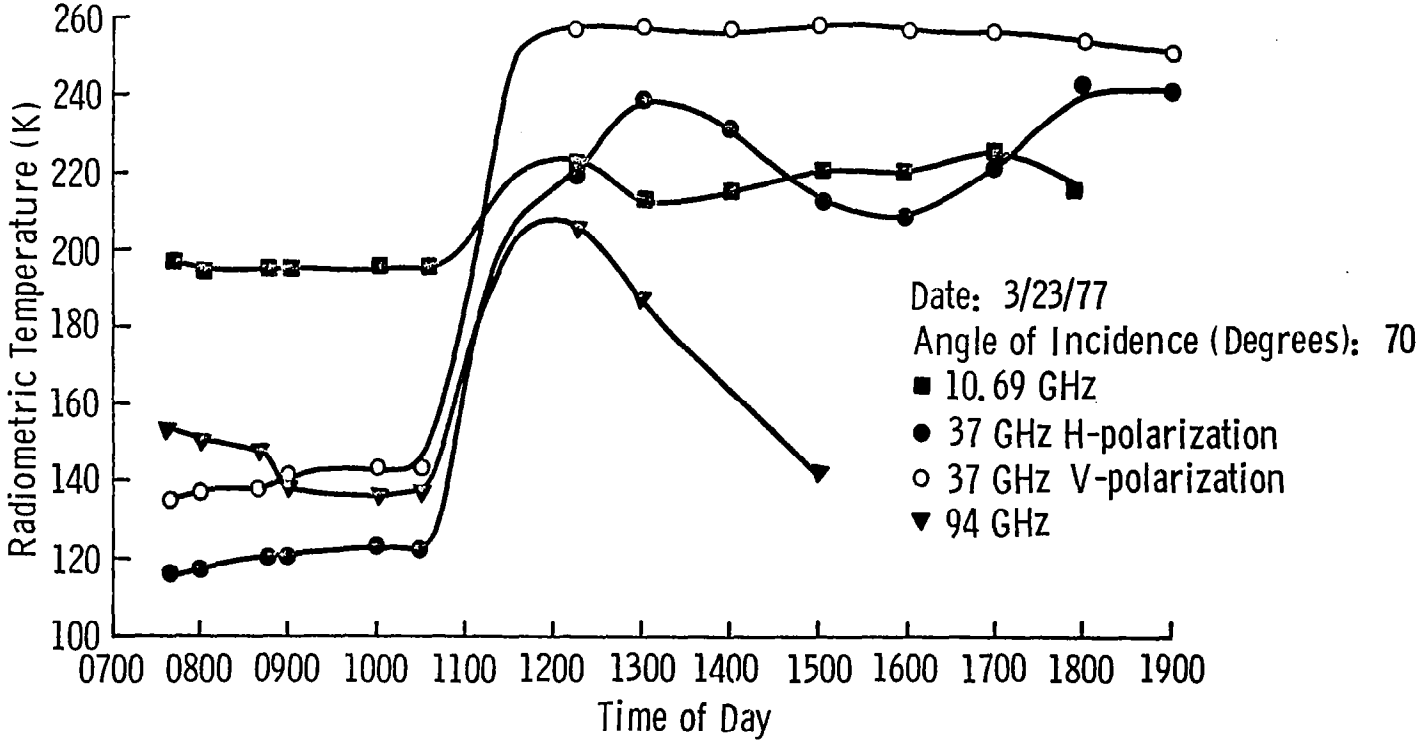


Figure 8-35b Time variation of the 70° radiometric temperature at 10.69, 37 and 94 GHz.

frequency from about 0 dB at 1.2 GHz to as much as 15 dB at 35.6 GHz (for 50° angle of incidence) in response to an m_v change from 0% to greater than 1.3%.

2) Also, this dynamic range decreases as θ approaches nadir.
3) The time rate of change of σ^o increases with increasing frequency. This phenomenon is related to the decreasing penetration depth with increasing frequency and the faster possible rate of change of m_v in the thinner layer to which the higher frequency σ^o values respond.
4) The dynamic range of T_{ap} (in response to changes in snow wetness in the surface layer) increases with frequency.
5) The passive dynamic range (in response to snow wetness) decreases only slightly as θ approaches nadir.
6) The time rate of change of T_{ap} in response to snow wetness variation increases, as did σ^o, with increasing frequency.
7) The trends exhibited by the single resolution cell diurnal experiment were similar to the trends observed for the whole field.

8.4 Response to Snow Wetness

Several types of analyses are included under this topic. First, the dynamic range variations of the diurnal experiments are examined. Then the hysteresis effect of snow wetness on the microwave measurements (σ^o and T_{ap}) is evaluated. Finally, regression curve fits are produced for the wetness variation influence on σ^o and T_{ap} when the other snow parameters were constant and other regression curve fits are determined for σ^o and T_{ap} over the seasonal variation with respect to snow wetness.

8.4.1 Active Microwave

Qualitative understanding of the effect of snow wetness on σ^o has to an extent been already covered in the previous sections. The response of σ^o to snow wetness is by no means a simple phenomenon. As a starting point, the magnitude of the σ^o response to wetness is examined for the diurnal periods. Each of the four diurnal experiments had relatively stable snow parameters with the exception of wetness and temperature. The peak-to-peak magnitude variation of σ^o and wetness at approximately 50° is given in Table 8-2 and Figure 8-36. These data indicate that

TABLE 8-2
Magnitudes of $\Delta\sigma^{o}$(dB) in Response to the Peak Snow Wetness Variations Observed during the Diurnal Experiments

		Frequency (GHz)					
Date	Angle	4.6	7.6	8.6	17	35.6	Peak m_v
2/17	25	---	---	6	8	13	2.6
2/17	55	---	---	6	9	12	2.6
3/3	20	2	---	4	8	14	1.3
3/3	50	3	---	4	8	15	1.3
3/16	50	7	10	11	12	14	4.5
3/24	50	---	---	14	16	15	4.0

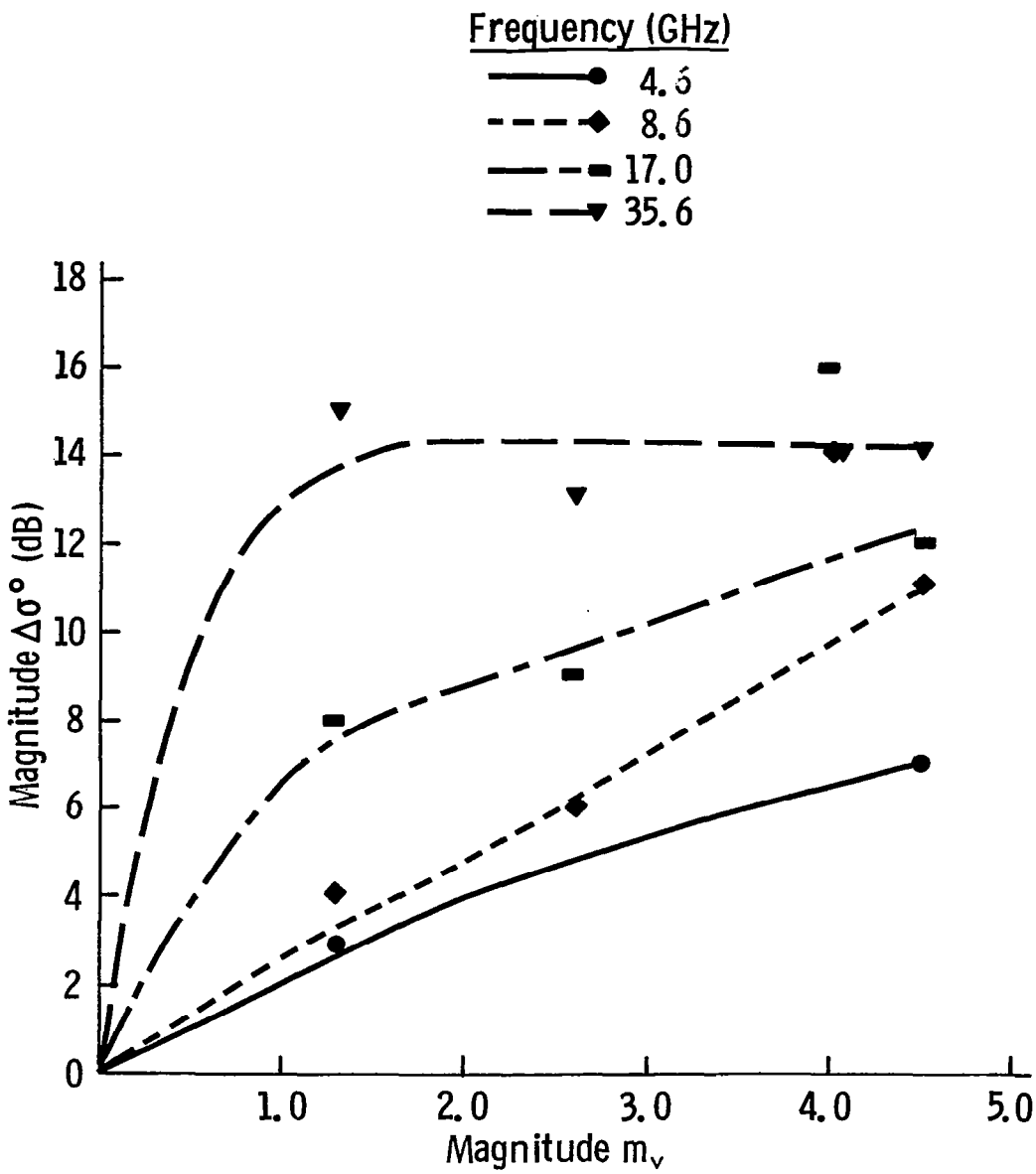


Figure 8-36 Magnitude of the σ^o diurnal responses versus the magnitude of the snow wetness response.

the σ^o response to snow wetness in the surface 5 cm layer is frequency dependent and can be non-linear. A plausible explanation for this variation is that the "effective depth" or the depth within the snow layer responsible for the majority of the backscatter contribution is not the same as the wetness sample depth (top 5 cm). The "effective depth" will decrease with increasing frequency and snow wetness. Also at a given frequency, the effective depth may be large when the snow is dry and decrease to a very small value if the snow is wet. If the effective depth is much less than the snow wetness sample layer, then since melt is from the surface down and a thinner layer becomes wet first, the σ^o response may exhibit a saturation response. This assumption is predicated on the idea that a saturation wetness exists. With the above inferences, it is seen that the 17.0 GHz and 35.6 GHz σ^o response exhibit this type of saturation behavior (Figure 8-36).

Because of the limited time resolution between the individual σ^o and ground truth measurements, the exact response of σ^o during the melt and freeze phases of the day is difficult to determine in relation to the measured ground truth parameters. The details of the response during the variational period do provide information on the nature of the snowpack dynamics.

Data from the first diurnal experiment are replotted in Figures 8-37a and 8-38a for two frequencies. Comparison of the diurnal variations suggests that σ^o leads m_v of the surface 5 cm layer during the melting phase. During the refreeze phase, the σ^o values at 8.6 GHz lag while the σ^o values at 35.6 GHz lead the m_v of the surface 5 cm layer. The variation between σ^o and m_v is shown in Figure 8-37b and 8-38b for 8.6 GHz and 35.6 GHz, respectively. The hysteresis effect of σ^o is relatively minor at 8.6 GHz and the response with m_v is approximately linear, while at 35.6 GHz, the hysteresis effect is significant. The shapes of the responses therefore indicate that while the behavior of m_v in the surface 5 cm layer is an adequate descriptor at 8.6 GHz in this case, it is not at 35.6 GHz.

The demonstrated "hysteresis" like behavior is ascribed to the fact that σ^o is governed by the entire wetness and density profile and not simply by the top 5 cm layer. In addition, the backscatter properties and attenuation properties of the surface layer and each succeeding layer affect the contribution of all layers deeper within the snowpack.

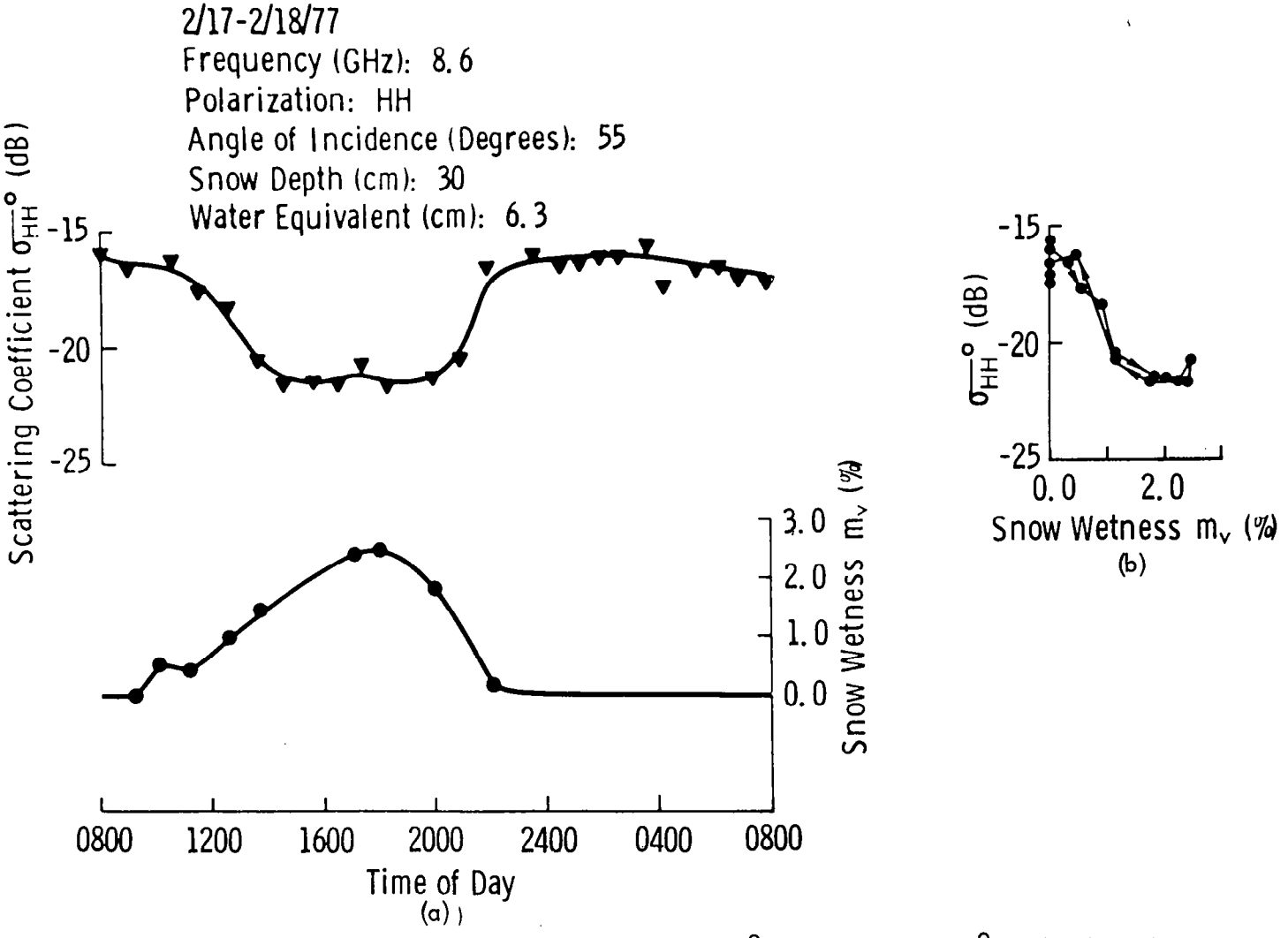


Figure 8-37 Diurnal Response and Hysteresis Effect of σ° at 8.6 GHz and 55° Angle of Incidence

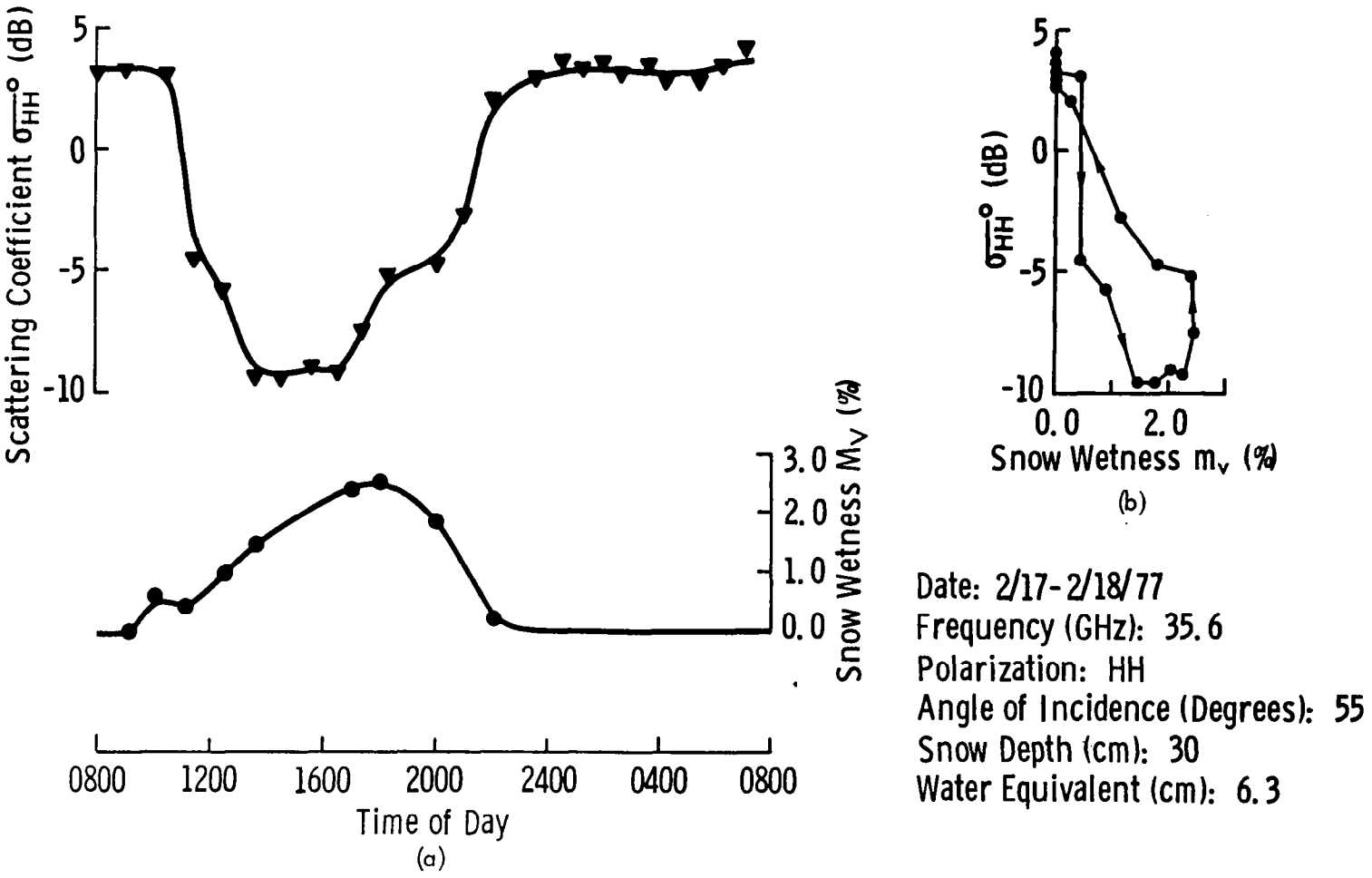


Figure 8-38 Diurnal Response and Hysteresis Effect of σ° at 35.6 GHz and 55° Angle of Incidence

The difficulty arises in determining the properties of each layer. Since attenuation and scattering loss within the snowpack increase with frequency, the effective depth at 35.6 GHz will be smaller than at 8.6 GHz. As stated in the previous sections, energy transfer at the air-snow boundary causes melt to occur from the surface down and therefore the top 1 cm layer for instance will lead the top 5 cm layer wetness during the melt period. The size of the time lag will depend on the rate of energy transfer. If the radar responds to a layer thinner than 5 cm during the melting phase, the σ^o values will lead the wetness values. During the refreeze phase, since the surface layer is the first layer to become dry, the σ^o values will have contributions from deeper wetter layers. Therefore, depending on the penetration depth at a given frequency, the σ^o values can either lead or lag with respect to the surface 5 cm layer snow wetness.

The hysteresis like behavior is not shown for the 3/3/77 diurnal experiment because of the paucity of σ^o data during wet snow conditions. The third diurnal experiment on 3/16/77 had the σ^o and snow wetness responses given in Figures 8-39 and 8-40. In this case, the hysteresis effect at 8.6 GHz is large. This response may be the result of snow wetness measurement error since if the σ^o value at approximately 1200 hours is removed, the σ^o versus m_v response becomes relatively linear, as in the 2/17/77 diurnal (Figure 8-37). With the exception of the questionable σ^o values near 1200 hours, the 35.6 GHz σ^o response leads m_v during the refreeze phase, indicating response to wetness in a thinner than 5 cm surface layer and also resembles the response on 2/17/77.

If the hysteresis effects are ignored, the curves in Figures 8-37b, 8-38b, 8-39b and 8-40b suggest that a linear regression of σ^o on m_v will provide a good fit. Linear regression fits were determined for σ^o of each diurnal; however, the small number of points per diurnal limited the significance of the tests. The exception was the diurnal experiment on 3/16/77. Figure 8-41 shows the σ^o response to m_v at four frequencies between 1 and 35 GHz. The sensitivity to wetness is zero at 1.2 GHz and approximately -2 dB/1% m_v at 8.6, 17.0 and 35.6 GHz. Figure 8-42 shows the spectral sensitivity and correlation coefficient. As frequency increases, a rapid increase in the magnitude of the correlation coefficient and sensitivity is observed, up to about 5 GHz, beyond which the levels remain approximately constant.

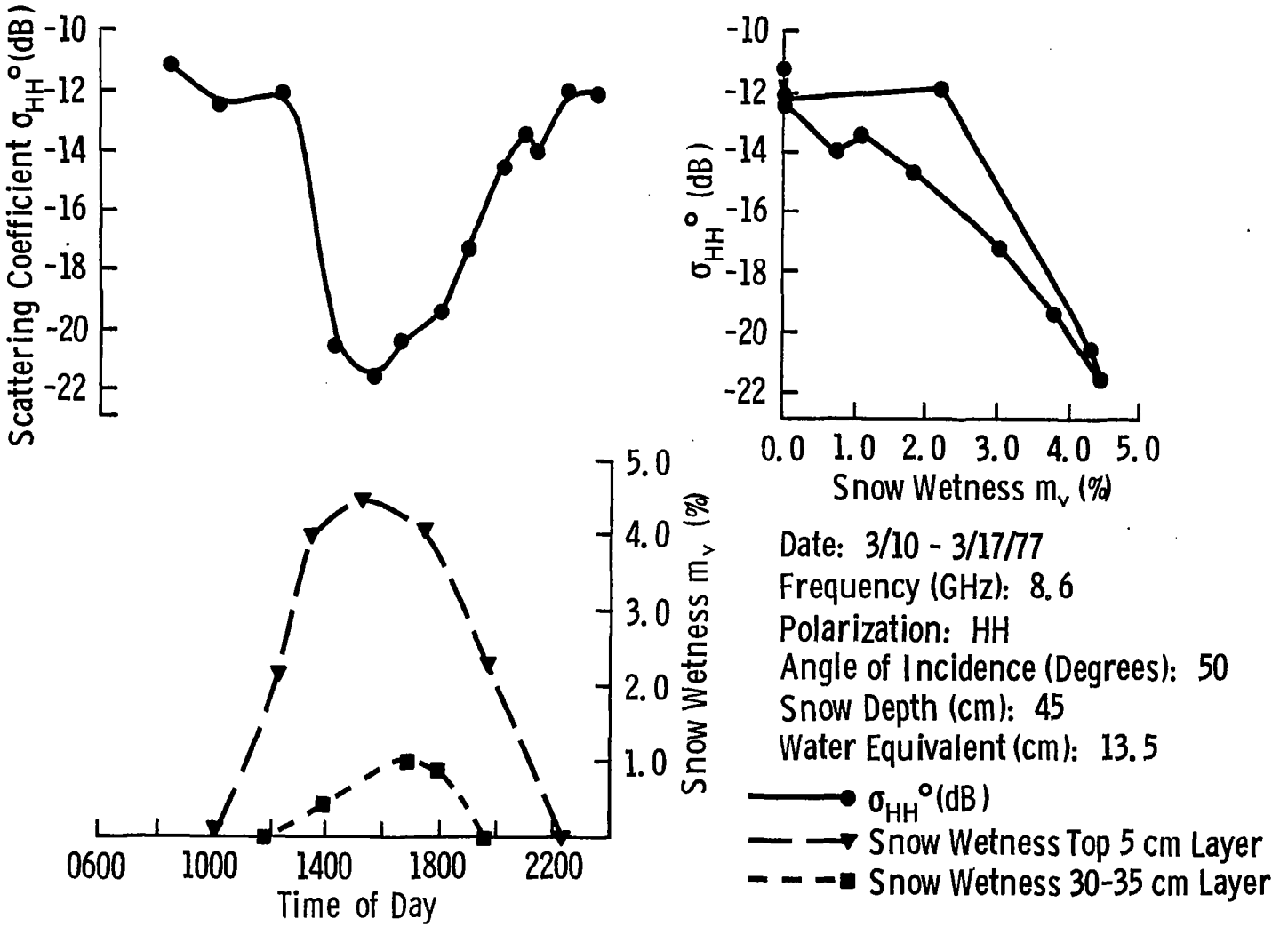


Figure 8-39 Diurnal response and hysteresis effect of σ° at 8.6 GHz and 50° angle of incidence.

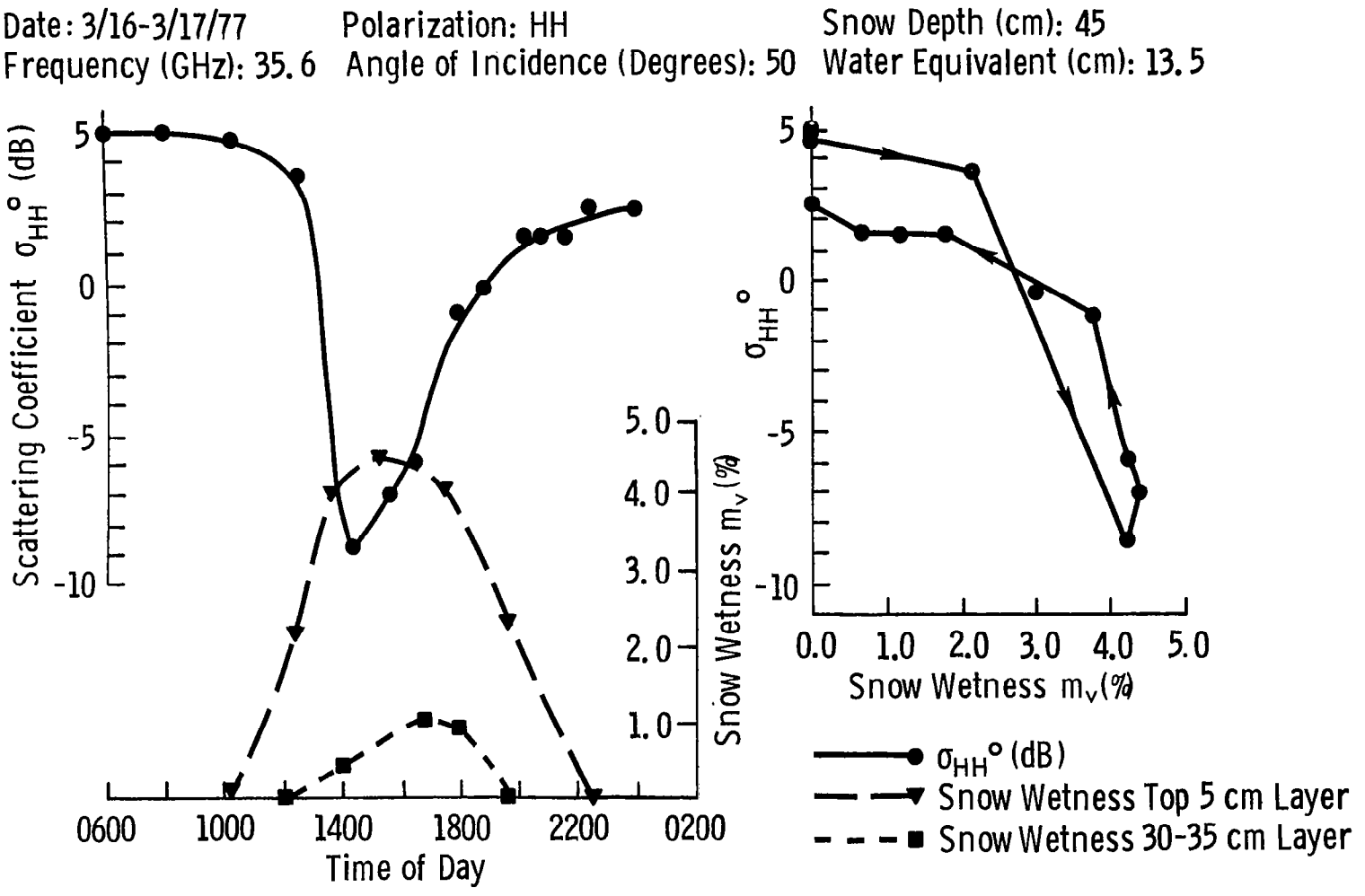


Figure 8-40 Diurnal response and hysteresis effect of σ° at 35.6 GHz and 50° angle of incidence.

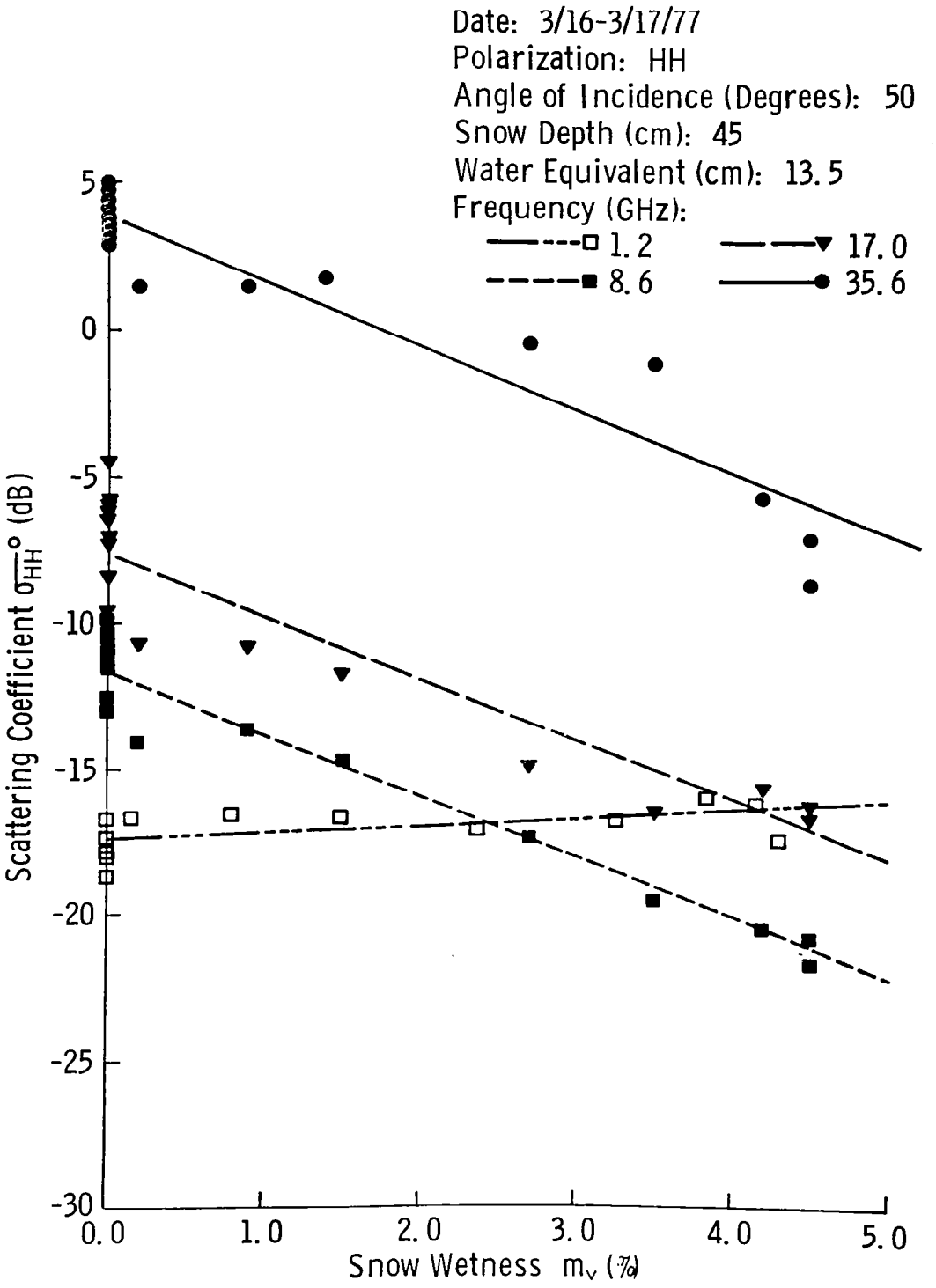


Figure 8-41 σ° Response to m_v at 50° Angle of Incidence on 3/16 - 3/17/77

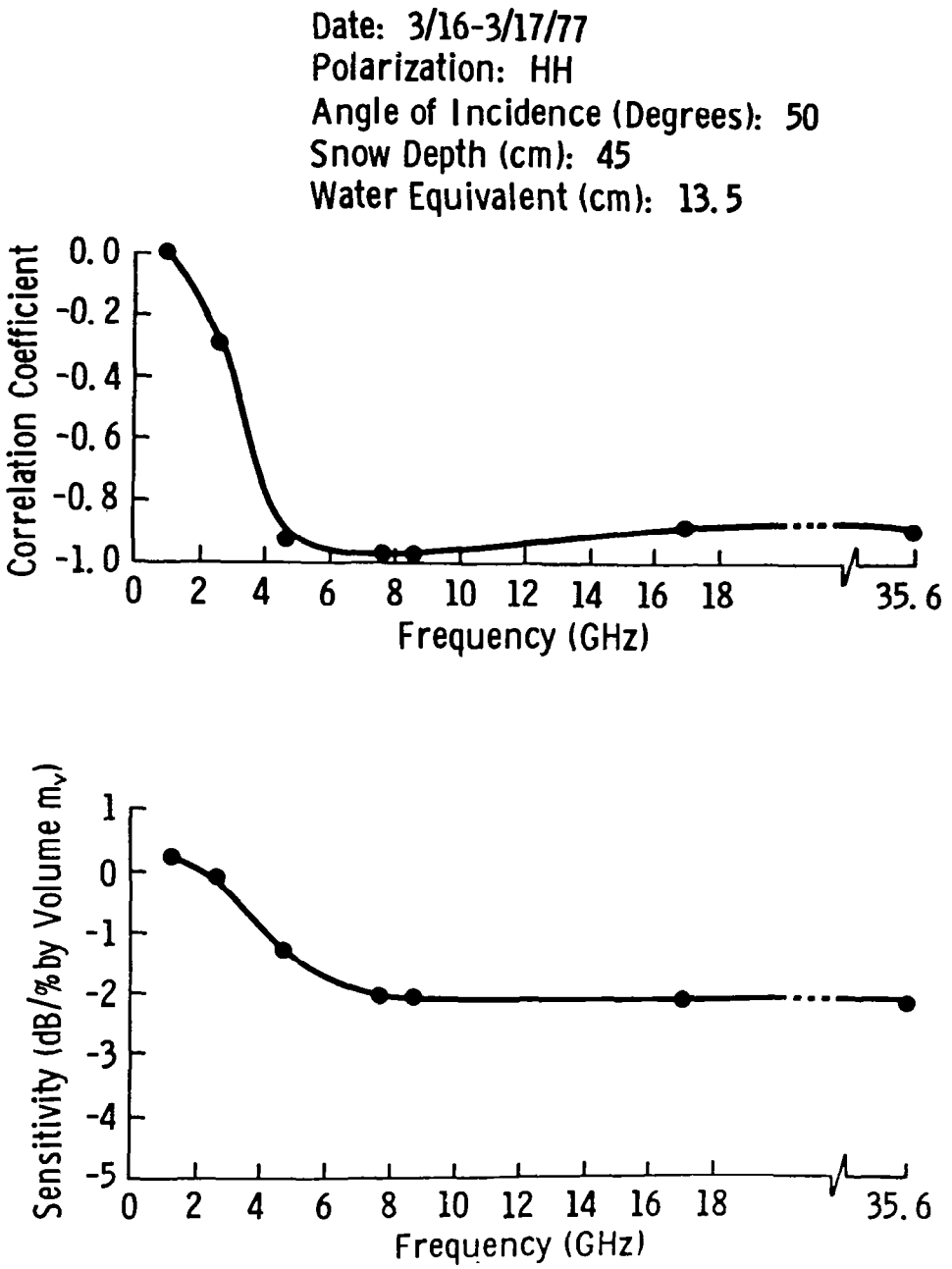


Figure 8-42 Correlation Coefficient and Sensitivity of σ° to m_v at 50° Angle of Incidence on 3/16 - 3/17/77

If the variation of all snow parameters with the exception of snow wetness are ignored and linear regressions applied to the σ^o data over the total measurement period, the resulting correlation coefficients and sensitivities given in Figure 8-43, are obtained. Although the pattern is similar to that of Figure 8-42, the correlation coefficient is generally smaller, which is attributed to the influence of the other snow parameter variations. The sensitivity is observed to increase in magnitude with frequency and angle of incidence. The positive correlation at low frequencies and especially 0° and 20° is believed to be due to ground contributions which can exhibit increased influence at small angles of incidence and low frequencies because the penetration capability is greater.

Obviously, there are short-comings in the above analyses. Better depth resolution on m_v is needed; probably m_v should be sampled in 1 cm increments. With a more detailed wetness profile, better models for the σ^o response to wetness could be developed. Also, the influence of other snow parameters need to be included. In Chapter 9, a model for σ^o is presented and evaluated which combines the dependence on snow wetness, water equivalent, and soil state.

8.4.2 Passive Microwave

The apparent temperature T_{ap} has been previously shown to increase with increasing snow wetness. The exact behavior with increasing snow wetness, however, is non-linear. In an analysis similar to the one for the active data, the magnitudes of the T_{ap} and surface 5 cm snow wetness responses are given in Table 8-3 and Figure 8-44 for the diurnal experiments. The magnitude response is observed to be relatively linear at 10.69 GHz, while exhibiting a saturation effect at 37 GHz. Comparison of the passive response with the σ^o and m_v response in Figure 8-36 indicates similar variations. The saturation response of T_{ap} at 37 GHz is not quite as apparent as the σ^o response at 35.6 GHz; however, the indications of similarity are clear. One reason for the increased variation is the inherent sensitivity of the passive data to thermometric temperature variations. The shape of the 10.69 GHz response is observed to be between that of the active 8.6 GHz and 17.0 GHz curves, as expected. The same argument given in the previous section relating sensor effective depth and sample wetness depth is applicable and explains the increasing exponential like response at 37 GHz over the 10.69 GHz response.

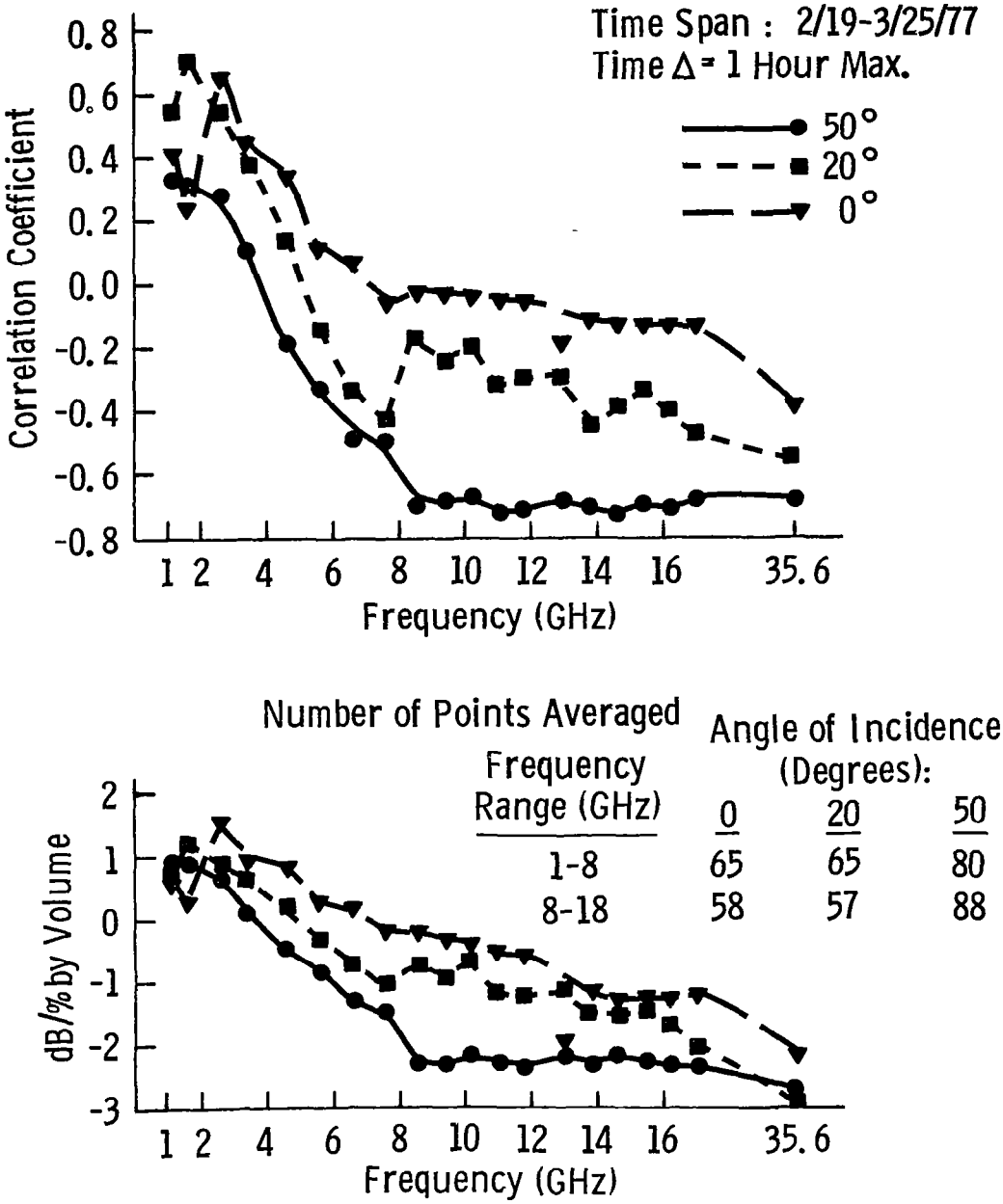


Figure 8-43 Correlation coefficient and sensitivity of σ^{o} and m_{v} at 0^{o}, 20^{o} and 50^{o} angles of incidence over the measurement period.

TABLE 8-3

Magnitudes of ΔT_{ap} in Response to the Peak Snow Wetness Variations Observed during the Diurnal Experiment

Date	Angle	10.69 GHz	37 GHz	Peak m_v
2/17	25	5	80	2.6
2/17	55	23	87	2.6
3/3	20	10	110	1.3
3/3	50	15	120	1.3
3/16	50	36	---	4.5
3/24	50	43	123	

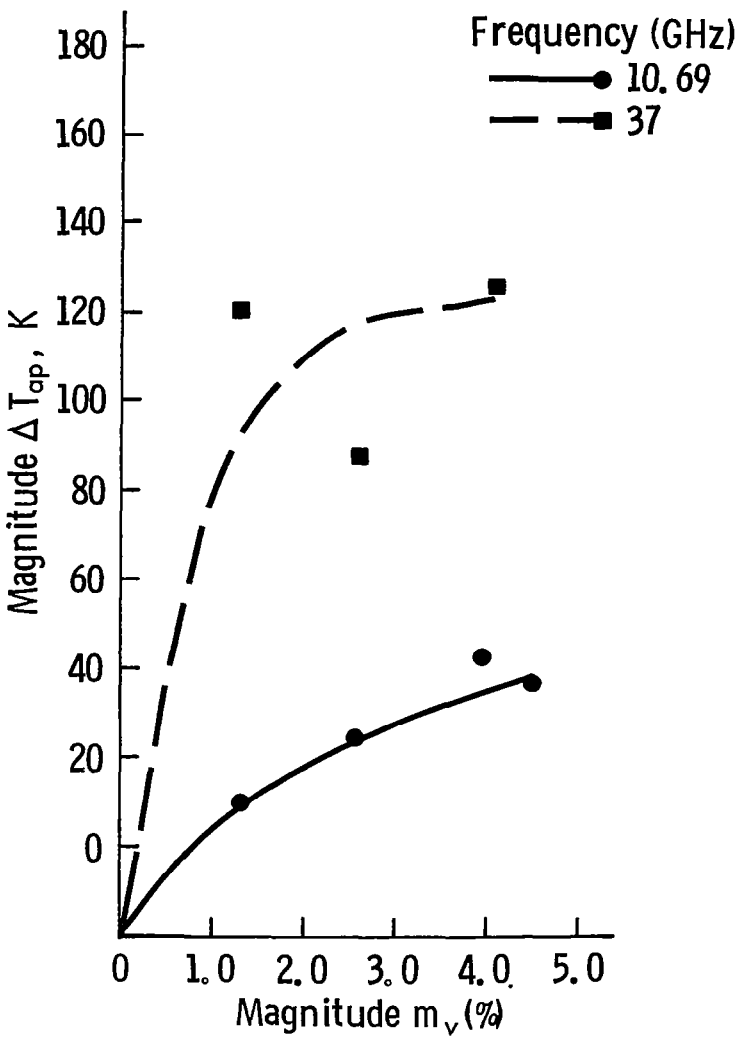


Figure 8-44 Magnitude of the T_{ap} diurnal responses versus the magnitude of the snow wetness response.

The detailed time responses of T_{ap} and m_v of the 2/17/77 diurnal experiment are replotted in Figure 8-45a and 8-46a for clarity. The hysteresis like patterns (Figures 8-45b and 8-46b) appear much more complex than the active patterns (Figures 8-37b and 8-38b). This complexity is in part due to sensitivity to physical temperature. The midday dip in the 10.69 GHz passive data (Figure 8-45a) complicates the analysis of the hysteresis phenomenon. This was the only diurnal experiment in which this type of behavior was observed, which may be due to a layering effect. A pronounced hysteresis like behavior is exhibited by the 37 GHz T_{ap} data (Figure 8-46b) as was shown by the σ^o values for the same diurnal experiment. The similarities to the active response indicate that the surface 5 cm snow wetness is not an adequate descriptor of T_{ap} at 37 GHz. The hysteresis effect at 10.69 GHz on 3/16/77 (Figure 8-47) shows a similar response to the 2/17/77 measurements; however, the absence of the midday dip in T_{ap} results in a smoother response.

Observation of Figures 8-45b, 8-46b and 8-47 suggest that an exponential fit of the form

$$T_{ap}\,(m_v) = A - B\,e^{-cm_v} \qquad (8\text{-}2)$$

could be used to fit the T_{ap} data if the hysteresis effect is ignored. For the first diurnal experiment the T_{ap} data were fit with the curves and equations given in Figure 8-48. Part of the scatter in the data points is the result of snow thermometric temperature variations. Although there was a wide scatter in the data points, the exponential fits for the T_{ap} data over the entire season were calculated. The regression equations for 10.69 GHz are:

$$\begin{aligned} T_{ap} &= 266.7 - 12.1\,e^{-0.17m_v} \text{ at } 0^o \\ &= 264.1 - 10.9\,e^{-0.165m_v} \text{ at } 20^o \\ &= 260.4 - 17.5\,e^{-0.185m_v} \text{ at } 50^o \end{aligned} \qquad (8\text{-}3)$$

and for 37 GHz the regression equations are:

$$\begin{aligned} T_{ap} &= 291.3 - 99.1\,e^{-0.41m_v} \text{ at } 0^o \\ &= 284.2 - 100.9\,e^{-0.472m_v} \text{ at } 20^o \\ &= 260.9 - 70.1\,e^{-0.635m_v} \text{ at } 50^o \end{aligned} \qquad (8\text{-}4)$$

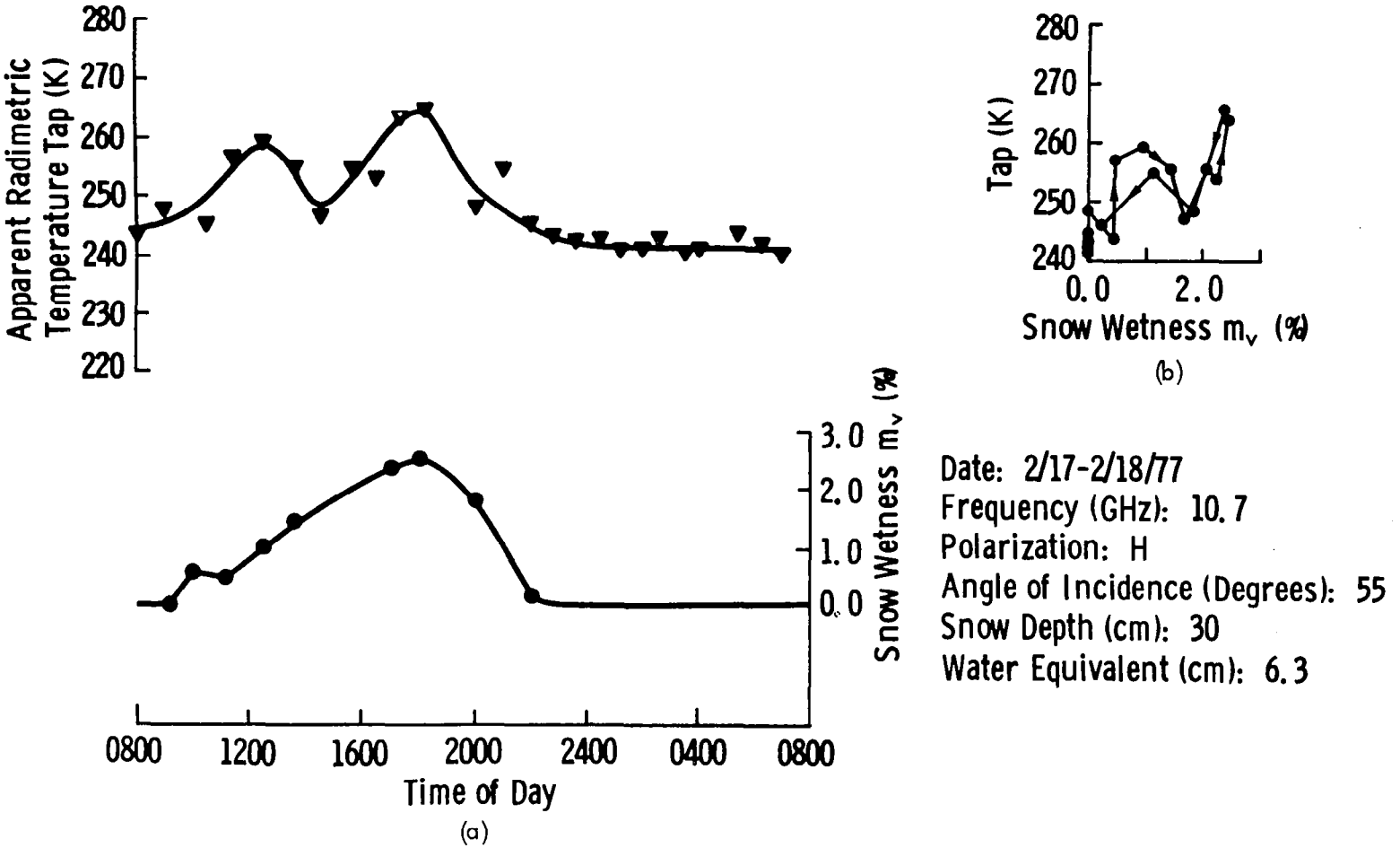


Figure 8-45 Diurnal Response and Hysteresis Effect of Tap at 10.7 GHz and 55° Angle of Incidence

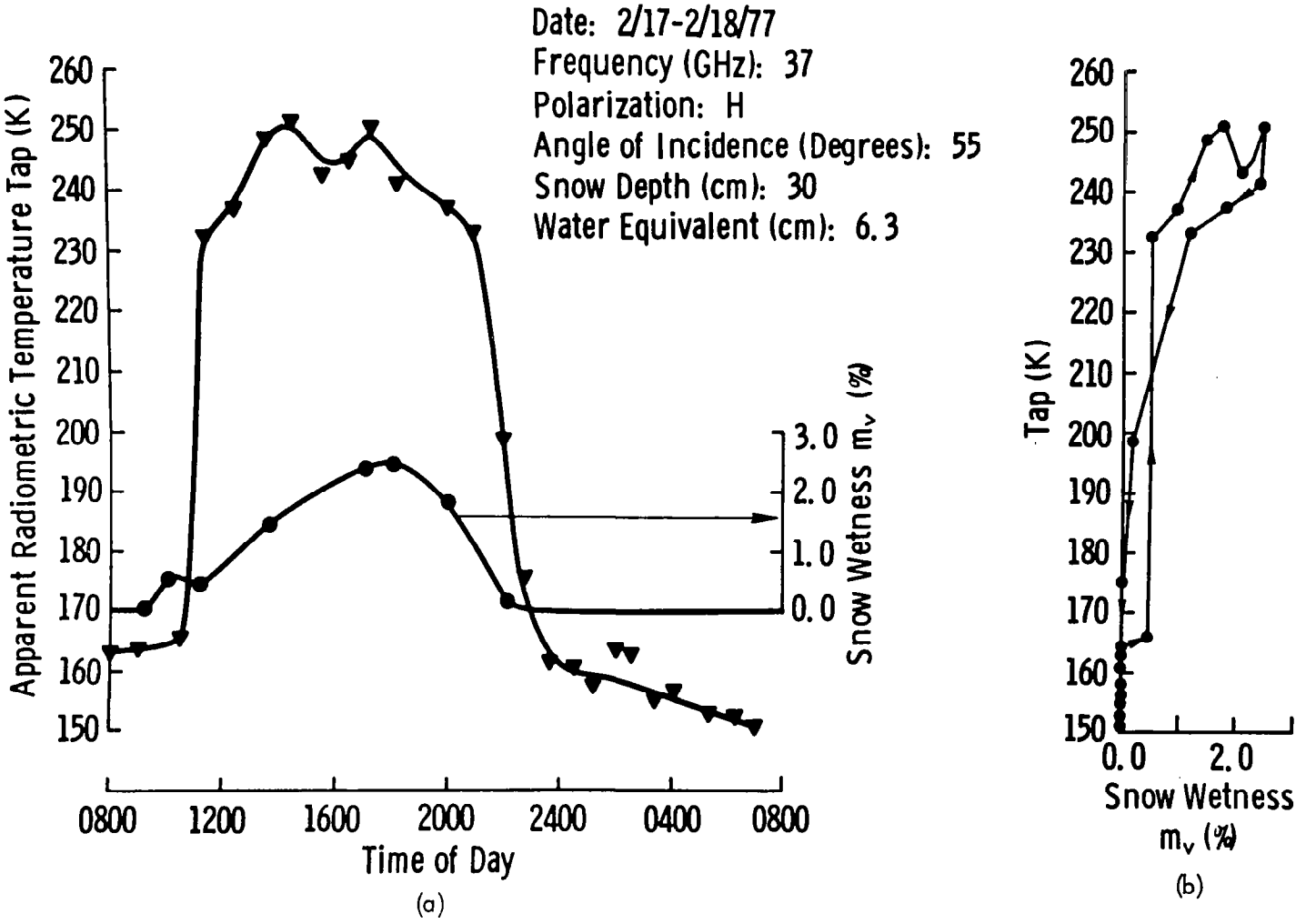


Figure 8-46 Diurnal Response and Hysteresis Effect of Tap at 37 GHz and 55° Angle of Incidence

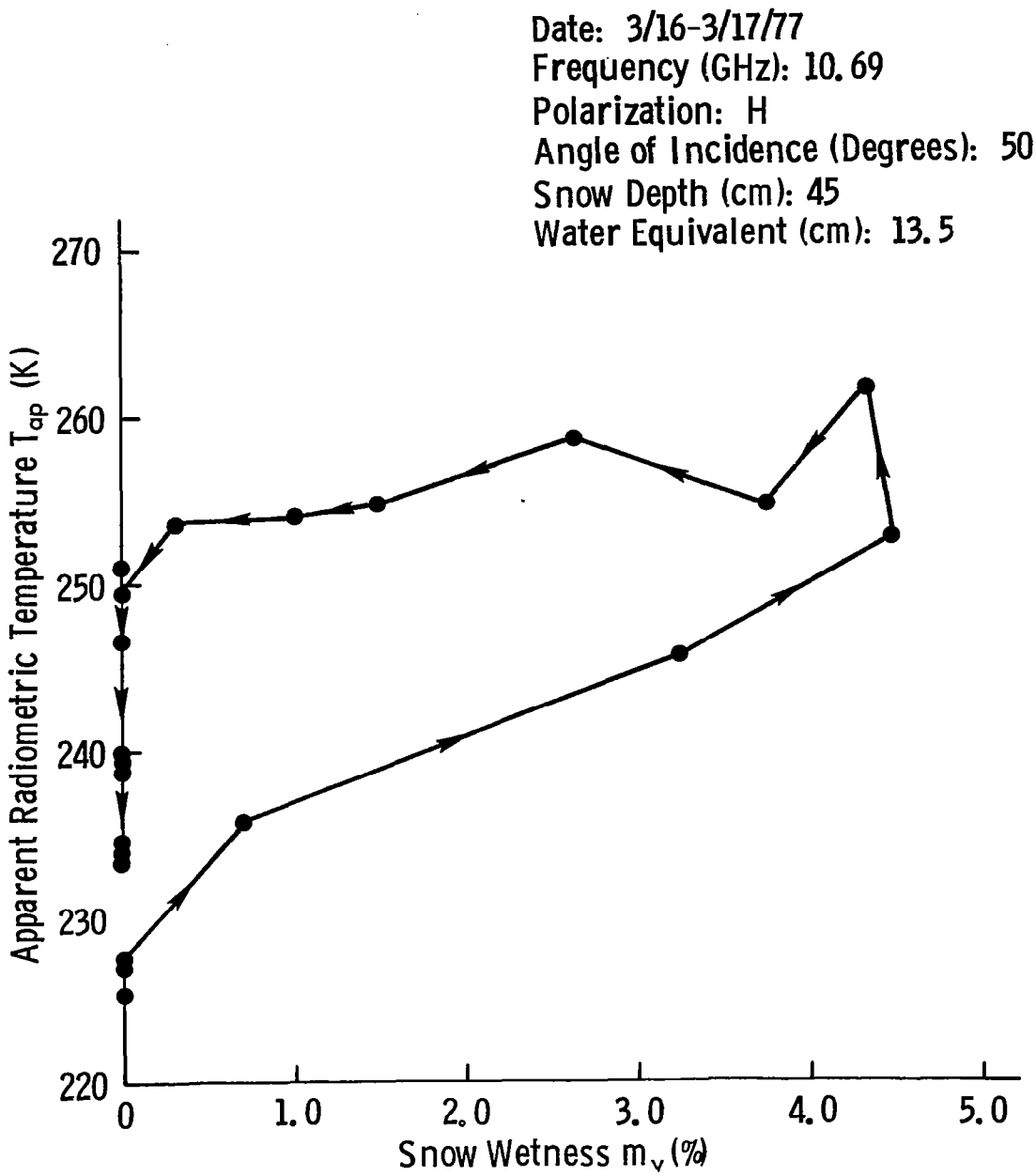


Figure 8-47 Hysteresis effect of T_{ap} at 10.69 GHz and 50^{o} angle of incidence.

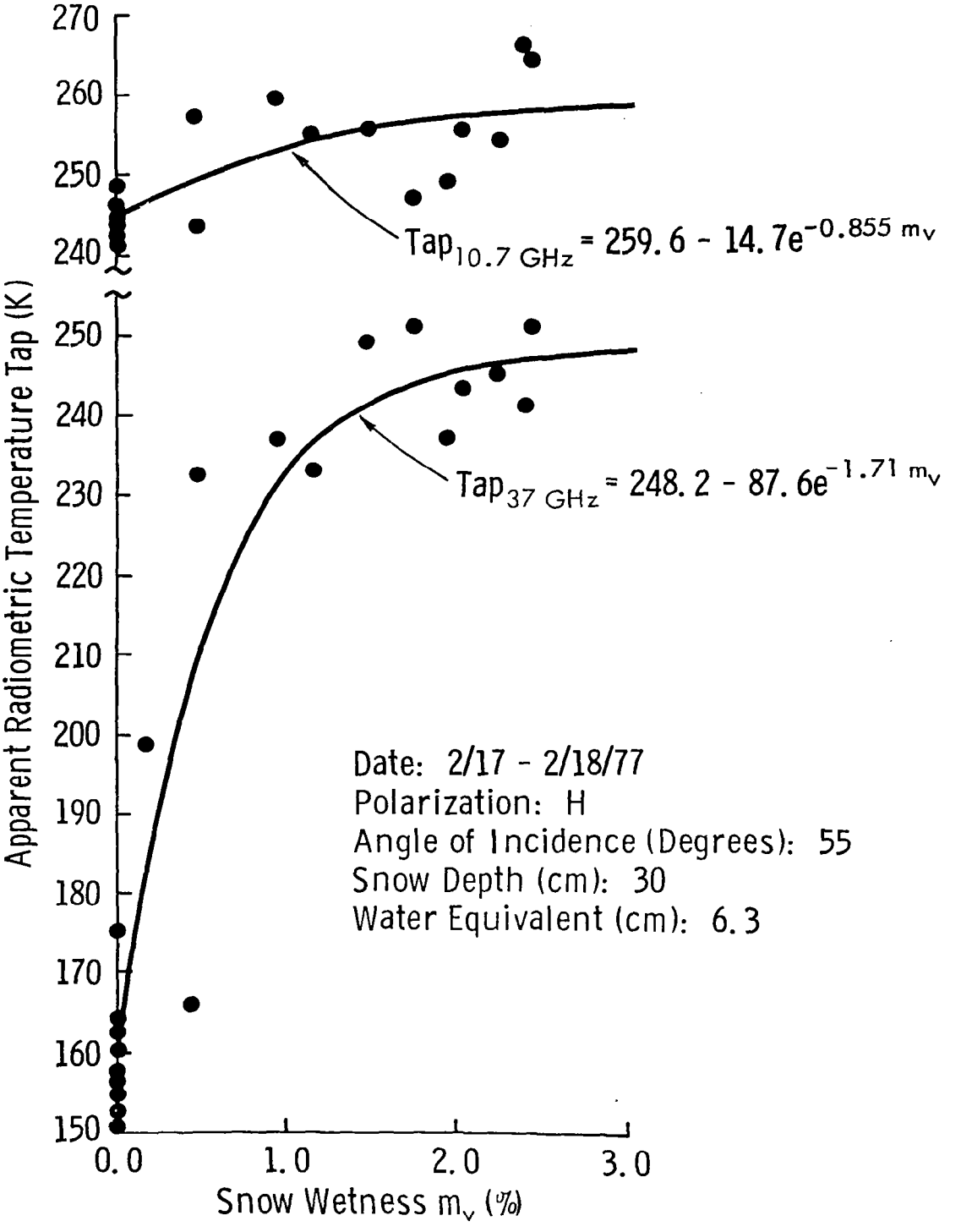


Figure 8-48 Tap Response to m_v at 50° Angle of Incidence

The scatter in the data points caused the exponential coefficients to be considerably smaller than the ones given in Figure 8-48 for a single diurnal experiment.

8.4.3 Summary of the Response to Snow Wetness

The conclusions from the analyses of the response to snow wetness are:

1) The peak-to-peak variation of σ^o to snow wetness indicates that the σ^o response is linear with wetness at low frequencies but becomes non-linear at the higher frequencies.
2) A hysteresis effect is seen between σ^o and m_v in the top 5 cm layer. The effect is related to the fact that the response is governed by the complete snow profile and the characterization by the wetness in the top 5 cm layer has varying validity.
3) The correlation coefficient and sensitivity of σ^o to changes in m_v becomes more negative with increasing frequency and angle of incidence.
4) The peak-to-peak variations of T_{ap} and m_v indicate a non-linear dependence.
5) A hysteresis effect similar to the active hysteresis is observed with T_{ap}.
6) The variation of T_{ap} with m_v can be represented by an exponential-like response.

8.5 Microwave Response to Water Equivalent

As a result of the limited snowfall during the experiment duration, the snow depth varied over a narrow range between 26 cm and 50 cm. The corresponding water equivalent variation was 6 cm to 14 cm. Although the data on the natural snowpack have provided information on the microwave response to several snow parameters, the response to water equivalent could not be determined because of its narrow range of values. Hence, three experiments were performed on artificially stacked snow. Since the spatial extent of the snowpile was limited, data were acquired at one angle of incidence per experiment. Passive data were obtained for all three experiments while σ^o data were acquired for only one experiment.

Table 8-4 gives a summary of the snow conditions and microwave parameters of each of the snowpile experiments. For the first experiment, snow

TABLE 8-4

Summary of the Snowpile Experiment Conditions

	Experiment 1	Experiment 2	Experiment 3
Date	2/24/77	3/21/77	3/22/77
Range of Snow Depth (cm)	0 - 144	0 - 170	0 - 170
Mean Snow Density (g/cm^3)	0.20	0.42	0.42
Mean Snow Temperature	-2^oC to -4^oC	-1^oC to -2^oC	-2^oC to -8^oC
Data Acquired With:			
a) 10.69 GHz radiometer	yes	no	yes
b) 37 GHz radiometer	yes	yes	yes
c) 94 GHz radiometer	no	yes	yes
d) MAS 8-18/35 scatterometer	no	no	yes
Angle of Incidence, θ	27^o	57^o	57^o
$T_{sky}(\theta)$			
10.69 GHz	6k	---	9.5k
37 GHz	15k	23k	23k
94 GHz	---	75k	75k

was piled up to a depth of 144 cm in five steps. In the second experiment, it was piled up to a depth of 170 cm in six steps and then reduced to ground level in nine steps in the third experiment. Ground truth samples were obtained for each layer added or removed from the snowpiles. Table 8-5 gives the ground truth data for the experiments.

All snowpile measurements were for dry snow conditions. This determination was either from calorimeter measurements or snow temperature measurements. The air temperature was below 0°C for all experiments. The density of the snow in Experiment 1 was approximately half the density of the snow in Experiments 2 and 3, resulting from the fact that fresh snow was used in the former and old metamorphosed snow was used in the latter.

For dry snow, the scattering and emission processes are governed by d, the snowpack depth, and ρ, the snowpack density. If d is electromagnetically commensurate to the snow skin depth or smaller, then the measured σ^o or T_{ap} will include contributions from the underlying surface. Dry snow is a scattering medium; however, in the absence of knowledge of the exact particle size and density distributions, the particles will be assumed to be uniform in size. With this assumption, for each snowpile experiment, σ^o and T_{ap} should be functions of the snow water equivalent W where

$$W = \rho d \qquad (8\text{-}3)$$

The units of W are centimeters.

8.5.1 Active Microwave

Since the scatterometer systems require spatial averaging to decrease the confidence limits on the measurement and as a result of the large volumes of snow required to create a snowpile, σ^o data were obtained only for Experiment 3. Since the snowpile size dictated a single look, adjacent frequencies were averaged to decrease the confidence limits. The confidence limits of σ^o were +1.5 dB to -2.0 dB at 9.0 GHz and +2.1 dB to -2.8 dB at 16.6 GHz at 57°. The results are given in Figures 8-49 and 8-50. An exponential like increase in σ^o is observed with water equivalent. Also the water equivalent at which the σ^o response begins to saturate is seen to decrease with frequency. The variation in σ^o is apparently almost complete at 16.6 GHz while the 9.0 GHz response is still rising.

Using a similar functional dependence to that used by Attema and Ulaby (1978) for vegetation, the following form was hypothesized for representing the effects of the snow medium and the underlying soil,

TABLE 8-5

Ground Truth for Snowpile Experiments

Experiment	Layer Depth top (cm)	Density (g/cm^3)	Snow Temp(°C)	Water Equivalent Layer(cm)	Water Equivalent Cumulative(cm)	Notes
1	0	----	0	----	----	
1	12	.10	-2.0	1.2	1.2	
1	40	.226	-2.4	6.3	7.5	
1	80	.220	-2.2	8.8	16.3	
1	113	.176	-2.1	5.8	22.2	
1	144	.196	-1.8	6.1	28.2	
1	43	.137	-2	5.9	----	old snow
2	0	----	0	----	----	
2	13	.340	-2.5	4.4	4.4	
2	32	.512	-1.6	9.7	14.1	
2	51	.510	-1.8	9.7	23.8	
2	71	.413	-2.0	8.3	32.1	
2	120	.425	-1.9	20.8	50.9	
2	170	.456	-2.5	22.8	73.7	
2	49	.275	-2	13.5	----	old snow
3	0	----	0	----	----	
3	14	.462	-2	6.5	6.5	
3	37	.462	-2	10.6	17.1	
3	52	.420	-3	6.3	23.4	
3	70	.420	-4	7.6	31.1	
3	85	.411	-5	6.2	37.2	
3	105	.382	-6	7.6	44.9	
3	120	.381	-7	5.7	50.6	
3	140	.385	-8	7.7	58.3	
3	170	.447	-8	13.4	71.7	

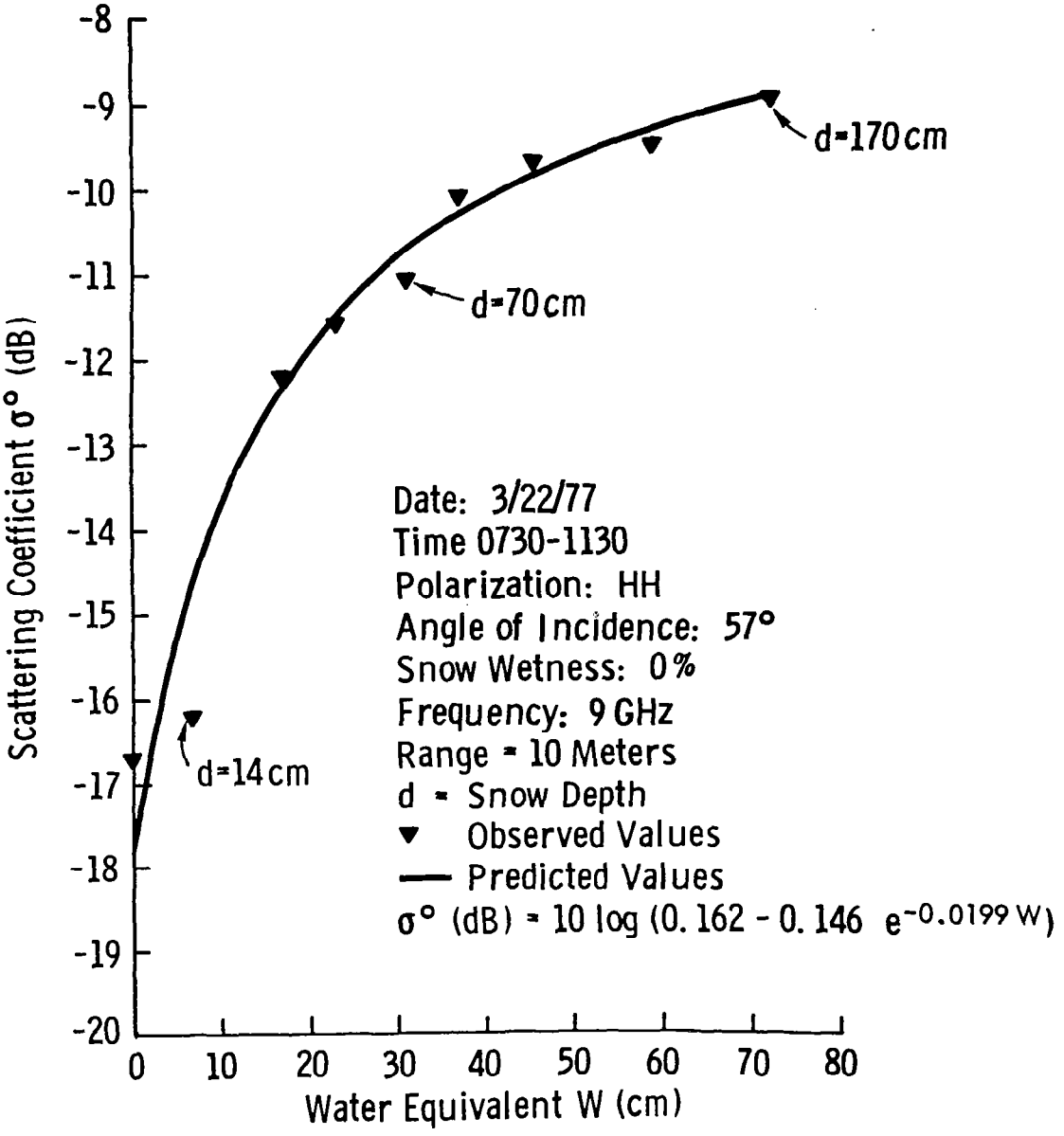


Figure 8-49 Scattering Coefficient Response to Snow Water Equivalent at 9 GHz

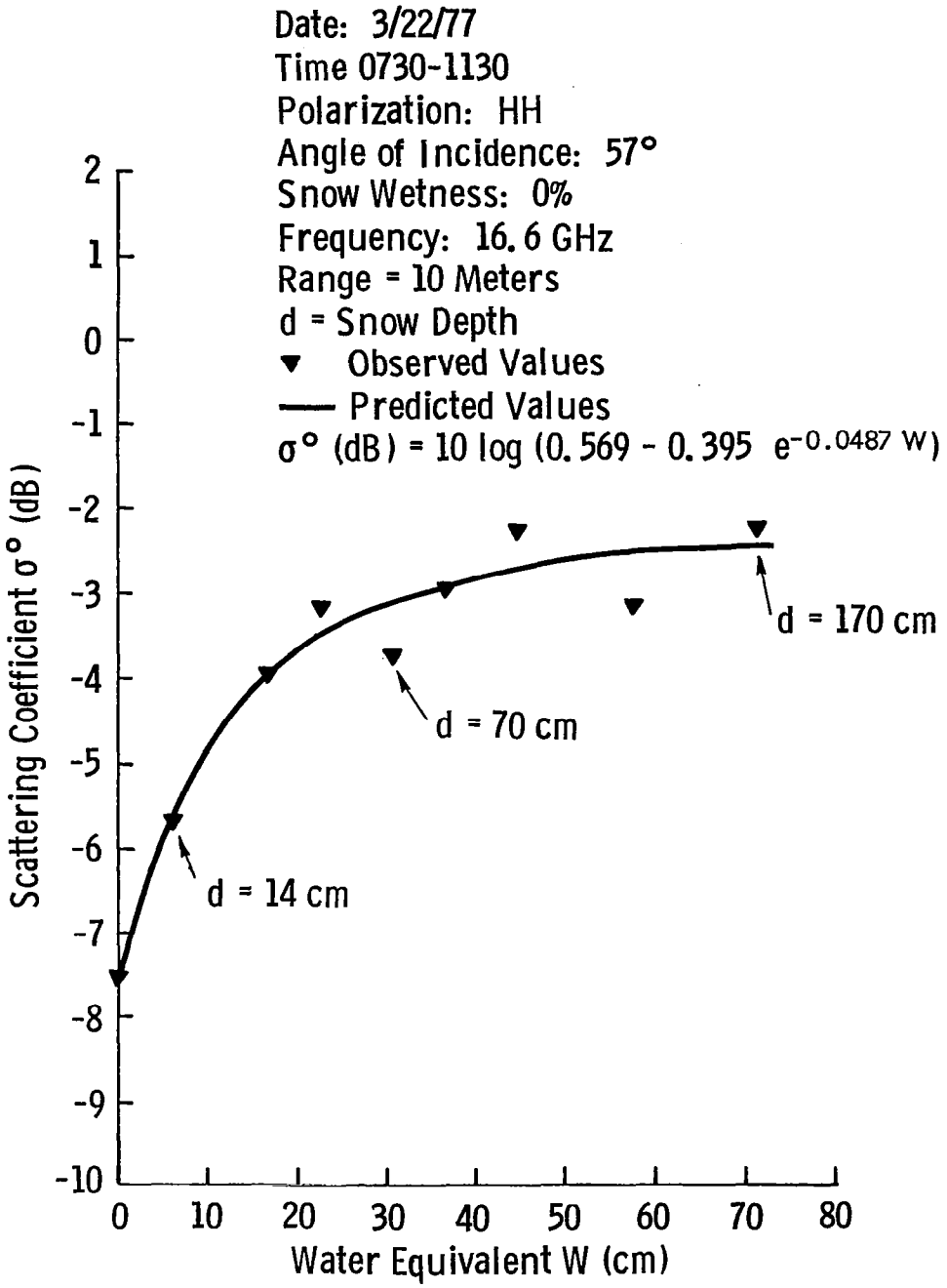


Figure 8-50 Scattering coefficient response to snow water equivalent at 16.6 GHz.

$$\sigma^o = C - D \exp(\kappa'_{eff} W) \qquad (8\text{-}4)$$

where κ'_{eff} is an effective mass extinction coefficient. The σ^o data were then fit by a non-linear regression of the above form. The results were

$$\sigma^o_{9.0}(dB) = 10 \log [0.162 - 0.146 \exp(-0.0199W)] \qquad (8\text{-}5)$$

$$\sigma^o_{16.6}(dB) = 10 \log [0.569 - 0.395 \exp(-0.0487W)] \qquad (8\text{-}6)$$

and are shown in Figures 8-49 and 8-50.

The results of equations (8-5) and (8-6) will be used in the model evaluation in Section 9.1.

8.5.2 Passive Microwave

The variation of T_{ap} with W is illustrated at all three frequencies in Figures 8-51 to 8-53. In addition to the T_{ap}'s measured in this study, Figure 8-52 also shows the results from Meier and Edgerton (1971) at a 45° angle of incidence.

Apparent temperature shows an exponential-like decrease with increasing water equivalent. The saturation water equivalent, or the W at which the soil contribution becomes neglible and further additions of snow do not affect T_{ap}, is observed to be frequency dependent. At 10.69 GHz, the saturation W was not reached, while the response leveled off at about W = 30 cm at 37 GHz and W = 15 cm at 94 GHz. The saturation values of T_{ap} at 57° are around 200 K at 10.69 GHz, 170 K at 37 GHz and 170 K at 94 GHz. Although the saturation levels are approximately the same at 37 GHz and 94 GHz, the emissivity at 94 GHz is lower (Section 8.2.2).

Data were also obtained on the adjacent undisturbed snowpack to allow comparison to natural conditions (Figures 8-51, 8-52 and 8-53). One observes that the natural snow values at both 27° and 57° are close to the snowpile values at comparable water equivalents, however the 37 GHz values are considerably lower even though the temperatures and ground conditions were approximately the same. The difference in T_{ap} of natural and artificially packed snow is attributed to the presence of ice layers in the natural snowpack. These layers would contribute to scattering loss and thus lower the emission. The spatial inhomogeneity in the snow volume introduced by the ice layers would be expected to have a substantially

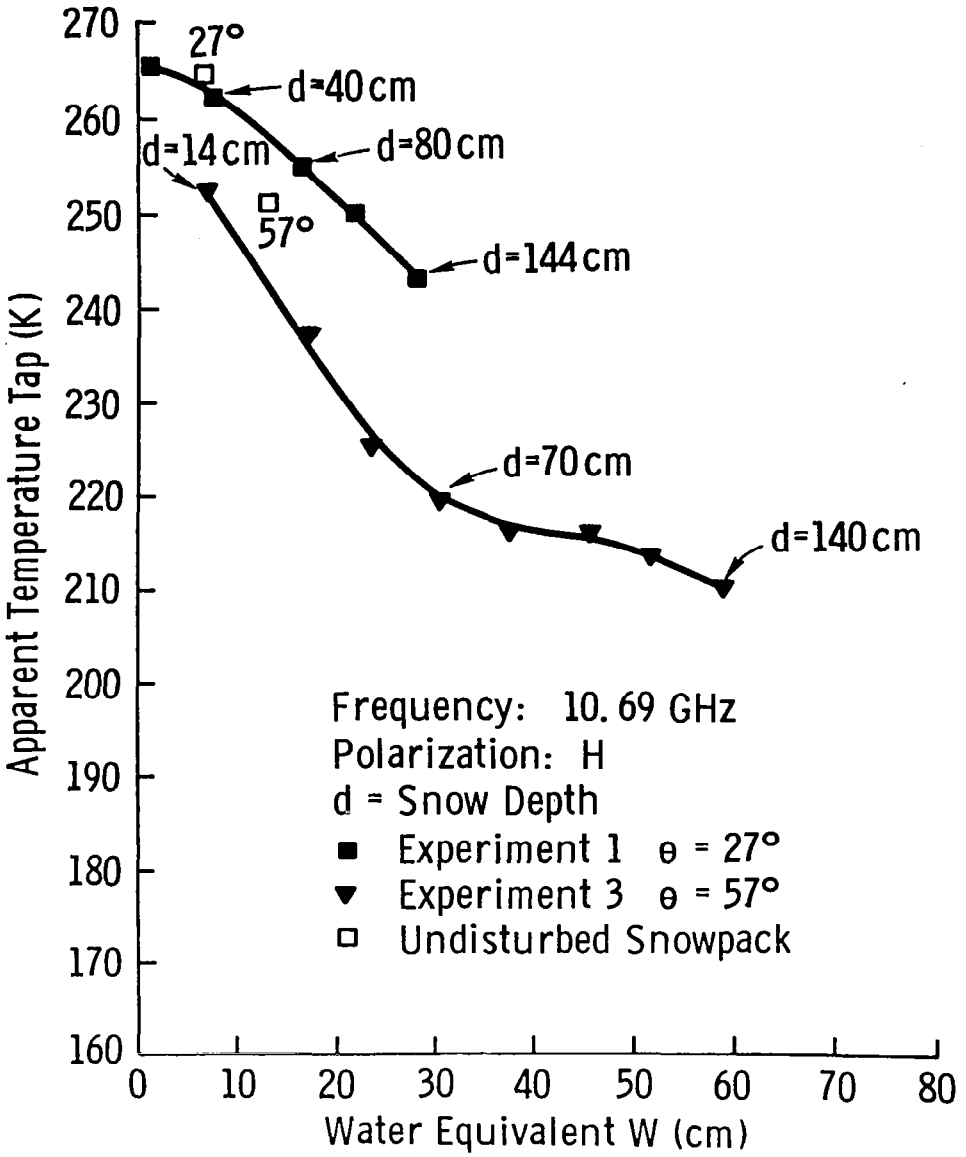


Figure 8-51 Radiometric apparent temperature response to snow water equivalent at 10.69 GHz.

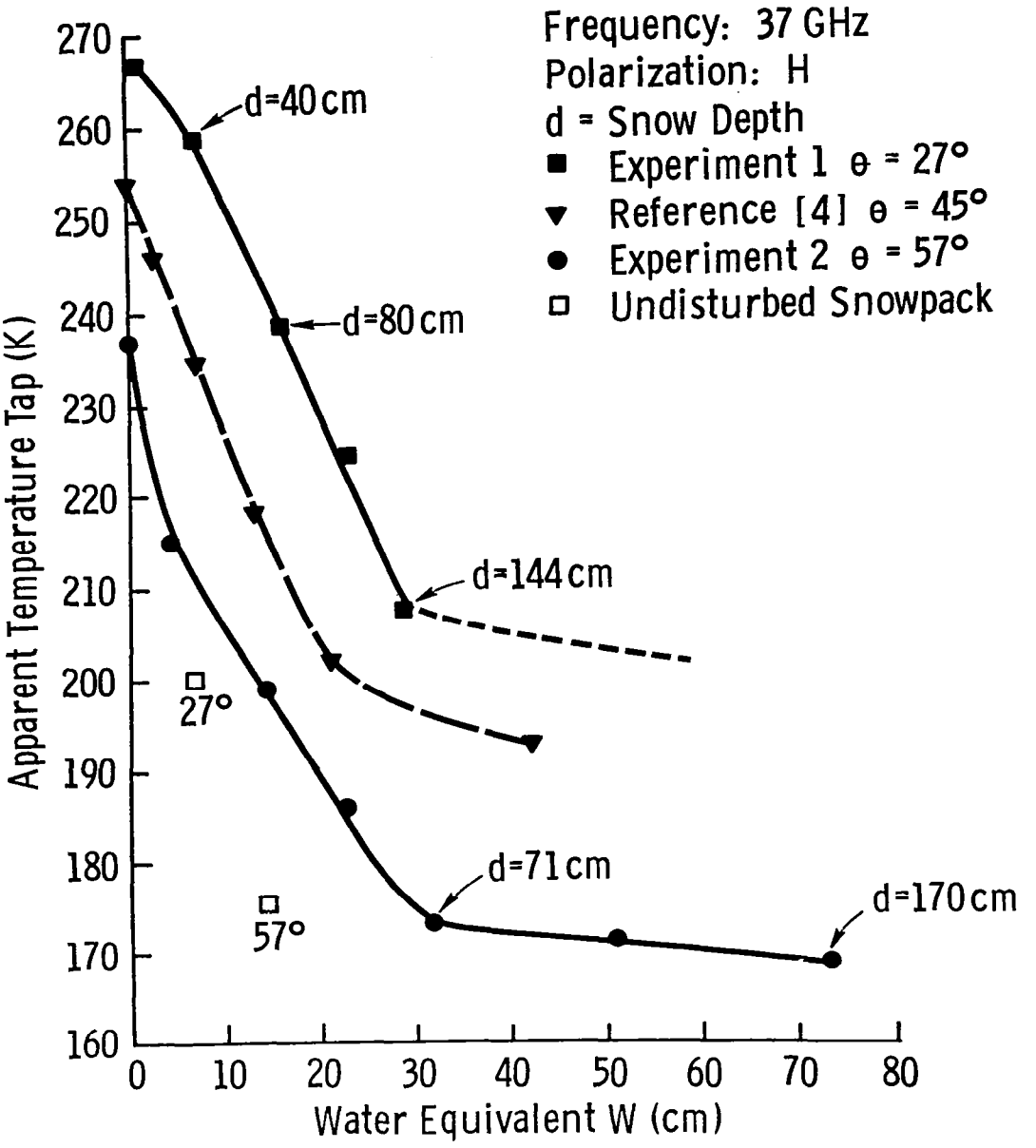


Figure 8-52 Radiometric apparent temperature response to snow water equivalent at 37 GHz.

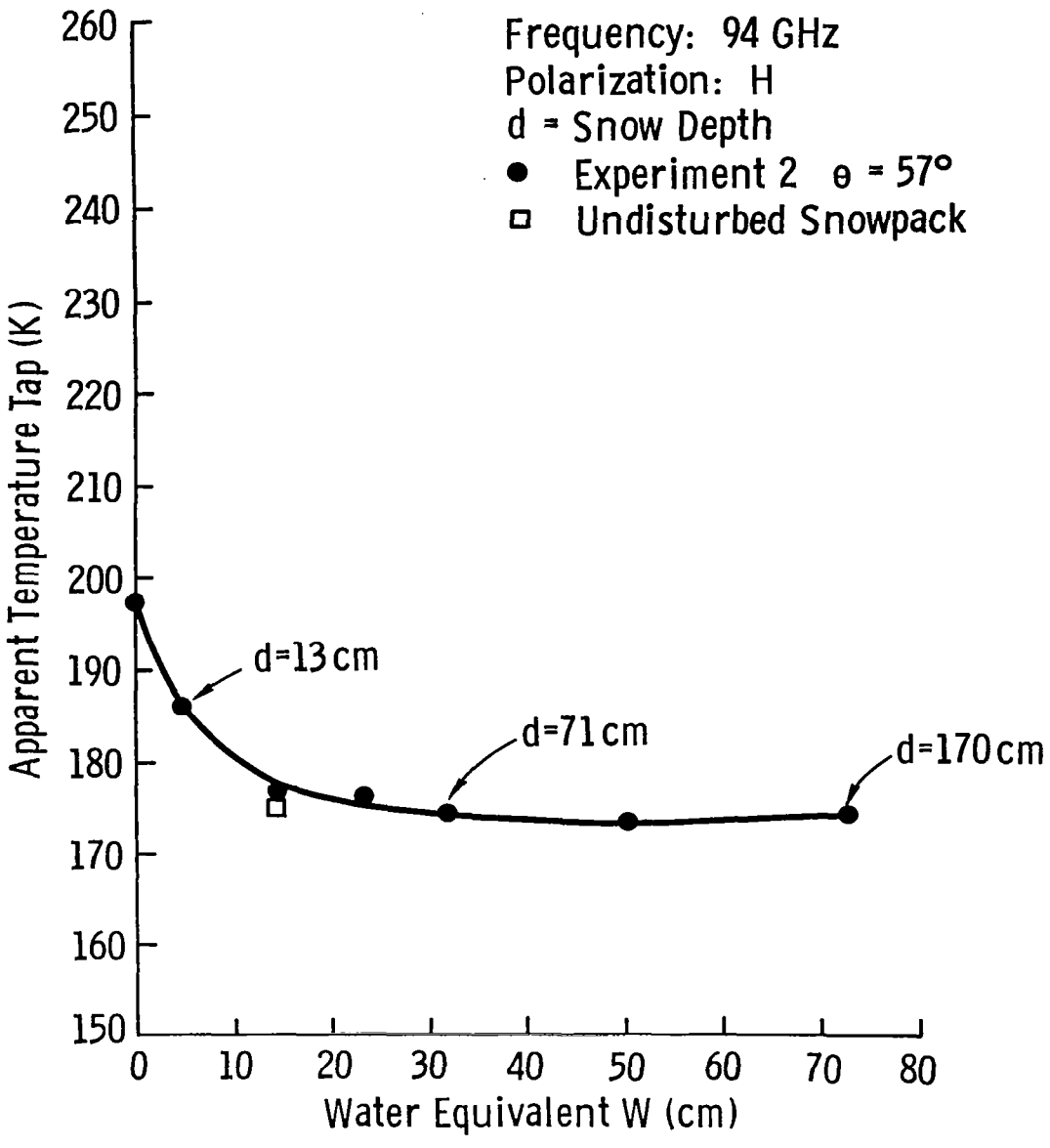


Figure 8-53 Radiometric apparent temperature response to snow water equivalent at 94 GHz.

greater influence at the shorter wavelength, 0.81 cm (37 GHz), than at the longer wavelength, 2.8 cm (10.7 GHz), which may explain the difference in behavior between 10.69 GHz and 37 GHz. Naturally packed "old" snow therefore should exhibit a faster exponential decay with W than the curves illustrated in Figure 8-52. It is also noted that the saturation values of T_{ap} are about the same as the natural snow values at 37 GHz and 94 GHz.

A model for expressing T_{ap} in terms of water equivalent is developed in Section 9.2.

8.5.3 Summary of the Microwave Response to Water Equivalent

The following conclusions were generated from the snowpile experiments.

1) The σ° data exhibit an exponential-like increase with increasing water equivalent at 57°.
2) The T_{ap} data exhibit an exponential-like decrease with increasing water equivalent at 57°.
3) The saturation levels reached by T_{ap} were frequency dependent and were reached at smaller water equivalent values for old metamorphosed snow.

8.5 Attenuation of Snow

The attenuation experiment, described in Section 6.5.3, was successful only to a limited extent because the condition of the snow layer over the antenna boxes was not representative of the plot on which the σ° and T_{ap} data were collected. Ice layers which formed during the extended period of no snow (near 2/23) were not present in the plot on which σ° and T_{ap} data were acquired. The path loss for wet and dry snow conditions was illustrated in Figure 8-2. A description of the response shown in Figure 8-2 is given in Section 8.1.1.

All of the path loss measurements at a given frequency are plotted as a function of time of day in Figures 8-54 to 8-57. The positive values of loss are the result of mismatch. The maximum loss values varied from 8.3 dB at 2.125 GHz to greater than 20 dB (system sensitivity limited) at 17.0 GHz. The envelopes of these values are also given. The peak loss values occur between 1200 and 1800 hours as expected when the snow was the wettest. On cold days, however, the attenuation values remained low.

Figure 8-58 gives the measured loss values obtained at 35 GHz. Unfortunately, the wetness measurements were inadequate. Nonetheless, the loss for the wet snow case is observed to be very high.

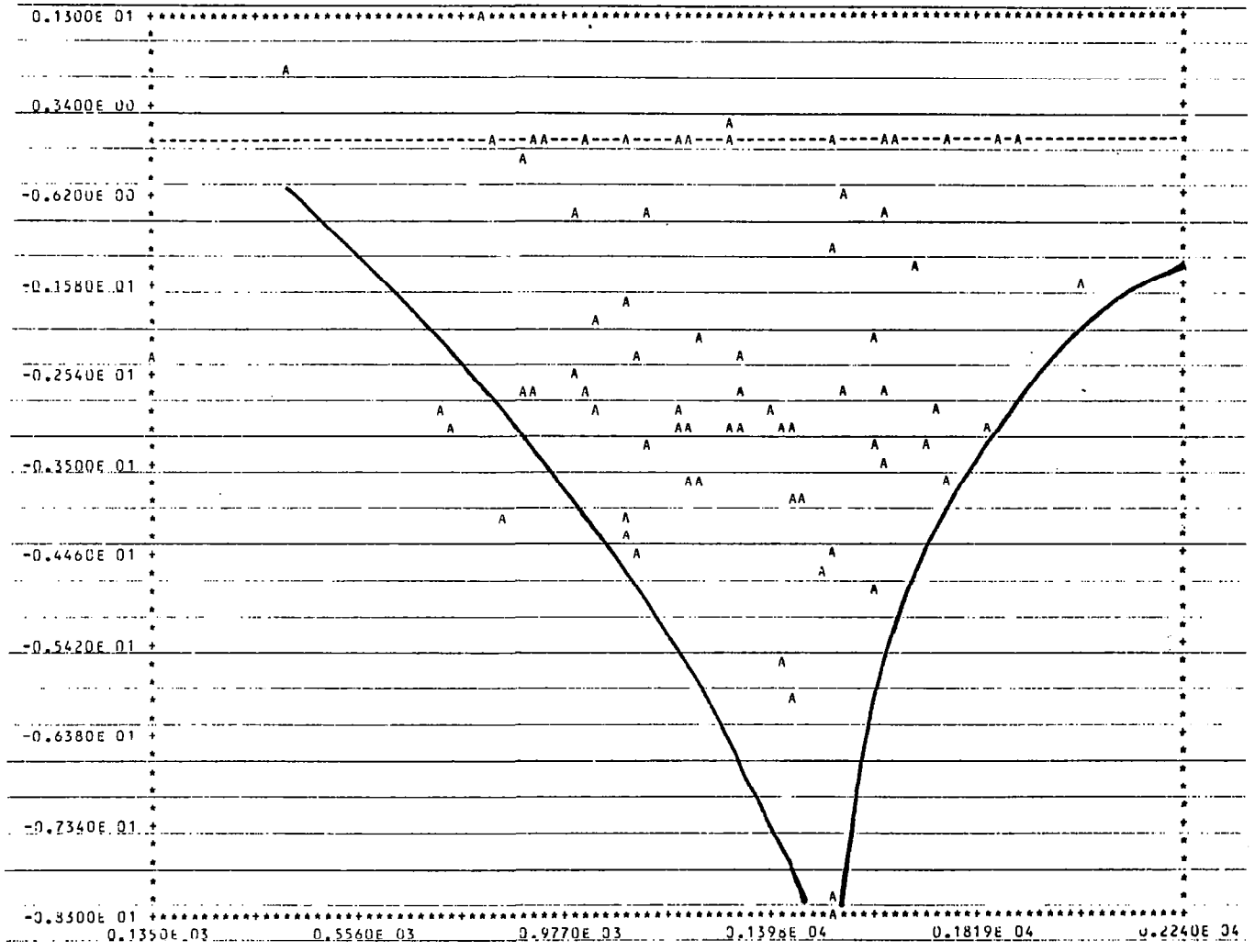


Figure 8-54 Dynamic range of snow attenuation values at 2.125 GHz.

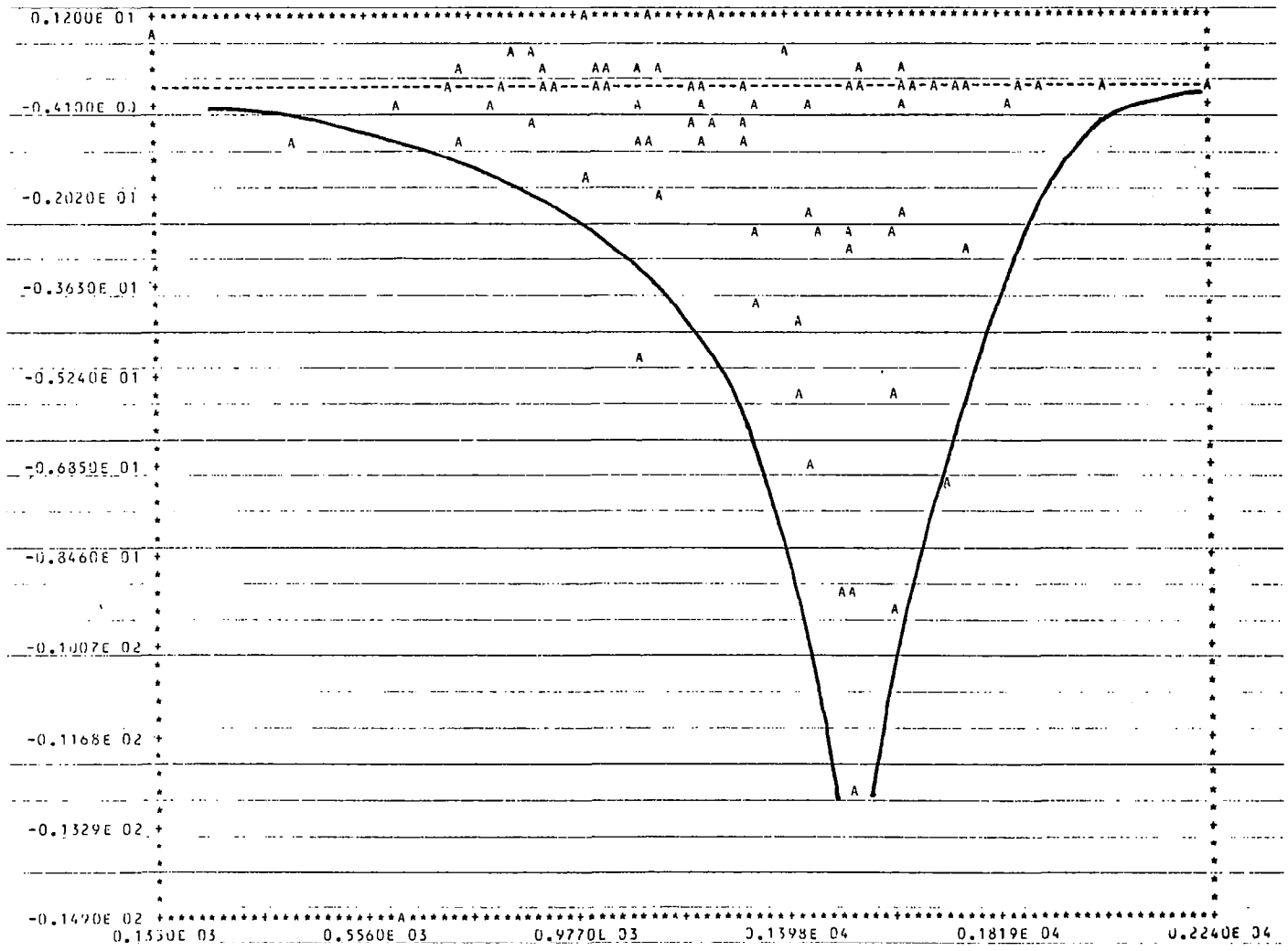


Figure 8-55 Dynamic range of snow attenuation values at 5.125 GHz.

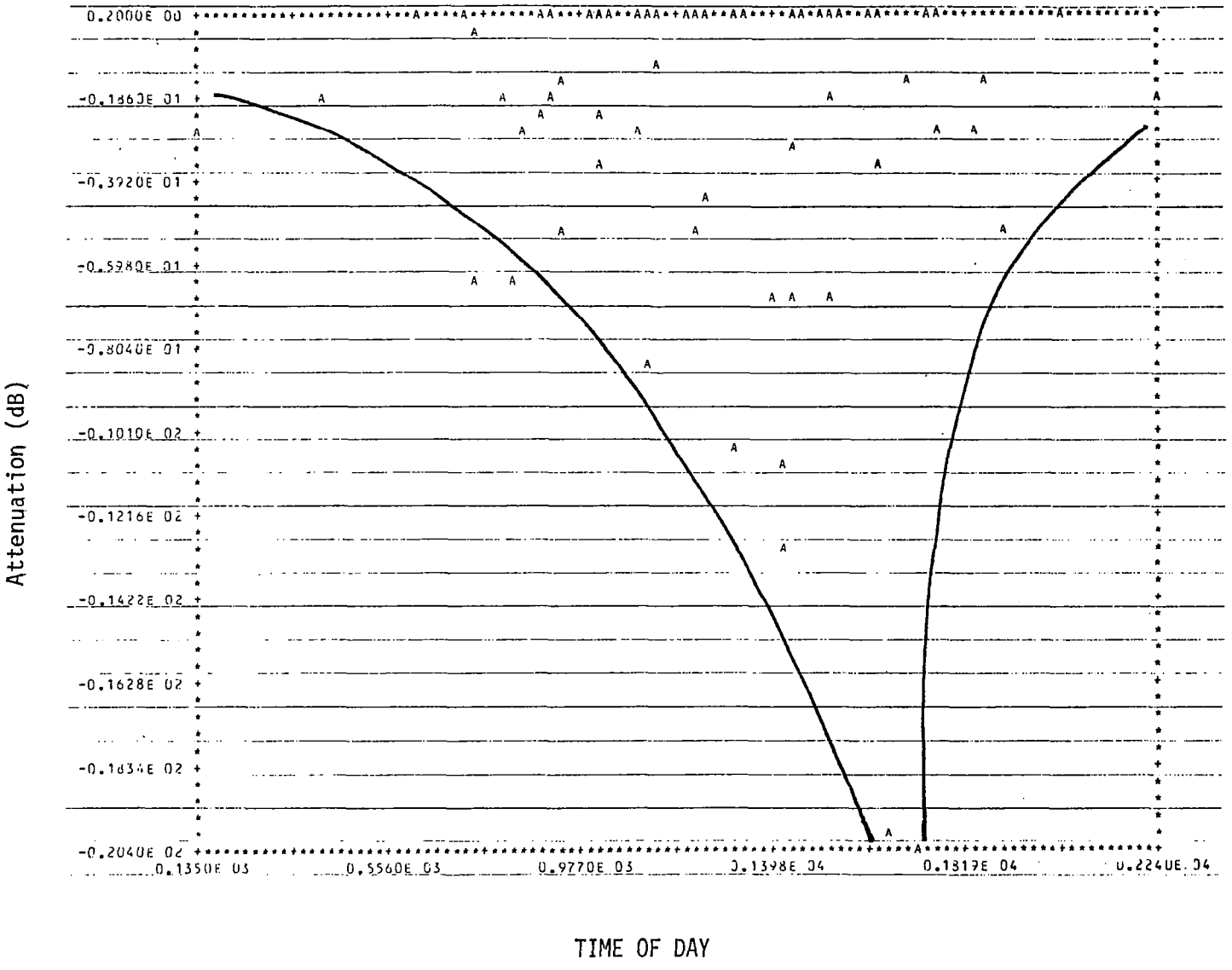


Figure 8-56 Dynamic range of snow attenuation values at 13.8 GHz.

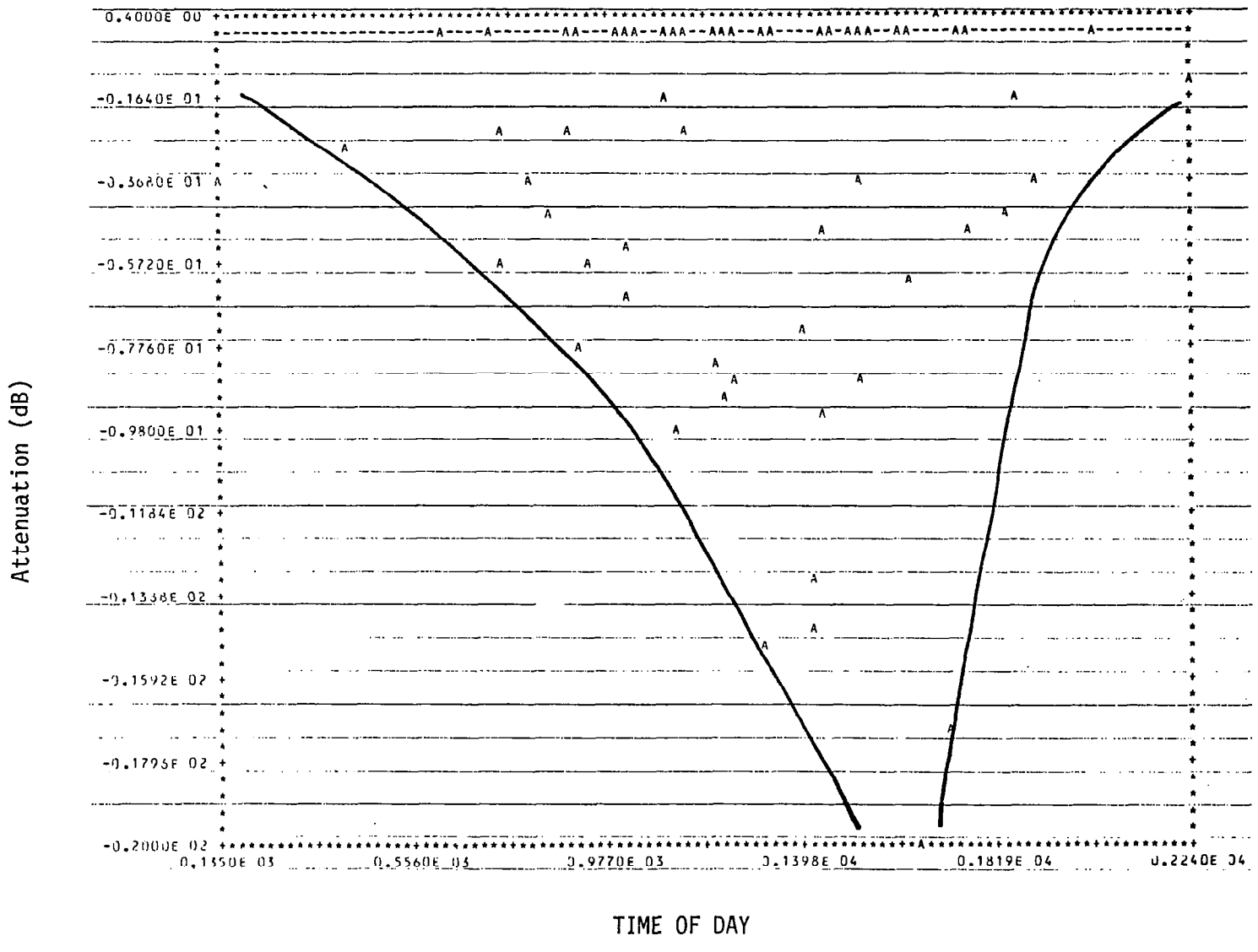


Figure 8-57 Dynamic range of snow attenuation values at 17.0 GHz.

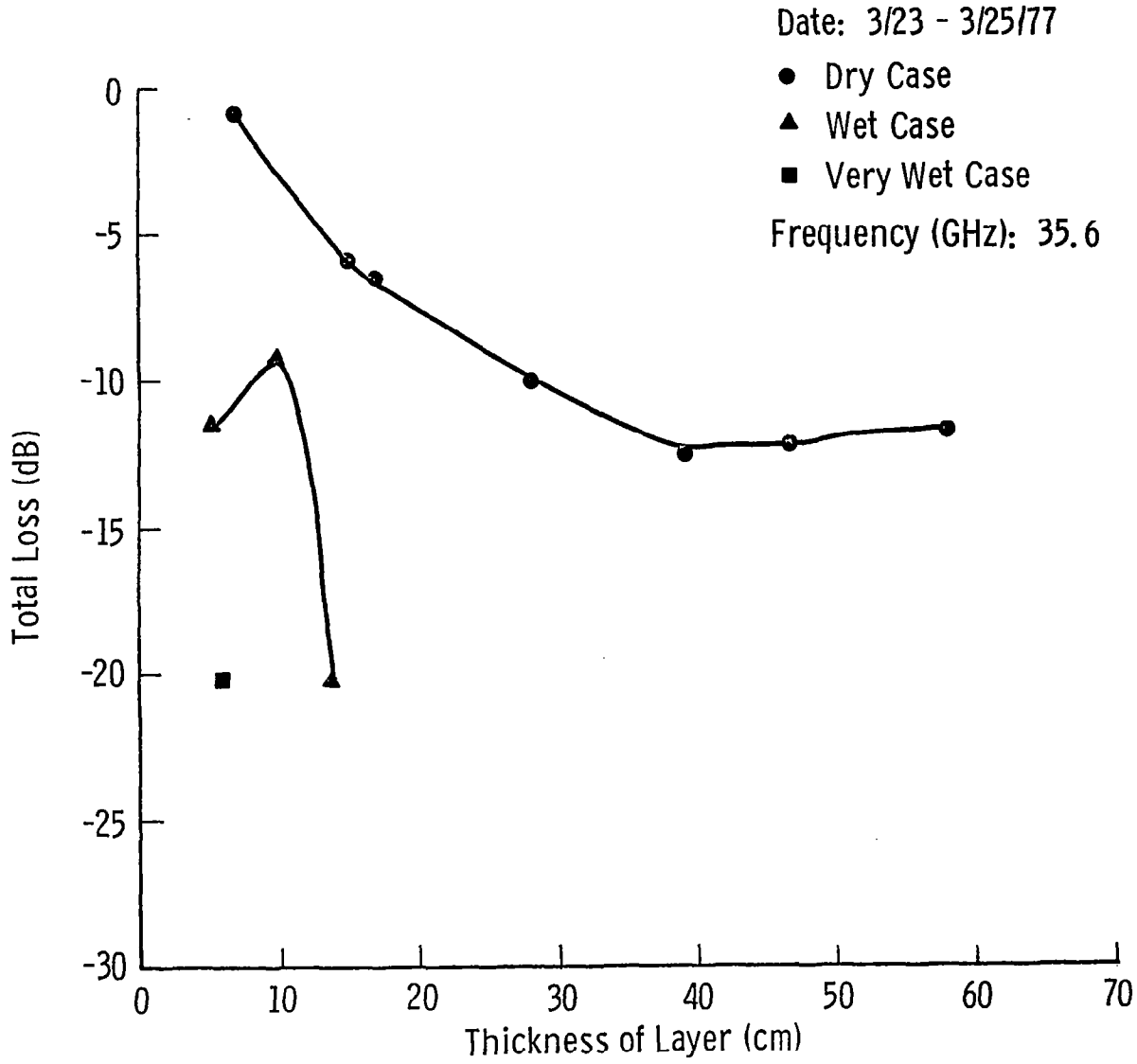


Figure 8-58 Measured path loss as a function of snow thickness for three snow conditions.

9.0 SIMPLE MODELS FOR σ^o AND ε OF SNOWPACK

The relationship between σ^o and ε and the physical and dielectric parameters of a snowpack can be better understood through the development of simple models. These models are based upon measurable ground truth parameters. A review of the more detailed theoretical modeling studies, which often require inputs not normally measured or measurable, is given in Section 2.2.

9.1 Active Microwave

9.1.1 Proposed Backscattering Coefficient Model

Although in general a snowpack consists of several layers of slightly varying density and crystalline structure, for simplicity it will be modeled as a single uniform dielectric layer. Figure 2-1 illustrates the target configuration.

The backscattering coefficient of the snow-covered soil target will be represented as the incoherent sum of the contributions from the ground and from the snow. Since the snow layer is a scattering and a lossy medium at microwave frequencies, it contributes to the backscattering coefficient directly and attenuates the backscattering coefficient of the ground.

The loss L_d through the snow layer of thickness d is given by equation 2-8. The ground contribution is σ^o_{gnd}, reduced by the round-trip loss L_d^2. If the snow and ground contributions are independent and add incoherently, then:

$$\sigma^o = \frac{\sigma^o_{gnd}}{L_d^2} + \sigma^o_{snow} \qquad (9\text{-}1)$$

The backscattering coefficient of bare soil has been determined by Ulaby, et al (1978b) to be of the following form:

$$\sigma^o_{gnd} = A \exp(Bm_s) \qquad (9\text{-}2)$$

where m_s is the soil moisture content and A and B are constants which are functions of frequency, polarization and angle of incidence. The backscatter of the snow is assumed to be related to the loss through the layer and backscatter within the layer in a manner similar to the emission in a

radiometric transfer model (Section 9.2). The following form is assumed:

$$\sigma^o_{snow} = \sigma^o_s \frac{\kappa_s}{\kappa_e} \left(1 - \frac{1}{L_d^2}\right) \tag{9-3}$$

where $\sigma^o_s \kappa_s/\kappa_e$ is the saturation value of the scattering coefficient when L is large. κ_s/κ_e is the scattering albedo and σ^o_s is a constant which scales the saturation scattering coefficient. This form is a variation of that used by Attema and Ulaby (1977) to model scattering from a vegetation canopy. With reference to Figure 2-1, L_d is given in terms of the transmission angle θ',

$$L_d = \exp(\tau_d \sec \theta') = \exp(\kappa_e d \sec \theta') \tag{9-4}$$

Equation 9-1 may be rewritten as:

$$\sigma^o = \frac{\sigma^o_{gnd}}{L_d^2} + \sigma^o_s \frac{\kappa_s}{\kappa_e} \left(1 - \frac{1}{L_d^2}\right) \tag{9-5}$$

The two snow parameters that will be included in this model are snow wetness m_v and snow depth d. The variation with depth is straightforward and affects σ^o through the loss factor L_d. The variation with snow wetness m_v, on the other hand, affects κ_s, κ_a, κ_e, and L_d. Therefore, the behavior of κ_s, κ_a and κ_e with m_v must be investigated.

Based on available experimental data (Figure 4-18), κ_a will be assumed to vary linearly with m_v:

$$\kappa_a = \kappa_{ao} + N_a m_v \tag{9-6}$$

where κ_{ao} is the dry snow absorption coefficient and N_a is a constant. The scattering coefficient κ_s is related to the dielectric inhomogeneity of the snow medium. In dry snow, the inhomogeneity is due to the contrast in dielectric constant between that of the ice crystals (k' = 3.2) and the snow medium (k' = 1.6 for a typical snow density of 0.3 g/cm^3 (see Figure (4-10)). As the snow becomes wet, the dielectric constant of the medium increases (Figures 4-13 and 4-14) to about k' = 3.5 for m_v = 10 percent, which results in a decrease in the contrast, and therefore less volume

scattering. Thus κ_s should slowly decrease with m_v. The following form will be assumed for κ_s:

$$\kappa_s = \kappa_{so} - N_s m_v \approx \kappa_{so} \tag{9-7}$$

where κ_{so} is the dry snow scattering coefficient and N_s is a positive constant. As a first order approximation, it will be assumed that κ_s is independent of wetness.

In the lower microwave frequency region, where the wavelength is much larger than the dimensions of the ice crystals, scattering in the volume is small, and therefore $\kappa_e \cong \kappa_a$. In the millimeter region, on the other hand, volume scattering plays a very important role in both the emission and backscattering processes, particularly for dry snow conditions.

The variation of κ_e with wetness, can be found from combining equations 2-6, 9-6, and 9-7:

$$\kappa_e = \kappa_{ao} + \kappa_{so} + N_a m_v = \kappa_{eo} + N_a m_v \tag{9-8}$$

Substitution of equations 9-4, 9-7 and 9-8 into equation 9-5 yields:

$$\sigma^o = \sigma^o_{gnd} \exp(-2\tau_d \sec\theta') + \sigma^o_s \left(\frac{\kappa_{so}}{\kappa_{ao} + \kappa_{so} + N_a m_v}\right) [1 - \exp(-2\tau_d \sec\theta')] \tag{9-9}$$

The general behavior of the above equation may be seen from the limiting cases of the snow parameters. If no snow is present, then $\tau_d = 0$ and:

$$\sigma^o = \sigma^o_{gnd} \tag{9-10}$$

If the depth of snow becomes very large, therefore $\tau_d >> 1$ and if the snow is dry:

$$\sigma^o = \sigma^o_s \frac{\kappa_{so}}{\kappa_{ao} + \kappa_{so}} = \sigma^o_{sat} \tag{9-11}$$

which is the saturation value of σ^o for dry snow. If the wetness is not constrained to zero then:

$$\sigma^o = \sigma^o_s \frac{\kappa_{so}}{\kappa_{ao} + \kappa_{so} + N_a m_v} \tag{9-12}$$

which decreases as m_v increases. A saturation value should exist for σ^o; however, since m_v is effectively limited by water drainage from the snow, there is an effective lower saturation limit on equation 9-12. For dry snow of an intermediate depth:

$$\sigma^o = \sigma^o_{gnd} \exp(-2\kappa_{eo} d \sec\theta') + \sigma^o_s \frac{\kappa_{so}}{\kappa_{eo}} [1 - \exp(-2\kappa_{eo} d \sec\theta')] \quad (9\text{-}13)$$

Equation 9-13 can be rewritten in a different form:

$$\sigma^o = \sigma^o_s \frac{\kappa_{so}}{\kappa_{eo}} + \left(-\sigma^o_s \frac{\kappa_{so}}{\kappa_{eo}} + \sigma^o_{gnd}\right) \exp(-2\kappa_{eo} d \sec\theta') \quad (9\text{-}14)$$

which is the same form (equation 8-4) as was applied to the dry snow snowpile σ^o data. Therefore, it is observed that in all of the limiting cases, equation 9-9 reduces to reasonable expressions for σ^o.

This model disregards many of the parameters which also affect σ^o; however, it can be used to generate empirical results from which insight into the dependence of σ^o on snow parameters can be gained. If the optical depth τ_d in equation 9-9 is small, then the ground contribution will dominate. If on the other hand the optical depth is large, then the major contribution of σ^o is from the snow layer. The microwave specturm is valuable for remote sensing purposes since for the snow conditions of interest, the total σ^o contribution can result from both snowpack and ground or by proper selection of system parameters the contributions may be separated.

In the next section, the variaion with the snow and ground parameters affecting σ^o will be described and the model will be applied to the data acquired in this investigation.

9.1.2 Evaluation of the Backscattering Coefficient Model

To apply equation 9-9 to the measured σ^o data, it will be convenient to use mass absorption, scattering, and extinction coefficients (equation 2-7):

$$\kappa_{ao} = \kappa'_{ao}\rho \qquad \kappa_{eo} = \kappa'_{eo}\rho$$
$$\kappa_{so} = \kappa'_{so}\rho \qquad N_a = N'_a\rho \quad (9\text{-}15)$$

Use of the mass coefficients allows the snow parameters to be expressed in terms of water equivalent W thus removing the effects of snow density ρ on κ_a, κ_s, and κ_e. Substitution of equations 2-7 and 9-15 into equation 9-9

gives:

$$\sigma^o = \sigma^o_{gnd} \exp\left(-2[\kappa'_{ao} + \kappa'_{so} + N'_a m_v] W \sec\theta'\right) \quad (9\text{-}16)$$
$$+ \sigma^o_s \frac{\kappa'_{so}}{\kappa'_{ao} + \kappa'_{so} + N'_a m_v} \left\{1 - \exp(-2[\kappa'_{ao} + \kappa'_{so} + N'_a m_v] W \sec\theta')\right\}$$

The constants (σ^o_{gnd}, κ'_s, κ'_a, κ'_e, N'_a, θ', and σ^o_s) in this equation will then be determined through observations and non-linear regressions of the data. First of all, the variation of these parameters with angle and frequency is determined and then the model is evaluated.

The angle of propagation in the snow layer is determined through the use of Snell's law:

$$\sec\theta' = \frac{\sqrt{k_s}}{\sqrt{k_s - \sin^2\theta}} \quad (9\text{-}17)$$

where k_s is the relative dielectric constant of a homogeneous snow layer.

The value of k_s is a function of wetness, therefore the effective water equivalent, $W_{eff} = W \sec\theta'$, of the snowpack is also a function of snow wetness. Since the dielectric constant varies from about 1.5 for low density dry snow to 4.5 for very wet snow, the corresponding W_{eff} values vary from about 1.37W to 1.09W, respectively. The following form was assumed for k_s:

$$k_s = 1.5 + 0.3\, m_v \quad (9\text{-}18)$$

which results from the slope of Sweeny and Colbeck's (1974) dependence on snow wetness (Figure 4-14) and assuming a dry k_s value of 1.5.

The next step is to determine the behavior of σ^o_{gnd}, σ^o_s and κ'_e with angle of incidence, frequency and soil state. The dry snow spectral response to water equivalent (Figure 9-1) is obtained by replotting the snowpile data described in Section 8.5.1. It is apparent that the response of σ^o(dB) with frequency at a given value of W is approimately linear. Equations (8-5) and (8-6) show that the behavior of σ^o is exponential with increasing water equivalent. If the exponential term is assumed to be linear with frequency, then the following spectral responses can be determined from these equations:

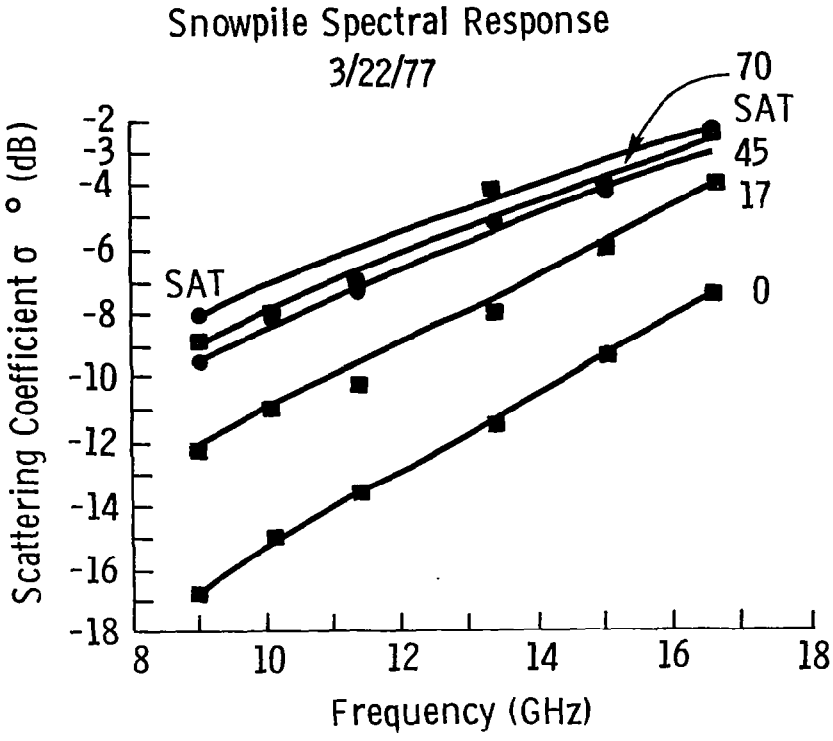


Figure 9-1 Snowpile Spectral Response

$$\left.\begin{aligned} \sigma^{o}_{gnd}(dB) &= 1.368\ f - 30.3 \\ \sigma^{o}_{sat}(dB) &= 0.7184f - 14.4 \\ 2\kappa'_{e} &= 0.00353f - .01187 \end{aligned}\right\} : m_v = 0 \qquad (9\text{-}19)$$

Since the snowpile measurements were at a single angle (57^{o}), determiation of the angular response of the above parameters at other angles of incidence was desired. Several data sets were averaged for the early and late periods of the experiment. Then the slopes, assuming a linear fit between 20^{o} and 70^{o}, were estimated and the following sensitivities to angle determined at two frequencies.

Before 3/3/77

$$S_{8.6} \cong 0.2 \quad dB/degree$$

$$S_{17.0} \cong 0.16 \quad dB/degree \qquad (9\text{-}20)$$

After 3/7/77

$$S_{8.6} \cong 0.2 \quad dB/degree$$

$$S_{17.0} \cong 0.1 \quad dB/degree$$

Since the scattering coefficient of the underlying target σ^{o}_{gnd} could not be measured except during the snowpile experiment, these values were estimated using equation (9-13) applied to dry snow conditions for two of the diurnal experiments when the soil conditions were different. Using the extinction coefficients from the snowpile experiments, σ_{sat} values of equations (9-19) and the following values of σ^{o} on dry snow and substituting into (9-13), σ^{o}_{gnd} can be solved for frozen soil conditions (2/17/77) and thawed soil conditions (3/16/77). The σ^{o} values of 55^{o} on 2/17/77 were -15.5 dB and -8.0 dB at 8.6 GHz and 17.0 GHz, respectively, while on 3/16/77 the σ^{o} values were -10.5 dB and -4.5 dB, respectively. The calculated values of σ^{o}_{gnd} are -19.8 dB and -19.5 dB on 2/17/77 at 55^{o} and -11.7 dB and -7.7 dB on 3/16/77 at 50^{o} for 8.6 GHz and 17.0 GHz, respectively. These values agree reasonably well with the ones calculated from equation (9-19) on thawed ground. The variation of σ^{o}_{gnd} with angle of incidence will be assumed to be the same as given in equation (9-20).

The constants (κ'_{eo}, $\sigma^o_s\kappa'_{so}$, and N'_a) in equation 9-16 were determined by applying the model to the σ^o data from the 2/17/77 and 3/16/77 diurnal experiments. A non-linear regression routine from the BMDP computer program package from the Health Sciences Computing Facility at the University of California was employed. The predicted σ^o response and the observed values are plotted versus m_v in Figures 9-2 and 9-3. The fit to the data is good at both 8.6 GHz and 17.0 GHz, even though the predicted σ^o values on 2/17/77 seem to be a little high. The trends of the data are also observed to be correct; as the snow wetness increases, the effects of the ground and snow depth variation decrease and the σ^o curves for each diurnal experiment converge. For dry snow, on the other hand, contributions from the ground and the different snow depths result in a wider variation in σ^o value than for the wet snow cases. Also, the scattering albedo, $\kappa'_{so}/\kappa'_{eo}$, increases with increasing frequency, as was expected.

The next step in the application of the model was to apply it to the σ^o data over the experiment duration. The frozen or thawed state of the soil was inferred from the temperature measurements and soil samples. The σ^o data taken before 2/19/77 were converted to 50^o using equation (9-20). Then the model was applied to the σ^o values at 50^o for 8.6 GHz and 17.0 GHz. Figure 9-4 shows the seasonal variation of m_v, W, σ^o_{HH} and the predicted values from the model evaluated at 8.6 GHz. The predicted response is most sensitive to m_v variations; however the effects of increasing W are also observed in the increasing values of σ^o for dry snow conditions as the snow depth increased. Figure 9-5 presents the predicted σ^o values at 17.0 GHz. The fit is not quite as good as at 8.6 GHz; the sensitivity to m_v does not appear to be large enough. However, the coefficients agree with the results in Figures 9-2 and 9-3 and show an expected increase in the coefficients from 8.6 GHz to 17.0 GHz.

Two deficiencies in the ground truth sampling (soil state and the wetness measurement sample size) limit improvement of the model. Out of necessity, the σ^o_{gnd} value had to be assumed to have only two values, corresponding to either frozen or thawed soil. Previous analyses have also shown that better vertical snow wetness resolution would better model the σ^o variation. Even with these deficiencies, however, the model is observed to fit the measurements. The differences between the constants from Figures 9-2 and 9-3 and Figures 9-4 and 9-5 result from the expanded data sets of the latter figures.

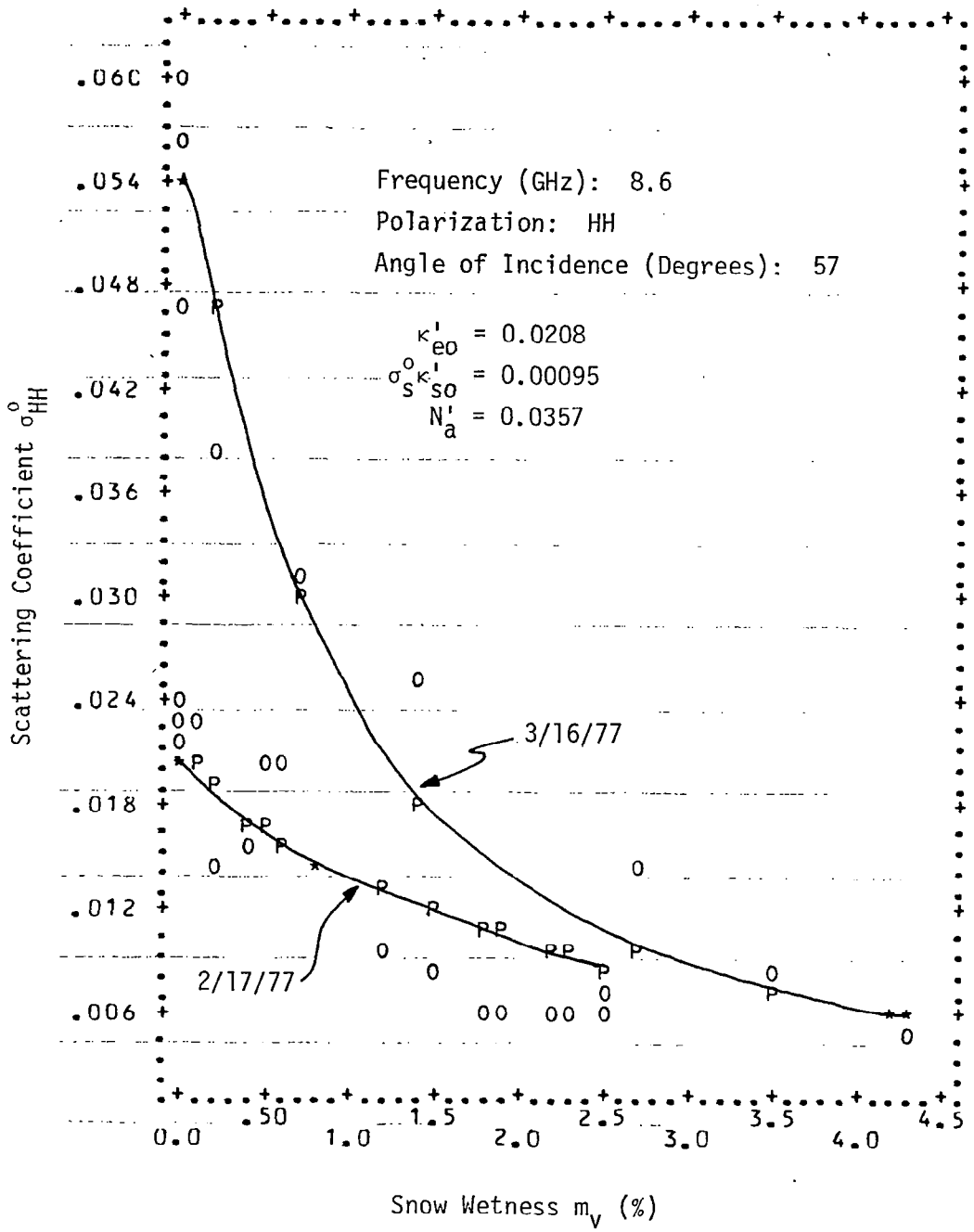


Figure 9-2 Scattering coefficient model applied to two diurnal data groups at 8.6 GHz.

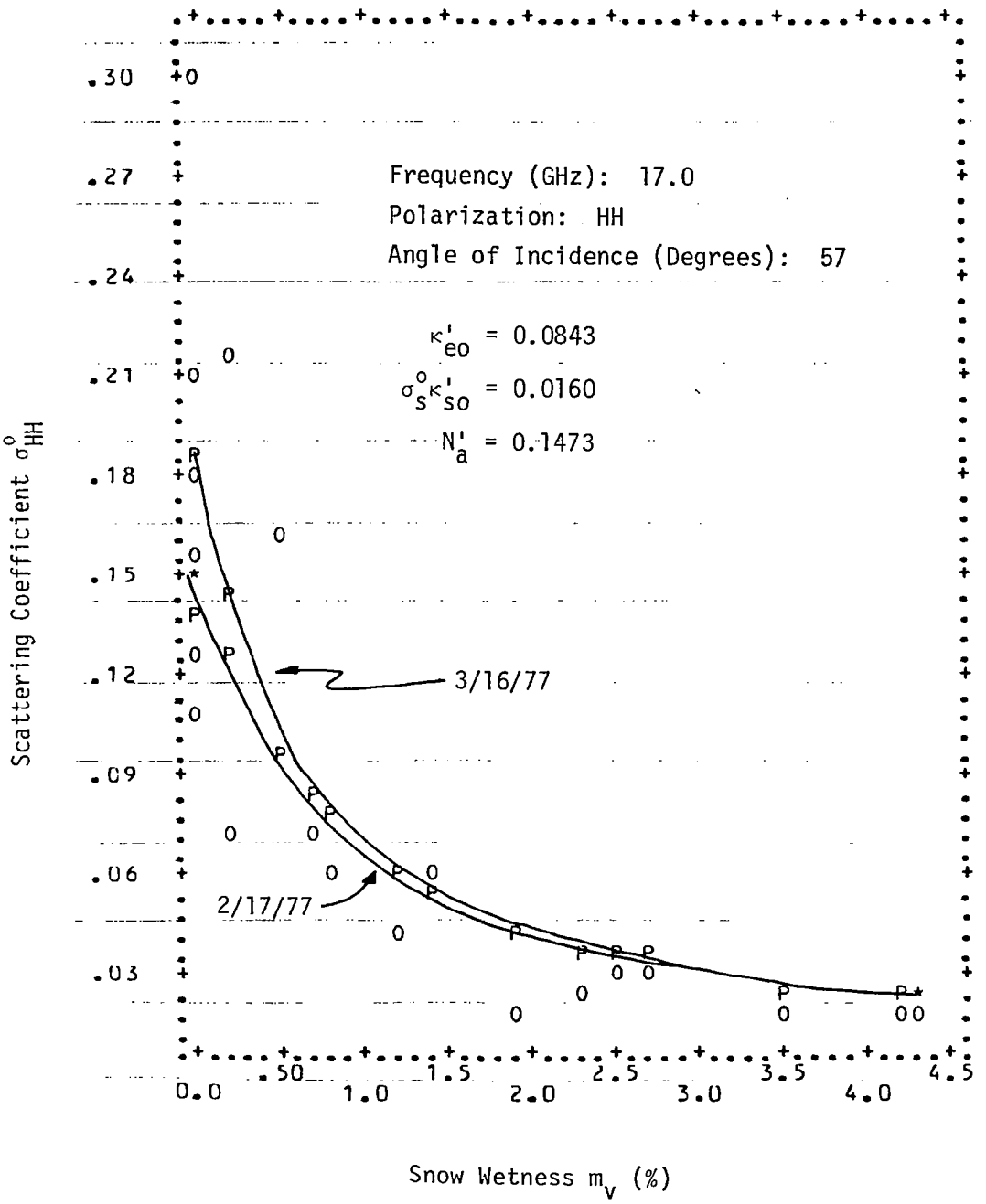


Figure 9-3 Scattering coefficient model applied to two diurnal data groups at 17.0 GHz.

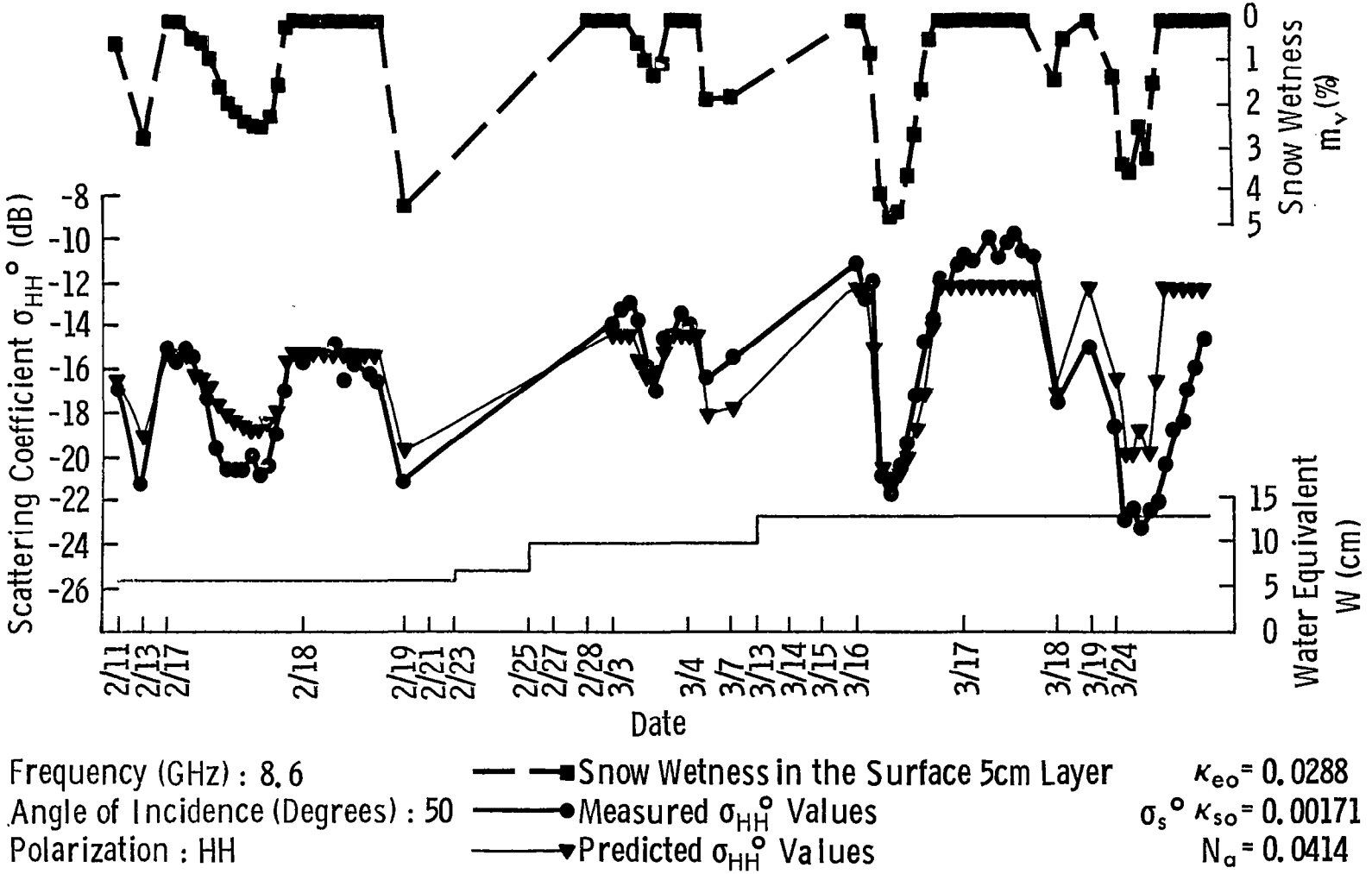


Figure 9-4 Scattering coefficient model and observed σ° value comparison over the experiment duration at 8.6 GHz and 50° angle of incidence.

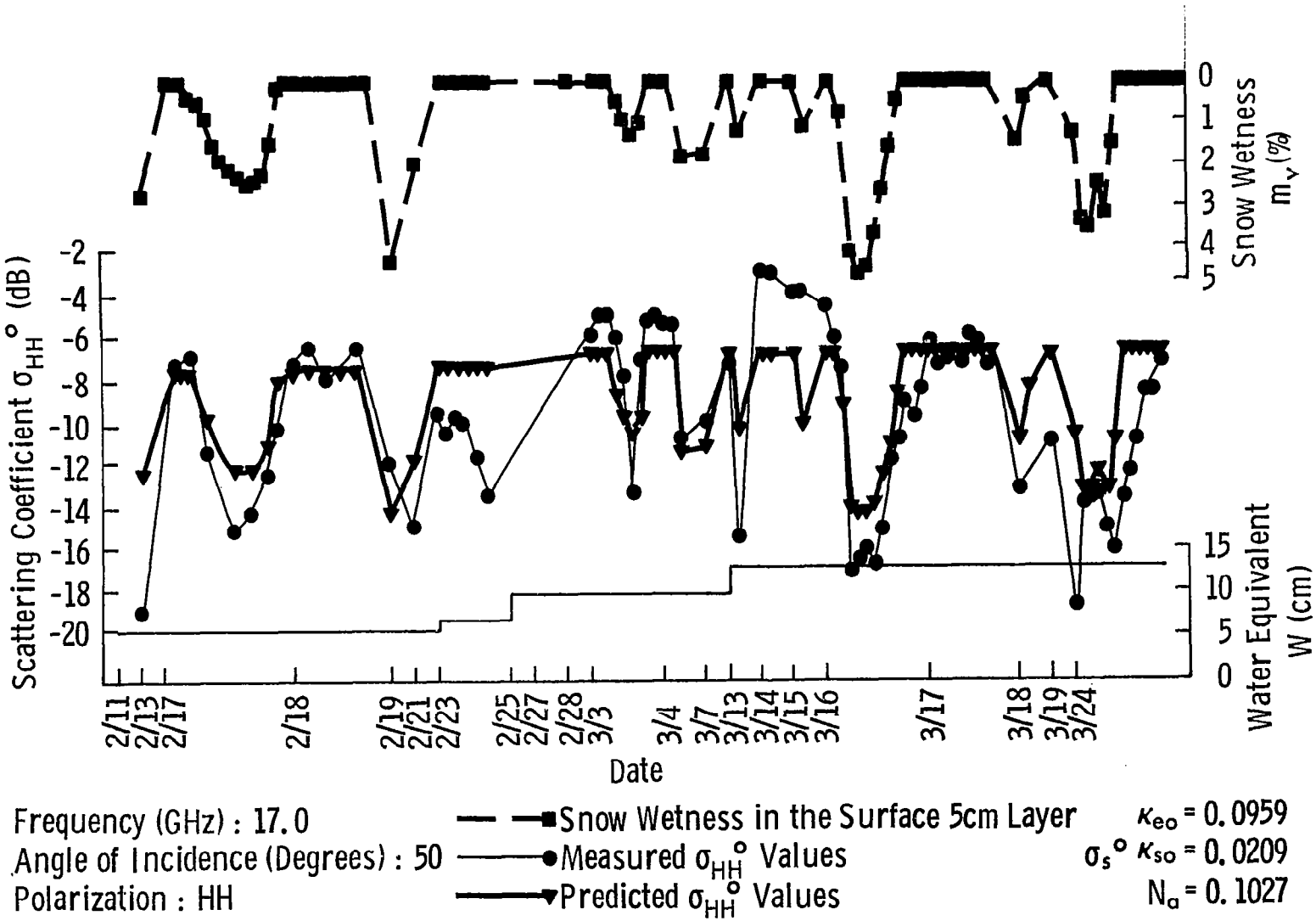


Figure 9-5 Scattering coefficient model and observed σ° value comparison over the experiment duration at 17.0 GHz and 50° angle of incidence.

The variation of σ^o in the limiting case of deep snow (given by equation 9-12) is illustrated in Figure 9-6 as a function of snow wetness. The higher σ^o value at 17.0 GHz results from the higher κ'_{so} values relative to κ'_{eo} at 17.0 GHz. The spectral variation of σ^o for deep snow is illustrated in Figure 9-7. The slope of these curves closely match the spectral response curves of Figure 8-17c, implying that the spectral response of the model is reasonable. Also note the saturation effect as the m_v values become high ($\approx$5%). The variation with snow wetness and water equivalent is seen in Figure 9-8. For the frozen ground cases and dry snow, the σ^o variation of the target with water equivalent between 5 and 30 cm is significant; while for $m_v > 2$, above W = 5 cm there is little variation with greater water equivalent values. For the thawed ground case, at 17.0 GHz, the effect of the ground is insignificant above W = 5 cm; while at 8.6 GHz, a 2.5 dB variation is seen between the σ^o values for W between 5 and 30 cm. This behavior indicates that ground contributions are more significant at 8.6 GHz than at 17.0 GHz. The model was also applied to the σ^o data at 20^o angle of incidence. The methodology was the same as for the 50^o σ^o data. Firstly, the σ^o_{gnd} values were estimated from the 2/17/77 diurnal experiment using the previously outlined procedure. The σ^o_{gnd} values were -12 dB and -5 dB at 8.6 GHz and 17.0 GHz, respectively. σ^o_{gnd} values for thawed ground were estimated to be -7 dB at 8.6 GHz and -2 dB at 17.0 GHz. Then the model was applied at 8.6 GHz and 17.0 GHz and the results are given in Figures 9-9 and 9-10. It should be noted that the regression fits in this case again show the correct trends, however, the fits are not as good as those at 50° angle of incidence.

The quantities $\sigma^o_s \kappa'_{so}$ at 20^o and 50^o are different because of the difference in value of σ^o_s at 20^o and 50^o. Calculation of the scattering albedo requires separation of these two terms. This was not done for the purposes of this model. One other problem with the previous development is the limited range of W over which σ^o data were obtained. For this reason, the model may not fit very well outside the range of W that was observed. A simplified, more empirical model was then developed and in some cases gives a better fit to the data. The following form was used:

$$\sigma^o = \sigma^o_{gnd} \exp\left[-2(\kappa'_{eo} + N'm_v)W\right] + \sigma^o_s \exp\left[-Em_v\right] \left[1 - \exp\left(-2[\kappa'_{eo} + N'm_v]W \sec\theta'\right)\right] \quad (9\text{-}21)$$

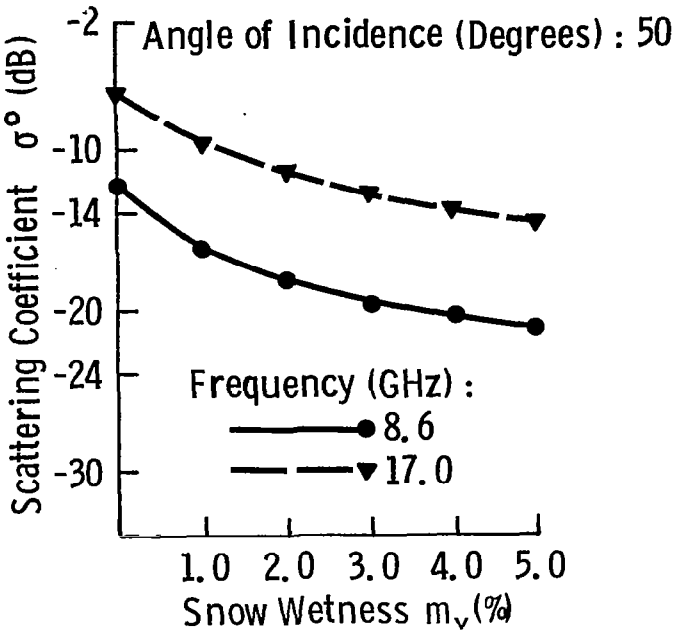


Figure 9-6 Sensitivity of σ^o of deep snow to snow wetness.

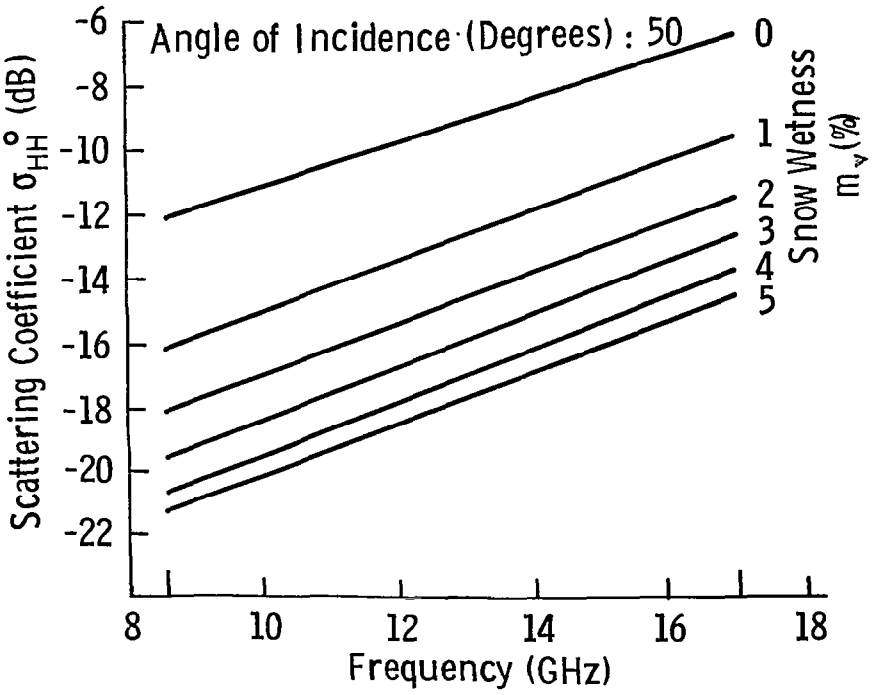


Figure 9-7 Spectral response of the σ^o model to snow wetness.

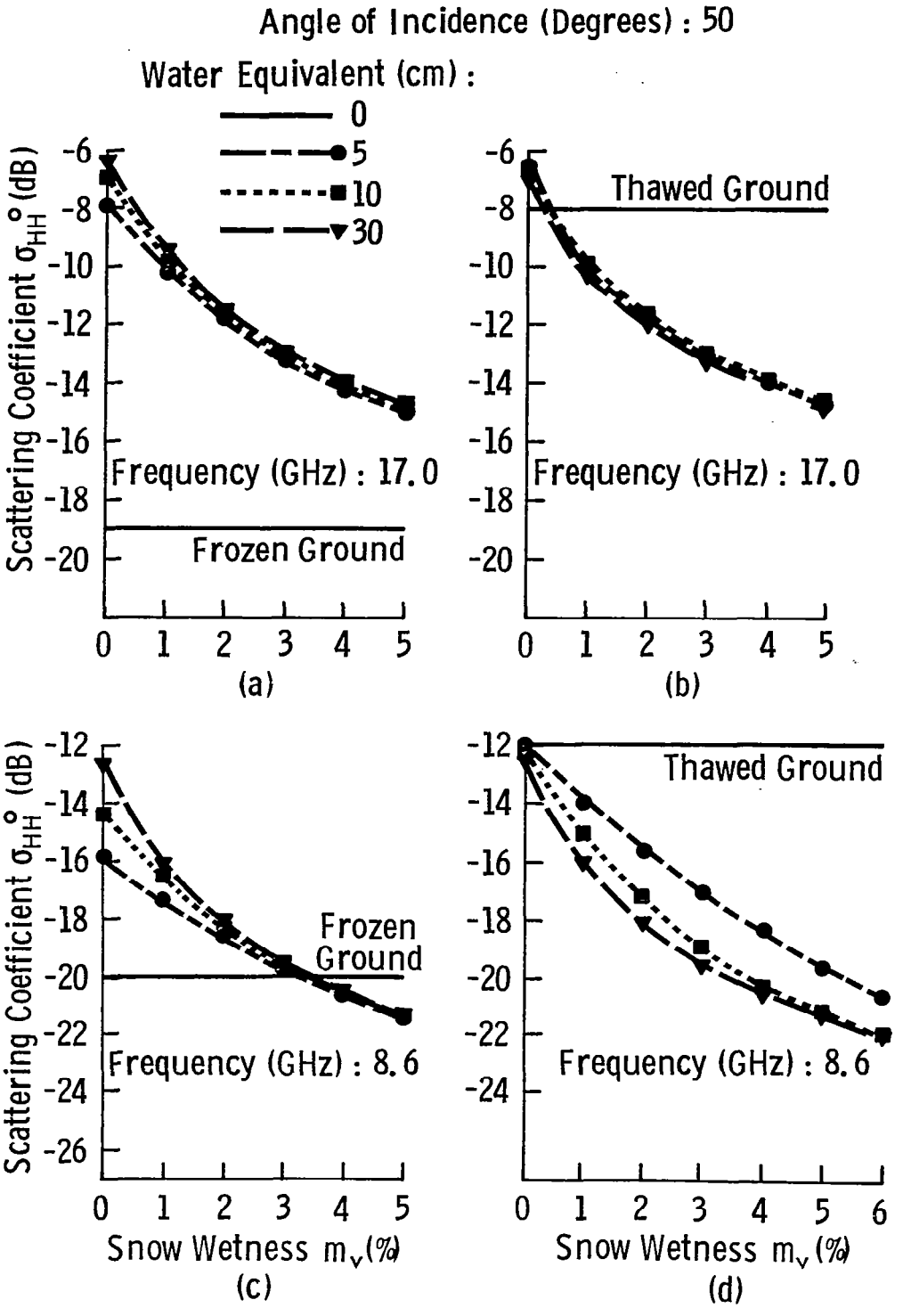


Figure 9-8 Sensitivity of σ^o model to water equivalent and snow wetness for (a) frozen ground at 17.0 GHz, (b) thawed ground at 17.0 GHz, (c) frozen ground at 8.6 GHz, and (d) thawed ground at 8.6 GHz.

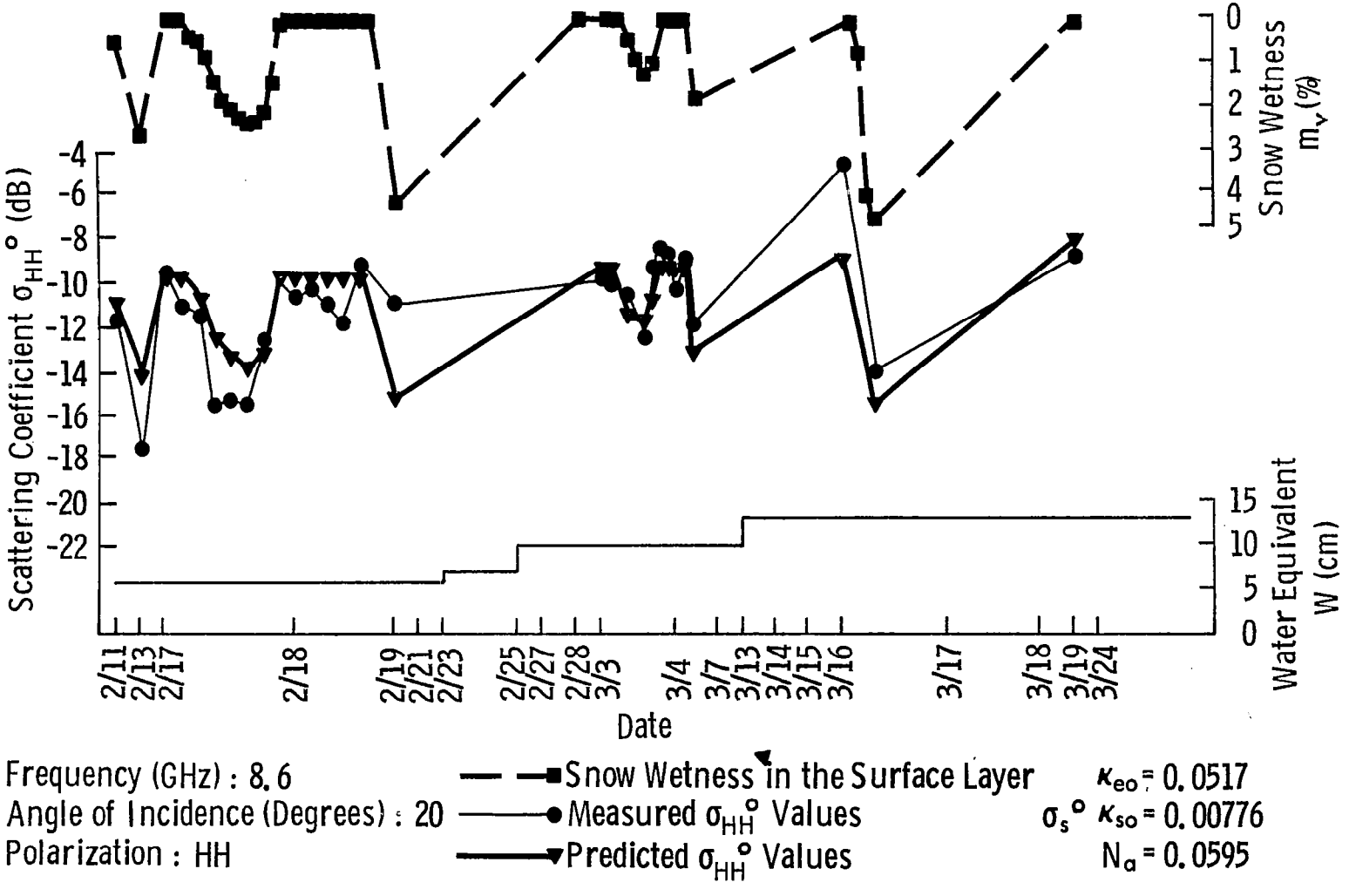


Figure 9-9 Scattering coefficient model and observed σ° value comparison at 8.6 GHz and 20° angle of incidence.

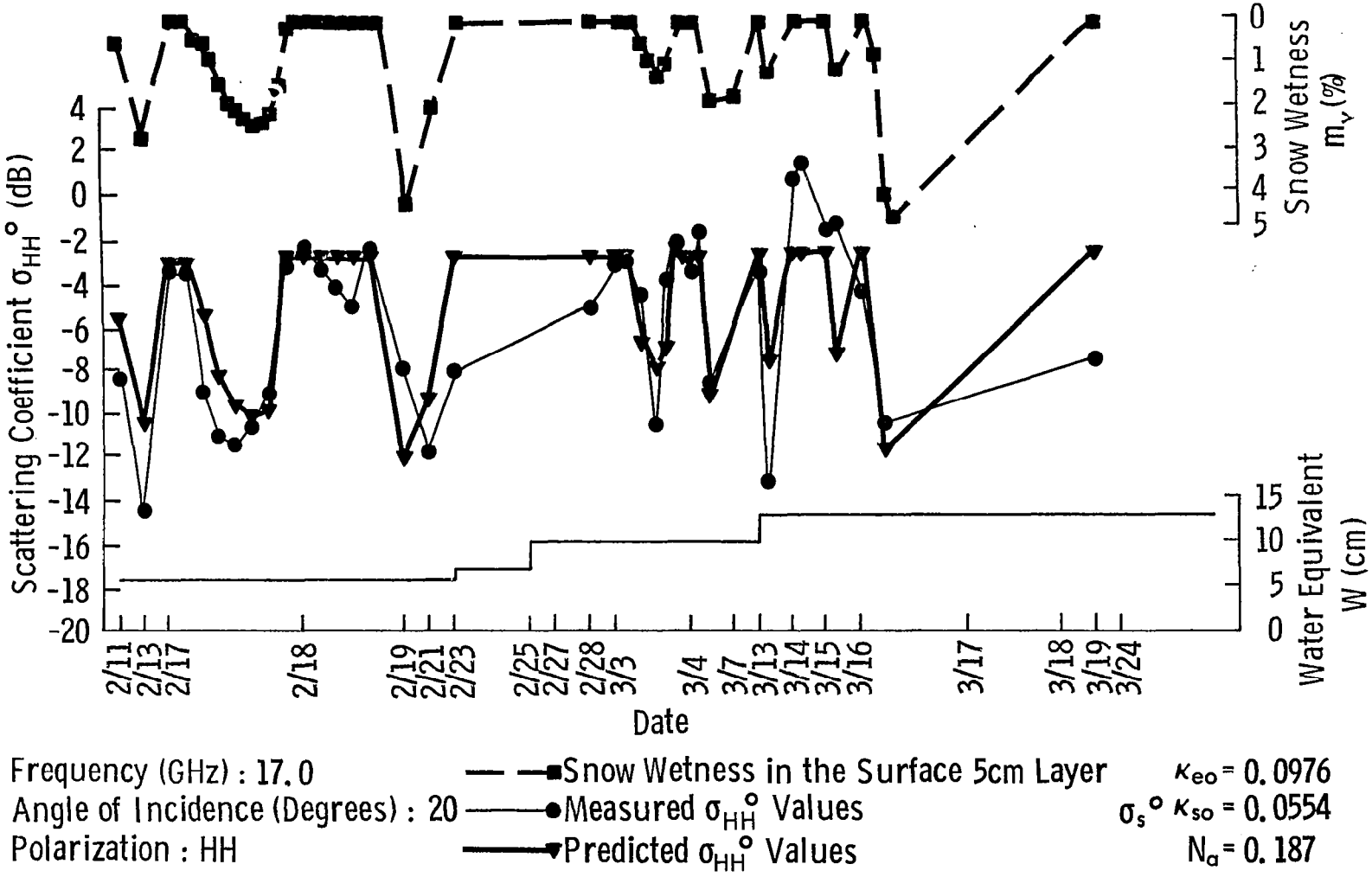


Figure 9-10 Scattering coefficient model and observed σ° value comparison at 17.0 GHz and 20° angle of incidence.

where E and N are constants and the term exp $[-Em_v]$ is used to express the variation of σ^o_{sat} with m_v and is given by:

$$\sigma^o_{sat} = \sigma^o_s \exp [-Em_v] \tag{9-22}$$

The values used for κ'_{eo} were obtained from equation 9-19, as was σ^o_{sat} and σ^o_{gnd}. Application of equation 9-21 to the σ^o data from the two diurnal data groups on 2/17/77 and 3/16/77 is shown in Figures 9-11 and 9-12. Then for the seasonal variation, σ^o predicted on the basis of equation 9-21 is given in Figures 9-13 to 9-16. The regression fits are observed to be better than the more theoretical model, indicating that improved snow ground truth or a better theoretical model is needed.

The spectral variation of σ^o for a very deep snow is illustrated in Figure 9-17 for several snow wetness values. The backscatter coefficient is observed to decrease with increasing wetness, while increasing with frequency. The slope of the $m_v = 0$ and $m_v = 1$ curves closely match the spectral response curve of Figure 8-17c, implying that the spectral response of the model is reasonable. The levels between Figures 9-17 and 9-7 are different because of the differences in the estimates of σ^o_{sat}.

The variation with snow wetness and water equivalent is shown in Figure 9-18. For the no snow case, W = 0, snow wetness has no effect. As the water equivalent of the snow layer increases, the variation due to wetness has a much wider dynamic range. As can be seen from the W = 15 cm curves, the dynamic range of the σ^o variation from $m_v = 0$ to $m_v = 4\%$ is 9 dB at 8.6 GHz and 15 dB at 17.0 GHz which agree well with the dynamic range variation in Figure 8-36 and is greater than the variation of the model of equation 9-16.

In summary, both models (equations 9-16 and 9-21) give good representations of the σ^o variation with m_v and W. Each has advantages and disadvantages. The models, however, do show the behavior of σ^o and point to the need for more extensive ground truth data so that more sophisticated models can be applied.

9.2 Passive Microwave

9.2.1 Proposed Emissivity Model

For a homogeneous snow layer covering a soil medium (Figure 2-1), the brightness temperature is assumed to consist of two components:

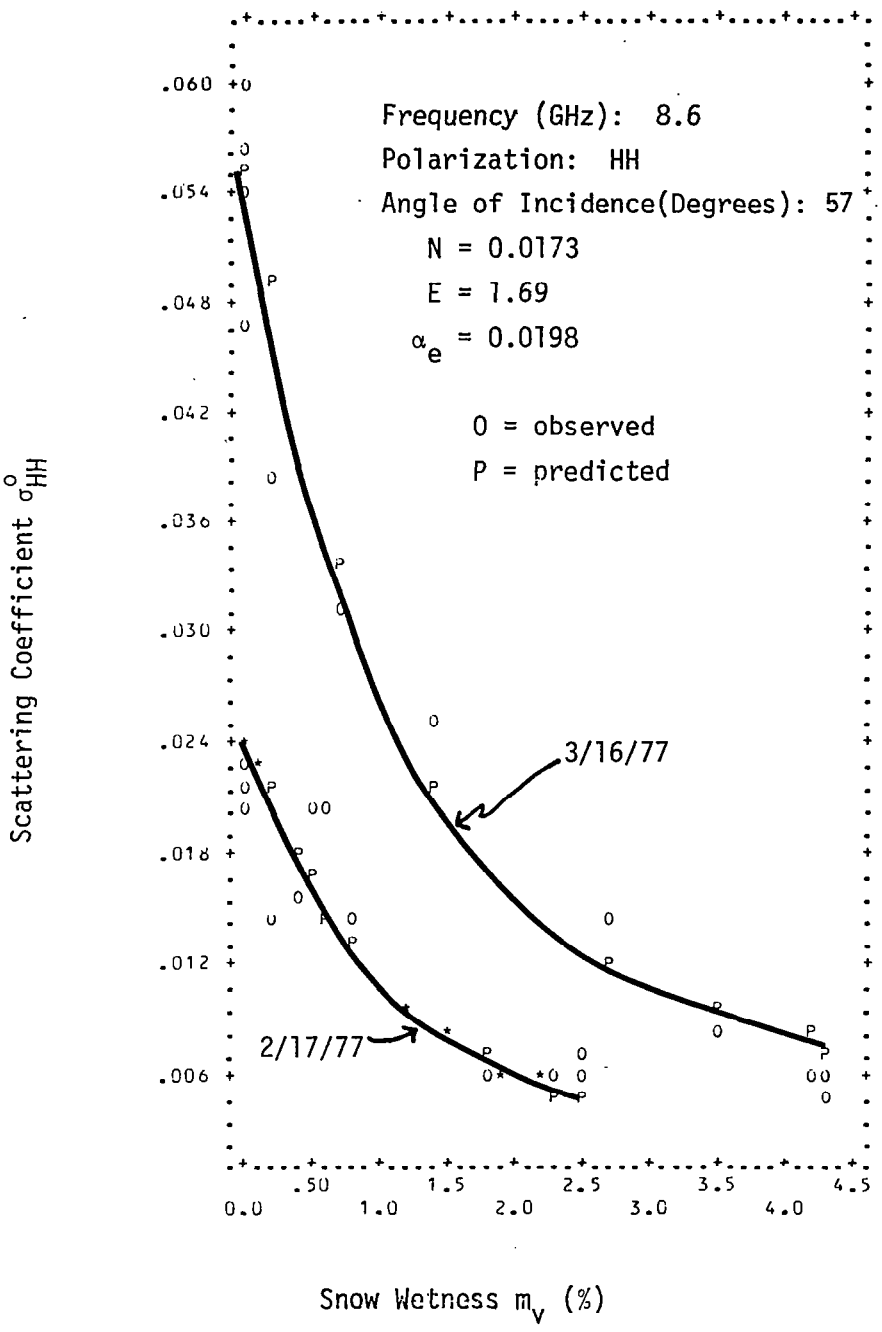


Figure 9-11 Scattering coefficient model applied to two diurnal data groups at 8.6 GHz.

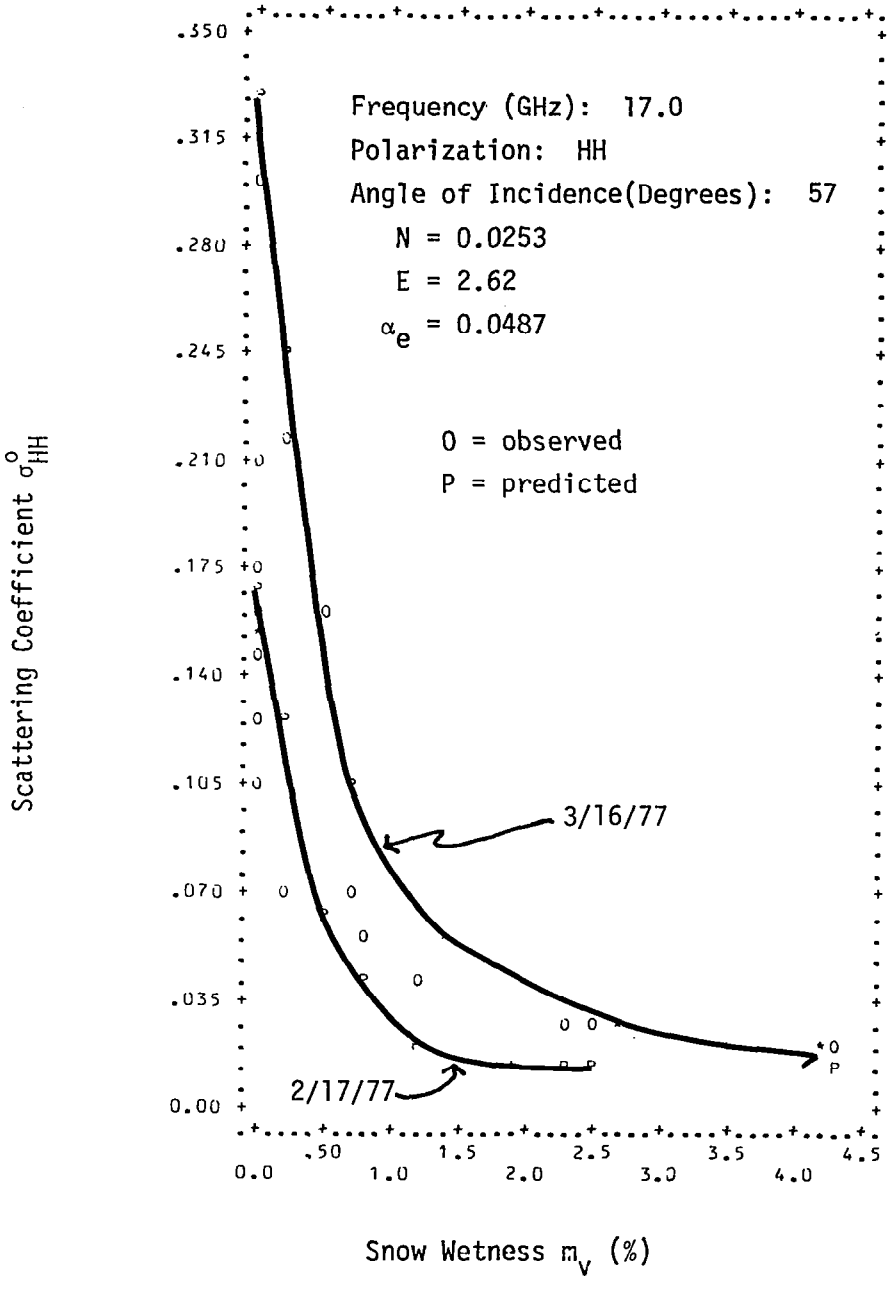


Figure 9-12 Scattering coefficient model applied to two diurnal data groups of 17.0 GHz.

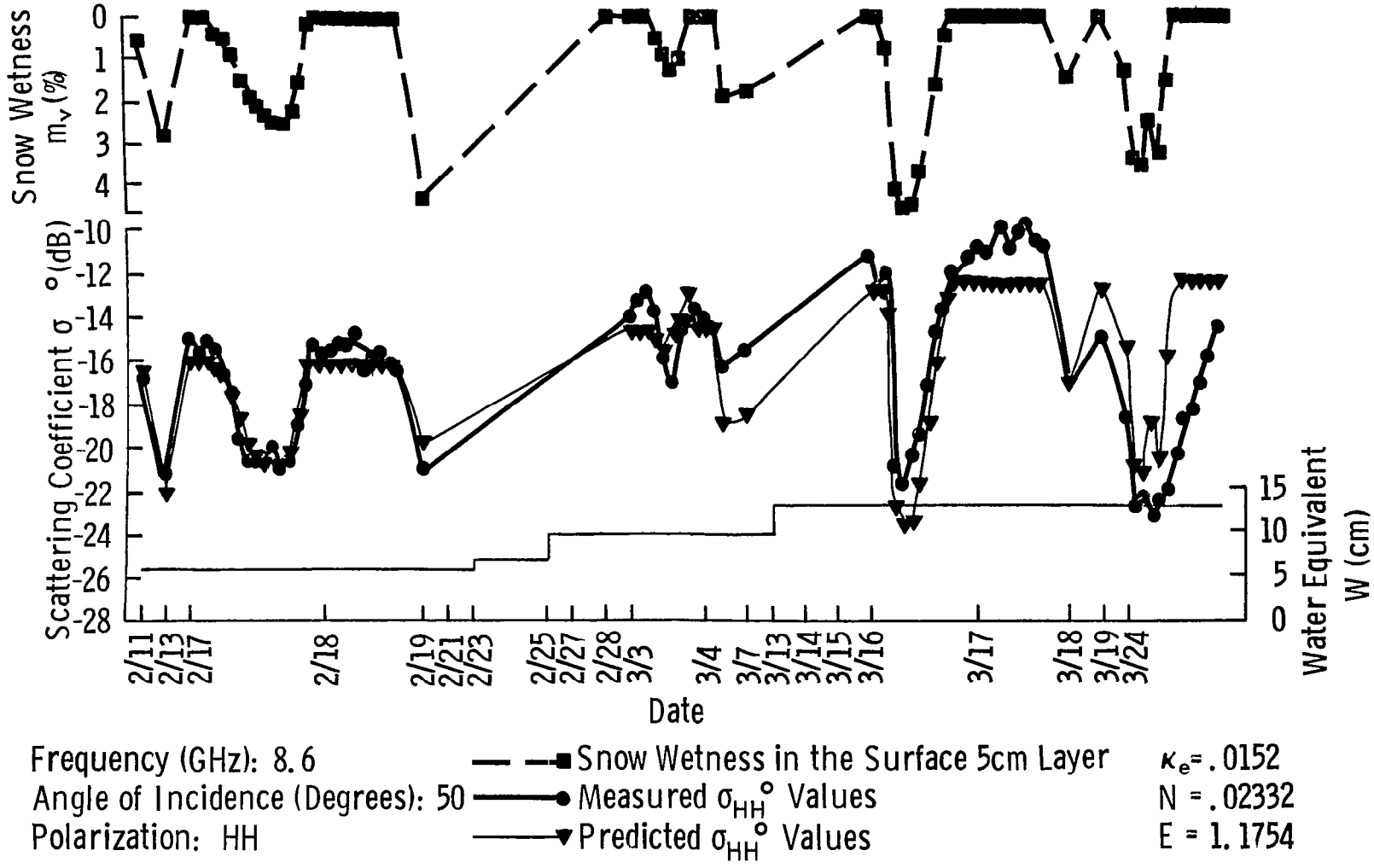


Figure 9-13 Scattering coefficient model and observed σ^o values over the experiment duration at 8.6 GHz and 50° angle of incidence.

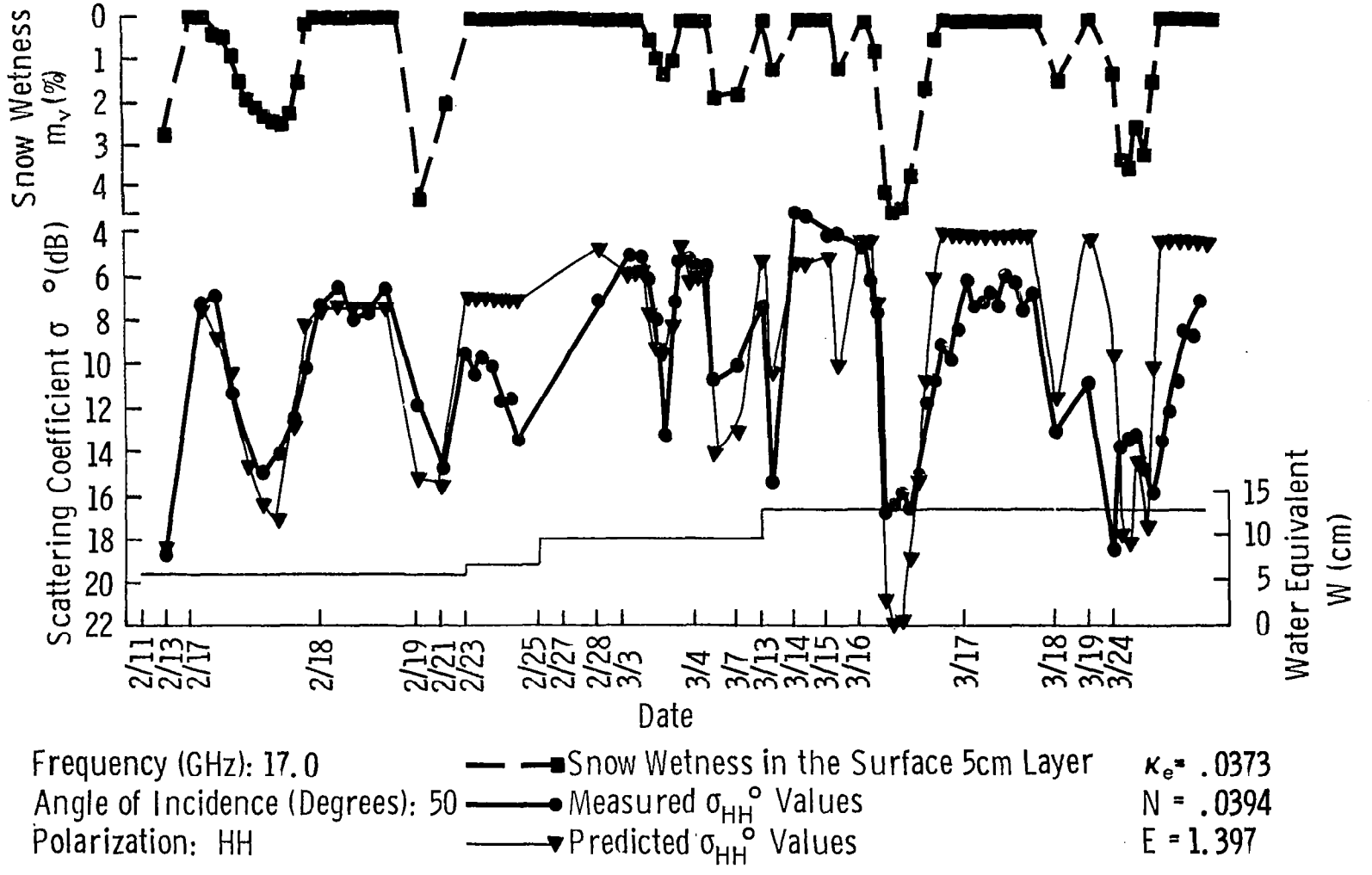


Figure 9-14 Scattering coefficient model and observed σ° values over the experiment duration at 17.0 GHz and 50° angle of incidence.

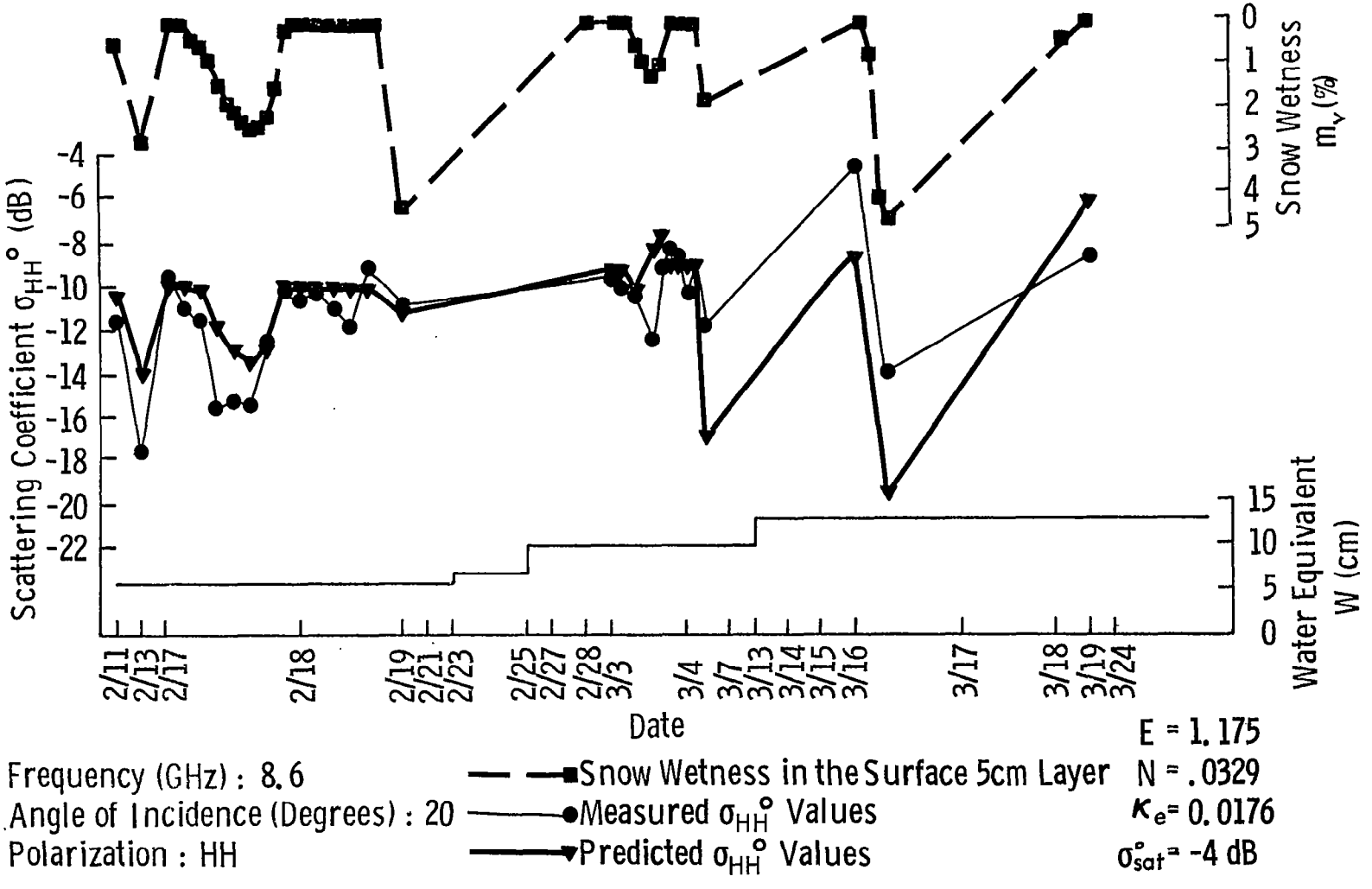


Figure 9-15 Scattering coefficient model and observed σ° values over the experiment duration at 8.6 GHz and 20° angle of incidence.

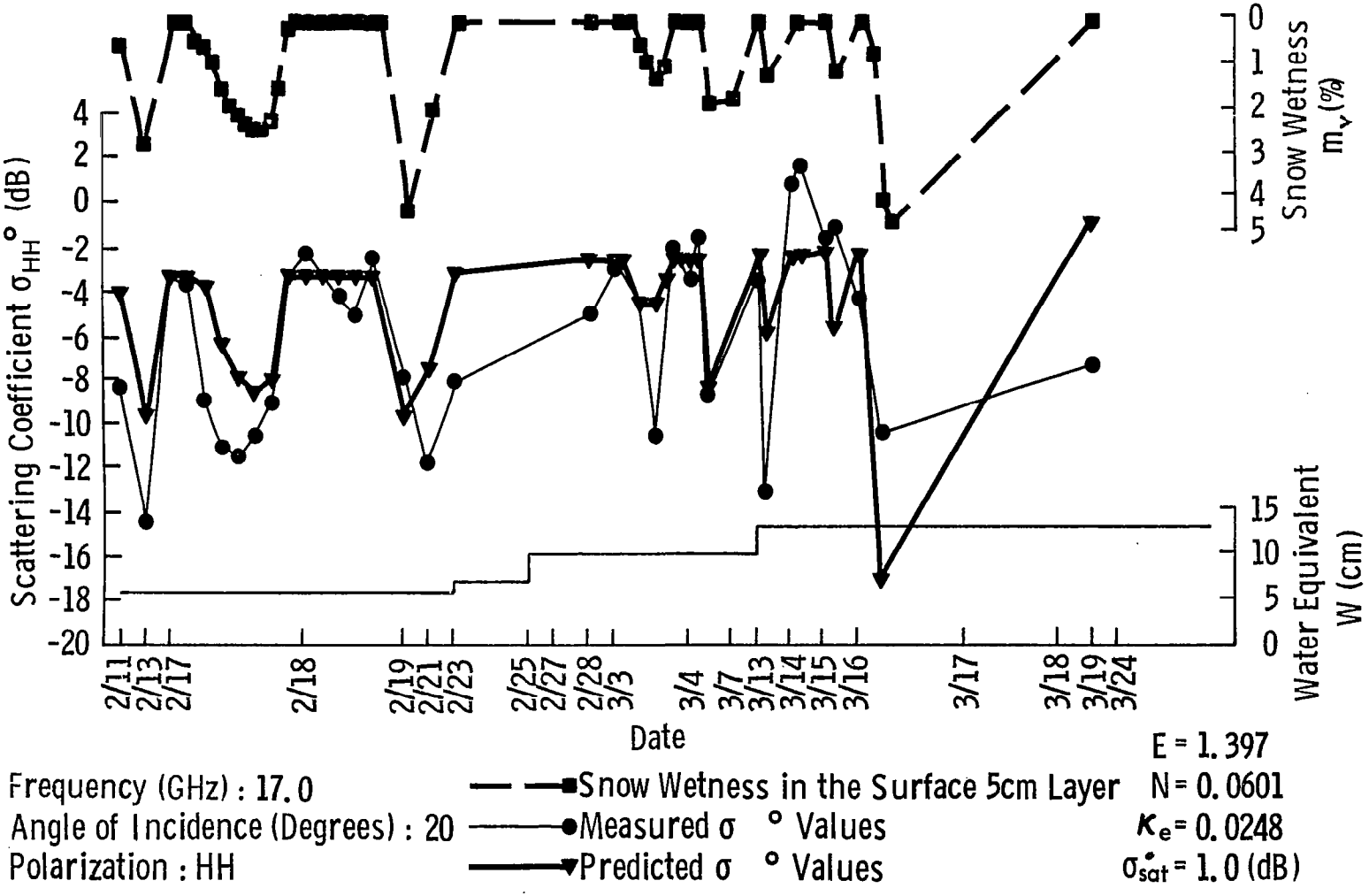


Figure 9-16 Scattering coefficient model and observed σ° values over the experiment duration at 17.0 GHz and 20° angle of incidence.

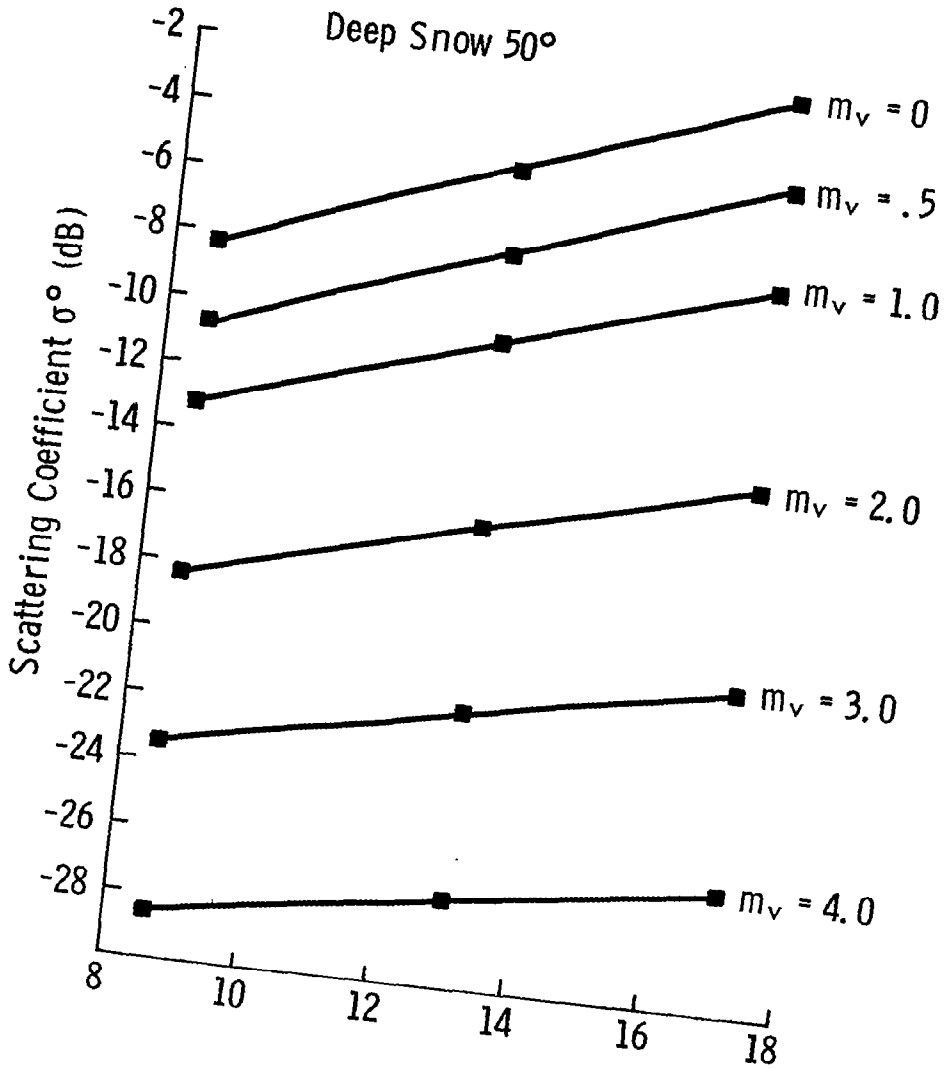


Figure 9-17 Sensitivity of σ^o to snow wetness.

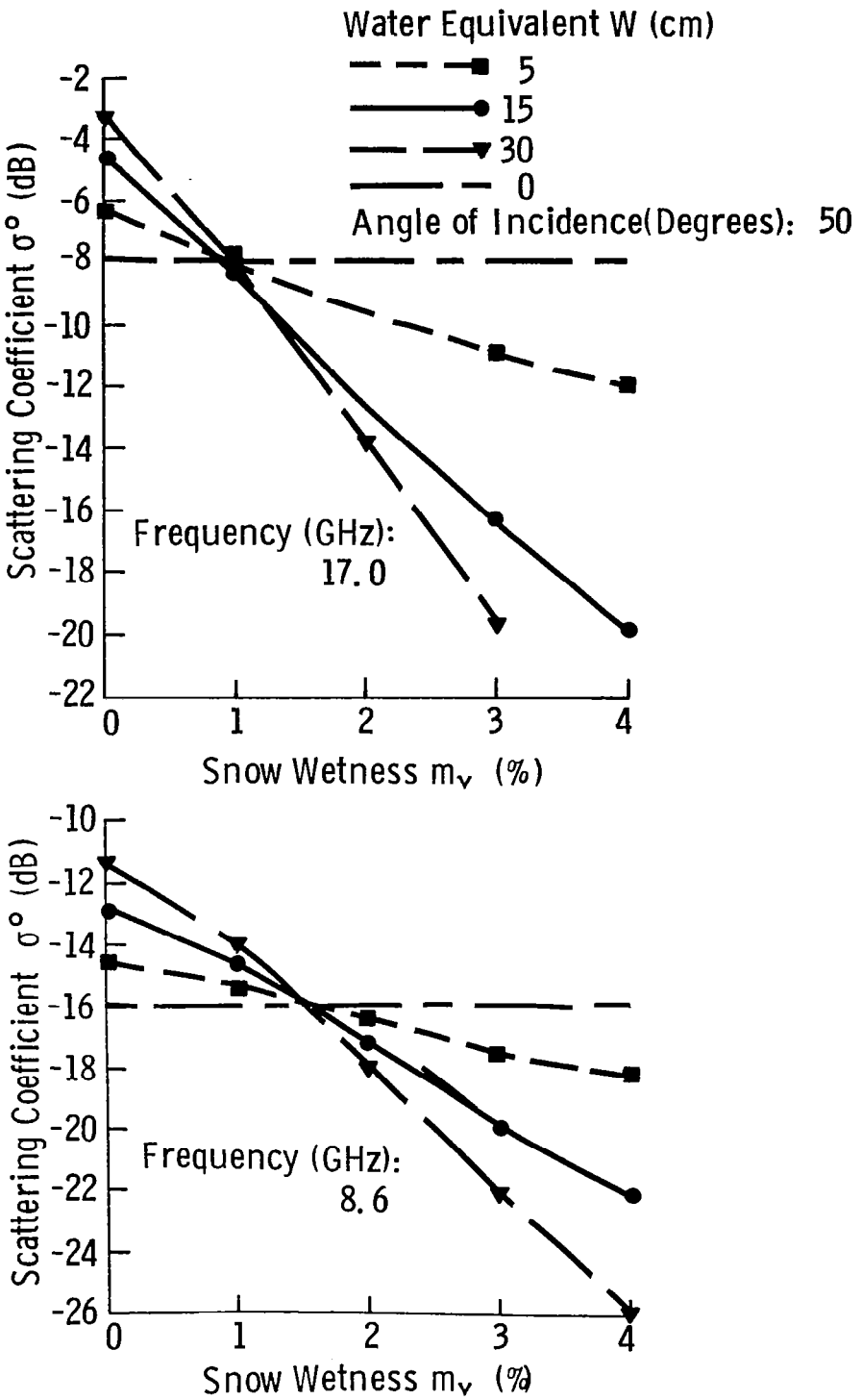


Figure 9-18 Sensitivity of σ° to water equivalent and snow wetness.

$$T_B = T_g + T_s \tag{9-23}$$

where T_B is the brightness temperature, T_g is the emission contribution of the ground, and T_s is the emission contribution of the snow layer. Ignoring multiple scattering within the snow medium, self emission by a thin snow layer of depth Δh is given by:

$$T_{se} = T_o \left[1 - \exp(-\kappa_a \sec \theta' \, \Delta h)\right] \cong T_o \, \kappa_a \sec \theta' \tag{9-24}$$

where T_o is the snow physical temperature and κ_a is the absorption coefficient. Hence, the total emission by the snow layer is (Moore et al., 1975 in Manual of Remote Sensing):

$$T_s = \tau_{sa} \left\{ T_o \int_o^d \kappa_a \sec \theta' \exp[-\kappa_e (d - h) \sec \theta'] \, dh \right\} \tag{9-25}$$

where τ_{sa} is the snow-air transmission coefficient and κ_e is the extinction coefficient. After integration, equation 9-25 reduces to:

$$T_s = \tau_{sa} \, T_o \frac{\kappa_a}{\kappa_e} \left[1 - \exp(-\kappa_e \, d \sec \theta')\right] \tag{9-26}$$

If τ_{gs} is the transmission coefficient at the ground-snow interface, the ground contribution after transmission through the snow layer is:

$$T_g = \tau_{gs} \, \tau_{sa} \, T_o \exp(-\kappa_e \, d \sec \theta') \tag{9-27}$$

where the ground is also assumed to have a physical temperature T_o. The emissivity of the snow scene can then be defined as:

$$\varepsilon = \frac{T_B}{T_o} = \frac{T_s + T_g}{T_o} \tag{9-28}$$

$$= \tau_{sa} \left\{ \frac{\kappa_a}{\kappa_e} \left[1 - \exp(-\kappa_e \, d \sec \theta')\right] + \tau_{gs} \exp(-\kappa_e \, d \sec \theta') \right\}$$

The above equation can also be expressed in terms of the snowpack optical depth τ_d (equation 2-10):

$$\varepsilon = \tau_{sa} \left\{ \frac{\kappa_a}{\kappa_e} \left[1 - \exp(\tau_d \sec \theta')\right] + \tau_{gs} \exp(\tau_d \sec \theta') \right\} \tag{9-29}$$

As with the active microwave case, if τ_d is small, the ground contribution dominates and for large values of τ_d, the snow contribution dominates.

The above result provides an explicit dependence on snow depth d. The dependence on snow wetness m_v is embedded in the values of κ_a, κ_s, κ_e, τ_{sa}, and τ_{gs}. The dependence of κ_a, κ_s, and κ_e on m_v are given in equations 9-6 through 9-8. Introducing these equations into equation 9-29, we have:

$$\varepsilon = \tau_{sa} \left\{ \frac{\kappa_{ao} + N_a m_v}{\kappa_{ao} + \kappa_{so} + N_a m_v} \left[1 - \exp(-[\kappa_{ao} + \kappa_{so} + N_a m_v] d \sec \theta') \right] + \tau_{gs} \exp(-[\kappa_{ao} + \kappa_{so} + N_a m_v] d \sec \theta') \right\} \quad (9\text{-}30)$$

which is the general equation for wet or dry snow.

For $\tau_d = 0$ (no snow), $\tau_{sa} = 1$, $\tau_{gs} = \tau_{ga}$ and equation 9-30 reduces to:

$$\varepsilon = \tau_{ga} \quad (9\text{-}31)$$

and for $\tau_d >> 1$ (large optical depth):

$$\varepsilon = \tau_{sa} \frac{\kappa_a}{\kappa_e} \quad (9\text{-}32)$$

If m_v is large (very wet snow) in the above equation, $\kappa_a >> \kappa_s$. Hence:

$$\frac{\kappa_a}{\kappa_e} = \frac{\kappa_a}{\kappa_a + \kappa_{so}} \cong 1 \quad (9\text{-}33)$$

which leads to:

$$\varepsilon \cong \tau_{sa} \quad (9\text{-}34)$$

which is the blackbody like behavior observed for wet snow. The application of this model to the T_{ap} data obtained during this investigation follows in the next section.

9.2.2 Evaluation of the Emissivity Model

Equation 9-30 was first evaluated for the dry snowpile data. In this case, the constants may be determined from the experimental data by rewriting

equation 9-30 in the form:

$$\varepsilon = \tau_{sa}\left\{\left(\frac{\kappa'_{ao}}{\kappa'_{eo}}\right) + \left(\tau_{gs} - \frac{\kappa'_{ao}}{\kappa'_{eo}}\right)\exp\left(-\kappa'_{eo}\ W \sec\theta'\right)\right\} \qquad (9\text{-}35)$$

$$= A + B \exp\left(-C\ W\right)$$

where A, B, and C represent the constant terms inside the parentheses. The experimental values of ε determined according to equation 2-18 are shown in Figure 9-19 along with the best fit curves of the form given by equation 9-35. The values of A, B, and C are given in Figure 9-19 and Table 9-1 for each curve. This simple model provides the correct form for the dependence of ε on W, as judged by the curve fit; however, the following remarks are noted:

a) The exponential coefficient C is much larger at $\theta = 57^{o}$ (than the sec θ' dependence predicts) than the $\theta = 27^{o}$ value. This inconsistency is attributed to the difference in snow type; whereas the snow observed at $\theta = 27^{o}$ was freshly fallen snow, the snow observed at $\theta = 57^{o}$ was old methamorphosed snow.

b) Although the value of C, which is related to κ'_{eo}, was expected to increase with frequency, the curve fits gave approximately the same values at 10.69 GHz and 37 GHz. The 94 GHz coefficient, however, was considerably larger.

The next step in the evaluation was the application of the model to the seasonal variation. This model was applied at 50° angle of incidence only. The following constants were used in the passive modeling:

$$\begin{aligned} \tau_{gs}\ &\text{(frozen ground)} = 0.9 \\ \tau_{gs}\ &\text{(thawed ground)} = 0.8 \\ \tau_{sa} &= 0.95 \end{aligned} \qquad (9\text{-}36)$$

The angular variation is given by equations 9-17 and 9-18.

Also employed was the ratio $\kappa'_{ao}/\kappa'_{eo}$ which was obtained from Table 9-1 where:

$$A = \tau_{sa}\frac{\kappa'_{ao}}{\kappa'_{eo}} \qquad (9\text{-}37)$$

The values for $\kappa'_{ao}/\kappa'_{eo}$ used were 0.95 and 0.6 at 10.69 GHz and 37 GHz,

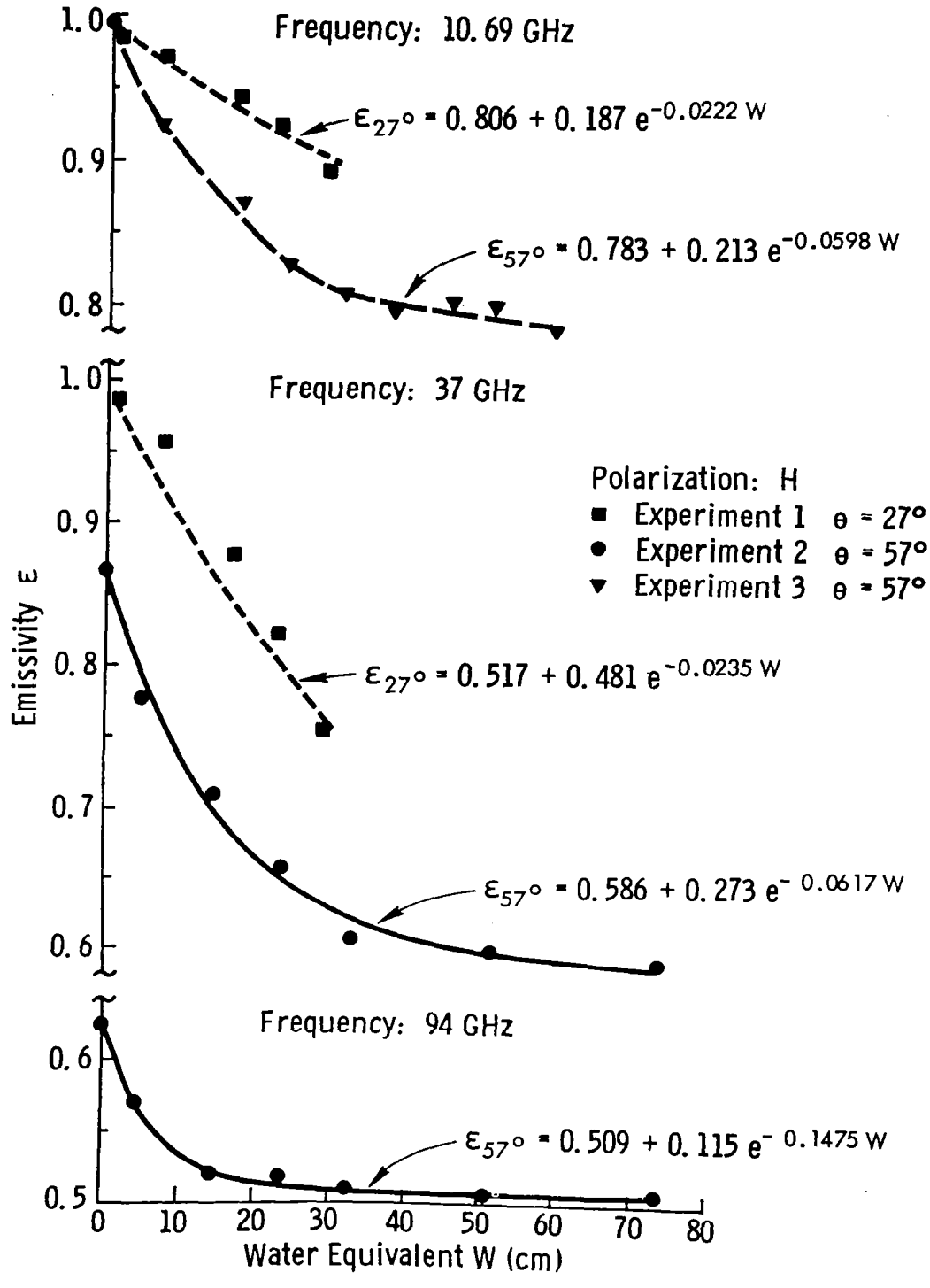


Figure 9-19 Measured Radiometric Emissivity Response to Dry Snow Water Equivalent at 10.69 GHz, 37 GHz, and 94 GHz

TABLE 9-1

Coefficients for the Emissivity
Model Applied to the Dry Snowpile Data

Frequency (GHz)	θ	A	B	κ'_{eo}(nep/cm)	Maximum Error*
10.69	27^o	0.806	0.187	0.0207	0.01
10.69	57^o	0.783	0.213	0.0440	0.01
37	27^o	0.517	0.481	0.0219	0.02
37	57^o	0.586	0.273	0.0454	0,02
94	57^o	0.509	0.115	0.108	0.01

* Maximum Error = $|\varepsilon_c - \varepsilon_m|$; ε_c = calculated from best fit equation, ε_m = measured

respectively; with these values, a non-linear regression routine was applied to T_{ap} and the ground truth data. The results are given in Figures 9-20 and and 9-21.

At 10.69 GHz, the results were poor. The reason is believed to be the wide scatter in the T_{ap} data independent of the ground truth parameters. The absorption coefficient was most noticeably too large, much larger than the active coefficients, and also much greater than the 37 GHz coefficient in Figure 9-21.

For the 37 GHz radiometer data, the regression fit was very good; it predicted the decrease in T_{ap} with increasing values of water equivalent and fit the wet case T_{ap} values also. Note that the κ'_{so} and N'_a values at 37 GHz (passive) are a reasonable five and seven times the 17.0 GHz active values; while κ'_{ao} is approximately 2.5 times the calculated κ'_{ao} value using the coefficients of Figure 9-5. Therefore, the model results at 37 GHz are good, indicating a valid representation of the T_{ap} variation with the ground truth parameters. Figure 9-22 illustrates the exponential behavior of T_{ap} with snow wetness and water equivalent. It is observed that 5 cm water equivalent effectively masks the ground contribution. It is also noted that the emission from snowpack can be either higher or lower than the emission from the underlying ground, thus complicating any scheme to separate the emission from snow or ground.

9.3 Summary of Simple Models

The active microwave model results are given by rewriting equation 9-16:

$$\sigma^o = \sigma^o_{gnd} \exp(-2[\kappa'_{ao} + \kappa'_{so} + N'_a m_v] W\sec\theta') + \sigma^o_s \frac{\kappa'_{so}}{\kappa'_{ao}+\kappa'_{so}+N'_a m_v} \left\{1-\exp(-2[\kappa'_{ao}+\kappa'_{so}+N'_a m_v]W\sec\theta')\right\} \quad (9\text{-}38)$$

where Table 9-2 gives the coefficients. The model should be valid over the 20° to 50° angular range with adjustment of the coefficients.

The passive microwave model results are given by rewriting equation 9-30:

$$\varepsilon = \tau_{sa} \left\{ \frac{\kappa'_{ao}+N'_a m_v}{\kappa'_{ao}+\kappa'_{so}+N'_a m_v} \left[1-\exp(-[\kappa'_{ao}+\kappa'_{so}+N'_a m_v]W\sec\theta')\right] + \tau_{gs} \exp(-[\kappa'_{ao}+\kappa'_{so}+N'_a m_v]W\sec\theta') \right\} \quad (9\text{-}39)$$

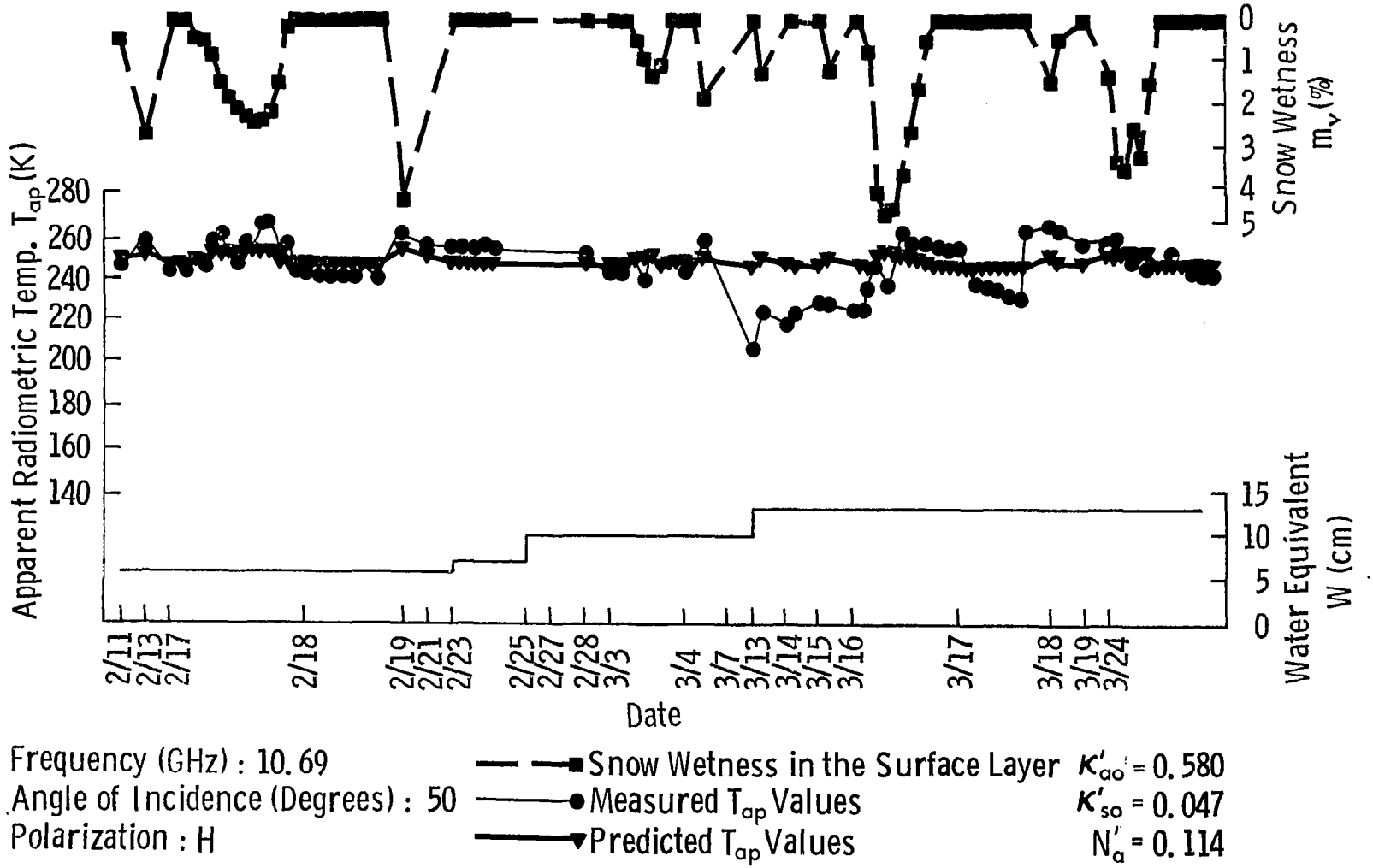


Figure 9-20 Emissivity model (x273.2) and observed apparent temperature comparison at 10.69 GHz.

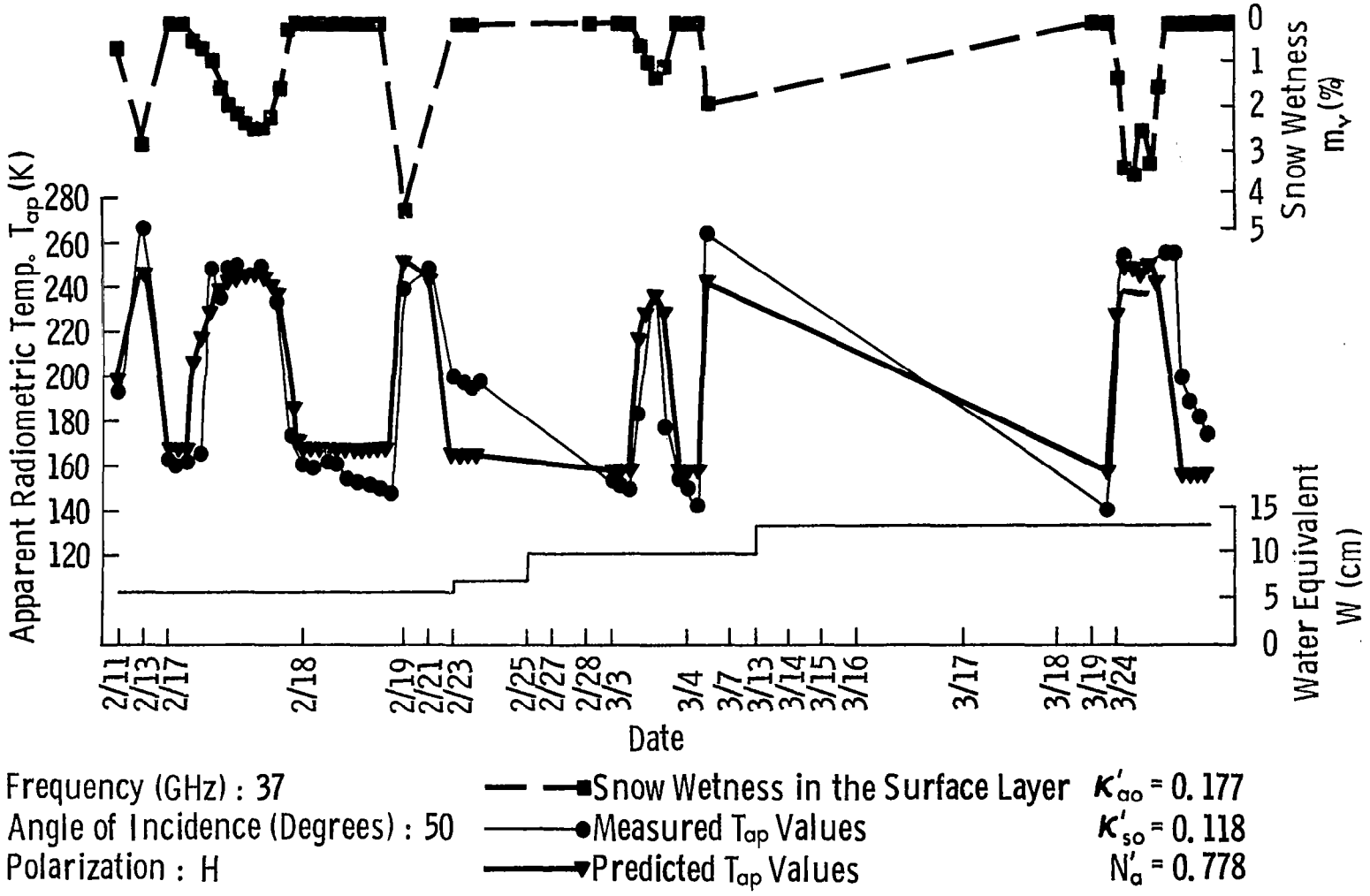


Figure 9-21 Emissivity model (x273.2) and observed apparent temperature comparison at 37 GHz.

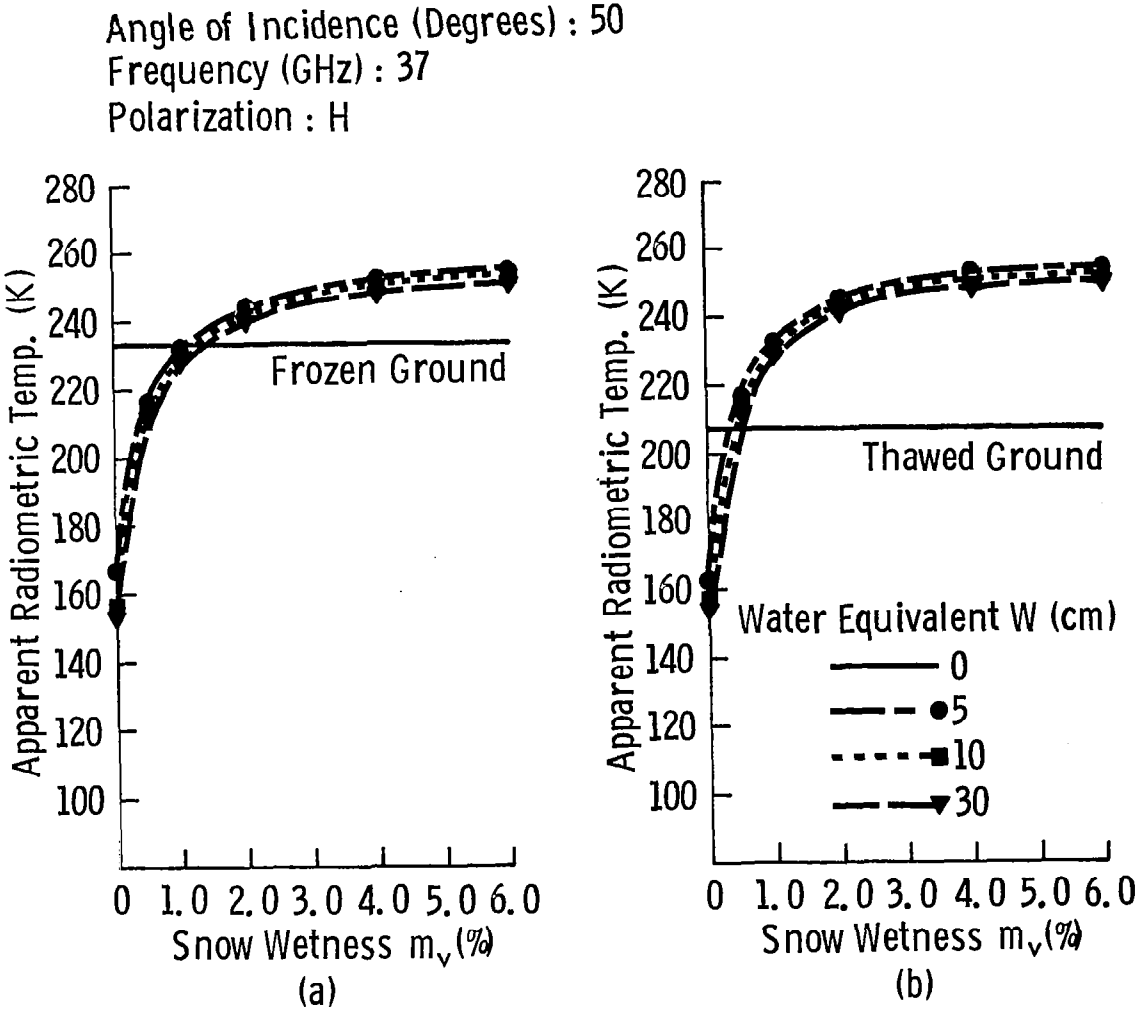


Figure 9-22 Sensitivity of T_{ap} model to water equivalent and wetness at 37 GHz for (a) frozen ground and (b) thawed ground.

TABLE 9-2

Coefficients for the Scattering Coefficient Model

Frequency	Angle	κ'_{eo}	$\sigma^o_s \kappa'_{so}$	N'_a
8.6	20°	0.0517	0.00776	0.0595
8.6	50°	0.0288	0.00171	0.0414
17.0	20°	0.0976	0.0554	0.187
17.0	50°	0.0959	0.0209	0.1027

where the coefficients at 37 GHz and 50° angle of incidence are:

$$\kappa'_{ao} = 0.177$$
$$\kappa'_{so} = 0.118 \qquad (9\text{-}40)$$
$$N'_a = 0.778$$

The fit for this model at 10.69 GHz was not good enough to warrant its use.

10.0 CONCLUSIONS AND RECOMMENDATIONS FOR FUTURE EXPERIMENTS

The objective of this investigation was to evaluate microwave remote sensing for obtaining snowpack information. Measurements of σ^o and T_{ap} were interpreted and then modeled in terms of the ground truth measurements. The following sections summarize the major conclusions of this investigation, list unanswered questions, and give recommendations for future experiments to answer these questions.

10.1 Conclusions

The following major conclusions were made:

1) The scattering coefficient σ^o is sensitive to both snow wetness and snow water equivalent. Snow wetness causes σ^o to decrease at angles away from nadir. Snow water equivalent, on the other hand, causes σ^o to increase at angles away from nadir.

2) The sensitivity of σ^o to snow wetness m_v generally increases with both increasing frequency and increasing angle of incidence. At frequencies below 4 GHz, the sensitivity to snow wetness in the top 5 cm layer was low at all angles of incidence, while the sensitivity was high for frequencies greater than 13 GHz. Sensitivities of σ^o(dB) at 50^o angle of incidence to m_v in the surface 5 cm layer varied from about -1 dB/%m_v at 6 GHz to almost -3 dB/%m_v at 35.6 GHz. The variation of σ^o with m_v in the surface 5 cm layer, however, becomes increasingly non-linear with increasing frequency due to increasing difference between the microwave penetration depth and the m_v sample depth.

3) The variation of σ^o(dB) with snow water equivalent was observed to be exponential. The 8 to 18 GHz σ^o data indicated a wider dynamic range for the lower frequencies (8 GHz).

4) The apparent radiometric temperature T_{ap} is also sensitive to both snow wetness and snow water equivalent; however, the responses to these two parameters are the inverse of the σ^o responses.

5) The sensitivity of T_{ap} to snow wetness increased from 10.69 to 37 to 94 GHz while remaining relatively constant with angle of incidence. The response was observed to be approximately exponential with increasing m_v, however a hysteresis effect was apparent.

6) The variation of T_{ap} with water equivalent was observed to be exponential with the exponential coefficients increasing with increasing frequency.

7) Snow surface roughness exhibits a small effect on either σ^o or T_{ap} for dry snow conditions, while surface roughness plays an important role in scattering and emission for wet snow conditions.

8) Volume scatter occurs within the dry snowpack leading to high σ^o values at angles away from nadir and low T_{ap} values at all angles of incidence at the higher microwave frequencies.

9) A simple model for σ^o incorporating the effects of snow wetness, snow water equivalent and soil state (frozen or thawed) was shown to give a good representation of σ^o in terms of the measured ground truth values.

10) A simple model for T_{ap} on dry snow was also shown to give a good representation of the emission as a function of water equivalent. The model applied to wet snow was not successful at 10.7 GHz, but was successful at 37 GHz.

Specific conclusions of this experiment were given in the above list. In general terms, the significant achievement of this experiment was in advancing the knowledge of the combined effects of snow wetness and water equivalent, especially for active microwave remote sensing purposes. Very little was known concerning quantitative responses of σ^o between 1 and 35 GHz before this experiment. It is felt that with the information gained in these analyses that the potential for microwave remote sensing of snow has been shown and the need for further investigations demonstrated. The following sections present some of the areas which need to be covered for a more complete understanding of the snow-microwave interaction mechanism.

10.2 Unanswered Questions

The following topics could not be answered from this experiment or from a review of the literature.

1) The dielectric properties of snow, especially the imaginary part, are not well understood. Effects of wetness and crystalline structure have yet to be measured between 8 and 35 GHz.

2) In a related problem, attenuation and penetration depths need to be better quantified for different wetness and crystal size conditions.

3) Crystal size effects on σ^o and T_{ap} have not been quantified.

4) The σ^o and T_{ap} response to snow water equivalent under naturally occurring conditions such as varying crystalline size is not known.

5) The surface roughness effects on wet snow need to be investigated in more detail.

6) The fading statistics for both intrafield and interfield variation on snow are not well known.

A better understanding of the above questions will allow specification of optimum parameters for a microwave system to remotely sense and potentially profile snowpack.

10.3 Recommendations for Future Experiments

Several experiments must be performed to answer the previously mentioned questions. This section summarizes the recommendations which can achieve the desired knowledge.

1) Dielectric constant measurements should be made preferably in an environmental chamber such that snow can be made with different properties. The desired range of snow parameters over which measurements need to be obtained are given in Table 10-1.

2) Better ground truth of both the snowpack and underlying target is needed to facilitate model improvement and implementation. Table 10-2 lists the needed ground truth parameters.

3) The variation in penetration depths at different frequencies affecting both σ^o and T_{ap} holds the promise of allowing profile information to be obtained. The vertical spatial and time resolution of m_v in this experiment, however, was not adequate for this purpose. It is proposed that wetness be monitored using calorimetric techniques in the following intervals from the snow surface: 0-1 cm, 1-2 cm, 2-5 cm, 5-15 cm, 15-30 cm, and greater depths, if necessary. The time resolution should be related to the rate of change in wetness; therefore, the surface sampling rate should be the highest and should be at a maximum of 30-minute intervals during the melt and freeze cycles of each day.

4) Measurements of σ^o and T_{ap} over widely varying snow depth and crystal sizes are needed. It is recommended that measurements of σ^o, T_{ap}, and ground truth be conducted at several sites such that at least the following conditions are included: snow depths greater than 1 meter, snow depths less than 0.5 meter, snow over frozen ground, snow over thawed ground and snow over asphalt or concrete. These experiments need to be conducted at a wide range of elevations with different snow accumulation rates and crystal sizes. Each of these sites should be observed periodically over a

TABLE 10-1

Desired Range of Parameters for Determining Dielectric Properties of Snow

Parameter	
Frequency	1-18, 35, 95 GHz
Density	.1 to .5 g/cm^3
Wetness (free water content by volume)	0 to 15%
Crystal Size	.2 mm to 1 cm
Temperature	-20^oC to 0^oC

TABLE 10-2

Ground Truth Parameters

A. Snowpack Parameters:

1. Depth & Stratification
2. Density Profile by Layer
3. Water Equivalent by Layer
4. Wetness Profile 0-1 cm, 1-2 cm, 2-5 cm, 5-15 cm, etc.
5. Temperature Profile (2 cm increments)
6. Crystal Structure (shape and size)
7. Surface Roughness (close-up photograph)

B. Underlying Surface Parameters:

1. Type (soil, concrete, etc.)
2. Moisture Content Profile (0-2 cm, 2-5 cm, 5-10 cm)
3. Temperature Profile (down to 10 cm in 2 cm increments)
4. Surface Structure (roughness)

C. Atmospheric and Environmental Parameters:

1. Atmospheric Pressure
2. Air Temperature
3. Humidity
4. Incident Solar Radiation
5. Reflected Solar Radiation
6. Cloud Cover Conditions

period that includes parts of the snow accumulation and depletion seasons. Either knowledge of σ^{o} or T_{ap} of the underlying target or loss values through the snow must also be known for interpretation of the results.

5) It is also strongly recommended that passive microwave measurements be again conducted simultaneously with the active measurements for:

(a) Savings in the cost of logistics.

(b) Savings in the cost of ground truth data acquisition.

(c) Providing the means for evaluating the advantages of combined use of active and passive microwave sensors over either one alone.

REFERENCES

Aeroject General Corporation, "Operations and Maintenance Manual for X-band Microwave Radiometer," prepared for NASA Langley Research Center, Hampton, Virginia.

Amback, W., "Zur Bestimmung des Schmelwassergehaltes des Schnecs durch dielektrische Messungen, " Zeltschrift fur Gletscherkunde und Glazialgeologie, Bd. 4, Ht. 1-2, pp. 1-8, 1958.

Attema, E. P. W. and F. T. Ulaby, "Vegetation Models as a Water Cloud," Radio Science, 13(2):357-364, March-April, 1978.

Barabanenkov, Yu. N., Karvtsov, Yu. A., Rytov, S. M. and V. I. Tamarskii, "Status of the Theory of Propagation of Waves in a Randomly Inhomogeneous Medium," Soviet Physics, USPEKHI, vol. 13, no. 15, pp. 551-680, March-April, 1971.

Barnes, J. C. and C. J. Bowley, "Snow Cover Distribution as Mapped from Satellite Photography," Water Resources Research, 4(2):257-272, 1968a.

Barnes, J. C. and C. J. Bowley, "Operational Guide for Mapping Snow Cover from Satellite Photography," Report 8G-48-F, Allied Research Assoc., Inc., Concord, Mass., 1968b.

Barnes, J. C. and C. J. Bowley, "Snow Studies Using Thermal Infrared Measurements from Earth Satellites," Final Report 8G92-F, Contract No. I-35350, Allied Research Assoc., Inc., Baltimore, Maryland, 1972.

Bassanini, P. C. et al., "Scattering of Waves by a Medium with Strong Fluctuations of Refractive Index," Radio Science, vol. 2, no. 1, pp. 1-18, 1967.

Battles, J. W. and D. E. Crane, "Millimeter Wave Attenuation Through Snow," U.S. Naval Ordnance Lab., NAVWEPS Report 8816, Corona, California, July, 1965.

Battles, J. W. and D. E. Crane, "Attenuation of Ka-Band Energy by Snow and Ice," U.S. Naval Ordnance Lab., NOLC Report 670, Corona, California, August, 1966 (AD 638303).

Benoit, A., "Signal Attenuation due to Neutral Oxygen and Water Vapor, Rain and Clouds," Microwave Journal, 11(11):73-80, 1968.

Bentley, W. A. and W. J. Humphreys, Snow Crystals, 1931.

Blue, M. D., "Permittivity of Water at Millimeter Wavelengths," Final Report, Engineering Experiment Station, Georgia Tech., Atlanta, Georgia, August, 1976.

Blue, M. D., "Reflectance of Ice and Seawater at Millimeter Wavelengths," Proceedings of IEEE MTT-S Symposium, Orlando, Florida, May, 1979.

Bourret, R. C., Propagation of Randomly Perturbed Fields," Canadian Journal of Physics, vol. 40, pp. 782-790, 1962.

Brown, A. J., "Long Range Goal and Information Needs of the Coordinated Snow Survey Program in California," Proc. of Adv. Concepts and Techniques in the Study of Snow and Ice Resources, Wash., D.C., 1974.

Brunfeldt, D. R., F. T. Ulaby and W. H. Stiles, "System Description and Hardware Specification of MAS 1-8,: RSL Technical Report 264-17, University of Kansas Center for Research, Inc., Lawrence, Kansas, February, 1979.

Bryan, M. L., "The Study of Fresh-Water Lake Ice Using Multiplexed Imaging Radar," Journal of Glaciology, 14(72), 1975.

Burke, J. E. and V. Twersky, "On Scattering of Waves by Many Bodies," Radio Science, vol. 68D, pp. 500-510, 1964.

Bush, T. F. and F. T. Ulaby, "Cropland Inventories Using an Orbital Imaging Radar," RSL Technical Report 330-4, University of Kansas Center for Research, Inc., Lawrence, Kansas, January, 1977.

Bush, T. F. and F. T. Ulaby, "Fading Characteristics of Panchromatic Radar Backscatter from Several Agricultural Targets," IEEE Transactions on Geoscience Electronics, GE-13(4):149-157, October, 1975.

Chandrasekhar, S., Radiative Transfer, Dover, 1960.

Chang, T. C., P. Gloersen, T. Schmugge, T. T. Wilheit, and H. J. Zwally, "Microwave Emission from Snow and Glacier Ice," Journal of Glaciology, 16(74):23-39, 1976.

Chang, A. T. C. and B. J. Choudhury, "Microwave Emission from Polar Firm," NASA Tech. Paper 1212, 1978.

Choudhury, B. J. and A. T. C. Chang, "The Solar Reflectance of a Snow Field," NASA Tech. Memo. 78085, Goddard Space Flight Center, Greenbelt, Maryland, 1978.

Cihlar, J. and F. T. Ulaby, "Dielectric Properties of Soils as a Function of Soil Moisture Content," RSL Technical Report 177-47, University of Kansas Center for Research, Inc., Lawrence, Kansas, November, 1974

Cole, K. S. and R. H. Cole, Journal of Chemical Physics, 9, 1941.

Committee of Polar Research, Polar Research: A Survey, 204 pp., National Research Council, National Academy of Sciences, Washington, DC, 1970.

Cosgriff, R. L., W. H. Peake and R. C. Taylor, "Terrain Scattering Properties for Sensor System Design (Terrain Handbook II)," Ohio State University Experimental Station, 1960.

Cumming, W., "The Dielectric Properties of Ice and Snow at 3.2 Centimeters Journal of Applied Physics, 23(7), 1952.

Currie, N.C., F. B. Dyer and G. W. Ewell, "Radar Millimeter Backscatter Measurements from Snow," Final Report, Engineering Experiment Station, Georgia Tech., Atlanta, Georgia, January, 1977.

Dence, D. and J. E. Spence, Wave Propagation in Random Anisotropic Media, Probabilistic Methods in Applied Mathematics, ed. A. T. Bharucha-Reid Vol. 3, Academic Press, 1973.

Eagleman, J. R., E. C. Pogge, R. K. Moore, et al., "Detection of Soil Moisture and Snow Characteristics from Skylab," Final Report 239-23 ERP No. 540-A2, Contract NAS 9-13273, Atmospheric Science Laboratory, University of Kansas Center for Research, Inc., Lawrence, Kansas, October, 1975.

Edgerton, A. T., R. M. Mandle, G. A. Poe, J. E. Jenkins, F. Soltis and S. Sakamoto, "Passive Microwave Measurements of Snow, Soils and Snow-Ice-Water Systems," Technical Report No. 4 for Geography Branch Earth Sciences Division, Office of Naval Research, Washington, DC, February, 1968.

Edgerton, A. and S. Sakamoto, "Microwave Radiometric Investigations of Snowpacks," Interim Report No. 2 for U.S.G.S., Aerojet-General Corp., El Monte, California, 1970.

Edgerton, A. T., A. Stogryn and G. Poe, "Microwave Radiometric Investigations of Snowpacks," Final Report No. 1285 R-4 for U.S.G.S. Contract No. 14-08-001-11828, Aerojet-General Corporation, Microwave Division, El Monte, California, July, 1971.

Ellerbruch, D. A., W. E. Little, H. S. Boyne, and D. D. Bachman, "Microwave Characteristics of Snow," Proc. of the Western Snow Conference, 1977.

Ellerbruch, D. A., R. L. Jesch, R. N. Jones, H. E. Bussey, H. S. Boyne, "Electromagnetic Scattering Properties of Soils and Snow," Proc. 12th International Symposium on Remote Sensing of Environment, Vol. II, Ann Arbor, Michigan, 1978.

England, A. W., "Thermal Microwave Emission from a Halfspace Containing Scatterers," Radio Science, 9(4):447-454, April, 1974.

England, A. W., "Thermal Microwave Emission from a Scattering Layer," Journal of Geophysical Research, 80(32):4484-4496, November, 1975.

Evans, S., "Dielectric Properties of Ice and Snow: A Review," Journal of Glaciology, v. 5, pp. 773, 1965.

Fowler, W. B., "Thermal Conductivity-Basis of a Potential Method for Determining in-situ Snow Density," Proc of 42nd Western Snow Conference, Anchorage, Alaska, 1974.

Frisch, U., "Wave Propagation in Random Media," Probabilistic Methods in Applied Math, vol. 1, ed. by A. T. Bharucha-Reid, Academic Press, 1968.

Fritz, S., "Satellite Pictures of the Snow-Covered Alps During April, 1960," Archiv fur Meteorologie, Geophysik und Bioklimatologie, Ser. A., Bd. 13, Ht. 2, pp. 186-198.

Fung, A. K. and H. S. Fung, "Application of First-Order Renormalization Method to Scattering from a Vegeation-Like Half-Space, IEEE Trans. Geoscience Electronics, vol. 15, no. 4, pp. 189-195, October, 1977.

Fung, A. K., "Scattering from a Vegetation Layer," IEEE Geoscience Electronics, vol. GE-17, no. 1, January, 1979.

Fung, A. K., and F. T. Ulaby, "A Scatter Model for Leafy Vegetation," IEEE Trans. Geoscience Electronics, vol. GE-16, no. 4, October, 1978.

Gloersen, P. and V. V. Salomonson, "Satellites--New Global Observing Techniques for Ice and Snow," Journal of Glaciology, 15(73):373-389, 1975.

Gough, S. R., "Comment on the Microwave 'Dielectric Constant' of Ice," J. Appl. Phys., 43(10):4251, October, 1972.

Grant, L. O. and J. O. Rhea, "Elevation and Meterological Controls on the Density of New Snow," Proc. of Adv. Concepts and Techniques in the Study of Snow and Ice Resources, National Academy of Sciences, Washington, D.C., 1974.

Grasty, R. L., H. S. Loijens and H. L. Faguson, "An Experimental Gamma-Ray Spectrometer Snow Survey Over Southern Ontario," Advanced Concepts and Techniques in the Study of Snow and Ice Resources, National Academy of Sciences, Washington, D.C., 1974.

Hall, D. K., A. Chang, J. L. Foster, A. Rango and T. Schmugge, "Passive Microwave Studies of Snowpack Properties," NASA Technical Memorandum 78089, Goddard Space Flight Center, Greenbelt, Maryland, April, 1978.

Hayes, D., V. H. W. Lammers, R. Marr and J. McNally, "Millimeter Wave Backscatter from Snow," Proc. of the Workshop on Radar Backscatter from Terrain, RSL Technical Report 374-2, University of Kansas Center for Research, Inc., Lawrence, Kansas, January, 1979.

Hoekstra, P. and D. Spanogle, "Radar Cross Section Measurements of Snow and Ice," Cold Regions Research and Engineering Laboratory, Technical Report 235, Hanover, New Hampshire, November, 1972.

Hoekstra, P. and A. Delaney, "Dielectric Properties of Soils at UHF and Microwave Frequencies," Journal of Geophysical Research, 79(11):1699-1708, April, 1974.

Hofer, R. and C. Matzler, "Investigations on Snow Parameters by Radiometry in the 3-60 mm Wavelength Region, submitted to Journal of Geophysical Research, January, 1979.

Hobbs, P. V., Ice Physics, Clarendon Press, Oxford, Great Britain, 1974.

Hydrology, Summer Study, Panel 3, "Useful Applications of Earth-Oriented Satellites: Hydrology," National Academy of Sciences, Washington, D.C., 1969.

Ishimaru, A., "Correlation Functions of a Wave in a Random Distribution of Stationary and Moving Scatterers," Radio Science, 10:45-52, 1975.

Janza, F. J., R. K. Moore and B. D. Warner, "Radar Cross-Sections of Terrain Near Vertical Incidence at 4.5 Mc, 3800 Mc and Extension of Analysis to X-Band," University of New Mexico Engineering Experiment Station Technical Report EE-21, March, 1959.

Karal, F. C. Jr., and J. B. Keller, "Elastic, Electromagnetic and Other Waves in a Random Medium," J. Math Phys., vol. 5, no. 4, pp. 537-547, April, 1964.

Klein, L. A. and C. T. Swift, "An Improved Model for the Dielectric Constant of Sea Water at Microwave Frequencies," URSI, Boulder, Colorado, 1975.

Kunzi, K. F., A. D. Fisher, D. H. Staelin and J. W. Waters, "Snow and Ice Surfaces Measured by the Nimbus-5 Microwave Spectrometer," Journal of Geophysical Research, (81):4965-4980, 1976.

Kupiec, I., L. B. Felsen, and S. Rosenbaum, "Reflection and Transmission by a Random Medium," Radio Science, vol. 4, no. 11, pp. 1067-1077, November, 1969.

LaChapelle, E. R., Field Guide to Snow Crystals, University of Washington Press, Seattle, Washington, 1969.

Lamb, J., "Measurements of the Dielectric Properties of Ice," Transactions of the Faraday Society, 42A:238-244, 1946.

Lamb, J. and A. Turney, "The Dielectric Properties of Ice at 1.25 cm Wavelength," Proc. Phys. Soc., B 62, pp. 272, London, England, 1949.

Leaf, C. F., "Free Water Content of Snowpack in Subalpine Areas," Proc. of the Western Snow Conference, 1966.

Limpert, Fred A., "Operational Applications of Satellite Snow Cover Observations--Northwest United States," Oper. Applic. of Satellite Snow Cover Obsv., Ed. A. Rango, NASA Goddard Space Flight Center, Washington, D.C., 1975.

Lin, J. C. and A. Ishimaru, "Multiple Scattering of Waves by a Uniform Random Distribution of Discrete Isotropic Scatterers, J. Acoust. Soc. Amer., 56:1695-1700, 1974.

Linlor, W. I., "Remote Sensing and Snowpack Management," Journal American Water Works Assn., 66(9), September, 1974.

Linlor, W. I., J. L. Smith, M. F. Meier, F. C. Clapp and D. Angelakos, "Measurement of Snowpack Wetness," Proc. 43rd Ann. Western Snow Conference, San Diego, California, April, 1975a.

Linlor, W. I., F. D. Clapp, M. E. Meier and J. L. Smith, "Snow Wetness Measurements for Melt Forecasting," NASA Special Publications SP391, in Operational Applications of Satellite Snowcover Observations, ed. by A. Rango, Proc. Workshop, Waystation, South Lake Tahoe, California, August 18-20, 1975b.

Macrakis, M. S., "Scattering from Large Fluctuations," J. Geophys. Res., vol. 70, no. 19, pp. 4987-4989, October, 1965.

Magono, C. and C. Lee, "Meterological Classification of Natural Snow Crystals," J. Fac. Sci., Hokkaido, Univ., Ser. VII, 2, 321-35, 1966.

Malkevich, M. S., Yu. V. Samsonov and L. I. Koprovs, "Vodyanoy par v stratosfere (Water Vapor in the Stratosphere)," Ukr. Fiz. Ah., 80(1), 1963.

Manual of Remote Sensing, R. G. Reeves, ed., American Soceity of Photogrammetry, Falls Church, Virginia, 1975.

Matzler, C., R. Hofer, D. Wyssen and E. Schanda, "On the Penetration of Microwaves in Snow and Soil," Proc. of 13th International Symp. on Remote Sensing of the Environment, Ann Arbor, Michigan, April, 1979.

Meier, M. F. and A. T. Edgerton, "Microwave Emission from Snow: A Progress Report, " Proc. 7th Intl. Symp. on Remote Sensing of Environment, Vol. II, Ann Arbor, Michigan, 1971.

Meier, M. F., "Measurement of Snow Cover Using Passive Microwave Radiation," Intl. Symp. on Role of Snow and Ice in Hydrology, UNESCO-WMO, Banff, vol. 1, pp. 739-750, September, 1972.

Meier, M. F., "Application of Remote Sensing Techniques to the Study of Seasonal Snow Cover," Journal of Glaciology, 15(73), 1975.

NASA, "Survey on Space Applications," NASA SP-142, Office of Tech. Utilization, Washington, D.C., April, 1967.

Peck, E. L., V. C. Bissel, E. B. Jones and D. L. Burge, "Evaluation of Snow Water Equivalent by Airborne Measurement of Passive Terrestial Gamma Radiation," Water Resources Research, 7(5):1151-1159, 1971.

Perry, J. W. and A. W. Straiton, "Dielectric Constant of Ice at 35.3 and 94.5 GHz," Journal of Applied Physics, 43(2), February, 1972.

Poe, G., "Remote Sensing of the Near-Surface Moisture Profile of Specular Soils with Multifrequency Microwave Radiometry," in Remote Sensing of Earth Resources and the Environemnt, ed. by Y. H. Katz, Proc. of the Society of Photo-optical Instrumentation Engineers, Palo Alsto, California, November, 1971.

Poulin, A. O., "Hydrologic Characteristics of Snow-Covered Terrain from Thermal Infrared Imagery," Proc. of Adv. Concepts and Techniques in the Study of Snow and Ice Resources, Washington, D.C., 1974.

Ramo, S., J. R. Whinnery and T. van Dvzer, Fields and Waves in Communication Electronics, Wiley and Sons, New York, 1965.

Rango, A. and V. V. Salomonson, "Employment of Satellite Snow Cover Observations for Improving Seasonal Runoff Estimates," Operational Applications of Satellite Snow Cover Observations, ed. A. Rango, NASA Goddard Space Flight Center, Washington, D.C., 1975.

Rango, A., "Operational Applications of Satellite Snowcover Observations Project," Proc. 10th Intl. Symp. on Remote Sensing of Environment, Vol. II, Ann Arbor, Michigan, 1975.

Rango, A., A. T. C. Chang and J. L. Foster, "The Utilization of Spaceborne Microwave Radiometers for Monitoring Snowpack Properties," Journal of Nordic Hydrology, February, 1979.

Rooney, J., "The Economic and Social Implications of Snow and Ice," in Water, Earth and Man, pp. 389-401, ed. by R. J. Chorley, Methuen and Company, Ltd., London, 1969.

Rosenbaum, S., "On the Coherent Wave Motion in Bounded, Randomly Fluctuating Regions," Radio Science, vol. 4, no. 8, pp. 709-719, August, 1967.

Rosenbaum, S., "On Energy Conserving Formulations in a Randomly Fluctuating Medium," in Proc. Symp. on Turbulence of Fluid and Plasmas, Polytechnic Institute of Brooklyn, New York, pp. 163-185, 1968.

Rosenbaum, S., "The Mean Green's Function: A Nonlinear Approximation," Radio Science, vol. 6, no. 3, pp. 379-386, March, 1971.

Royer, G. M., "The Dielectric Properties of Ice, Snow, and Water at Microwave Frequencies and the Measurement of the Thickness of Ice and Snow Layers with Radar," Communications Research Centre, Technical Report No. 1242, Ottawa, Canada, 1973.

Sackinger, W. M. and R. C. Byrd, "Backscatter of Millimeter Waves from Snow, Ice and Sea Ice," Final Technical Report, No. 7207, Institute of Arctic Environmental Engineering, Fairbanks, Alaska, 1972.

Sancer, M. I. and A. D. Varvatsis, "An Investigation of the Renormalization and Rytov Methods as Applied to Propagation in a Turbulent Medium," Northrop Corporate Laboratories, NCL 69-28R, Hawthorne, California, April, 1969.

Schanda, E. and R. Hofer, "Microwave Multispectral Investigations of Snow," Proc. of the Eleventh International Symposium on Remote Sensing of Environment, Univ. Michigan, Ann Arbor, 1977.

Schmugge, T., T. T. Wilheit, P. Gloersen, M. F. Meier, D. Frank and I. Dirmhirn, "Microwave Signatures of Snow and Fresh Water Ice," Advanced Concepts and Techniques in the Study of Snow and Ice Resources, pp. 551-562, National Academy of Sciences, Washington, D.C., 1974.

Schmugge, T., P. Gloersen, T. Wilheit and F. Geiger, "Remote Sensing of Soil Moisture with Microwave Radiometers," Journal of Geophysical Research, 79(2):317-323, 1974b.

Schuster, A., Astrophys. J., 21(1), 1905.

Sharp, J. M., "A Cost-effectiveness Comparison of Existing and LANDSAT-aided Snow Water Content Estimation Systems," Proc. of 10th Intl. Symp. on Remote Sensing of Environment, Ann Arbor, Michigan, 1975.

Shiue, J. C., A. T. C. Chang, H. Boyne and D. Ellerbruch, "Remote Sensing of Snowpack with Microwave Radiometers for Hydrologic Applications," Proc. of the 12th International Symposium on Remote Sensing of Environment, ERIM, Ann Arbor, Michigan, 1978.

Sperry Microwave Electronics Co., "Technical Manual-94 GHz Radiometer," prepared for Air Force Avionics Laboratory, Air Force Systems Command U.S.A.F., Wright-Patterson AFB, 1977.

Stiles, W. H., F. T. Ulaby, B. C. Hanson and L. F. Dellwig, "Snow Backscatter in the 1-8 GHz Region," RSL Technical Report 177-61, University of Kansas Center for Research, Inc., Lawrence, Kansas, 1976.

Stiles, W. H., B. C. Hanson and F. T. Ulaby, "Microwave Remote Sensing of Snow: Experiment Description and Preliminary Results," RSL Technical Report 340-1, University of Kansas Center for Research, Inc., Lawrence, Kansas, June, 1977.

Stiles, W. H. and F. T. Ulaby, "The Active and Passive Microwave Response to Snow Parameters, Part I: Wetness," RSL Technical Report 340-2, University of Kansas Center for Research, Inc., Lawrence, Kansas, October, 1978.

Stiles, W. H., D. Brunfeldt and F. T. Ulaby, "Performance Analysis of the MAS (Microwave Active Spectrometer) Systems: Calibration, Precision and Accuracy," RSL Technical Report 360-4, University of Kansas Center for Research, Inc., Lawrence, Kansas, April, 1979.

Stogryn, A., "The Brightness Temperature of a Vertically Structured Medium," Radio Science, 5(12):1397-1406, December, 1970.

Stogryn, A., "Equations for Calculating the Dielectric Constant of Saline Water," IEEE Trans. on Microwave Theory and Techniques, MTT-16(8):733-736, August, 1971.

Stogryn, A., "Electromagnetic Scattering by Random Dielectric Constant Fluctuations in a Bounded Medium," Radio Science, vol. 9, no. 5, pp. 509-518, May, 1974.

Suzuki, M. and T. Hasegawa, "Studies on the Reflection of Microwaves on a Snow-covered Terrain," in Microwave Propagation in Snowy Districts ed. by Y. Asami, Research Institute of Applied Electricity, Hokkaido University, Sapporo, Japan, 1958.

Sweeney, B. D. and S. C. Colbeck, "Measurements of the Dielectric Properties of Wet Snow using a Microwave Technique," Research Report 325, U.S. Army Cold Regions Research and Engineering Laboratory, Hanover, New Hampshire, October, 1974.

Tan, H. S. and A. K. Fung, "The Mean Green's Dyadic for a Half-Space Random Medium--A Non-linear Approximation," IEEE International Symposium, Washington, D. C., May, 1978.

Tatarskii, V. I. and M. E. Gertsenshtein, "Propagation of Waves in a Medium with Strong Fluctuations of the Refractive Index," Soviet Physics JETP, 17(2):458-469, August, 1963.

Tatarskii, V. I., "Propagation of Electromagnetic Waves in a Medium with Strong Dielectric-Constant Fluctuations," Soviet Physics JETP, 19(4):946-953, October, 1964.

Tiuri, Martti, Martti Hallikainen, Pekka Jakkula, and Henrik Schultz, "Microwave Signatures of Snow Measured in Finalnd," Helsinki University of Technology, Radio Laboratory, Report S 109, 1978.

Tolbert, C. W., C. C. Krause and A. W. Straiton, "Attenuation of the Earth's Atmosphere between the Frequencies of 100 and 140 Gigacycles per Second," Journal of Geophysical Research, 69(7), April 1, 1964.

Tsang, L. and J. A. Kong, "The Brightness Temperature of a Half-Space Random Medium with Non-Uniform Temperature Profile," Radio Science, 10(12):1025-1033, December, 1975.

Tsang, L. and J. A. Kong, "Microwave Remote Sensing of a Two-Layer Random Medium, IEEE Trans. Ant. and Prop., 24(3):283-287, May, 1976a.

Tsang, L. and J. A. Kong, "Thermal Microwave Emission from Half-Space Random Media," Radio Science, vol. 11, no. 7, pp. 599-609, July, 1976b.

Tsang, L. and J. A. Kong, "Thermal Microwave Emission from a Random Imhomogeneous Layer over a Homogeneous Medium Using the Method of Invariant Imbedding," Radio Science, vol. 12, no. 2, pp. 185-194, March, 1977a.

Tsang, L. and J. A. Kong, "Theory for Thermal Microwave Emission from a Bounded Medium Containing Spherical Scatterers," J. Appl. Phys., 48(8):3593-3599, August, 1977b.

Tsang, L. and J. A. Kong, "Wave Theory for Microwave Remote Sensing of a Half-Space Random Medium with Three-Dimensional Variations," Radio Science, (to be published), 1978a.

Tsang, L. and J. A. Kong, "Radiative Transfer Theory for Active Remote Sensing of Half-Space Random Media," Radio Science (to be published), 1978b.

Twersky, V., "On Multiple Scattering of Waves," J. Research Nat. Bur. Standards, vol. 64D, pp. 715-730, 1960.

Twersky, V., "On Scattering of Waves by Random Distribution," J. Math Phys., vol. 3, no. 4, pp. 700-715, July-August, 1962a

Twersky, V., "On a General Class of Scattering Problems," J. Math Phys., vol. 3, no. 4, pp. 716-723, July-August, 1962b.

Twersky, V., "On Scattering of Waves by Random Distributions," J. Math Phys., vol. 3, no. 4, pp. 724-734, July-August, 1962c.

Twersky, V., "Multiple Scattering of Electromagnetic Waves by Arbitrary Configurations," J. Math Phys., vol. 8, no. 3, pp. 589-610, March, 1967a.

Twersky, V., "Theory and Microwave Measurements of Higher Statistical Moments of Randomly Scattered Fields," in Electromagnetic Scattering, ed. by R. L. Rowell and R. S. Stein, Gordon and Breach Science Publishers, New York, pp. 579-695, 1967b.

Twersky, V., "Coherent Electromagnetic Waves in Pair-Correlated Random Distributions of Aligned Scatterers, J. Math Phys., 19(1), January, 1978.

Ulaby, F. T., W. H. Stiles, L. F. Dellwig and B. C. Hanson, "Experiments on the Radar Backscatter of Snow," IEEE Trans. on Geoscience Electronics, GE-15(4):185-189, October, 1977.

Ulaby, F. T. and C. Dobson, "Analysis of the Active Microwave Response to Soil Moisture, Part I: Bare Ground," RSL Technical Report 264-18, University of Kansas Center for Research, Inc., Lawrence, Kansas, November, 1977.

Ulaby, F. T. and W. H. Stiles, "Backscatter and Emissivity of Snow," Proceedings Microwave Remote Sensing Symposium, Houston, Texas, December, 1977.

Ulaby, F. T., A. K. Fung and W. H. Stiles, "Backscatter and Emission of Snow: Literature Review and Recommendations for Future Investigations," RSL Technical Report 369-1, University of Kansas Center for Research, Inc., Lawrence, Kansas, June, 1978.

Ulaby, F. T. and W. H. Stiles, "The Active and Passive Microwave Response to Snow Parameters, Part II: Water Equivalent of Dry Snow," RSL Technical Report 340-2, University of Kansas Center for Research, Inc., Lawrence, Kansas, October, 1978.

Ulaby, F. T., P. P. Batlivala and M. C. Dobson, "Microwave Backscatter Dependence on Surface Roughness, Soil Moisture and Soil Texture: Part 1: Bare Soil," IEEE Trans. on Geoscience Electronics, GE-15(4):286-296, October, 1978b.

Ulaby, F. T. and W. H. Stiles, "The Active and Passive Microwave Response to Snow Parameters, Part II: Water Equivalent of Dry Snow," RSL Technical Report 340-2, University of Kansas Center for Research, Inc., Lawrence, Kansas, October, 1978.

Ulaby, F. T., W. H. Stiles, D. R. Brunfeldt and M. E. Lubben, "MAS 8-18/35 GHz Scatterometer," RSL Technical Report 360-5, University of Kansas Center for Research, Inc., Lawrence, Kansas, February, 1979.

U.S. Department of the Interior, "Project Skywater," Bureau of Reclamation, Atmospheric Water Resources Program, 16 pp., U.S. Government Printing Office, Washington, D.C., 1970.

U.S. Department of the Interior, "Snow Mapping and Runoff Forecasting: Examination of ERTS-1 Capabilities and Potential Benefits from an Operational ERS System," Interim Report, Contract No. 14-08-13519, Office of Economic Analysis, Washington, D.C., 1974.

Valley, S. L., editor, "Handbook of Geophysics and Space Environments," AFCRL, 1965.

Varvatsis, A. D. and M. I. Sancer, "On the Renormalization Method in Random Wave Propagation," Radio Science, 6(1):87-97, Janaury, 1971.

Venier, G. O. and F. R. Cross, "An Experimental Look at the Use of Radar to Measure Snow and Ice Depths," Communications Research Centre Technical Note No. 646, Ottawa, Canada, 1972.

Vickers, R. S. and G. C. Rose, "High Resolution Measurements of Snowpack Stratigraphy Using a Short Pulse Radar," Proc. 8th International Symposium on Remote Sensing of Environment, Ann Arbor, Michigan, 1972.

Vickers, R. S., J. Heighway and R. Gedney, "Airborne Profiling of Ice Thickness Using a Short Pulse Radar," NASA Technical Memorandum TMX-78481, December, 1973.

Von Hippel, A., Dielectric Materials and Applications, MIT Press, Cambridge, Massachusetts, 1954.

Waite, W. P. and H. C. MacDonald, "Snowfield Mapping with K-Band Radar," Journal of Remote Sensing of Environment, 1:143-150, 1970.

Weiner, O., "Zur Theorie der Refraktion Skonstanter, Berichte Gesellschaft der Wissen Schaften zu Leipzig, Mathematisch-physikalische Klasse, Bd. 62, Ht. 5, pp. 256-268, 1910.

Yosida, Zyungo, "Free Water Content of Wet Snow," Proceedings of the International Conference on Low Temperature Science, Sapporo, Japan, 1968.

Zwally, H. J., "Microwave Emissivity and Accumulation Rate of Polar Firm," J. Glaciology, 18(79):195-215, 1977.

1. Report No.	2. Government Accession No.	3. Recipient's Catalog No.
NASA CR-3263		

4. Title and Subtitle	5. Report Date
MICROWAVE REMOTE SENSING OF SNOWPACKS	June 1980
	6. Performing Organization Code

7. Author(s)	8. Performing Organization Report No.
William H. Stiles and Fawwaz T. Ulaby	RSL Tech. Rep. 340-3
	10. Work Unit No.

9. Performing Organization Name and Address	11. Contract or Grant No.
University of Kansas Center for Research, Inc. Remote Sensing Laboratory 2291 Irving Hill Drive—Campus West Lawrence, Kansas 66045	NAS5-23777
	13. Type of Report and Period Covered Contractor Report

12. Sponsoring Agency Name and Address	14. Sponsoring Agency Code
National Aeronautics and Space Administration Washington, D.C. 20546	

15. Supplementary Notes

A companion report, NASA CR-3263, includes the basic data collected during this experiment. Both ground-truth and microwave data are listed.

Goddard Technical Monitor: Albert Rango Final Report

16. Abstract

The possibility of simultaneous wide areal coverage and profile information makes the microwave band an attractive spectral region for remote sensing. In this study, the interaction mechanisms responsible for the microwave backscattering and emission behavior of snow were investigated, and models were developed relating the backscattering coefficient σ^o and apparent temperature T_{ap} to the physical parameters of the snowpack. An experiment was designed and conducted to obtain σ^o and T_{ap} data at several combinations of the sensor parameters (angle of incidence, frequency and polarization coefficient), along with snow ground-truth measurements.

The microwave responses to snow wetness, snow water equivalent, snow surface roughness, and to diurnal variations were investigated in detail. Snow wetness was shown to have an increasing effect with increasing frequency and angle of incidence for both active and passive cases. Increasing snow wetness was observed to decrease the magnitude of σ^o and increase T_{ap}. Snow water equivalent was also observed to exhibit a significant influence on σ^o and T_{ap}. Snow surface configuration (roughness) was observed to be significant only for wet snow surface conditions. Diurnal variations were as large as 15 dB for σ^o at 35 GHz and 120 K for T_{ap} at 37 GHz.

Simple models for σ^o and T_{ap} of a snowpack scene were developed in terms of the most significant ground-truth parameters. The coefficients for these models were then evaluated; the fits to the σ^o and T_{ap} measurements were generally good.

Finally, areas of needed additional observations were outlined and experiments were specified to further the understanding of the microwave-snowpack interaction mechanisms.

17. Key Words (Suggested by Author(s))	18. Distribution Statement
Microwave backscatter Microwave radiometry Radar remote sensing Microwave emission, snow Snow wetness, snow water equivalent	Unclassified - Unlimited Subject Category 43

19. Security Classif. (of this report)	20. Security Classif. (of this page)	21. No. of Pages	22. Price*
Unclassified	Unclassified	404	$13.25

* For sale by the National Technical Information Service, Springfield, Virginia 22161

NASA-Langley, 1980